Iron-Alkyne Based Organometallic Molecules as Functional Building Blocks for Molecular Junctions

DISSERTATION

zur

Erlangung der naturwissenschaftlichen Doktorwürde
(**Dr. sc. nat**.)

vorgelegt der

Mathematisch-naturwissenschaftlichen Fakultät

der

Universität Zürich

von

FRANZISKA LISSEL

aus

Deutschland

Promotionskomitee

Prof. Dr. Heinz Berke (Vorsitz und Leitung der Dissertation)
Prof. Dr. Roger Alberto
Prof. Dr. Jürg Hutter
Dr. Emmanuel Lörtscher

Zürich 2014

For my goddaughter,

Luise Annelie Gauthey

TABLE OF CONTENTS

LIST OF ABBREVIATIONS

Cp	Cyclopentadienyl
CT	Charge transfer
CV	Cyclic voltammetry
DCM	Dichloromethane
dmpe	1,2-Bis(dimethylphosphino)ethane
depe	1,2-Bis(diethylphosphino)ethane
DFT	Density functional theory
e^-	Electron
E	Energy
EPR	Electron paramagnetic resonance
Et	Ethyl
ET	Electron transfer
eV	electron volt
G	Gibbs free energy
G_0	Standard Gibbs free energy
h	Planck constant
H_{ab}	Electronic coupling matrix element
HOMO	Highest occupied molecular orbital
Hz	Hertz
IR	Infrared
IVCT	Intervalence charge transfer

k_B	Boltzmann constant
K_C	Comproportionational constant
LUMO	Lowest unoccupied molecular orbital
MCBJ	Mechanically controllable break junction
MV	Mixed valence
Me	Methyl
MO	Molecular Orbital
MS	Mass spectrometry
NIR	Near infrared
nm	Nanometer
NMR	Nuclear magnetic resonance
Nu	Nucleophile
Otf	Triflate
ppm	Parts per million
ψ	Wave function
rt	Room temperature
R^F	Perfluorinated organic rest
s, sec	Second
STM	Scanning tunneling microscopy
SQUID	Superconducting quantum interference device
TBAF	Tetra-n-butyl ammonium fluoride
THF	Tetrahydrofuran
UV	Ultraviolet
υ	Frequency
Vis	Visible

1. INTRODUCTION

1.1 MOLECULAR ELECTRONICS

1.1.1 Molecular Electronics

Molecular-scale electronics seek to assemble appropriate molecular components for exerting specific functions[1,2] in order to design and fabricate electronic circuits and ultimately devices on the molecular level.[1-7] Both electronic transport through and functional operations by molecules depend on chemical structure, thus interfacing physics and chemistry.[8] Richard Feynman's lecture of 1959 entitled "There´s Plenty of Room at the Bottom"[9] is considered a milestone in the exploitation of non-colligative properties at the single-atom level and is marked as a seminal event in the history of nanotechnology, still inspiring new concepts in the field decades later. He considered the possibility of direct manipulation of individual atoms to further the fields of electronics and optics. But replacing single atoms by single molecules would not make a great difference considering the physical principles of a microscopic world and the functional exploitation of such units. Furthermore, molecules are in general more stable than single atoms and carry distinct and device-related properties, such as the option to manipulate structural, electronic or spectroscopic characteristics by e.g. photo- or electrochemical input.[10] Also, the theoretical foundations and experimental techniques to design and build systems with specific properties are established for molecules, while the manipulation of single atoms is still in its infancy.

The evolution of molecular electronics has strongly progressed and gained momentum through interdisciplinary efforts, joining forces of theory, physics and chemistry.[11] From the chemistry side, the main contribution towards single-molecule electronics is to provide a rational design for the synthesis of unique molecular entities suitable of probing structure-function relationships,[12-14] which is a categorical prerequisite to comprehensively understand the processes underlying electronic transport on the single-molecule level. Ultimately this know-how is expected to be the basis for creating tailored functional molecular building blocks for electronic tasks as e.g. conductance switching or charge storing, and to eventually enable the implementation of molecular-scale devices to provide novel functionalities based on intrinsic molecular mechanisms, such as multi-level redox activity or quantum interference.

To build a basic electronic circuit on the molecular scale, two different molecular components are needed:[2,15] (1) π-conjugated molecules, so-called “molecular wires” combining a rigid-rod structural layout with favorable orbital overlaps along the electronic charge pathway to allow efficient resonant transport of electric charge over distances of several nanometres, and (2) an intrinsic functional moiety capable of enabling operations such as rectification, conductance switching, e.g. via quantum interference or charge storing.

1.1.2 Techniques for Single Molecule Conductance Measurements

The experimental techniques to investigate molecular transport are evolving at a fast pace and by now allow the probing of single molecules in so-called molecular junctions, which can be subdivided into three main components:[16] an experimental setup providing atomic-sized electrodes separated by a tunable gap of molecular dimensions (0-3 nm), a functional molecular unit providing a pathway for electrons to travel between the two electrodes under an applied field, and the termini of the molecular unit, the so-called anchoring groups or endgroups. These functional groups establish the mechanical and electronic contact between the functional molecular unit - the molecular “backbone” - and the electrodes by chemical means thereby immobilizing the molecule in the junction and forming a solid-state device. Suitable molecular entities are structurally rigid and consist of molecular orbitals (MOs) that are coupled/overlapping along the electronic pathway to facilitate resonant electron transport. The conductance can be modulated by varying the level of MO coupling, the energetic position of the MOs in respect to the Fermi energy E_F of the electrodes or the injection barrier from the electrodes to the MOs. In that context, the anchoring groups are key to establish a mechanically stable contact and to control the electronic coupling between the molecule and the electrodes.[17] The chemical design defines the type of transport mechanism and its efficiency by tuning the electronic overlap between MOs and orbitals of the metallic electrodes.

A number of different experimental methods were developed to investigate the transport properties of single molecules:[18] scanning tunneling microscopy (STM), conductive probe atomic force microscopy (CP-AFM), scanning tunneling microscopy break junctions (STM-BJs), crossed wires, nanoparticle assemblies, electromigration break junctions (E-BJs), nanopores, and liquid metal junctions employing mercury or gallium−indium eutectic alloys (EGaIn).

Currently, one of the the most sophisticated method of investigating the electron transport properties of a single molecule is the so-called "Mechanically Controllable Break Junction (MCBJ) technique"[19] (Figure 1).

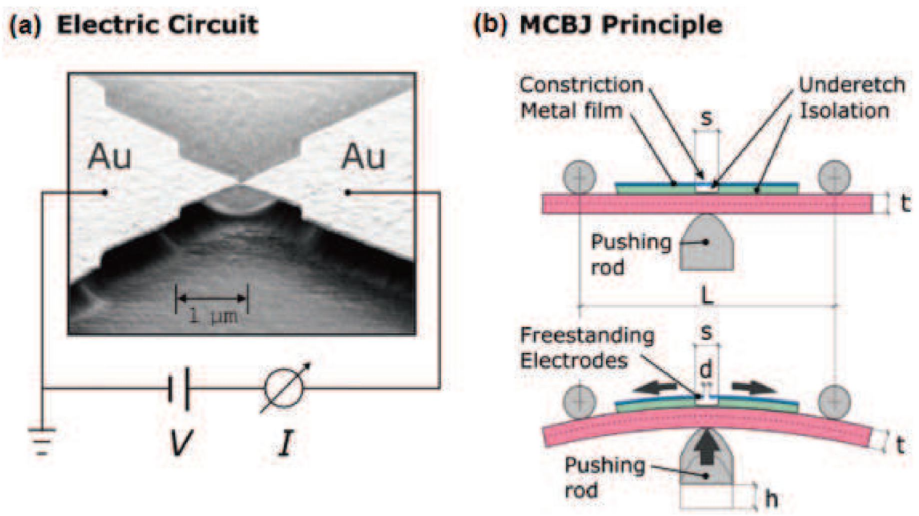

Figure 1. (a) Scanning electron microscopy image of microfabricated MCBJ sample with a schematically drawn electrical circuit; (b) the MCBJ principle.[20]

Here, a prefabricated thin gold strand is placed on a flexible and insulating substrate. Two counter supports are placed firmly on both sides of the strand. Then, controlled by a rotator motor, a rod is positioned directly under the gold strand before pushing upwards against the substrate base. Being hold in place by the counter supports, the elastic substrate bends convex. By this movement, the gold strand is stretched and finally breaks, creating a gap which can be controlled in size by a careful and controlled bending of the flexible substrate. By contacting the outer ends of the broken gold strand electronically, an open electrical circuit on the molecular level is created. This circuit can be closed by molecules of a suitable size carrying terminal substituents with a high affinity to gold.[21] After the junction is formed, measurements at temperatures of 4 – 300 K allow to study the electron transport and the used molecular orbitals in detail.[22]

Figure 2[23] depicts the sequence of such a measurement and the energetic changes induced by the molecule-electrode contact and the subsequent application of a potential gradient across the junction. In a first step, the molecule establishes contact with the metal electrodes (a),

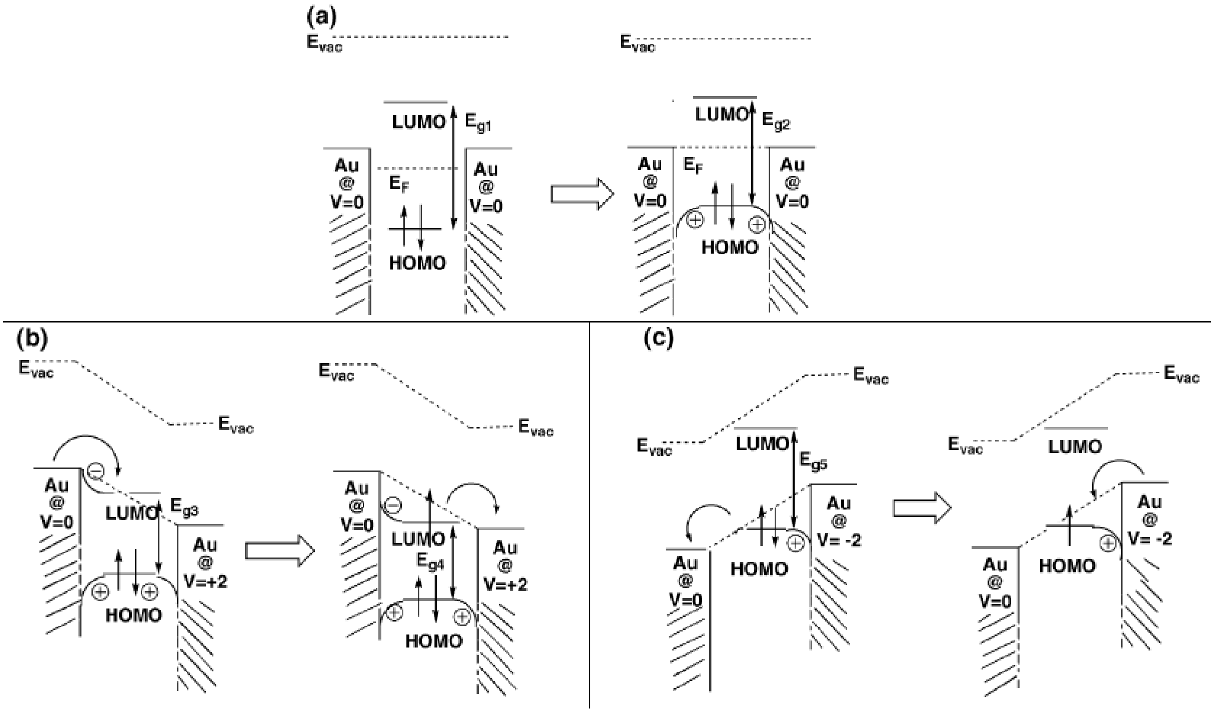

Figure 2. Electronic processes in the molecule-electrode junction. (a) chemisorption of the molecule on the electrodes and broadening of the molecular energy levels; (b) transport through the LUMO; (c) transport through the HOMO.[23,99]

resulting in a significant broadening of the molecular energy levels due to the hybridization with the metal states.[99]

Upon the application of a field gradient, transport through the LUMO (b) or the HOMO (c) is possible. The rounded arrows show the electron transfer that is about to happen.[23]

Two different experimental procedures can be carried out to probe the trapped molecule (Figure 3):[22] Keeping the applied bias constant while stepwise varying the electrode gap distance allows the recording of individual conductance-distance G(d) curves (a). The statistical analyses of sets of individual curves allow the compilation of histograms (counts vs. conductance), where peaks at distinct conductance values may be correlated to the single-molecule conductance. Stepwise stopping allows the measurement of an entire I-V curve at a given electrode distance (b).[22]

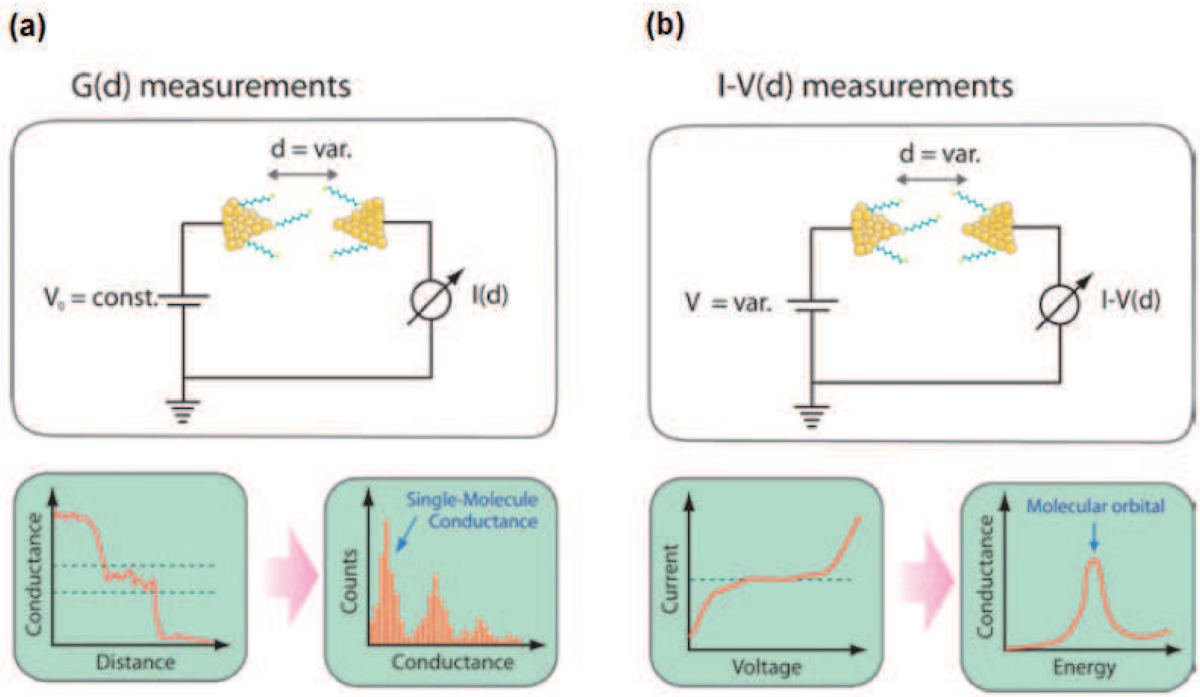

Figure 3. Different experimental procedures to probe a single molecule trapped between electrodes. (a) Varying the gap distance under constant bias allows G(d) measurements and the compilation of statistical histograms; (b) measuring the current at a given bias and constant electrode gap gives individual I-V curves to probe molecular orbitals.[22]

1.1.3 Molecules for Single Molecule Conductance Measurements

At the present stage of development, a search has been started for suitable molecules, starting with the most simple molecular electronic component, the molecular wire. Conjugated organic moieties, especially those consisting of sp hybridized carbon atoms, have been proven to constitute materials that accomplish high electron transfer rates, since they provide well-defined, fully conjugated, rigid-rod structures with strongly delocalized frontier orbitals.[24]

The through space tunneling between two molecular sized electrodes is given by:[25,26]

$$G = G_0 e^{-\beta L} \qquad \text{(Eq. 1)}$$

where G_0 is the contact conductance quantum achieved by a direct atomic Au-Au contact, β the tunneling decay constant and L the length of the charge transport pathway. As can be seen from Equation 1, this type of conductance is temperature independent but decays exponentially with the electrode – electrode length.

When a molecule bridges the electrodes, thus forming a molecular junction, the charge transport can proceed via two charge transport mechanisms:[25,26,99] coherent transport via tunneling or superexchange and incoherent thermally activated hopping. The transport mode depends to a great extent on the alignment of the two frontier molecular orbitals to the Fermi level of the metal electrode.[27,99]

The first dominates the charge transport through short molecules, and the conductance is given by

$$G = A_0 e^{-\beta L} \qquad \text{(Eq. 2)}$$

Here the temperature depending system-specific conductance A_0 takes place of the contact conductance G_0. In this type of transport, an electron crosses the molecular junction in a single step and without appreciable abidance on the molecule.

The incoherent and thermally activated hopping follows an Arrhenius relation given by:

$$G \propto \exp(-E_A/k_BT) \qquad \text{(Eq. 3)}$$

where E_A is the hopping activation energy, T is the temperature in Kelvin, and k_B is the Boltzmann constant. Here, the electron first enters into the molecular orbitals from the source electrode, and then takes a series of discrete steps (hopping) to reach the drain electrode. For this resonant conductance, the molecular resistance depends on each site-to-site hopping barrier and this type of charge transport has a relatively weak length dependence.[27]

For very short molecular junctions (≤ 1 nm), a direct through space electron tunneling according to Equation 1 has to be taken into consideration.[28] This direct electrode - electrode tunneling forms a parallel conductance channel, and its contribution to the overall conductance cannot be easily ascertained.[28]

It has been shown that the charge transport rates of purely organic "conducting" systems decay exponentially with the distance until, at certain length, the hopping based current transport becomes predominant, albeit in a very low conductance regime.[25,29,30] Also, the molecular frontier orbitals are not in an energetic range with the Fermi Level of the electrodes, thus requiring a large bias to be applied over the molecular junction and reducing the transport efficiencies. This is constraining severely the dimensions of the molecular systems and complicates the implementation of intrinsic molecular functionalities.[29-32]

A number of simple organic molecules, among them alkanes,[33,34] phenyl systems,[3,22,34-36] carotenoids,[32,37] and oligothiophenes,[38] have been investigated so far using different single molecule and ensemble methods (Figure 4).

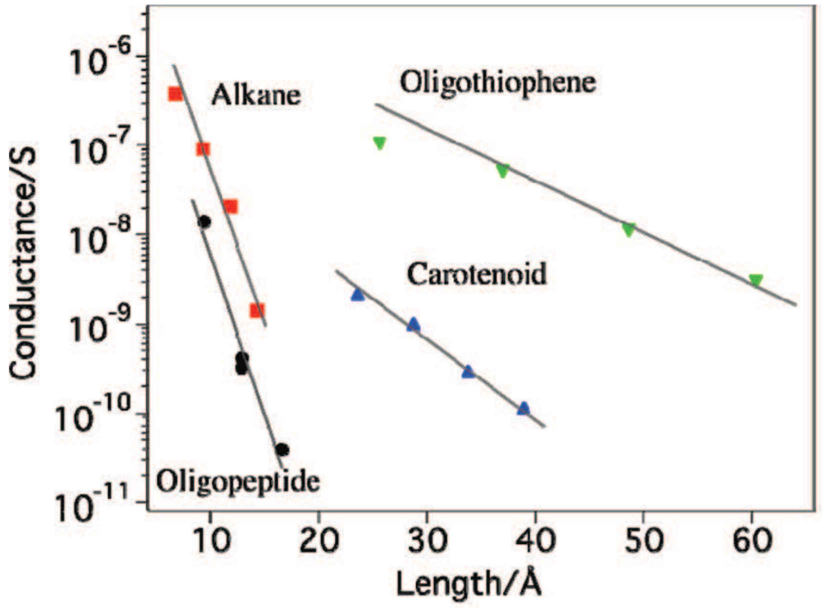

Figure 4. Length dependence of conductance for saturated chains and conjugated molecules. The conductance in each system decreases exponentially with the length but with a different slope (decay constant β) and zero-length conductance A_0. [23,42]

Research interest focused mainly on three areas: (1) the investigation of suitable anchoring groups to reproducibly form stable junctions and achieve a strong molecule-electrode coupling as well as a high charge injection into the molecular backbone,[14,21,39] (2) the influence of molecular and orbital geometry on the charge conductance,[6,22,35,40,41] and (3) the length dependent changes in conductance due to the different shares of elastic tunneling and inelastic hopping.[25,29,30,32]

To achieve resonant transport to occur through MOs at relatively low bias for energy-efficient applications and a high conductance, the position of the energy levels of the MOs needs to be aligned to the Fermi-Level E_F of the molecular electronic Au leads. It was shown that Au electrodes are comparably soft according to the HSAB concept developed by Pearson.[43] The HSAB concept states that the chemical hardness can be correlated to the HOMO-LUMO gap $\Delta E_{(H\text{-}L)}$, and allows the strength of donor - acceptor interactions to be predicted.[44] A small HOMO/LUMO gap is denoted as soft, a large HOMO/LUMO gap as hard, while (I+A)/2 (I = ionization potential, A = electron affinity) at high negative energy means high electronegativity and vice versa. Molecules should therefore be soft and have a relatively low electronegativity (be polarizable), to be adjusted to E_F.

In contrast to purely organic entities, where MO and E_F levels are usually energetically separated by several eV (in the isolated case), the introduction of metal centers into molecular topologies dominated by carbon frameworks allows to tune the energetic position of the electron carrying molecular orbitals (absolute electronegativity according to Pearson[44]). Such organometallic compounds enable a facile tuning of the MO energies because of the strong dependence on the kind of the metal center.[45-49] and are expected to cope energetically with the Fermi level of the macroscopic electronic leads. Furthermore organometallic molecules can be tuned for a certain size in the HOMO/LUMO gap, which again provides adjustment of the orbital interactions of the molecules with the electronic leads helping to accomplish an electronic charge pathway and certain intrinsic functions of the molecules.

These basic facts, together with the rich structural chemistry of ligands and the high tunability of transition metals in an ancillary ligand environment, make organometallic molecules highly promising candidates for applications in molecular electronics. Nonetheless, investigations into organometallic entities are restrained by the lack of suitable series of molecules including their endgroups, which allow to probe the interdependencies of structure and electronic properties at the molecular level.

Up to date, only a few organometallic structures were probed for their molecular charge transport properties. Stepwise assembled coordinatively bounded terpyridine/M^{2+} (M = Fe, Co) frameworks[50,51], ferrocene/oligo(p-phenyleneethynylene)s (OPEs) architectures[27] and a series of mono-, di- and trinuclear Ru(II) σ-arylacetylide complexes[52-54] were investigated as self-assembled monolayers (SAMs). In this method, the current is measured in bulk and the resulting current density J (A/cm^2) gives the conductance of a high number of molecules.

The so-called "relay approach", that is the introduction of redox-active metal centers into the rigid-rod molecular architectures, was shown to enhance the overall conductance.[50,51] Figure 5 depicts the stepwise build-up of rigid-rod terpyridine/M^{2+} (M = Fe, Co) based ensembles on an Au surface.

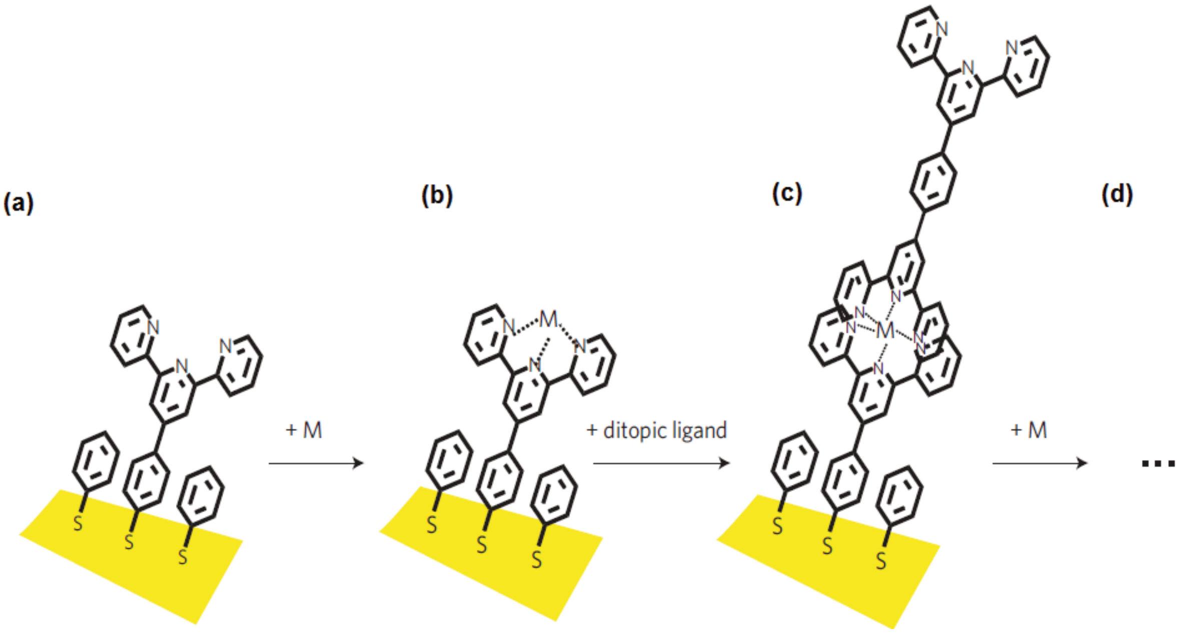

Figure 5. The relay approach: building up rigid-rod terpyridine/M^{2+} based ensembles on an Au surface. (a) Assembly of the anchor on the gold surface; (b) coordination of M^{2+} to the ligand; (c) coordination of the terpyridine ligand; (d) iterative repetitions of (b) and (c).[50]

The found high conductance rates were attributed to the promotion of a hopping based charge transport by providing defined donor−acceptor sites. The resulting low distance dependence (Figure 6) reinforced the interest in organometallic molecular ensembles.

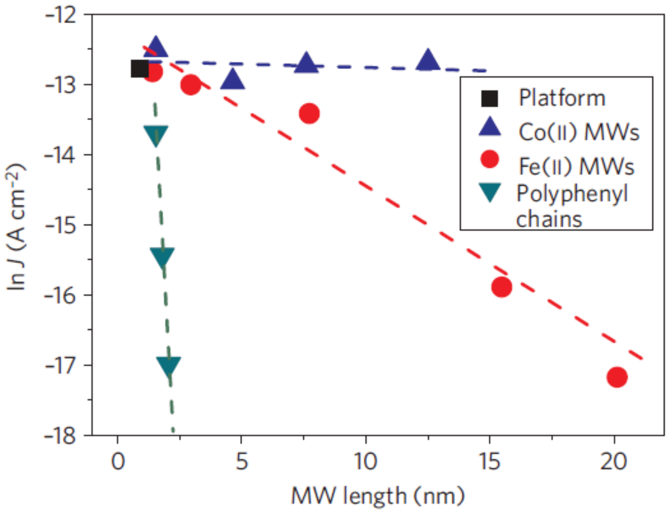

Figure 6. The relay approach: ln J (J = current density A/cm^2) versus length of the Fe(II)- and Co(II)-based SAMs.[50]

Likewise, the insertion of ferrocene units into oligo(p-phenyleneethynylene)s (OPEs) based SAMs lead to higher rates of resonant transport compared to simple OPEs of the same length, and furthermore showed that the molecular conductance of a long molecule in the hopping regime can exceed the molecular conductance of a short one in the tunneling regime at room temperature.[27] This observation was attributed to the better alignment of the MOs, in this case the LUMO, to the Fermi level of the electrodes.[27]

A series of mono-, di- and trinuclear Ru (II) σ-arylacetylide complexes (Figure 7) were the first example of organometallic molecules with an all-covalent bonded charge transport pathway to be examined. [52-55]

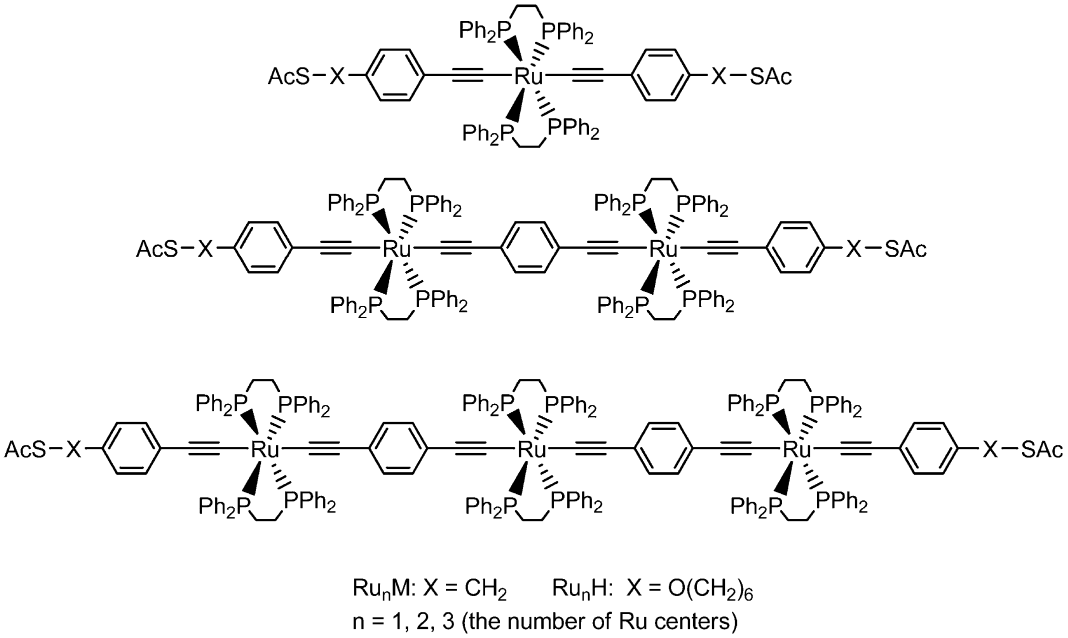

Figure 7. A series of mono-, di- and trinuclear Ru (II) σ-arylacetylide complexes examined as SAMs.[52-54] The thioate group cleaves off upon contact with the electrodes, thereby forming a S-Au bond.

Two structural factors were being varied in the study:[54] the first being the number of the Ru(dppe) (dppe = 1,2-bis(diphenylphospino)ethane); the second the anchorgroup, which allowed a more direct electron injection for the -CH_2SAc termination, while the -$O(CH_2)_6SAc$ group decoupled the redox-active functional core from the electrodes. The length dependent study exhibited a very weak length dependence of the wire resistance, indicative of a high degree of electronic coupling between the redox centers. The electronic decoupling by insertion of the -$O(CH_2)_6SAc$ functional groups promoted hopping based transport, while the non-decoupled -CH_2SAc terminated molecules were found to transport charge by direct tunneling.[54] It has to be noted however, that the introduction of an insulating -$O(CH_2)_6$-building block also significantly increases the molecular length, thereby disfavoring direct tunneling. Measurements of a mononuclear Ru(dppe)($C_2PhC_2SiMe_3$) complex showed higher conductance compared to an OPE type framework, which was attributed to the better alignment of the molecular HOMO with the Fermi levels of the gold contacts.[56]

Conductance measurements of organometallic compounds on the single molecule level are limited to a few examples up so far. The insertion of ferrocene into an OPE framework (Figure 8) gave promising results in single-molecule conductance measurements, with a resonant transport based single-molecule conductance exceeding 70% of the conductance quantum G_0.[57] This unprecedented level of conductance, which is significantly higher than the tunneling based conductance found for a similar-in-length, all-organic conjugated phenylethynyl oligomer molecular framework, was attributed to the low-lying molecular resonance and extended orbital network.[57]

The design concept illustrated that the introduction of transition metal centers into organic wires allows to shift orbital alignments and energies to achieve resonant hopping transport even for comparably short structures.

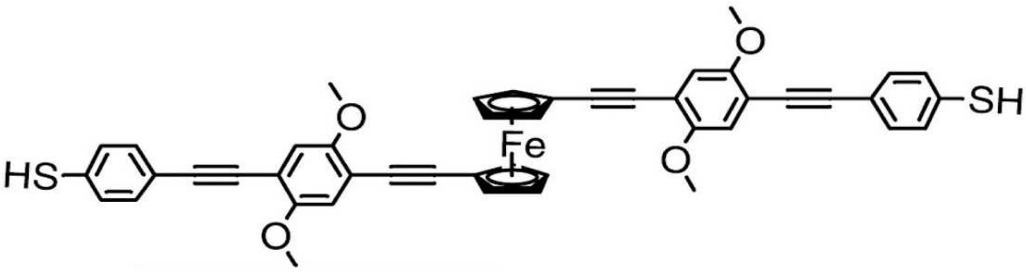

Figure 8. Molecular structure of an OPE framework functionalized with a ferrocene unit.[57]

The conductance profiles of a mononuclear Ru(II) terpyridine complex, termed "cardan-joint" because of the molecular geometry, were investigated at different temperatures from 300 K - 5 K and the results compared with detailed DFT studies.[20] Charge transport most likely occurs through the LUMO, which is mostly located on the organic ligand. In a relaxed or stretched molecular orientation, the octahedral symmetry ensures that the t_{2g} orbitals direct the current through a narrow region close to the Ru(II) core. Upon bending these states are again remixed, causing the wavefunction overlap to increase again. As the bending does not require a high energy, the room temperature measurements can be interpreted as an incoherent average over many microscopic junction configurations. At low temperatures, however, the junction is frozen, and captures the molecule in a certain molecular geometry, causing distinct features to appear, which is nonetheless not known.[20]

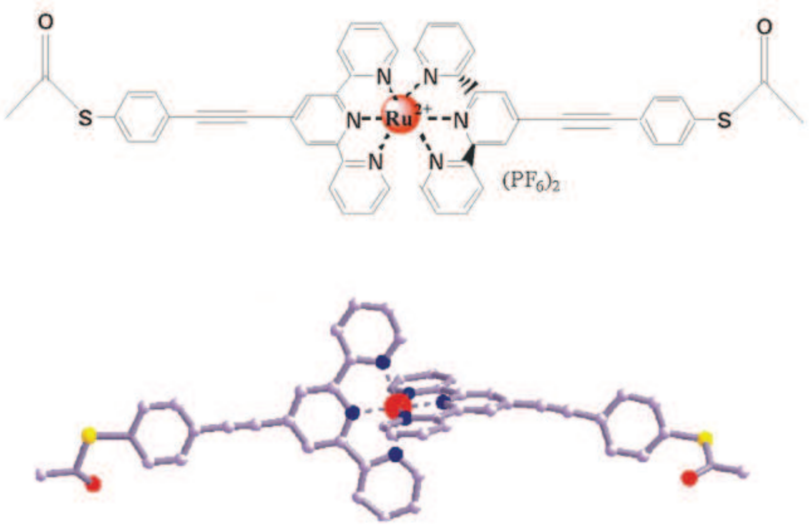

Figure 9. Chemical (top) and molecular (bottom) structure of a mononuclear Ru(II) terpyridine complex investigated with MCBJ.[20] Counter ions are omitted for the molecular plot (bottom).

Three dinuclear Ru(II) complexes (Figure 10) were investigated using the MCBJ technique.[13] Whereas the redox active metal centers are covalently connected by a C_4 bridging ligand, the anchorgroups are not covalently attached to the Ru(II) cores, but instead bind to the chelating ancillary terpyridine ligands. For all three complexes, the attachment to the molecular electrode is established via an Au-S bond, thus shortening the charge transport pathway in the sequence **1** > **2** > **3**.[13]

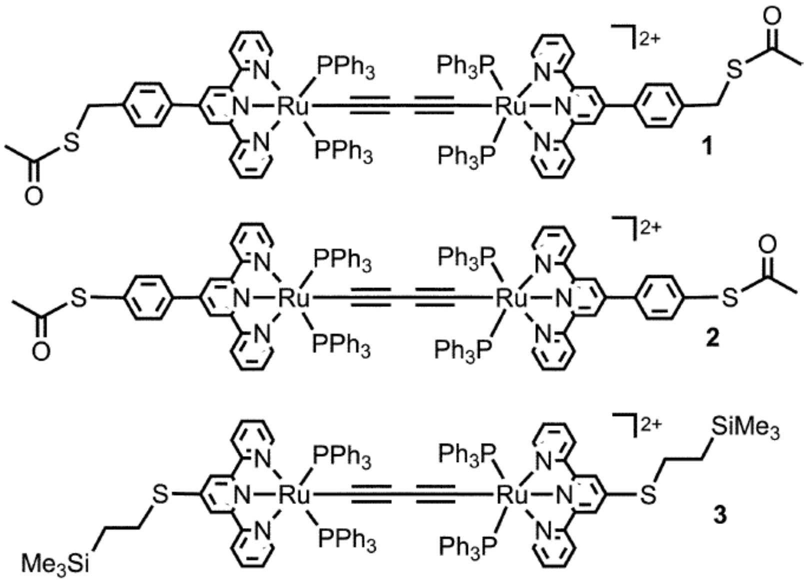

Figure 10. Chemical Structures of three dinuclear Ru(II) complexes. The perchlorate counterions are not noted.[13]

For all complexes, low HOMO–LUMO gaps (Eg ≈ 1.7 eV) were found. The histograms of **1**, **2** and **3** display considerably distinct peaks at 3.0 x 10^{-4} G_0, 1.0 x 10^{-3} G_0, and 1.4 x 10^{-3} G_0.[13] The molecular conductance found for each of the molecules is about one order of magnitude higher compared to organic molecules of comparable length. The single-molecule conductance of **2** is about three times as large as that of **1**, implying that the insertion of methylene (–CH_2–) functions and the resulting break of the π-conjugated system significantly prohibits charge transport along the molecular backbones.

While the charge transport pathway was further shortened for **3**, the increase in molecular conductance was found to be moderate, suggesting a less length dependant conductance behavior compared with organic molecules.[13]

A mononuclear Pt(II) with a covalently linked and sp/sp^2 hybridized charge transport pathway (Figure 11) was investigated with the MCBJ technique, but found to act as an insulator, with a molecular resistance about three orders of magnitude larger than that observed for two organic compounds of the same length.[58] The origin of the insulating behavior of the Pt complex was explained with the pure σ character of the Pt-C(sp) bonds of the Pt(II) centre and the acetylenic ligand.[58]

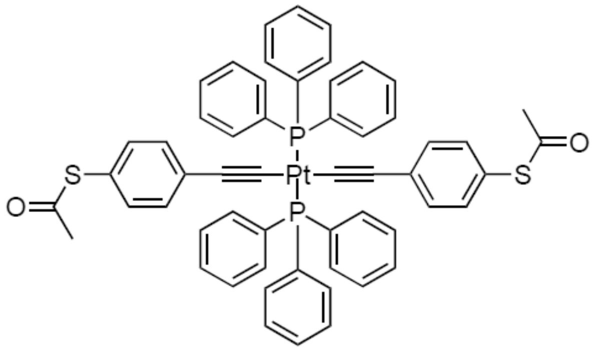

Figure 11. A Pt(II) complex acting as a molecular insulator. The terminal thioate functional group cleaves off upon contact with the gold electrodes.[58]

1.2 DINUCLEAR POLYCARBYL COMPLEXES

1.2.1 Bimetallic Complexes in Molecular Electronics

The design and synthesis of the Creutz-Taube[59] ion established that in bimetallic (binuclear) complexes containing two redox-active metal centers linked through a bridging ligand, charge transport between the centers can occur. This cooperative effect depends on the nature of the bridging ligand, which has to facilitate a favorable overlap with the metal's frontier orbitals to act as an intramolecular electron pathway.[60,61]

In recent years, there has been a great interest in molecules in which the two metal centers show a pronounced electronic interaction across the bridging ligand, as they might be interesting for applications in molecular electronics, non-linear optics and catalysis. In addition, these systems can be used as models for electron-transfer (ET) processes in biological processes.[60,62,63]

1.2.2 Dinuclear Polycarbyl Complexes

Transition metal polycarbyl complexes of the type (Cp*)(PP)MC_nM(PP)(Cp*) (Cp* = η^5-C_5Me_5, P = monodentate phosphine ligand or PP = bidentate phosphine ligand, C_n organic bridging ligand) have received considerable attention to study intramolecular charge transport[60,61,63] and due to their potential as molecular wires.[60-67]

The covalently bonded and electronically delocalized bridge poses a structurally well-defined rigid-rod electron pathway, whereas the options to alter the incorporated metal centers,[64,68] the bridging[69,70] and ancillary ligands[71] (Figure 12) in order to vary the MO alignment open the possibility to gain in-depth understanding of the electronic processes taking place at the molecular level. Electrochemical and spectroscopic experiments evidenced that, depending on the chosen metal centers and bridging ligand, the electronic delocalization extends over the entire length of the organometallic unit.[72-74] The extent of the electronic delocalization also depends on the absolute metal-metal distance.[60-75]

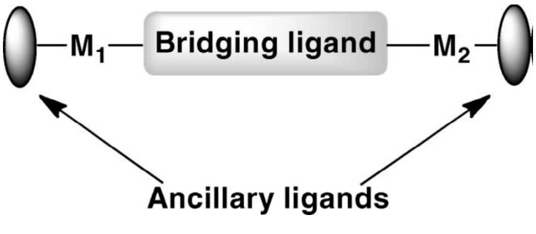

Figure 12. Schematic representation of a dinuclear metal complex. The metal centers M_1 and M_2 are connected by a bridging ligand.[60]

1.2.3 Electron Transfer and Mixed-Valence complexes

If an electron is removed from such a symmetric system chemically or electronically, the equivalent metal centers can become non-equivalent due to the electron transport occurring via the organic bridging ligand, resulting in so-called mixed valence systems in which the metal centers at least formally carry a different charge. The magnetic, spectroscopic and redox properties of these mixed valence complexes depend on the strength of the electronic interactions between the metal centers.[76-78]

The equilibrium displayed in Figure 13 depicts the formation of mixed-valence systems. Two redox-active metal centers M_1 and M_2, in the oxidation states n and $n + 1$ are linked by a bridging ligand L. K_c is the comproportionation constant representing the relative stability of the mixed valence species and large values of K_c are an essential prerequisite for the isolation of the mixed-valence compounds.[79] While strongly delocalized systems are usually characterized by large K_c values, the K_c values cannot be used as a direct measurement of the delocalization of mixed-valence complexes. [79-81]

$$M_1^n{-}L{-}M_2^n \;+\; M_1^{n+1}{-}L{-}M_2^{n+1} \xrightleftharpoons{K_c} M_1^n{-}L{-}M_2^{n+1} \;+\; M_1^{n+1}{-}L{-}M_2^n$$

Figure 13. Formation of mixed-valence compounds $M_1^{n+1}{-}L{-}M_2^n$ and $M_1^n{-}L{-}M_1^{n+1}$ with the comproportionation constant K_c.

If the bridging ligand is symmetric and the metal centers become unequivalent solely through different oxidation states, electron transfer (ET) processes via the bridging ligand are possible

(Figure 14). The metal centre in the higher oxidation state can be denoted as an acceptor, the centre in the lower oxidation state as a donor, both having different solvent configurations. The ET processes can be described in terms of the motion of the system on an energy surface from the initial state toward the activated complex and then to the final state passing over an interconversion barrier. Depending on the interactions between the nuclear and electronic frequencies, this process can be adiabatic or nonadiabatic. A system is considered to be weakly coupled when a nonadiabatic electron-transfer occurs and strongly coupled when an adiabatic transfer happens.[82,83]

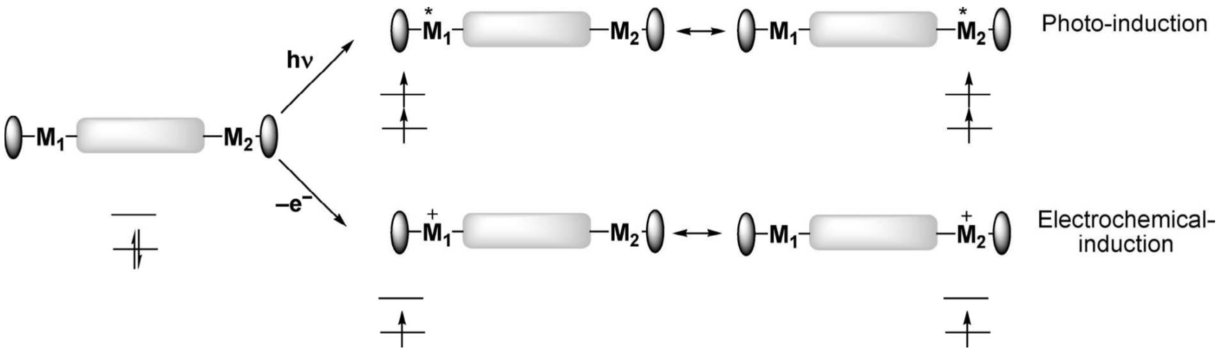

Figure 14. Photoinduced (top) and electrochemical (bottom) of an organometallic molecular wire model.[60]

The movement of an electron from the donor to the acceptor can be described in terms of a redox-reaction without the formation or breaking of bonds. For such structurally continual systems, Markus Theory (see Equation 3) takes the place of the transition state theory of Eyring. Where for the latter the reaction partners become strongly coupled in the course of the reaction to form a structurally defined activated complex, in the Marcus theory, donor and acceptor stay weakly coupled and retain their individuality. Still, the nuclear configuration, e.g. the metal-ligand and intraligand bond lengths and angles, and the surrounding media, e.g. changes in the solvent molecule orientation, have to adjust after the electron jump.

$$k_{\mathrm{ET}} = k_{\mathrm{el}}\nu_n \exp[-(\lambda + \Delta G°)^2 / 4\lambda k_{\mathrm{B}}T\,] \qquad \text{(Eq. 3)}$$

Equation 3 gives the Markus equation, the expression of the kinetic rate constant for a generic electron-transfer process (k_{ET}), with k_{el} the transmission coefficient, ν_{n} the frequency of passage (nuclear motion) through the transition state, k_{B} is the Boltzmann constant, λ is the reorganization energy, $\Delta G°$ is the total Gibbs free energy change for the electron-transfer reaction, and T is the temperature.

The Marcus theory was developed for so-called outer sphere electron transfer (OSET) reactions, where donor and acceptor are not connected via chemical bonds, but instead the electron moves through space. For so-called inner sphere electron transfer (ISET) reactions, i.e. systems in which donor and acceptor are connected by chemical bonds like in the case of dinuclear mixed-valence polycarbyl complexes, the Marcus theory was modified by Hush to be applied to stable mixed-valence systems.[84-86] These species can be studied by spectroscopic analyses that, along with cyclic voltammetry (CV) studies, often allow the determination of the type (class) of mixed-valence complexes.

The categorization of mixed-valence systems as proposed by Robin and Day[80] groups the systems in different classes based on the strength of the electronic interactions between the two metal centers M_1 and M_2. The interaction varies from zero or weak (class I) to moderate (class II) and to very strong (class III).

In class I, optical and electronic properties for the separate sites are present, and activated electron-transfer either does not occur at all or only at a very slow rate.

Complexes belonging to the class II display new optical and electronic properties in addition to those of the separate sites. Yet the interaction is weak, leading to valence trapped or charge localized systems.

The electronic coupling is very strong in complexes belonging to class III, the odd electron is fully delocalized and the systems show unique electronic and optical properties due to the full delocalization of the charge.

Mixed valence complexes often exhibit an intervalence charge transfer (IVCT) band characteristic in the near-infrared (NIR) spectral area, which corresponds to the optically induced intramolecular electron-transfer. This band is absent in the spectra of the reduced and oxidized states.

The position, form and intensity of the IVCT band allow to determine the two most important electron-transfer parameters, the reorganization energy λ and the electronic matrix coupling *H*ab. The latter one arises from donor and acceptor coupling. Figure 15 displays the potential-energy surfaces for the three primary Robin-Day classes.

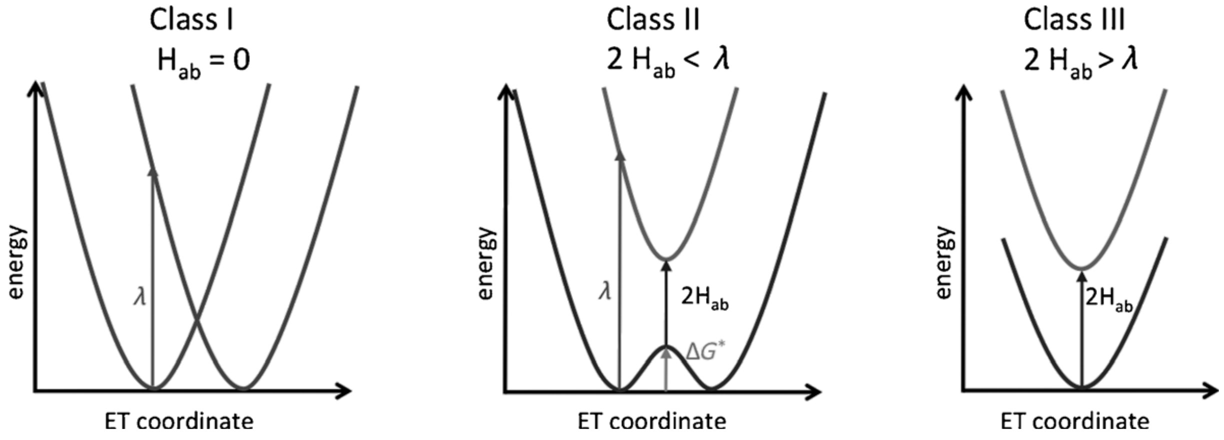

Figure 15. Potential-energy surfaces for the three primary Robin–Day classes: class I (left), class II (middle), and class III (right).[89]

It has to be noted, however, that more classes have been denoted. Mixed-valence complexes at the borderline II/III exhibit a very fast thermal electrontransfer due to small activation barriers.[87] A class IV was proposed taking the vibronic progression into consideration.[88] Recently, Low and coworkers showed that in bimetallic complexes, the conformation of the metal centers and the ancillary and bridging ligand influence the electronic coupling and can result in valence-trapped conformations.[89] Also the nature of the bridging ligand has to be taken into account, as so-called non-innocent ligands change the potential-energy surface.[61,81]

Different techniques are used to probe the delocalization of suitable systems. Cyclic voltammetry (CV) allows the extraction of ΔE and K_c. Investigating complexes with $J \neq 0$ using magnetization measurements determines ferromagnetic or antiferromagnetic coupling between spins.

X-Ray spectroscopy details structural information, such as geometry and bond lengths. UV/Vis-NIR allows to determine shape, energy, intensity and half-height bandwidth of the IVCT band, EPR to identify the location of the unpaired electron based on hyperfine splitting and *g* anisotrophy. For iron containing complexes, Mössbauer-spectroscopy can be performed to help placing a time-scale on the electron transfer.

1.2.4 Dinuclear Polycarbyl Complexes as Molecular Wires

Transition metal complexes exhibiting a charge delocalization over the length of the molecular backbone, i.e. belonging to class III, are highly interesting candidates for the realization of molecular wires.[60-67] It was demonstrated that the chemical reversibility of the redox process is highest for C_4 bridged complexes and decreases rapidly with increasing chain lengths or when other forms of sp/sp^2 type bridges are employed.[69] Consequently, the electronically versatile C_4 fragment[61,90] (Figure 16) is an ideal linker for the construction of relay-type conducting molecular entities.

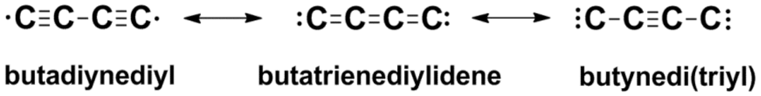

Figure 16. Canonical forms of a C_4 unit in $[M]C_4[M]$ structures

Lapinte and coworkers showed that butadiynediyl bridged diiron complexes have outstanding electrochemical properties,[64,91,92] especially with regard to the high stabilization of the various oxidized forms and the high metal character of the delocalized HOMOs in all accessible oxidation states.[93]

Investigations of this kind were mainly focused on molecules of the type (Cp*)(PP)M–C_n–M(PP)(Cp*) (Cp* = η^5-C_5Me_5, P = mono-dentate phosphine ligand or PP = bidentate phosphine ligand, C_n = organic bridging ligand),[11,17] which might be called dinuclear stopper-type as they do not possess endgroups that allow their connection to electrodes or further extension of the conjugated system.

Intrinsically open dinuclear systems of the type X–(PP)M–C_4–M(PP)–X (X = halide) are known, but are quite rare.[94-97] The construction of terminally open, metal containing analogues of higher nuclearities as genuine representatives of the relay approach is synthetically challenging and was up to date only reported for three $C_2C_6H_4C_2$ bridged trinuclear ruthenium[52,54,55] and iron[98] complexes, a mixed ditungsten diiron tetranuclear complex where a central ditungsten ethynylbis(carbyne) fragment was capped with terminal butadiynyl iron moieties[94] as well as a series of C_8 bridged platinum complexes.[95]

Still, the prospect of employing organometallic polycarbyl complexes as molecular wires is intriguing, as the covalently bonded and electronically delocalized bridge poses a structurally well-defined rigid-rod electron pathway, whereas the options to alter the incorporated metal centers[68,64], the bridging[69,70] and ancillary ligands[71] in order to vary the MO alignment open the possibility to gain in-depth understanding of the electronic processes taking place at the molecular level. Yet up to date, single-molecule transport measurements were only carried out on a limited number of the X(PP)MC_nM(PP)X type of fragments (see above): a mononuclear ruthenium[56] and a mononuclear platinum[58] complex and selected di- and trinuclear ruthenium entities.[13,52-54] Hence, the rich ligand chemistry and the high tunability of transition metals, which make the (PP)MC_nM(PP) class very attractive for molecular electronic applications, is so far not sufficiently exploited and needs further chemical realization and physical transport experiments.

1.3 GOAL OF THE THESIS

1.3.1 Iron-Alkyne Based Organometallic Molecules as Functional Building Blocks for Molecular Junctions

Single molecules constitute the smallest discrete units to build electronic devices at the molecular level. Key requirements for suitable molecular units are structural rigidity, resonant conductivity along chosen pathways and the option to manipulate and thus modulate the charge transport. One route towards such molecular units is to embed redox active metal centers in conjugated organic moieties, thereby deploying the metal centers as relays for the transported charge. Such organometallic architecture is also attractive due to the possibility to vary structural motifs, electron density and work functions, thus obtaining fundamental knowledge on the relationship between molecular structure and electronic properties.

This work aims at constructing such organometallic fully conjugated systems by incorporating Fe centers into alkyne based scaffolds and to investigate their physico-chemical and electronic properties. The stability of the redox pair Fe(II)/Fe(III), the natural abundancy and low toxicity of the iron(II) dihalide precursor make the utilization of this transition metal desirable. The outstanding electrochemical properties found for butadiynediyl bridged diiron complexes recommend the implementation of Fe centers into the targeted complexes.

Strongly electron donating diphosphines were chosen as ancillary ligands (PP = depe = 1,2-bis(diethylphosphino)ethane) to the iron centers (Figure 17) to obtain complexes of high solubility in organic solvents, stable ligand environments and an absolute electronegativity in the range needed for appropriate interaction with the gold leads of a mechanically controllable break junction (MCBJ) technique.

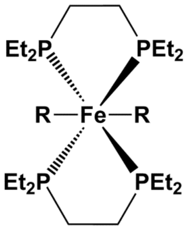

Figure 17. Chemical structure of the mononuclear subunit *trans*-Fe(depe)$_2$R$_2$.

1.3.2 Synthesis, Characterization and Properties of a Tetranuclear Homometallic Pentakis(butadiynediyl) Based Framework (see Chapter 2)

The first part of the thesis targets the stepwise incorporation of four Fe(II) centers into a pentakis(butadiynediyl) based framework to obtain a linear homometallic tetranuclear species (Figure 18).

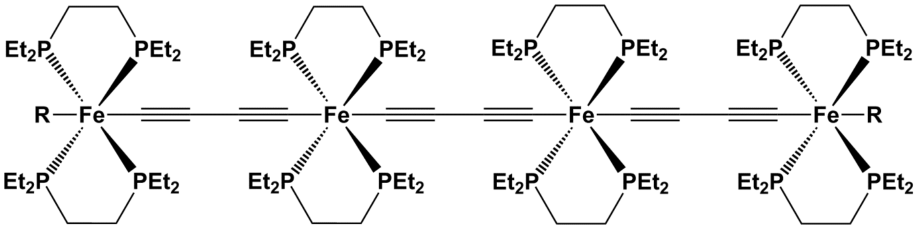

Figure 18. Chemical structure of a tetranuclear, homometallic pentakis(butadiynediyl) based framework.

As the chosen iron fragments possess potentially open terminal binding sites, smaller dinuclear units can be used as building blocks and elaborated into larger rigid-rod entities containing up to four metal atoms and five C_4 ligands. Establishing synthetic routes to terminally open mono, di- and tetranuclear complexes is a fundamental prerequisite to further investigate the properties and structure-function relationship of organometallic molecular wires. The target complexes as well as the dinuclear precursors obtained for the iterative synthesis will be investigated using *in-situ* spectroelectrochemistry to probe the electronic coupling over the length of the conjugated chain.

1.3.3 Diiron C_4 Bridged Complexes with Different Electrode-Binding Terminal Substituents (see Chapters 3 and 4)

The second part of the thesis aims to introduce electrode-binding ligands to the terminal substitution sites of a dinuclear butadiyne bridged unit (Figure 19) and probe selected complexes for their molecular charge transport properties using the mechanically controllable break junction (MCBJ) technique. The knowledge gained in the first part of the thesis is a prerequisite to access and terminally modify the dinuclear fragments. The inherent length of the FeC_4Fe core compared to mononuclear complexes is expected to significantly reduce the contribution of direct electrode-electrode tunneling, thus improving the accuracy of the measurements. Butadiyne was chosen as a bridging ligand for the structural rigidity and electronic versatility. The rich ligand chemistry of transition metals allows the introduction of a wide range of possible electrode-binding anchorgroups. The obtained series of complexes will be investigated using spectroscopic and electrochemical methods. To gain insight into the influence of the terminal groups on the energetic regime of the molecular orbitals, the molecular geometries of selected complexes together with the corresponding HOMO/LUMO energy levels and chemical hardness will be investigated at the density functional theory (DFT) level.

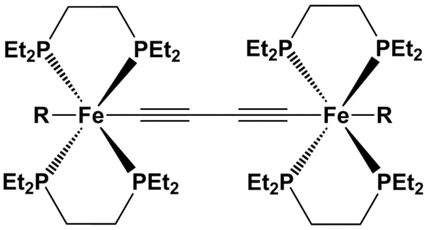

.

Figure 19. Chemical structure of a diiron C_4 bridged complex with electrode-binding terminal substituents R.

The dinuclear FeC_4Fe core is electronically functional due to the two redox-active metal centers and an sp bridging ligand enabling charge transport across the entire length of the molecular backbone due to strong electronic delocalization. selected complexes will be probed using mechanically controllable break junction (MCBJ) technique to investigate the transport properties of the FeC_4Fe core and to probe the influence of the different molecule - electrode coupling on the charge transport and junction stability.

To further investigate the influence on comparably stronger or weaker molecule - electrode coupling on the charge transport and junction stability, deep temperature MCBJ experiments as well as DFT calculations of the energetic regimes of the electrode-molecule-electrode systems under applied bias are planned.

1.3.4 Carbyl/Methyne-Based Bridges in Di- and Trinuclear Redox-Active Iron Complexes (see Chapter 5)

In the third part of the thesis, redox-active Fe(depe)$_2$ cores will be connected with different sets of unsaturated organic bridging ligands to probe the effect of a gradual decoupling of the metal centers on the molecular orbital energies and the resulting chemical hardness (Figure 20).

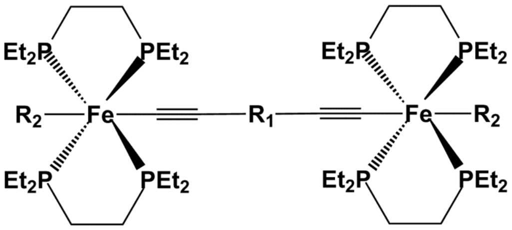

Figure 20. Chemical structure of diiron complexes bridged with different sp/sp^2 ligands and carrying different terminal ligands R$_2$.

The introduction of electrode-binding terminal ligands to further lay down synthetic routes to access organometallic molecular wires will be investigated. All complexes are intrinsically functional due to the redox-active metal centers embedded in a structurally rigid and covalent sp/sp^2 framework. Again, DFT calculations will be used to explore the influence of the bridging ligands on the energetic regime of the molecular orbitals and the chemical hardness of the compounds.

1.4 IMPACT OF THE PRESENTED WORK

The incooperation of Fe centres into a charge delocalized molecular backbone could pave the way to materials with unique electronic properties. The proposed molecules constitute consangious series of organometallic molecular wires and wire models, and the scope of structural modification and planned theoretical and experimental investigations is unprecedented. The elucidation of the individual transfer sites in such systems, the interpretation of vibrational patterns and of the nature of the electronic transitions will contribute significantly to the understanding of the interdependencies of structure and electric and electronic properties on the molecular level.

All targeted molecules are intrinsically functional due to the incorporation of redox-active transition metal centers directly into the sp hybridized pathway of electrons. Furthermore, the stepwise synthetic build-up allows for a variety of structural motifs, involving the metal centers, the bridging ligand and the equatorial ligand sphere, to be modulated to probe the charge transport and understand the relationship betwenic properties on a molecular level. The terminal substituents are conjugated moieties and covalently bind to the Fe centers to establish a conjugated bridge between the Fe centers. The complexes are excellent starting materials for even longer scaffolds with even or odd numbers of metal centers along a fully conjugated rigid-rod like metal-organic framework.

The presented work contributes to the field of molecular electronics by providing modifiable organometallic molecular wires, and to the general field of organometallic chemistry by exploring new synthetic strategies to obtain electronically functional poly-iron complexes. The gained understanding of synthetic routes and of structure-property dependencies can contribute to the design of novel functional organometallic entities for molecular electronics, spintronics and catalysis.

1.5 REFERENCES

(1) Metzger, R. M. *J. Mater. Chem.* **2008,** *18* (37), 4364–4396.

(2) Carroll, R. L.; Gorman, C. B. *Angew. Chem. Int. Ed.* **2002** (41), 4378–4400.

(3) Reed, M. A. *Science*. **1997,** *278* (5336), 252–254.

(4) Aviram, A.; Ratner, M. A. *Chemical Physics Letters*. **1974,** *29* (2), 277–283.

(5) Akita, M.; Chung, M.-C.; Sakurai, A.; Sugimoto, S.; Terada, M.; Tanaka, M.; Moro-oka, Y. *Organometallics*. **1997,** *16* (22), 4882–4888.

(6) Lörtscher, E.; Ciszek, J. W.; Tour, J.; Riel, H. *Small*. **2006,** *2* (8-9), 973–977.

(7) Tour, J. M.; Kozaki, M.; Seminario, J. M. *J. Am. Chem. Soc.* **1998,** *120* (33), 8486–8493.

(8) Tour, J. M. *Acc. Chem. Res.* **2000,** *33* (11), 791–804.

(9) Richard Feynman gave the talk "There's Plenty of Room at the Bottom" on December 29th, 1959 at the Californian Institute of Technology.

(10) Balzani, V.; Credi, A.; Venturi, M. *Molecular devices and machines: Concepts and perspectives for the nanoworld;* Wiley-VCH: Weinheim, **2008**.

(11) Cuniberti, G. *Introducing molecular electronics;* Springer: Berlin, **2005**.

(12) Kaliginedi, V.; Moreno-García, P.; Valkenier, H.; Hong, W.; García-Suárez, V. M.; Buiter, P.; Otten, Jelmer L. H.; Hummelen, J. C.; Lambert, C. J.; Wandlowski, T. *J. Am. Chem. Soc.* **2012,** *134* (11), 5262–5275.

(13) Wen, H.-M.; Yang, Y.; Zhou, X.-S.; Liu, J.-Y.; Zhang, D.-B.; Chen, Z.-B.; Wang, J.-Y.; Chen, Z.-N.; Tian, Z.-Q. *Chem. Sci.* **2013,** *4* (6), 2471.

(14) Hong, W.; Manrique, D. Z.; Moreno-García, P.; Gulcur, M.; Mishchenko, A.; Lambert, C. J.; Bryce, M. R.; Wandlowski, T. *J. Am. Chem. Soc.* **2012,** *134* (4), 2292–2304.

(15) Cuniberti, G.; Fagas, G.; Richter, K. *Introducing molecular electronics;* Springer: Berlin, New York, **op. 2005**.

(16) Chen, F.; Hihath, J.; Huang, Z.; Li, X.; Tao, N. J. *Annu. Rev. Phys. Chem.* **2007,** *58* (1), 535–564.

(17) Zotti, L. A.; Kirchner, T.; Cuevas, J.-C.; Pauly, F.; Huhn, T.; Scheer, E.; Erbe, A. *Small.* **2010,** *6* (14), 1529–1535.

(18) Meyer, E.; Glatzel, T. *Science.* **2009,** *324* (5933), 1397–1398.

(19) Xiang, D.; Jeong, H.; Lee, T.; Mayer, D. *Adv. Mater.* **2013,** *25* (35), 4845–4867.

(20) Ruben, M.; Landa, A.; Lörtscher, E.; Riel, H.; Major, M.; Görls, H.; Weber, H. B.; Arnold, A.; Evers, F. *Small.* **2008,** *4* (12), 2229–2235.

(21) Lörtscher, E.; Cho, C. J.; Major, M.; Tschudy, M.; Rettner, C.; Riel, H. *ChemPhysChem.* **2011,** *12* (9), 1677–1682.

(22) Lörtscher, E.; Riel, H. *CHIMIA.* **2010,** *64* (6), 376–382.

(23) Metzger, R. M. *J. Mater. Chem.* **2008,** *18* (37), 4364.

(24) Brédas, J.-L.; Beljonne, D.; Coropceanu, V.; Cornil, J. *Chem. Rev.* **2004,** *104* (11), 4971–5004.

(25) Hines, T.; Diez-Perez, I.; Hihath, J.; Liu, H.; Wang, Z.-S.; Zhao, J.; Zhou, G.; Müllen, K.; Tao, N. *J. Am. Chem. Soc.* **2010,** *132* (33), 11658–11664.

(26) Nitzan, A. *Science.* **2003,** *300* (5624), 1384–1389.

(27) Lu, Q.; Yao, C.; Wang, X.; Wang, F. *J. Phys. Chem. C.* **2012,** *116* (33), 17853–17861.

(28) Gotsmann, B.; Riel, H.; Lörtscher, E. *Phys. Rev. B.* **2011,** *84* (20).

(29) Ho Choi, S.; Kim, B.; Frisbie, C. D. *Science.* **2008,** *320* (5882), 1482–1486.

(30) Lu, Q.; Liu, K.; Zhang, H.; Du, Z.; Wang, X.; Wang, F. *ACS Nano.* **2009,** *3* (12), 3861–3868.

(31) Luo, L.; Choi, S. H.; Frisbie, C. D. *Chem. Mater.* **2011,** *23* (3), 631–645.

(32) He, J.; Chen, F.; Li, J.; Sankey, O. F.; Terazono, Y.; Herrero, C.; Gust, D.; Moore, T. A.; Moore, A. L.; Lindsay, S. M. *J. Am. Chem. Soc.* **2005,** *127* (5), 1384–1385.

(33) Xu, B. *Science.* **2003,** *301* (5637), 1221–1223.

(34) Salomon, A.; Cahen, D.; Lindsay, S.; Tomfohr, J.; Engelkes, V. B.; Frisbie, C. *Adv. Mater.* **2003,** *15* (22), 1881–1890.

(35) Venkataraman, L.; Klare, J. E.; Nuckolls, C.; Hybertsen, M. S.; Steigerwald, M. L. *Nature.* **2006,** *442* (7105), 904–907.

(36) Reichert, J.; Ochs, R.; Beckmann, D.; Weber, H.; Major, M.; Löhneysen, H. *Phys. Rev. Lett.* **2002,** *88* (17).

(37) Ramachandran, G. K.; Tomfohr, J. K.; Li, J.; Sankey, O. F.; Zarate, X.; Primak, A.; Terazono, Y.; Moore, T. A.; Moore, A. L.; Gust, D.; Nagahara, L. A.; Lindsay, S. M. *J. Phys. Chem. B.* **2003,** *107* (25), 6162–6169.

(38) Kergueris, C.; Bourgoin, J.-P.; Palacin, S.; Esteve, D.; Urbina, C.; Magoga, M.; Joachim, C. *Phys. Rev. B.* **1999,** *59* (19), 12505–12513.

(39) Xing, Y.; Park, T.-H.; Venkatramani, R.; Keinan, S.; Beratan, D. N.; Therien, M. J.; Borguet, E. *J. Am. Chem. Soc.* **2010,** *132* (23), 7946–7956.

(40) Lörtscher, E.; Elbing, M.; Tschudy, M.; Hänisch, C. von; Weber, H. B.; Major, M.; Riel, H. *ChemPhysChem*. **2008,** *9* (15), 2252–2258.

(41) Hong, W.; Valkenier, H.; Mészáros, G.; Manrique, D. Z.; Mishchenko, A.; Putz, A.; García, P. M.; Lambert, C. J.; Hummelen, J. C.; Wandlowski, T. *Beilstein J. Nanotechnol.* **2011,** *2*, 699–713.

(42) Chen, F.; Tao, N. J. *Acc. Chem. Res.* **2009,** *42* (3), 429–438.

(43) Nath, S.; Ghosh, S.; Kundu, S.; Praharaj, S.; Panigrahi, S.; Pal, T. *J Nanopart Res*. **2006,** *8* (1), 111-116.

(44) Pearson, R. G. *Chemical hardness;* Wiley-VCH: Weinheim, Germany, New York, **1997**.

(45) Zhao, X.; Huang, C.; Gulcur, M.; Batsanov, A. S.; Baghernejad, M.; Hong, W.; Bryce, M. R.; Wandlowski, T. *Chem. Mater.* **2013,** *25* (21), 4340–4347.

(46) Prins, F.; Monrabal-Capilla, M.; Osorio, E. A.; Coronado, E.; van der Zant, Herre S. J. *Adv. Mater.* **2011,** *23* (13), 1545–1549.

(47) Low, P. J. *Dalton Trans.* **2005** (17), 2821.

(48) Wuttke, E.; Hervault, Y.-M.; Polit, W.; Linseis, M.; Erler, P.; Rigaut, S.; Winter, R. F. *Organometallics*. **2014,** 140207082351004.

(49) O'Hanlon, D. C.; Cohen, B. W.; Moravec, D. B.; Dallinger, R. F.; Hopkins, M. D. *J. Am. Chem. Soc.* **2014**.

(50) Tuccitto, N.; Ferri, V.; Cavazzini, M.; Quici, S.; Zhavnerko, G.; Licciardello, A.; Rampi, M. A. *Nat Mater*. **2008,** *8* (1), 41–46.

(51) Sakamoto, R.; Ohirabaru, Y.; Matsuoka, R.; Maeda, H.; Katagiri, S.; Nishihara, H. *Chem. Commun.* **2013,** *49* (64), 7108.

(52) Benameur, A.; Brignou, P.; Di Piazza, E.; Hervault, Y.-M.; Norel, L.; Rigaut, S. *New J. Chem.* **2011,** *35* (10), 2105.

(53) Kim, B.-S.; Beebe, J.; Olivier, C.; Rigaut, S.; Touchard, D.; Kushmerick, J.; Zhu, X.-Y.; Frisbie, C. *J. Phys. Chem. C.* **2007,** *111* (20), 7521–7526.

(54) Luo, L.; Benameur, A.; Brignou, P.; Choi, S. H.; Rigaut, S.; Frisbie, C. D. *J. Phys. Chem. C.* **2011,** *115* (40), 19955–19961.

(55) Olivier, C.; Kim, B.; Touchard, D.; Rigaut, S. *Organometallics*. **2008,** *27* (4), 509–518.

(56) Marques-Gonzalez, S.; Yufit, D. S.; Howard, Judith A. K.; Martin, S.; Osorio, H. M.; Garcia-Suarez, V. M.; Nichols, R. J.; Higgins, S. J.; Cea, P.; Low, P. J. *Dalton Trans*. **2013,** *42* (2), 338–341.

(57) Getty, S.; Engtrakul, C.; Wang, L.; Liu, R.; Ke, S.-H.; Baranger, H.; Yang, W.; Fuhrer, M.; Sita, L. *Phys. Rev. B*. **2005,** *71* (24).

(58) Major, M.; Hänisch, C. von; Weber, H. B.; Reichert, J.; Beckmann, D. *Angewandte Chemie International Edition*. **2002,** *41* (7), 1183–1186.

(59) Creutz, C.; Taube, H. *J. Am. Chem. Soc.* **1973,** *95* (4), 1086–1094.

(60) Aguirre-Etcheverry, P.; O’Hare, D. *Chem. Rev.* **2010,** *110* (8), 4839–4864.

(61) Costuas, K.; Rigaut, S. *Dalton Trans.* **2011,** *40* (21), 5643.

(62) Ceccon, A.; Santi, S.; Orian, L.; Bisello, A. *Coordination Chemistry Reviews*. **2004** (248), 683.

(63) Low, P. J. *Coordination Chemistry Reviews*. **2013,** *257* (9-10), 1507–1532.

(64) Bruce, M. I.; Costuas, K.; Davin, T.; Ellis, B. G.; Halet, J.-F.; Lapinte, C.; Low, P. J.; Smith, M. E.; Skelton, B. W.; Toupet, L.; White, A. H. *Organometallics*. **2005,** *24* (16), 3864–3881.

(65) Bruce, M. I.; Le Guennic, B.; Scoleri, N.; Zaitseva, N. N.; Halet, J.-F. *Organometallics*. **2012,** *31* (13), 4701–4706.

(66) Yu, Marie Pui Yin; Yam, V. W.-W.; Cheung, K.-K.; Mayr, A. *Theory and Mechanistic Studies*. **2006,** *691* (21), 4514–4531.

(67) Gauthier, N.; Argouarch, G.; Paul, F.; Humphrey, M. G.; Toupet, L.; Ababou-Girard, S.; Sabbah, H.; Hapiot, P.; Fabre, B. *Adv. Mater.* **2008,** *20* (10), 1952–1956.

(68) Szafert, S.; Paul, F.; Meyer, W. E.; Gladysz, J. A.; Lapinte, C. *C. R. Chimie*. **2008,** *11* (6-7), 693–701.

(69) Montigny, F. de; Argouarch, G.; Costuas, K.; Halet, J.-F.; Roisnel, T.; Toupet, L.; Lapinte, C. *Organometallics*. **2005,** *24* (19), 4558–4572.

(70) Lissel, F.; Blacque, O.; Venkatesan, K.; Berke, H. *submitted*. **2014**.

(71) Haines, D. E.; O’Hanlon, D. C.; Manna, J.; Jones, M. K.; Shaner, S. E.; Sun, J.; Hopkins, M. D. *Inorg. Chem.* **2013,** *52* (16), 9650–9658.

(72) Low, P. J.; Bock, S. *Electrochimica Acta*. **2013**.

(73) Pevny, F.; Di Piazza, E.; Norel, L.; Drescher, M.; Winter, R. F.; Rigaut, S. *Organometallics*. **2010,** *29* (22), 5912–5918.

(74) Wuttke, E.; Pevny, F.; Hervault, Y.-M.; Norel, L.; Drescher, M.; Winter, R. F.; Rigaut, S. *Inorg. Chem.* **2012,** *51* (3), 1902–1915.

(75) Dembinski, R.; Bartik, T.; Bartik, B.; Jaeger, M.; Gladysz, J. A. *J. Am. Chem. Soc.* **2000,** *122* (5), 810–822.

(76) Barlow, S.; O'Hare, D. *Chem. Rev.* **1997** (97), 637.

(77) McCleverty, J. A.; Ward, M. D. *Acc. Chem. Res.* **1998,** *31* (12), 842–851.

(78) Ward, M. D. *Chem. Soc. Rev.* **1995,** *24* (2), 121.

(79) Ernst, S.; Kasack, V.; Kaim, W. *Inorg. Chem.* **1988,** *27* (7), 1146–1148.

(80) Robin, M. B.; Day, P.; Elsevier, **1968; Vol.** 10; pp 247–422.

(81) Winter, R. F. *Organometallics*. **2014**.

(82) Brunschwig, B. S.; Creutz, C.; Sutin, N. *Chem. Soc. Rev.* **2002,** *31* (3), 168–184.

(83) Marcus, R. A. *Can. J. Chem.* **1959,** *37* (1), 155–163.

(84) Hush, N. S. *Coord. Chem. Rev.* **1985** (64), 135.

(85) Hush, N. S. *Prog. Inorg. Chem.* **1967** (8), 391.

(86) Hush, N. S. *Electrochim. Acta*. **1968** (13), 1005.

(87) Demadis, K. D.; Hartshorn, C. M.; Meyer, T. J. *Chem Rev*. **2001,** *101* (9), 2655–2686.

(88) Kaim, W.; Lahiri, G. K. *Angew. Chem. Int. Ed.* **2007,** *46* (11), 1778–1796.

(89) Parthey, M.; Gluyas, Josef B. G.; Fox, M. A.; Low , Paul J.; Kaupp, M. *Chem. Eur. J.* **2014,** *20* (23), 6895–6908.

(90) Frohnapfel, D. S.; Woodworth, B. E.; Thorp, H. H.; Templeton, J. L. *J. Phys. Chem. A*. **1998,** *102* (28), 5665–5669.

(91) Paul, F.; Lapinte, C. *Electron Transfer in Coordination Chemistry*. **1998,** *178–180, Part 1* (0), 431–509.

(92) Halet, J.-F.; Lapinte, C. *Electron Transfer in Coordination Chemistry*. **2013,** *257* (9–10), 1584–1613.

(93) Guillemot, M.; Toupet, L.; Lapinte, C. *Organometallics*. **1998,** *17* (10), 1928–1930.

(94) Semenov, S. N.; Taghipourian, S. F.; Blacque, O.; Fox, T.; Venkatesan, K.; Berke, H. *J. Am. Chem. Soc.* **2010,** *132* (22), 7584–7585.

(95) Zheng, Q.; Hampel, F.; Gladysz, J. A. *Organometallics*. **2004,** *23* (25), 5896–5899.

(96) Venkatesan, K.; Blacque, O.; Berke, H. *Dalton Trans.* **2007** (11), 1091.

(97) Egler-Lucas, C.; Blacque, O.; Venkatesan, K.; López-Hernández, A.; Berke, H. *Eur. J. Inorg. Chem.* **2012,** *2012* (9), 1536–1545.

(98) Field, L. D.; Turnbull, A. J.; Turner, P. *J. Am. Chem. Soc.* **2002,** *124* (14), 3692–3702.

(99) Goddard, W.; Brenner, D.; Lyshevski, S., Iafrate, G. (Edt.) . *Nanoscience, Engineering and Technology Handbook*, CRC Press **2003**

2. STEPWISE CONSTRUCTION OF AN IRON-SUBSTITUTED RIGID-ROD MOLECULAR WIRE: TARGETING A TETRAFERRA-TETRACOSA-DECAYNE

2.1 MANUSCRIPT

The manuscript and associated supplementary information were published as a full paper in the Journal of the American Chemical Society as:

F. Lissel, T. Fox, O. Blacque, W. Polit, R. F. Winter, K. Venkatesan, H. Berke "*Stepwise Construction of an Iron-Substituted Rigid-Rod Molecular Wire: Targeting a Tetraferra-Tetracosa-Decayne*", *J. Am. Chem. Soc.* **2013**, 135 (10), 4051-4060

JACS
JOURNAL OF THE AMERICAN CHEMICAL SOCIETY
Article
pubs.acs.org/JACS

Stepwise Construction of an Iron-Substituted Rigid-Rod Molecular Wire: Targeting a Tetraferra−Tetracosa−Decayne

Franziska Lissel,[†] Thomas Fox,[†] Olivier Blacque,[†] Walther Polit,[#] Rainer F. Winter,[#] Koushik Venkatesan,[†] and Heinz Berke*,[†]

[†]Institute of Inorganic Chemistry, University of Zürich, Winterthurerstrasse 190, CH-8057 Zürich, Switzerland
[#]Faculty of Chemistry, University of Konstanz, Universitätsstrasse 10, D-78457 Konstanz, Germany

Supporting Information

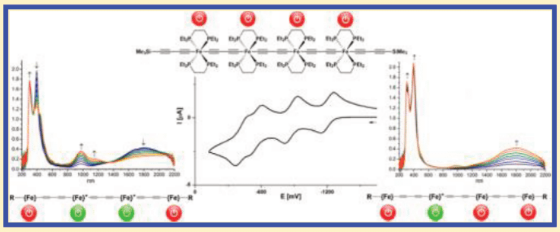

ABSTRACT: *trans*-Fe(depe)$_2$I$_2$ (depe =1,2-bis(diethylphosphino)ethane) was employed to stepwise incorporate Fe(II) centers into a rigid-rod butadiyne based 5,10,15,20-tetraferratetracosa-1,3,6,8,11,13,16,18,21,23-decayne. The iterative synthesis first connects two Fe(II) centers via a central butadiynediyl ligand to provide I-Fe(depe)$_2$-C$_4$-Fe(depe)$_2$-I (**2**), then extends the system by substituting the terminal halides of **2** to yield Me$_3$SiC$_4$-Fe(depe)$_2$-C$_4$-Fe(depe)$_2$-C$_4$SiMe$_3$ (**3**). Further modification of the termini gives the deprotected and stannylated compounds RC$_4$-Fe(depe)$_2$-C$_4$-Fe(depe)$_2$-C$_4$R (**4** and **5**; R = H, Sn(CH$_3$)$_3$, respectively). Transmetalation with two more mononuclear units furnishes the homometallic tetranuclear compound I-Fe(depe)$_2$-C$_4$-Fe(depe)$_2$-C$_4$-Fe(depe)$_2$-C$_4$-Fe(depe)$_2$-I (**6**), to which two more butadiynyl units were attached to give Me$_3$SiC$_4$-Fe(depe)$_2$-C$_4$-Fe(depe)$_2$-C$_4$-Fe(depe)$_2$-C$_4$-Fe(depe)$_2$-C$_4$SiMe$_3$ (**7**). All compounds were characterized by NMR, IR, and Raman spectroscopies and by elemental analyses. X-ray diffraction studies were carried out on the dinuclear complexes revealing highly symmetrical rigid-rod structures. Cyclic voltammetric studies showed that compounds **2**−**7** undergo reversible and well-defined oxidations with high K_c values indicating thermodynamically stable mixed valence species. While the number of the oxidation waves of compounds **2**, **6**, and **7** are equivalent to the number of metal centers, the dinuclear complexes **3**, **4**, and **5** exhibit three reversible oxidation waves, one at significantly more positive potential. Two redox waves were attributed to the oxidation of the metal centers, while the remaining one is due to the oxidation of the butadiynediyl ligand. The electronic properties of complexes **2**, **3**, and **7** were investigated by spectroelectrochemical measurements.

■ INTRODUCTION

Molecular-scale electronics seeks to assemble appropriate molecular components for exerting specific functions in molecular electronic devices.[1,2] One of the basic functions required for many types of electronic devices on the molecular level is based on the design of π-conjugated rigid-rod molecules, so-called "molecular wires", that are able to transport electric charge over distances of several nanometres.[3] The electron transport through single molecules and ultimately the relationship between molecular structure and electric or electronic properties is as yet not fully understood.[4] Nevertheless, conjugated organic moieties, especially those consisting of sp-hybridized carbon atoms, constitute materials that accomplish high electron transfer rates, since they provide well-defined, fully conjugated, rigid-rod structures with strongly delocalized frontier orbitals.[5] Tunnelling-based charge transfer rates of purely organic "conducting" systems are known to decay exponentially with the distance until, at certain length, the tunnelling turns into a multistep hopping having a nonexponential distance dependence.[6,7] As has been exemplified by terpyridine-based frameworks, the so-called "relay approach", that is the insertion of metal centers into rigid-rod architectures, promotes transport based on electron hopping by providing defined donor−acceptor sites, thus enhancing the overall conductivity.[8]

Transition metal polycarbyl complexes of the type L$_m$M-(C$_n$)-ML$_m$ have received considerable attention in recent years due to their potential as molecular wires.[9−14] Electronic delocalization over the length of the unsaturated carbon bridge could be probed by using spectroelectrochemical methods.[15,16] Investigations of this kind were mainly focused on molecules of the type (Cp*)(PP)M-C$_n$-M(PP)(Cp*) (Cp*= η^5-C$_5$Me$_5$, P = monodentate phosphine ligand or PP = bidentate phosphine ligand, C$_n$ = organic bridging ligand),[11,17] which might be called dinuclear stopper-type as they do not possess end groups that allow their connection to electrodes or further extension of the conjugated system. Intrinsically open dinuclear systems of the type X-(PP)M-C$_4$-M(PP)-X (X = halide) are known, but are quite rare.[18−21] The construction of terminally open, metal-containing analogues of higher nuclearities as genuine representatives of the relay approach is synthetically challenging and was up to date only reported for three C$_2$C$_6$H$_4$C$_2$ bridged trinuclear ruthe-

Received: January 4, 2013
Published: February 13, 2013

nium[22−24] and iron[25] complexes, a mixed ditungsten diiron tetranuclear complex where a central ditungsten ethynylbis(carbyne) fragment was capped with terminal butadiynyl iron moieties,[26] as well as a series of C_8 bridged platinum complexes.[21]

It was demonstrated for dinuclear stopper type molecules that the chemical reversibility of the redox process is highest for C_4 bridged complexes and decreases rapidly with increasing chain lengths or when other forms of sp/sp^2 type bridges are employed.[27] Consequently, the electronically versatile butadiynediyl fragment[28,29] is an ideal linker for the construction of relay-type conducting molecular entities. Also, among the stopper-type molecules, Lapinte and co-workers showed that butadiynediyl bridged diiron complexes have outstanding electrochemical properties,[30,31] especially with regard to the high stabilization of the various oxidized forms[32] and the high metal character of the delocalized HOMOs in all accessible oxidation states.[33]

In this context we targeted the stepwise incorporation of four Fe(II) centers into a pentakis(butadiynediyl)-based framework to obtain a linear homometallic tetranuclear species. Such architecture is, to the best of our knowledge, unprecedented. Electron-donating bidentate diphosphine ligands occupying the equatorial positions were employed to ensure *trans* configuration of the rigid-rod butadiynediyl units and favorable redox properties. As the chosen iron fragments possess potentially open terminal binding sites, smaller dinuclear units could be used as building blocks and elaborated into larger rigid-rod entities containing up to four metal atoms and five C_4 ligands.

■ SYNTHESIS AND CHARACTERIZATION OF THE DI- AND TETRANUCLEAR COMPLEXES

Synthetic access to dinuclear iron complexes of the general type (Cp*)(PP)Fe-C_n-Fe(PP)(Cp*) can generally be accomplished via the reaction of a mononuclear fragment of the type (Cp*)(PP)FeCl with silylated alkynes in the presence of MeOH and a fluoride source yielding either directly the targeted dinuclear complex[27] or a mononuclear vinylidene complex that can be subjected to oxidative homocoupling.[34,35] Attempts to employ these conditions to prepare a butadiynediyl-bridged dinuclear iron complex with terminal chloro substituents of the type $Cl(PP)_2Fe$-C_4-$Fe(PP)_2Cl$ turned out to be unsuccessful, yielding an interesting non-rigid-rod trinuclear complex instead.[36] Remarkably, only a few examples of dinuclear complexes of the type $X(PP)_2Fe$-C_n-$Fe(PP)_2X$ (X = halide, CH_3) with modifiable end groups are described in the literature,[25,37,38] but as yet they are bridged by bis(ethynyl)-arylene spacers and their synthetic access is based on complex and not generally applicable routes.[19,20,25]

One should also note that in complexes of the type *trans*-$Fe(PP)_2Cl_2$ (PP = 1,2-bis(dimethylphosphino)ethane, 1,2-bis(diethylphosphino)ethane, 1,2-bis(diisopropylphosphino)-ethane) the bidentate phosphine ligands can reversibly dissociate.[39] While this characteristic property allows substitution reactions on the metal center,[40,41] it simultaneously limits the synthetic options for assembling oligonuclear rigid-rod moieties with two bridging ligands in *trans* position[36] as targeted for this work. Although the lability of a bidentate phosphine ligand increases with the sterical demand,[39] we still chose the depe (depe =1,2-bis(diethylphosphino)ethane) ligand over the less bulky methyl-substituted dmpe (dmpe =1,2-bis-(dimethylphosphino)ethane) to maintain a reasonable solubility of the targeted di- and tetranuclear compounds. Instead of the mononuclear dichloro compound, the corresponding diiodo complex *trans*-$Fe(depe)_2I_2$ was chosen as starting material, since the iodides are more reactive and furthermore known to dissociate readily.[42] Also, the lower solubility of the diiodo complex was perceived to be advantageous for the purification of the targeted compounds as it allows a facile separation of the mononuclear precursor. On the basis of earlier work from our group[26,43] we aimed at utilizing transmetalation reactions for the stepwise construction of a tetrairon chain.

As shown in Scheme 1, transmetalating two units of the mononuclear precursor *trans*-$Fe(depe)_2I_2$[44] (**1**) with $Me_3Sn—C{\equiv}C—C{\equiv}C—SnMe_3$[45] in refluxing tetrahydrofuran gave the butadiyne-bridged dinuclear complex **2** as a burgundy red solid of low solubility in good yield (88%). The $^{31}P\{^1H\}$ NMR of **2** showed a singlet at 69.8 ppm for the eight equivalent P atoms, which is shifted slightly downfield compared to the mononuclear precursor (δ = 65.9 ppm). The shift can be attributed to the introduction of the carbon-rich C_4 bridging ligand, which, in a resonance form best described as a butadiynediyl, reduces the electron density at the metal center, thus leading to an increased σ-donation of the equatorial ligands toward the iron. The $^{13}C\{^1H\}$ NMR spectrum of **2** did not exhibit signals relating to sp-hybridized carbon atoms. As indicated by NMR studies at 193 K, this is not caused by a fluxional behavior as for instance found in the case of $[CpFe(dppe)]_2(\mu\text{-}C_4)$[35] but originates from the low solubility of compound **2**. A second transmetalation process to substitute the terminal iodides in **2** was not successful even in the presence of catalytic amounts of Cu(I).[46]

Related to the reactions of (Cp*)(PP)FeCl and *trans*-$Fe(PP)_2Cl_2$ cores with lithium-acetylide[47] and sodium-acetylide[37,38] reagents, the targeted elongation was finally achieved by substitution of the terminal iodo ligands with a freshly prepared $Li—C{\equiv}C—C{\equiv}C—SiMe_3/LiBr$[48] reagent in toluene. Compared to the diiodo precursor **2**, the yellow compound **3** with two terminal C_4TMS (TMS = trimethylsilyl, $SiMe_3$) ligands was found to be highly soluble in nonpolar organic solvents, even in pentane. The increased solubility allowed full characterization by ^1H, $^{13}C\{^1H\}$, $^{31}P\{^1H\}$, and $^{29}Si\{^1H\}$ NMR spectroscopies. The resonances for the $SiMe_3$ groups were observed at 0.17 ppm in the ^1H NMR, at −21.8 ppm in the $^{29}Si\{^1H\}$ NMR, and at 1.39 ppm in the $^{13}C\{^1H\}$ NMR spectra. Besides the expected signals for the primary and secondary carbon atoms of the phosphine ligands and the $SiMe_3$ groups, the $^{13}C\{^1H\}$ NMR spectrum showed six signals of sp-hybridized carbon atoms. This is consistent with the centrosymmetric structure of **3** with one central butadiynediyl and two terminal butadiynyl ligands. Each signal corresponds to two chemically and magnetically equivalent carbon atoms. The signals of the carbon atoms in α-position to the iron centers split into multiplets due to the coupling with the four equatorial P atoms. The $^{31}P\{^1H\}$ NMR spectrum exhibited a singlet at 76.3 ppm, which is markedly shifted downfield compared to **2** due to the influence of two additional butadiynyl units.

The TMS groups were removed under mild conditions employing TBAF in THF (containing 5% H_2O) at room temperature. The resulting C_4H derivative **4** was characterized by ^1H, $^{13}C\{^1H\}$, and $^{31}P\{^1H\}$ NMR spectroscopies. It could be stannylated by using NEt_2SnMe_3[49] in refluxing THF to give the trimethyltin capped species **5**. Both complexes were obtained in reasonably high yields (76% and 89%, respectively).

As for compounds **2** and **3**, no column chromatography was needed to obtain the compounds in an analytically pure state. The deprotection and subsequent stannylation of the terminal

Scheme 1. Stepwise Synthesis of the Tetraferra−Tetracosa−Decayne Complex 7

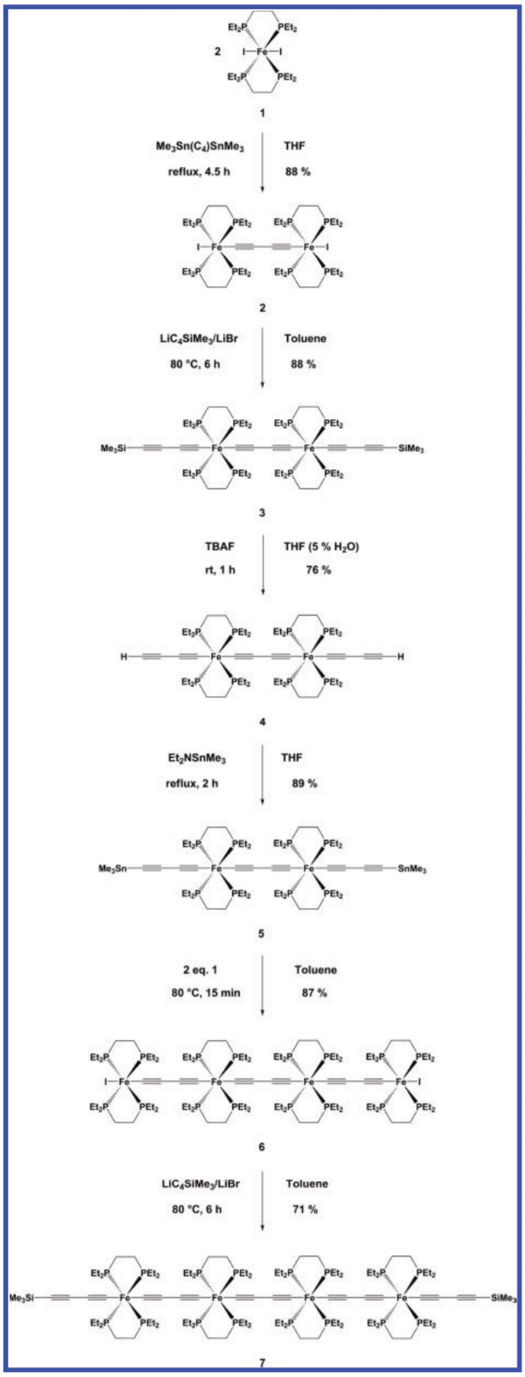

butadiynyl functions has only minor influence on the physical properties.

Similar to the $SiMe_3$ protected **3**, compounds **4** and **5** were yellow solids and highly soluble compared to the diiodo precursor **2**, although **4** was not soluble in pentane. The $^{31}P\{^1H\}$ NMR spectra of both the deprotected and the stannylated diiron complexes displayed singlets at 76.2 or 76.1 ppm, respectively. The $^{13}C\{^1H\}$ NMR spectra showed six signals related to a total of 12 sp-hybridized carbon atoms confirming the centrosymmetry of these rigid-rod molecules. The quintets expected for the carbon atoms in α-position to the iron centers are clearly distinguishable in the spectra of **4**, whereas in the $^{13}C\{^1H\}$ NMR spectrum of the $SnMe_3$-substituted complex **5** only multiplets could be observed for the corresponding signals. The acetylenic proton of **4** was observed as a singlet at 1.26 ppm in the ^1H NMR spectrum in C_6D_6, whereas it coincides with the signals of the methyl groups in THF-d_8. The $SnMe_3$ group of **5** gave rise to a singlet at 0.06 ppm in the ^1H NMR spectrum, at −36.3 ppm in the $^{119}Sn\{^1H\}$ and at −7.47 ppm in the $^{13}C\{^1H\}$ NMR spectra. Both the ^1H and the $^{13}C\{^1H\}$ signals show tin satellites as expected for the $SnMe_3$ functional group. Additional two-dimensional NMR spectra of complexes **2**, **3**, and **4** are displayed in the Supporting Information (see Figures S1−S7).

Transmetalation of **5** with two more mononuclear *trans*-$Fe(depe)_2I_2$ units in toluene (see Scheme 1) resulted in the pale red tetranuclear compound **6**, where four Fe(II) centers are bridged by three butadiynediyl units. The short reaction time of 15 min at 80 °C demonstrated an enhanced reactivity of the terminal C_4SnMe_3 moiety of **5** in comparison with the $Me_3Sn—C{\equiv}C—C{\equiv}C—SnMe_3$ reagent used for the first transmetalation. Similar to the dinuclear diiodo complex **2**, the tetranuclear diiodo complex **6** is poorly soluble, thus limiting the possibilities to characterize this complex by NMR spectroscopy. Two singlets with equivalent integrals appeared in the $^{31}P\{^1H\}$ NMR spectrum, one at 68.3 ppm, in good agreement with the chemical shift of the dinuclear diiodo complex **2** (68.3 ppm), and the other resonance at 77.6 ppm, shifted slightly downfield in comparison with the signals of the three dinuclear C_4R-disubstituted compounds (76.3, 76.2, 76.1 ppm for R = $SiMe_3$, H, $SnMe_3$, respectively).

Substitution of the iodo ligands of **6** with $Li—C{\equiv}C—C{\equiv}C—SiMe_3/LiBr$ gave the targeted compound **7**, which was isolated as a dark yellow solid. In the $^{31}P\{^1H\}$ NMR spectrum the signal of the outer $Fe(depe)_2$ centers was found to be shifted downfield to 77.5 ppm, as it is also seen in the other cases of replacement of the iodo ligands with butadiynyl units. Similarly, the $^{31}P\{^1H\}$ NMR signal of the inner $Fe(depe)_2$ entities showed a small shift to 79.3 ppm compared to 77.6 ppm in **6**. Complex **7** contains a centrosymmetric chain of 20 sp-hybridized carbon atoms. As expected, the $^{13}C\{^1H\}$ NMR spectrum exhibits 10 signals for all 20 carbon atoms. Four of these signals correspond to carbon atoms that are directly bonded to the iron centers and are split into multiplets due to the coupling with the P atoms of the depe ligands, while the remaining six signals are singlets.

The $SiMe_3$ functional group was observed as a singlet at 0.18 ppm in the ^1H NMR, at −22.1 ppm in the $^{29}Si\{^1H\}$ NMR and at 1.43 ppm in the $^{13}C\{^1H\}$ NMR spectra. Like the dinuclear molecules **2**−**5**, both tetranuclear complexes **6** and **7** were obtained in relatively high yields of 87% and 71%, respectively. Additionally, two-dimensional NMR spectra of complex **7** confirmed its structure (see the Supporting Information, Figures S8−S11).

■ STRUCTURAL STUDIES

Single crystals of compounds **2**−**5** were obtained and provide detailed structural information on all four dinuclear species. X-ray diffraction analysis of compound **2** (see Figure 1, Table 1 and Table S1 in the Supporting Information) showed a highly symmetric molecule possessing an inversion center located between C_B and $C_{B'}$ and revealed pseudo-octahedral geometries of the iron centers (see Figure 2 for the labeling of selected atoms).

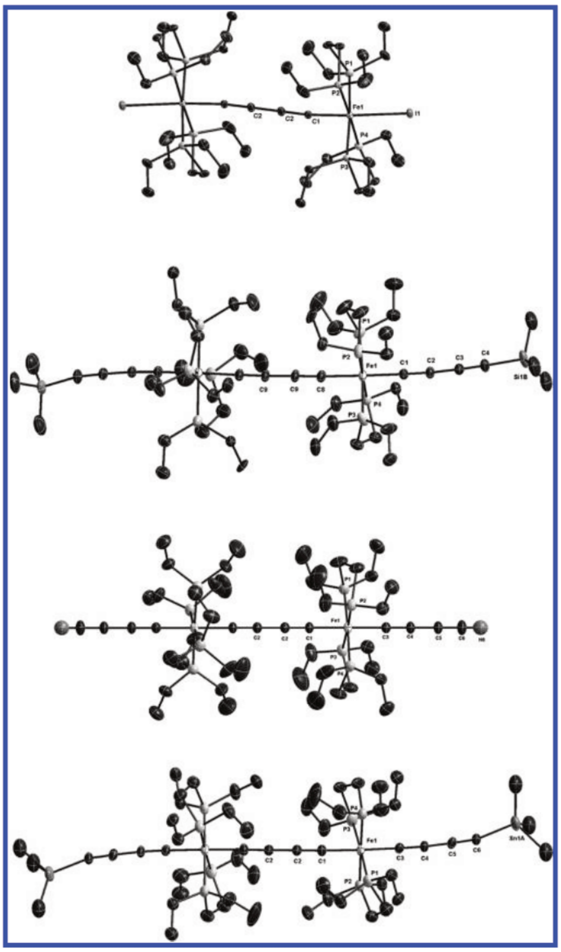

Figure 1. Molecular structures of **2** (top), **3** (upper middle), **4** (lower middle), and **5** (bottom). Ellipsoids are set at the 30% probability level. Solvent molecules and selected hydrogen atoms are omitted for clarity. See Table 1 for selected bond lengths, distances, and angles.

The introduction of the bridging butadiynediyl ligand causes a contraction of the average Fe−P distance to 2.2469(6) Å compared to 2.309 Å in the mononuclear diiodo precursor,[42] which is consistent with an increase of σ-donation from the phosphine ligands to the iron centers. The length of the Fe−I bond remains at 2.7070(4) Å. The Fe−C_A bond is 1.889(2) Å, which agrees well with reported Fe−C(sp) bond lengths,[26,27,32] while the C_A—C_B (1.229(3) Å) and C_B—$C_{B'}$ (1.380(5) Å) bonds are in the range of C≡C and C—C bond lengths expected for a 1,3-butadiynediyl bridge.[50] The Fe−Fe distance is 7.6038(8) Å and is thus between the reported values of $[CpFe(dppe)](\mu\text{-}C_4)$[50] and $[(\eta^5\text{-}C_5Me_5)(CO)_2Fe_2](\mu\text{-}C_4)$[51] of 7.564 and 7.653 Å, respectively. The Fe−C_4−Fe axis in **2** shows a slight deviation from linearity (173.8(2)° for Fe−C_A−C_B and 179.3(4)° for C_A−C_B−$C_{B'}$), which is commonly observed in $L_mM\text{−}(C_4)\text{−}ML_m$ type complexes and mostly attributed to crystal packing effects.[52,53]

Table 1. Selected Bond Lengths [Å], Nonbonding Distances [Å], and Angles [deg] of Compounds 2−5[a]

	2	3	4	5
Fe−C_A	1.889(2)	1.919(3)	1.916(6)	1.924(7)
C_A−C_B	1.229(3)	1.216(5)	1.221(9)	1.223(9)
C_B−$C_{B'}$	1.380(5)	1.389(7)	1.379(13)	1.381(12)
Fe−I	2.7070(4)			
Fe−C_C		1.907(3)	1.907(7)	1.908(6)
C_C−C_D		1.226(5)	1.220(9)	1.228(8)
C_D−C_E		1.371(5)	1.374(10)	1.371(9)
C_E−C_F		1.218(5)	1.181(10)	1.208(9)
Fe−P^b	2.2469(6)	2.2292(12)	2.2250(9)	2.233(7)
Fe−Fe′	7.6038(8)	7.6525(8)	7.6515(12)	7.6590(9)
C_F−$C_{F'}$		19.048(5)	19.015(12)	19.035(9)
Fe−C_A−C_B	173.8(2)	178.3(3)	180	175.9(7)
C_A−$C_{B'}$−$C_{B'}$	179.3(4)	178.4(4)	180	178.5(7)
Fe−C_C−C_D		178.2(4)	180	177.8(7)
C_C−C_D−C_E		175.6(4)	180	176.3(7)
C_D−C_E−C_F		178.0(5)	180	177.9(9)

[a] Please refer to Figure 2 for the labeling. [b] Average bond length.

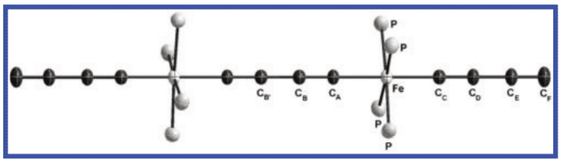

Figure 2. Labeling of selected atoms of the dinuclear complexes **3**−**5**. The atoms of complex **2** are labeled congruently.

X-ray diffraction analyses of the three C_4R-disubstituted compounds (see Figure 1 for R = $SiMe_3$, H, and $SnMe_3$, respectively) showed structures with rigid-rod RC_4-{Fe}-C_4-{Fe}-C_4R backbones. Compared to the diiodo complex **2**, the Fe−Fe distance is clearly elongated (7.6525(8), 7.6515(12), and 7.6590(9) Å for R = $SiMe_3$, H, and $SnMe_3$, respectively) and assumes a value close to that of 7.653 Å found for $[(\eta^5\text{-}C_5Me_5)(CO)_2Fe_2](\mu\text{-}C_4)$.[51] This can be attributed to the even more pronounced butadiynediyl character of the bridge, marked by a slight contraction of the C_A−C_B triple bonds (see Figure 2 for the labeling of selected atoms), which is overcompensated by elongations of the Fe−C_A and C_B−$C_{B'}$ single bonds (see Table 1).

The symmetry of the structures is reduced compared to **2**, as the phosphine ligands are more staggered and, in case of **3** and **5**, the trimethylsilyl and trimethylstannyl groups capping the terminal butadiynyl ligands bend slightly out of plane. High symmetry is nevertheless retained for all three dinuclear C_4R substituted complexes. In particular, the C_4-Fe-C_4-Fe-C_4 backbone displays a rigid linearity with angles in the range of 175°−180° (see Table 1) and significantly less distortion than the dinuclear tungsten complexes described earlier.[18,26] The average Fe−P distance shows further contraction from the dinuclear diiodo **2** (2.2469(6) Å) to the C_4TMS capped compound **3** (2.2292(12) Å). This is consistent with a further decrease of the electron density of the metal centers due to the introduction of additional butadiynyl ligands and a resulting increase of the σ-donation of the phosphine ligands. Changes in the substitution of the terminal C_F in the series from **2** to **5** have only a minor influence on the Fe−P distances (2.2250(9) and 2.233(7) Å on average for **4** and **5**, respectively). Further details on all structures are provided in the Supporting Information (Tables S1 and S2 and crystallographic information files).

CYCLIC VOLTAMMETRY

The cyclic voltammogram of **2** in THF/NBu_4PF_6 (see Figure S12 in the Supporting Information) exhibited two well-separated and reversible oxidation waves at $E_{1/2}$ = −905 and −362 mV vs Ag/AgCl ($Fc^{0/+}$ used as an external calibrant), marking the successive oxidation of the two metal centers. The K_c value of 1.9 × 10^9 (see Table 2) is in a very high range, indicating the large thermodynamic stabilization of the mixed valence species. No further waves were detected showing that the oxidation of the bridging ligand as described in the literature[33] lies outside the accessible solvent range or does not take place as the poorly π-donating iodo substituents in *trans* position to the bridge do not support this.

Table 2. Electrochemical Data of the Dinuclear Complexes[a]

compd	$E_{1/2}$(0/+1) [mV]	$E_{1/2}$(+1/+2) [mV]	ΔE [mV]	K_c	$E_{1/2}$(+2/+3) [mV]
2	−905	−362	543	1.9 × 10^9	
3	−863	−423	440	3.3 × 10^7	306
4	−880	−421	459	6.9 × 10^7	316
5	−893	−446	447	4.3 × 10^7	268

[a] Measurements at room temperature in THF/NBu_4PF_6 (0.1 M) with an Au working electrode, a Pt counter electrode, and a nonaqueous reference electrode (Ag/AgCl). Calibrated against $Fc^{0/+}$ as an external calibrant.

Three well-separated and reversible oxidation waves (see Figure 3, Table 2 and section Spectroelectrochemical Studies) were observed in the cyclic voltammogram of **3**, marking the successive oxidation of the two metal centers and subsequently the oxidation of the bridging ligand. While the K_c value for the radical cation decreased by 2 orders of magnitude when compared to **2**, it is still very high, indicating the high stability of the mixed valence Fe(II)/Fe(III) form.

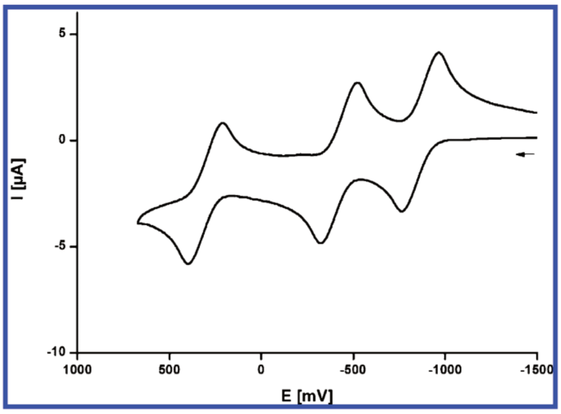

Figure 3. Cyclic voltammogram for **3** in THF/NBu_4PF_6 (0.1 M) at room temperature; Au electrode; *E* vs $Fc^{0/+}$ (external).

The electrochemical properties of compounds **4** and **5** were found to be similar to complex **3**. Both showed three reversible oxidation waves occurring at potentials similar to **3** (see Table 2 and Figures S13 and S14 in the Supporting Information) as well as K_c values in a similar range. This is in line with our expectations due to the high structural similarity of complexes **3**, **4**, and **5**.

The cyclic voltammetric study of **6** in CH_2Cl_2/NBu_4PF_6 (vs Ag/AgCl, $Fc^{0/+}$ used as an external calibrant) exhibited four individually resolved, reversible oxidation waves (see Figure 4 and Table 3), marking the successive oxidation of all four metal centers. The oxidations were observed at very negative potentials with $E°$ = −1434, −1099, −650, and −435 mV. Similar to **6**, the second tetranuclear compound **7** underwent four successive oxidations in the cyclic voltammogram (see Figure S15 in the Supporting Information, Table 3, and section Spectroelectrochemical Studies), attributable to the stepwise oxidation of the four metal centers.

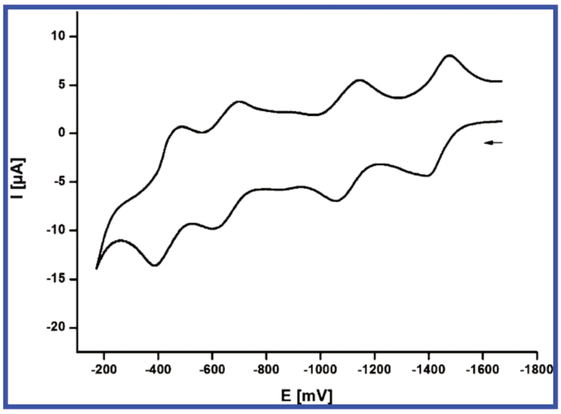

Figure 4. Cyclic voltammogram for **6** in CH_2Cl_2/NBu_4PF_6 (0.1M) at room temperature; Au electrode; *E* vs $Fc^{0/+}$ (external).

Neither complex **6** nor complex **7** exhibited further reversible oxidation waves within the potential window of the given electrolyte that could be attributed to redox processes of the organic units. It has to be noted that the successive oxidations of the metal centers occur at very negative potentials, while the oxidation of the carbon-rich bridging ligand of **3**, **4**, and **5** was observed at a much more positive potential. The separations of individual half-wave potentials for both tetranuclear compounds are not as large as for the dinuclear complexes, but still substantial and well sufficient to allow a spectroelectrochemical probing of individual oxidation states.

SPECTROELECTROCHEMICAL STUDIES

Complexes **2**, **3**, and **7** were selected for spectroelectrochemical experiments that aimed at probing the electron delocalization along the metal−organic π-conjugated chain through the changes in the ν(C≡C) band pattern and intensities upon stepwise oxidation. Complex **2** features only the internal butadiynediyl ligand and can thus be used to identify the vibrational bands of the $[\{Fe\}{-}C{\equiv}C{-}C{\equiv}C{-}\{Fe\}]^{n+}$ core without interference of the additional C_4R ligands of complexes **3** and **7**.

Spectroelectrochemical studies on complex **2** suffered from its low solubility in the THF/NBu_4PF_6 supporting electrolyte and its inherent instability in chlorinated solvents, such that the signal-to-noise ratio of the spectra is rather poor (see Figures S16 and S17 of the Supporting Information).

Table 3. Electrochemical Data for the Tetranuclear Complexes[a]

compd	$E_{1/2}(0/+1)$ [mV]	$E_{1/2}(+1/+2)$ [mV]	$\Delta E_{(1,2)}$ [mV]	$E_{1/2}(+2/+3)$ [mV]	$\Delta E_{(2,3)}$ [mV]	$E_{1/2}(+3/+4)$ [mV]	$\Delta E_{(3,4)}$ [mV]
6[b]	−1434	−1099	335	−650	449	−435	215
7[c]	−1204	−873	331	−553	320	−421	135

[a] Measurements performed with an Au working electrode and a Pt counter electrode, and a nonaqueous reference electrode (Ag/AgCl). Calibrated against $Fc^{0/+}$ as an external calibrant. [b] In THF/Bu_4NPF_6 (0.1M) at room temperature. [c] In CH_2Cl_2/Bu_4NPF_6 (0.1M) at room temperature.

Table 4. IR $\nu(C{\equiv}C)$ data (in cm^{-1}) for the Complexes in Their Various Oxidation States

	$n = 0$	$n = 1$	$n = 2$
$\mathbf{2}^{n+}$ [a]	1951	1972, 1880	not observed
$\mathbf{3}^{n+}$ [b]	2157, 2100(sh), 2068, 1967(sh), 1951	2153, 2106, 2080(sh), 1990, 1964, 1955(sh), 1878	2157, 2104, 2080(sh), 2030, 1958(sh), 1937, 1878
$\mathbf{7}^{n+}$	2155, 2073, 2043(sh), 1965(sh), 1947, 1924, 1885	2152, 2096(sh), 2085, 2035, 1947(sh), 1930, 1882	2152, 2102, 2075(sh), 2037, 1925, 1882(sh), 1799

[a] In THF/NBu_4PF_6 (0.2 M) as the supporting electrolyte. [b] In $1,2\text{-}C_2H_4Cl_2/NBu_4BAr^F{}_4$ ($BAr^F{}_4 = B\{C_6H_3(CF_3)_2\text{-}3,5\}_4{}^-$) (0.1 M) as the supporting electrolyte.

In contrast to Lapinte's butadiynediyl-bridged diiron complexes with Cp*Fe(LL) half-sandwich type end groups, neutral **2** displays just one C≡C IR stretch in its IR spectrum at almost the same energy as the higher energy band of the Cp*Fe(dppe) analogue.[54] We note, however, that similar C_4-bridged diruthenium, diosmium, or dirhenium complexes usually display just one C≡C band in their IR spectra[17,55−59] while other rigid-rod like dimetal complexes with the higher local D_{2h} symmetry of **2** may display no IR-active C≡C vibration at all.[60,61]

Upon oxidation, the single $\nu(C{\equiv}C)$ band of **2** at 1951 cm^{-1} evolves into a two-band pattern with peaks at 1972 and 1880 cm^{-1} (see Table 4). One might argue that this observation points to the loss of a centrosymmetric structure upon oxidation and hence to a valence-localized structure with discernible Fe(II) and Fe(III) sites on the IR time scale. The observation of a pattern of two $\nu(C{\equiv}C)$ bands for mixed-valent butadiynediyl-bridged dimetal complexes of Class III with intrinsic charge delocalization is, however, not without precedence, in particular in iron chemistry.[54,62] We also note the growth of an intense, broad near-infrared (NIR) band of electronic origin peaking at 6400 cm^{-1} (1560 nm) (see Figure S16). With reference to the mixed-valent radical cations of the aforementioned half-sandwich diiron complexes this band is assigned as the Fe(II)→Fe(III) intervalence charge transfer (IVCT) absorption. This IVCT band is truncated at the low energy side with half widths of 1270 cm^{-1} at higher energy of the maximum and 1020 cm^{-1} at the lower energy side. Both half-widths are substantially lower than the value expected of a Class II system, $\Delta\nu_{1/2} = (2310\nu_{max})^{1/2} = 3750\ cm^{-1}$, derived from Hush's theory.[63,64] Brunschwig, Creutz, and Sutin have introduced the Γ value with $\Gamma = 1 - \nu_{1/2,obsd}/\nu_{1/2,calc}$ as a measure of ground state delocalization.[65] The value of 0.66 obtained for the half-width at the higher energy realm clearly exceeds the value of 0.50 delimiting the Class II−III transition and hence points to extensive charge delocalization in this mixed-valence species.

Further oxidation at a potential positive of the +/2+ couple results in a further increase of the intensity of the $\nu(C{\equiv}C)$ IR band at the lower energy and a slight shift to 1883 cm^{-1} as well as a partial bleaching of the low-energy electronic band. Longer electrolysis times and a further increase of the applied potential led to an intensity loss of all vibrations that precludes a firm assignment of the spectroscopic properties of that species. Preliminary studies of chemically oxidized $\mathbf{2}^+$ and $\mathbf{2}^{2+}$ showed that they are reasonably stable compounds. It was however observed that $\mathbf{2}^{2+}$ is completely insoluble in THF, which could be a reason for the observed behavior.

Replacement of the terminal iodo ligands by trimethylsilylbutadiynyl ones leads to extensive vibrational coupling along the unsaturated $-C_4-\{Fe\}-C_4-\{Fe\}-C_4-$ backbone as can be inferred from the large number of alkynyl stretching vibrations for neutral **3** that spread over the 2157 to 1951 cm^{-1} range. Upon oxidation to its radical cation in the $1,2\text{-}C_2H_4Cl_2/NBu_4BAr^F{}_4$ ($BAr^F{}_4{}^- = B\{C_6H_3(CF_3)_2\text{-}3,5\}_4{}^-$) electrolyte, the number of IR active vibrations further increases (see Table 4 and Figure 5).

By inference from $\mathbf{2}^{0/+}$, the stretches at 1951 cm^{-1} of **3** and at 1964 and 1878 cm^{-1} of $\mathbf{3}^+$ can be assigned to vibrational modes of the central butadiynediyl ligand. The $\nu(C{\equiv}C)$ band positions of that entity thus seem to be only little affected by substitution at the *trans*-disposed terminal ligands. Oxidation of one of the core

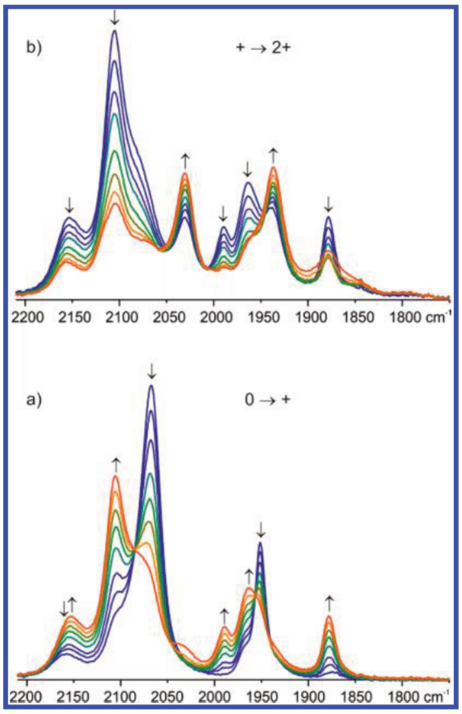

Figure 5. IR spectroscopic changes during (a) the first and (b) the second oxidation of complex **3** in an OTTLE cell ($1,2\text{-}C_2H_4Cl_2/NBu_4BAr^F{}_4$ 0.2 M at room temperature).

Fe atoms likewise seems to have rather little influence on the energies of the $\nu(C{\equiv}C)$ modes of the terminal ligands while there are changes in terms of relative band intensities. This is most clearly seen for the prominent band of the butadiynyl ligands, where the pattern of a high-energy shoulder at 2100 cm^{-1} and a main peak at 2068 cm^{-1} just inverses upon oxidation with only slight shifts to result in a strong peak at 2106 cm^{-1} and a shoulder at 2080 cm^{1}. We concede, however, that such reasoning might be too simplistic when considering the strong coupling between the individual vibrators along the unsaturated TMS–C$_4$–{Fe}–C$_4$–{Fe}–C$_4$–TMS chain.

Further oxidation to 3^{2+} bleaches the bands at 1990 and 1964 cm^{-1}, while the remaining ones experience only small shifts but larger changes in intensity. Again, this second oxidation process could not be pursued to full conversion before the onset of irreversible spectroscopic changes which might again be due to insufficient solubility of oxidized 3^{2+}. This unfortunately precludes us from assessing the spectroscopic changes associated with the third oxidation. Similar experiments in the THF/NBu$_4$PF$_6$ electrolyte produced almost identical results for the $3/3^+$ pair of compounds as in the 1,2-C$_2$H$_4$Cl$_2$/NBu$_4$BAr^F$_4$ electrolyte (see Figure S18 of the Supporting Information) but failed to produce reliable results for even 3^{2+}. Of note is the observation of a low-energy electronic band at 6040 cm^{-1} (1655 nm) that grows in during the first oxidation of **3** and bleaches during the second one. This feature is also seen as a strong band at 6145 cm^{-1} (1627 nm) in UV/vis/NIR spectroelectrochemistry (see Figure 6) with additional shoulders at 7300 and 8064 cm^{-1} (1370 and 1240 nm). The energy of this band falls close to the equivalent absorption of 2^+ at 1560 nm (6400 cm^{-1}) and is again assigned as an Fe(II)→Fe(III) IVCT. As for 2^+ this band is truncated at the low energy side with half widths of 1510 and 1290 cm^{-1}, respectively, for the high- and low-energy realms of the peak. The ratio θ between the observed half-width and the calculated one of a Class II system is 0.40, which in turn yields a Γ value of 0.60. This value is again larger than the one of 0.50 marking the Class II–III transition. This argues for strong electronic coupling between the C$_4$-bridged {Fe} sites in 3^+. Other changes in the UV/vis part of the spectrum include the shift of the original UV band from 341 to 322 nm and the growth of weaker shoulders at 394 and 420 nm as well as an additional small peak at 720 nm. On oxidation to the 3^{2+} dication the original NIR absorption is bleached with the concomitant growth of a new structured band of like absorptivity at 1015 nm and a shoulder to the blue at 970 nm. For this band we propose $\pi{\rightarrow}\pi^*$-parentage, most probably with strong ligand-to-metal charge-transfer contributions. Like bands, albeit usually at lower energies, are routinely observed for Fe(III) alkynyl complexes including other butadiynediyl-bridged diiron complexes with half-sandwich-type {Fe} sites.[54,62,66]

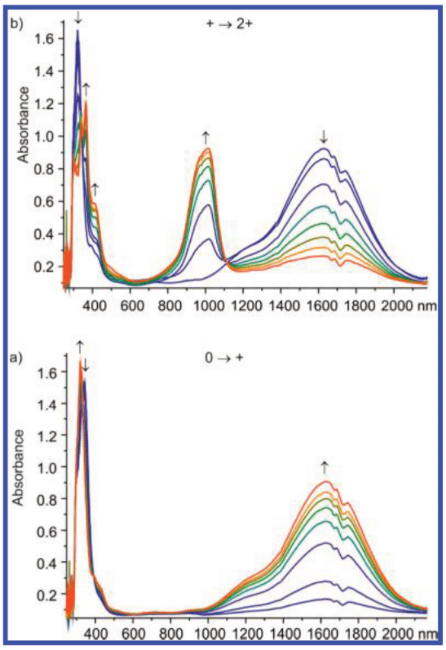

Figure 6. UV/vis/NIR spectroscopic changes during (a) the first and (b) the second oxidation of complex **3** in an OTTLE cell (1,2-C$_2$H$_4$Cl$_2$/NBu$_4$BAr^F$_4$ 0.2 M at room temperature).

Further elongation of the rigid-rod metal organic π-system to the tris(butadiynediyl)-bridged tetrairon complex **7** results in a further increase of the number of IR active modes in the 1965 to 1885 cm^{-1} range along with a red shift of the prominent C≡C absorption from 1951 to 1924 cm^{-1} (see Figure 7). This is probably the result of further vibrational coupling between the two central butadiynediyl ligands. Similar to **3**, oxidation of **7** to its radical cation caused a blue shift of the main peak of the bands assigned to the terminal butadiynyl ligands from 2073 to 2085 cm^{-1} and an intensity increase of the vibrations at 1947 and 1924 cm^{-1}, but hardly any change in their positions. The second oxidation likewise causes changes in band intensities rather than band positions with the exception of the growth of an intense band at 1799 cm^{-1}. This feature resembles the low-energy band formed upon the first oxidation of complexes **2** and **3**, yet with a

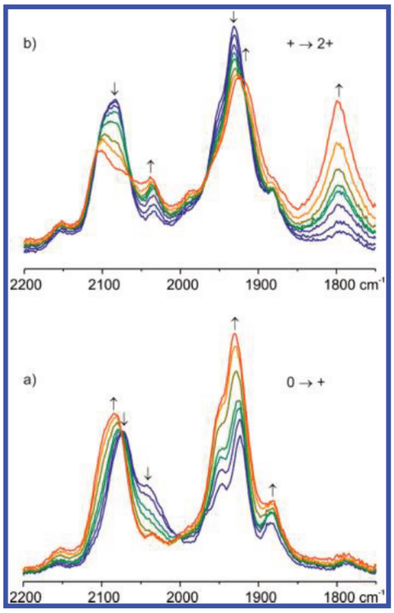

Figure 7. IR spectroscopic changes during (a) the first and (b) the second oxidation of complex **7** in the mid-IR in an OTTLE cell (1,2-C$_2$H$_4$Cl$_2$/NBu$_4$BAr^F$_4$ 0.2 M at room temperature).

substantial red shift of ca. 80 cm^{-1}. Just like $\mathbf{2}^+$ and $\mathbf{3}^+$, radical cation $\mathbf{7}^+$ displays a broad, strong NIR absorption at ca. 5500 cm^{-1} (1820 nm, see Figure 8). This band has a rather symmetrical shape.

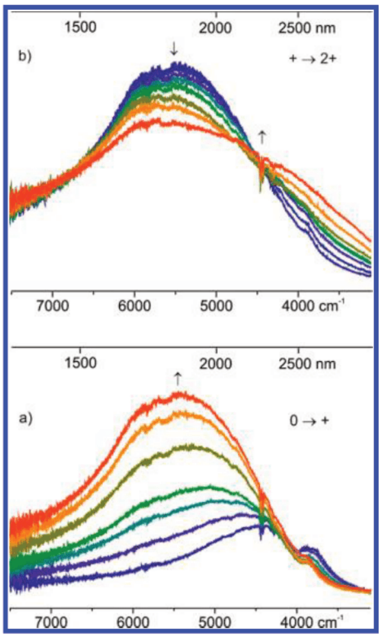

Figure 8. IR spectroscopic changes during (a) the first and (b) the second oxidation of complex **7** in the NIR in an OTTLE cell (1,2-$C_2H_4Cl_2$/$NBu_4BAr^F{}_4$ 0.2 M at room temperature).

As shown in Figure 9, this band is also observed in UV/vis/NIR spectroelectrochemical experiments and displays a half width of ca. 1750 cm^{-1}, which is again appreciably smaller than the value of 3565 cm^{-1} derived from the Hush formula for a Class II system but appreciably larger as for $\mathbf{2}^+$ and $\mathbf{3}^+$. The calculated Γ value of 0.51 places $\mathbf{7}^+$ still in the regime of strongly delocalized systems, yet at the Class II/III borderline. Spectral deconvolution of the NIR part of the electronic spectrum reveals the presence of a second, broader NIR band peaking at 6920 cm^{-1} (1445 nm) with a half-width of 3010 cm^{-1} (see Figure S19 of the Supporting Information). The calculated Γ value of 0.25 is typical of an IVCT transition within a mixed-valent system of Class II parentage. Other spectroscopic changes along the $\mathbf{7}/\mathbf{7}^+/\mathbf{7}^{2+}$ redox system are similar to complex **3**, i.e. some slight shift and intensity increase of the prominent UV and vis bands and the growth of a shoulder at 495 nm during the first oxidation and the development of a structured NIR band with resolved peaks at 977 and 1177 nm upon the second oxidation. Of note is a moderate red shift of these bands when compared to $\mathbf{3}^{2+}$, obviously as a consequence of the further extension of the π-conjugated pathway. At variance with $\mathbf{3}^{2+}$, doubly oxidized $\mathbf{7}^{2+}$ still retains a rather strong NIR band at 5065 cm^{-1} (1970 nm), that is at a just slightly higher energy as the equivalent IR band of $\mathbf{7}^+$.

Deconvolution of the NIR part of the electronic spectrum of $\mathbf{7}^{2+}$ (see Figure S19 of the Supporting Information) provides an excellent fit to the experimental spectra and indicates that the low-energy NIR absorption originates from a single absorption with a half-width of 2690 cm^{-1}, corresponding to a Γ value of 0.21.

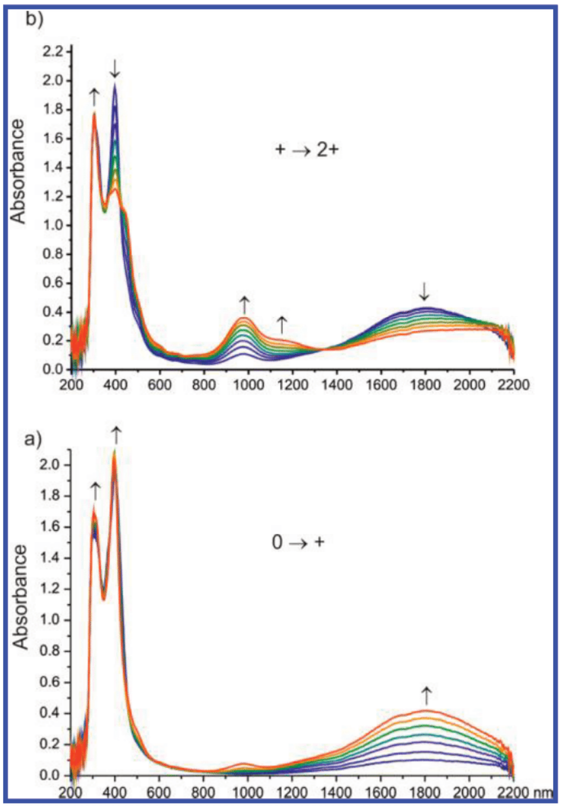

Figure 9. UV/vis/NIR spectroscopic changes during (a) the first and (b) the second oxidation of complex **7** in an OTTLE cell (1,2-$C_2H_4Cl_2$/$NBu_4BAr^F{}_4$ 0.2 M at room temperature).

This finding possibly provides a clue to the sequence of oxidations within the bis(butadiynediyl)-bridged tetrairon core. One can reasonably assume that a Fe(depe)$_2$-substituted butadiynyl moiety is more electron rich than a TMS-substituted one. Hence, one of the inner two {Fe} sites with two attached $-C_4-\{Fe\}-C_4-$TMS "ligands" is a more likely candidate for the primary oxidation site. For the TMS$-C_4-\{Fe\}-C_4-\{Fe\}^+-C_4-\{Fe\}-C_4-\{Fe\}-C_4-$TMS system thus formed one might expect two IVCT transitions from electronically different neighboring {Fe} sites. This assumes that IVCT from the next-to-nearest neighbors, i.e. from the remote TMS$-C_4-\{Fe\}-$ moiety, is not observed. The second oxidation could then occur at either the remaining central or one of the remote terminal {Fe(depe)$_2$bis(butadiynyl)} sites (see Figure 10). Oxidation of the remaining inner moiety (I in Figure 10) would lead to a system where only one type of IVCT transition, that is from each of the outer to the neighboring inner site, is observed.

In that case one would also expect that the remaining IVCT band is the one displaying the weaker electronic coupling. Both these expectations match with our experimental observations. We also note that the appreciably smaller Γ value for the IVCT transition between the inner sites when compared to $\mathbf{2}^+$ and $\mathbf{3}^+$ correlates with the likewise smaller $\Delta E_{1/2}$ and K_c values for radical cation $\mathbf{7}^+$ when compared to $\mathbf{2}^+$ and $\mathbf{3}^+$.

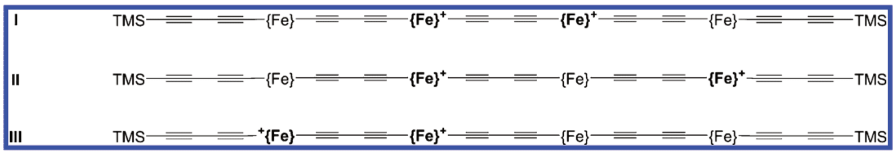

Figure 10. Possible electronic structures of the dication 7^{2+}.

Considering that the only difference between 2^+, 3^+, and 7^+ is the identity of the peripheral ligand (−I, $-C_4-$TMS or $-C_4-${Fe}$-C_4-$TMS) and that spatial distances between the {Fe}-based redox sites in these complexes are virtually identical, the decrease of the $\Delta E_{1/2}$ and K_c values is very likely of true electronic origin as opposed to electrostatic effects, changes in the inductive effects or magnetic exchange term.[67−69] The other possibility is that the second oxidation involves one of the terminal {Fe} sites. Electrostatic repulsion between like unipositively charged redox centers one would make an oxidation of the remote moiety more feasible than that of the one neighboring the already oxidized site, thus rendering a dication with two chemically different oxidized $\{Fe\}^+$ sites (II in Figure 10). In such a case one would expect to see three IVCT transitions, one arising from charge transfer from the reduced inner to the oxidized inner, one from the reduced inner to the oxidized outer, and one from the reduced outer to the oxidized inner {Fe} moiety. The third, least likely scenario of the second oxidation involues the outer {Fe} moiety neighboring the already oxidized inner one (III in Figure 10). Here, one would also expect to see a single IVCT band, but this time the one with the stronger coupling. This is, of course, under the assumption that our assignments of the IVCT transitions of 7^+ are correct. Unfortunately, all attempts to assess the higher oxidized forms of **7** proved to be in vain.

CONCLUSION

In summary, we have demonstrated that a stepwise construction of homometallic tetranuclear species starting from a diiron *trans* diiodo complex could be achieved proving that long and well-defined rigid-rod organometallic molecules with tunable redox properties are accessible via a controlled and iterative synthesis. To the best of our knowledge this is the first report of a tetranuclear homometallic species that still has intrinsically open terminal binding sites. Also, the investigated compounds display IVCT between the metal centers as well as a high stabilization of its oxidized forms. Complexes **2**, **5**, and **6** are excellent starting materials for even longer scaffolds with even or odd numbers of metal centers along a fully conjugated rigid-rod like metal−organic backbone that could pave the way to materials with unique electronic properties. We also note that the elucidation of the individual transfer sites in such systems, the interpretation of vibrational patterns, and the nature of the electronic transitions becomes a more and more demanding task as the number of redox sites increases.

ASSOCIATED CONTENT

Ⓢ Supporting Information

Experimental details including more detail on NMR spectroscopy (Figures S1−S11), cyclic voltammetry (Figures S12−S15), and spectroeletrochemical studies (Figures S16−S19) as well as summaries of the X-ray diffraction studies (Table S1 and S2). This material is available free of charge via the Internet at http://pubs.acs.org.

AUTHOR INFORMATION

Corresponding Author

hberke@aci.uzh.ch

Notes

The authors declare no competing financial interest.

ACKNOWLEDGMENTS

Funding from the National Research Programme “Smart Materials” (NRP 62, grant no. 406240-126142) of the Swiss National Science Foundation (SNSF) and the University of Zürich is gratefully acknowledged.

REFERENCES

(1) Metzger, R. M. *J. Mater. Chem.* **2008**, *18*, 4364.
(2) Vuillaume, D. *C. R. Phys.* **2008**, *9*, 78.
(3) Carroll, R. L.; Gorman, C. B. *Angew. Chem., Int. Ed.* **2002**, *41*, 4378.
(4) Luo, L. A.; Choi, S. H.; Frisbie, C. D. *Chem. Mater.* **2011**, *23*, 631.
(5) Brédas, J.-L.; Beljonne, D.; Coropceanu, V.; Cornil, J. *Chem. Rev.* **2004**, *104*, 4971.
(6) Choi, S. H.; Kim, B.; Frisbie, C. D. *Science* **2008**, *320*, 1482.
(7) Lu, Q.; Liu, K.; Zhang, H. M.; Du, Z. B.; Wang, X. H.; Wang, F. S. *ACS Nano* **2009**, *3*, 3861.
(8) Tuccitto, N.; Ferri, V.; Cavazzini, M.; Quici, S.; Zhavnerko, G.; Licciardello, A.; Rampi, M. A. *Nat. Mater.* **2009**, *8*, 359.
(9) Aguirre-Etcheverry, P.; O’Hare, D. *Chem. Rev.* **2010**, *110*, 4839.
(10) Ceccon, A.; Santi, S.; Orian, L.; Bisello, A. *Coord. Chem. Rev.* **2004**, *248*, 683.
(11) Low, P. J. *Coord. Chem. Rev.* **2012**, DOI: 10.1016/j.ccr.2012.08.008.
(12) Bruce, M. I.; Le Guennic, B.; Scoleri, N.; Zaitseva, N. N.; Halet, J.-F. *Organometallics* **2012**, *31*, 4701.
(13) Yu, M. P. Y.; Yam, V. W.-W.; Cheung, K.-K.; Mayr, A. *J. Organomet. Chem.* **2006**, *691*, 4514.
(14) Gauthier, N.; Argouarch, G.; Paul, F.; Humphrey, M. G.; Toupet, L.; Ababou-Girard, S.; Sabbah, H.; Hapiot, P.; Fabre, B. *Adv. Mater.* **2008**, *20*, 1952.
(15) Wuttke, E.; Pevny, F.; Hervault, Y. M.; Norel, L.; Drescher, M.; Winter, R. F.; Rigaut, S. *Inorg. Chem.* **2012**, *51*, 1902.
(16) Pevny, F.; Di Piazza, E.; Norel, L.; Drescher, M.; Winter, R. F.; Rigaut, S. *Organometallics* **2010**, *29*, 5912.
(17) Bruce, M. I.; Low, P. J.; Costuas, K.; Halet, J.-F.; Best, S. P.; Heath, G. A. *J. Am. Chem. Soc.* **2000**, *122*, 1949.
(18) Semenov, S. N.; Blacque, O.; Fox, T.; Venkatesan, K.; Berke, H. *J. Am. Chem. Soc.* **2010**, *132*, 3115.
(19) Venkatesan, K.; Blacque, O.; Berke, H. *Dalton Trans.* **2007**, 1091.
(20) Egler-Lucas, C.; Blacque, O.; Venkatesan, K.; López-Hernández, A.; Berke, H. *Eur. J. Inorg. Chem.* **2012**, *2012*, 1536.
(21) Zheng, Q.; Hampel, F.; Gladysz, J. A. *Organometallics* **2004**, *23*, 5896.
(22) Olivier, C.; Kim, B.; Touchard, D.; Rigaut, S. *Organometallics* **2008**, *27*, 509.
(23) Benameur, A.; Brignou, P.; Di Piazza, E.; Hervault, Y. M.; Norel, L.; Rigaut, S. *New J. Chem.* **2011**, *35*, 2105.
(24) Luo, L.; Benameur, A.; Brignou, P.; Choi, S. H.; Rigaut, S.; Frisbie, C. D. *J. Phys. Chem. C* **2011**, *115*, 19955.
(25) Field, L. D.; Turnbull, A. J.; Turner, P. *J. Am. Chem. Soc.* **2002**, *124*, 3692.

(26) Semenov, S. N.; Taghipourian, S. F.; Blacque, O.; Fox, T.; Venkatesan, K.; Berke, H. *J. Am. Chem. Soc.* **2010**, *132*, 7584.

(27) De Montigny, F.; Argouarch, G.; Costuas, K.; Halet, J. F.; Roisnel, T.; Toupet, L.; Lapinte, C. *Organometallics* **2005**, *24*, 4558.

(28) Frohnapfel, D. S.; Woodworth, B. E.; Thorp, H. H.; Templeton, J. L. *J. Phys. Chem. A* **1998**, *102*, 5665.

(29) Costuas, K.; Rigaut, S. *Dalton Trans.* **2011**, *40*, 5643.

(30) Paul, F.; Lapinte, C. *Coord. Chem. Rev.* **1998**, *178−180* (Part 1), 431.

(31) Halet, J.-F.; Lapinte, C. *Coord. Chem. Rev.* **2012**, DOI: 10.1016/j.ccr.2012.09.007.

(32) Bruce, M. I.; Costuas, K.; Davin, T.; Ellis, B. G.; Halet, J. F.; Lapinte, C.; Low, P. J.; Smith, M. E.; Skelton, B. W.; Toupet, L.; White, A. H. *Organometallics* **2005**, *24*, 3864.

(33) Guillemot, M.; Toupet, L.; Lapinte, C. *Organometallics* **1998**, *17*, 1928.

(34) Iyer, R. S.; Selegue, J. P. *J. Am. Chem. Soc.* **1987**, *109*, 910.

(35) Le Narvor, N.; Toupet, L.; Lapinte, C. *J. Am. Chem. Soc.* **1995**, *117*, 7129.

(36) Hoffert, W. A.; Rappe, A. K.; Shores, M. P. *Chem. Commun.* **2010**, *46*, 4710.

(37) Colbert, M. C. B.; Lewis, J.; Long, N. J.; Raithby, P. R.; Younus, M.; White, A. J. P.; Williams, D. J.; Payne, N. N.; Yellowlees, L.; Beljonne, D.; Chawdhury, N.; Friend, R. H. *Organometallics* **1998**, *17*, 3034.

(38) Field, L. D.; George, A. V.; Laschi, F.; Malouf, E. Y.; Zanello, P. *J. Organomet. Chem.* **1992**, *435*, 347.

(39) Baker, M. V.; Field, L. D.; Hambley, T. W. *Inorg. Chem.* **1988**, *27*, 2872.

(40) Allen, O. R.; Dalgarno, S. J.; Field, L. D.; Jensen, P.; Tumbull, A. J.; Willis, A. C. *Organometallics* **2008**, *27*, 2092.

(41) Field, L. D.; Li, H. L.; Dalgarno, S. J.; Turner, P. *Chem. Commun.* **2008**, 1680.

(42) Barclay, J. E.; Hills, A.; Hughes, D. L.; Leigh, G. J. *J. Chem. Soc., Dalton Trans.* **1988**, 2871.

(43) Taghipourian, S. F.; Berke, H. Unpublished Results.

(44) Bancroft, G. M.; Mays, M. J.; Prater, B. E. *J. Chem. Soc. A* **1970**, 956.

(45) Semenov, S. N.; Blacque, O.; Fox, T.; Venkatesan, K.; Berke, H. *Organometallics* **2010**, *29*, 6321.

(46) Lewis, J.; Khan, M. S.; Kakkar, A. K.; Raithby, P. R.; Fuhrmann, K.; Friend, R. H. *J. Organomet. Chem.* **1992**, *433*, 135.

(47) Adams, R. D.; Davison, A.; Selegue, J. P. *J. Am. Chem. Soc.* **1979**, *101*, 7232.

(48) Holmes, A. B.; Jones, G. E. *Tetrahedron Lett.* **1980**, *21*, 3111.

(49) Jones, K.; Lappert, M. F. *J. Chem. Soc.* **1965**, 1944.

(50) Jiao, H. J.; Costuas, K.; Gladysz, J. A.; Halet, J. F.; Guillemot, M.; Toupet, L.; Paul, F.; Lapinte, C. *J. Am. Chem. Soc.* **2003**, *125*, 9511.

(51) Akita, M.; Chung, M. C.; Sakurai, A.; Sugimoto, S.; Terada, M.; Tanaka, M.; Morooka, Y. *Organometallics* **1997**, *16*, 4882.

(52) Dembinski, R.; Lis, T.; Szafert, S.; Mayne, C. L.; Bartik, T.; Gladysz, J. A. *J. Organomet. Chem.* **1999**, *578*, 229.

(53) Szafert, S.; Gladysz, J. A. *Chem. Rev.* **2003**, *103*, 4175.

(54) Le Narvor, N.; Toupet, L.; Lapinte, C. *J. Am. Chem. Soc.* **1995**, *117*, 7129.

(55) Bruce, M. I.; Ellis, B. G.; Low, P. J.; Skelton, B. W.; White, A. H. *Organometallics* **2003**, *22*, 3184.

(56) Bruce, M. I.; Costuas, K.; Davin, T.; Halet, J.-F.; Kramarczuk, K. A.; Low, P. J.; Nicholson, B. K.; Perkins, G. J.; Roberts, R. L.; Skelton, B. W.; Smith, M. E.; White, A. H. *Dalton Trans.* **2007**, 5387.

(57) Meyer, W. E.; Amoroso, A. J.; Horn, C. R.; Jaeger, M.; Gladysz, J. A. *Organometallics* **2001**, *20*, 1115.

(58) Brady, M.; Weng, W.; Zhou, Y.; Seyler, J. W.; Amoroso, A. J.; Arif, A. M.; Böhme, M.; Frenking, G.; Gladysz, J. A. *J. Am. Chem. Soc.* **1997**, *119*, 775.

(59) Roberts, R. L.; Puschmann, H.; Howard, J. A. K.; Yamamoto, J. H.; Carty, A. J.; Low, P. J. *Dalton Trans.* **2003**, 1099.

(60) Fernández, F. J.; Blacque, O.; Alfonso, M.; Berke, H. *Chem. Commun.* **2001**, 1266.

(61) Mohr, W.; Stahl, J.; Hampel, F.; Gladysz, J. A. *Chem.—Eur. J.* **2003**, *9*, 3324.

(62) Le Narvor, N.; Lapinte, C. *J. Chem. Soc., Chem. Commun.* **1993**, 357.

(63) Hush, N. S. *Prog. Inorg. Chem.* **1967**, *8*, 391.

(64) Hush, N. S. *Coord. Chem. Rev.* **1985**, *64*, 135.

(65) Brunschwig, B.; Creutz, C.; Sutin, N. *Chem. Soc. Rev.* **2002**, *31*, 168.

(66) Paul, F.; Toupet, L.; Thépot, J.-Y.; Costuas, K.; Halet, J.-F.; Lapinte, C. *Organometallics* **2005**, *24*, 5464.

(67) Sutton, J. E.; Sutton, P. M.; Taube, H. *Inorg. Chem.* **1979**, *18*, 1017.

(68) Evans, C. E. B.; Naklicki, M. L.; Rezvani, A. R.; White, C. A.; Kondratiev, V. V.; Crutchley, R. J. *J. Am. Chem. Soc.* **1998**, *120*, 13096.

(69) Lin, Y.-C.; Chen, W.-T.; Tai, J.; Su, D.; Huang, S.-Y.; Lin, I.; Lin, J.-L.; Lee, M. M.; Chiou, M. F.; Liu, Y.-H.; Kwan, K.-S.; Chen, Y.-J.; Chen, H.-Y. *Inorg. Chem.* **2009**, *48*, 1857.

2.1 SUPPLEMENTARY INFORMATION

Stepwise Construction of an Iron-Substituted Rigid-Rod Molecular Wire: Targeting a Tetraferra-Tetracosa-Decayne

Supporting Information

Stepwise Construction of an Iron-Substituted Rigid-Rod Molecular Wire: Targeting a Tetraferra-Tetracosa-Decayne

Franziska Lissel[†], Thomas Fox[†], Olivier Blacque[†], Walther Polit[#], Rainer F. Winter[#],

Koushik Venkatesan[†] and Heinz Berke[*,†]

† Department of Inorganic Chemistry, University of Zürich, Winterthurerstrasse 190, CH-8057 Zürich, Switzerland

 # Faculty of Chemistry, University of Konstanz, Universitätsstraße 10, D-78457 Konstanz, Germany

* hberke@aci.uzh.ch

General Procedures

All experiments and measurements were carried out under a nitrogen atmosphere using Schlenk techniques or in a glove box (M. Braun 150B-G-II). Reagent grade benzene, toluene, pentane, diethyl ether and tetrahydrofuran were dried and distilled from sodium prior to use. Reagent grade dichloromethane and acetonitrile were dried and distilled from CaH_2. Deuterated solvents were dried and distilled likewise.
1,4-Bis(trimethylsilyl)buta-1,3-diyne was recrystallized from pentane prior to use. 1,2-Bis(diethylphosphinoethane) (depe)[1], 1,4-bis(trimethylstannyl)buta-1,3-diyne[2], 4-lithium-1-(trimethyl-silyl)-buta-1,3-diyne[3] and N,N-diethyl-1,1,1-trimethyl-stannyl-amine[4] were prepared based on literature protocols, *trans*-dichloro-di[1,2-bis(diethylphosphino)ethane]-iron(II) ($Fe(depe)_2Cl_2$)[5] and *trans*-diiodo-di[1,2-bis(diethylphosphino)-ethane]-iron(II) ($Fe(depe)_2I_2$)[6] in a variation of literature protocols.

NMR spectra were measured on a Bruker-DRX-500 spectrometer at 500 MHz for ^1H, 125.8 MHz for $^{13}C\{^1H\}$, 202.5 MHz for $^{31}P\{^1H\}$, 99.4 MHz for $^{29}Si\{^1H\}$, 168.5 MHz for $^{119}Sn\{^1H\}$, and on a Bruker Biospin at 500 MHz for ^1H and 202.5 MHz for $^{31}P\{^1H\}$. Low temperature measurements were carried out on a Varian Gemini-2000 spectrometer at 300.1 MHz for ^1H, 75.5 MHz for $^{13}C\{^1H\}$ and 121.5 MHz for $^{31}P\{^1H\}$. Chemical shifts for ^1H and ^{13}C are given in ppm relative to the solvent,[7] for ^{31}P relative to phosphoric acid, for ^{119}Sn relative to $SnMe_4$ and for ^{29}Si relative to $SiMe_4$. Unless noted otherwise, all NMR were recorded at room temperature. IR spectra were measured in KBr and recorded on a Perkin-Elmer Spectrum Two FT-IR spectrometer. Raman spectra were recorded on a Renishaw Ramanscope spectrometer (785 nm, 633 nm, 514 nm). CHN elemental analyses were performed with a LECO CHN-932 microanalyzer. Cyclic voltammograms were obtained with a BAS 100W Voltammetric Analyzer (low volume cell). The cell was equipped with an Au working electrode and a Pt counter electrode, and a nonaqueous reference electrode (Ag/AgCl). All sample solutions were 0.1M in Bu_4NPF_6 and recorded with a scan rate of 100 mV/s. Ferrocene was used as an external standard (in THF: $E_{1/2}$ = 927 mV, in CH_2Cl_2: $E_{1/2}$ = 1172 mV under the chosen conditions). A BAS 100W program was employed for the data analysis.

X-ray diffraction analyses: single-crystal X-ray diffraction data were collected at 183(2) K on a Xcalibur diffractometer (Agilent Technologies, Ruby CCD detector) for all compounds using a single wavelength Enhance X-ray source with MoKα radiation (λ= 0.71073 Å).[8] The selected suitable single crystals were mounted using polybutene oil on the top of a glass fiber fixed on a goniometer head and immediately transferred to the diffractometer. Pre-experiment, data collection, data reduction and analytical absorption corrections[9] were performed with the program suite *CrysAlis*^{Pro}.[8] The crystal structures were solved with SHELXS97[10] using direct methods. The structure refinements were performed by full-matrix least-squares on F^2 with SHELXL97.[11] All programs used during the crystal structure determination process are included in the WINGX software.[11] PLATON[12] was used to check the result of the X-ray analyses and to obtain the values of long distances as Fe···Fe in the dinuclear species. For more details about the refinements, see the Refine_special_details and Iucr_refine_instructions_details sections in the Crystallographic Information files (Supporting Information). CCDC-916041 (for **2**), CCDC-916042 (for **3**), CCDC-916043 (for **4**), and CCDC-916044 (for **5**) contain the supplementary crystallographic data (excluding structure factors) for this paper. These data can be obtained free of charge from The Cambridge Crystallographic Data Centre via www.ccdc.cam.ac.uk/data_request/cif

The OTTLE cell was home-built and comprises a Pt-mesh working and counter electrode and a thin silver wire as a pseudo-reference electrode sandwiched between the CaF_2 windows of a conventional liquid IR cell. The working electrode is positioned in the center of the spectrometer beam. FT-IR spectra were recorded on a Thermo is10 instrument. UV/Vis/NIR spectra were obtained on a TIDAS fiberoptic diode array spectrometer (combined MCS UV/NIR and PGS NIR instrumentation) from j&m.

Syntheses

Syntheses of the starting materials

Trans-dichloro-di[1,2-bis(diethylphosphino)ethane]-iron(II) ($\mathrm{Fe(depe)_2Cl_2}$)[5]

$\mathrm{FeCl_2}$ (2.54 g, 20 mmol) was suspended in THF (150 mL) and a solution of 1,2-Bis(diethylphosphino)ethane (9.4 mL, 8.27 g, 40.1 mmol) in THF (50 mL) was added. After stirring at rt for 12h, the solution was filtered over a plug of diatomaceous earth. The solvent was removed *in vacuo* and the obtained green solid washed with pentane (3 x 50 mL) and dried *in vacuo*. Yield: 10.41 g, 19.3 mmol, 97%.

Anal. Calcd. for $\mathrm{C_{20}H_{48}FeCl_2}$: C, 44.55; H, 8.97. **Found**: C, 44.74; H, 8.76. **^{1}H NMR** (300.1 MHz, 243 K, $\mathrm{CD_2Cl_2}$): δ = 2.30 - 2.14 (m, 8H, $\mathrm{C}\mathit{H}_2$-$\mathrm{C}\mathit{H}_2$), 2.06 - 1.88 (m, 8H, $\mathrm{C}\mathit{H}_2$-$\mathrm{CH_3}$), 1.88 - 1.69 (m, 8H, $\mathrm{C}\mathit{H}_2$-$\mathrm{CH_3}$), 1.35 - 1.14 (m, 24H, $\mathrm{CH_2}$-$\mathrm{C}\mathit{H}_3$). **^{13}C{^{1}H} NMR** (75.5 MHz, 243 K, $\mathrm{CD_2Cl_2}$): δ = 20.7 - 19.9 (m, $\mathrm{CH_2}$-$\mathrm{CH_3}$), 17.8 - 16.8 (m, $\mathrm{CH_2}$-$\mathrm{CH_2}$), 10.2 - 9.5 (m, $\mathrm{CH_2}$-$\mathrm{CH_3}$). **^{31}P{^{1}H} NMR** (121.5 MHz, 243 K, $\mathrm{CD_2Cl_2}$): δ = 59.0 (s). **^{31}P{^{1}H} NMR** (121.5 MHz, 193 K, THF-d_8): δ = 63.7 (s).

Trans-diiodo-di[1,2-bis(diethylphosphino)ethane]-iron(II) ($\mathrm{Fe(depe)_2I_2}$)[6]

$\mathrm{Fe(depe)_2Cl_2}$ (1.08 g, 2 mmol) and NaI (6 g, 40 mmol) were refluxed in toluene (150 mL) for 2 h. The yellow solution was filtered over a plug of diatomaceous earth and the solvent removed *in vacuo*. Yield: 1.42 g, 1.96 mmol, 98%.

Anal. Calcd. for $\mathrm{C_{20}H_{48}FeI_2}$: C, 33.26; H, 6.70. **Found**: C, 33.63; H, 6.59. **^{1}H NMR** (300.1 MHz, 243 K, $\mathrm{CD_2Cl_2}$): δ = 2.24 - 2.05 (m, 8H, $\mathrm{C}\mathit{H}_2$-$\mathrm{CH_3}$), 1.66 - 1.48 (m, 8H, $\mathrm{C}\mathit{H}_2$-$\mathrm{CH_3}$), 1.44 - 1.34 (m, 8H, $\mathrm{C}\mathit{H}_2$-$\mathrm{C}\mathit{H}_2$), 1.23 - 1.08 (m, 24H, $\mathrm{CH_2}$-$\mathrm{C}\mathit{H}_3$). **^{13}C{^{1}H} NMR** (75.5 MHz, 243 K, $\mathrm{CD_2Cl_2}$): δ = 26.9 - 25.5 (m, $\mathrm{CH_2}$-$\mathrm{CH_3}$), 11.9 - 10.7 (m, $\mathrm{CH_2}$-$\mathrm{CH_3}$), 10.7 - 9.3 (m, $\mathrm{CH_2}$-$\mathrm{CH_2}$). **^{31}P{^{1}H} NMR** (121.5 MHz, 243 K, $\mathrm{CD_2Cl_2}$): δ = 60.5 (s). **^{31}P{^{1}H} NMR** (121.5 MHz, 193 K, THF-d_8): δ = 65.9 (s).

Syntheses of compounds 2 - 7

[I–Fe(depe)$_2$–C$_4$–Fe(depe)$_2$–I] 2

$\mathrm{Fe(depe)_2I_2}$ (289 mg, 0.4 mmol) and 1,4-bis(trimethylstannyl)buta-1,3-diyne (77 mg, 0.205 mmol) were suspended in THF (5 mL) and heated to reflux for 4.5 h. After addition of diethyl ether (5 mL) the solution was decanted and the obtained burgundy red solid was washed with THF/diethyl ether (1:4) until the washings were colourless. The obtained product was dried *in vacuo*. Yield: 210 mg, 0.17 mmol, 88%. Crystals suitable for X-ray diffraction were grown by slow evaporation of benzene at rt.

Anal. Calcd. for $\mathrm{C_{44}H_{96}Fe_2I_2P_8}$: C, 42.67; H, 7.81. **Found**: C, 42.39; H, 8.02. **IR** (KBr, cm^{-1}): 1940 ($\nu_{\mathrm{C\equiv C}}$). **Raman** (785 nm, cm^{-1}): 2085 ($\nu_{\mathrm{C\equiv C}}$). **ESI-MS** ($\mathrm{C_{44}H_{96}Fe_2\,I_2P_8}$): m/z = 1238 ($[\mathrm{M}]^+$, 100%). **^{1}H NMR** (500 MHz, $\mathrm{C_6D_6}$): δ = 2.76 - 2.65 (m, 8H, $\mathrm{C}\mathit{H}_2$-$\mathrm{CH_3}$), 2.39 - 2.27 (m, 8H, $\mathrm{C}\mathit{H}_2$-$\mathrm{CH_3}$), 1.96 - 1.83 (m, 16H, $\mathrm{C}\mathit{H}_2$-$\mathrm{CH_3}$ and $\mathrm{C}\mathit{H}_2$-$\mathrm{C}\mathit{H}_2$), 1.83 - 1.72 (m, 8H, $\mathrm{C}\mathit{H}_2$-$\mathrm{C}\mathit{H}_2$), 1.67 - 1.56 (m, 8H, $\mathrm{C}\mathit{H}_2$-$\mathrm{CH_3}$), 1.18 - 1.08 (m, 48H, $\mathrm{CH_2}$-$\mathrm{C}\mathit{H}_3$). **^{13}C{^{1}H} NMR** (125.8 MHz, $\mathrm{C_6D_6}$): δ = 22.50 (d, $^1J_{\mathrm{C\text{-}P}}$ = 563.5 Hz, $\mathrm{CH_2}$-$\mathrm{CH_3}$), 22.07 - 21.58 (m, $\mathrm{CH_2}$-$\mathrm{CH_2}$), 10.31 (d, $^2J_{\mathrm{C\text{-}P}}$ = 49.1 Hz, $\mathrm{CH_2}$-$\mathrm{CH_3}$). **^{31}P {^{1}H} NMR** (202.5 MHz, $\mathrm{C_6D_6}$): δ = 68.3 (s). **^{1}H NMR** (300.1 MHz, 193 K, THF-d_8): δ = 2.54 - 2.24 (m, 16H, $\mathrm{C}\mathit{H}_2$-$\mathrm{CH_3}$), 1.98 - 1.59 (m, 32H, $\mathrm{C}\mathit{H}_2$-$\mathrm{CH_3}$ and $\mathrm{C}\mathit{H}_2$-$\mathrm{C}\mathit{H}_2$, overlaps with THF peak), 1.26 - 1.01 (m, 48H, $\mathrm{CH_2}$-$\mathrm{C}\mathit{H}_3$). **^{13}C{^{1}H} NMR** (300.1 MHz, 193 K, THF-d_8): δ = 10.96 - 10.21 (m, $\mathrm{CH_2}$-$\mathit{C}\mathrm{H_3}$, low intensity). **^{31}P{^{1}H} NMR** (121.5 MHz, 193 K, THF-d_8): δ = 69.8 (s).

[($\mathbf{Me_3Si{-}C_4}$)–Fe(depe)$_2$–$\mathbf{C_4}$–Fe(depe)$_2$–($\mathbf{C_4{-}SiMe_3}$)] 3

1,4-bis(trimethylsilyl)buta-1,3-diyne (292 mg, 1.5 mmol) was reacted with MeLi/LiBr solution (2.2 M in diethyl ether, 545 μL, 1.2 mmol) according to literature protocols[3] to give Li-C≡C-C≡C-$SiMe_3$/LiBr. The obtained solid was dried *in vacuo* and used without further purification. The lithiated reagent and **2** (248 mg, 0.2 mmol) were dispersed in toluene (15 mL) and heated to 80 °C. The color of the solution changed from red to orange. Monitoring with $^{31}P\{^1H\}$ NMR showed the complete consumption of the starting material after 6 hours. The solution was filtered over a plug of diatomaceous earth and the toluene removed *in vacuo*. The obtained solid was washed with acetonitrile and the product, a yellow powder, was extracted with diethyl ether, filtered over a plug of diatomaceous earth and dried *in vacuo*. Yield: 218 mg, 0.18 mmol, 88%. Crystals suitable for X-ray diffraction were obtained by slow evaporation of benzene at rt.

Anal. Calcd. for $C_{58}H_{114}Fe_2P_8Si_2$: C, 56.77; H, 9.36. **Found**: C, 56.59; H, 9.31. **IR** (KBr, cm^{-1}): 2160, 2079 (sh at 2106), 1978, 1951 ($\nu_{C\equiv C}$). **Raman** (785 nm, cm^{-1}): 2093, 2076 ($\nu_{C\equiv C}$). **ESI-MS** ($C_{58}H_{114}Fe_2P_8Si_2$): *m/z* = 1227 ($[M]^+$, 100%). **^{1}H NMR** (500 MHz, C_6D_6): δ = 2.38 - 2.28 (m, 8H, $\mathrm{C}\mathit{H}_2\mathrm{-CH_3}$), 2.24 - 2.13 (m, 8H, $\mathrm{C}\mathit{H}_2\mathrm{-CH_3}$), 1.66 - 1.46 (m, 32H, $\mathrm{C}\mathit{H}_2\mathrm{-CH_3}$ and $\mathrm{C}\mathit{H}_2\mathrm{-C}\mathit{H}_2$), 1.12 - 1.01 (m, 48H, $\mathrm{CH_2-C}\mathit{H}_3$), 0.17 (s, 18H, $Si(CH_3)_3$). **^{13}C{^{1}H} NMR** (125.8 MHz, C_6D_6): δ = 145.72 - 145.14 (m, C_α (FeC_4Si chain)) 106.36 (s, C_β (FeC_4Fe chain)), 99.16 - 98.46 (m, C_α (FeC_4Fe chain)), 98.84 (s, C_β (FeC_4Si chain)), 95.25 (s, C_γ (FeC_4Si chain)), 62.37 (s, C_δ (FeC_4Si chain)), 21.32 (d, $^1J_{C\text{-}P}$ = 154.7 Hz, $\mathrm{CH_2-CH_3}$), 21.30 - 20.86 (m, $\mathrm{CH_2-CH_2}$), 9.82 (d, $^2J_{C\text{-}P}$ = 42.8 Hz, $\mathrm{CH_2-CH_3}$), 1.39 (s, $Si(CH_3)_3$). **^{31}P{^{1}H} NMR** (121.5 MHz, C_6D_6): δ = 76.3 (s). **^{29}Si{^{1}H} NMR** (99.4 MHz, C_6D_6): δ = - 21.82 (s).

[(H–$\mathbf{C_4}$)–Fe(depe)$_2$–$\mathbf{C_4}$–Fe(depe)$_2$–($\mathbf{C_4}$–H)] 4

3 (245 mg, 0.2 mmol) was dissolved in THF (10 mL) and stirred at rt. TBAF solution (1 M in THF containing 5% H_2O, 0.6 mL, 0.6 mmol) was diluted with 4.4 mL of THF and added dropwise. The mixture was stirred for 1 h at rt, then acetonitrile (10 mL) was added and the solution was concentrated *in vacuo* to a volume of 10 mL (removal of THF). The yellow precipitate forming upon concentration was filtered off and washed with acetonitrile and pentane. The product, a yellow solid, was extracted with THF/diethyl ether (1:4), filtered over a plug of diatomaceous earth and dried *in vacuo*. Yield: 164.6 mg, 0.152 mmol, 76%. Crystals suitable for X-ray diffraction were obtained from THF/acetonitrile at –20 °C.

Anal. Calcd. for $C_{52}H_{98}Fe_2P_8$: C, 57.68; H, 9.12. **Found**: C, 57.35; H, 9.06. **IR** (KBr, cm^{-1}): 3309, 3267 ($\nu_{C\equiv C-H}$); 2090, 1944 (sh at 1962) ($\nu_{C\equiv C}$). **Raman** (785nm, cm^{-1}): 2108, 2078 ($\nu_{C\equiv C}$). **ESI-MS** ($C_{52}H_{98}Fe_2P_8$): *m/z* = 1082 ($[M]^+$, 100%). **^{1}H NMR** (500 MHz, C_6D_6): δ = 2.38 - 2.28 (m, 8H, $\mathrm{C}\mathit{H}_2\mathrm{-CH_3}$), 2.27 - 2.17 (m, 8H, $\mathrm{C}\mathit{H}_2\mathrm{-CH_3}$), 1.71 - 1.51 (m, 32H, $\mathrm{C}\mathit{H}_2\mathrm{-CH_3}$ and $\mathrm{C}\mathit{H}_2\mathrm{-C}\mathit{H}_2$), 1.26 (s, 2H, FeC_4H), 1.14 - 1.05 (m, 48H, $\mathrm{CH_2-C}\mathit{H}_3$). **^{13}C{^{1}H} NMR** (125.8 MHz, C_6D_6): δ = 140.04 (p, $^2J_{C\text{-}P}$ = 25.8 Hz, C_α (FeC_4H chain)), 106.36 (s, C_β (FeC_4Fe chain)), 98.79 (p, $^2J_{C\text{-}P}$ = 28.9 Hz, C_α (FeC_4Fe chain)), 97.26 (s, C_β (FeC_4H chain)), 74.50 (s, C_γ (FeC_4H chain)), 48.93 (s, C_δ (FeC_4H chain)), 21.36 (d, $^1J_{C\text{-}P}$ = 125.8 Hz, $\mathrm{CH_2-CH_3}$), 21.42 - 20.98 (m, $\mathrm{CH_2-CH_2}$), 9.82 (d, $^2J_{C\text{-}P}$ = 30.2 Hz, $\mathrm{CH_2-CH_3}$). **^{31}P{^{1}H} NMR** (202.5 MHz, C_6D_6): δ = 76.2 (s).

[($\mathbf{Me_3Sn{-}C_4}$)–Fe(depe)$_2$–$\mathbf{C_4}$–Fe(depe)$_2$–($\mathbf{C_4{-}SnMe_3}$)] 5

4 (217 mg, 0.2 mmol) was dissolved THF (15 mL) and a solution of N,N-diethyl-1,1,1-trimethylstannanamine (190 mg, 0.8 mmol) in 5 mL THF was added. The mixture was heated to reflux for 2 h, then the solvent was removed *in vacuo* and the resulting yellow solid washed with acetonitrile. The yellow product was extracted with diethyl ether/pentane (1:1), filtered over a plug of diatomaceous earth and dried *in vacuo*. Yield: 251 mg, 0.178 mmol, 89%. Crystals suitable for X-ray diffraction were obtained in THF/benzene/acetonitrile at – 20 °C.

Anal. Calcd. for $C_{58}H_{114}Fe_2P_8Sn_2$: C, 49.46; H, 8.16. **Found**: C, 49.38; H, 8.05. **IR** (KBr, cm^{-1}): 2113, 2085, 1951 (sh at 1970) ($\nu_{C\equiv C}$). **Raman** (785nm, cm^{-1}): 2102 ($\nu_{C\equiv C}$). **ESI-MS** ($C_{58}H_{114}Fe_2P_8Sn_2$): *m/z* = 1408 ($[M]^+$, 100%). **^{1}H NMR** (500 MHz, C_6D_6): δ = 2.41 - 2.30 (m, 8H, $\mathrm{C}\mathit{H}_2\mathrm{-CH_3}$), 2.25 - 2.13 (m, 8H, $\mathrm{C}\mathit{H}_2\mathrm{-CH_3}$), 1.68 - 1.48 (m, 32H, $\mathrm{C}\mathit{H}_2\mathrm{-CH_3}$ and $\mathrm{C}\mathit{H}_2\mathrm{-C}\mathit{H}_2$), 1.13 - 1.02 (m, 48H, $\mathrm{CH_2-C}\mathit{H}_3$), 0.06 (s,(d, satellites, $^2J_{H\text{-}Sn}$ = 60 MHz), 18H, $Sn(CH_3)_3$). **^{13}C{^{1}H} NMR** (125.8 MHz, C_6D_6): δ = 139.82 (p, $^2J_{C\text{-}P}$ = 24.5 Hz, C_α (FeC_4Sn chain)), 106.40 (s, C_β (FeC_4Fe chain)), 99.74 - 98.28 (m, C_α (FeC_4Fe chain)), 99.34 (s, C_β (FeC_4Sn chain)), 99.26 (s, C_γ (FeC_4Sn chain)), 61.78 (s, C_δ (FeC_4Sn chain)), 21.34 (d, $^1J_{C\text{-}P}$ = 144.7 Hz, $\mathrm{CH_2-CH_3}$), 21.33 - 20.88 (m, $\mathrm{CH_2-CH_2}$), 9.83 (d, $^2J_{C\text{-}P}$ = 37.7 Hz, $\mathrm{CH_2-CH_3}$), -7.47 (s, $Sn(CH_3)_3$). **^{31}P{^{1}H} NMR** (202.5 MHz, C_6D_6): δ = 76.1 (s). **^{119}Sn{^{1}H} NMR** (168.5 MHz, C_6D_6): δ = - 36.33 (s).

[I–Fe(depe)$_2$–C$_4$–Fe(depe)$_2$–C$_4$–Fe(depe)$_2$–C$_4$–Fe(depe)$_2$–I] 6

5 (141 mg, 0.1 mmol) and Fe(depe)$_2$I$_2$ (148 mg, 0.205 mmol) were suspended in toluene (15 mL). The mixture was heated to 80 °C under vigorous stirring. Monitoring with ^{31}P{^{1}H} NMR showed a complete consumption of the starting material after 15 minutes. Pentane (20 ml) was added and the pale red precipitate separated from the solution by centrifugation. The precipitate was washed with pentane (3 x 10 mL) and dried *in vacuo* to give the title compound. Yield: 199 mg, 0.087 mmol, 87%.

Anal. Calcd. for $C_{92}H_{192}Fe_4I_2P_{16}$: C, 48.65; H, 8.52. **Found**: C, 48.32; H, 8.35. **IR** (KBr, cm^{-1}): 2089, 2025, 1940, 1878 ($\nu_{C\equiv C}$). **Raman** (514nm, cm^{-1}): 2099, 2002 ($\nu_{C\equiv C}$). **ESI-MS** ($C_{92}H_{192}Fe_4I_2P_{16}$): *m/z* = 2271 ([M]$^+$, 100%), 1136 ([M]$^{2+}$, 2%), 1033 ([M-(depe)]$^{2+}$, 15%), 929 ([M-(depe)$_2$]$^{2+}$, 23%), 826 ([M-(depe)$_3$]$^{2+}$, 30%). **^{1}H NMR** (500 MHz, C_7D_8): Signal intensity was too low due to poor solubility. **^{31}P{^{1}H} NMR** (202.5 MHz, C_7D_8): δ = 77. 6 (s, 8P, inner Fe(depe$_2$)$_2$ cores), 68.3 (s, 8P, outer Fe(depe)$_2$ cores).

[(Me$_3$SiC$_4$)–Fe(depe)$_2$–C$_4$–Fe(depe)$_2$–C$_4$–Fe(depe)$_2$–C$_4$–Fe(depe)$_2$–(C$_4$–SiMe$_3$)] 7

1,4-bis(trimethylsilyl)buta-1,3-diyne (73 mg, 0.375 mmol) was reacted with MeLi/LiBr solution (2.2 M in diethyl ether, 136 µL, 0.3 mmol) according to literature protocols[3] to give Li-C≡C-C≡C-SiMe$_3$/LiBr. The obtained solid was dried *in vacuo* and used without further purification. The lithiated reagent and **6** (113.5 mg, 0. 05 mmol) were dispensed in toluene (15 mL) and heated to 80 °C. Monitoring with ^{31}P{^{1}H} NMR showed a complete consumption of the starting material after 6 hours. The solution was filtered over a plug of diatomaceous earth and the toluene removed *in vacuo*. The obtained solid was washed with pentane and the product extracted with toluene and dried *in vacuo*. Yield: 80.2 mg, 0.0355 mmol, 71%.

Anal. Calcd. for $C_{106}H_{210}Fe_4P_{16}Si_2$: C, 56.34; H, 9.37. **Found**: C, 56.17; H, 9.29. **IR** (KBr, cm^{-1}): 2161, 2078 (sh at 2037), 1973, 1941 (sh at 1924), 1879 ($\nu_{C\equiv C}$). **Raman** (633nm, cm^{-1}): 2095, 1985 ($\nu_{C\equiv C}$). **ESI-MS** ($C_{106}H_{210}Fe_4P_{16}Si_2$): *m/z* = 2260 ([M]$^+$, 41%), 1130 ([M]$^{2+}$, 100%). **^{1}H NMR** (500 MHz, C_6D_6): δ = 2.44 - 2.20 (m, 32H, C*H*$_2$-CH$_3$), 1.75 - 1.49 (m, 64H, C*H*$_2$-CH$_3$ and C*H*$_2$-C*H*$_2$), 1.27 - 1.17 (m, 48H, CH$_2$-C*H*$_3$, inner Fe(depe)$_2$ cores), 1.17 - 1.10 (m, 24H, CH$_2$-C*H*$_3$, outer Fe(depe)$_2$ cores), 1.10 - 1.03 (m, 24H, CH$_2$-C*H*$_3$, outer Fe(depe)$_2$ cores), 0.18 (s, 18H, Si(CH$_3$)$_3$). **^{13}C{^{1}H} NMR** (125.8 MHz, C_6D_6): δ = 146.85 - 146.00 (m, C_α (FeC$_4$Si chain)), 107.18 (s, Fe-C≡*C*), 106.49 (s, Fe-C≡*C*), 105.69 (s, Fe-C≡*C*), 103.95 - 103.05 (m, Fe-*C*≡C), 99.32 - 98.43 (m, Fe-*C*≡C), 98.71 (s, C_β (FeC$_4$Si chain)), 95.40 (s, C_γ (FeC$_4$Si chain)), 95.07 - 94.10 (m, Fe-*C*≡C), 61.97 (s, C_δ (FeC$_4$Si chain)), 21.74 - 21.52 (m, *C*H$_2$-CH$_3$ and *C*H$_2$-*C*H$_2$), 21.39 (dm, $^1J_{C\text{-}P}$ = 150.9 Hz, *C*H$_2$-CH$_3$), 21.33 - 20.93 (m, *C*H$_2$-*C*H$_2$), 9.97 (s, CH$_2$-*C*H$_3$, inner Fe(depe)$_2$ cores), 9.86 (d, $^2J_{C\text{-}P}$ = 44.0 Hz, CH$_2$-*C*H$_3$, outer Fe(depe)$_2$ cores), 1.43 (s, Si(CH$_3$)$_3$). **^{31}P{^{1}H} NMR** (202.5 MHz, C_6D_6): δ = 79. 3 (s, 8P, inner Fe(depe)$_2$ cores), 77.5 (s, 8P, outer Fe(depe)$_2$ cores). **^{29}Si{^{1}H} NMR** (99.4 MHz, C_6D_6): δ = - 22.08 (s).

NMR - Studies

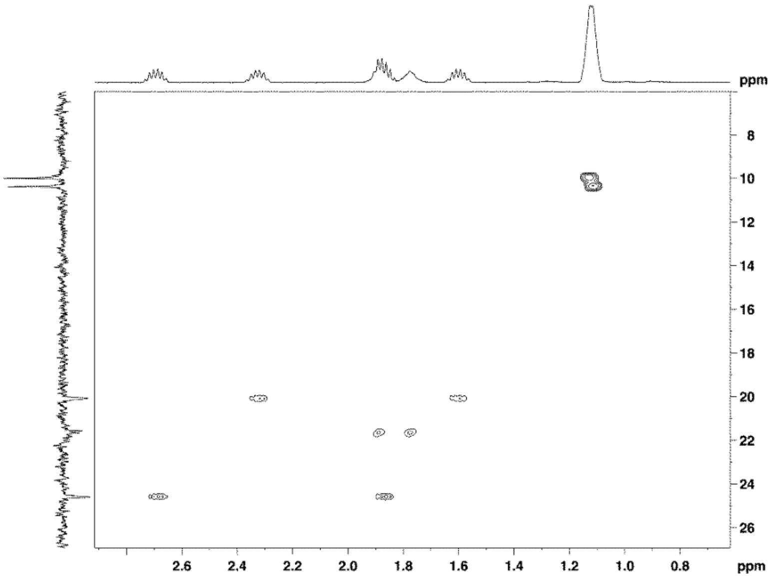

Figure S1. C, H - Correlation of **2** in C_6D_6.

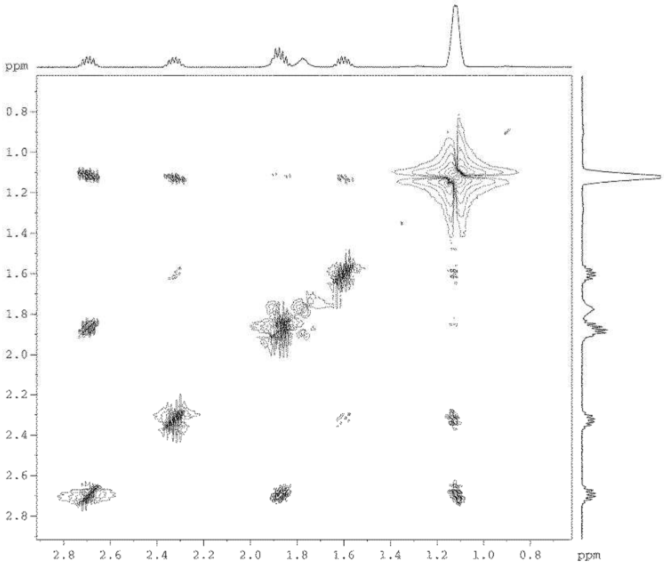

Figure S2. ^{1}H - COSY of **2** in C_6D_6.

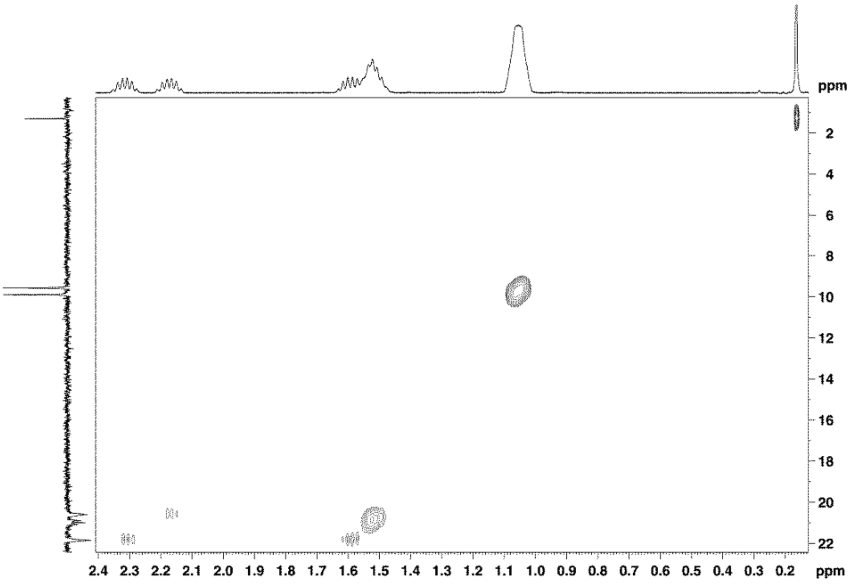

Figure S3. C, H - Correlation of **3** in C_6D_6.

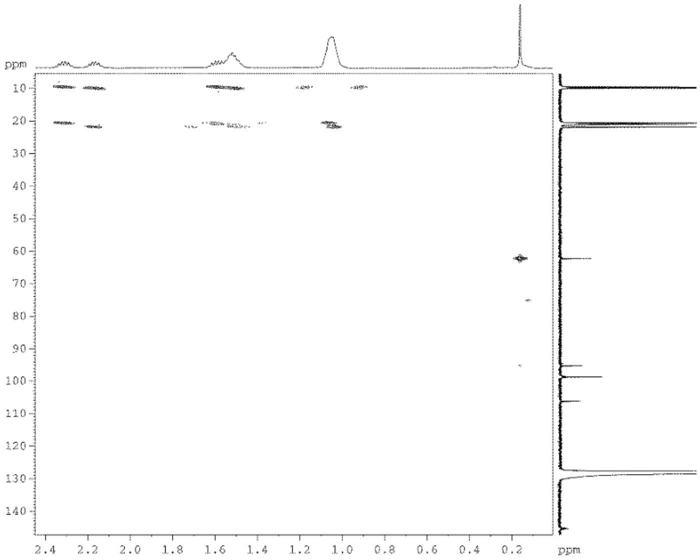

Figure S4. C, H - Correlation (long range) of **3** in C_6D_6.

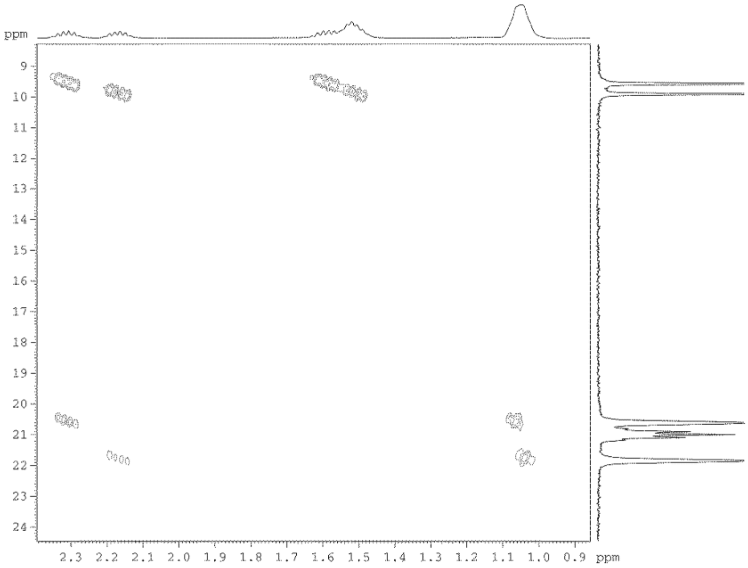

Figure S5. C, H - Correlation (long range) of **3** in C_6D_6.

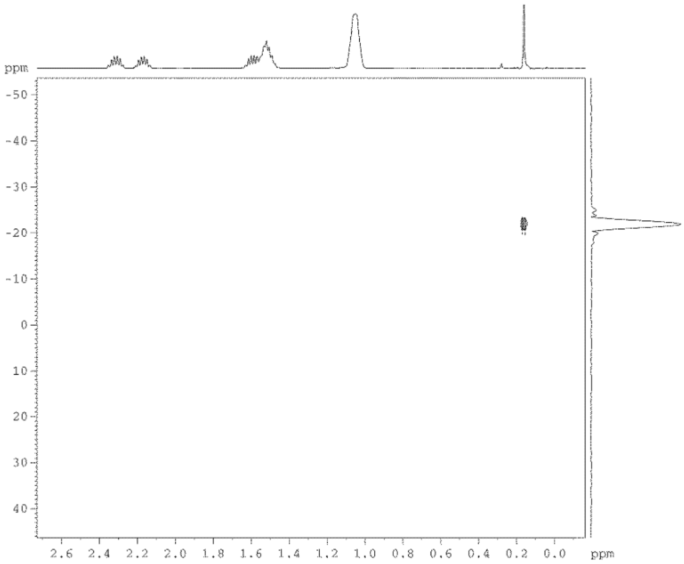

Figure S6. ^{1}H, ^{29}Si - HMBC of **3** in C_6D_6.

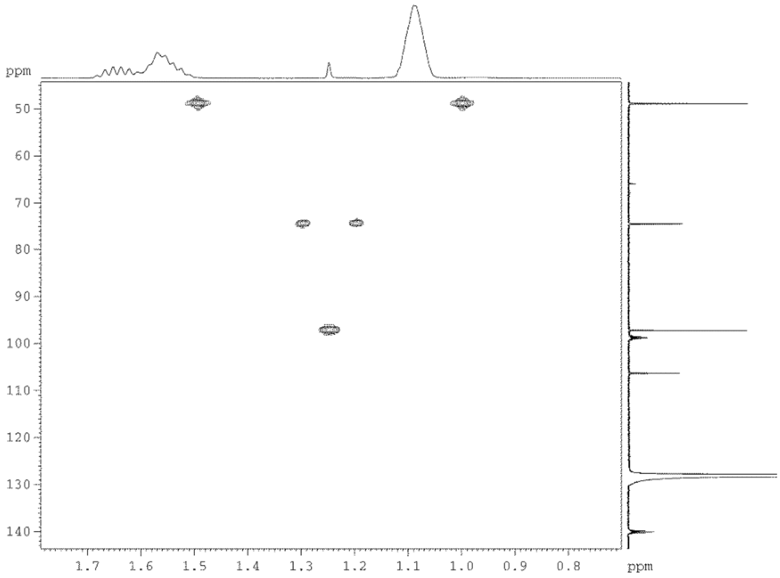

Figure S7. C, H - Correlation (long range) of **4** in C_6D_6.

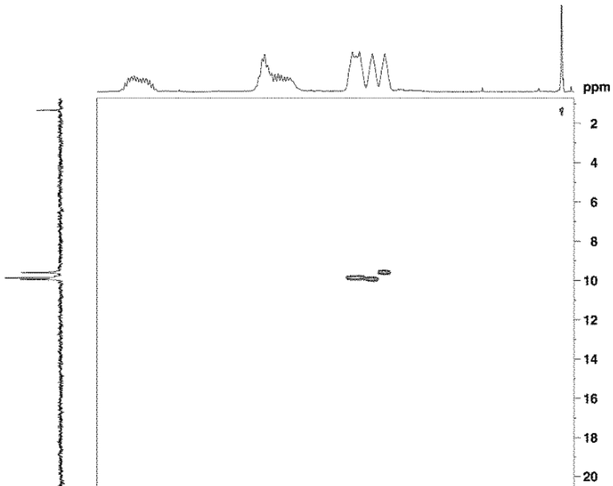

Figure S8. C, H - Correlation of **7** in C_6D_6.

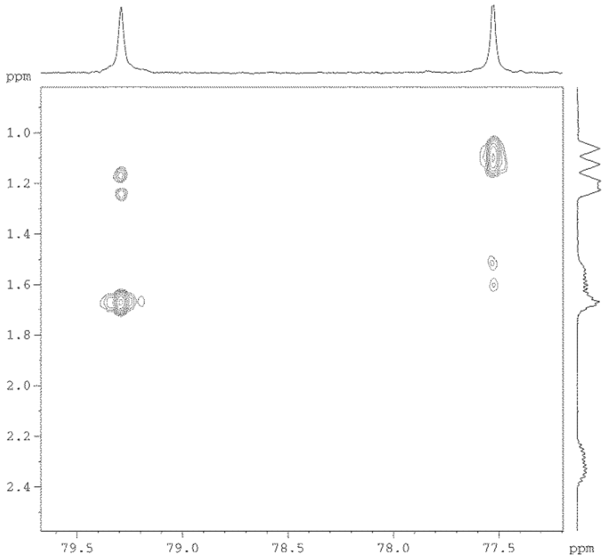

Figure S9. P, H - Correlation of **7** in C_6D_6.

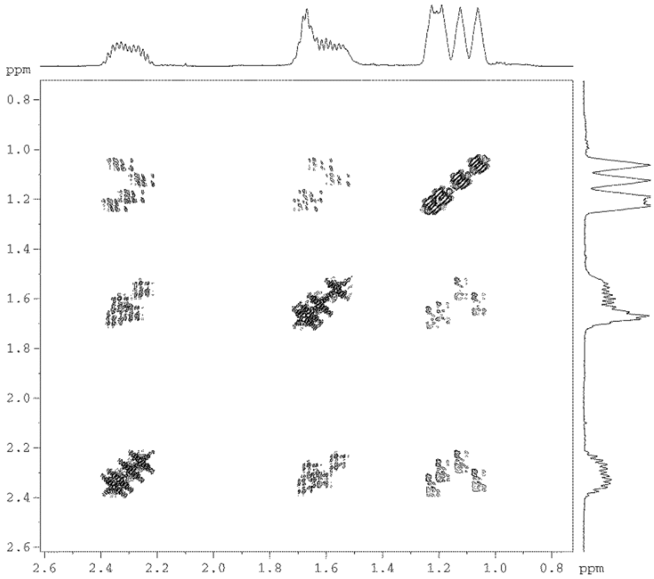

Figure S10. ^{1}H - COSY of **7** in C_6D_6.

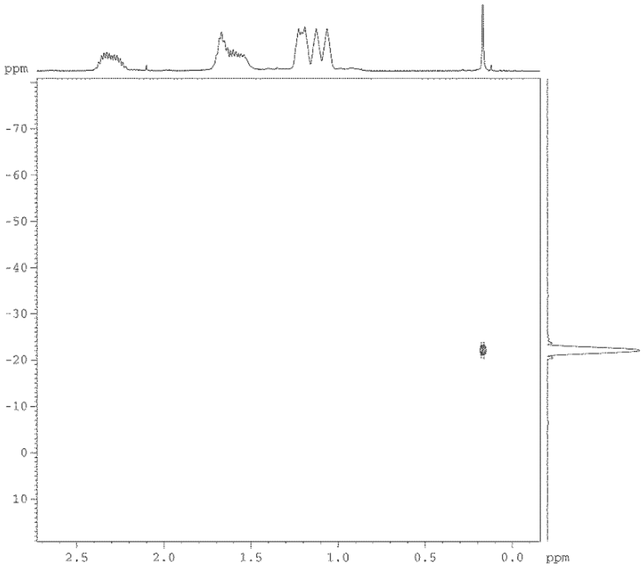

Figure S11. ^{1}H, ^{29}Si - HMBC of **7** in C_6D_6.

X-ray diffraction

Table S1. Summary of the X-ray diffraction studies of compounds **2** and **3**.

	2	**3**
CCDC	916041	916042
empirical formula	$C_{44}H_{96}Fe_2I_2P_8$	$C_{58}H_{114}Fe_2P_8Si_2$, C_6H_6
formula weight (g·mol^{-1})	1238.47	1305.24
temperature (K)	183(2)	183(2)
wavelength (Å)	0.71073	0.71073
crystal system, space group	triclinic, $P\bar{1}$	orthorhombic, *F* d d d
a (Å)	10.1979(9)	20.5030(5)
b (Å)	11.5601(10)	25.9009(6)
c (Å)	12.8120(9)	55.7178(9)
α (deg)	106.968(7)	90
β (deg)	95.428(7)	90
γ (deg)	103.682(8)	90
volume (Å^3)	1381.7(2)	29588.7(11)
Z, density (calcd) (Mg·m^{-3})	1, 1.488	16, 1.172
abs coefficient (mm^{-1})	1.902	0.632
F(000)	638	11264
crystal size (mm^3)	0.13 x 0.10 x 0.06	0.34 x 0.31 x 0.28
θ range (deg)	2.79 to 30.51	2.59 to 25
reflections collected	25809	48658
reflections unique	8437 / R_{int} = 0.0338	6527 / R_{int} = 0.0286
completeness to θ (%)	99.9	99.9
absorption correction	analytical	analytical
max/min transmission	0.917 / 0.824	0.885 / 0.853
data / restraints / parameters	6501 / 6 / 282	5013 / 161 / 444
goodness-of-fit on F^2	0.979	1.061
final R_1 and wR_2 indices [$I > 2\sigma(I)$]	0.0327, 0.0704	0.0582, 0.1580
R_1 and wR_2 indices (all data)	0.0479, 0.0732	0.0733, 0.1663

The unweighted R-factor is $R_1 = \Sigma(Fo - Fc)/\Sigma Fo$; $I > 2\ \sigma(I)$,*the weighted R-factor is* $wR_2 = \{\Sigma w(Fo^2 - Fc^2)^2/\Sigma w(Fo^2)^2\}^{1/2}$.

Table S2. Summary of the X-ray diffraction studies of compounds **4** and **5**.

	4	**5**
CCDC	916043	916044
empirical formula	$C_{52}H_{98}Fe_2P_8$	$C_{58}H_{114}Fe_2P_8Sn_2$, C_6H_6
formula weight (g·mol^{-1})	1082.76	1486.48
temperature (K)	183(2)	183(2)
wavelength (Å)	0.71073	0.71073
crystal system, space group	tetragonal, *P* 4/n n c	orthorhombic, *F* d d d
a (Å)	10.4243(2)	20.1791(6)
b (Å)	10.4243(2)	26.1862(11)
c (Å)	28.0294(9)	56.2511(12)
α (deg)	90	90
β (deg)	90	90
γ (deg)	90	90
volume (Å^3)	3045.84(13)	29723.9(17)
Z, density (calcd) (Mg·m^{-3})	2, 1.181	16, 1.329
abs coefficient (mm^{-1})	1164	1.254
F(000)	638	12416
crystal size (mm^3)	0.31 x 0.21 x 0.02	0.18 x 0.12 x 0.09
θ range (deg)	2.76 to 26.37	2.55 to 25.35
reflections collected	14925	47527
reflections unique	1567 / R_{int} = 0.0607	6806 / R_{int} = 0.0750
completeness to θ (%)	99.9	99.9
absorption correction	analytical	analytical
max/min transmission	0.987 / 0.861	0.921 / 0.874
data / restraints / parameters	942 / 0 / 103	4386 / 146 / 408
goodness-of-fit on F^2	1.038	1.044
final R_1 and wR_2 indices [$I > 2\sigma(I)$]	0.0552, 0.1183	0.0773, 0.1834
R_1 and wR_2 indices (all data)	0.1181, 0.1376	0.1197, 0.2081

The unweighted R-factor is $R_1 = \Sigma(Fo - Fc)/\Sigma Fo$; $I > 2\,\sigma(I)$,*the weighted R-factor is* $wR_2 = \{\Sigma w(Fo^2 - Fc^2)^2/\Sigma w(Fo^2)^2\}^{1/2}$.

Cyclic Voltammetry Studies

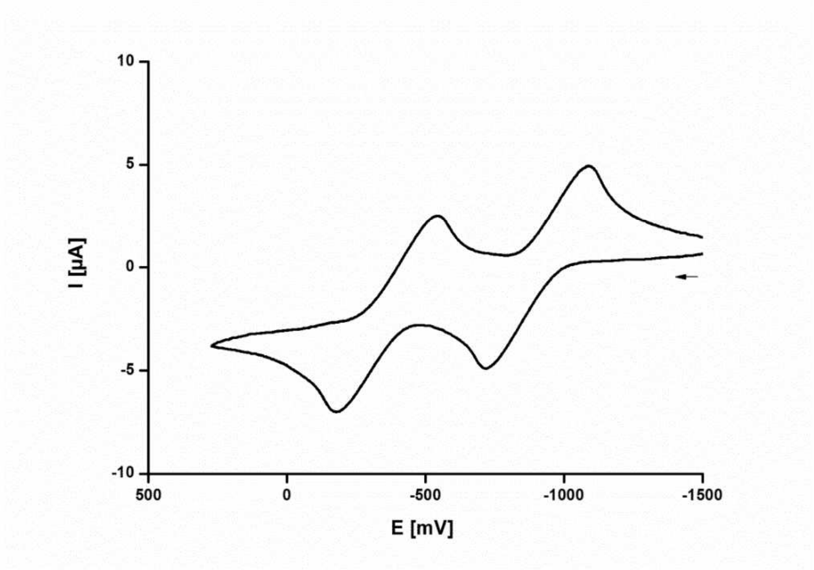

Figure S12. Cyclic voltammogram for **2** in NBu_4PF_6 (0.1M) at rt, Au electrode; E vs. $Fc^{0/+}$ (external).

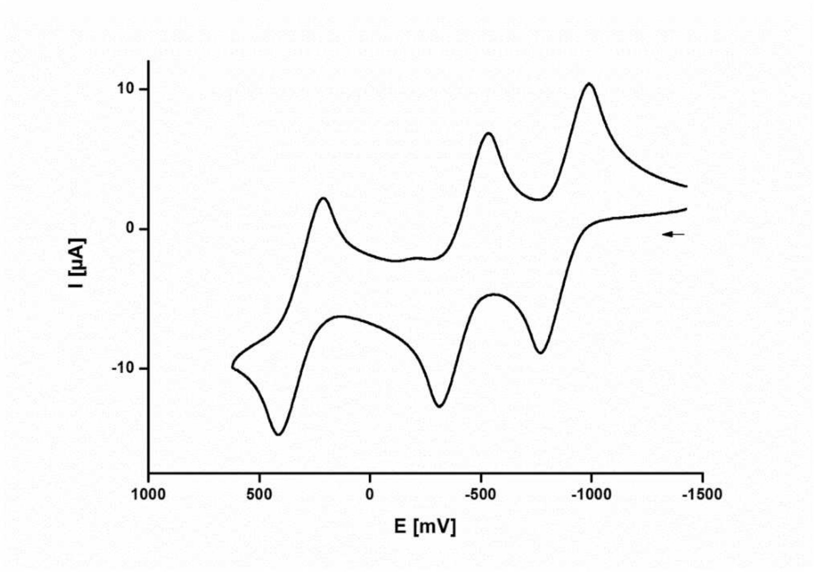

Figure S13. Cyclic voltammogram for **4** in NBu_4PF_6 (0.1M) at rt, Au electrode; E vs. $Fc^{0/+}$ (external).

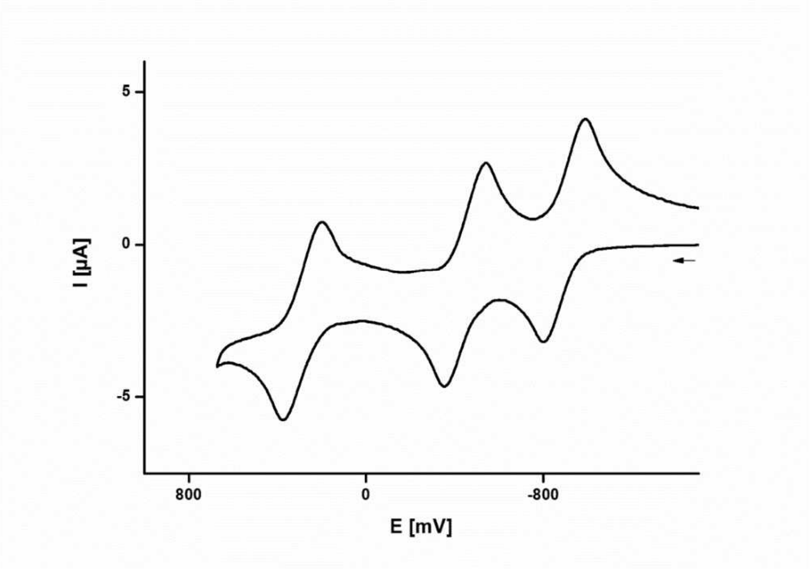

Figure S14. Cyclic voltammogram for **5** in NBu_4PF_6 (0.1M) at rt, Au electrode; E vs. $Fc^{0/+}$ (external).

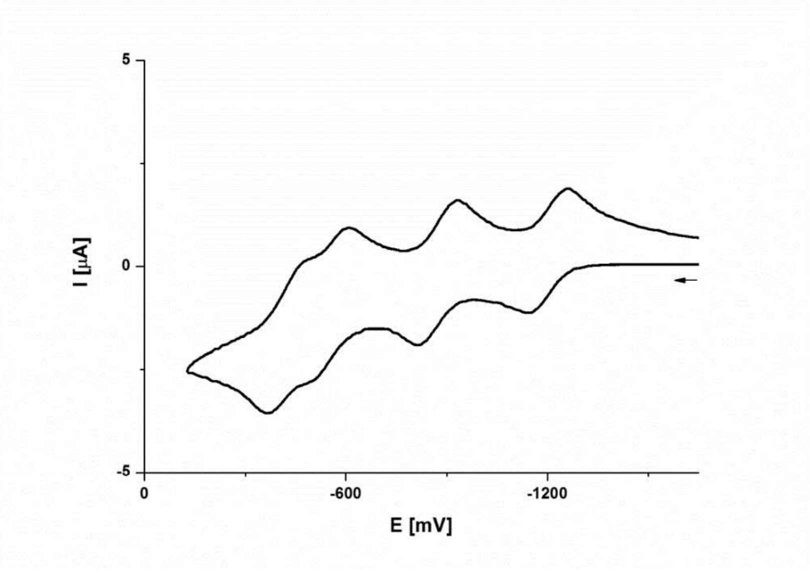

Figure S15. Cyclic voltammogram for **7** in NBu_4PF_6 (0.1M) at rt, Au electrode; E vs. $Fc^{0/+}$ (external).

Spectroelectrochemical Studies

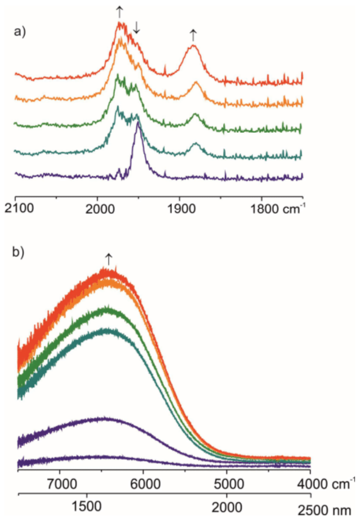

Figure S16. IR spectroscopic changes during the first oxidation of complex **2** in an OTTLE cell (THF/NBu_4PF_6 0.2 M at rt); top (a)): changes in the ν(C≡C) region of the mid IR; bottom (b)): changes at the NIR region.

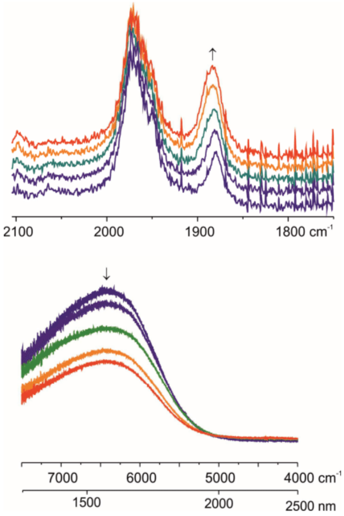

Figure S17. IR spectroscopic changes during the initial stages of the second oxidation of complex **2** in an OTTLE cell (THF/NBu_4PF_6 0.2 M at rt); top (a)): changes in the ν(C≡C) region of the mid IR; bottom (b)): changes at the NIR region.

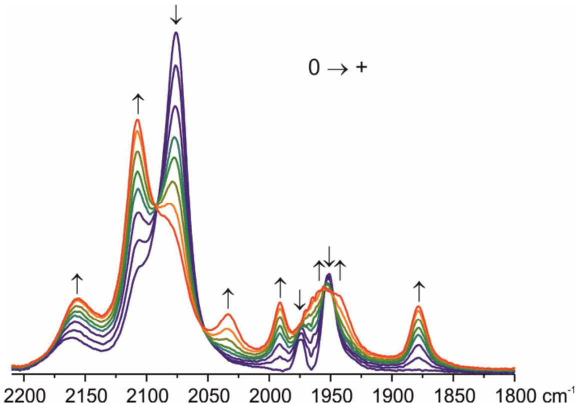

Figure S18. IR spectroscopic changes during the first oxidation of complex **3** in an OTTLE cell (THF/NBu$_4$PF$_6$ 0.2 M at rt).

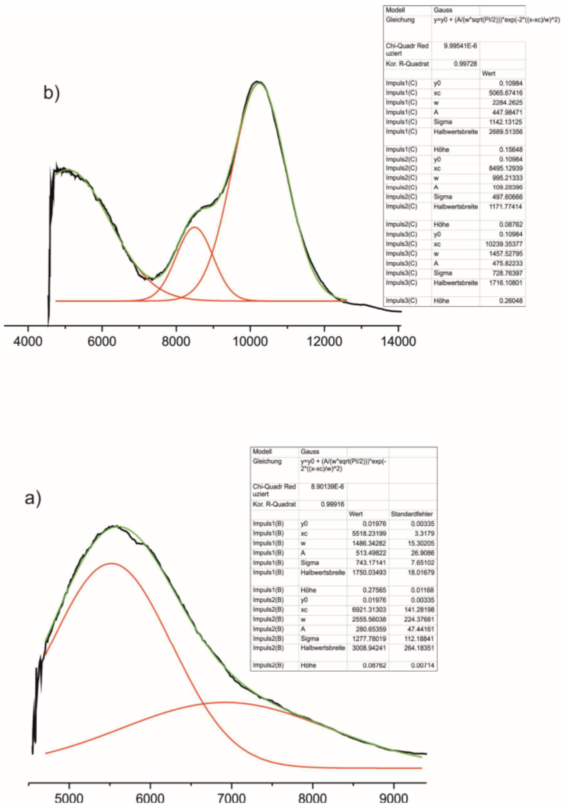

Modell	Gauss	
Gleichung	y=y0 + (A/(w*sqrt(PI/2)))*exp(-2*((x-xc)/w)^2)	
Chi-Quadr Reduziert	9.99541E-6	
Kor. R-Quadrat	0.99728	
		Wert
Impuls1(C)	y0	0.10984
Impuls1(C)	xc	5065.67416
Impuls1(C)	w	2284.2625
Impuls1(C)	A	447.98471
Impuls1(C)	Sigma	1142.13125
Impuls1(C)	Halbwertsbreite	2689.51356
Impuls1(C)	Höhe	0.15648
Impuls2(C)	y0	0.10984
Impuls2(C)	xc	8495.12939
Impuls2(C)	w	995.21333
Impuls2(C)	A	109.28396
Impuls2(C)	Sigma	497.60666
Impuls2(C)	Halbwertsbreite	1171.77414
Impuls2(C)	Höhe	0.08762
Impuls3(C)	y0	0.10984
Impuls3(C)	xc	10239.35377
Impuls3(C)	w	1457.52795
Impuls3(C)	A	475.82233
Impuls3(C)	Sigma	728.76397
Impuls3(C)	Halbwertsbreite	1716.10801
Impuls3(C)	Höhe	0.26048

Modell	Gauss		
Gleichung	y=y0 + (A/(w*sqrt(PI/2)))*exp(-2*((x-xc)/w)^2)		
Chi-Quadr Reduziert	8.90139E-6		
Kor. R-Quadrat	0.99916		
		Wert	Standardfehler
Impuls1(B)	y0	0.01976	0.00335
Impuls1(B)	xc	5518.23199	3.3179
Impuls1(B)	w	1486.34282	15.30205
Impuls1(B)	A	513.49822	26.9086
Impuls1(B)	Sigma	743.17141	7.65102
Impuls1(B)	Halbwertsbreite	1750.03493	18.01679
Impuls1(B)	Höhe	0.27565	0.01168
Impuls2(B)	y0	0.01976	0.00335
Impuls2(B)	xc	6921.31303	141.28198
Impuls2(B)	w	2555.56038	224.37681
Impuls2(B)	A	280.65359	47.44161
Impuls2(B)	Sigma	1277.78019	112.18841
Impuls2(B)	Halbwertsbreite	3008.94241	264.18351
Impuls2(B)	Höhe	0.08762	0.00714

Figure S19. Deconvolution of the NIR part of the electronic spectra of complexes **7**$^+$ (bottom) and **7**$^{2+}$ (top).

References

(1) Burt, R. J.; Chatt, J.; Hussain, W.; Leigh, G. J. *J. Organomet. Chem.* **1979**, *182*, 203.
(2) Semenov, S. N.; Blacque, O.; Fox, T.; Venkatesan, K.; Berke, H. *Organometallics* **2010**, *29*, 6321.
(3) Holmes, A. B.; Jones, G. E. *Tetrahedron Lett.* **1980**, *21*, 3111.
(4) Jones, K.; Lappert, M. F. *J. Chem. Soc.* **1965**, 1944.
(5) Chatt, J.; Hayter, R. G. *J. Chem. Soc.* **1961**, 5507.
(6) Bancroft, G. M.; Mays, M. J.; Prater, B. E. *J. Chem. Soc. A* **1970**, 956.
(7) Gottlieb, H. E.; Kotlyar, V.; Nudelman, A. *J. Org. Chem.* **1997**, *62*, 7512.
(8) Agilent Technologies (formerly Oxford Diffraction), Yarnton, England **2011**.
(9) Clark, R. C.; Reid, J. S. *Acta Crystallogr. A* **1995**, *51*, 887.
(10) Sheldrick, G. *Acta Crystallogr. A* **2008**, *64*, 112.
(11) Farrugia, L. *J. Appl. Crystallogr.* **1999**, *32*, 837.
(12) Spek, A. L. *J. Appl. Crystallogr.* **2003**, *36*, 7.

3. ORGANOMETALLIC SINGLE-MOLECULE ELECTRONICS: TUNING ELECTRON TRANSPORT THROUGH $X(DIPHOSPHINE)_2FEC_4FE(DIPHOSPHINE)_2X$ BUILDING BLOCKS BY VARYING THE FE-X-AU ANCHORING SCHEME FROM COORDINATIVE TO COVALENT

3.1 MANUSCRIPT

The manuscript and associated supplementary information were accepted as a full paper to the Journal of the American Chemical Society as:

F. Lissel, F. Schwarz, O. Blacque, H. Riel, E. Lörtscher, K. Venkatesan, H. Berke: *"Organometallic Single-Molecule Electronics: Tuning Electron Transport through* $X(diphosphine)_2FeC_4Fe(diphosphine)_2X$ *Building Blocks by Varying the Fe-X-Au Anchoring Scheme from Coordinative to Covalent"*

JACS JOURNAL OF THE AMERICAN CHEMICAL SOCIETY
Article
pubs.acs.org/JACS

Organometallic Single-Molecule Electronics: Tuning Electron Transport through X(diphosphine)$_2$FeC$_4$Fe(diphosphine)$_2$X Building Blocks by Varying the Fe–X–Au Anchoring Scheme from Coordinative to Covalent

Franziska Lissel,[†] Florian Schwarz,[‡] Olivier Blacque,[†] Heike Riel,[‡] Emanuel Lörtscher,*[,‡] Koushik Venkatesan,*[,†] and Heinz Berke*[,†]

[†]Department of Chemistry, University of Zurich, Winterthurerstrasse 190, CH-8057 Zürich, Switzerland
[‡]Science & Technology Department, IBM Research - Zurich, Säumerstrasse 4, CH-8803 Rüschlikon, Switzerland

S Supporting Information

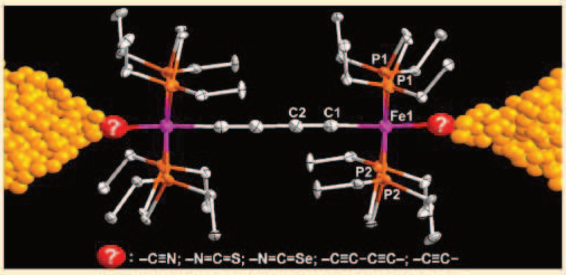

ABSTRACT: A series of X(depe)$_2$FeC≡C–C≡CFe(depe)$_2$X complexes (depe =1,2-bis(diethylphosphino)ethane; X = I **1**, NCMe **2**, N$_2$ **3**, C$_2$H **4**, C$_2$SnMe$_3$ **5**, C$_4$SnMe$_3$ **6**, NCSe **7**, NCS **8**, CN **9**, SH **10**, and NO$_2$ **11**) was designed to study the influence of the anchor group on organometallic molecular transport junctions to achieve high-conductive molecular wires. The FeC$_4$Fe core is electronically functional due to the redox-active Fe centers and sp-bridging ligands allowing a strong electronic delocalization. **1**–**11** were characterized by elemental analyses, X-ray diffraction, cyclic voltammetry, NMR, IR, and Raman spectroscopy. DFT calculations on model compounds gave the HOMO/LUMO energies. **5**–**9** were investigated in mechanically controllable break-junctions. For **9**, unincisive features at 8.1×10^{-7} G_0 indicate that sterical reasons prevent stable junctions to form or that the coordinative binding motif prohibits electron injection. **7** and **8** with the hitherto unexploited coordinatively binding end groups NCSe and NCS yielded currents of 1.3×10^{-9} A (**7**) and 1.8×10^{-10} A (**8**) at ±1.0 V. The SnMe$_3$ in **5** and **6** splits off, yielding junctions with covalent C–Au bonds and currents of 6.5×10^{-7} A (**Au–5′–Au**) or 2.1×10^{-7} A (**Au–6′–Au**). Despite of a length of almost 2 nm, the **Au–5′–Au** junction reaches 1% of the maximum current assuming one conductance channel in quantum point contacts. Additionally, the current noise in the transport data is considerably reduced for the covalent C–Au coupling compared to the coordinative anchoring of **7**–**9**, endorsing C–Au coupled organometallic complexes as excellent candidates for low-ohmic molecular wires.

INTRODUCTION

The field of molecular electronics aims at employing intrinsic molecular functionalities for specific electronic operations.[1−4] Electronic transport through molecular junctions depends on the chemical structure of the molecules, which however is hard to predict in such a solid-state type-of-device,[5] as the properties of the isolated molecule change substantially when it is coupled to metal leads. Nonetheless the evolution of atomic and molecular manipulation and molecular electronics has strongly progressed and gained momentum through interdisciplinary efforts, joining forces of theory, physics and chemistry.[6] From the chemistry side, the main contribution toward single-molecule electronics is to provide a rational design for the synthesis of unique molecular entities suitable of probing structure–function relationships,[7−9] which is a categorical prerequisite to comprehensively understand the processes underlying electronic transport on the single-molecule level.

Ultimately this know-how is expected to be the basis for creating tailored functional molecular building blocks for specific electronic tasks, as e.g. conductance switching, and eventually enabling the implementation of single-molecule devices to provide novel functionalities based on intrinsic molecular mechanisms, such as multilevel redox activity. A molecular transport junction can be divided into three main parts:[10] an experimental setup providing atomic-sized electrodes separated by a tunable gap of molecular dimensions (0–3 nm), a (functional or passive) molecular backbone providing a pathway for electrons to travel between the two electrodes under an applied field, and the termini of the molecular unit, the so-called end groups. These end groups establish the mechanical and electronic contact between the backbone and the electrodes by chemical means, thereby immobilizing the molecule in the junction to form a solid-state device. Suitable molecular entities are structurally rigid and consist of molecular orbitals (MOs) that are ideally coupled in an overlapping way along the

Received: August 2, 2014

dx.doi.org/10.1021/ja507672g | J. Am. Chem. Soc. XXXX, XXX, XXX−XXX

electronic pathway to facilitate electron transport. The junction's conductance can now be modulated by varying the level of MO coupling, the energetic position of the MOs in respect to the Fermi energy, E_F, of the electrodes and the injection barriers from the electrodes to the MOs. In that context, the end groups are key to establish a mechanically stable contact and to control the electronic coupling between the molecule and the electrodes.[11] The molecular topologies are expected to determine the type of transport mechanism and its efficiency, namely the anchor group to determine the charge injection barrier and the molecular orbitals the pathways for electrons to tunnel through. Whereas the experimental techniques to investigate molecular transport are evolving at a fast pace and enable meanwhile even measurements at the single-molecule level, the number of suitable homologous series of molecules for a systematic study of the structure−function relationship is rather limited. Also, the conductance of commonly used purely organic molecules for single-molecule electronics is reported to be rather low and to decay generally exponentially with increasing molecular length until, at a certain length, the hopping-based low-conductance regime is reached. This constrains severely the dimensions of the molecular systems,[12−15] in particular to achieve long wires, and complicates the implemention of intrinsic molecular functionalities.

To achieve high conductance at relatively low bias for energy-efficient applications, the positions of the energy levels of the MOs need to be aligned with E_F for resonant transport to occur through MOs. In contrast to purely organic entities, where MO and E_F levels are usually energetically separated by several eV (in the isolated case), organometallic compounds enable a facile tuning of the MO energies, because of their strong dependence on the kind of the metal center.[16−20] The design and synthesis of the Creutz−Taube[21] ion furthermore established that an organic ligand connecting two or more redox-active metal cores allows a delocalized electronic system to be formed between the metal centers which act as an intramolecular electron pathway for transport. Additionally, the insertion of redox-active metal centers into organic frameworks, termed "relay approach", was shown to improve the molecular conductance of the entire framework by providing defined donor−acceptor sites.[22]

In recent years, organometallic complexes of the type (Cp*)(PP)MC$_n$M(PP)(Cp*) (Cp* = η^5-C$_5$Me$_5$, P = monodentate phosphine ligand or PP = bidentate phosphine ligand, C$_n$ organic bridging ligand) were intensively employed to study intramolecular charge transport.[23−25] The covalently bonded and electronically delocalized bridge poses a structurally well-defined rigid-rod electron pathway, whereas the options to alter the incorporated metal centers,[26,27] the bridging[28,29] and nonbridging ligands[30] in order to vary the MO alignment open the possibility to gain in-depth understanding of the electronic processes taking place at the molecular level. Electrochemical and spectroscopic experiments evidenced that the electronic delocalization can extend over the entire length of the organometallic unit.[31−33] The reversibility of the intramolecular redox process was found to be highest for the unsaturated, rigid-rod type and electronically versatile C$_4$ ligand and decreased dramatically if other types of sp/sp^2 systems were employed.[28,29,34−36] Among the C$_4$-bridged bimetallic systems, the homonuclear (Cp*)(PP)FeC$_4$Fe(PP)(Cp*) class is highlighted by an exceptionally large charge delocalization and a high stabilization of the oxidized species.[27,37−39] First experimental evidence suggests that spectroelectrochemical data derived from solution-based bulk measurements can tentatively be related to the electronic properties expressed on a single-molecule level.[40] Despite this, single-molecule transport measurements of compounds of the (PP)MC$_n$M(PP) class are rare, as the design and realization of organometallic fragments with open terminal sites that would allow for the insertion of electrode binding end groups constitute significant synthetic challenges. Up to date, only a mononuclear ruthenium[41] and platinum[42] complex as well as selected di- and trinuclear ruthenium entities[8,43−45] were investigated. Another experimental challenge is the required backbone length. As the direct electron tunneling between the Au electrodes is a non-negligible conductance channel in a molecular junction,[46] the electrode spacing of the corresponding metal−molecule−metal system has to be taken into account when comparing molecular conductances in general and molecule−metal coupling strengths in particular. As the direct electron tunneling contribution is strong for short electrode separations, longer compounds are better suited for such comparative studies, adding to synthetic challenges. Hence, the rich ligand chemistry and the high tunability of transition metals, which make the (PP)MC$_n$M(PP) class very attractive for molecular electronic applications, is so far not sufficiently exploited and needs further chemical realization and physical transport experiments.

We recently reported the stepwise assembly of a homometallic tetranuclear Me$_3$SiC$_4${Fe}C$_4${Fe}C$_4${Fe}C$_4${Fe}-C$_4$SiMe$_3$ ({Fe} = Fe(depe)$_2$, depe = 1,2-bis(diethylphospino)-ethane) unit, which showed extensive charge delocalization and vibrational coupling over the entire unsaturated organometallic backbone.[34] Based on these findings, we targeted to attach electrode-binding terminal groups to the {Fe}−C≡C−C≡C−{Fe} unit, thus combining the favorable properties of the Fe(II) core(s) with those of the butadiyne bridging ligand while realizing molecular junctions in the length range of 1.3−2.0 nm to reduce the direct electron tunneling contribution.

Toward this end, we first designed a triad of organometallic precursors of the type X{Fe}C$_4${Fe}X (X = I **1**,[34] NCMe **2**, and N$_2$ **3**) with reactive terminal ligands X. Starting from these source compounds, synthetic strategies were devised to modify the end groups for contact to Au electrodes. Using different synthetic pathways, we capped the central {Fe}C$_4${Fe} unit with X = C≡CH **4**, C≡CSnMe$_3$ **5**, C$_4$SnMe$_3$ **6**,[34] NCSe **7**, NCS **8**, CN **9**, SH **10**, and NO$_2$ **11** to study the influence of molecule−metal coupling on the transport properties. The **4**−**11** series of complexes consists of principally two different types of electrode-binding molecules. Those with terminal H atoms or Me$_3$Sn moieties attach to the Au surface by elimination of these moieties, forming junctions with X = C$_2$ (**5′**) or X = C$_4$ (**6′**). **5′** and **6′** are expected to establish covalent bonds to the Au surface, while complexes with Lewis basic end groups (**7**−**9** and **11**) form coordinative bonds. It seems reasonable to expect that the utilization of covalent C−Au bonds will lead to an increased stability of the molecular junction compared to the coordinative bonding case. Moreover, a stronger MO overlap due to the shorter electrode−molecule distance and therefore a higher overall conductance is anticipated for C−Au bonds. The presently best conducting molecular wires are those with poly *p*-phenylene junctions possessing also a direct C−Au binding.[47] Here, tunneling between the distinct π-system of the phenyls mediates transport, whereas in our case a delocalized electron system enables electron transport between the metal centers.

To achieve resonant transport, the MOs of the molecule have to be aligned to E_F, so that the electronegativity is similar. It was

Scheme 1. Reaction Pathways to Modify the Terminal X Functional Group of the X{Fe(depe)$_2$}C$_4${Fe(depe)$_2$}X Unit

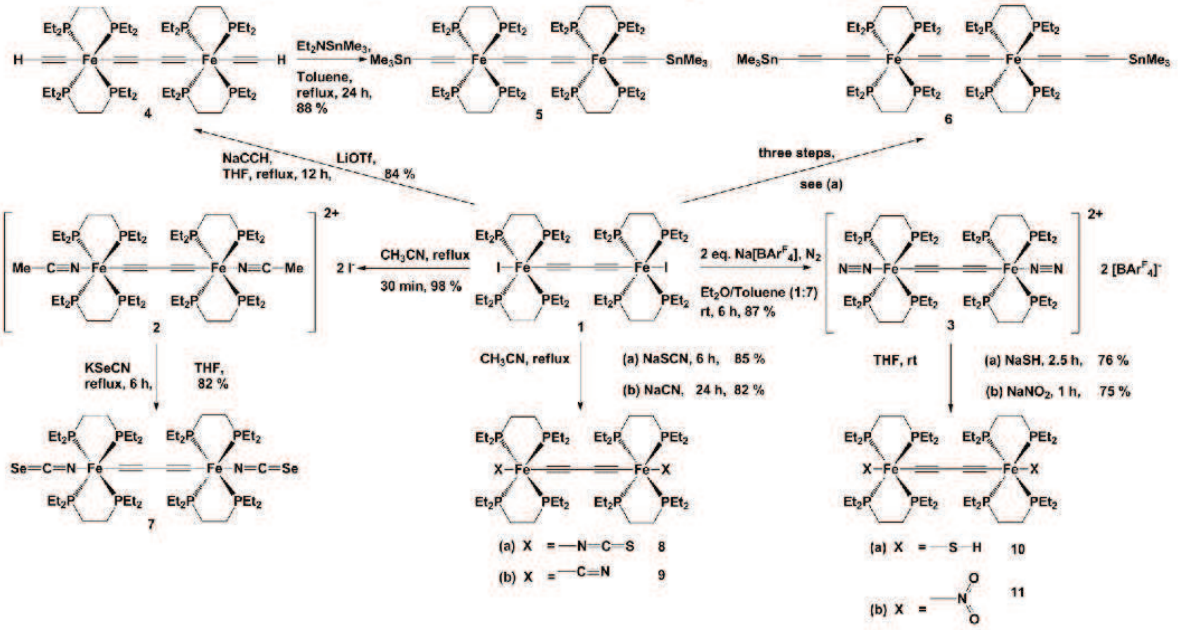

^{a}Three step synthesis.[34] [BAr$^F_4$]$^-$ = tetrakis[(3,5-trifluoromethyl)phenyl]borate.

shown that Au electrodes are comparably soft according to the HSAB concept developed by Pearson.[48] The same concept states that the chemical hardness can be correlated to the energy difference between the highest occupied molecular orbital (HOMO) and the lowest unoccupied molecular orbital (LUMO), called the HOMO−LUMO gap $\Delta E_{(H-L)}$, and allows the strength of donor−acceptor interactions to be predicted.[49] A small HOMO/LUMO gap means soft, and a large HOMO/LUMO gap means hard in character, while the Mulliken electronegativity $(I + A)/2$ (I = ionization potential, A = electron affinity) at high negative energies means high electronegativity and vice versa. Following this line of thought, molecules prone for high resonant conductivity should be soft in character and have a relatively low electronegativity to adjust to E_F of the Au electrodes. To gain insight into the influence of the terminal groups on the energetic regime of the molecular orbitals, the molecular geometries of selected model complexes **5**-Me, **6**$_H$-Me, **7**-Me, **8**-Me, **9**-Me, **10**-Me, and **11**-Me were optimized at the PBE1PBE/LANL2DZ level, and the HOMO/LUMO energies and chemical hardnesses of the compounds were obtained by single-point calculations with the 6-311+g(d) basis set and the same PBE1PBE functional.

All terminal substituents chosen possess a conjugation scheme that allows charge delocalization of the central {Fe}C$_4${Fe} unit to be extended over the molecule−metal interfaces. The strong electronic delocalization, the relatively high chemical stability, and the rigid-rod conjugated structures make a possible deployment of the {Fe}C$_4${Fe} unit attractive for applications as molecular wires. While cyanide,[50] isocyanide,[51] thiol,[52,53] and nitro substituents[8] are frequently employed as end groups, sp carbons are as yet rarely used,[7,54,55] and the utilization of NCS and NCSe as end groups is, to the best of our knowledge, unprecedented in molecular electronics. The affinity of S toward Au is well established, and one can reasonably assume that replacing S with the softer Se could enhance the orbital interaction of the soft Au electrode and the anchor groups[56] and additionally reinforce the stability of the formed junction. As mentioned before, capping a carbon function with either trimethylsilyl[57] or trimethylstannyl[58] substituents allows strong C−Au σ-bonds to be established after deprotection of the EMe$_3$ group (E = Si, Sn). The utilization of trimethylstannyl groups is preferable since due to the weaker Sn−C bond the cleavage of the C−Sn bonds occurs spontaneously at the electrodes and pre-experiment deprotection by a suitable reagent is not required. The linear structure, rigidness, and orbital arrangement of sp-hybridized C make these end groups highly interesting for the investigation of molecular transport.[54,55,59]

■ EXPERIMENTAL SECTION

Syntheses and Spectroscopic Characterizations. All experiments and measurements were carried out under a dinitrogen atmosphere using Schlenk techniques or in a glovebox (M. Braun 150B-G-II). All compounds were worked up to an analytically pure state without the use of column chromatography. The experimental part containing the description of the syntheses, one- and two-dimensional NMR experiments (Figures S1−S28), IR (Figures S29−S38) and Raman data (Table S1), and cyclic voltammetry experiments at different scan rates (Figures S42−S50) as well as the results of the elemental analyses can be found in the Supporting Information.

X-ray Structure Analyses. The molecular structures of complexes **5**, and **7**−**9** are depicted in Figure 2. The dicationic complexes [**2**]$^{2+}$ and [**3**]$^{2+}$ are illustrated in Figure S39, and the molecular structures of the compounds **5**, **10** and **11** are shown in Figure S40. Selected bond lengths, intramolecular distances, and angles are summarized in Table S2. The data collection and structure-refinement data for compounds **2**, **3**, and **5**−**11** are presented in Tables S3−S5. Single-crystal X-ray diffraction data were collected at 183(2) K on a Xcalibur diffractometer (Ruby CCD detector) or on a SuperNova area-detector diffractometer (for **6**), using a single wavelength enhance X-ray source with MoK$_\alpha$

radiation (λ = 0.71073 Å).[60] The selected suitable single crystals were mounted using polybutene oil on the top of a glass fiber fixed on a goniometer head and immediately transferred to the diffractometer. Pre-experiment, data collection, data reduction, and analytical absorption corrections[61] were performed with the program suite CrysAlis^{Pro}.[60] Using WinGX[62] or Olex,[63] the crystal structures were solved with SHELXS97[64] using direct methods, and the structure refinements were performed by full-matrix least-squares on F^2 with SHELXL97[64] for **3**, **5**, **8**–**11** and SHELXL2013[64] for **2**, **4** and **7**. PLATON[65] was used to check the results of the X-ray analyses. For more details about the refinements, see the Supporting Information and/or the refine_special_details and iucr_refine_instructions_details sections in the Crystallographic Information files (Supporting Information). CCDC-986825 (for **2**), CCDC-986826 (for **3**), CCDC-986827 (for **4**), CCDC-986828 (for **5**), CCDC-986829 (for **7**), CCDC-986830 (for **8**), CCDC-986831 (for **9**), CCDC-986832 (for **10**), and CCDC-986833 (for **11**) contain the supplementary crystallographic data for this paper. These data can be obtained free of charge from The Cambridge Crystallographic Data Center via www.ccdc.cam.ac.uk/data_request/cif.

Computational Details. DFT calculations were performed with the Gaussian03 program package[66] using the hybrid functional PBE1PBE[67] in conjunction with the LanL2DZ basis set[68−70] for the geometry optimizations and with the 6-311+G(d) basis set[71−73] on all atoms for the determination of the energy levels. Geometries were optimized with a C_i (inversion center) or a C_2 (2-fold axis) symmetry, and the ethyl groups of the depe ligands were replaced by methyl groups. The results are summarized in Table 3 and Figure S51.

Single-Molecule Transport Measurements. Transport measurements were taken at 300 K under ultrahigh vacuum conditions (pressure $<2 \times 10^{-9}$ mbar) by repeated opening and closing of the molecular junction using a three-point bending mechanism upon simultaneous current−voltage ($I-V$) data acquisition[74] using a Hewlett-Packard HP4156B Parameter Analyzer with 1 fA current resolution. After initial breaking of the Au−Au junction, the dinuclear Fe compounds were deposited onto the open junction from a 4×10^{-5} mol/L solution in tetrahydrofuran (THF), forming a submonolayer coverage on the two Au surfaces by the various bonding motifs. After evaporation of the solvent, the junction is slowly and stepwise closed until an electrical resistance of 1 MΩ at 1.2 V is being measured. Then the junction is opened again until a resistance of 3 TΩ at 1.2 V is reached, indicating a fully opened junction. In the subsequent opening and closing cycles, molecules can bridge the two electrodes, and metal−molecule−metal junctions are formed repeatedly. Statistical analysis, typically covering several hundred $I-V$ curves during junction forming and breaking events, is performed to identify the most probable transport characteristics[74] during this mechanical manipulation procedure.

■ EXPERIMENTAL RESULTS

Synthesis and Spectroscopic Properties of the Different Dinuclear Complexes. Mononuclear iron complexes of the type $Fe(PP)_2X_2$ (PP = bidentate phosphine ligand, X = Cl, Br, I) are known to react with organic nitriles yielding the mono- or dinitrile coordinating complexes[75,76] as well as allowing the abstraction of the terminal halides by sterically hindered bases to obtain the corresponding dinitrogen complexes.[77] The dinuclear I{Fe}C_4{Fe}I complex **1** (Scheme 1) is easily accessible and allows a facile substitution of the terminal iodo functions.[34] We targeted the dinuclear bis-nitrile (**2**) and bis-dinitrogen (**3**) species as synthetic intermediates to assemble a triad of reactive precursors to access entities based on the {Fe}C_4{Fe} motif, which terminal functional groups are chemically "tunable". The di-iodo complex **1** reacted with refluxing acetonitrile to give the bis-acetonitrile coordinated dinuclear complex [**2**] as the di-iodo salt in very high yield (98%, Scheme 1). Treating **1** with two equivalents of sodium tetrakis[(3,5-trifluoromethyl)phenyl]borate under a dinitrogen atmosphere and apolar conditions gave the bis-dinitrogen complex [**3**] as the tetrakis[(3,5-trifluoromethyl)phenyl]-borate salt in good yield (87%, Scheme 1). The reaction of mononuclear (Cp*)(PP)FeCl and $Fe(PP)_2Cl_2$ cores with lithium acetylide[78] and sodium acetylide[79,80] reagents is well established. In a previous paper we could show that by reacting **1** with a freshly prepared lithiated $[C_4]^{2-}$ unit and subsequent deprotection and stannylation of the termini, the C_4SnMe_3 capped dinuclear complex **6** is accessible.[34] In a similar fashion the reaction of **1** with sodium acetylide in the presence of lithium triflate gave the acetylide capped compound **4**, which was stannylated using NEt_2SnMe_3 to yield the C_2SnMe_3 capped complex **5** (Scheme 1). Both compounds were isolated in good yields of 84% and 88%, respectively. The signal of the acetylenic proton of **4** in the ^1H NMR appears as a quintet at 1.03 ppm due to a $^4J_{H-P}$ coupling with the four phosphorus atoms of the depe ligand (see Figure S10 for the ^1H and ^1H {^{31}P} spectra as well as Figure S13 for the P,H correlation spectrum). The stannylation to give **5** has a distinct influence on the spectroscopic properties (see NMR and IR parts of the Supporting Information), most notably on the $^{13}C\{^1H\}$ resonance of the C_α carbon atom of the terminal acetylide group, which experiences a considerable low-field shift from 129.9 ppm for **4** to 170.2 ppm for **5**. Despite the stannyl substituent, the signal of the C_β atom is likewise shifted low-field, albeit to a lesser extent, from 99.4 to 111.6 ppm (for **4** and **5**, respectively). In the $^{119}Sn\{^1H\}$ NMR, the trimethyltin group of **5** appears as a quintet at −121.0 ppm due to the $^4J_{Sn-P}$ coupling (Figure S18). Compared to the corresponding singlet of the C_4SnMe_3 capped **6**, which is found at −36.3 ppm,[34] the signal is shifted considerably toward the lower field.

Starting from the bis-acetonitrile complex $[\mathbf{2}]^{2+}$ and using KSeCN as a reagent, the isoselenocyanate capped complex **7** was obtained in good yield (82%, Scheme 1).

In a similar line, reacting the di-iodo complex **1** in refluxing acetonitrile with NaSCN and NaCN yielded the isothiocyanate capped **8** and the cyanide substituted complex **9** in good yields of 85% and 82%. *In situ* $^{31}P\{^1H\}$ NMR measurements indicated the formation of the bis(acetonitrile) substituted $[\mathbf{2}]^{2+}$ as an intermediate. **7** and **8**, which differ from each other solely in the heteroatom of the terminal function, show a distinct consistency in their respective spectroscopic properties (Table 1 and Supporting Information).

Table 1. IR and Raman $\nu(C_4)$ Bands of the Bridging Butadiyne Unit of Compounds 2–10

compd.	IR [cm^{-1}] $\nu_{as}(C_4)$	Raman [cm^{-1}] $\nu_s(C_4)$
2	1946 (m)	2088(s)
3	2109 (m)	2122(vs)
4	1952 (w)	2098(s)
5	1936 (vs)	2086(s)
6[b]	1951 (m) (sh at 1967)[a]	2102(vs)
7	1950 (m)	2097(vs)
8	1950 (m)	2097(vs)
9	1955 (m)	2103(vs)
10	1940 (m)	2094(s)
11	1956 (m)	2098(s)

[a] $\nu(C_2)$. [b] Described in literature.[34]

The thiol and nitro capped dinuclear compounds **10** and **11** were obtained in yields of 74% and 75% (Scheme 1) by reacting the bis-dinitrogen complex $[\mathbf{3}]^{2+}$ with the corresponding sodium salts at room temperature, indicative of the facile replacement of the coordinated dinitrogen ligands. The bis-thiol compound **10** is prone to decomposition in solution or in air, apparently under oxidative conditions, presumably resulting in the formation of dithio bridged compounds. In the ^1H NMR, the SH group gives rise to a quintet due to the $^3J_{H-P}$ coupling with the four phosphorus atoms of the depe ligand and is shifted considerably upfield to −6.34 ppm (Figure S25). For the ligand exchange reactions, an intermediate $[\{Fe\}{\equiv}C{-}C{\equiv}C{-}C{\equiv}\{Fe\}]^{2+}$ structure seems reasonable (see Figure 1), as in this mesomeric form of the C_4 bridge both metal centers attain a 18-electron configuration.

The C_4 bridge of all described compounds gives rise to two signals in the $^{13}C\{^1H\}$ NMR, consistent with a centrosymmetric $\{Fe\}{-}C_\alpha{\equiv}C_\beta{-}$

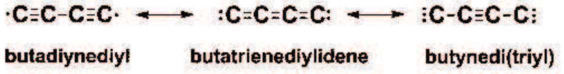

Figure 1. Possible mesomeric forms of the C$_4$ bridging ligand.

C$_\beta$≡C$_\alpha$–{Fe} butadiyne structure and an inversion center located between the C$_\beta$ and C$_\beta$′ of the bridging unit. The signal of the carbon atoms in α position to the iron centers is a quintet for all complexes due to the coupling with the four equatorial P atoms. Also, for centrosymmetric structures with octahedral geometry around the Fe(II) centers and with the electron-rich phosphine ligands arranged equatorially, we expected a singlet in the ^{31}P{^{1}H}NMR, which was indeed found for all complexes. All complexes are expected to have a local $D_{\infty h}$ symmetry of the {Fe}–C≡C–C≡C–{Fe} arrangement and due to this the complexes are anticipated to give rise to one IR active ν_{as}(C$_4$) band. This band is found to possess a prominent and well-distinguishable feature in all IR spectra (Figures S29 – S38). As for **4**–**11** the structure of the central {Fe}C$_4${Fe} motif remains constant, changes of the stretching frequencies of this band can be attributed to the different donor/acceptor properties of the terminal anchor groups *trans* to the bridging ligand (Table 1).

Within the homologous series of compounds, the ν_{as}(C$_4$) IR band shifts only slightly. For **4**–**11**, the lowest value of 1936 cm^{-1} is found for the C$_2$SnMe$_3$ capped compound **5** and the highest value of 1956 cm^{-1} for the dinitro derivative **11**. For the ν_s(C$_4$) Raman band, the lowest value of 2086 cm^{-1} is again found for the C$_2$SnMe$_3$ capped compound **5**, yet the by far highest values of 2103 and 2102 cm^{-1} stem from the vibrational bands of the CN and C$_4$SnMe$_3$ capped complexes **9** and **6**. A possible explanation for these at first glance unexpected values could be a vibrational coupling between the ν_s(C$_4$) band of the bridging ligand and the respective vibrations of the terminal ligands, putting the high-energy band to higher energies and the low-energy band to lower energies.

X-ray Structure Analyses. Single crystals were grown of all compounds and allowed a structural characterization using X-ray diffraction studies. The crystal structures of **1** and **6** are discussed elsewhere.[34] Figure 2 depicts the molecular structures of **5** and **7**–**9**, the structures of **2** and **3** are given in Figure S39, and the ones of **4**, **10**, and **11** are in Figure S40. For all complexes discussed here, the bond between the Fe and the C$_\alpha$ of the bridging ligand lies between the values of 1.900(3) Å for **10** and 1.935(5) Å for **5**, which is consistent with a Fe–C single bond. The C$_\alpha$–C$_\beta$ bonds are between 1.215(8) Å for **8** and 1.225(3) Å for **11** and thus still fall into the range of C≡C triple bond separations, whereas the C$_\beta$–C$_\beta$′ bond lengths with values between 1.373(8) Å for **7** and 1.390(7) Å for **10** are slightly shorter than expected for a C(sp)–C(sp) single bond. The Fe–Fe distances are between 7.6117(8) Å for **10** and 7.701(1) Å for **5** and are thus in good accord with the values reported for other terminally open dinuclear compounds, with the {Fe(depe)$_2$}C$_4${Fe(depe)$_2$} motif,[34] and are also in range of stopper-type C$_4$ bridged iron dinuclears, such as [CpFe(dppe)](μ-C$_4$)[81] and [(η^5-C$_5$Me$_5$)(CO)$_2$Fe$_2$](μ-C$_4$),[82] which have nonbonding Fe····Fe distances of 7.564 and 7.653 Å, respectively. The values document a butadiynediyl character of the bridging C$_4$ unit, albeit with participation of a butatrienediylidene mesomeric form (Figure 1).

For both complexes **4** and **5** the terminal C$_2$ unit displays bond lengths which correspond to an acetylide structure, i.e., the length of the Fe–C bonds is consistent with a single bond (1.935(5) Å and 1.926(5) Å for **5**, 1.926(2) Å for **4**), and the C–C bonds are in the range expected for triple bonds (1.220(5) Å, and 1.210(8) Å for **5**, 1.207(4) Å for **4**). For all molecules, the ligand geometry around the Fe cores is pseudo octahedral, with the four P atoms occupying equatorial positions, whereas the end group is lying on an axial position *trans* to the bridging ligand. The average Fe–P distance of the neutral compounds lies between 2.220 Å for the C$_2$SnMe$_3$ capped compound **5** and 2.248 Å for the NO$_2$ terminated **11**. The average Fe–P distance of the dicationic compounds **2** and **3** (2.252 and 2.271 Å, respectively) is slightly elongated compared to the neutral compounds, yet all values lie in the range of {Fe(depe)$_2$} centers reported earlier. The comparably long Fe–P distance of **3** apparently causes a high-field shift of the signal in the ^{31}P{^{1}H} spectrum as described above.

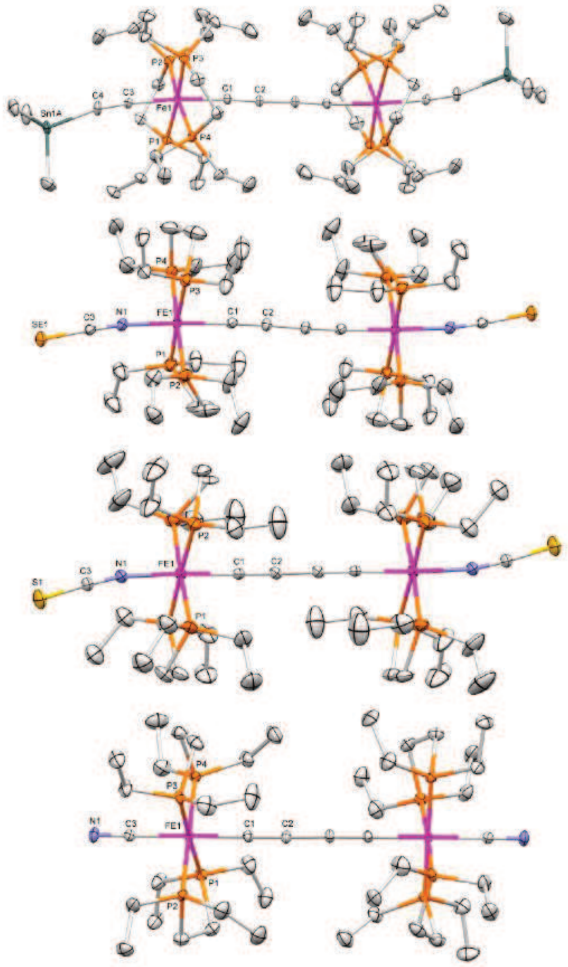

Figure 2. Molecular structures of **5** and **7**–**9** (from top to bottom). Ellipsoids are set at 30% probability level. Solvent molecules and selected hydrogen atoms are omitted for clarity. See Table S2 for selected bond lengths, distances, and angles.

The *cisoid* (bow-shaped) and *transoid* (S-shaped) distortions, which are a common phenomenon for C$_n$ (with $n \geq 4$) bridged dinuclear {M}C$_n${M} compounds, are unincisive for the structures discussed here. Compounds **4**, **9**, and **11** show minor *cisoid* distortions along the metal–C$_4$–metal backbone, yet the Fe–C$_\alpha$–C$_\beta$ angle, which makes the largest contribution to this distortion, lies in the range of 175.9(3)–176.7(2)° (Table S2) and is almost linear. Compounds [**2**]$^{2+}$, [**3**]$^{2+}$, **5** and **7**–**10** could be described as *transoid* distorted, yet this distortion is only distinct for the thiol capped compound **9**, where the Fe–C$_\alpha$–C$_\beta$ angle is 173.4(3)°. Gladysz et al. showed via DFT calculations that the energetic barrier for *cisoid* distortions for {M}C$_n${M} fragments is quite small[83] and also noted the tendency that distortions from linearity are often located at the end of the linear chain.[84] When the lengths of the terminal ligands are taken into account, this tendency can indeed be observed for the presented molecules, in particular for terminal groups consisting of three or more atoms, which are linearly arranged, i.e., complexes **5**–**8** and, albeit to a lesser extent, the C$_2$H capped **4**. Interestingly, the distortion of the linearity is emanating from the iron center for compounds **7** and **8** illustrated by a Fe–N–C bond angle deviating considerably from linearity (172.9(4) and 169.4(5)° for

NCSe **7** and NCS **8**, respectively). For **4** and **5** the distortion is located completely on the terminal ligand, with the C−C−Sn angles of **5** at 162.9(5)° and 158.0(5)°. However, these values cannot considered with confidence because of the disorder observed on the terminal ligands. For both **7** and **8**, the Fe−N−C bond angle was expected to be <180° due to the lone electron pair on the N nuclei but instead found to be close to 180° ($\angle_{(C3-N1-Fe1)}$ = 177.6(4)° for **7** and 176.2(6)° for **8**, Table S2).

The comparably short N−C bond (1.161(6)Å for **7** and 1.135(7) Å for **8**, Table S2) suggests a considerable influence of the $M{-}N^{+}{\equiv}C{-}Se^{-}$ and $M{-}N^{+}{\equiv}C{-}S^{-}$ canonical structures.[85] Neither of the terminal ligands chosen for this project nor the depe ligands are sterically excessively demanding. Consequently it can be reasoned that the observed deviations from linearity stem from intermolecular interactions and crystal packing effects.[84,86]

Cyclic Voltammetry. Cyclic voltammetry experiments were carried out to probe the thermodynamic stability of the reported complexes in all accessible oxidation states. Compounds **4**, **6**, **8**, **9**, and **11** exhibit three and complexes **5** and **7** two well-defined and reversible oxidation waves, while for **10** no reversible process was found (Table 2 and Supporting Information).

Table 2. Cyclic Voltammetry Data of the Complexes **4**−**11**[a]

compd.	$E_{1/2}$ (0/+1) [mV]	$E_{1/2}$ (+1/+2) [mV]	ΔE [mV]	K_c	$E_{1/2}$ (+2/+3) [mV]
4	−453	10	462	7.7×10^7	799
5	−458	5	463	7.9×10^7	–
6	−503	−48	456	6.0×10^7	671
7	−428	24	452	5.1×10^7	–
8	−372	106	478	14.5×10^7	848
9	−421	10	431	2.2×10^7	729
10	–	–	–	–	–
11	−497	−14	483	17.7×10^7	735

[a] Measurements at 300 K in THF/Bu_4NPF_6 (0.1M) with an Au working electrode, a Pt counter electrode, and an Ag reference electrode. *E* vs $Fc^{0/+}$ (external).

Two oxidation waves are associated with the consecutive oxidation of the two metal centers, whereas the third one, positioned at a significantly more positive potential, is associated with the oxidation of the bridging ligand.[34,37] The existence of two metal-based oxidations for a highly symmetric molecule possessing a formal inversion center in the middle of the bridging ligand is a strong indicator for high charge delocalization over the length of the rigid-rod molecule,[23] which demonstrates that the butadiyne bridging ligand is actively supporting charge transport between the redox-active iron centers.[87]

The thiol-capped compound **10** does not exhibit any reversible oxidation process in the THF/Bu_4NPF_6 electrolyte, an electrochemical behavior which would be consistent with the oxidative formation of dithio species. This explanation is also in agreement with the observed disposition of **10** to decompose in solution and deposit as a thin film on the electrodes during the cyclic voltammetry experiments. The C_2SnMe_3 capped **5** and the NCSe capped **7** both only show two reversible oxidation waves, both in a range associated with metal-based oxidations (Figure S47 for **7** and S44 for **5**). For **5**, the absence of a third reversible oxidation wave is interesting as the structurally highly similar C_2H capped **4** shows the carbon based oxidation. When recording cyclic voltammograms of **5** with a broader electrochemical window (Figure S43), one can observe that, while there is no reversible third oxidation wave, the first two oxidations are still present and furthermore still reversible. This indicates that processes linked to a cleavage of the trimethylstannyl group in the higher potential range might be responsible for the absence of a carbon based oxidation. For the NCSe capped complex **7** all three oxidations are observable, but the re-reduction processes are not reversible (Figure S46). Upon narrowing the potential window, two fully reversible oxidation waves were detected (Figure S47). This behavior could be interpreted in terms of insolubility of the 3-fold oxidized species in the electrolyte. Except for the thiol-capped complex **10** the mixed valence forms show very good thermodynamic stabilization as derived from the high K_c values in the range of 10^7 (Table 2).[23]

Based on the MC_4M in common motif molecules, **4**−**11** show high structural uniformity. Nonetheless, number and position of the oxidation waves as well as the peak separation evidence a noticeable variance (Table 2). Peak separation and K_c values depend on the distance between the metal centers,[88] the electron density at the metal centers, electrostatic interactions, solvation, ion pairing with the electrolyte, and structural distortions.[23] For the complexes reported here, the differences in the nonbonding Fe···Fe distances (see Table 3) are small and can only partially explain the variance. The ΔE values are expected to increase with the electron density of the metal center, yet, similar to the IR and Raman data, the interpretation based on the electron-donating and -accepting properties of the terminal anchoring ligand is however not fully conclusive. Still, the cyclic voltammetry data corroborate that by changing one structural motif in an otherwise homologous series of organometallic wire-type molecules allows modification of their physical, spectroscopic, and electronic properties.

Table 3. Selected Distances (Å) Computed at the According to the HSAB Principle (ref 49)[a]

X	X···X (X-ray) (Å)	X···X (DFT)[c] (Å)	LUMO (eV)	HOMO (eV)	$\Delta E_{(H-L)}$ (eV)	χ (eV)
SH	S···S = 12.3435(17)	12.54	−0.33	−4.16	3.83	2.25
NO_2	O···O = 12.830(3)	13.15	−0.57	−4.58	4.01	2.58
CN	N···N = 13.738(4)	13.93	−0.39	−4.41	4.02	2.40
C_2H	C···C = 13.896(6)	14.08	−0.28	−4.07	3.79	2.18
NCS	S···S = 16.940(3)	17.34	−0.57	−4.60	4.03	2.59
NCSe	Se···Se = 17.3280(15)	17.59	−0.60	−4.62	4.02	2.61
C_4H	C···C = 19.015(12)[b]	19.26	−0.40	−4.33	3.93	2.37

[a] An increase of the HOMO/LUMO gap is PBE1PBE/LANL2DZ level and derived from X-ray studies, HOMO and LUMO energies (eV), HOMO/LUMO gap (eV), and absolute electronegativity χ computed at the PBE1PBE/LANL2DZ//PBE1PBE/6-311+g(d) level. [b] See ref 34. [c] See Computational Details section.

■ DFT CALCULATIONS

The molecular geometries of the model complexes **4**-Me, $\mathbf{6_H}$-Me, **7**-Me, **8**-Me, **9**-Me, **10**-Me, and **11**-Me were optimized with the Gaussian 03 program package[66] using the hybrid functional PBE1PBE[67] in conjunction with the LanL2DZ basis set.[67−70] Geometries were optimized with a C_i (inversion center) or a C_2 (2-fold axis) symmetry, and the ethyl groups of the depe ligands were replaced by methyl groups (dmpe = 1,2-bis(dimethylphosphino)ethane). As the $SnMe_3$ groups of **5** and **6** are expected to cleave off to form a covalent C−Au bond, calculations were carried out for the H terminated models **4**-Me ($HC{\equiv}C(dmpe)_2Fe{-}C_4{-}Fe(dmpe)_2C{\equiv}CH$) and $\mathbf{6_H}$-Me ($HC_4(dmpe)_2Fe{-}C_4{-}Fe(dmpe)_2C_4H$).

The computed distances for the model complexes compare well with the structural data derived from the X-ray studies (Tables 3 and S2). In all cases, the computed distances are slightly elongated, which is attributed to intermolecular interactions and packing effects within the crystal structures.[84,89] The deviation is highest for the NO_2 terminated complexes **11** and **11**-Me, where the computed O···O′ distance of 13.15 Å is longer by about 2.5% compared to the distance of 12.83 Å found in the X-ray experiment. Single-point calculations were carried out with the PBE1PBE functional and the 6-311+G(d) basis set for the determination of the molecular orbital energies. The HOMO and LUMO energies are given in Table 3 and in Figure S51 arranged in the order of the increasing molecular length. The absolute energies of the HOMO lie between −4.62 eV for **7**-Me and −4.07 eV for **4**-Me, and the ones of the LUMO are between −0.60 eV for **7**-Me and −0.28 eV for **4**-*Me*. To achieve a resonant transport, the molecular orbitals of the probed molecule should be aligned to E_F of the macroscopic electronic leads. As expected for 18-electron metal complexes, the HOMO/LUMO gap $\Delta E_{(H-L)}$ is relatively large and lies between 3.79 eV for **4**-Me and 4.03 eV for **8**-Me. The work of Pearson established that $\Delta E_{(H-L)}$ derived from DFT calculations can be correlated to hardness associated with a weakening of polarizability and therefore an increase in chemical hardness. For the discussed molecules, the hardness is consequently increasing in the order **4**-Me < **10**-Me < **6$_H$**-Me < **11**-Me < **9**-Me = **7**-Me < **8**-Me, whereas for the electronegativity χ the opposite trend is followed (Table 3 and Figure S51).

The Fermi energy of the Au electrodes is reasonably close to the energetic range of the HOMO's of all complexes discussed here. Assuming no charge transfer and MO broadening upon coupling the compounds to leads and taking the calculated HOMO levels of the isolated compounds as a measure for the resonant transport conditions, their alignment to and interaction with E_F would be in the order **8**-Me < **9**-Me = **7**-Me < **11**-*Me* < **6$_H$**-Me. It has to be noted, however, that the calculations were carried out for isolated molecules in the gas phase, whereas for the MCBJ experiments, a solid-state behavior of the complexes has to be assumed. The interactions with the Au electrodes, such as charge transfer, hybridization, and broadening of MO due to coupling, which are especially for the understanding of the covalently bonded **Au−5′−Au** and **Au−6′−Au** junctions, are not considered by the chosen level of DFT.

A more detailed computational study of the C$_4$SnMe$_3$, C$_2$SnMe$_3$, NCS, NCSe, and CN terminated molecules and their conductance behavior under bias, taking the interactions with the Au electrodes into account, is reported elsewhere.[90]

Still, the calculations show that the energetic positions of the molecular orbitals and the extent of the HOMO/LUMO gap can be tuned by varying the terminal ligand of a X{M}C$_4${M}X, even if metal center, bridging, and equatorial ligands are kept unaltered.

Single-Molecule Transport Measurements. Based on the results of the spectroscopic and electrochemical studies as well as of the computational findings, the coordinatively binding complexes **7**−**9** and the SnMe$_3$ capped compounds **5** and **6** were chosen for transport measurements at the single-molecule level using a mechanically controllable break-junction. The results are summarized in Figure 3 and Table 4. As the direct electron tunneling between the Au electrodes is an non-negligible conductance channel in a molecular transport junction,[46] the electrode spacing of the corresponding metal−molecule−metal system has to be taken into account. The junction **Au−5′−Au** formed after the cleavage of the SnMe$_3$ group has a resulting junction length (C$_\beta$−C$_\beta$ distance of 13.95 Å after cleavage) comparable to **Au−9−Au** (with a N−N distance of 13.74 Å), whereas the **Au−6′−Au** junction (C$_\beta$-C$_\beta$ distance of 19.02 Å after cleavage) is in a length range with the NCS (S−S distance of 16.94 Å) and NCSe (Se−Se distance of 17.33 Å) junctions **Au−8−Au** and **Au−7−Au**.

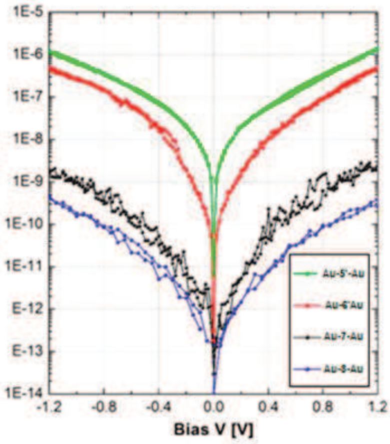

Figure 3. Current−voltage (*I*−*V*) characteristics taken at 300 K for the junctions **Au−5′−Au** (green), **Au−6′−Au** (red), **Au−7−Au** (black), and **Au−8−Au** (blue).

Table 4. Typical Current Values for 5′, 6′, 7, and 8 Averaged From the *I*−*V* Double Sweeps at 200 mV and at 1 V

	current level [A] extracted at different bias	
compd.	200 mV	1 V
5′	2.03×10^{-8}	6.51×10^{-7}
6′	5.56×10^{-9}	2.13×10^{-7}
7	6.66×10^{-12}	1.29×10^{-9}
8	1.79×10^{-12}	1.77×10^{-10}

For the C$_2$ and C$_4$ terminal substituents of the **Au−5′−Au** and **Au−6′−Au** junctions, acetylenic-, vinylidenic-, and (alkynyl vinylidenic)-configured bonding schemes can be postulated upon binding to the Au electrodes. A computational study of the possible bonding motifs of the C$_4$SnMe$_3$ terminated molecule suggested that the different bonding schemes do not differ significantly in their conductance behavior.[90] To elucidate the bonding schemes of the C$_2$ and C$_4$ anchor groups, further spectroscopic experiments are planned, e.g., XPS and Raman spectroscopy.

For **9**, only histograms have been acquired revealing a less pronounced accumulation at 8.1×10^{-7} G$_0$, most likely due to unstable binding situations as the phosphine ligands sterically hinder the short CN anchor to bind to the Au surface. The low conductance and the sterical hindrance renders the CN end group rather inefficient for electron injection. In contrast to **9**, the statistical transport measurements of **5′**, **6′**, **7**, and **8** provided reproducible and consistent results that are displayed in Figure 3. The data presented show representative and individual four-step (from 0.0 to −1.2 to 0.0 V and from 0.0 to +1.2 and 0.0 V) *I*−*V* characteristics for **Au−5′** (green), **6′** (red), **7** (black), and **8** (blue) acquired at room temperature and extracted from large statistical data sets of more than 1000 *I*−*V* characteristics.[74,90] On the first glance, the *I*−*V* characteristics at 300 K look similar regarding their functional behavior and differ strongly in: (A) the current amplitude at both low and high bias, (B) the current onset (at zero bias), and (C) the signal-to-noise ratio. These parameters differ for the four end groups because of the following reasons: At 300 K, a finite local density of states (LDOS) is arising at $E_{F,Au}$ from the energy level of the MOs being broadened thermally and by coupling the MO to leads.[91]

Additionally, E_F is broadened at 300 K giving rise to a finite conductance and hence a finite current at zero bias. In Figure 3, the current is generally increasing with increasing bias for all compounds, indicating that the frontier MOs get energetically better aligned with the chemical potentials of left or right leads. In contrast to measurements taken at low temperatures (<100 K), where resonant transport properties are being revealed by distinct steps in the $I-V$ curves,[92] at 300 K the MOs are smeared out, and generally a nonlinear (almost exponential) functional $I-V$ behavior with only a few distinguishable features is found.

We will discuss in the following the two comparative parameters current level and current increase and further quantify the current fluctuations as measure for the junction's high-field stability:

(A) The current levels of compound **8** (blue; (1.5−2.2) × 10^{-10} A at ±1.0 V) and **7** (black; (1.0−1.8) × 10^{-9} A at ±1.0 V) differ by almost 1 order of magnitude, rendering NCS coupling the weakest among all coupling motifs studied here. Compounds **5′** and **6′** with direct C−Au coupling reveal current levels ranging between (6.0−7.2) × 10^{-7} and (2.0−2.4) × 10^{-7} A at ±1.0 V, an approximately 100- and a 1000-fold increase in current compared to −NCSe and −NCS termination. As the Fe−C_4−Fe molecular backbone is kept equal in all four compounds, charging effects that may shift the MO's energy levels in Au−molecule−Au systems significantly compared to the isolated molecules are expected to be similar for all compounds. Hence, the current levels represent in a first-order approximation the electronic coupling strength of the corresponding end group. Consequently the NCSe termination provides a better coupling compared to NCS as the current is increased by a factor of 10. The direct C−Au bond, as established during cleavage of the $SnMe_3$ group, reveals an at least 2 orders of magnitude higher current level compared to NCSe (**7**) and 3 orders of magnitude compared to the NCS (**8**) termination. This relative increase in the transport characteristics is in agreement with findings on the low-bias conductance of S−Au and C−Au coupled oligophenylenes[47] as well as DFT calculations[90] that indicate a strong electronic hybridization between molecular and metal states.

(B) The functional current increase when starting the bias sweep at zero is similar for NCS and NCSe termination, in contrast to a very abrupt increase in current for the direct C−Au coupling. In the latter case, the current increases, e.g., from 0.4 pA to 0.4 nA (**4**) or 1.0 nA (**5′**) within only 20 mV. This indicates that resonant MOs or MOs close-to-resonance are available at E_F, presumably established by spatial overlap of molecular and metal states leading to electronic hybridization[90] as discussed above. Additional to the zero-bias current level, the slopes of the $I-V$ curves differ. They are found to behave almost linear on the semilog representation at biases larger than approximately ±0.3 V for **5′** and larger than ±0.4 V for **6′**, respectively. This indicates that for the C−Au coupling, the contribution of the MOs next to the frontier ones to transport is minor in the bias window available. From the DFT calculations, it seems that the "conducting" orbitals in the molecule−metal interface are assumed to be of π type as they constitute the HOMO/LUMO region and are therefore more suited for electron transport.

(C) The last comparative parameter concerns the noise in the current as a measure for the junction stability under electrical load. Despite of the 3 orders of magnitude higher current, the current fluctuations are 1 order of magnitude smaller for C−Au coupling compared with NCS coupling, in particular for voltages larger than ±0.4 V (Figure S52).

This indicates that even under large current densities, the C−Au bond has very limited bond fluctuations and that the electron−phonon-coupling in the Fe−C_4−Fe backbone is rather small in all compounds.

We summarize from the transport properties of **5′**, **6′**, **7**, and **8** as displayed in Figure 3 and Table 4 that variations of the anchoring motif strongly and directly influence the transport properties of the corresponding Au−molecule−Au system. A strong increase in conductance occurs in particular when employing covalent C−Au bonds. The end group therefore enables to tune the transport properties over more than 3 orders of magnitude.

■ CONCLUSION

It was demonstrated that the class of {Fe}−C≡C−C≡C−{Fe} ({Fe} = Fe(depe)$_2$, depe = 1,2-bis(diethylphospino)ethane) organometallic complexes can be modified to incorporate terminal substituents capable of binding to Au electrodes to form stable single-molecular junctions by establishing either covalent or coordinative bonds to Au electrodes. A triad of precursor molecules with highly reactive ligands in *trans* position to the bridging butadiyne was designed to target this terminal substituent function. Synthetic strategies were developed to introduce CN, SH and NO_2, C_2H, C_2SnMe_3, C_4SnMe_3, NCSe, and NCS substituents at the terminal sites.

The molecular design of the precursor molecules as well as the strategy for the synthetic pathways enable a facile modification of the termini of the X{Fe}−C≡C−C≡C−{Fe}X system to tailor the molecule−metal coupling for specific applications.

The systematic synthetic approach allows a variation of the structural motifs, involving the metal centers, the bridging ligand, and the equatorial ligand sphere, to be modified in order to modulate the charge transport properties. The end groups chosen are conjugated moieties and covalently bound to the Fe centers. Various binding motifs to Au electrodes were tested that form coordinative to covalent bonds, enabling to electronically extend the electron delocalization of the {Fe}−C≡C−C≡C−{Fe} core toward the leads by hybridization of MO and metal states as it takes place upon a covalent C−Au binding. The C−Au end groups allow a direct charge injection into the redox active molecules. The utilization of the sp-hybridized and electronically highly versatile butadiyne bridging ligand was demonstrated to drastically increase charge transport rates by lowering the injection barrier across the molecule−metal interface. DFT model studies suggest that the HOMO/LUMO gap can be tuned by varying the X groups of a X{M}C_4{M}X system even if the metal centers and bridging and equatorial ligands are kept unaltered.

To allow a comparison of the current levels, molecules with comparable overall molecular lengths were chosen for single-molecule transport measurements at 300 K under ultrahigh vacuum conditions. For the C_2 terminated **5′** a current level of approximately 6.5 × 10^{-7} A at 1.0 V was achieved, reaching 1% of the maximal current available for Au−Au quantum point contacts (77.6 × 10^{-6} A at 1.0 V assuming one conductance channel). Additionally, both C−Au bonded systems exhibited a higher stability and less fluctuations in the transport properties. When comparing the conductance of the organometallic compounds as a function of wire length, the Fe-based molecules **5′** and **6′** outperform the currently best conductive molecular wire systems (at comparable length), the poly-*p*-phenylene possessing a C−Au coupling.[47] The covalently bonded C_2 and C_4 molecular junctions behave like highly conjugated systems.

Therefore, the utilization of covalent C(sp)−Au bonds and of strongly electronically delocalized polycarbyl chains with embedded metal centers into the molecular backbone is an attractive concept to achieve low-ohmic molecular wires generating hybridized metal−molecule interfaces, close MO level alignments with E_F and electron pathways delocalized across the backbone. These three parameters provide high-conductive molecular wires that are strongly required for future nanoelectronics.

■ ASSOCIATED CONTENT

Ⓢ Supporting Information

Experimental details describing the syntheses as well as giving details of the NMR spectroscopy (Figures S1−S28, Table S1), IR spectroscopy (Figures S29−S38), cyclic voltammetry (Figures S42−S50) experiments, refinement details and crystallographic data (Tables S2−S5, Figures S39−S41 and CIFs) for the X-ray diffraction studies, computational results (Figure S51, and a XYZ file with the Cartesian coordinates of all optimized geometries) and additional transport results (Figure S52). This material is available free of charge via the Internet at http://pubs.acs.org.

■ AUTHOR INFORMATION

Corresponding Authors

hberke@chem.uzh.ch
venkatesan.koushik@chem.uzh.ch
eml@zurich.ibm.com

Notes

The authors declare no competing financial interest.

■ ACKNOWLEDGMENTS

Funding from the National Research Program "Smart Materials" (NRP 62, grant 406240-126142) of the Swiss National Science Foundation (SNSF) and the University of Zürich is gratefully acknowledged. We thank T. Fox for his help with the NMR studies. We acknowledge the technical support of U. Drechsler, M. Tschudy, and Ch. Rettner and the scientific discussions with R. Stadler, G. Kastlunger, M. Koch, N. Mosso, and G. Puebla-Hellmann.

■ REFERENCES

(1) Carroll, R. L.; Gorman, C. B. *Angew. Chem., Int. Ed.* **2002**, No. 41, 4378−4400.

(2) Lörtscher, E.; Ciszek, J. W.; Tour, J.; Riel, H. *Small* **2006**, *2* (8−9), 973−977.

(3) Reed, M. A. *Science* **1997**, *278* (5336), 252−254.

(4) Aviram, A.; Ratner, M. A. *Chem. Phys. Lett.* **1974**, *29* (2), 277−283.

(5) Tour, J. M. *Acc. Chem. Res.* **2000**, *33* (11), 791−804.

(6) Cuniberti, G. *Introducing molecular electronics*; Springer: Berlin, 2005.

(7) Kaliginedi, V.; Moreno-García, P.; Valkenier, H.; Hong, W.; García-Suárez, V. M.; Buiter, P.; Otten, J. L. H.; Hummelen, J. C.; Lambert, C. J.; Wandlowski, T. *J. Am. Chem. Soc.* **2012**, *134* (11), 5262−5275.

(8) Wen, H.-M.; Yang, Y.; Zhou, X.-S.; Liu, J.-Y.; Zhang, D.-B.; Chen, Z.-B.; Wang, J.-Y.; Chen, Z.-N.; Tian, Z.-Q. *Chem. Sci.* **2013**, *4* (6), 2471.

(9) Hong, W.; Manrique, D. Z.; Moreno-García, P.; Gulcur, M.; Mishchenko, A.; Lambert, C. J.; Bryce, M. R.; Wandlowski, T. *J. Am. Chem. Soc.* **2012**, *134* (4), 2292−2304.

(10) Chen, F.; Hihath, J.; Huang, Z.; Li, X.; Tao, N. J. *Annu. Rev. Phys. Chem.* **2007**, *58* (1), 535−564.

(11) Zotti, L. A.; Kirchner, T.; Cuevas, J.-C.; Pauly, F.; Huhn, T.; Scheer, E.; Erbe, A. *Small* **2010**, *6* (14), 1529−1535.

(12) Luo, L.; Choi, S. H.; Frisbie, C. D. *Chem. Mater.* **2011**, *23* (3), 631−645.

(13) Lu, Q.; Liu, K.; Zhang, H.; Du, Z.; Wang, X.; Wang, F. *ACS Nano* **2009**, *v3* (12), 3861−3868.

(14) He, J.; Chen, F.; Li, J.; Sankey, O. F.; Terazono, Y.; Herrero, C.; Gust, D.; Moore, T. A.; Moore, A. L.; Lindsay, S. M. *J. Am. Chem. Soc.* **2005**, *127* (5), 1384−1385.

(15) Ho Choi, S.; Kim, B.; Frisbie, C. D. *Science* **2008**, *320* (5882), 1482−1486.

(16) Zhao, X.; Huang, C.; Gulcur, M.; Batsanov, A. S.; Baghernejad, M.; Hong, W.; Bryce, M. R.; Wandlowski, T. *Chem. Mater.* **2013**, *25* (21), 4340−4347.

(17) Prins, F.; Monrabal-Capilla, M.; Osorio, E. A.; Coronado, E.; van der Zant, Herre S. J. *Adv. Mater.* **2011**, *23* (13), 1545−1549.

(18) Low, P. J. *Dalton Trans.* **2005**, No. 17, 2821.

(19) Wuttke, E.; Hervault, Y.-M.; Polit, W.; Linseis, M.; Erler, P.; Rigaut, S.; Winter, R. F. *Organometallics* **2014**, *33*, 4672−4686.

(20) O'Hanlon, D. C.; Cohen, B. W.; Moravec, D. B.; Dallinger, R. F.; Hopkins, M. D. *J. Am. Chem. Soc.* **2014**, *136*, 3127−3136.

(21) Creutz, C.; Taube, H. *J. Am. Chem. Soc.* **1973**, *95* (4), 1086−1094.

(22) Tuccitto, N.; Ferri, V.; Cavazzini, M.; Quici, S.; Zhavnerko, G.; Licciardello, A.; Rampi, M. A. *Nat. Mater.* **2008**, *8* (1), 41−46.

(23) Aguirre-Etcheverry, P.; O'Hare, D. *Chem. Rev.* **2010**, *110* (8), 4839−4864.

(24) Costuas, K.; Rigaut, S. *Dalton Trans.* **2011**, *40* (21), 5643.

(25) Low, P. J. *Coord. Chem. Rev.* **2013**, *257* (9−10), 1507−1532.

(26) Szafert, S.; Paul, F.; Meyer, W. E.; Gladysz, J. A.; Lapinte, C. *C. R. Chim.* **2008**, *11* (6−7), 693−701.

(27) Bruce, M. I.; Costuas, K.; Davin, T.; Ellis, B. G.; Halet, J.-F.; Lapinte, C.; Low, P. J.; Smith, M. E.; Skelton, B. W.; Toupet, L.; White, A. H. *Organometallics* **2005**, *24* (16), 3864−3881.

(28) Montigny, F. de; Argouarch, G.; Costuas, K.; Halet, J.-F.; Roisnel, T.; Toupet, L.; Lapinte, C. *Organometallics* **2005**, *24* (19), 4558−4572.

(29) Lissel, F.; Blacque, O.; Venkatesan, K.; Berke, H. *Organometallics* **2014**, submitted.

(30) Haines, D. E.; O'Hanlon, D. C.; Manna, J.; Jones, M. K.; Shaner, S. E.; Sun, J.; Hopkins, M. D. *Inorg. Chem.* **2013**, *52* (16), 9650−9658.

(31) Low, P. J.; Bock, S. *Electrochim. Acta* **2013**, *110*, 681−692.

(32) Pevny, F.; Di Piazza, E.; Norel, L.; Drescher, M.; Winter, R. F.; Rigaut, S. *Organometallics* **2010**, *29* (22), 5912−5918.

(33) Wuttke, E.; Pevny, F.; Hervault, Y.-M.; Norel, L.; Drescher, M.; Winter, R. F.; Rigaut, S. *Inorg. Chem.* **2012**, *51* (3), 1902−1915.

(34) Lissel, F.; Fox, T.; Blacque, O.; Polit, W.; Winter, R. F.; Venkatesan, K.; Berke, H. *J. Am. Chem. Soc.* **2013**, *135* (10), 4051−4060.

(35) Ward, M. D. *Chem. Soc. Rev.* **1995**, *24* (2), 121.

(36) Frohnapfel, D. S.; Woodworth, B. E.; Thorp, H. H.; Templeton, J. L. *J. Phys. Chem. A* **1998**, *102* (28), 5665−5669.

(37) Guillemot, M.; Toupet, L.; Lapinte, C. *Organometallics* **1998**, *17* (10), 1928−1930.

(38) Paul, F.; Lapinte, C. *Coord. Chem. Rev.* **1998**, *178−180, Part 1* (0), 431−509.

(39) Halet, J.-F.; Lapinte, C. *Coord. Chem. Rev.* **2013**, *257* (9−10), 1584−1613.

(40) Quardokus, R. C.; Lu, Y.; Wasio, N. A.; Lent, C. S.; Justaud, F.; Lapinte, C.; Kandel, S. A. *J. Am. Chem. Soc.* **2012**, *134* (3), 1710−1714.

(41) Marques-Gonzalez, S.; Yufit, D. S.; Howard, Judith A. K.; Martin, S.; Osorio, H. M.; Garcia-Suarez, V. M.; Nichols, R. J.; Higgins, S. J.; Cea, P.; Low, P. J. *Dalton Trans.* **2013**, *42* (2), 338–341.

(42) Mayor, M.; Hänisch, C. von; Weber, H. B.; Reichert, J.; Beckmann, D. *Angew. Chem., Int. Ed.* **2002**, *41* (7), 1183–1186.

(43) Benameur, A.; Brignou, P.; Di Piazza, E.; Hervault, Y.-M.; Norel, L.; Rigaut, S. *New J. Chem.* **2011**, *35* (10), 2105.

(44) Luo, L.; Benameur, A.; Brignou, P.; Choi, S. H.; Rigaut, S.; Frisbie, C. D. *J. Phys. Chem. C* **2011**, *115* (40), 19955–19961.

(45) Kim, B.-S.; Beebe, J.; Olivier, C.; Rigaut, S.; Touchard, D.; Kushmerick, J.; Zhu, X.-Y.; Frisbie, C. *J. Phys. Chem. C* **2007**, *111* (20), 7521–7526.

(46) Gotsmann, B.; Riel, H.; Lörtscher, E. *Phys. Rev. B* **2011**, *84*, 205408.

(47) Chen, W.; Widawsky, J. R.; Vazquez, H.; Schneebeli, S. T.; Hybertsen, M. S.; Breslow, R.; Venkataraman, L. *J. Am. Chem. Soc.* **2011**, *133* (43), 17160–17163.

(48) Nath, S.; Ghosh, S.; Kundu, S.; Praharaj, S.; Panigrahi, S.; Pal, T. *J. Nanopart. Res.* **2006**, *8* (1), 111–116.

(49) Pearson, R. G. *Chemical hardness*; Wiley-VCH: Weinheim, Germany, 1997.

(50) Mishchenko, A.; Zotti, L. A.; Vonlanthen, D.; Bürkle, M.; Pauly, F.; Cuevas, J. C.; Mayor, M.; Wandlowski, T. *J. Am. Chem. Soc.* **2011**, *133* (2), 184–187.

(51) Lörtscher, E.; Cho, C. J.; Mayor, M.; Tschudy, M.; Rettner, C.; Riel, H. *ChemPhysChem* **2011**, *12* (9), 1677–1682.

(52) Vazquez, H.; Skouta, R.; Schneebeli, S.; Kamenetska, M.; Breslow, R.; Venkataraman, L.; Hybertsen, M. *Nat. Nanotechnol.* **2012**, *7* (10), 663–667.

(53) Reed, M. A. *Science* **1997**, *278* (5336), 252–254.

(54) Sheridan, M. V.; Lam, K.; Geiger, W. E. *J. Am. Chem. Soc.* **2013**, *135* (8), 2939–2942.

(55) Sheridan, M. V.; Lam, K.; Geiger, W. E. *Angew. Chem., Int. Ed.* **2013**, *52* (49), 12897–12900.

(56) Pearson, R. G. *J. Chem. Sci.* **2005**, *117*, 369.

(57) Hong, W.; Li, H.; Liu, S.-X.; Fu, Y.; Li, J.; Kaliginedi, V.; Decurtins, S.; Wandlowski, T. *J. Am. Chem. Soc.* **2012**, *134* (47), 19425–19431.

(58) Cheng, Z.-L.; Skouta, R.; Vazquez, H.; Widawsky, J. R.; Schneebeli, S.; Chen, W.; Hybertsen, M. S.; Breslow, R.; Venkataraman, L. *Nat. Nanotechnol.* **2011**, *6* (6), 353–357.

(59) Ballesteros, L. M.; Martín, S.; Momblona, C.; Marqués-González, S.; López, M. C.; Nichols, R. J.; Low, P. J.; Cea, P. *J. Phys. Chem. C* **2012**, *116* (16), 9142–9150.

(60) *CrysAlis*^{Pro}; Agilent Technologies (formerly Oxford Diffraction): Yarnton, England, 2011.

(61) Clark, R. C.; Reid, J. S. *Acta Crystallogr., Sect. A: Found. Crystallogr.* **1995**, *51* (6), 887–897.

(62) Farrugia, L. J. *J. Appl. Crystallogr.* **1999**, *32* (4), 837–838.

(63) Dolomanov, O. V.; Bourhis, L. J.; Gildea, R. J.; Howard, Judith A. K.; Puschmann, H. *J. Appl. Crystallogr.* **2009**, *42* (2), 339–341.

(64) Sheldrick, G. M. *Acta Crystallogr., Sect. A: Found. Crystallogr.* **2008**, *64* (1), 112–122.

(65) Spek, A. L. *J. Appl. Crystallogr.* **2003**, *36* (1), 7–13.

(66) Frisch, M. J.; Trucks, G. W.; Schlegel, H. B.; Scuseria, G. E.; Rob, M. A.; Cheeseman, J. R.; Montgomery, J. A., Jr.; Vreven, T.; Kudin, K. N.; Burant, J. C.; Millam, J. M.; Iyengar, S. S.; Tomasi, J.; Barone, V.; Mennucci, B.; Cossi, M.; Scalmani, G.; Rega, N.; Petersson, G. A.; Nakatsuji, H.; Hada, M.; Ehara, M.; Toyota, K.; Fukuda, R.; Hasegawa, J.; Ishida, M.; Nakajima, T.; Honda, Y.; Kitao, O.; Nakai, H.; Klene, M.; Li, X.; Knox, J. E.; Hratchian, H. P.; Cross, J. B.; Bakken, V.; Adamo, C.; Jaramillo, J.; Gomperts, R.; Stratmann, R. E.; Yazyev, O.; Austin, A. J.; Cammi, R.; Pomelli, C.; Ochterski, J. W.; Ayala, P. Y.; Morokuma, K.; Voth, G. A.; Salvador, P.; Dannenberg, J. J.; Zakrzewski, V. G.; Dapprich, S.; Daniels, A. D.; Strain, M. C.; Farkas, O.; Malick, D. K.; Rabuck, A. D.; Raghavachari, K.; Foresman, J. B.; Ortiz, J. V.; Cui, Q.; Baboul, A. G.; Clifford, S.; Cioslowski, J.; Stefanov, B. B.; Liu, G.; Liashenko, A.; Piskorz, P.; Komaromi, I.; Martin, R. L.; Fox, D. J.; Keith, T.; Al-Laham, M. A.; Peng, C. Y.; Nanayakkara, A.; Challacombe, M.; Gill, P. M. W.; Johnson, B.; Chen, W.; Wong, M. W.; Gonzalez, C.; Pople, J. A. *Gaussian 03*, revision D.01; Gaussian Inc.: Wallingford, CT, 2003.

(67) Adamo, C.; Barone, V. *Chem. Phys. Lett.* **1999**, *314* (1–2), 152–157.

(68) Hay, P. J.; Wadt, W. R. *J. Chem. Phys.* **1985**, *82* (1), 270.

(69) Wadt, W. R.; Hay, P. J. *J. Chem. Phys.* **1985**, *82* (1), 284.

(70) Hay, P. J.; Wadt, W. R. *J. Chem. Phys.* **1985**, *82* (1), 299.

(71) Krishnan, R.; Binkley, J. S.; Seeger, R.; Pople, J. A. *J. Chem. Phys.* **1980**, No. 72, 650.

(72) McLean, A. D.; Chandler, G. S. *J. Chem. Phys.* **1980**, No. 72, 5639.

(73) Wachters, A. J. H. *J. Chem. Phys.* **1970**, No. 52, 1033.

(74) Lörtscher, E.; Weber, H.; Riel, H. *Phys. Rev. Lett.* **2007**, *98* (17), 176807.

(75) Barclay, J. E.; Leigh, G. J.; Houlton, A.; Silver, J. *J. Chem. Soc., Dalton Trans.* **1988**, No. 11, 2865.

(76) George, A. V.; Field, L. D.; Malouf, E. Y.; McQueen, A. E. D.; Pike, S. R.; Purches, G. R.; Hambley, T. W.; Buys, I. E.; White, A. H.; Hockless, D. C. R.; Skelton, B. W. *J. Organomet. Chem.* **1997**, *538* (1–2), 101–110.

(77) Hughes, D. L.; Leigh, G. J.; Jimenez-Tenorio, M.; Rowley, A. T. *J. Chem. Soc., Dalton Trans.* **1993**, No. 1, 75.

(78) Adams, R. D.; Davison, A.; Selegue, J. P. *J. Am. Chem. Soc.* **1979**, *101* (24), 7232–7238.

(79) Field, L. D.; George, A. V.; Laschi, F.; Malouf, E. Y.; Zanello, P. *J. Organomet. Chem.* **1992**, *435* (3), 347–356.

(80) Colbert, M. C. B.; Lewis, J.; Long, N. J.; Raithby, P. R.; Younus, M.; White, A. J. P.; Williams, D. J.; Payne, N. N.; Yellowlees, L.; Beljonne, D.; Chawdhury, N.; Friend, R. H. *Organometallics* **1998**, *17* (14), 3034–3043.

(81) Jiao, H.; Costuas, K.; Gladysz, J. A.; Halet, J.-F.; Guillemot, M.; Toupet, L.; Paul, F.; Lapinte, C. *J. Am. Chem. Soc.* **2003**, *125* (31), 9511–9522.

(82) Akita, M.; Chung, M.-C.; Sakurai, A.; Sugimoto, S.; Terada, M.; Tanaka, M.; Moro-oka, Y. *Organometallics* **1997**, *16* (22), 4882–4888.

(83) Zhuravlev, F.; Gladysz, J. A. *Chem.—Eur. J.* **2004**, *10* (24), 6510–6522.

(84) Szafert, S.; Gladysz, J. A. *Chem. Rev.* **2003**, *103* (11), 4175–4206.

(85) Forster, D.; Goodgame, D. M. L. *J. Chem. Soc.* **1965**, No. 0, 268–274.

(86) Dembinski, R.; Lis, T.; Szafert, S.; Mayne, C. L.; Bartik, T.; Gladysz, J. *J. Organomet. Chem.* **1999**, *578* (1–2), 229–246.

(87) Le Narvor, N.; Toupet, L.; Lapinte, C. *J. Am. Chem. Soc.* **1995**, *117* (27), 7129–7138.

(88) Dembinski, R.; Bartik, T.; Bartik, B.; Jaeger, M.; Gladysz, J. A. *J. Am. Chem. Soc.* **2000**, *122* (5), 810–822.

(89) Dembinski, R.; Lis, T.; Szafert, S.; Mayne, C. L.; Bartik, T.; Gladysz, J. *J. Organomet. Chem.* **1999**, *578* (1–2), 229–246.

(90) Schwarz, F.; Kastlunger, G.; Lissel, F.; Riel, H.; Venkatesan, K.; Stadler, R.; Berke, H.; Lörtscher, E. *Nano Lett.* **2014**, DOI: 10.1021/nl5029045.

(91) Goddard, W. A. *Handbook of nanoscience, engineering and technology*; CRC Press: Boca Raton, 2003.

(92) Lörtscher, E.; Elbing, M.; Tschudy, M.; von Hänisch, C.; Weber, H. B.; Mayor, M.; Riel, H. *ChemPhysChem* **2008**, *9* (15), 2252–2258.

3.2 SUPPLEMENTARY INFORMATION

Submitted Manuscript (J. Am. Chem. Soc. 2014): F. Lissel, F. Schwarz, O. Blacque, H. Riel, E. Lörtscher, K. Venkatesan, H. Berke: *"Organometallic Single-Molecule Electronics: Tuning Electron Transport through X(diphosphine)$_2$FeC$_4$Fe(diphosphine)$_2$X Building Blocks by Varying the Fe-X-Au Anchoring Scheme from Coordinative to Covalent"*

Organometallic Single-Molecule Electronics: Tuning Electron Transport through X(diphosphine)$_2$FeC$_4$Fe(diphosphine)$_2$X Building Blocks by Varying the Fe-X-Au Anchoring Scheme from Coordinative to Covalent

Franziska Lissel[†], Florian Schwarz[‡], Olivier Blacque[†], Heike Riel[‡], Emanuel Lörtscher*[‡],
Koushik Venkatesan*[†] and Heinz Berke*[†]

† Department of Chemistry, University of Zurich, Winterthurerstrasse 190, CH-8057 Zürich, Switzerland

‡ IBM Research - Zurich, Science & Technology Department, Säumerstrasse 4, CH-8803 Rüschlikon, Switzerland

* hberke@chem.uzh.ch

* venkatesan.koushik@chem.uzh.ch

* eml@zurich.ibm.com

General Procedures

Reagent grade toluene, pentane, diethylether and tetrahydrofuran were dried and distilled from sodium prior to use. Reagent grade benzene and dichloromethane were dried and distilled from CaH_2, acetonitrile from P_2O_5. Deuterated solvents were dried and distilled likewise.

$[\{FeI(\eta^2\text{ - depe})_2\}_2(\mu\text{ - }C{\equiv}C{-}C{\equiv}C)]$[1] **1** and $[\{Fe({-}C{\equiv}C{-}C{\equiv}C{-}SnMe_3)(\eta^2\text{ - depe})_2\}_2(\mu\text{ - }C{\equiv}C{-}C{\equiv}C)]$ **6**[1], and N,N-diethyl-1,1,1-trimethyl-stannyl-amine[2] were prepared based on literature protocols. Sodium acetylide was purchased in a xylene slurry. Prior to use, the xylene was removed by filtration, the reagent washed with pentane and dried in vacuo. Commercially available KSeCN, NaSCN and NaCN were recrystallised from methanol, sodium tetrakis[(3,5-trifluoromethyl)phenyl]borate ($Na[BAr^F_4]$) from diethylether. High quality NaSH and $NaNO_2$ were purchased and used without further purification.

NMR spectra were measured on a Bruker-DRX-500 spectrometer at 500 MHz for ^1H, 125.8 MHz for $^{13}C\{^1H\}$, 202.5 MHz for $^{31}P\{^1H\}$, 168.5 MHz for $^{119}Sn\{^1H\}$, on a Bruker Biospin at 500 MHz for ^1H, 125.8 MHz for $^{13}C\{^1H\}$ and 202.5 MHz for $^{31}P\{^1H\}$ and on a Varian Gemini-2000 spectrometer at 300.1 MHz for ^1H, 121.5 MHz for $^{31}P\{1H\}$, 282.4 MHz for $^{19}F\{^1H\}$ and 96.3 MHz for $^{11}B\{^1H\}$. Chemical shifts for ^1H and ^{13}C are given in ppm relative to the solvent[3], for ^{31}P relative to phosphoric acid, for ^{119}Sn relative to $SnMe_4$ for ^{19}F relative to $CFCl_3$ and for ^{11}B relative to $BF_3{\cdot}Et_2O$. Unless noted otherwise, all NMR were recorded at room temperature. IR spectra were measured using an ATR bridge and recorded on a Perkin-Elmer Spectrum Two FT-IR spectrometer. Raman spectra were recorded on a Renishaw Ramanscope spectrometer (514 nm). CHN elemental analyses were performed with a LECO CHN-932 microanalyzer. Cyclic voltammograms were obtained with a BAS 100W Voltammetric Analyzer (low volume cell). The cell was equipped with an Au working electrode and a Pt counter electrode, and an Ag reference electrode. All sample solutions were 0.1M in Bu_4NPF_6 and recorded with a scan rate of 50, 100 and 200 mV/s. Ferrocene was used as an external standard A BAS 100W program was employed for the data analysis.

Syntheses

[{Fe(−N≡C−CH$_3$)(η^2 - depe)$_2$}$_2$(μ - C≡C−C≡C)]$^{2+}$ [I$^-$]$_2$ 2

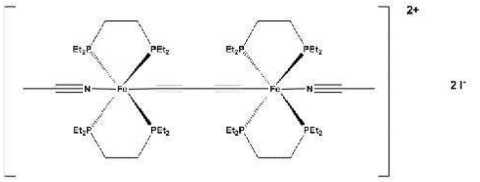

[{FeI(η^2 - depe)$_2$}$_2$(μ - C≡C−C≡C)] **1** (247.7 mg, 0.2 mmol) was suspended in CH$_3$CN (20 mL) and heated to reflux for 30 min. The diiodo complex dissolved under reflux conditions, yielding an orange solution. The solution was filtered over diatomite and the solvent removed in vacuo. The obtained orange solid was washed with toluene and dried in vacuo. Yield: 257.7 mg = 0.195 mmol = 97.6%. Crystals suitable for X-ray were grown in CH$_3$CN at -30 °C.

Anal. Calcd. for $C_{48}H_{106}Fe_2I_2N_2P_8$: C: 43.65; H: 7.78; N: 2.12. **Found**: C: 43.64; H: 7.80; N: 2.08. **IR** (ATR, cm^{-1}): 2248 (m, $\nu_{C\equiv N}$); 1946 (m, $\nu_{C\equiv C}$). **Raman** (514 nm, cm^{-1}): 2245 ($\nu_{C\equiv N}$), 2088 ($\nu_{C\equiv C}$). **^{1}H NMR** (500.3 MHz, CD$_3$CN, after 0 hours): δ = 2.24 - 2.11 (m, 8H, C**H**$_2$-CH$_3$), 2.09 (s, 6H, Fe-N≡C-C**H$_3$**), 1.92 - 1.83 (m, 8H, C**H**$_2$-CH$_3$), 1.82 - 1.65 (m, 32H, C**H**$_2$-CH$_3$ and C**H**$_2$-C**H**$_2$), 1.24 - 1.08 (m, 48H, CH$_2$-C**H**$_3$). **^{13}C{^{1}H} NMR** (125.8 MHz, CD$_3$CN): δ = 128.8 (s, Fe-N≡**C**-CH$_3$ and Fe-N≡**C**-CHD$_2$), 118.2 (s, free N≡**C**-CH$_3$ and N≡**C**-CHD$_2$), 108.6 (s, **C$_\beta$** (FeC$_4$Fe)), 90.1 (p, $^2J_{C-P}$ = 31.5 Hz, **C$_\alpha$** (FeC$_4$Fe chain)), 21.3 - 20.8 (m, **C**H$_2$-CH$_3$), 19.8 - 19.6 (m, **C**H$_2$-**C**H$_2$), 19.5 - 19.3 (m, **C**H$_2$-CH$_3$), 9.4 (d, $^2J_{C-P}$ = 54.1 Hz, CH$_2$-**C**H$_3$), 5.4 (s, Fe-N≡C−**C**H$_3$), 5.0 (sep, $^1J_{C-D}$ = 20.8 Hz, Fe-N≡C−**C**HD$_2$), 1.8 (s, free N≡**C**−CH$_3$). **^{31}P{^{1}H} NMR** (121.5 MHz, CD$_3$CN): δ = 70.9 (s).

[{Fe(−N≡N)(η^2 - depe)$_2$}$_2$(μ - C≡C−C≡C)]$^{2+}$ [B$_{Ar}$$^{F-}$]$_2$ 3

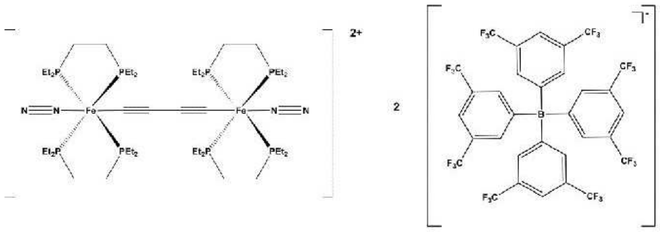

Na[BAr^F$_4$] (443.1 mg, 0.5 mmol) was dissolved in diethylether (5 mL) and stirred vigorously at rt under an dinitrogen atmosphere. [{FeI(η^2 - depe)$_2$}$_2$(μ - C≡C−C≡C)] (247.7 mg, 0.2 mmol) was dispensed in toluene (35 mL) and added to the Na[BAr^F$_4$] solution. The mixture was stirred vigorously for 6 h. A yellow precipitate formed which was filtered off over diatomite and washed with toluene (3 x 10 mL) and diethylether (3 x 20 mL). The product was extracted with hot chlorobenzene (100 °C, 60 mL). The solution was cooled to -30 °C for 12 h, causing the product to precipitate again. The supernatant solution was removed by centrifugation and the obtained yellow solid dried in vacuo. Yield: 480.8 mg = 0.174 mmol = 86.9%. Crystals suitable for X-ray were grown in C$_6$H$_5$Cl at -30 °C.

Anal. Calcd. for $C_{108}H_{120}B_2F_{48}Fe_2N_4P_8$: C: 46.88; H: 4.37; N: 0.78. **Found**: C: 46.65; H: 4.21; N: 0.75. **IR** (ATR, cm^{-1}): 2109 (m, $\nu_{C\equiv C}$); 1980, 1971(w, $\nu_{N\equiv N}$). **Raman** (514 nm, cm^{-1}): 2122 ($\nu_{C\equiv C}$); **^{1}H NMR** (500.3 MHz, THF-d$_8$): δ = 7.81 - 7.78 (m, 16H, m-Ar-**H**), 7.59 (s, 8H, p-Ar-**H**), 2.3 - 2.20(m, 8H, C**H**$_2$-CH$_3$), 2.10 - 2.00 (m, 8H, C**H**$_2$-CH$_3$), 1.98 - 1.89 (m, 32H, C**H**$_2$-CH$_3$ and C**H**$_2$-C**H**$_2$), 1.28 - 1.21 (m, 48H, CH$_2$-C**H**$_3$). **^{13}C{^{1}H} NMR** (125.8 MHz, THF-d$_8$): δ = 162.9 (q (1:1:1:1), $^1J_{C\text{-}B}$ = 49.7 Hz, Aryl, **i-C**), 135.8 - 135.6 (m, Aryl, **m-C**), 130.1 (qq, $^2J_{C\text{-}F}$ = 31.5 Hz, $^4J_{C\text{-}F}$ = 3.8 Hz, Aryl, **o-C**), 125.6 (q, $^1J_{C\text{-}F}$ = 271.7 Hz, **C**F$_3$), 118.4 - 118.2 (m, Aryl, **p-C**), 106.8 (s, **C$_\beta$** (FeC$_4$Fe chain)), 91.2 (p, $^2J_{C\text{-}P}$ = 33.3 Hz, **C$_\alpha$** (FeC$_4$Fe chain)), 21.1 - 20.7 (m, **C**H$_2$-CH$_3$), 20.4 - 20.2 (m, **C**H$_2$-**C**H$_2$), 19.5 - 19.2 (m, **C**H$_2$-CH$_3$), 9.3 (d, $^2J_{C\text{-}P}$ = 74.22 Hz, CH$_2$-**C**H$_3$). **^{31}P{^{1}H} NMR** (121.5 MHz, THF-d$_8$): δ = 64.5 (s). **^{19}F{^{1}H} NMR** (282.4 MHz, THF-d$_8$): δ = - 64.5 (s, -C**F**$_3$). **^{11}B{^{1}H} NMR** (96.3 MHz, THF-d$_8$): δ = - 6.0 (s, **B**-Ar$_4$).

[{Fe(−C≡C−H)(η^2 - depe)$_2$}$_2$(μ - C≡C−C≡C)] 4

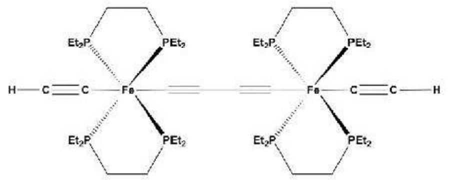

[{FeI(η^2 - depe)$_2$}$_2$(μ - C≡C−C≡C)] **1** (247.7 mg, 0.2 mmol), LiOTf (187.2 mg, 1.2 mmol) and NaC≡CH (28.8 mg, 0.6 mmol) were suspended in THF (25 mL) and heated to reflux for 12 h. The brown solution was filtered over diatomite and the solvent removed in vacuo. After extraction with benzene/pentane (1:1, 50 mL), the solution was again filtered over diatomite. Drying in vacuo gave the title compound as a yellow-brownish solid. Yield: 172.8 mg = 0.167 mmol = 83.5%. Crystals suitable for X-ray diffraction were obtained in THF/acetonitrile at −30 °C.

Anal. Calcd. for $C_{48}H_{98}Fe_2P_8$: C: 55.71; H: 9.55. **Found**: C: 55.99; H: 9.62. **IR** (ATR, cm^{-1}): 3281 (w, $\nu_{C\equiv C-H}$), 1952 (w, $\nu_{C\equiv C}$, C$_4$ bridge), 1901 (s, $\nu_{C\equiv C}$, terminal acetylide). **Raman** (514 nm, cm^{-1}): 2098 (s, $\nu_{C\equiv C}$, C$_4$ bridge), 2008 (w, $\nu_{C\equiv C}$, terminal acetylide), 1907 (w, $\nu_{C\equiv C}$, terminal acetylide); **ESI-MS** ($C_{48}H_{98}Fe_2P_8$): m/z = 1035 ([M]$^+$, 100%). **^{1}H NMR** (500.3 MHz, THF-d$_8$): δ = 2.45 - 2.35 (m, 8H, C**H**$_2$-CH$_3$), 2.33 - 2.23 (m, 8H, C**H**$_2$-CH$_3$), 1.78 - 1.60 (m, 32H, C**H**$_2$-CH$_3$ and C**H**$_2$-C**H**$_2$, overlapping with THF signal), 1.22 - 1.10 (m, 48H, CH$_2$-C**H**$_3$), 1.03 (p, $^4J_{H\text{-}P}$ = 2.5 Hz, 2H, C≡C−**H**). **^{1}H{^{31}P} NMR** (500.3 MHz, THF-d$_8$): δ = 2.40 (dq, 8H, $^2J_{H\text{-}H}$ = 15 Hz, $^3J_{H\text{-}H}$ = 7.5 Hz, C**H**$_2$-CH$_3$), 2.28 (dq, 8H, $^2J_{H\text{-}H}$ = 15 Hz, $^3J_{H\text{-}H}$ = 7.5 Hz, C**H**$_2$-CH$_3$), 1.78 - 1.60 (m, 32H, C**H**$_2$-CH$_3$ and C**H**$_2$-C**H**$_2$, overlapping with THF signal), 1.19 (t, 24H, $^3J_{H\text{-}H}$ = 7.5 Hz, CH$_2$-C**H**$_3$), 1.14 (t, 24H, $^3J_{H\text{-}H}$ = 7.5 Hz, CH$_2$-C**H**$_3$), 1.03 (s, 2H, C≡C−**H**). **^{13}C{^{1}H} NMR** (125.8 MHz, THF-d$_8$): δ = 129.8 (p, $^2J_{C\text{-}P}$ = 25.2 Hz, Fe−**C**≡C−H), 107.5 (s, **C$_\beta$** (FeC$_4$Fe chain)), 99.4 (s, Fe−C≡**C**−H), 98.8 (p, $^2J_{C\text{-}P}$ = 27.7 Hz, **C$_\alpha$** (FeC$_4$Fe chain)), 22.2 - 22.0 (m, **C**H$_2$-CH$_3$), 21.9 - 21.6 (m, **C**H$_2$-**C**H$_2$ and **C**H$_2$-CH$_3$), 10.3 (d, $^2J_{C\text{-}P}$ = 54.1 Hz, CH$_2$-**C**H$_3$). **^{31}P{^{1}H} NMR** (202.5 MHz, THF-d$_8$): 78.5 (s).

[{Fe(−C≡C− SnMe$_3$)(η^2 - depe)$_2$}$_2$(μ - C≡C−C≡C)] 5

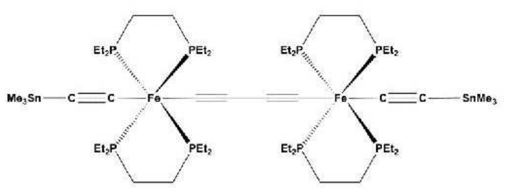

4 (103.5 mg, 0.1 mmol) was dissolved in toluene (15 mL) and a solution of N,N-diethyl-1,1,1-trimethylstannanamine (94.4 mg, 0.4 mmol) in 5 mL toluene was added. The mixture was heated to reflux for 24h, and then the solution was concentrated to 5 mL. Addition of acetonitrile (15 mL) caused the product to precipitate. The supernatant solution was removed and the solid washed with acetonitrile (3 x 5 mL). After extraction with pentane the solution was filtered over diatomite. Drying in vacuo gave the title compound as a yellow-brownish solid. Yield: 119.1 mg, 0.0875 mmol, 87.5%. Crystals suitable for X-ray diffraction were obtained in THF/acetonitrile at −30 °C.

Anal. Calcd. for $C_{54}H_{114}Fe_2P_8Sn_2$: C: 47.68; H: 8.45. **Found**: C: 47.92; H: 8.40. **IR** (ATR, cm^{-1}): 1936 (vs, $\nu_{C\equiv C}$, C_4 bridge), 1904 (m, $\nu_{C\equiv C}$, terminal acetylide). **Raman** (514 nm, cm^{-1}): 2086 (s, $\nu_{C\equiv C}$, C_4 bridge), 2011 (w, $\nu_{C\equiv C}$, terminal acetylide), 1947 (w, $\nu_{C\equiv C}$, terminal acetylide); **ESI-MS** ($C_{48}H_{98}Fe_2P_8$): m/z = 1359 ([M-H]$^+$, 100%), 1199 ([M-SnMe$_3$]$^+$, 16%). **^{1}H NMR** (500.3 MHz, C_6D_6): δ = 2.65 - 2.53 (m, 8H, $C\mathbf{H}_2$-CH_3), 2.42 -2.30 (m, 8H, $C\mathbf{H}_2$-CH_3), 1.77 - 1.63 (m, 32H, $C\mathbf{H}_2$-CH_3 and $C\mathbf{H}_2$-$C\mathbf{H}_2$), 1.27 - 1.1.15 (m, 48H, CH_2-$C\mathbf{H}_3$), 0.23 (s (d, satellites, $^2J_{H\text{-}}119_{Sn}$ = 60.0 MHz; $^2J_{H\text{-}}117_{Sn}$ = 55.0 MHz), 18H, Sn($C\mathbf{H}_3$)$_3$). **^{13}C{^{1}H} NMR** (125.8 MHz, C_6D_6): δ = 170.2 (p, $^2J_{C\text{-}P}$ = 23.9 Hz, Fe−**C**≡C−SnMe$_3$), 111.6 (s, Fe−C≡**C**−SnMe$_3$), 106.7 (s, $\mathbf{C_\beta}$ (FeC$_4$Fe chain)), 99.4 (p, $^2J_{C\text{-}P}$ = 27.7 Hz, $\mathbf{C_\alpha}$ (FeC$_4$Fe chain)), 21.7 - 21.1 (m, $\mathbf{C}H_2$-CH_3 and $\mathbf{C}H_2$-CH_3), 10.1 (d, $^2J_{C\text{-}P}$ = 7.5 Hz, CH_2-$\mathbf{C}H_3$), -6.8 (s,(d, satellites; $^1J_{C\text{-}}119_{Sn}$ = 381.2 MHz and $^1J_{C\text{-}}117_{Sn}$ = 364.8 MHz), Sn($\mathbf{C}H_3$)$_3$). **^{31}P{^{1}H} NMR** (202.5 MHz, C_6D_6): δ = 76.7 (s). **^{119}Sn{^{1}H} NMR** (168.5 MHz, THF-d$_8$): δ = -121.9 (p, $^4J_{Sn\text{-}P}$ = 13.8 Hz, C≡C−**Sn**Me$_3$).

[{Fe(−N=C=Se)(η^2 - depe)$_2$}$_2$(μ - C≡C−C≡C)] 7

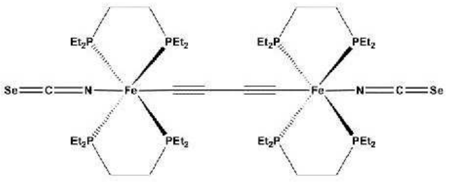

2 (132.1 mg, 0.1 mmol) and KSeCN (288.2 mg, 2 mmol) were suspended in THF (25 mL) and heated to reflux for 6h. The bright orange solution was filtered over a plug of diatomite and the THF removed in vacuo. After washing with cold acetonitrile (3 x 5 mL, -30 °C), the product was extracted with benzene and the solution again filtered over a plug of diatomite. Drying in vacuo gave the title compound as a bright orange solid. Yield: 98.1 mg = 0.0821 mmol = 82.1%. Crystals suitable for X-ray were grown in benzene at rt.

Anal. Calcd. for $C_{46}H_{96}Fe_2N_2P_8Se_2$: C: 46.25; H: 8.10; N: 2.34. **Found**: C: 46.28; H: 8.15; N: 2.27. **IR** (ATR, cm^{-1}): 2094 (s, $\nu_{C=N}$); 1950(m, $\nu_{C\equiv C}$). **Raman** (514 nm, cm^{-1}): 2097 ($\nu_{C\equiv C}$); **^{1}H NMR** (500.3 MHz, C_6D_6): δ = 2.04 - 1.95 (m, 8H, $C\mathbf{H}_2$-CH_3), 1.93 - 1.83 (m, 8H, $C\mathbf{H}_2$-CH_3), 1.66 - 1.53 (m, 16H, $C\mathbf{H}_2$-CH_3 and $C\mathbf{H}_2$-$C\mathbf{H}_2$), 1.52 - 1.42 (m, 16H, $C\mathbf{H}_2$-CH_3 and $C\mathbf{H}_2$-$C\mathbf{H}_2$), 1.10 - 1.04 (m, 24H, CH_2-$C\mathbf{H}_3$), 1.02 - 0.95 (m, 24H, CH_2-$C\mathbf{H}_3$). **^{13}C{^{1}H} NMR** (125.8 MHz, C_6D_6): δ = 129.5 (s, N=**C**=Se), 109.4 (s, $\mathbf{C_\beta}$ (FeC$_4$Fe)), 89.8 (p, $^2J_{C\text{-}P}$ = 29.6 Hz, $\mathbf{C_\alpha}$ (FeC$_4$Fe chain)), 21.0 - 20.6 (m, $\mathbf{C}H_2$-CH_3), 20.0 - 19.8 (m, $\mathbf{C}H_2$-$\mathbf{C}H_2$), 19.6 - 19.3 (m, $\mathbf{C}H_2$-CH_3), 9.3 (d, $^2J_{C\text{-}P}$ = 37.7 Hz, CH_2-$\mathbf{C}H_3$). **^{31}P{^{1}H} NMR** (202.5 MHz, C_6D_6): δ = 73.0 (s).

S5

[{Fe(−N=C=S)(η^2 - depe)$_2$}$_2$(μ - C≡C−C≡C)] 8

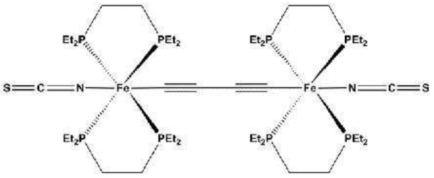

[{FeI(η^2 - depe)$_2$}$_2$(μ - C≡C−C≡C)] **1** (123.9 mg, 0.1 mmol) and NaSCN (162 mg, 2 mmol) were suspended in CH_3CN (20 mL) and heated to reflux for 6h. The acetonitrile was removed in vacuo. After extraction with benzene (25 mL), the solution was filtered over diatomite and the solvent was removed in vacuo. The obtained product was washed with cold CH_3CN (3 x 5 mL, -30 °C) and dried in vacuo. Yield: 93.8 mg = 0.0852 mmol = 85.2%. Crystals suitable for X-ray were obtained by slow diffusion of pentane into a benzene solution at rt.

Anal. Calcd. for $C_{46}H_{96}Fe_2N_2P_8S_2$: C: 50.19; H: 8.79; N: 2.54. **Found**: C: 50.28; H: 8.66; N: 2.49. **IR** (ATR, cm^{-1}): 2096 (s, $\nu_{C=N}$); 1950(m, $\nu_{C\equiv C}$). **Raman** (514 nm, cm^{-1}): 2097 ($\nu_{C\equiv C}$). **^{1}H NMR** (500.3 MHz, C_6D_6): δ = 2.07 - 1.97 (m, 8H, $C\mathbf{H}_2$-CH_3), 1.94 - 1.84 (m, 8H, $C\mathbf{H}_2$-CH_3), 1.67 - 1.56 (m, 16H, $C\mathbf{H}_2$-CH_3 and $C\mathbf{H}_2$-$C\mathbf{H}_2$), 1.55 - 1.44 (m, 16H, $C\mathbf{H}_2$-CH_3 and $C\mathbf{H}_2$-$C\mathbf{H}_2$), 1.12 - 1.04 (m, 24H, CH_2-$C\mathbf{H}_3$), 1.04 - 0.97 (m, 24H, CH_2-$C\mathbf{H}_3$). **^{13}C{^{1}H} NMR** (125.8 MHz, C_6D_6): δ = 142.0 (s, N=**C**=S), 108.8 (s, $\mathbf{C}_\beta$ (FeC_4Fe)), 89.8 (p, $^2J_{C\text{-}P}$ = 29.6 Hz, $\mathbf{C}_\alpha$ (FeC_4Fe)), 21.2 - 20.7 (m, $\mathbf{C}H_2$-CH_3), 20.1 - 19.8 (m, $\mathbf{C}H_2$-$\mathbf{C}H_2$), 19.8 - 19.5 (m, $\mathbf{C}H_2$-CH_3), 9.3 (d, $^2J_{C\text{-}P}$ = 46.5 Hz, CH_2-$\mathbf{C}H_3$). **^{31}P{^{1}H} NMR** (202.5 MHz, C_6D_6): δ = 74.1 (s).

[{Fe(−C≡N)(η^2 - depe)$_2$}$_2$(μ - C≡C−C≡C)] 9

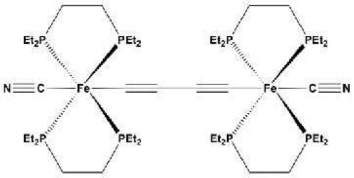

[{FeI(η^2 - depe)$_2$}$_2$(μ - C≡C−C≡C)] **1** (123.9 mg, 0.1 mmol) and NaCN (98 mg, 2 mmol) were suspended in CH_3CN (20 mL) and heated to reflux for 24h. The solvent was removed in vacuo. After extraction with CH_2Cl_2, the solution was filtered over diatomite and concentrated to a volume of 5 mL before CH_3CN (10 mL) was added. At -30 °C, the product crystallized from the solution in the course of 12 h. The product was washed with diethylether (3 x 10 mL) and dried in vacuo. Yield: 85.3 mg = 0.0823 mmol =82.3%. Crystals suitable for X-Ray were obtained from THF/pentane at -30 °C.

Anal. Calcd. for $C_{46}H_{96}Fe_2N_2P_8$: C: 53.29; H: 9.33; N: 2.70. **Found**: C: 53.21; H: 9.30; N: 2.67. **IR** (ATR, cm^{-1}): 2056 (s, $\nu_{C\equiv N}$); 1955 (m, $\nu_{C\equiv C}$). **Raman** (514 nm, cm^{-1}): 2103 ($\nu_{C\equiv C}$). **^{1}H NMR** (500.3 MHz, C_6D_5Cl): δ = 2.31 - 1.18 (m, 16H, $C\mathbf{H}_2$-CH_3), 1.77 - 1.52 (m, 32H, CH_2-CH_3 and $C\mathbf{H}_2$-$C\mathbf{H}_2$), 1.17 - 1.06 (m, 48H, CH_2-$C\mathbf{H}_3$). **^{13}C{^{1}H} NMR** (125.8 MHz, C_6D_5Cl): δ = 156.1 (br, **C**≡N), 106.6 (br, $\mathbf{C}_\beta$ (FeC_4Fe)), 97.7 (br, $\mathbf{C}_\alpha$ (FeC_4Fe)), 23.0 - 22.6 (m, $\mathbf{C}H_2$-CH_3), 21.5 - 20.9 (m, $\mathbf{C}H_2$-$\mathbf{C}H_2$), 20.6 - 20.2 (m, $\mathbf{C}H_2$-CH_3), 9.6 (d, $^2J_{C\text{-}P}$ = 34.0 Hz, CH_2-$\mathbf{C}H_3$). **^{31}P{^{1}H} NMR** (202.5 MHz, C_6D_5Cl): δ = 73.8 (s).

[{Fe(−S−H)(η^2 - depe)$_2$}$_2$(μ - C≡C−C≡C)] 10

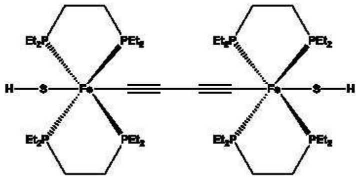

3 (279.3 mg, 0.1 mmol) and NaSH (112 mg, 2 mmol) were suspended in THF (40 mL) and stirred vigorously at rt for 2.5h. The colour of the solution changed from yellow to red-brown, monitoring with ^{31}P{^{1}H} showed a full consumption of the starting material. The solution was freed from solids using centrifugation and the solvent removed in vacuo. The obtained solid was washed with diethylether (3 x 5 mL). After extraction with benzene (20 mL), the solution was again freed from solids by centrifugation. Drying in vacuo gave the title compound as a pale orange-red solid. Yield: 80.2 mg = 0.0763 mmol =76.3%. Crystals suitable for X-ray diffraction studies were obtained in THF at -30 °C.

Anal. Calcd. for $C_{44}H_{98}Fe_2P_8S_2$: C: 50.29; H: 9.40. **Found**: C: 50.10; H: 9.31. **IR** (ATR, cm^{-1}): 2545 (w, $\nu_{S\text{-}H}$), 1940 (m, $\nu_{C\equiv C}$). **Raman** (514 nm, cm^{-1}): 2094 ($\nu_{C\equiv C}$). **^{1}H NMR** (500.3 MHz, THF-d$_8$): δ = 2.38 - 2.28 (m, 8H, C**H**$_2$-CH$_3$), 2.27 - 2.17 (m, 8H, C**H**$_2$-CH$_3$), 1.85 - 1.58 (m, 32H, C**H**$_2$-CH$_3$ and C**H**$_2$-C**H**$_2$, overlapping with solvent peak), 1.22 - 1.09 (m, 48H, CH$_2$-C**H**$_3$), -6.35 (p, $^3J_{H\text{-}P}$ = 6.7 Hz, 2H, S-**H**). **^{13}C{^{1}H} NMR** (125.8 MHz, THF-d$_8$): δ = 109.5 (s, **C**$_\beta$ (FeC$_4$Fe)), 93.2 (p, $^2J_{C\text{-}P}$ = 29.6 MHz, **C**$_\alpha$ (FeC$_4$Fe)), 21.8 - 21.3 (m, **C**H$_2$-CH$_3$ and **C**H$_2$-**C**H$_2$), 20.1 - 19.9 (m, **C**H$_2$-CH$_3$), 10.4 (d, $^2J_{C\text{-}P}$ = 26.4 Hz, CH$_2$-**C**H$_3$). **^{31}P{^{1}H} NMR** (202.5 MHz, THF-d$_8$): δ = 70.8 (s).

[{Fe(−NO$_2$)(η^2 - depe)$_2$}$_2$(μ - C≡C−C≡C)] 11

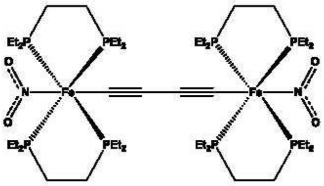

NaNO$_2$ (138 mg, 2 mmol) was suspended in THF (25 mL) and stirred vigorously. **3** (279.3 mg, 0.1 mmol) was dissolved in THF (15 mL) and added to the suspension. The colour of the solution changed from yellow to red, monitoring with ^{31}P{^{1}H} showed a full consumption of the starting material after 60 minutes. The solution was concentrated to a volume of 10 mL and freed from solids using centrifugation. Then the THF was removed in vacuo and the obtained solid washed with acetonitrile (5 x 5 mL). After extraction with benzene (25 mL), the solution was again freed from solids using centrifugation. Drying in vacuo gave the title compound as an orange solid. Yield: 80.9 mg = 0.0751 mmol = 75.1 %. Crystals suitable for X-ray were grown in THF/pentane at -30 °C.

Anal. Calcd. for $C_{44}H_{96}Fe_2N_2O_4P_8$: C: 49.08; H: 8.99; N: 2.60. **Found**: C: 48.97; H: 8.77; N: 2.49. **IR** (ATR, cm^{-1}): 1956 (m, $\nu_{C\equiv C}$), 1738 (w, $\nu_{N=O}$). **Raman** (514 nm, cm^{-1}): 2098 ($\nu_{C\equiv C}$). **^{1}H NMR** (500.3 MHz, CD$_2$Cl$_2$): δ = 2.28 - 2.17 (m, 8H, C**H**$_2$-CH$_3$), 2.07 - 1.91 (m, 16H, C**H**$_2$-CH$_3$ and C**H**$_2$-C**H**$_2$), 1.78 - 1.68 (m, 8H, C**H**$_2$-C**H**$_2$), 1.67 - 1.52 (m, 16H, C**H**$_2$-CH$_3$), 1.18 - 1.08 (m, 48H, CH$_2$-C**H**$_3$). **^{13}C{^{1}H} NMR** (125.8 MHz, CD$_2$Cl$_2$): δ = 110.5 (s, **C**$_\beta$ (FeC$_4$Fe)), 94.7 (p, $^2J_{C\text{-}P}$ = 29.6 MHz, **C**$_\alpha$ (FeC$_4$Fe)), 20.2 - 19.6 (m, **C**H$_2$-CH$_3$ and **C**H$_2$-**C**H$_2$), 18.9 - 18.7 (m, **C**H$_2$-CH$_3$), 9.7 (d, $^2J_{C\text{-}P}$ = 17.6 Hz, CH$_2$-**C**H$_3$). **^{31}P{^{1}H} NMR** (202.5 MHz, CD$_2$Cl$_2$): δ = 70.2 (s).

NMR - Studies

Unless noted otherwise, the depicted spectra were collected at 500.3 MHz for ^{1}H, 125.8 MHz for ^{13}C, 202.5 MHz for ^{31}P and 168.5 MHz for ^{119}Sn.

Table S1. Selected IR and Raman stretches as well as selected ^{13}C{^{1}H}NMR signals of the compounds **2** - **10**.

Compd.	**IR [cm^{-1}]**		**Raman [cm^{-1}] ν (C$_4$)**	**^{31}P{^{1}H}NMR [ppm]**	**^{13}C{^{1}H}NMR [ppm]**		
	$\nu_{(C\equiv C)}$ (C$_4$ bridge)	**ν (terminal ligand)**			**C$_\alpha$ (^{2}J$_{C\text{-}P}$)** [a]	**C$_\beta$**	**C$_{(Endgroup)}$**
2[b]	1946 (m)	2248 (m, $\nu_{C\equiv N}$)	2088	70.9	90.1 (31.5)	108.6	128.8 (Fe--N≡**C**–CH$_3$)
3[c]	2109 (m)	1980, 1971 (w, $\nu_{N\equiv N}$)	2122	64.5	91.5 (33.3)	106.8	--
4[c]	1952 (w)	3281 (w, $\nu_{C\equiv C\text{–}H}$), 1901 (s, $\nu_{C\equiv C}$)	2098	78.5	98.8 (27.7)	107.5	129.9 (Fe–**C**≡C–H), 99.4 (Fe–C≡**C**–H)
5[d]	1936 (vs)	1904 (m, $\nu_{C\equiv C}$)	2086	76.7	99.4 (27.7)	106.7	170.2 (Fe–**C**≡C–SnMe$_3$), 111.6 (Fe–C≡**C**–SnMe$_3$),
6[d, e]	1951 (m, sh at 1967)	2085 (s, sh at 2113, $\nu_{C\equiv C}$)	2102	76.1	99.7 - 98.3 (m)	106.4	139.8 (p, C$_\alpha$), 99.3 (s, C$_\beta$), 99.3 (s, C$_\gamma$), 61.8 (s, C$_\delta$)
7[d]	1950 (m)	2094 (s, $\nu_{C=N}$)	2097	73.0	89.8 (29.6)	109.4	129.5 (Fe–N=**C**=Se)
8[d]	1950 (m)	2096 (s, $\nu_{C=N}$)	2097	74.1	89.9 (29.6)	106.4	141.0 (Fe–N=**C**=S)
9[f, g]	1955 (m)	2056 (s, $\nu_{C\equiv N}$)	2103	73.8	97.7 [f]	106.6	156.2 (Fe–**C**≡N)
10[c]	1940 (m)	2545 (w, $\nu_{S\text{-}H}$)	2094	70.8	93.1 (29.6)	109.5	--
11[h]	1956 (m)	1738 (w, $\nu_{N=O}$)	2098	70.2	94.7 (29.6)	110.5	--

[a] signals split into quintets due to ^{2}J$_{C\text{-}P}$ coupling with the four equivalent phosphors of the depe ligand. The number in brackets refers to the coupling constant in ppm, [b] ^{13}C{^{1}H} NMR in CD$_3$CN, [c] ^{13}C{^{1}H} NMR in THF-d$_8$, [d] ^{13}C{^{1}H} NMR in C$_6$D$_6$, [e] see literature[1], [f] ^{13}C{^{1}H} NMR in C$_6$D$_5$Cl, [g] sp-hybridized carbons gave rise to broad signals in the ^{13}C{^{1}H}NMR, no splitting discernible (see Figure S25), [h] ^{13}C{^{1}H} NMR in CD$_2$Cl$_2$

NMR studies on the terminal ligand exchange of complex **2**

Monitoring the ^{1}H NMR in CD$_3$CN over the course of 24 hours illustrates a fluctuation in the ligand sphere (see Figures S1 and S2), which finally leads to a complete replacement of the CH$_3$CN ligands with the deuterated form. This reflects in the ^{1}H NMR spectra in the steady decline of the initial nitrile methyl peak at 2.09 ppm and the concurrent rise of a peak at1.96 ppm, which is assigned to free acetonitrile. A NOE experiment performed after three days (see Figure S3) is consistent with this interpretation. The existence of this exchange already at room temperature indicates the eligibility of this compound for substitution reactions at the terminal site. As the ^{13}C{^{1}H}NMR of this type of compounds requires long measurement times to allow the signals relating to sp-carbons to evolve, the ^{13}C{^{1}H}NMR of **2** exhibits a mixed spectrum with peaks relating to both the CH$_3$CN and CD$_3$CN coordinating form (see Figure S4). Of note is the low-field shift of the sp hybridized nitrile carbon to 128.8 ppm from 118.3 ppm for the free solvent, thus indicating a donation of the nitrile function towards the metal centre. This finding contrary to the high-field shift observed for mononuclear Fe centres upon nitrile complexation.[4]

Notes on the ^{13}C{^{1}H} NMR of complex **9**

The sp hybridized carbons of complex **9** only give rise to broad signals of low intensity in the ^{13}C{^{1}H} NMR (see Figure S25). This behavior was also observed in THF-d$_8$ and in C$_6$D$_5$Cl, in the latter solvent at room temperature as well as during elevated and low temperature ^{13}C{^{1}H} NMR measurements.

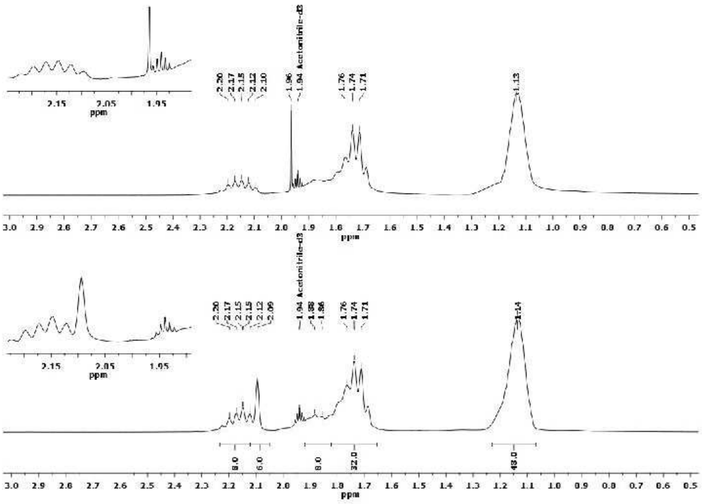

Figure S1. ^{1}H NMR of **2** in CD_3CN (300.1 Mhz): top: after 0 hours at rt; bottom: after 24 hours at rt

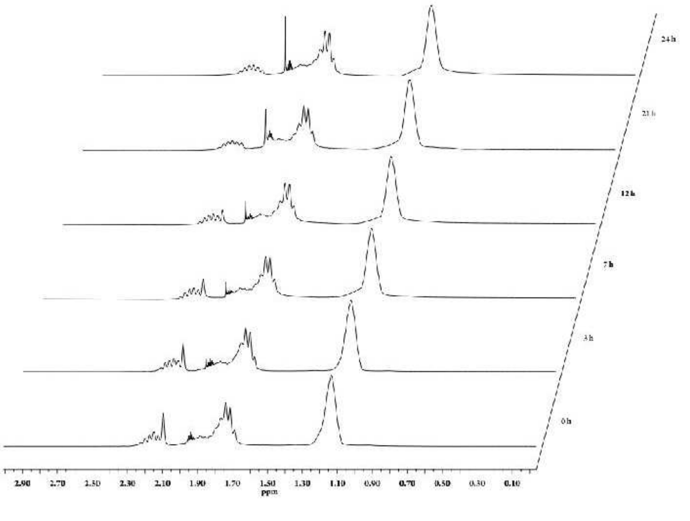

Figure S2. ^{1}H NMR of **2** in CD_3CN (300.1 Mhz): exchange of the coordinated acetonitrile over the course of 24 hours

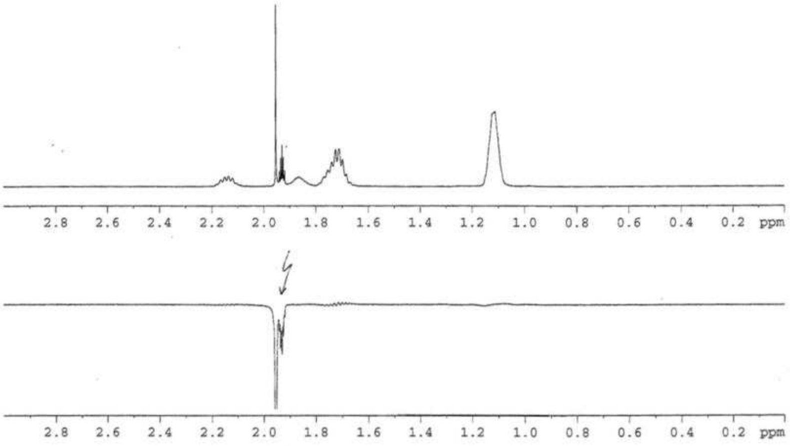

Figure S3. 1D-NOE of **2** in CD$_3$CN after 3 days at rt.

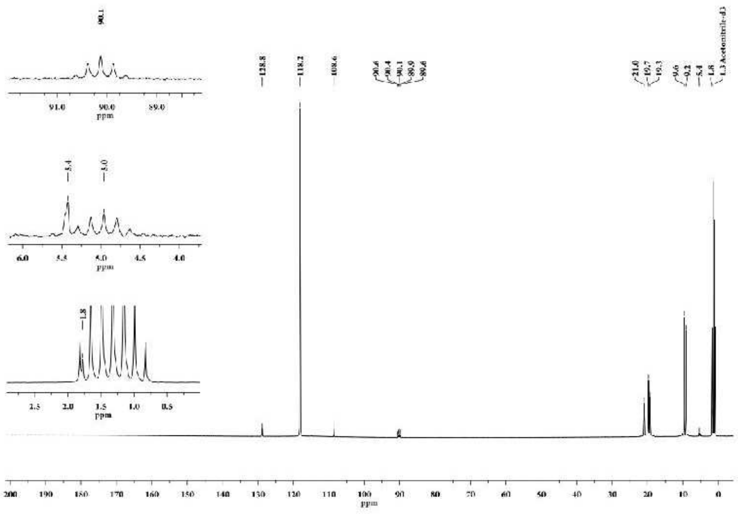

Figure S4. $^{13}C\{^1H\}$ NMR of **2** in CD$_3$CN

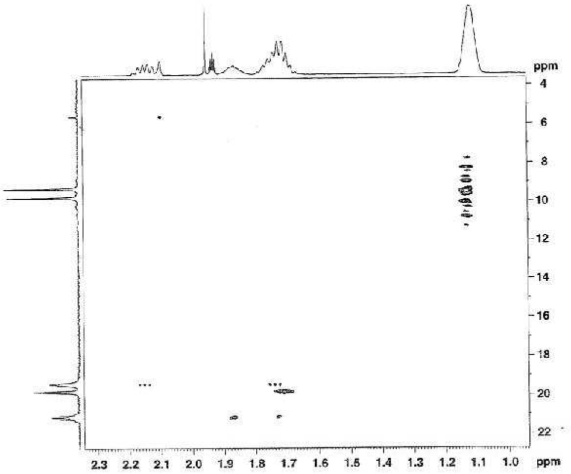

Figure S5. C,H Correlation of **2** in CD_3CN after 15 hours at rt

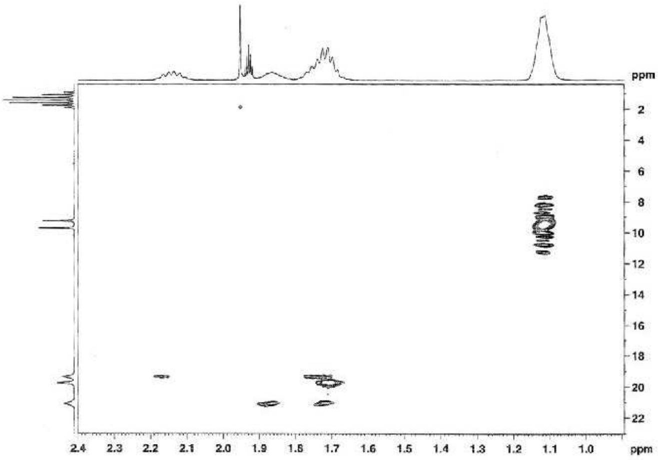

Figure S6. C,H Correlation of **2** in CD_3CN after 3 days at rt

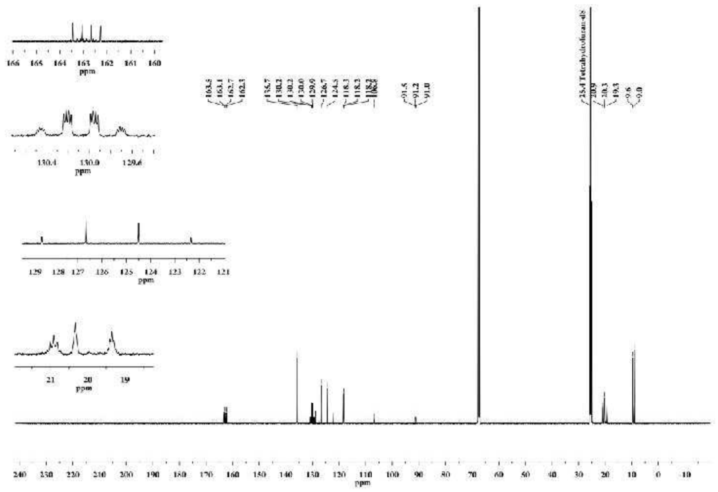

Figure S7. $^{13}C\{^1H\}$ NMR of **3** in THF-d$_8$

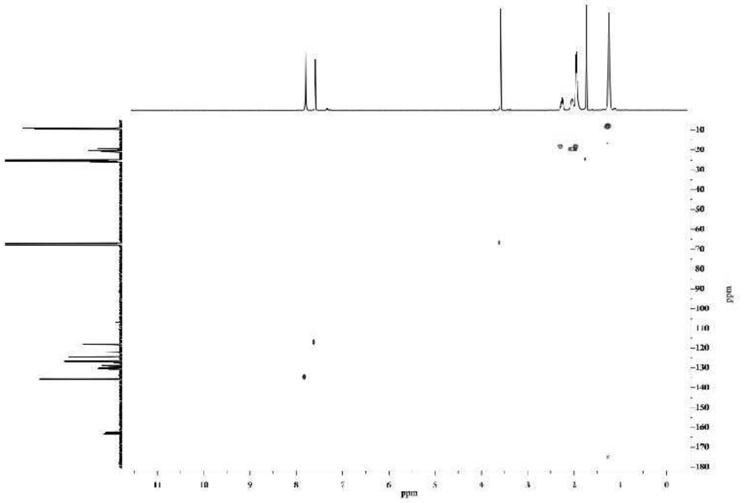

Figure S8. C,H - Correlation of **3** in THF-d$_8$.

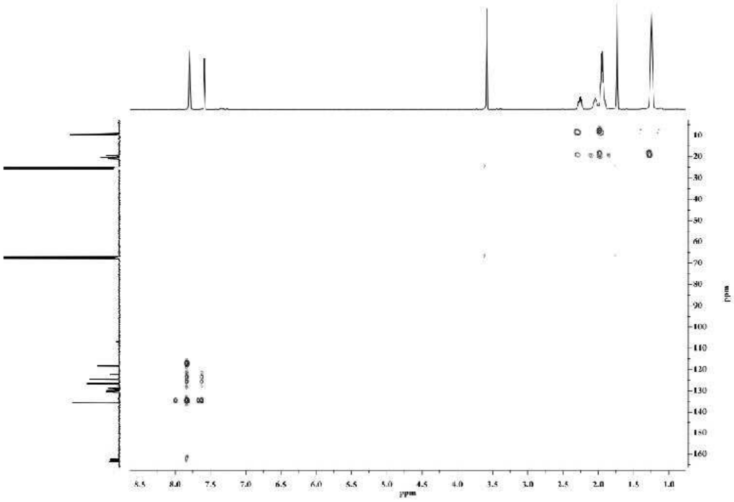

Figure S9. C,H - Correlation (long range) of **3** in THF-d_8.

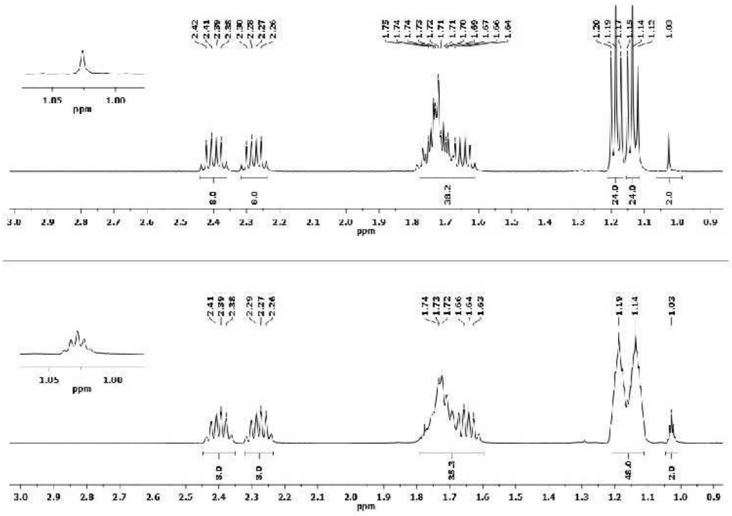

Figure S10. top: $^1H\{^{31}P\}$ NMR of **4** in THF-d_8; bottom: ^1H NMR of **4** in THF-d_8. The sample concentration is different. In both spectra, one of the methanediyl multiplets coincides with the solvent peak (THF, 1.73 ppm)

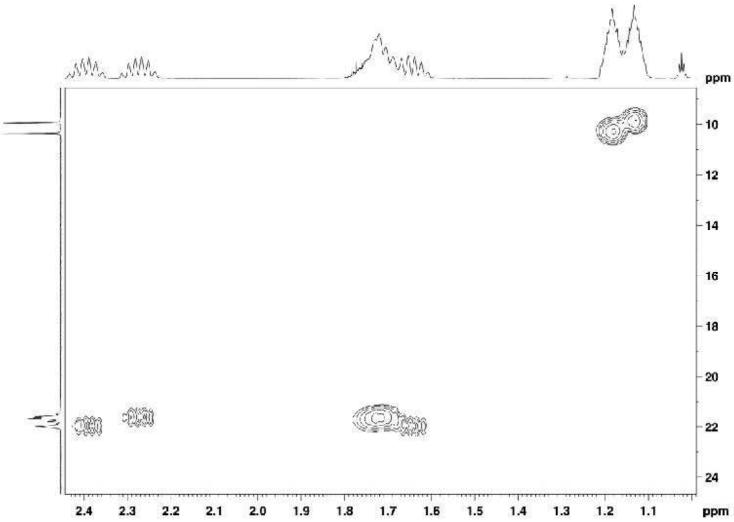

Figure S11. C,H - Correlation of **4** in THF-d_8.

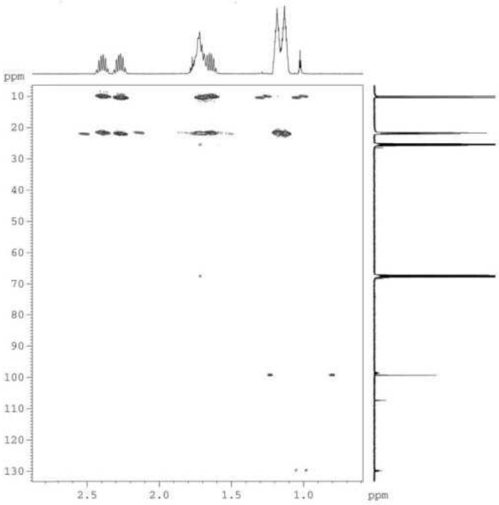

Figure S12. C,H - Correlation (long range) of **4** in THF-d_8.

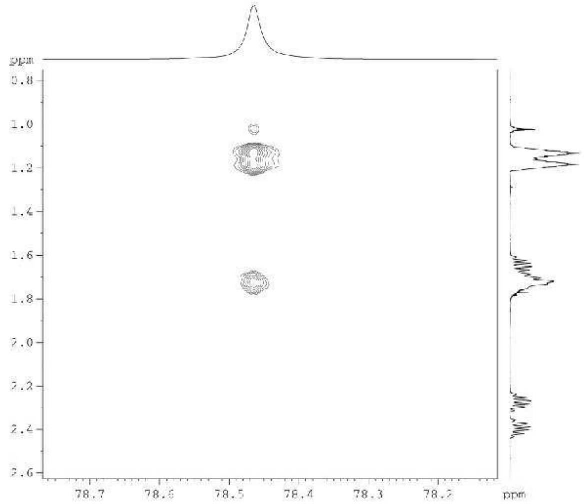

Figure S13. P,H - Correlation of **4** in THF-d_8.

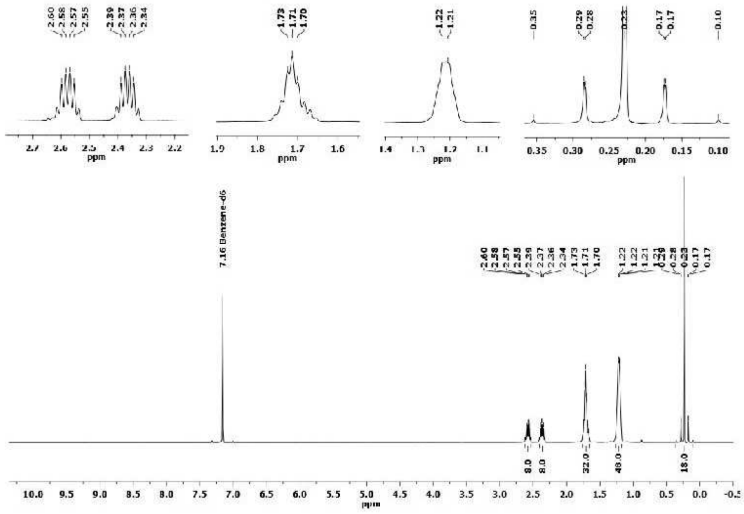

Figure S14. ^{1}H NMR of **5** in C_6D_6

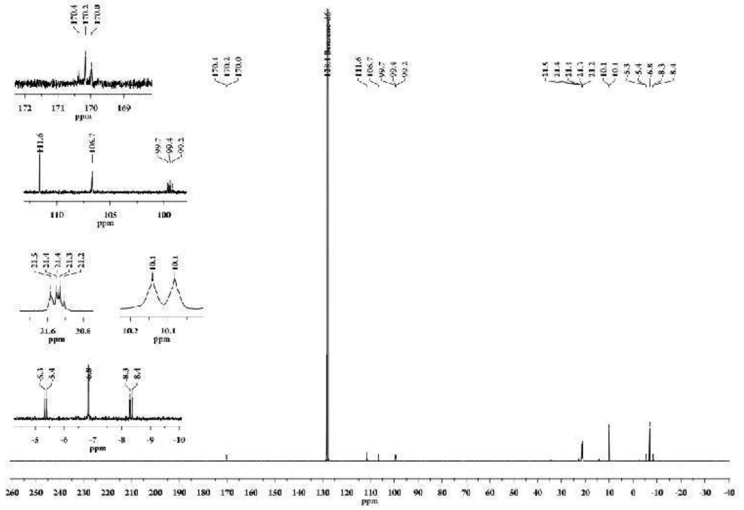

Figure S15. $^{13}C\{^1H\}$ NMR of **5** in C_6D_6

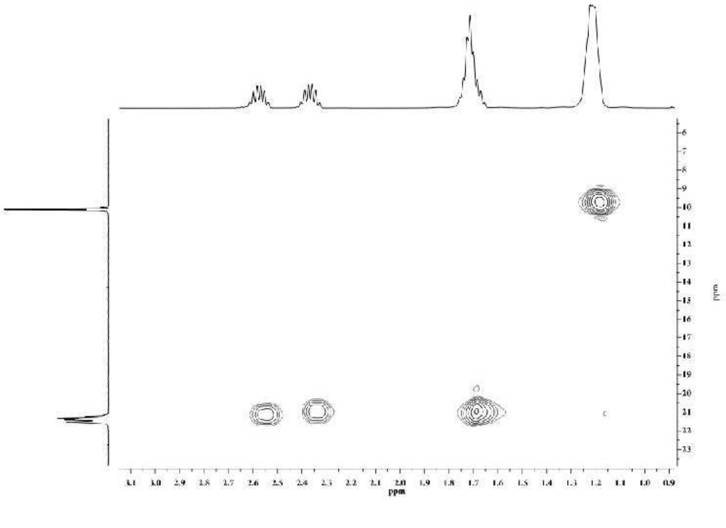

Figure S16. C,H Correlation of **5** in C_6D_6

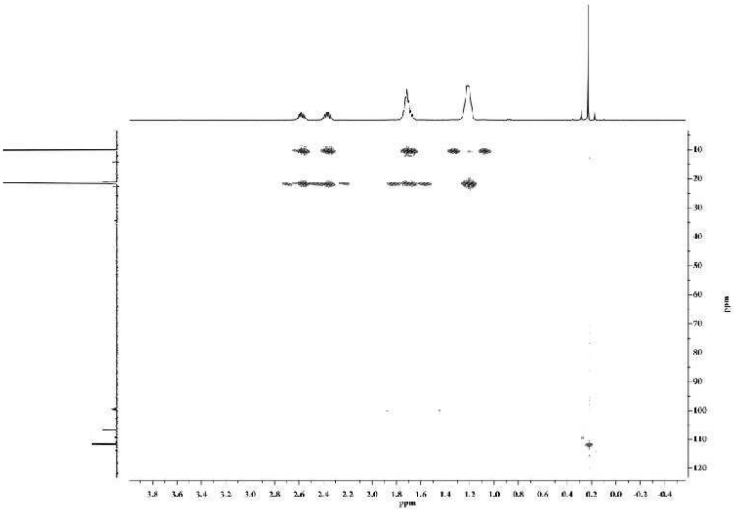

Figure S17. C,H Correlation (long range) of **5** in C_6D_6

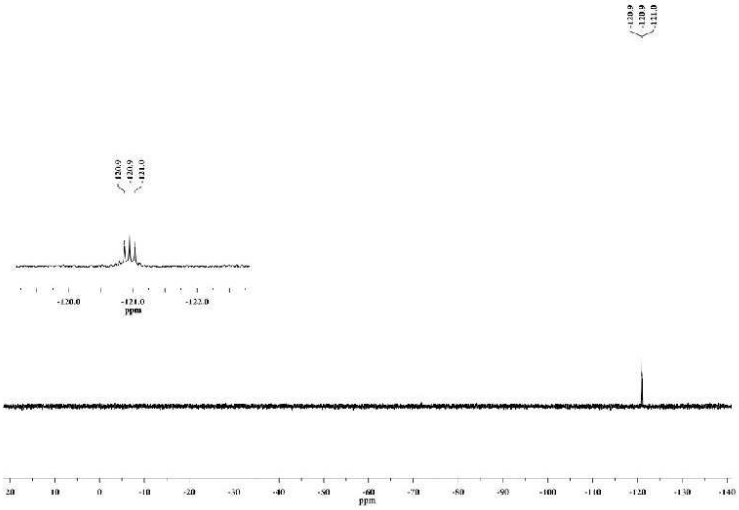

Figure S18. $^{119}Sn\{^1H\}$ NMR of **5** in THF-d_8

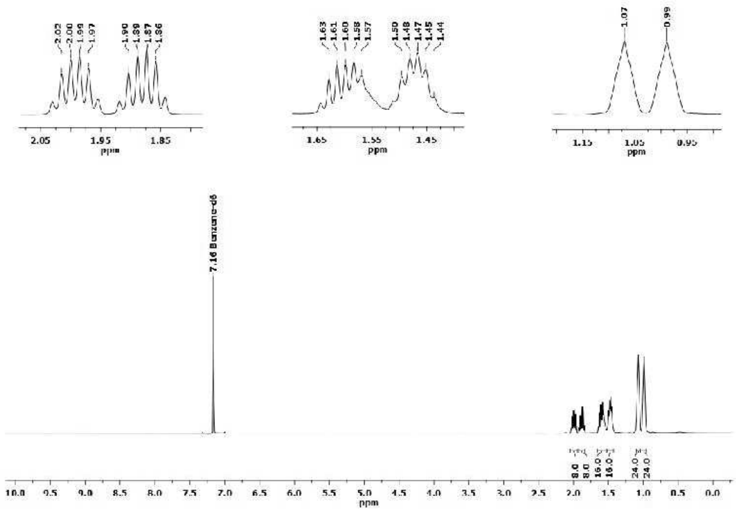

Figure S19. ^{1}H NMR of **7** in C_6D_6

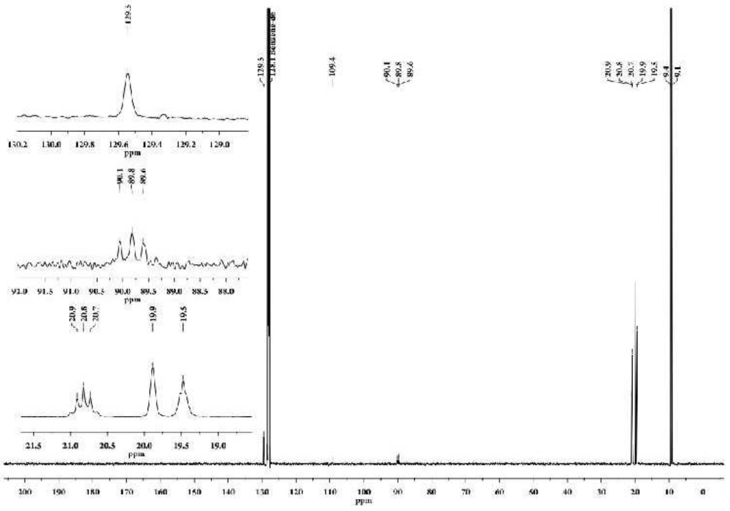

Figure S20. $^{13}C\{^1H\}$ NMR of **7** in C_6D_6

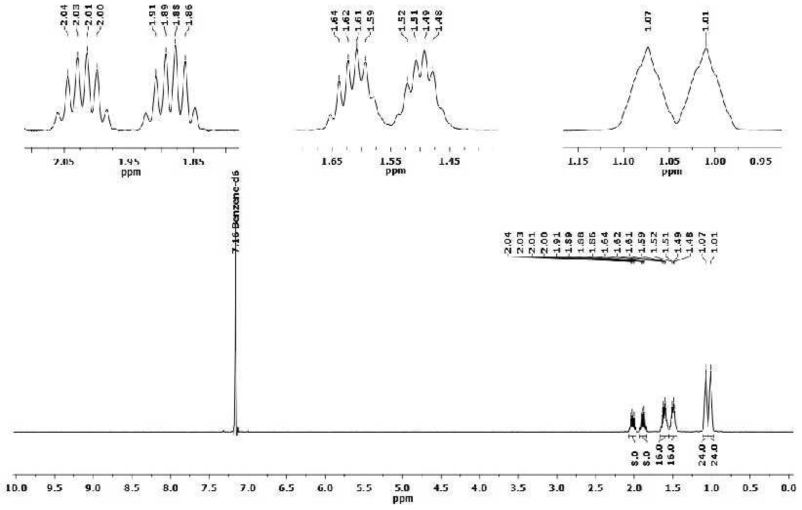

Figure S21. ^{1}H NMR of **8** in C_6D_6

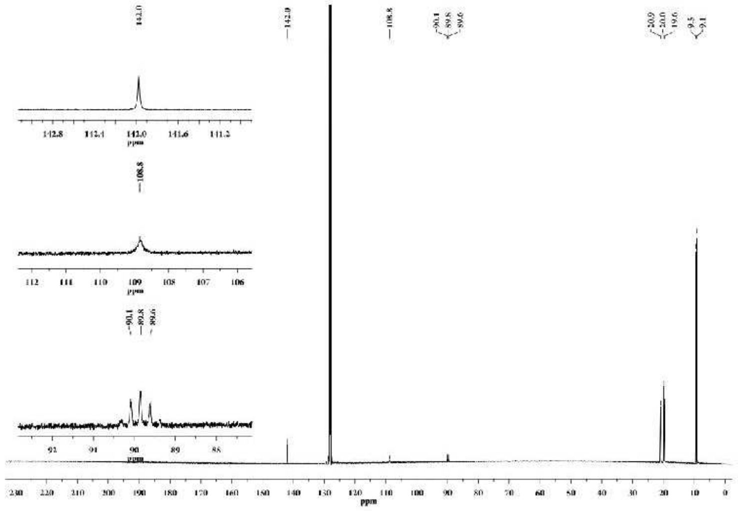

Figure S22. ^{13}C{^{1}H} NMR of **8** in C_6D_6

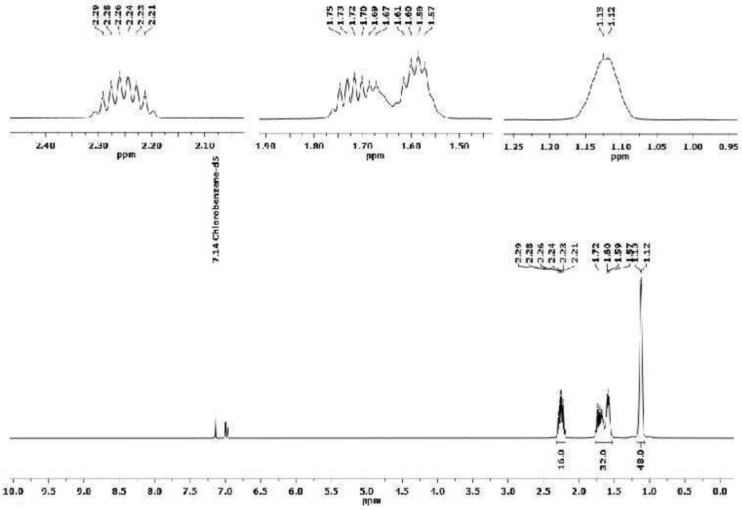

Figure S23.^{1}H NMR of **9** in C_6D_5Cl

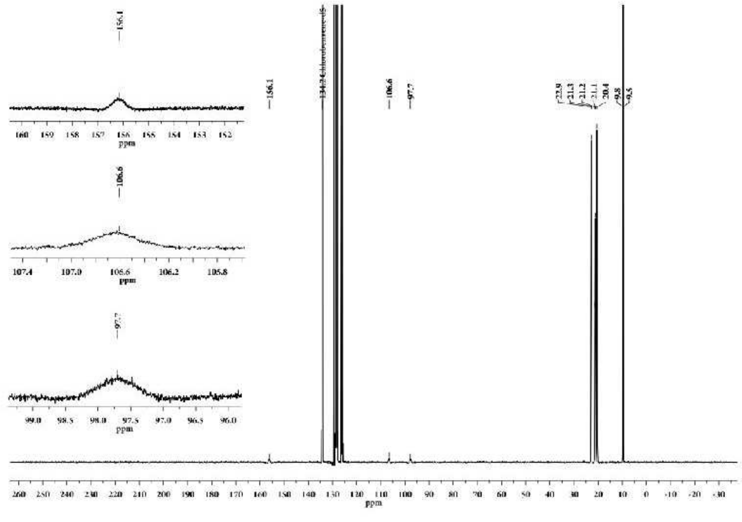

Figure S24. $^{13}C\{^1H\}$ NMR of **9** in C_6D_5Cl

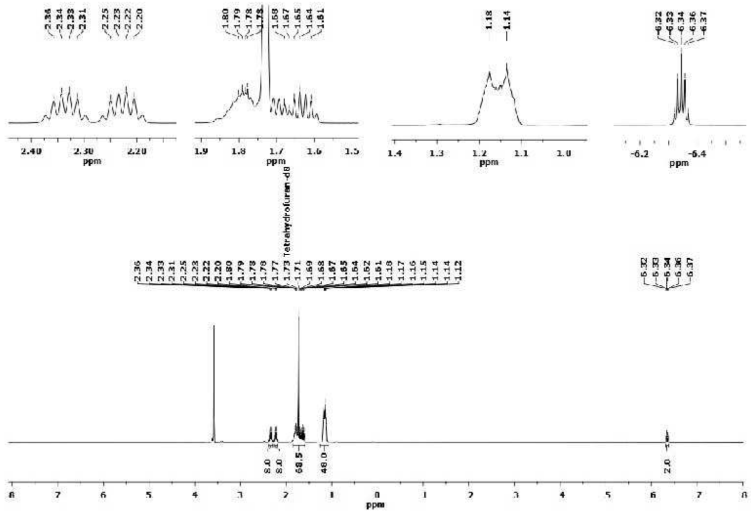

Figure S25. ^{1}H NMR of **10** in THF-d_8. The solvent peak at 1.73 ppm overlaps with methanediyl assigned multiplets

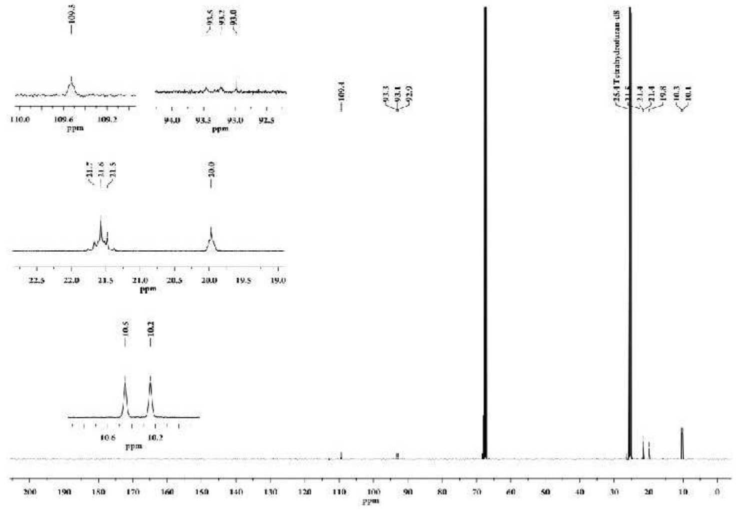

Figure S26. ^{13}C{^{1}H} NMR of **10** in THF-d_8

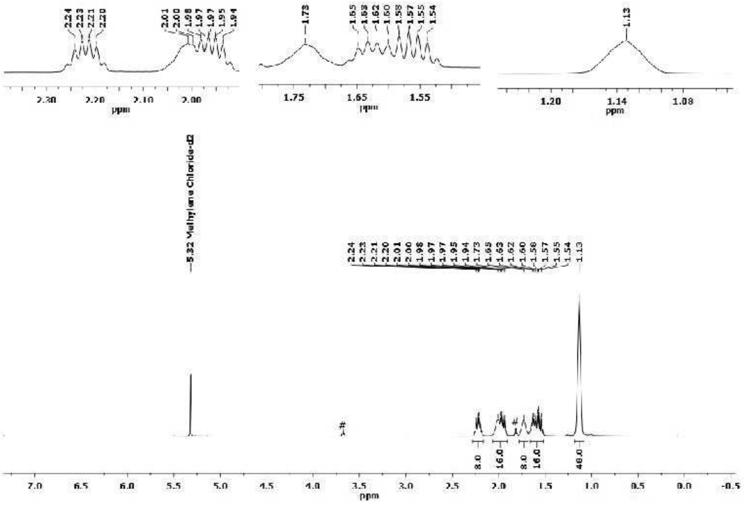

Figure S27. ^1H NMR of **11** in CD_2Cl_2. #: solvent impurity (THF)

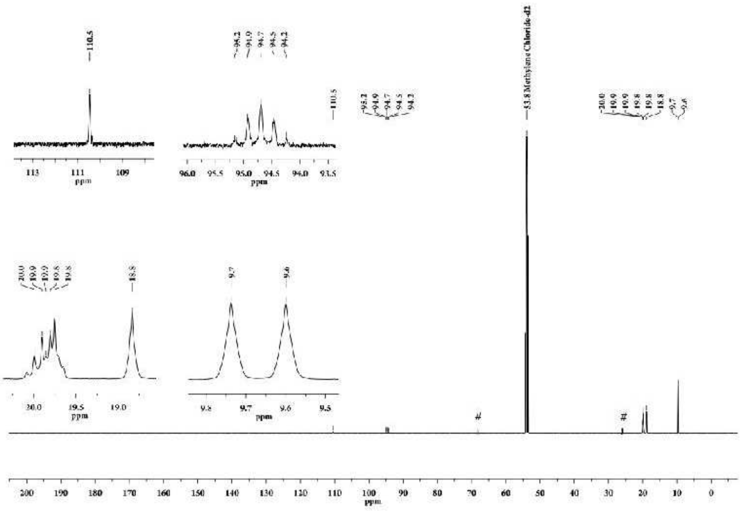

Figure S28. $^{13}C\{^1H\}$ NMR of **11** in CD_2Cl_2. #: solvent impurity (THF)

Infrared Spectra

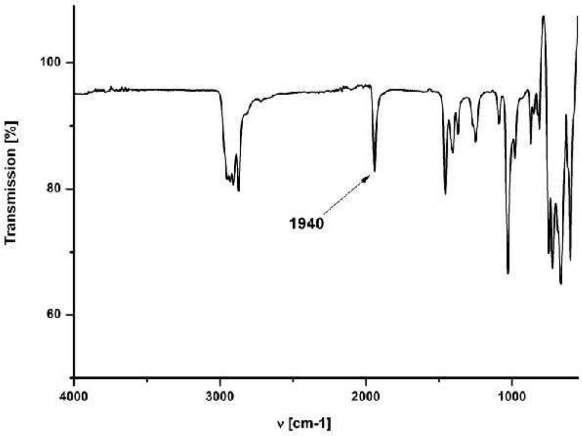

Figure S29. IR spectrum (ATR) of [{FeI(η^2 - depe)$_2$}$_2$(μ - C≡C−C≡C)] **1**

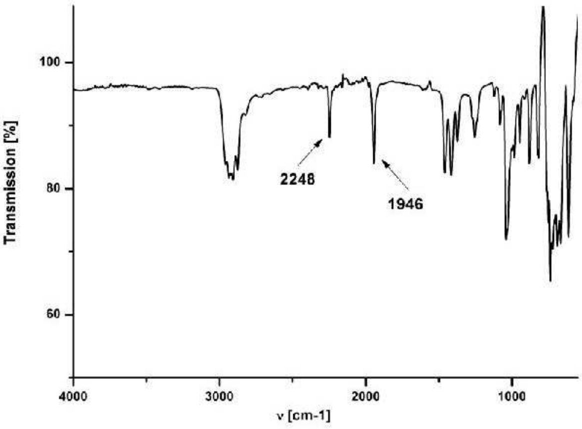

Figure S30. IR spectrum (ATR) of **2**

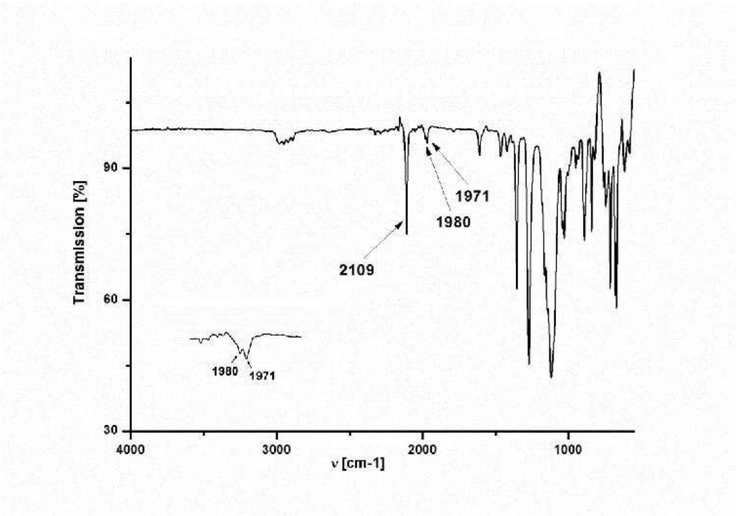

Figure S31. IR spectrum (ATR) of **3**

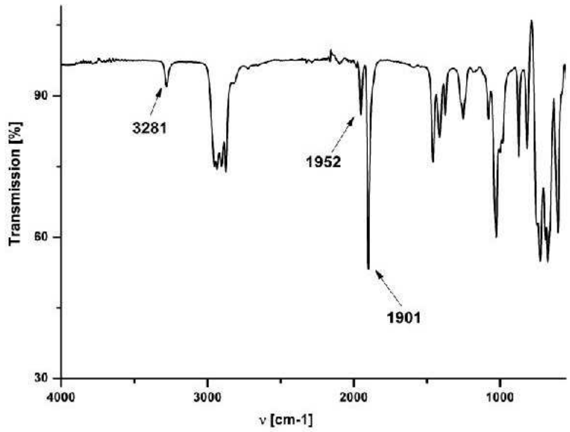

Figure S32. IR spectrum (ATR) of **4**

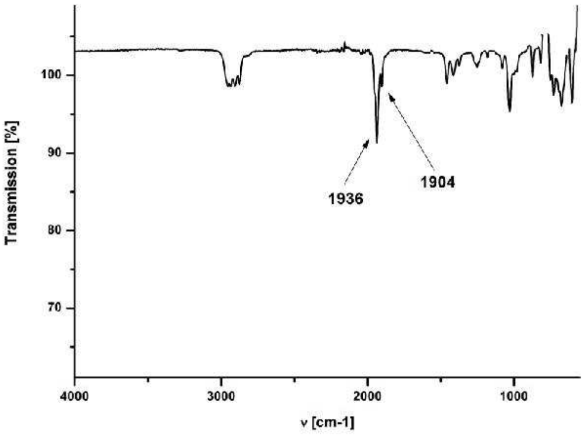

Figure S33. IR spectrum (ATR) of **5**

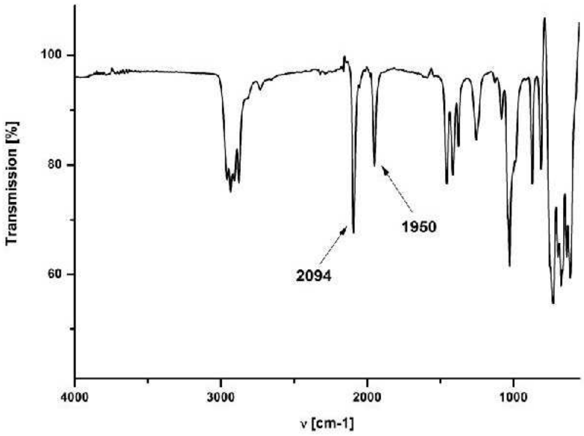

Figure S34. IR spectrum (ATR) of **7**

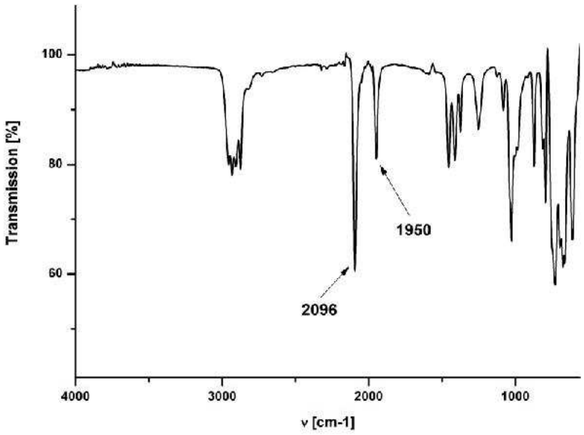

Figure S35. IR spectrum (ATR) of **8**

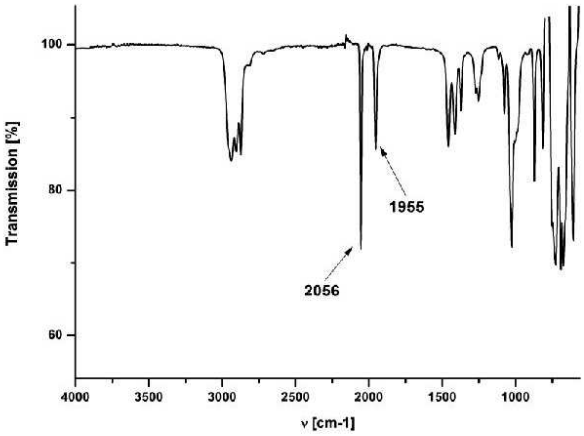

Figure S36. IR spectrum (ATR) of **9**

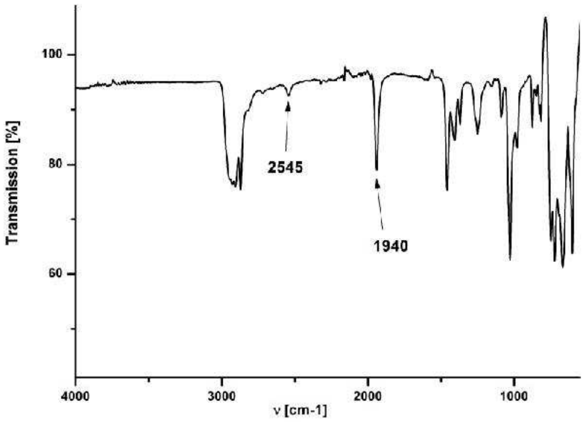

Figure S37. IR spectrum (ATR) of **10**

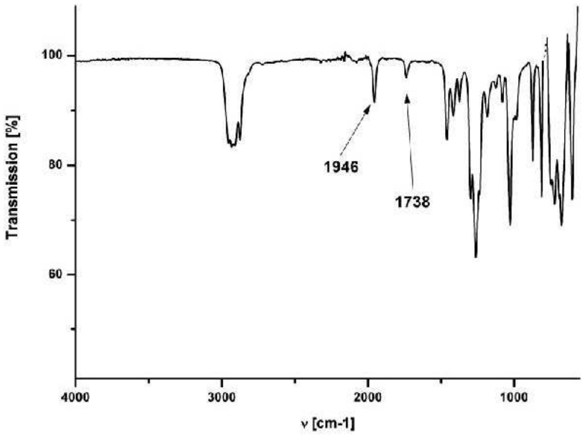

Figure S38. IR spectrum (ATR) of **11**

X-ray diffraction

Refinement details. The asymmetric unit of **2** contains one diiron species, two iodide conter ions, and three solvent molecules of acetonitrile. Three ethyl groups are disordered over two orientations, with site occupancy ratios of 0.48(2):0.52(2), 0.305(5):0.695(5) and 0.240(8):0.760(8). Many SHELXL restraints (62) had to be used to correct the geometry of the disordered parts (DANG, DFIX and SADI) and the thermal parameters of the corresponding atoms (SIMU). All hydrogen positions were calculated after each cycle of refinement using a riding model, with C—H = 0.97Å and $U_{iso}(H) = 1.2U_{eq}(C)$ for the methylene H atoms, and with C—H = 0.96Å and $U_{iso}(H) = 1.5U_{eq}(C)$ for the methyl H atoms. The asymmetric unit of **3** contains one half of the diiron species (which lies on an inversion center) and one $[BAr^F_4]^-$ counter-ion (tetrakis[(3,5-trifluoromethyl)phenyl]borate). Two ethyl groups and one ethane bridge are disordered over two orientations, with a related site occupancy ratio of 0.358(5):0.642(5). Many SHELXL restraints (113) had to be used to correct the geometry of the disordered parts (DFIX and SADI) and the thermal parameters of the corresponding atoms (DELU, EADP and SIMU). All hydrogen positions were calculated after each cycle of refinement using a riding model, with C—H = 0.93Å and $U_{iso}(H) = 1.2U_{eq}(C)$ for the aromatic and acetylenic H atoms, with C—H = 0.97Å and $U_{iso}(H) = 1.2U_{eq}(C)$ for the methylene H atoms, and with C—H = 0.96Å and $U_{iso}(H) = 1.5U_{eq}(C)$ for the methyl H atoms. The diiron species **4** lies on a two-fold axis located in the middle of the central bond C—C bond. Two ethyl groups are disordered over two orientations, with site occupancy ratios of 0.390(8):0.610(8) and 0.357(8):0.643(8). Many SHELXL restraints (82) had to be used to correct the geometry of the disordered parts (DFIX and SADI) and the thermal parameters of the corresponding atoms (SIMU). All hydrogen positions, except H4 which was located and freely refined, were calculated after each cycle of refinement using a riding model, with C—H = 0.97Å and $U_{iso}(H) = 1.2U_{eq}(C)$ for the methylene H atoms, and with C—H = 0.96Å and $U_{iso}(H) = 1.5U_{eq}(C)$ for the methyl H atoms. The asymmetric unit of **5** contains two halves of the diiron species (which lie on inversion centers) and solvent molecules of benzene in a ratio 1:1:2. The terminal CH_3 groups of two ethyl groups were disordered over two orientations with site occupancy ratios of 0.36(5):0.64(5) and 0.47(4):0.53(4). The $SnMe_3$ groups are also disordered but only the Sn metal positions could be refined since the minor components represent only 7.16(16) and 7.30(16) %, for Sn1B and Sn2B, respectively. Many SHELXL restraints (236) had to be used to correct the geometry of the disordered parts (SADI) and the thermal parameters of the corresponding atoms (SIMU). All non-H atoms were anisotropically refined. All hydrogen positions were calculated after each cycle of refinement using a riding model, with C—H = 0.93 Å and $U_{iso}(H) = 1.2U_{eq}(C)$ for aromatic H atoms, with C—H = 0.97 Å and $U_{iso}(H) = 1.2U_{eq}(C)$ for methylene H atoms, and with C—H = 0.96 Å and $U_{iso}(H) = 1.5U_{eq}(C)$ for methyl H atoms. The asymmetric unit of **7** contains one half of the diiron species (which lies on an inversion center) and one and half solvent molecules of benzene. Three ethyl groups and one ethane bridge are disordered over two orientations: two ethyl groups with a related site occupancy ratio of 0.382(8):0.618(8), the third ethyl group with a site occupancy ratio of 0.251(10):0.749(10), and the ethane group with 0.188(13):0.812(13). Many SHELXL restraints (124) had to be used to correct the geometry of the disordered parts (SADI) and the thermal parameters of the corresponding atoms (SIMU). All hydrogen positions were calculated after each cycle of refinement using a riding model, with C—H = 0.93 Å and $U_{iso}(H) = 1.2U_{eq}(C)$ for aromatic H atoms, with C—H = 0.97 Å and $U_{iso}(H) = 1.2U_{eq}(C)$ for methylene H atoms, and with C—H = 0.96 Å and $U_{iso}(H) = 1.5U_{eq}(C)$ for methyl H atoms. The diiron species **8** lies on an inversion center and on a mirror plane. One ethyl group is severely disordered over four orientations (for the terminal CH_3), with site occupancy factors of 0.128(11), 0.221(11), 0.279(11) and 0.372(11). The ethane bridge is also disordered over two different orientations with a site occupancy ratio of 0.5:0.5 due to the symmetry elements. Many SHELXL restraints (135) had to be used to correct the geometry of the disordered parts (DFIX and SADI) and the thermal parameters of the corresponding atoms (ISOR and SIMU). All hydrogen positions were calculated after each cycle of refinement using a riding model, with C—H = 0.97 Å and $U_{iso}(H) = 1.2U_{eq}(C)$ for methylene H atoms, and with C—H = 0.96 Å and $U_{iso}(H) = 1.5U_{eq}(C)$ for methyl H atoms. The asymmetric unit of **9** contains one half of the diiron species, the second half is generated by a symmetry operation corresponding to a two-fold axis. The terminal methyl groups of two ethyl ligands (and the corresponding methylene H atoms) are disordered over two orientations, with site occupancy ratios of 0.342(11):0.658(11) and 0.440(18):0.560(18). Some SHELXL restraints (12) had to be used to correct the thermal parameters of the disordered atoms (SIMU). All hydrogen positions were calculated after each cycle of refinement using a riding model, with C—H = 0.97 Å and $U_{iso}(H) = 1.2U_{eq}(C)$ for methylene H atoms, and with C—H = 0.96 Å and $U_{iso}(H) = 1.5U_{eq}(C)$ for methyl H atoms. The asymmetric unit of **10** contains one half of the diiron species, the second half is generated by a symmetry operation corresponding to a two-fold axis. One ethyl group is disordered over two orientations, with a site occupancy ratio of 0.274(10):0.726(12). One ethane bridge is also disordered over two different orientations, with a site occupancy ratio of 0.247(11):753(11). Some SHELXL restraints (36) had to be used to correct the thermal parameters of the disordered atoms (SIMU). All hydrogen positions were calculated after each cycle of refinement using a riding model, with C—H = 0.97 Å and $U_{iso}(H) = 1.2U_{eq}(C)$ for methylene H atoms, with C—H = 0.96 Å and $U_{iso}(H) = 1.5U_{eq}(C)$ for methyl H atoms, and with S—H = 1.20 Å and $U_{iso}(H) = 1.5U_{eq}(S)$. The asymmetric unit of **11** contains one half of the diiron species, the second half is generated by a symmetry operation corresponding to a two-fold axis. The terminal methyl group of one ethyl ligand (and the corresponding methylene H atoms) is disordered over two orientations, with a site occupancy ratio of 0.457(8):0.543(8). No restraints were used. All hydrogen positions were calculated after each cycle of refinement using a riding model, with C—H = 0.97 Å and $U_{iso}(H) = 1.2U_{eq}(C)$ for methylene H atoms, and with C—H = 0.96 Å and $U_{iso}(H) = 1.5U_{eq}(C)$ for methyl H atoms. For more details about all refinements, see the _iucr_refine_instructions_details sections of the corresponding Crystallographic Information File (Supporting Information).

Table S2. Selected bond lengths [Å], non-bonding distances [Å] and angles [°] of compounds **2 - 11**.

	2	**3**	**4**	**5**	**6**^{a}	**7**	**8**	**9**	**10**	**11**
Space group	$P\bar{1}$	$P2_1/c$	C 2/c	$P2_1/c$	F ddd	$P2_1/c$	C mca	I 2/c	C 2/c	I 2/a
Bond lengths [Å]	**Fe1-C1** 1.9029(18) **Fe2-C4** 1.9030(18)	**Fe1-C1** 1.927(5)	**Fe1-C1** 1.921(2)	**Fe1-C1** 1.935(5) **Fe2-C28** 1.927(5)	**Fe1-C1** 1.924(7)	**Fe1-C1** 1.911(5)	**Fe1-C1** 1.902(6)	**Fe1–C1** 1.922(3)	**Fe1–C1** 1.900(3)	**Fe1–C1** 1.912(2)
	C1-C2 1.220(2) **C3-C4** 1.222(3)	**C1-C2** 1.220(5)	**C1-C2** 1.224(3)	**C1-C2** 1.230(7) **C28-C29** 1.228(7)	**C1-C2** 1.223(9)	**C1-C2** 1.222(6)	**C1-C2** 1.215(8)	**C1–C2** 1.221(4)	**C1–C2** 1.218(5)	**C1–C2** 1.225(3)
	C2-C3 1.385(3)	**C2-C2'** 1.387(9)	**C2-C2'** 1.378(5)	**C2-C2'** 1.384(6) **C29-C29'** 1.379(10)	**C2-C2'** 1.381(12)	**C2-C2'** 1.373(8)	**C2-C2'** 1.386(11)	**C2–C2'** 1.383(6)	**C2–C2'** 1.390(7)	**C2–C2'** 1.382(4)
	Fe1-N1 1.9188(14) **Fe2-N2** 1.9250(15)	**Fe1-N1** 1.846(4)	**Fe1-C3** 1.926(2)	**Fe1-C3** 1.935(5) **Fe2-C30** 1.926(5)	**Fe1-C3** 1.908(6)	**Fe1-N1** 1.942(4)	**Fe1-N1** 1.950(5)	**Fe1– C3** 1.920(3)	**Fe1– S1** 2.3767(10)	**Fe1– N1** 1.9618(18)
	N1-C5 1.146(2) **N2-C7** 1.142(2)	**N1-N2** 1.105(5)	**C3-C4** 1.207(4)	**C3-C4** 1.220(5) **C30-C31** 1.210(8)	**C3-C4** 1.228 (8)	**N1-C3** 1.161(6)	**N1-C3** 1.135(7)	**C3–N1** 1.159(4)	----	**N1–O** **O1:** 1.244(3) **O2:** 1.260(3)
	C5-C6 1.452(3) **C7-C8** 1.453(2)	---	---	**C4-Sn1A** 2.082(6) **C31-Sn2A** 2.083(6)	**C4-C5** 1.371 (9)	**C3-Se1** 1.789(5)	**C3-S1** 1.635(6)	----	----	----
	---	---	---	---	**C5-C6** 1.208 (9)	---	---	---	---	---
	---	---	---	---	**C6-Sn1** 2.083(7)	---	---	---	---	---
	Fe1-P 2.2520^{b} **Fe2-P** 2.2517^{b}	**Fe1-P** 2.2715^{b}	**Fe1-P** 2.2224^{b}	**Fe1-P** 2.2201^{b} **Fe2-P** 2.2163^{b}	**Fe1-P** 2.233^{b}	**Fe1-P** 2.2439^{b}	**Fe1-P** 2.2343^{b}	**Fe1-P** 2.2280^{b}	**Fe1-P** 2.2299^{b}	**Fe1-P** 2.2481^{b}
Non-bonding distances [Å]	**Fe1···Fe2** 7.6272(3)	**Fe1···Fe1'** 7.6821(10)	**Fe1···Fe1'** 7.6556(9)	**Fe1···Fe1'** 7.701(1) **Fe2···Fe2'** 7.685(1)	**Fe1···Fe1'** 7.6590(9)	**Fe1···Fe1'** 7.6361(8)	**Fe1···Fe1'** 7.619(1)	**Fe1···Fe1'** 7.6406(6)	**Fe1···Fe1'** 7.6117(8)	**Fe1···Fe1'** 7.6255(4)
	---	---	**C4···C4'** 13.896(6)	**C4···C4'** 13.939(8) **C31···C31'** 13.956(8)	**C6···C6'** 19.015(9)	**Se1···Se1'** 17.329(1)	**S1···S1'** 16.940(3)	**N1···N1'** 13.738(4)	**S1···S1'** 12.3435(17)	**O1···O2** 12.830(3)
Bond angles [°]	**Fe1-C1-C2** 175.99(16) **Fe2-C4-C3** 176.88(17)	**Fe1-C1-C2** 178.7(4)	**Fe1-C1-C2** 176.7(2)	**Fe1-C1-C2** 176.1(5) **Fe2-C28-C29** 177.0(4)	**Fe1-C1-C2** 175.9(7)	**Fe1-C1-C2** 176.9(4)	**Fe1-C1-C2** 178.6(5)	**Fe1-C1-C2** 175.9(3)	**Fe1-C1-C2** 173.4(3)	**Fe1-C1-C2** 176.24(19)
	C1-C2-C3 178.8(2) **C4-C3-C2** 179.1(2)	**C1-C2-C2'** 178.6(6)	**C1-C2-C2'** 178.5(2)	**C1-C2-C2'** 177.8(7) **C28-C29-C29'** 178.2(7)	**C1-C2-C2'** 178.5(7)	**C1-C2-C2'** 177.5(7)	**C1-C2-C2'** 179.5(8)	**C1-C2-C2'** 177.3(3)	**C1-C2-C2'** 178.6(4)	**C1-C2-C2'** 176.61(19)
	C1-Fe1-N1 178.73(7) **C4-Fe2-N2** 178.57(7)	**C1-Fe1-N1** 178.15(16)	**C1-Fe1-C3** 178.39(10)	**C1-Fe1-C3** 175.2(2) **C28-Fe2-C30** 178.5(2)	**C1-Fe1-C3** 178.6(3)	**C1-Fe1-N1** 176.65(18)	**C1-Fe1-N1** 177.2(2)	**C1-Fe1-C3** 178.62(13)	**C1-Fe1-S1** 176.13(11)	**C1-Fe1-N1** 178.48(9)
	Fe1-N1-C5 178.30(15) **Fe2-N2-C7** 178.98(17)	**Fe1-N1-N2** 179.6(5)	**Fe1-C3-C4** 178.3(3)	**Fe1-C3-C4** 174.9(5) **Fe2-C30-C31** 178.1(5)	**Fe1-C3-C4** 177.8(7)	**Fe1-N1-C3** 172.9(4)	**Fe1-N1-C3** 169.4(5)	**Fe1-C3-N1** 179.4(3)	----	**Fe1-N1-O** **O1:**122.85(16) **O2:**121.52(16)
	N1-C5-C6 177.9(2) **N2-C7-C8** 179.7(2)	---	---	**C3-C4-Sn1A** 162.9(5) **C30-C31-Sn2A** 158.0(5)	**C3-C4-C5** 176.3(7)	**N1-C3-Se1** 177.6(4)	**N1-C3-S1** 176.2(6)	----	----	**O1-N1-O2** 115.63(19)
	---	---	---	---	**C4-C5-C6** 177.9(9)	---	---	---	---	---
	---	---	---	---	**C5-C6-Sn1** 166.0(6)	---	---	---	---	---

^{a} see reference^{1}. ^{b} average bond length.

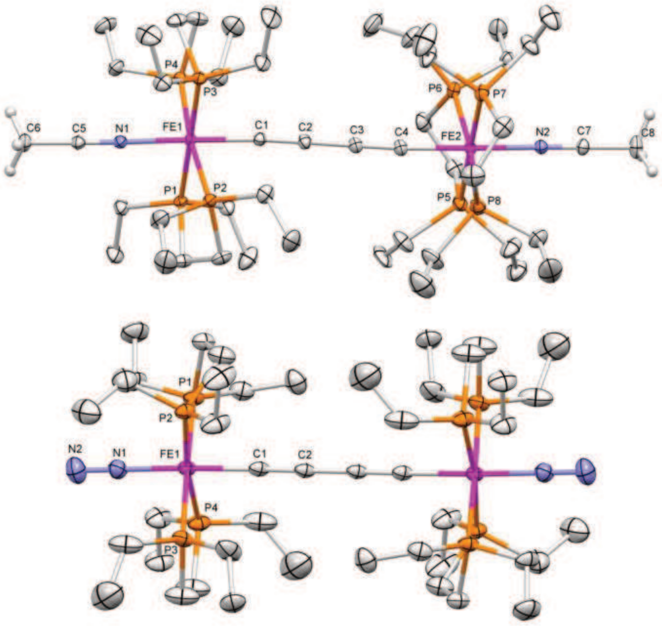

Figure S39. Molecular structures of [**2**]$^{2+}$ (top) and [**3**]$^{2+}$ (bottom). Ellipsoids are set at 30% probability level. Solvent molecules, counter ions and selected hydrogen atoms are omitted for clarity. See Table S2 for selected bond lengths, distances and angles.

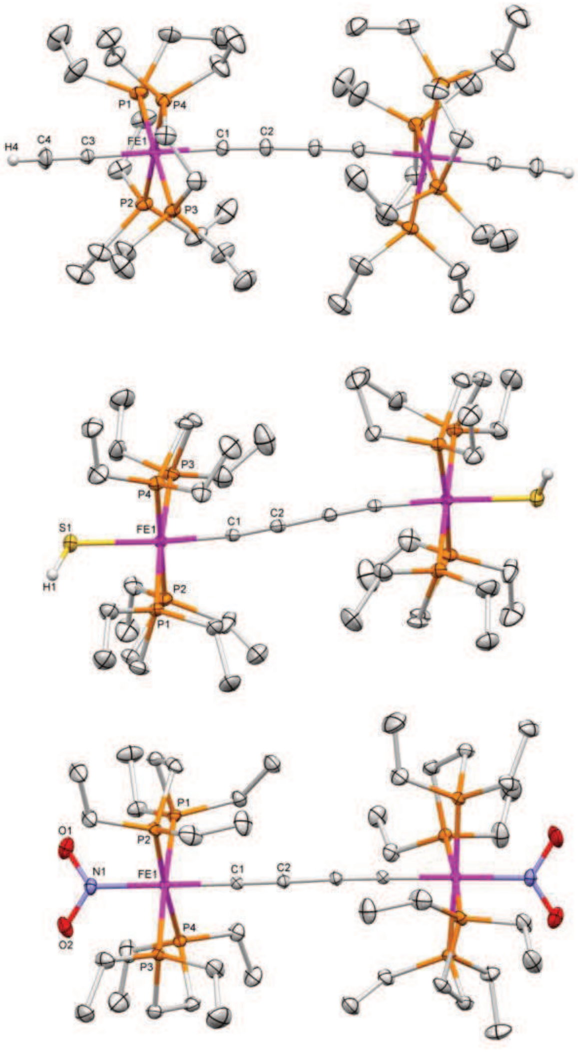

Figure S40. Molecular structures of (from top to bottom): **4**, **10** and **11**. Ellipsoids are set at 30% probability level. Solvent molecules and selected hydrogen atoms are omitted for clarity. See Table S2 for selected bond lengths, distances and angles.

For all compounds described, each of the two iron atoms is the centre of a plane spanned by the four P atoms surrounding it. These are perpendicular to the rigid-rod Fe-C_4-Fe line. For compounds **3**, **5**, **7**, **8** and **10**, the two planes are congruent, whereas for **4**, **6**, **9** and **11** there is an angle of 22.5° and for compound **2** the planes are staggered at a 90° angle (see Figure S41).

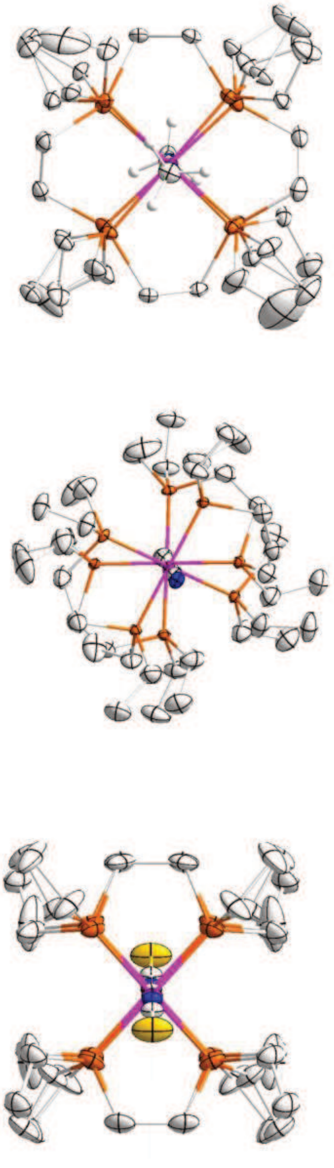

Figure S41. Examples detailing the different angles of the two planes spanned by the P atoms around the two iron centres. **top**: compound **2**, 90° angle. **middle**: compound **9**, 22.5° angle. **bottom**: compound **8**, congruent planes.

Table S3. Crystallographic data for compounds **2**, **3** and **4**.

	2	**3**	**4**
CCDC	986825	986826	986827
empirical formula	$[C_{48}H_{102}Fe_2N_2P_8]^{2+}[I^-]_2$ .3(C_2H_3N)	$[C_{44}H_{96}Fe_2N_4P_8]^{2+}[C_{32}H_{12}BF_{24}^-]_2$	$C_{48}H_{98}Fe_2P_8$
formula weight (g·mol^{-1})	1443.73	2767.16	1034.72
temperature (K)	183(2)	183(2)	183(2)
wavelength (Å)	0.71073	0.71073	0.71073
crystal system, space group	triclinic, P $\bar{1}$	monoclinic, P 2_1/c	monoclinic, C 2/c
a (Å)	10.3030(1)	14.0211(4)	29.5938(6)
b (Å)	17.4632(2)	26.5865(7)	10.0002(1)
c (Å)	20.3423(2)	17.9536(6)	21.1040(4)
α (deg)	94.204(1)	90	90
β (deg)	101.929(1)	111.308(3)	116.945(2)
γ (deg)	92.428(1)	90	90
volume (Å^3)	3565.17(7)	6235.1(3)	5567.59(19)
Z, density (calcd) (Mg·m^{-3})	2, 1.345	2, 1.471	4, 1.234
abs coefficient (mm^{-1})	1.487	0.453	0.781
F(000)	1496	2816	2232
crystal size (mm^3)	0.50 x 0.38 x 0.25	0.39 x 0.21 x 0.06	0.55 x 0.28 x 0.11
θ range (deg)	2.562 to 27.484	2.49 to 25.35	2.583 to 28.282
reflections collected	63750	37721	44136
reflections unique	16349 / R_{int} = 0.0218	11389 / R_{int} = 0.0448	6905 / R_{int} = 0.0261
completeness to θ (%)	99.9	99.8	99.9
absorption correction	analytical	analytical	analytical
max/min transmission	0.761 and 0.553	0.975 and 0.880	0.931 and 0.744
data / restraints / parameters	13434 / 62 / 703	5883 / 113 / 804	5800 / 82 / 314
goodness-of-fit on F^2	1.065	0.896	1.055
final R_1 and wR_2 indices [$I > 2\sigma(I)$]	0.0271, 0.0716	0.0582, 0.1487	0.0466, 0.1417
R_1 and wR_2 indices (all data)	0.0360, 0.0736	0.1134, 0.1627	0.0544, 0.1459
largest diff. peak and hole (e·Å^{-3})	0.985 and -0.381	0.803 and -0.482	0.846 and -0.552

The unweighted R-factor is $R_1 = \Sigma(Fo - Fc)/\Sigma Fo$; $I > 2\sigma(I)$ and the weighted R-factor is $wR_2 = \{\Sigma w(Fo^2 - Fc^2)^2/\Sigma w(Fo^2)^2\}^{1/2}$

Table S4. Crystallographic data for compounds **5**, **7** and **8**.

	5	**7**	**8**
CCDC	986828	986829	986830
empirical formula	$C_{54}H_{114}Fe_2P_8Sn_2$, C_6H_6	$C_{46}H_{96}Fe_2N_2P_8Se_2.3(C_6H_6)$	$C_{46}H_{104}Fe_2N_2P_8S_2$
formula weight (g·mol^{-1})	1438.39	1428.95	1108.89
temperature (K)	183(1)	183(2)	183(2)
wavelength (Å)	0.71073	0.71073	0.71073
crystal system, space group	monoclinic, P 2_1/c	monoclinic, P 2_1/c	orthorhombic, C mca
a (Å)	19.0064(3)	10.0294(7)	18.9951(16)
b (Å)	18.7974(4)	19.4329(7)	15.3883(8)
c (Å)	19.7398(3)	18.4637(10)	20.0151(13)
α (deg)	90	90	90
β (deg)	90.9394(16)	96.994(5)	90
γ (deg)	90	90	90
volume (Å^3)	7051.5(2)	3571.8(3)	5850.5(7)
Z, density (calcd) (Mg·m^{-3})	4, 1.355	2, 1.329	4, 1.259
abs coefficient (mm^{-1})	1.319	1.642	0.818
F(000)	3008	1504	2392
crystal size (mm^3)	0.20 x 0.12 x 0.07	0.18 x 0.09 x 0.07	0.31 x 0.12 x 0.03
θ range (deg)	2.310 to 27.10	2.930 to 25.350	2.84 to 25.67
reflections collected	65475	26409	14855
reflections unique	15409 / R_{int} = 0.0576	6537 / R_{int} = 0.0827	2869 / R_{int} = 0.0734
completeness to θ (%)	99.5	99.8	99.8
absorption correction	analytical	analytical	analytical
max/min transmission	0.913 and 0.800	0.905 and 0.799	0.978 and 0.864
data / restraints / parameters	12244 / 236 / 758	4341 / 124 / 426	2030 / 135 / 204
goodness-of-fit on F^2	1.088	1.059	1.043
final R_1 and wR_2 indices [I > 2σ(I)]	0.0647, 0.1661	0.0628, 0.1413	0.0667, 0.1588
R_1 and wR_2 indices (all data)	0.0799, 0.1769	0.0999, 0.1682	0.0990, 0.1779
largest diff. peak and hole (e·Å^{-3})	2.881 and -0.956	0.788 and -0.718	0.734 and -0.566

The unweighted R-factor is $R_1 = \Sigma(Fo - Fc)/\Sigma Fo$; $I > 2\sigma(I)$ and the weighted R-factor is $wR_2 = \{\Sigma w(Fo^2 - Fc^2)^2/\Sigma w(Fo^2)^2\}^{1/2}$

Table S5. Crystallographic data for compounds **9**, **10** and **11**.

	9	**10**	**11**
CCDC	986831	986832	986833
empirical formula	$C_{46}H_{96}Fe_2N_2P_8$	$C_{44}H_{98}Fe_2P_8S_2$	$C_{44}H_{96}Fe_2N_2O_4P_8$
formula weight (g·mol^{-1})	1036.71	1050.80	1076.69
temperature (K)	183(2)	183(2)	183(2)
wavelength (Å)	0.71073	0.71073	0.71073
crystal system, space group	monoclinic, I 2/c	monoclinic, C 2/c	monoclinic, I 2/a
a (Å)	21.0545(7)	14.1900(11)	20.9315(3)
b (Å)	10.0187(3)	19.2827(12)	10.0246(1)
c (Å)	26.9455(9)	20.1632(15)	27.2939(4)
α (deg)	90	90	90
β (deg)	107.922(4)	104.209(8)	108.157(2)
γ (deg)	90	90	90
volume (Å^3)	5408.1(3)	5348.3(7)	5441.90(14)
Z, density (calcd) (Mg·m^{-3})	4, 1.273	4, 1.305	4, 1.314
abs coefficient (mm^{-1})	0.805	0.889	0.808
F(000)	2232	2264	2312
crystal size (mm^3)	0.43 x 0.14 x 0.09	0.35 x 0.19 x 0.09	0.12 x 0.07 x 0.04
θ range (deg)	2.81 to 27.48	2.96 to 26.36	2.18 to 25.03
reflections collected	36996	19321	15048
reflections unique	6184 / R_{int} = 0.0481	5442 / R_{int} = 0.0643	4804 / R_{int} = 0.0234
completeness to θ (%)	99.8	99.8	99.8
absorption correction	analytical	analytical	analytical
max/min transmission	0.942 and 0.763	0.931 and 0.807	0.813 and 0.592
data / restraints / parameters	5338 / 12 / 292	3304 / 36 / 300	4326 / 0 / 290
goodness-of-fit on F^2	1.037	1.019	1.033
final R_1 and wR_2 indices [$I > 2\sigma(I)$]	0.0556, 0.1516	0.0537, 0.1202	0.0330, 0.0830
R_1 and wR_2 indices (all data)	0.0641, 0.1596	0.1019, 0.1467	0.0375, 0.0860
largest diff. peak and hole (e·Å^{-3})	1.402 and -0.594	0.817 and -0.629	1.031 and -0.427

The unweighted R-factor is $R_1 = \Sigma(Fo - Fc)/\Sigma Fo$; $I > 2\sigma(I)$ and the weighted R-factor is $wR_2 = \{\Sigma w(Fo^2 - Fc^2)^2/\Sigma w(Fo^2)^2\}^{1/2}$

Cyclic Voltammetry Studies

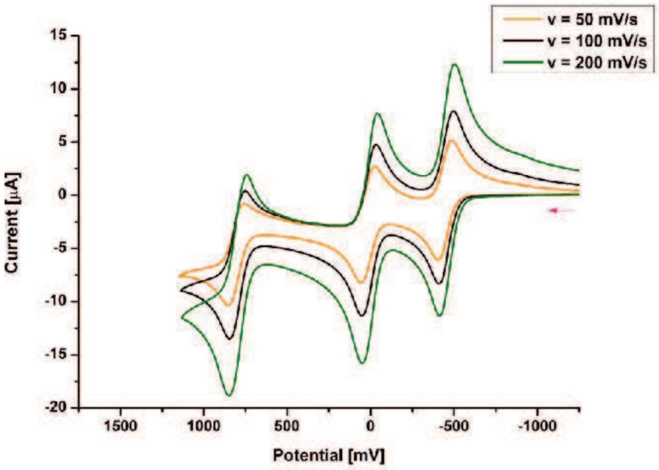

Figure S42. Cyclic voltammograms for **4** in NBu_4PF_6 (0.1M) at three different scan rates; rt, Au electrode; E vs. $Fc^{0/+}$ (external)

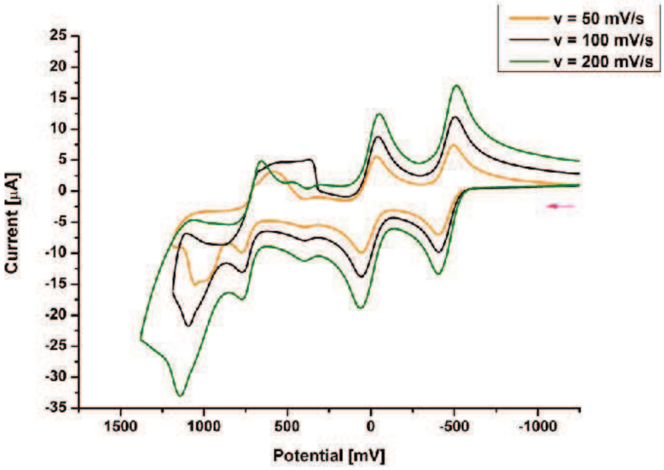

Figure S43. Cyclic voltammograms for **5** in NBu_4PF_6 (0.1M) at three different scan rates; broad potential range;rt, Au electrode; E vs. $Fc^{0/+}$ (external)

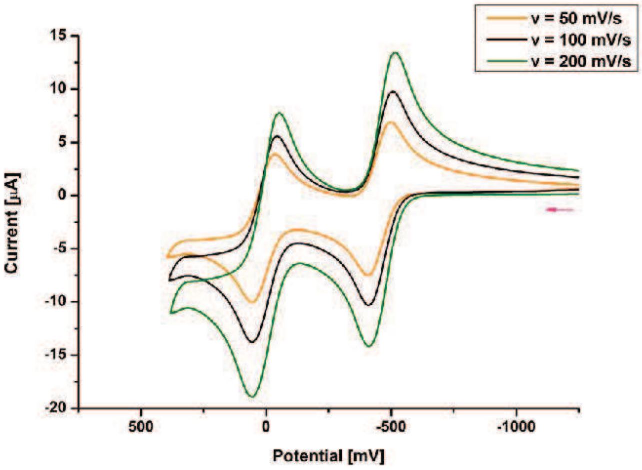

Figure S44. Cyclic voltammograms for **5** in NBu$_4$PF$_6$ (0.1M) at three different scan rates; narrow potential range; rt, Au electrode; E vs. Fc$^{0/+}$ (external)

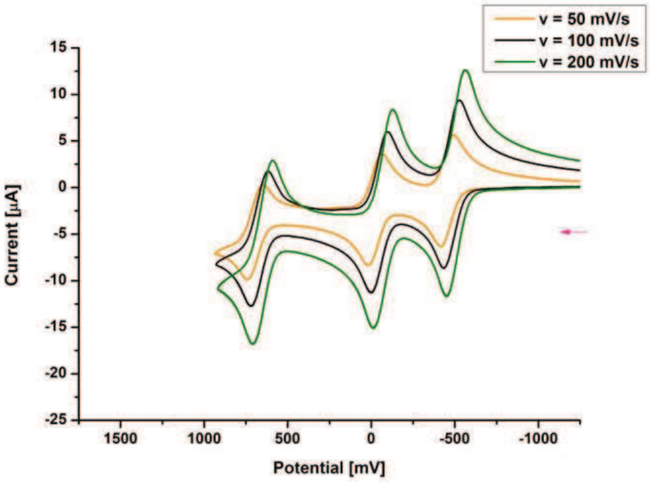

Figure S45. Cyclic voltammograms for **6** in NBu$_4$PF$_6$ (0.1M) at three different scan rates; rt, Au electrode; E vs. Fc$^{0/+}$ (external)

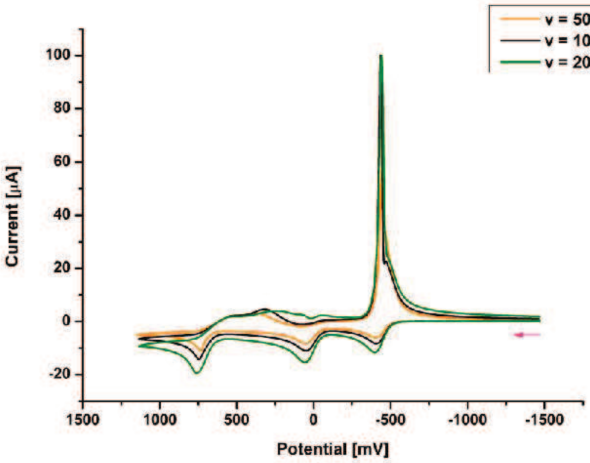

Figure S46. Cyclic voltammograms for **7** in NBu_4PF_6 (0.1M) at three different scan rates; broad potential range;rt, Au electrode; E vs. $Fc^{0/+}$ (external)

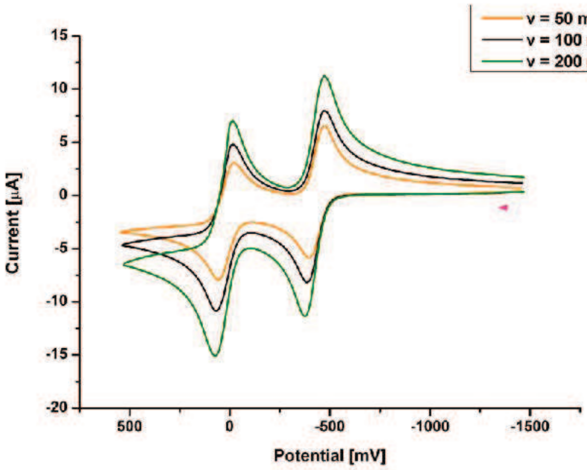

Figure S47. Cyclic voltammograms for **7** in NBu_4PF_6 (0.1M) at three different scan rates; narrow potential range; rt, Au electrode; E vs. $Fc^{0/+}$ (external)

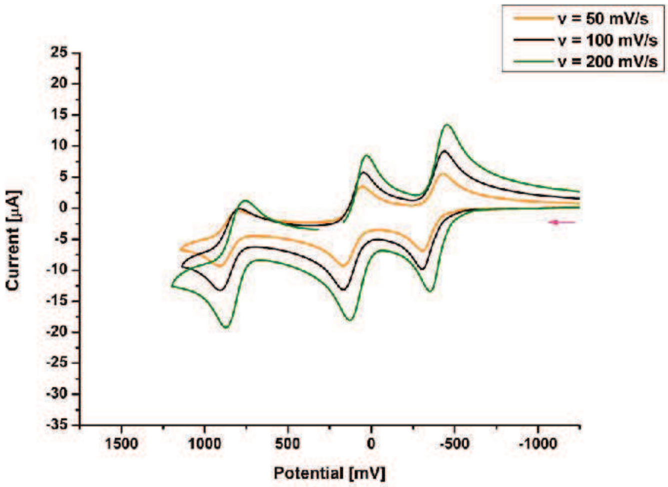

Figure S48. Cyclic voltammograms for **8** in NBu$_4$PF$_6$ (0.1M) at three different scan rates; rt, Au electrode; E vs. Fc$^{0/+}$ (external)

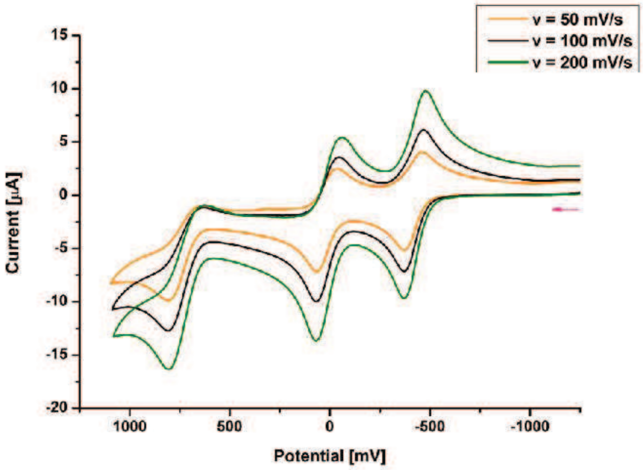

Figure S49. Cyclic voltammograms for **9** in NBu$_4$PF$_6$ (0.1M) at three different scan rates; rt, Au electrode; E vs. Fc$^{0/+}$ (external)

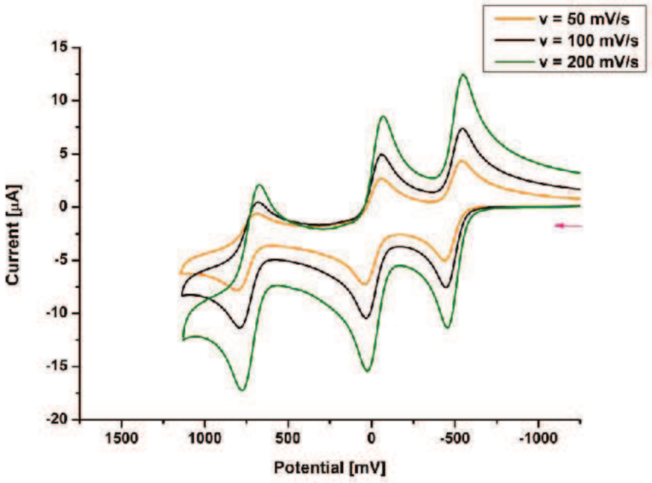

Figure S50. Cyclic voltammograms for **11** in NBu_4PF_6 (0.1M) at three different scan rates; rt, Au electrode; E vs. $Fc^{0/+}$ (external)

DFT Calculations

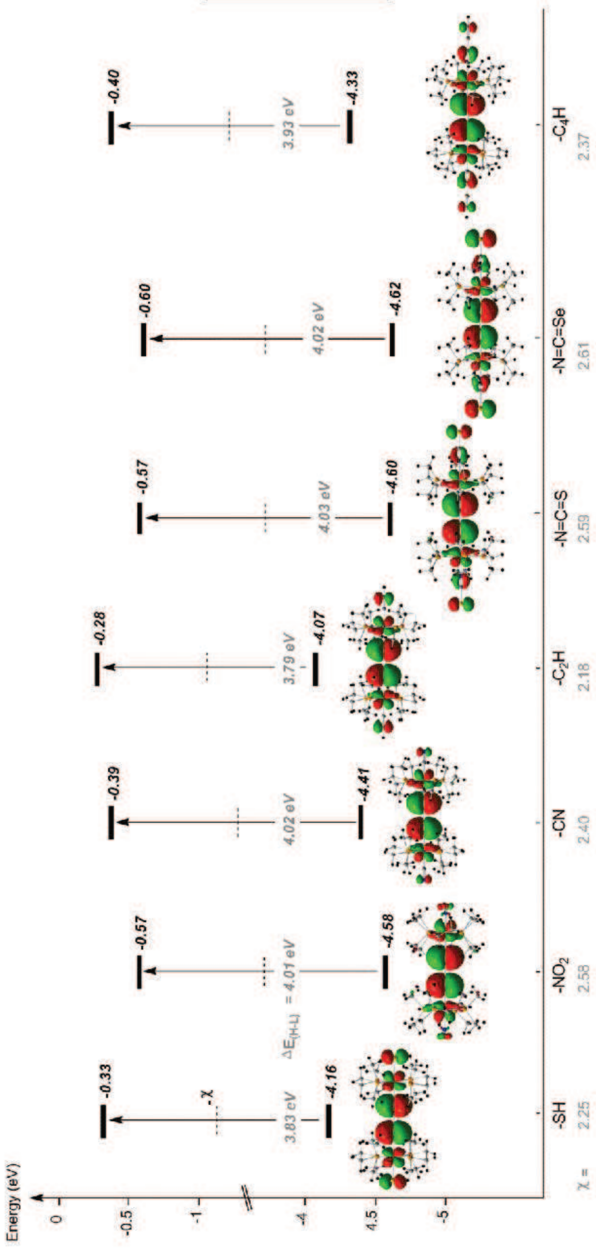

Figure S51. Energies of the HOMO and LUMO of the model complexes computed at the PBE1PBE/LANL2DZ//PBE1PBE/6-311+g(d) level and arranged in the order of the increasing molecular length. Spatial plots of the corresponding orbitals **and electronegativity values** χ (defined as (I+A)/2 with I = ionization potential, A = electron affinity), represented as a dashed line halfway between the HOMO and LUMO, are given.

Fluctuations in the Transport Measurements

Current-Voltage (I - V) curves are acquired using a mechanically controllable break-junction setup operated under UHV conditions (pressure < 2 x 10^{-9} mbar). The statistical measurement procedure is described elsewhere.[4] The raw I-V data acquired during each step in closing or opening cycles is mathematically derived to achieve differential conductance curves (G_{diff} – V). No filtering or data manipulation is applied. The data displayed represents opening traces.

In Figure S52 we have plotted ΔI / I to quantify the current fluctuations in the **Au-5'-Au** and **Au-7-Au** system. The current fluctuations are one to two orders of magnitude smaller for the C-Au coupled system **5'**.

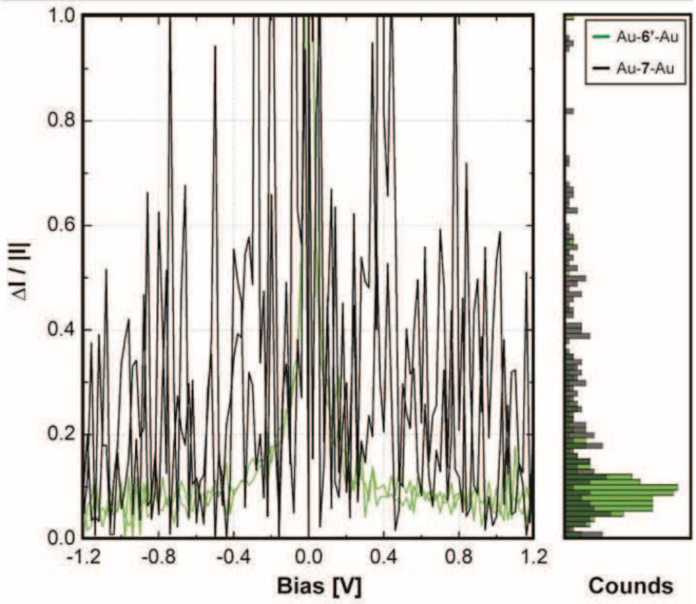

Figure S52: Current noise |ΔI/I| vs. voltage and represented as histograms taken at 300 K for the dinuclear Fe complexes **5'** (green) and **7** (black).

References

(1) Lissel, F.; Fox, T.; Blacque, O.; Polit, W.; Winter, R. F.; Venkatesan, K.; Berke, H. J. Am. Chem. Soc. **2013,** 135 (10), 4051–4060.
(2) Jones, K.; Lappert, M. F. J. Chem. Soc. **1965,** 1944.
(3) Fulmer, G. R.; Miller, A. J. M.; Sherden, N. H.; Gottlieb, H. E.; Nudelman, A.; Stoltz, B. M.; Bercaw, J. E.; Goldberg, K. I. Organometallics. **2010,** 29 (9), 2176–2179.
(4) Lörtscher, E.; Weber, H.; Riel, H. Phys. Rev. Lett. **2007,** 98 (17).

4. HIGH-CONDUCTIVE ORGANOMETALLIC MOLECULAR WIRES WITH DELOCALIZED ELECTRON SYSTEMS STRONGLY COUPLED TO METAL ELECTRODES

4.1 MANUSCRIPT

The manuscript and associated supplementary information were accepted as a communication to NanoLetters as:

F. Schwarz, G. Kastelunger, F. Lissel, H. Riel, K. Venkatesan, H. Berke, R. Stadler, E. Lörtscher: *"High-conductive Organometallic Molecular Wires with Delocalized Electron Systems Strongly Coupled to Metal Electrodes"*

High-conductive Organometallic Molecular Wires with Delocalized Electron Systems Strongly Coupled to Metal Electrodes

Florian Schwarz,[†] Georg Kastlunger,[‡] Franziska Lissel,[¶] Heike Riel,[†] Koushik Venkatesan,[¶] Heinz Berke,[¶] Robert Stadler,[‡] and Emanuel Lörtscher[*,†]

IBM Research - Zurich, Säumerstrasse 4, CH-8803 Rüschlikon, Switzerland, University of Vienna, Department of Physical Chemistry, Sensengasse 8/7, A-1090 Vienna, Austria, and Department of Chemistry, University of Zürich, Winterthurerstrasse 190, CH-8057 Zürich, Switzerland

Received August 13, 2014; E-mail: eml@zurich.ibm.com

Abstract *Besides active, functional molecular building blocks such as diodes or switches, passive components as, e.g., molecular wires, are required to realize molecular-scale electronics. Incorporating metal centers in the molecular backbone enables the molecular energy levels to be tuned in respect to the Fermi energy of the electrodes. Furthermore, by using more than one metal center and sp-bridging ligands, a strongly delocalized electron system is formed between these metallic "dopants", facilitating transport along the molecular backbone. Here, we study the influence of molecule–metal coupling on charge transport of dinuclear* $X(PP)_2FeC_4Fe(PP)_2X$ *molecular wires (PP =* $Et_2PCH_2CH_2PEt_2$*); X = CN (**1**), NCS (**2**), NCSe (**3**),* C_4SnMe_3 *(**4**) and* C_2SnMe_3 *(**5**)) under ultra-high vacuum and variable temperature conditions. In contrast to **1** which showed unstable junctions at very low conductance (*$8.1 \cdot 10^{-7}$ G_0*), **4** formed a Au-*$C_4FeC_4FeC_4$*-Au junction **4′** after* $SnMe_3$ *extrusion which revealed a conductance of* $8.9 \cdot 10^{-3}$ G_0*, three orders of magnitude higher than for **2** (*$7.9 \cdot 10^{-6}$ G_0*) and two orders of magnitude higher than for **3** (*$3.8 \cdot 10^{-4}$ G_0*). Density functional theory (DFT) confirmed the experimental trend in the conductance for the various anchoring motifs. The strong hybridization of molecular and metal states found in the C–Au coupling case enables the delocalized electronic system of the organometallic* Fe_2 *backbone to be extended over the molecule-metal interfaces to the metal electrodes.*

Molecular electronics aims at employing single molecules as functional building blocks in electronic circuits. Besides such active components which provide, e.g., current rectifying or switching properties, also passive components such as molecular wires are required for the realization of molecular-scale electronics. Generally, an ideal wire has lowest resistance with almost linear (ohmic) and length-independent (ballistic) transport properties. For molecular wires, the required high conductance can in principle be achieved if low injection barriers for charge-carriers are present at the molecule–metal interfaces, if molecular orbitals (MOs) are available close to the Fermi energy of the electrodes, and if a large degree of electronic conjugation across the backbone is present. Already the first task seems to be difficult to achieve: The most frequently used thiol anchoring[1,2] suffers from an electronically weak molecule–metal coupling. Additionally, multiple bonding sites available on the Au surface for the thiol bond give rise to alternating energy barriers for charge-carrier injection and hence large fluctuations in the transport properties. Therefore other anchoring schemes such as nitriles,[3] isocyanides,[4] amines,[5] and pyridines[6] were investigated. Dithiocarbamates[7] were demonstrated to increase the molecule–metal coupling compared to previously used single-bond anchors by at least one order of magnitude, and to simultaneously reduce fluctuations. The use of fullerenes as anchors[8–10] seems promising, because of the larger molecule–metal interface and the affinity of fullerenes for precious metals.[11] However, it turned out that the transport-limiting barriers shifted from the molecule–metal interfaces onto the molecular backbone, independently of the specific connection scheme to the fullerene.[12] In contrast to fullerenes with many, but weak sp^2 "bonds", a single, direct C–Au bond showed unprecedented high conductances for oligophenyls up to 0.9 G_0,[13] (for one phenyl ring) close to the theoretical maximum of 1 G_0 (with $G_0 = 2e^2/h \simeq 77$ μS the conductance quantum). The C–Au bond can be established either by extrusion of a trimethyltin moiety[13] or a trimethylsilyl moiety.[14] Currently, the direct C–electrode bond seems to be the most promising coupling scheme also for graphene electrodes[15,16] if polymerization via the free termini can be prevented.

Oligo(phenylene ethynylene)s (OPEs) were considered as one class of molecular wires as their conjugated backbone enables electron transport. In that respect, C–Au coupled OPEs are currently the highest conductive molecular wires[13,14] with an exponential conductance decay of approx. 1 order of magnitude per phenyl ring. For longer systems than OPE4, however, a transition from tunneling to hopping is found.[17] In contrast to tunneling between the conjugated moieties of the molecular backbone, delocalized electron systems would facilitate charge-carrier transport, yielding a lower - ideally no - length dependence. Organometallic molecules[18] with incorporated metal centers form such delocalized electron systems between two or more metal centers if appropriate ligand connections over unsaturated C bridges are chosen.[19] Motivated by this seminal idea, we have devised dinuclear Fe complexes[20] $X(PP)_2FeC_4Fe(PP)_2X$ consisting of a $[FeC_4Fe]$ backbone with highly delocalized electronic systems.[21] To investigate the effect of molecule–metal coupling on transport across the $[FeC_4Fe]$ backbone and its influence on the delocalized electronic system, we varied only the end groups coordinatively or covalently bonded to the $[FeC_4Fe]$ unit. All compounds can be considered as rigid-rod like structures with reduced conformational degrees of freedom. Fig. 1 C shows compounds **1**-**3** bound coordinatively via terminal CN, NCS and NCSe end-groups to Au, whereas the $SnMe_3$ end-capped compounds **4** and **5** (Fig. 1 D and 1 E) allow for different covalent bonding motifs (see SI), e.g. to form a direct covalent C–Au σ bond after extrusion of the $SnMe_3$ groups. The loss of the -$SnMe_3$ capping leads to a reduction in length of the anchoring groups and hence a shorter electrode–electrode distance for the resulting Au–molecule–Au system. The junction's length, however, determines also the direct electron-tunneling contribution between the electrodes, a non-negligible electron path parallel to the molecular-mediated one.[22] Accordingly, we couple C_4-$SnMe_3$ end groups to the Fe centers to achieve a length of 2.322 nm (distance between binding Au atoms) for the Au–**4′**–Au junction that is

---

[†] IBM Research - Zurich

[‡] University of Vienna

[¶] University of Zurich

comparable to the one of the Au–**2**–Au (2.257 nm) and Au–**3**–Au (2.328 nm) junctions. In order to investigate length-effects on the molecule–electrode coupling, we have designed additionally compound **5** with shorter C_2-$SnMe_3$ end groups which forms the Au–**5′**–Au system with an electrode separation comparable to Au–**1**–Au. All [FeC_4Fe] compounds exhibit a high charge-delocalization between the two metal centers and can be oxidized or reduced reversibly in solution with up to three oxidation states at relatively low potentials (< 1.0 V).[20,21] (see SI).

To perform transport measurements, we use electron-beam-structured break-junctions (Fig. 1 B) that are mechanically actuated in a three-point bending mechanism (Fig. 1 A) operated in an ultra-high vacuum environment (UHV; pressure $p < 2 \cdot 10^{-9}$ mbar) and at variable temperature ($10\ \mathrm{K} < T < 300\ \mathrm{K}$)[23] (see SI for details). Statistical data acquisition is performed by taking several hundred *I*–*V* characteristics curves in subsequent junction forming and breaking cycles.[23] We first report on the transport properties of the compounds **1** - **5** taken at room-temperature (300 K). The measurement of compound **1** upon initial junction closing and subsequent opening and closing cycles under a fixed bias of 50 mV resulted in histograms that showed less distinct molecular signatures with a small conductance accumulation located at around $8.1 \cdot 10^{-7}$ G_0 (see SI). *I*–*V* data acquisition was not possible due to highly unstable junctions. In contrast, compounds **2**, **3**, **4** and **5** (transformed into **4′**, and **5′** respectively, upon attachment to the Au electrodes) gave reproducible results during *I*–*V* data acquisition. The *I*–*V* data gathered was then mathematically derived to obtain (differential) conductance vs. voltage, G_{Diff}-V, curves. The entity of all these curves is displayed as a "density plot" in the left column of Fig. 2 with the color code representing the grade of accumulation. The data contains 1033 *I*–*V* characteristics taken for **2** (with a junction forming probability of 70%), 812 for **3** (70%), 636 **4** (98%), and 1929 for **5** (70%) as acquired during the identical measurement protocols of comparable cycle numbers. Based on the most probable accumulations, we have selected individual G_{Diff}-V characteristics (transparent blue curves) to display the functional behavior of individual curves. In addition, conductance histograms were constructed by taking the conductance data at ± 1.0 V from the opening curves (see SI for histograms extracted at other voltages and in absence of molecules). According to our measurement approach, the electrodes are brought in very close contact (approx. 0.1 nm) during every cycle, which results either in the formation of a direct Au–Au contact or multi-molecular junctions, depending primarily on the diffusion of surface Au atoms under the applied high field. Hence, the close-contact or high-conductance regime of (0.08 - 5.0) G_0 is therefore considered as not appropriately controlled at room temperature and henceforth indicated by a blue shaded background in the right column of Fig. 2.

Fig. 2 A) shows one broad and two narrow accumulations of G_{Diff}–V data for **2**. The corresponding conductance peaks in the histogram are located at 0.95 G_0, $1.5 \cdot 10^{-1}$ G_0 and $7.9 \cdot 10^{-6}$ G_0 as displayed in Fig. 2 B). The first distribution represents Au–Au QPCs that are formed repeatedly during the measurement process. The most dominant and hence most probable distribution at $7.9 \cdot 10^{-6}$ G_0 is attributed to the formation of a Au–**2**–Au junction. In contrast, transport measurements of compound **3** reveal no clear accumulation in the *G*–*V* data (Fig. 2 C). Instead, a spread in the G_{Diff}–V data from 10^{-5} G_0 to 10^{-2} G_0 is found. The conductance histogram confirms this finding by a broad peak located at $3.8 \cdot 10^{-4}$ G_0. Much more distinct are the results for compound **4**, where three peaks are found at 0.86 G_0, $8.9 \cdot 10^{-3}$ G_0 and $9.6 \cdot 10^{-7}$ G_0 (Fig. 2 F), as could also be presumed from the *G*–*V* distribution (Fig. 2 E). Here, the first peak again originates from Au–Au metal junctions, whereas the second and third one are due to the formation of a Au–**4′**–Au junction. From the peak height, i.e. the relative occurrence, we preliminarily conclude that the most probable conductance is $7.9 \cdot 10^{-6}$ G_0 for **2**, $3.8 \cdot 10^{-4}$ G_0 for **3**, and $8.9 \cdot 10^{-3}$ G_0 for **4′** (all taken at 1 V). Besides the difference in the conductance maxima, also the spread in conductance differs clearly for the three different anchor groups being studied. For NCS and NCSe anchoring, the widths of the conductance histograms are approx. 3-4 orders of magnitude (e.g., $G_{3,high}/G_{3,low} = 4 \cdot 10^3$, estimated from the Full Width at Half Max (FWHM) of a Gaussian-like peak), and much less for direct C–Au anchoring, approx. 1-2 orders of magnitude ($G_{4,high}/G_{4,low} = 2.5 \cdot 10$). This smaller conductance variation is also found for the second C–Au coupled and shorter Au– **5′**–Au system as displayed in Fig. 2 G) and H), which show an even higher conductance of $1.3 \cdot 10^{-2}$ G_0.

At room temperature, the MOs energy level are usually broadened and the Fermi energy of Au is broadened too, leading to rather monotonic and continuous *I*–*V* characteristics as displayed in Fig. 2 for all compounds. In contrast, the MOs usually become apparent in *G*–*V* characteristics at low temperatures, typically at less than 100 K, because of the reduced thermal broadening. We therefore investigated the transport properties exemplarily for **2** and **4′** at low temperatures (Fig. 3). The data exhibits a symmetric conductance gap of approx. 0.60 V for **2**, independent on the temperature (the data contains 120 *I*–*V* characteristics, 40 taken at 30 K, 50 K and 100 K each). In the low-voltage range up to ± 0.25 V, no MOs are available for electrons to tunnel through. At higher bias, however, the current starts to increase as frontier MOs (according to DFT the HOMO, see below) get into resonance. As can be seen best in the *G*-*V* representation, where the resonant MOs are represented by peaks, they are located at -0.85 V, -0.39 V, 0.39 V, and 0.87 V. They are spaced symmetrically with respect to bias polarity, as it is expected for symmetric molecules and symmetric coupling. In addition to the conductance gap and the appearance of discrete MO resonances in **2**, many *I*–*V* characteristics with the appearance of hysteretic conductance switching are found (see SI). All these findings differ strongly to those for compound **4′**, where only monotonous curves without a conductance gap were recorded at low temperatures. Fig. 3 shows 100 *I*–*V* (C), and G_{Diff}-V (D) characteristics of **4′**, taken at 50 K (similar data for 30 K and 100 K): Besides the absence of discrete MO peaks, the transport properties are more linear and the current levels are 3 to 4 orders of magnitude higher.

To study the MO alignment and landscape, we performed Density Functional Theory (DFT) calculations with a PBE XC-functional within a NEGF-DFT framework[24–26] using the GPAW-code[27,28] to compute transmission probabilities, $T(E)$. In order to account for selfinteraction errors and image charge effects present in DFT with local XC-functionals we applied a scissor operator (SO), according to Quek et al.,[5] to the weaker coupled molecules **1** to **3** (see SI). The results of the DFT calculations for the transmission functions and eigenenergies of the respective orbitals HOMO and HOMO-1 relative to E_F are presented in Fig. 4 for the compounds **1** to **5′**.

The Figure illustrates the relation between the energetic position of those two MOs and the characteristic double peaks in the transmission. Furthermore it shows the spatial distribution of these two MOs. Both the eigenvalues and the shape of the relevant MOs are similar for all systems, consisting of π-orbitals delocalized over the entire molecular backbone and containing equal amounts of both Fe d-states. For each system, the HOMO and HOMO-1 differ only in the sense that they are rotated by 90° to each other, which explains their energetical proximity and therefore the double-peak structure in the transmission function. The conductance at zero bias, which is given in Fig. 5 B) and compared to experimental findings, is mainly influenced by the tails of the HOMO and HOMO-1 peaks, leading

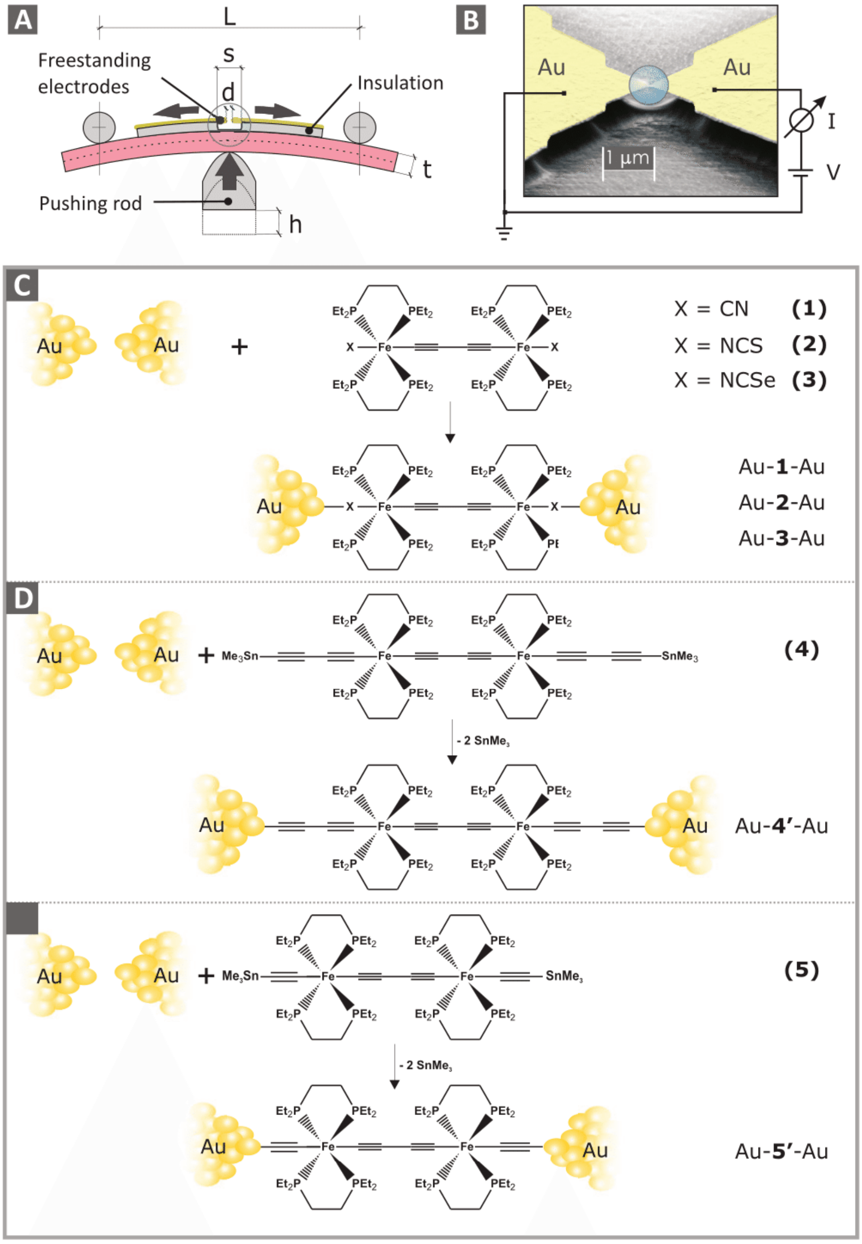

Figure 1. A) Operation principle of a mechanically controllable break-junction. B) Scanning electron microscope (SEM) image of a micro-structured sample. C) Compounds **1** - **3** with corresponding reaction schemes upon coupling to Au electrodes. In contrast to compounds **1** - **3**, the $SnMe_3$ end groups of **4** and **5** cleave off and direct C–Au bonds are formed yielding the Au–**4′**–Au (D) and the Au–**5′**–Au junction (E), respectively.

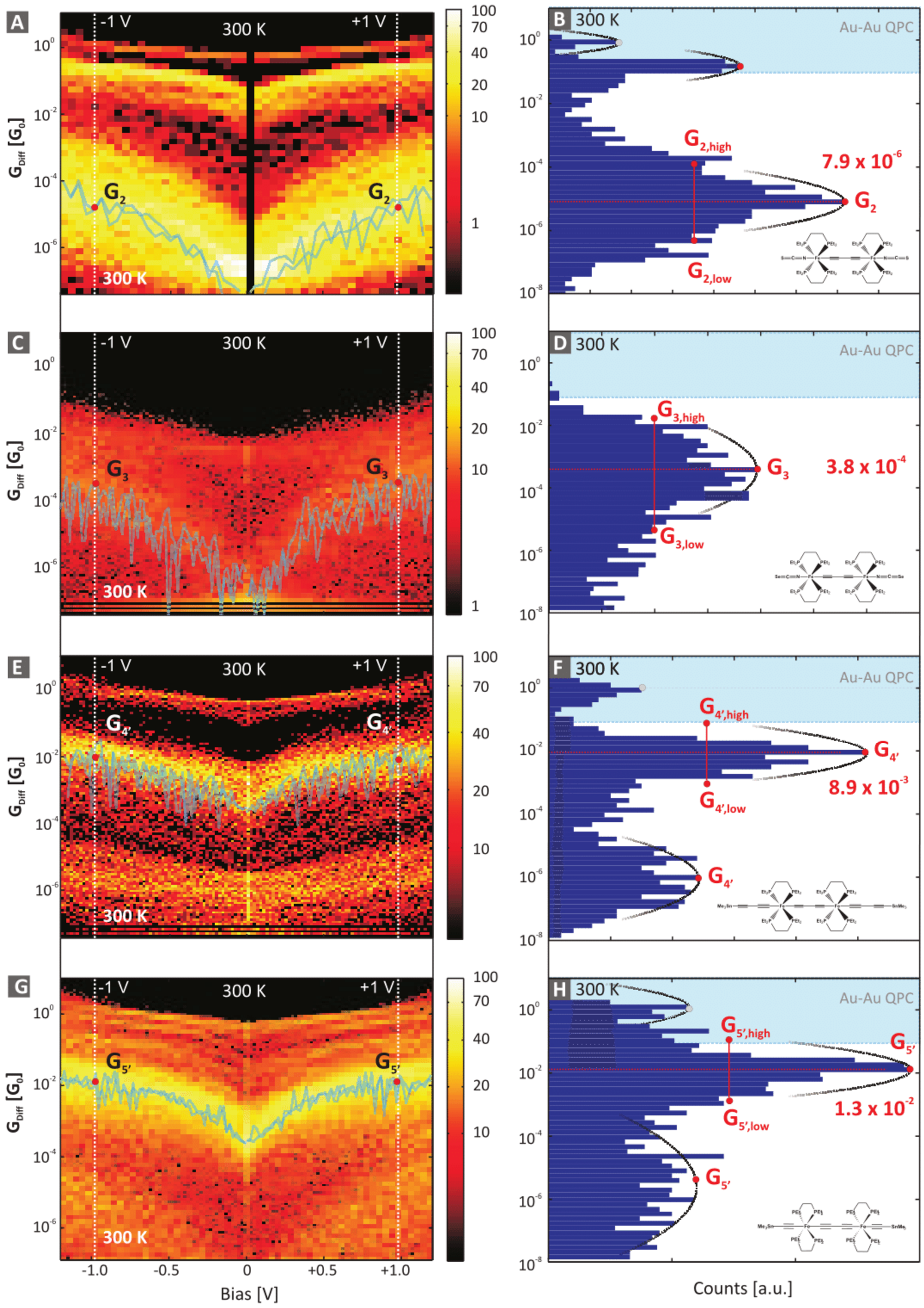

Figure 2. Density plots of the differential conductance, vs. voltage, G_{Diff}–V, characteristics acquired for compounds **2** in A), **3** in C), **4′** in E), and **5′** in G) at 300 K. Individual G_{Diff}–V curves (raw data) are plotted in transparent blue to display the functional behavior of an individual curve. Corresponding conductance histograms extracted at ± 1.0 V are displayed in B) for **2**, D) for **3**, F) for **4′**, and H) for **5′**. The blue area signals the smallest electrode separations that can either lead to a direct Au-Au contact (and hence a QPC) or multi-molecule junctions. The maximum conductance accumulation is labelled in red with a FWHM estimation for the peak width.

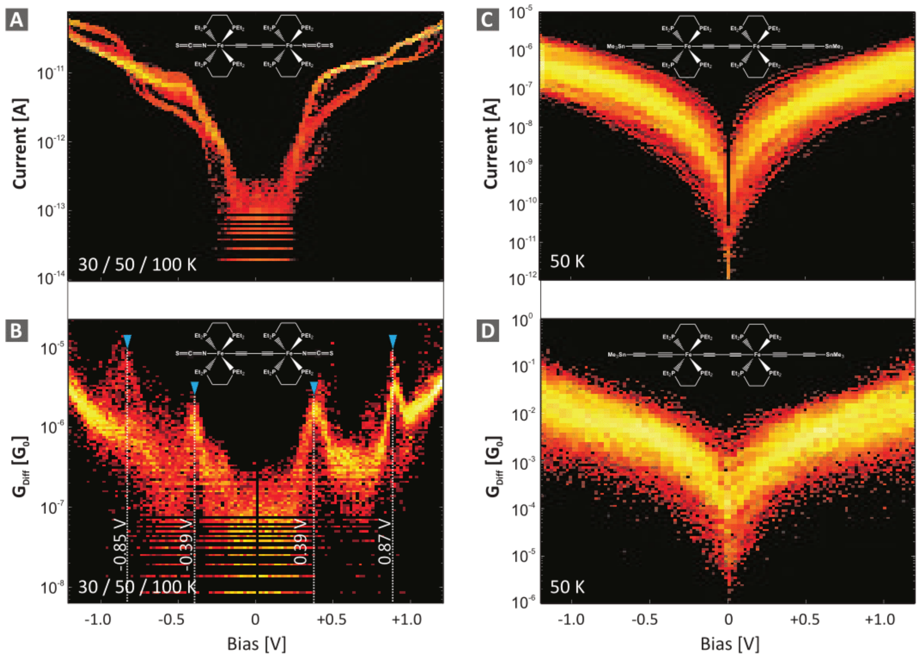

Figure 3. *I–V* and G_{Diff}-*V* characteristics taken at low temperatures for **2** in A) and B), and for **4′** in C) and D), respectively. For **2**, resonant transport through molecular orbitals gives rise to conductance peaks at specific voltages that are symmetric in respect to bias. In contrast, **4′** reveals exclusively monotonic curves without the appearance of discrete MOs. Furthermore, current levels are 3 orders of magnitude higher for the high-bias regime of **4′**, and 4 orders of magnitude higher for the low-bias regime due to the appearance of a conductance gap of approx. 0.60 V for **2**.

to quite different values among the compounds investigated. Although the metal–molecule coupling is quite high for all anchor groups, the two C–Au end groups surpass the others with rather strong covalent bonding, which leads not only to broad peaks in the transmission function, but also to a more distinct energy shift of the peaks towards E_F caused by hybridization of the MOs and the leads. It can be seen that the aligned MO eigenenergies for the different anchor schemes are rather similar, thereby ruling out structural variations in the charge transfer[29–31] as a possible source for the differences in the transmission peak energies, and leaving only variations in the hybridization strengths as explanation. As a consequence, even the rather long C_4 anchors of **4′** lead to a higher conductance than the coordinatively bonding end groups CN, NCS and NCSe, although the rate of coherent tunneling decreases rapidly with the Au–Au distance in a molecular junction. Similar to the arguments for the superior conductance provided by the C–metal end groups, also the conductance ordering for the thiol- and selenium anchors can be rationalized by the fact that the electronic coupling strength of Se–Au exceeds that of S–Au.[32,33]

We start the discussion of experimental and theoretical findings with compound **1**. The presence of only weak and rather unlikely molecular signatures (of $8.1 \cdot 10^{-7}$ G_0 at 50 mV bias) in the low-bias transport data of compound **1**, can have several reasons: First, the conductance of compound **1** is either below our experimental resolution ($\ll 1.0 \cdot 10^{-8}$ G_0), or, second, the CN binding to Au is weak and the resulting Au-**1**-Au junction is not stable even under very low bias, or, third, the bulky ligands prevent the terminals to bind to the Au electrodes due to the short distance to the Fe center. For compounds **2**, **3**, **4′** and **5′**, the room-temperature experiments worked reproducibly and the conductance data displayed in Fig. 2 shows values that range from slightly larger than 1 G_0 down to 10^{-8} G_0. It is hence ensured that all possible configurations during the junction forming and breaking procedure, from fully open Au contacts to Au–molecule–Au junctions and direct Au–Au QPCs were probed. The QPC peak at 1 G_0 confirms that the electrodes completely touched (at least in some of the cycles) in the required gentle way, i.e., not fusing the contact entirely. The data gathered, noticeably, represents conductances of all possible electrode distances. In case of **2**, a broad peak with a maximum at $7.9 \cdot 10^{-6}$ G_0 is formed. The fluctuations giving rise to this broad peak are typically generated by variations in the S–Au bond as multiple bonding sites (top, hollow, bridge etc.) are available on the Au surface. A peak of similar width is found for Se–Au in compound **3** indicating also multiple bonding sites also for this end group. For the case of C–Au in **4′** and **5′**, the narrower accumulations is a sign of fewer bonding sites or bonding sites with less distinct work functions. In the transport data of compound **4′** (and weaker also in case of **5′**), a second, broader but smaller peak compared to the main peak at $8.9 \cdot 10^{-3}$ G_0 is found at $9.6 \cdot 10^{-7}$ G_0. The appearance of a second peak at a lower average conductance for **4′** (and similar also for **5′**) is presumed to originate from the various bonding scenarios of the C end group: Incomplete cleavage of the $SnMe_3$ capping, formation of chemically reasonable alkynyl vinylidene trimethyltin species [(-C≡C)($SnMe_3$)C=C)] upon binding to the gold electrode resulting in the formation of a carbene type bond to the Au electrode ([Au-C_4FeC_4Fe-C≡C($SnMe_3$)C=C=Au] = Au–**4**”–Au) (see SI), transport through one of the bis(diethylphosphino)ethane ligands (as one or two arms of the phosphine ligands could lift-off to form Fe-PCH_2-CH_2-P → Au) and non-cleaved end groups cappings. Alternatively in our understanding, also dimerization forming a Au–$C_4FeC_4FeC_8FeC_4FeC_4$–Au (Au–**4′**-**4′**–Au) junctions (similarly for **5′**) can occur. As such details of the junction configuration are experimentally not directly accessible, the conductances of the Au-**4′**-**4′**-Au and Au-**5′**-**5′**-Au dimer junctions and the vinylidene-coupling case were exemplarily calculated (see SI). A conductance of $1.05 \cdot 10^{-5}$ G_0 was found for the dimer junction Au–**4′**-**4′**–Au.

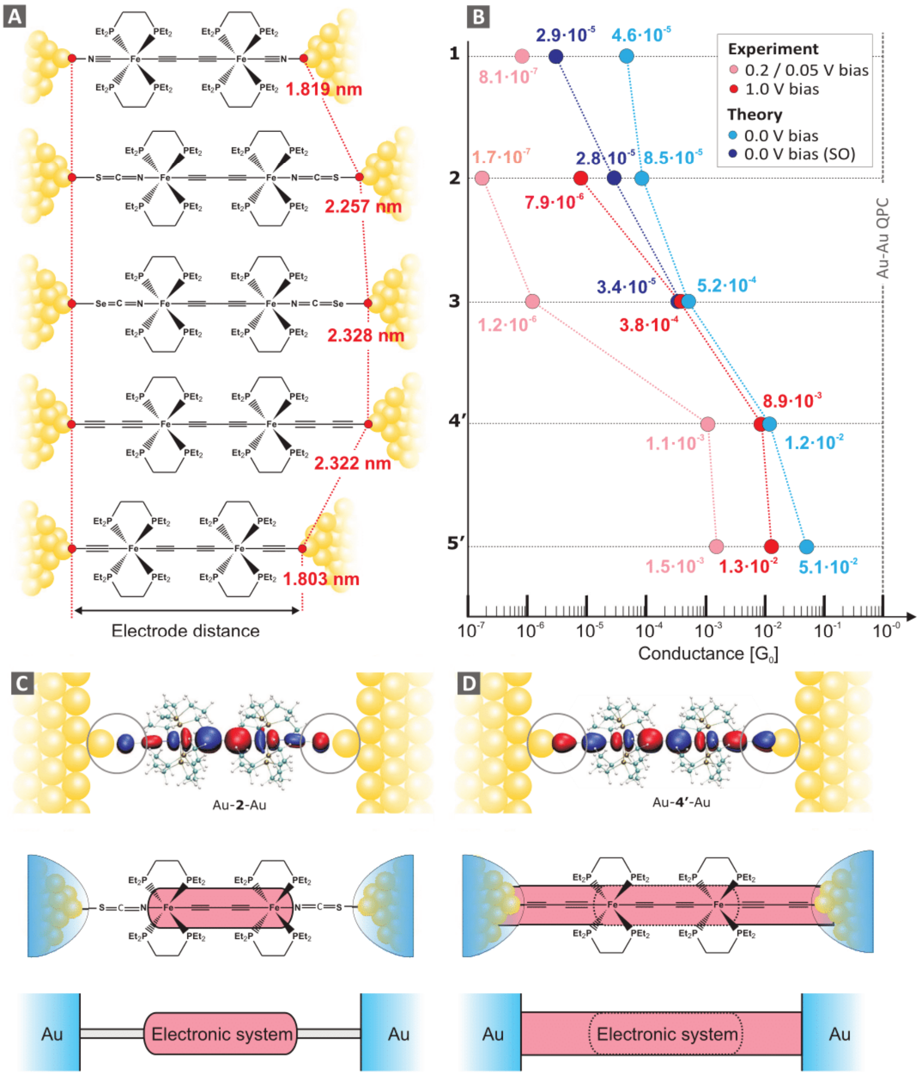

Figure 5. A) Calculated Au–Au distances of the resulting molecular junctions for compounds **1** to **5′**. B) Comparison of conductances for all compounds determined by experiment (300 K; 200 mV, 1.0 V) and DFT (0 K, zero bias, with and without scissor operator (SO) corrections). The experimental data point for **1** was achieved by low-bias measurements (50 mV). Schematic representation of the Au-**2**-Au (C) and the Au-**4′**-Au junction (D). The strong hybridization of metal and molecular states in the case of Au-**4′**-Au as evidenced by the DFT results (gray circles) leads to the formation of a strong molecule–metal bond and enables to extend the delocalized electronic system between the two Fe centers over the molecule–electrode interfaces, in contrast to the weakly bonded Au-**2**-Au system.

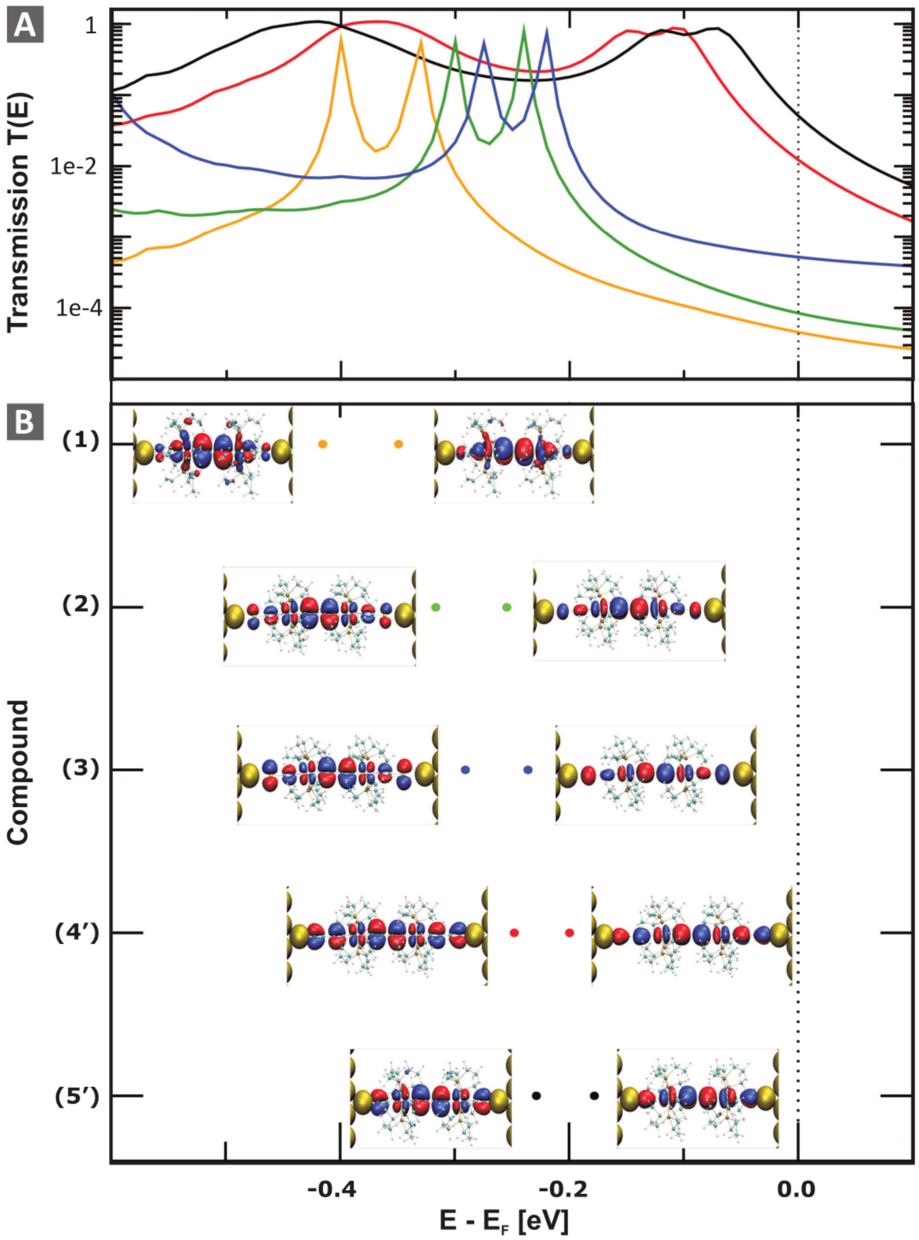

Figure 4. A) Transmission functions for compounds **1** to **5′** as calculated from DFT (color coding according to B)). B) Energetic positions of the HOMO and HOMO-1 of compounds **1** to **5′** represented as dots with different colors for the different systems with respect to the Fermi energy of the electrodes. Also given are the respective spatial distributions of these HOMO and HOMO-1. The slight shift of the transmission peaks toward the electrode Fermi Level results from the hybridization of the MOs with the gold bands, which is not regarded in the subdiagonalization process used to obtain the molecular states in the composite system.)

In the transmission function of the dimer, the slope at the Fermi level is relatively high, which means that a small energy shift of 0.1 eV would result in a lower calculated conductance. This notion is in agreement with the experimental finding as such a small shift in energy could also be argued to deficiencies of DFT such as gap underestimation. Due to the good agreement between DFT and experiments for both the 'monomer' and the 'dimer' compounds, we conclude that spontaneous dimerization is most likely the origin for the low-conductance peaks of compounds **4** (and also **5**).

When comparing only the main peaks in the conductance data at high bias (1.0 V) or low bias (0.2 V, see SI) of **2**, **3**, **4′** and **5′** measured at 300 K, a good qualitative agreement with DFT at zero-bias is found as directly compared in Fig. 5 B). The zero-bias conductance according to DFT and the low-bias current in the experiments are both much higher for **4′** or **5′** than for **2** and **3**, which indicates that the LDOS is much higher for the C–Au coupled systems than that of the others. This indicates that a strong hybridization of MOs and metal states takes places at the molecule–metal interfaces in the C–Au coupled system as evidenced directly by the DFT data (circles in Fig. 5 D)). This hybridization shifts HOMO and HOMO-1 closer to E_F, leading to an earlier onset in electron transport as indicated by the individual curves displayed in Fig. 2 A), C) and E). Injection barriers estimated from minima in the transition-voltage-spectroscopy representation ($\ln(I/V^2)$–$(1/V^{-1})$; see SI) reveal a similar barrier height of around (1.75 ± 0.3) V for **4′** and (1.85 ± 0.3) V for **5′** in contrast to (4.2 ± 1.5) V for **3**, and (5.5 ± 1.5) V for **2** at 300 K. The strong hybridization might also be the reason why the hysteretic switching behavior found in **2** at low temperatures (see SI) was not revealed in the C–Au coupled **4** as the MOs are more pinned and intrinsic functionality is prohibited. The energetic positions of the frontier MOs found for **2** at around ± 0.4 V are in good agreement with the energy difference between HOMO and E_F calculated by DFT to be around 0.25 - 0.30 eV.

In summary, we have theoretically and experimentally investigated the influence of molecule–metal coupling on the electron transport properties of dinuclear Fe complexes. We varied the molecule–metal coupling systematically by using different anchoring schemes, such as CN, NCS, NCSe, C_2SnMe_3 and C_4SnMe_3 with the latter two end groups leading to a direct C–Au bond after $SnMe_3$ extrusion. Whereas the CN termination did not result in stable junctions, all other end groups yielded reproducible transport junctions that enabled the determination of the room-temperature coupling strengths, which follow the order $\Gamma_{NCS-Au} < \Gamma_{NCSe-Au} < \Gamma_{C_4-Au} < \Gamma_{C_2-Au}$, in qualitative agreement with DFT calculations. Moreover, the reproducible binding of the C-Au motif upon extrusion or migration of the $SnMe_3$ end-group was demonstrated to occur also at low temperatures (50 K), leading to the formation of high-conductive molecular wires. Compared with trimethylsilyl-capped OPEs of equal length (after $SiMe_3$ cleavage),[14] e.g. OPE3, the conductance of compound **4′** is more than ten-fold higher. In the case of trimethyltin-capped xylylenes (after $SnMe_3$ cleavage),[13] a conductance of $1.4 \cdot 10^{-2}$ G_0 was found, similarly high as that of compound **4′**. By varying the anchor length from C_2 to C_4 we can create a preliminary length-dependence of dinuclear Fe compounds which results in similarly low decay constants as in oligothiophenes, β = 1.0 nm^{-1},[34] or Ru-based organometallic compounds, β = (1.02 - 1.64) nm^{-1},[35] (comparison between various molecular wires in SI). Regarding possible wire extensions starting from the dinuclear compound, it has to be mentioned that the trinuclear Fe compound is synthetically not accessible[21] and the next step in our research are strongly coupled tetranuclear Fe compounds, which, however, suppose major challenges to MCBJ measurements due to its length of almost 4.8 nm. Overall, the class of organometallic compounds with delocalized electron systems between two and more metal centers is a promising concept to achieve long and highly conductive wires due to an extension of the electronic system of the $[FeC_4Fe]$ unit over the molecule–metal interfaces to the electrodes by strong hybridization. Beyond that, organometallic compounds are an attractive framework for the integration of intrinsic functionality for future applications such as redox activity for conductance switching and memory application.

ASSOCIATED CONTENT

Supporting Information on the synthesis and compound handling, the experimental setup, control measurements, histograms at other voltages and DFT for various C–Au anchoring motifs. This material is available free of charge via the Internet at http://pubs.acs.org.

AUTHOR INFORMATION

Corresponding Author for chemistry: hberke@aci.uzh.ch (H.B.), venkatesan.koushik@chem.uzh.ch (K.V.); DFT calculations: robert.stadler@univie.ac.at (R.S.); experiments: eml@zurich.ibm.com (E.L.)

NOTES

The authors declare no competing financial interest.

ACKNOWLEDGMENTS

We are grateful to B. Gotsmann, V. Schmidt, and W. Riess for scientific discussions, and to M. Tschudy, U. Drechsler and Ch. Rettner for technical assistance. Funding from the National Research Programme "Smart Materials" (NRP 62, grant 406240-126142) of the Swiss National Science Foundation (SNSF) and the University of Zürich is gratefully acknowledged. G.K. and R.S. are currently supported by the Austrian Science Fund FWF, project Nr. P22548. We are deeply indebted to the Vienna Scientific Cluster VSC, on whose computing facilities all DFT calculations presented in this article have been performed (project Nr. 70174).

References

(1) Bumm, L. A.; Arnold, J. J.; Cygan, M. T.; Dunbar, T. D.; Burgin, T. P.; Jones II, L.; Allara, D. L.; Tour, J. M.; Weiss, P. S. *Science* **1996**, *271*, 1705–1707.
(2) Reed, M. A.; Zhou, C.; Muller, C. J.; Burgin, T. P.; Tour, J. M. *Science* **1997**, *278*, 252–254.
(3) Metzger, R. M.; Chen, B.; Höpfner, U.; Lakshmikantham, M. V.; Vuillaume, D.; Kawai, T.; Wu, X.; Tachibana, H.; Hughes, T. V.; Sakurai, H.; Baldwin, J. W.; Hosch, C.; Cava, M. P.; Brehmer, L.; Ashwell, G. J. *J. Am. Chem. Soc.* **1997**, *119*, 10455–10466.
(4) Chen, J.; Calvet, L. C.; Reed, M. A.; Carr, D. W.; Grubisha, D. S.; Bennett, D. W. *Chem. Phys. Lett.* **1999**, *313*, 741–748.
(5) Quek, S. Y.; Neaton, J. B.; Hybertsen, M. S.; Venkataraman, L.; Choi, C. H.; Louie, S. G. *Nano Lett.* **2007**, *7*, 3477–3482.
(6) Kamenetska, M.; Su, Y. Q.; Whalley, A. C.; Steigerwald, M. L.; Choi, H. J.; Louie, S. G.; Nuckolls, C.; Hybertsen, M. S.; Neaton, J. B.; Venkataraman, L. *J. Am. Chem. Soc.* **2010**, *132*, 6817–6821.
(7) von Wrochem, F.; Gao, D.; Scholz, F.; Nothofer, H.-G.; Nelles, G.; Wessels, J. M. *Nature Nanotech.* **2010**, *5*, 618–623.
(8) Martin, C. A.; Ding, D.; Sørensen, J. K.; Bjørnholm, T.; van Ruitenbeek, J. M.; van der Zant, H. S. J. *J. Am. Chem. Soc.* **2008**, *130*, 13198–13199.
(9) Fock, J.; Sørensen, J. K.; Lörtscher, E.; Vosch, T.; Martin, C. A.; Riel, H.; Kilså, K.; T., B.; van der Zant, H. *Phys. Chem. Chem. Phys.* **2011**, *13*, 14325–14332.
(10) Lörtscher, E.; Geskin, V.; Gotsmann, B.; Fock, J.; Sørensen, J. K.; Bjørnholm, T.; Cornil, J.; van der Zant, H. S. J.; Riel, H. *Small* **2013**, *9*, 209–214.
(11) Joachim, C.; Gimzewski, J. K.; Schlittler, R.; Chavy, C. *Phys. Rev. Lett.* **1995**, *74*, 2102–2105.
(12) Leary, E.; Gonzalez, T. M.; van der Pol, C.; Bryce, M. R.; Filippone, S.; Martin, N.; Rubio Bollinger, G.; Agraït, N. *Nano Lett.* **2011**, *11*, 2236–2241.
(13) Chen, W.; Widawsky, J. R.; Vazquez, H.; Schneebeli, S. T.; Hybert-

sen, M. S.; Breslow, R.; Venkataraman, L. *J. Am. Chem. Soc.* **2011**, *133*, 17160–17163.
(14) Hong, W.; Li, H.; Liu, S.-H.; Fu, Y.; Li, J.; Kaliginedi, V.; Decurtins, S.; Wandlowski, T. *J. Am. Chem. Soc.* **2012**, *134*, 19425–19431.
(15) Cao, Y.; Dong, S.; Liu, S.; Liu, Z.; Guo, X. *Angew. Chem. Int. Ed.* **2013**, *52*, 3906–3910.
(16) Lörtscher, E. *Nature Nanotech.* **2013**, *8*, 381–384.
(17) Zhao, X.; Huang, C.; Gulcur, M.; Batsanov, A. S.; Baghernejad, M.; Hong, W.; Bryce, M. R.; Wandlowski, T. *Chem. Mater.* **2013**, *25*, 4340–4347.
(18) Ceccon, A.; Santi, S.; Orian, L.; Bisello, A. *Coord. Chem. Rev.* **2004**, *248*, 683–724.
(19) Pevny, F.; Di Piazza, E.; Norel, L.; Drescher, M.; Winter, R. F.; Rigaut, S. *Organometallics* **2010**, *29*, 5912.
(20) Lissel, F.; Schwarz, F.; Blaque, O.; Riel, H.; Lörtscher, E.; Venkatesan, K.; Berke, H. *Submitted* **2014**,
(21) Lissel, F.; Fox, T.; Blacque, O.; Polit, W.; Winter, R. F.; Venkatesan, K.; Berke, H. *J. Am. Chem* **2013**, *135*, 4051–4060.
(22) Gotsmann, B.; Riel, H.; Lörtscher, E. *Phys. Rev. B* **2011**, *84*, 205408.
(23) Lörtscher, E.; Weber, H. B.; Riel, H. *Phys. Rev. Lett.* **2007**, *98*, 176807.
(24) Brandbyge, M.; Mozos, J.-L.; Taylor, J.; Stokbro, K. *Phys. Rev. B* **2002**, *65*, 165401.
(25) Xue, Y.; Datta, S.; Ratner, M. A. *Chem. Phys.* **2002**, *281*, 151.
(26) Rocha, A. R.; Garcia-Suarez, V. M.; Bailey, S. W.; Lambert, C. J.; Ferrer, J.; Sanvito, S. *Nature Mater.* **2005**, *4*, 335.
(27) Mortensen, J. J.; Hansen, L. B.; Jacobsen, K. W. *Phys. Rev. B* **2005**, *71*, 035109.
(28) Enkovaara, J.; Rostgaard, C.; Mortensen, J. J.; Chen, J.; Dulak, M.; Ferrighi, L.; Gavnholt, J.; Glinsvad, C.; Haikola, V.; Hansen, H. A.; Kistoffersen, H.; Kuisma, M.; Larsen, A. H.; Lehtovaara, L. *J. Phys.: Conf. Ser.* **2010**, *22*, 253202.
(29) Stadler, R.; Jacobsen, K. W. *Phys. Rev. B* **2006**, *74*, 161405.
(30) Stadler, R. *J. Phys.: Conf. Ser.* **2006**, *61*, 1097–1101.
(31) Stadler, R. *Phys. Rev. B* **2010**, *81*, 16429.
(32) Patrone, L.; Palacin, S.; Bourgoin, J.-P.; Lagoute, J.; Zambelli, T.; Gauthier, S. *Chem. Phys.* **2002**, *281*, 325–332.
(33) Yaliraki, S. N.; Kemp, M.; Ratner, M. A. *J. Am. Chem. Soc.* **1999**, *121*, 3428–3434.
(34) Yamada, R.; Kumazawa, H.; Noutoshi, T.; Tanaka, S.; Tada, H. *Nano Lett.* **2008**, *8*, 1237–1240.
(35) Luo, L.; Benameur, A.; Brignou, P.; Choi, S. H.; Rigaut, S.; Frisbie, C. D. *J. Phys. Chem. C* **2011**, *115*, 19955–19961.

4.2 SUPPLEMENTARY INFORMATION

Submitted Manuscript (**NanoLetters**, *in revision*): F. Schwarz, G. Kastelunger, F. Lissel, H. Riel, K. Venkatesan, H. Berke, R. Stadler, E. Lörtscher: *"High-conductive Organometallic Molecular Wires with Delocalized Electron Systems Strongly Coupled to Metal Electrodes"*

Supporting information for: High-conductive Organometallic Molecular Wires with Delocalized Electron Systems Strongly Coupled to Metal Electrodes

Florian Schwarz,[†] Georg Kastlunger,[‡] Franziska Lissel,[¶] Heike Riel,[†] Koushik Venkatesan,[¶] Heinz Berke,[¶] Robert Stadler,[‡] and Emanuel Lörtscher[*,†]

IBM Research - Zurich, Säumerstrasse 4, CH-8803 Rüschlikon, Switzerland, University of Vienna, Department of Physical Chemistry, Sensengasse 8/7, A-1090 Vienna, Austria, and Department of Chemistry, University of Zürich, Winterthurerstrasse 190, CH-8057 Zürich, Switzerland

E-mail: eml@zurich.ibm.com

---

[*] To whom correspondence should be addressed

[†] IBM Research - Zurich

[‡] University of Vienna

[¶] University of Zurich

Contents

1 Synthetic Information and Compound Handling

Synthetic Information reporting on the synthetic steps and the characterization of all compounds by elemental analysis, X-ray diffraction, cyclic voltammetry, IR, and Raman spectroscopy can be found elsewhere.[1]

Due to the high sensitivity of the compounds, in particular for the -$SnMe_3$ capped wires with highly toxic precursors, all compounds were treated under argon or dinitrogen atmosphere throughout all procedures.

2 Sample Fabrication, Setup and Instrumentation

Break-junction samples are fabricated by first spin-coating polyimide on beryllium copper substrates (250 μm thickness, 10 cm x 10 cm size), thereby creating an insulating layer of 6-8 μm. Then, large contact pads are created using a photolithography step (AZ6612) and metallization (20 nm Ti, 100 nm Au). The constrictions are patterned into a positive-tone electron-beam resist (PMMA 950 K) using a 100 kV electron-beam lithography system from Leica or a 30 kV system from Raith (eline). As a next step, Au is evaporated to a thickness of 80 nm, and the resist is removed by a lift-off step in acetone followed by a dry process in UHV to planarize the sample after lift-off. As a result, channels with transversal constrictions of 100x100 nm^2 are fabricated.

Finally, a freestanding junction is created by an isotropic reactive-ion etching step (O_2, 6 min at 80 W forward power in an Oxford system) where the plasma removes partially the uncovered polyimide layer by combining physical and chemical material removal processes. Depending on the geometry and etching time, the bridge is freestanding over a distance of 200 - 800 nm. As a last step, junctions are laser-cut in 5 mm x 18 mm pieces from the large metal plates to yield the individual samples for measurements.

The above described break-junction samples are mounted into a three-point bending mechanism with a distance between the upper supports of 11.8 mm (see Fig. 1 A) in the manuscript). The middle support, a so-called "pushing rod", is attached to the bottom of the substrate and remains fixed in position, whereas the upper supports are driven via a thread and a high-resolution rotatory motor (Newport URS50BPP). They are attached to a mechanical rail system to ensure mechanical stability, reduced slippage and smooth operation.

For transport measurements, a HP4156B parameter analyzer without current amplifier is used. The current resolution is 1 fA, typical step sizes in voltage are 20 mV (resolution 60 μV). One current–voltage sweep requires 2-20 seconds. Typical step sizes are 1 to 5 degrees for the rotatory motor, at every point the electrode motion is stopped and 1-5 current–voltage characteristics are acquired. The electrode motion is controlled by measuring the electrical conductance. The entire MCBJ system is controlled and automated using LabView software.

3 Statistical Measurement Approach

For most organic and organometallic molecules, the molecular orbitals (MOs), e.g., the highest occupied (HOMO) or lowest unoccupied MO (LUMO), are generally not energetically aligned with the Fermi energy of the Au electrodes ($E_F \simeq$ -(5.1–5.4) eV). Hence, transport measurements at low bias ($V \leq 100$ mV) probe the local density of states (LDOS) near E_F of the electrodes. The LDOS at E_F is finite as the MO's energy level get broadened thermally and also by the molecule-metal coupling;[2] also as E_F is broadened at 300 K. Hence, for resonant transport through MOs to occur, a large bias has to be applied to align the MO's energy level with E_F. Therefore, we perform current–voltage (I–V) sweeps during repeated opening and closing procedures[3] to trap molecules in the junction and to measure their transport properties accessing MOs in resonance. The simultaneous mechanical manipulation of the junction provides a comprehensive transport picture as multiple configurations of the junctions are generated and electrically probed. No filtering by selection criteria of the acquired data is applied. Hence, junction-forming probabilities and fluctuations in the transport properties originating from the various geometries of the junctions can be quantified.

To perform the transport measurements, we use electron-beam-structured samples (Fig. 1 B of the manuscript) that are mechanically actuated in a three-point bending mechanism (see Fig. 1 A of the manuscript) operated in an ultra-high vacuum environment (UHV; pressure $p < 2 \cdot 10^{-9}$ mbar) and at variable temperature (10 K $< T <$ 300 K).[3] After initial rupture of the Au metal film constriction, the leads created are conditioned until a clear 1 G_0 peak is revealed, indicating atomic-sized Quantum Point Contacts (QPC). Molecules are then deposited onto a fully open junction (electrode separation approx. 3 - 4 nm) from a highly diluted solution in dry tetrahydrofuran (THF; $4 \cdot 10^{-5}$ Mol/l) such that molecules can assemble on each electrode surface and form a sub-monolayer coverage. After evaporation of the solvent, the electrical characterization is started by driving the electrodes in dependence of the electrical current being measured. The junction is opened stepwise and incrementally until a current of $<$ 1 pA at 1.0 V is being detected, representing a fully open junction. Then, the electrode motion is reversed until a current of $>$ 1 μA at 1.0 V is reached. In every opening or closing cycle, molecules can bridge the two electrodes. Despite the use of a lower threshold of 1 μA instead of 77.6 μA for a direct Au–Au contact, the electrodes are found to still gently touch because of the high mobility of the Au surface atoms at elevated temperatures and the electric field applied. If this threshold is reached, the electrode motion is reversed, and a new cycle is started. In every cycle, *I–V* characteristics are acquired using a Hewlett-Packard HP4156B parameter analyzer (current resolution 1 fA), with one bias sweep per position, providing several hundreds of *I–V* curves per cycle. Typically several dozen cycles are acquired. For every compound, the measurements are repeated on at least two independent chips.

4 Histograms in Absence of Molecules

Before molecular transport measurements are started, the properties of a pristine junction are measured for a few dozens cycles to ensure proper functionality and no presence of artificial features. When performing 200 opening and closing traces in absence of molecules using a pristine junction with a fixed bias of 10 mV, a histogram created from the opening traces has no accumulations appearing below 1 G_0 and the background is flat until 10^{-6} G_0. The Au–Au QPC features are shown at higher conductances than 1 G_0. Fig. 1 shows exemplarily a histogram created from 100 opening taken at 300 K under a bias of 10 mV.

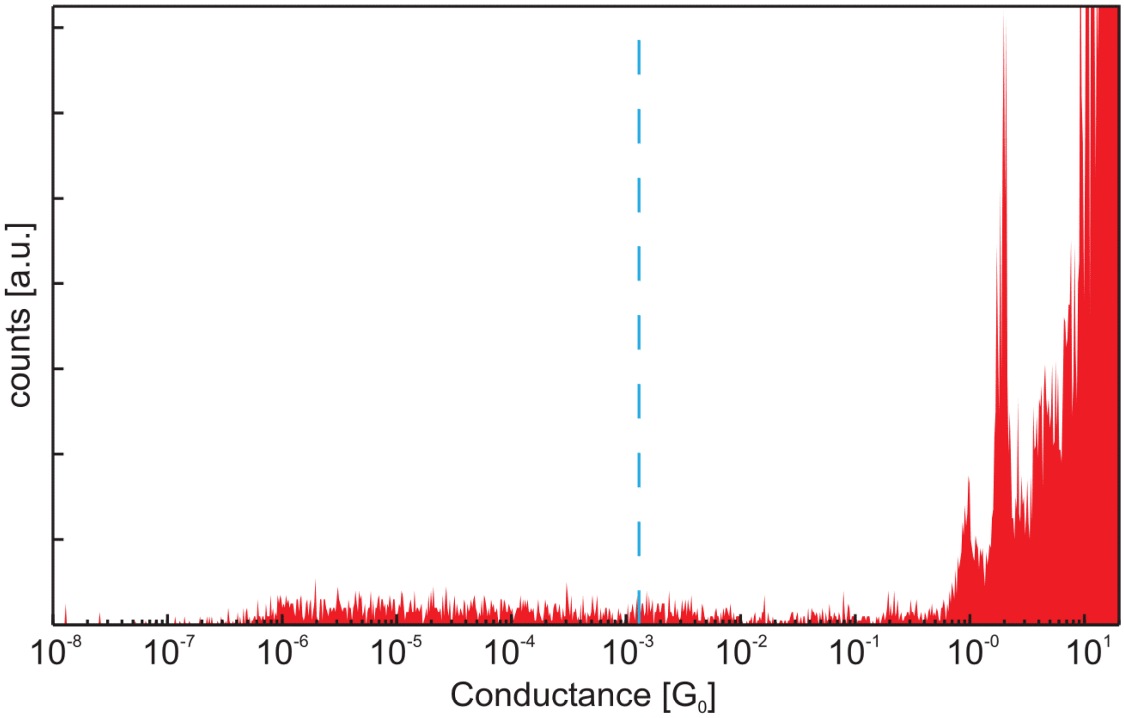

Figure 1: Histogram measured at 10 mV for 100 opening traces acquired in absence of molecules (pristine junction).

5 Transport Data of the -C≡N-terminated Compound 1

The transport data of compound **1** gave non-reproducible results on all three independent samples being characterized. In contrast to compounds **2**, **3** and **4**, only fixed bias histograms could be acquired at 10 mV, 50 mV, and 100 mV and 300 K which revealed all exclusively weak or masked molecular features within the experimental resolution available. Fig. 2 shows the histogram that gave the largest accumulations among all the 9 measurements performed on three different samples under identical measurement protocols. Only a very weak conductance accumulation is revealed at approx. $8.1 \cdot 10^{-7}\ G_0$ with around 40 counts (on a large background of 10 - 20 counts), giving a relative peak height (peak counts/background counts) of only 2-4. As a comparison, the corresponding histogram for compound **2** depicted in Fig. 2 A) of the manuscript shows a peak height of 150 counts (on a background of only 3 counts), resulting in tenfold higher relative peak height of around 50. The other histograms acquired for compound **1** show even fewer features in the sense that there were no statistically relevant conductance accumulations sticking out from the background with reasonably high relative peak heights. The green data in Fig. 1 shows raw data histograms with smaller logarithmic bins whereas the blue-bar histogram is constructed by using the same bins as the other results displayed throughout this work. Please note further that the shoulder arising from the direct Au–Au QPC located at $1.0 \cdot\ G_0$ is very broad as it achieves more than 1800 counts in this representation. This clearly indicates that the junction is fully closed during the repeated cycles (maximum conductance during closing: G_{max} = (5 - 20)$\cdot\ G_0$) and that the entire conductance range is probed down to $1.0 \cdot 10^{-8}\ G_0$. Both *I–V* measurements and higher-bias histograms (at 500 mV) did not reveal any molecular signatures that were stable and reproducible.

Given the very weak features in the histograms at 50 mV for compound **1** with -C≡N termination, we conclude that the conductance of compound **1** is either below our experimental resolution ($G_{Au-\mathbf{1}-Au} \ll 1.0 \cdot 10^{-8}\ G_0$), that the Au-**1**-Au junction is not stable even under very low bias, or that the bulky ligands prevent the terminals to bind to the Au electrodes due to the shorter bridge (leading also to an unstable junction).

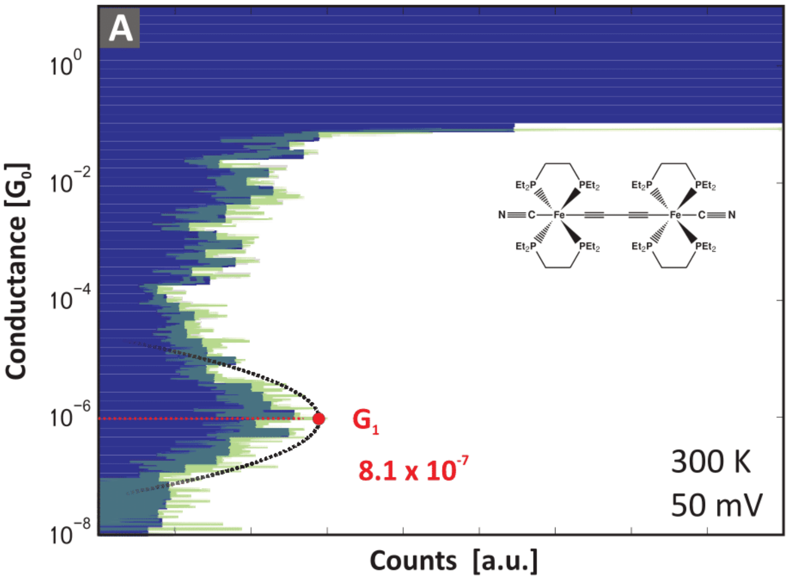

Figure 2: Low-bias histograms acquired under a fix bias of 50 mV at 300 K for compound **1**.

6 Histogram for 50/60 mV, 100 mV and 500 mV Bias

Low-bias histograms at 300 K were calculated by mathematically deriving the differential conductance dI/dV from I–V raw data at 50 mV, 100 mV and 500 mV for compound **2**, and for 60 mV, 100 mV and 500 mV for compounds **3** and **4** (the difference in the lowest bias point results from different step sizes (50 mV, 20 mV) during I–V data acquisition). The results are displayed in Fig. 3.

The conductance peak of compound **2** in Fig. 2 A) of the manuscript is located at $1.7 \cdot 10^{-7}$ G_0 for 50 mV and remains at $1.2 \cdot 10^{-7}$ G_0 for an increased bias of 100 mV in B). However, for a bias of 500 mV a ten-fold increase relative to A) and B) in the conductance to a value of $1.5 \cdot 10^{-6}$ G_0 in C) is found.

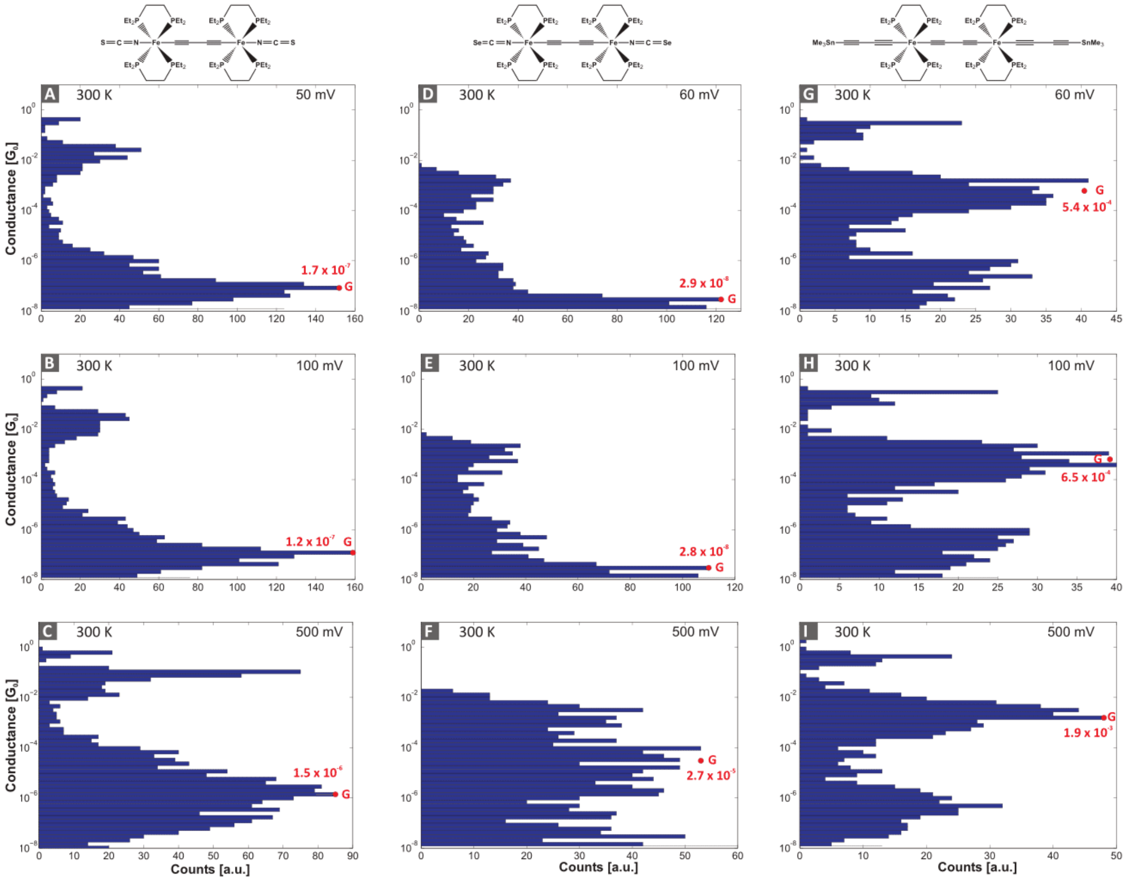

Figure 3: Low-bias histograms of compound **2** extracted from raw $I-V$ curves at 50 mV (A), 100 mV (B), and 500 mV (C). Histograms for compound **3** extracted at 60 mV (D), 100 mV (E), and at 500 mV (F). Histograms for compound **4** extracted at 60 mV (G), 100 mV (H), and at 500 mV (I).

Conductance histograms of compound **3** at 60 mV in D), 100 mV in E) and at 500 mV in F) show a similar behavior where the main peak is identified at $2.9 \cdot 10^{-8}$ G_0, $2.8 \cdot 10^{-8}$ G_0 and at $2.7 \cdot 10^{-5}$ G_0 respectively. Again, an increase in conductance is only observed if the bias is raised to 500 mV. The peak in F) is broadened whereas in D) and E) the highest peak has a steep shape and a tendency to lie close to the noise region.

In contrast, the low bias histograms of compound **4** clearly indicated that the main peak in conductance falls within the region of higher conductance. The conductance peak of **4** is located at $5.4 \cdot 10^{-4}$ G_0 for 60 mV in G), $6.5 \cdot 10^{-4}$ G_0 for 100 mV in H) and at $1.9 \cdot 10^{-3}$ G_0 for 500 mV in I).

Fig. 4 summarizes the most probable conductance (determined by the main histogram peaks) for the compounds **2**, **3** and **4** as a function of histogram extraction bias. For small bias, i.e. ≤ 100 mV, the conductance does not significantly increase. However, an increase of each molecule's most probable conductance relative to the low-bias conductance is revealed at higher bias as expected from the non-linear transport properties. The increase is around one order of magnitude for compound **4**, and two orders of magnitude for **3**.

7 Comparison of Histogram for 0.2 and 1.0 V Bias

As DFT calculations are performed at zero bias and the experimental results are most conclusive, we plotted the histograms also at a low bias of 0.2 V to be better comparable to zero bias. The results are shown in Fig. 5.

The insets contain evolution plots in which the conductance at +1.0 V is plotted versus the measurement number upon changing the electrode distance. The plot indicates that the entire range from a fully open to a direct metal–metal junction is probed.

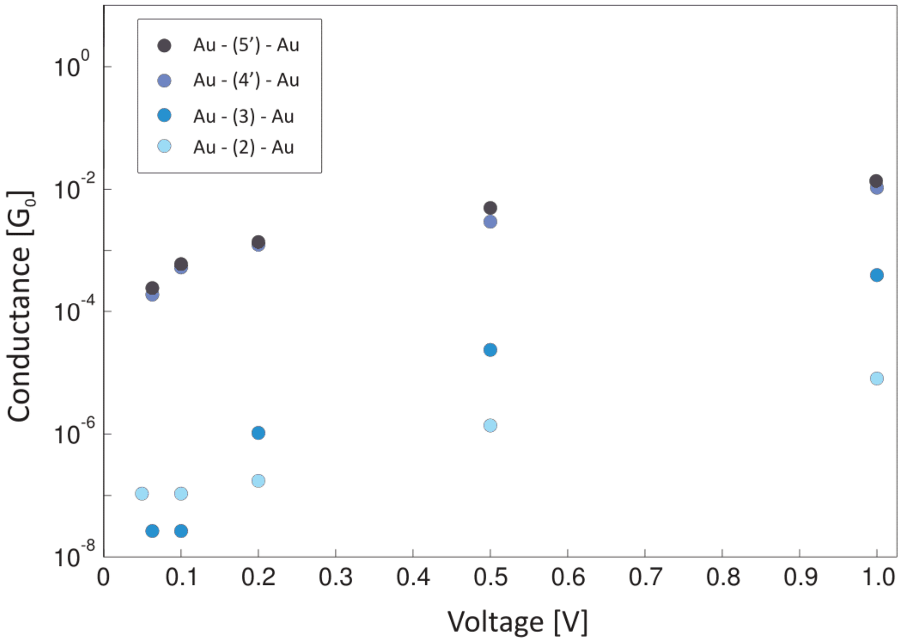

Figure 4: Main peaks found in the conductance histogram extracted at various biases for compounds **2**, **3**, **4′** and **5′**.

8 Density Functional Theory Calculations

All calculations of transmission probabilities $T(E)$ were performed within a NEGF-DFT framework[4–6] with the GPAW code.[7,8] We chose a linear combination of atomic orbitals (LCAO) on a double zeta level with polarization functions (DZP) for the basis set, a spacing of 0.18 Å for the real space grid describing the potential energy term in the Hamiltonian, and a Perdew-Burke-Ernzerhof (PBE) parametrization for the exchange-correlation (XC) functional. All conductance values have been obtained from a 4x4x1 **k** point sampling which resulted in eight **k** points in the irreducible Brillouin zone. Optimal distances between the two leads in the junction separated by the molecule were found by means of total energy minimization. The MO eigenenergies were calculated by decoupling the basis functions localized on the molecule from those of the surface states via a sub-diagonalization of the transport Hamiltonian.[9]

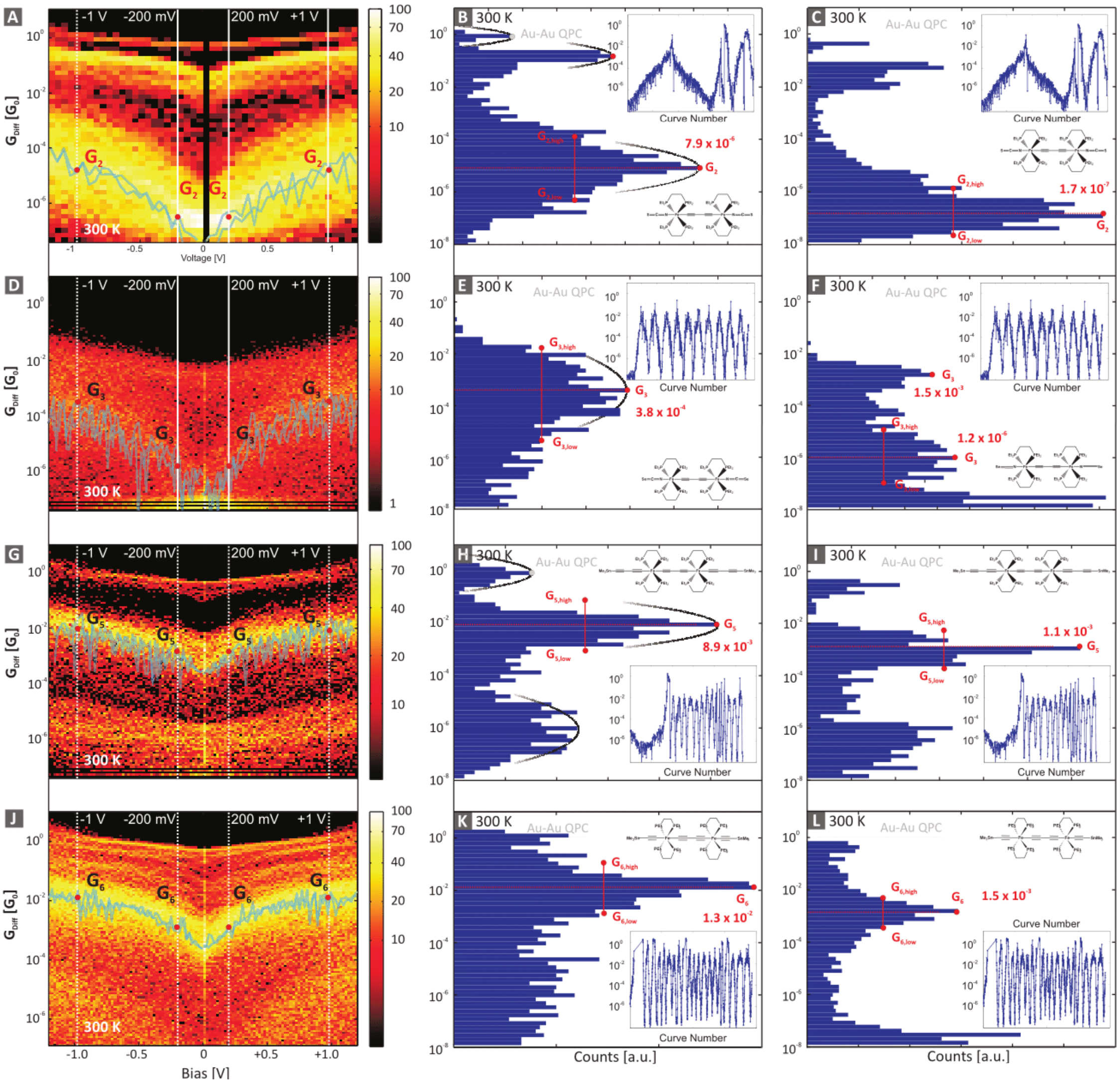

Figure 5: Histogram for all compounds extracted at 1.0 V (middle row) and 0.2 V bias (right row).

In order to account for self interaction and image charge effects a scissor operator, as introduced by Quek et al.,[10] was applied. Since the the molecular ionisation potential in vacuum is used as a reference in this correction, it is only justified for weakly coupled molecular systems, while the charge would spill into the leads because it occupies an orbital formed from the hybridization of the HOMO with Au surface states in the strongly coupled species. Therefore the SO operator was not applied to the **4′** and **5′** systems, since the direct C–Au bond leads to a significant change in the coupling (as can also be seen in Fig. 4 in the main text).

Because of the rather large size of the central molecule, we had to use gold slabs with a 6x6 unit cell in the surface plane to ensure that neighboring molecules do not interact. With the two Au ad-atoms directly coupling to the molecule, the device region contains a total of 254 Au atoms in addition to the atoms of the molecule itself. As a consequence, the part of the Hamiltonian used in the NEGF formalism reaches a size which was beyond our computational capabilities. To reduce the memory, we cut out very high- and very low-lying MOs from the transport Hamiltonian after sub-diagonalizing it with respect to molecular basis functions.[9] Here, we profit from the fact that we can disregard MOs further than 5 eV apart from E_F for the zero-bias conductance.

9 Possible Bonding Motifs for $SnMe_3$ capped Fe_2 compounds

The terminal substituents of compound **4** allow to postulate two different bonding reactions towards the Au surface. Fig. 6 A shows the compound **4** as synthesized. Two alternative bonding schemes to the Au electrode are plausible, leading to three different junction configurations as illustrated in Fig. 6 B, C and D. They differ by no $SnMe_3$ side group (forming a direct C_4 bridge to both electrodes) (B), one $SnMe_3$ side group towards right (or left) electrode (forming an alkynyl vinylidene configuration towards the right electrode) (C) or two $SnMe_3$ side groups towards both electrodes (forming both-sided alkynyl vinylidene-configured bridges) (D).

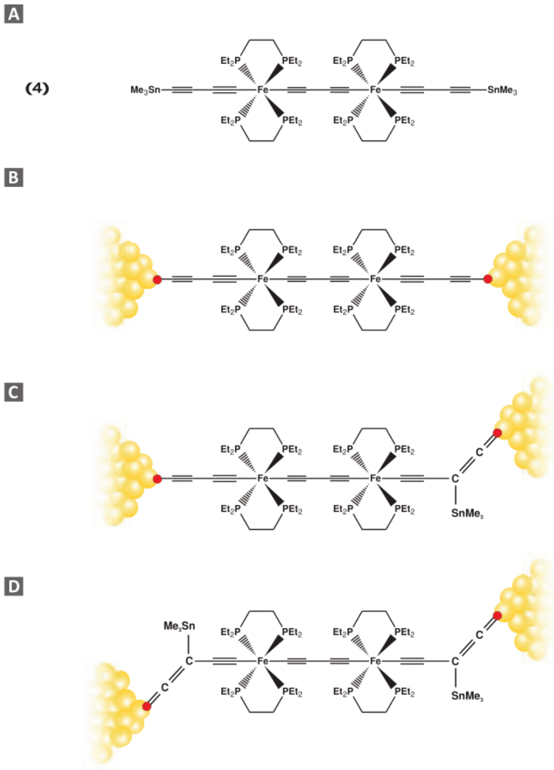

Figure 6: A) The terminal substituents of **4** allow for two different bonding reactions towards the Au surface giving rise to three different junction configurations: B) Cleavage of the $SnMe_3$ capping resulting in a C_4 bridge to the Au surface on both electrode sides. C) Asymmetric cleavage of the $SnMe_3$ capping on the left hand side electrode with alkynyl vinylidene configuration on the right electrode side. D) Both-sided alkynyl vinylidene-configured bonding scheme.

In the DFT calculations of the three plausible junction configurations, the $SnMe_3$ side groups as depicted in Fig. 6 have only minimal effect on the conductance when comparing the transmission function at the Fermi energy E_F. The conductances differ by less than one order of magnitude. In Fig. 7, it can be seen that although the $SnMe_3$ side groups result in additional MOs slightly lower than the Fermi energy, these MOs are entirely localized on the $SnMe_3$ side groups. Therefore, they do not result in additional peaks in the transmission function and hence do not contribute to the conductance.

If comparing relative conductances for these three distinctly different anchored junctions, the side groups have an indirect effect as they reduce the coupling slightly. This explains why the blue curve (one $SnMe_3$ side group) is shifted more downward in energy compared with the black curve and the peaks come closer to the energetic position of the MOs. This is also reflected in a slightly reduced conductance when blue is compared with black. For the red curve (two $SnMe_3$ side groups), this effect is more pronounced in the sense that the peaks are more shifted and coincide almost with the MO energies, which indicates an even weaker coupling than for the other curves.

Based on the DFT calculations alone, the alkynyl vinylidene-configured bonding scheme does not show distinctly different conductances than the direct C_4-Au bridge after cleavage of the $SnMe_3$. The small differences extracted for the three configurations from simulations is masked in the experiments by the large conductance fluctuations given. Hence, the DFT calculations for these different bonding schemes do not reflect the additional conductance accumulation in the current–voltage curves shown in Fig. 2 F) of the main text at approx. $9.6 \cdot 10^{-7}$ G_0. We therefore conclude that only dimerization of the compound **4** can explain the second low conductance peak as discussed in the main text and as evidenced in the next section and its Fig. 8.

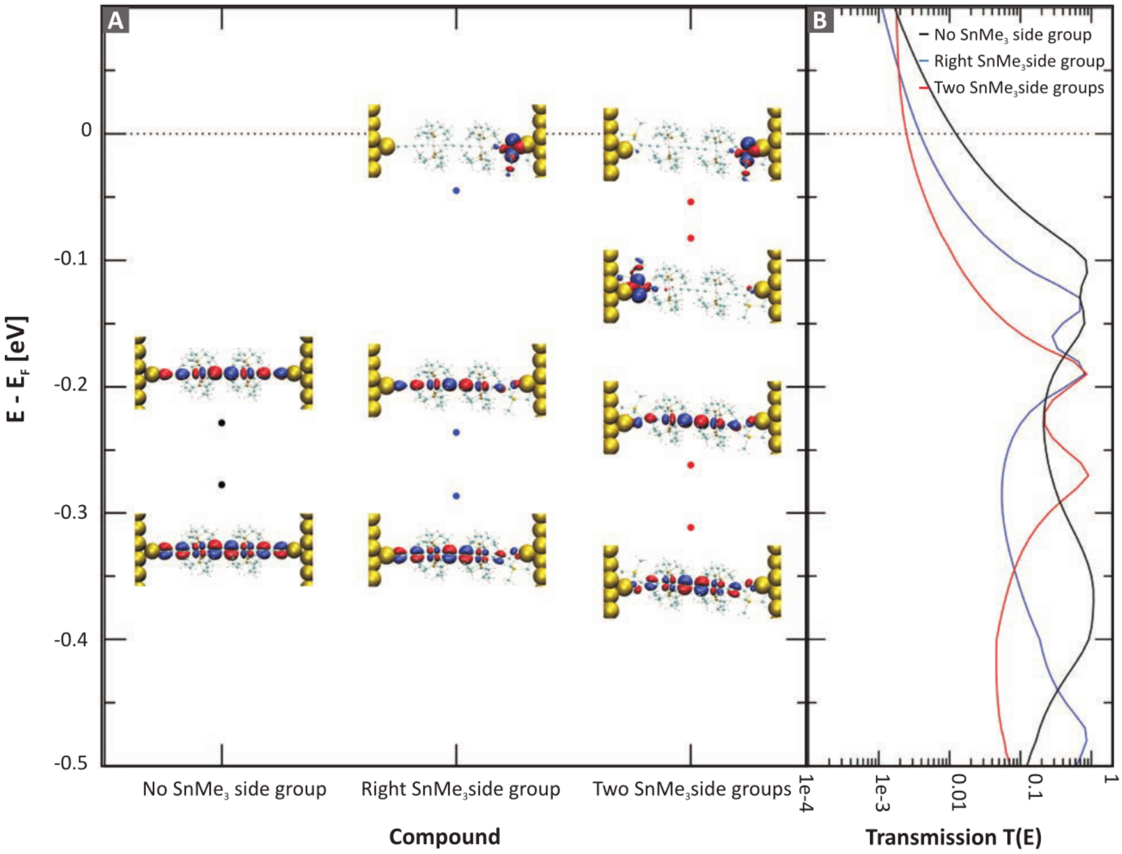

Figure 7: A) Comparison of MO eigenenergies and MO shapes as a function the number of $SnMe_3$ side groups (no $SnMe_3$ side group, $SnMe_3$ side group towards right electrode, and two $SnMe_3$ side groups towards left and right electrode.) B) Transmission function for the three junctions.

10 Dimerization of 4 and 5

We also calculated the conductance of the dimer compounds of **4′** and **5′** using DFT, where Au–**4′**–**4′**–Au, and Au–**5′**–**5′**–Au junctions were formed, respectively. The results are depicted in Fig. 8 A) for the molecular junctions shown in Fig. 8 B).

Comparing the DFT results with experimental values for the second highest conductance accumulation, a good qualitative agreement with the same relative offset is found. We hence conclude that the second highest accumulations are most probably due to spontaneous dimerization of the compounds **4′** or **5′**.

11 Hysteretic effects of compound 2

An additional effect found in the transport properties of **2** is a hysteretic behavior with a voltage-induced conductance switching in the bias regime from 1.08 - 1.20 V. The hysteresis is absent for data acquired above 200 K, rather unlikely to occur at 150 K (fewer than 5% of all curves), and occurs more reproducibly at 100 K (approx. 25%) and 30 K ($>$ 30%). Fig. 3 A) and B) of the main text display more than 50 transport characteristics that all show voltage-induced conductance switching and hysteretic behavior. These findings are in contrast to those for compound **4′**, where only monotonous curves without occurrence of a switching event or hysteretic behavior were recorded at low temperatures. Fig. 3 of the main text shows the corresponding I–V (C), and G_{Diff}-V (D) characteristics of **4′**, respectively, taken at 50 K: In addition to the absence of a hysteresis, the functional behavior of the transport properties is entirely different as no MOs can be identified due to a more linear transport behavior as found in Au–**4′**–Au junctions.

Fig. 3 A) of the main text shows bundles of I–V curves, a representation that is important, e.g. to determine statistically the most probable energies for the MOs (in respect to E_F) or the probability

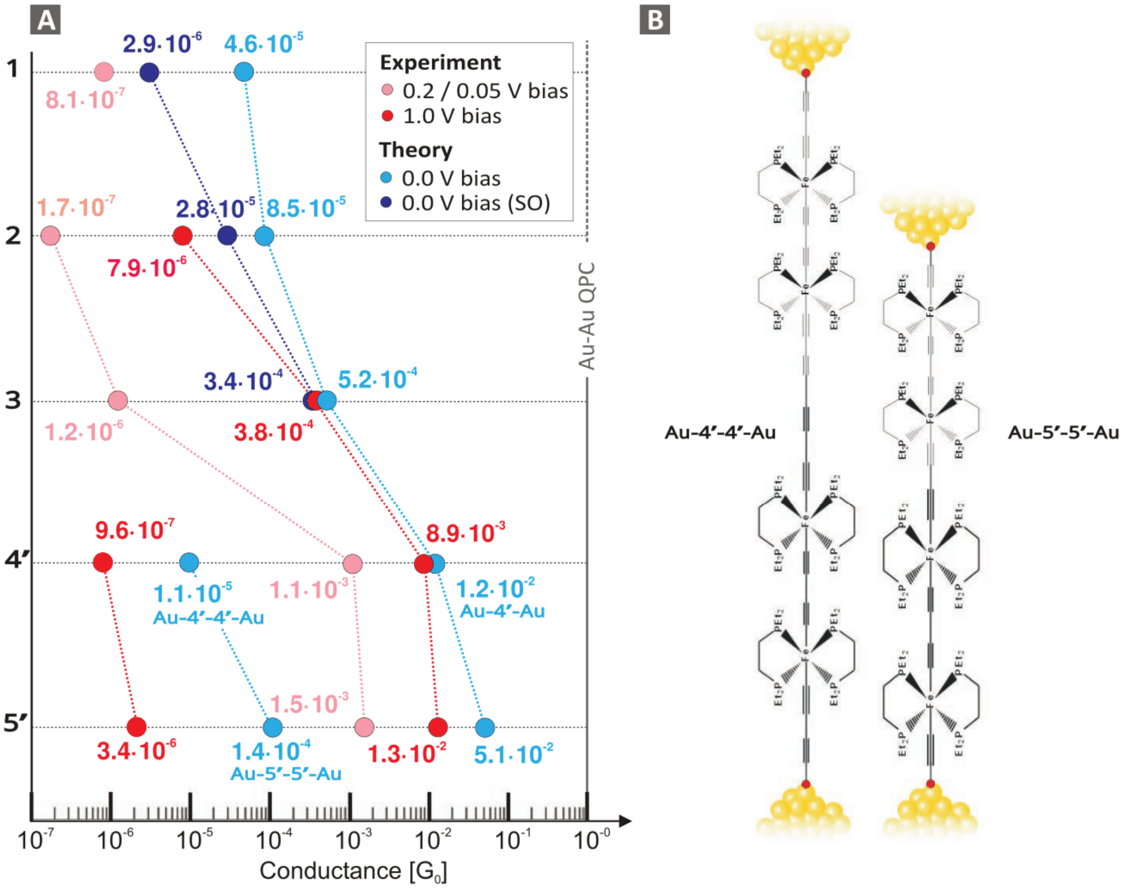

Figure 8: A) Transport results and conductances according to DFT for dimers of **4** and **5**. B) Dimer junctions Au–**4**′–**4**′–Au and Au–**5**′–**5**′–Au.

of a hysteresis to occur. However, in this representation it is difficult to understand the functional behavior of individual transport characteristics, in particular the hysteretic behavior. Fig. 9) shows individual *I–V* curves selected from the bundles of curves displayed in Fig. 3 A) and B) of the main text. In addition, Fig. 9 shows the direction of a bias sweep, when starting either at 0 V (Fig. 9 A) or negative bias (-1.2 V, B). Irrespective of the starting point for the bias sweep, the hysteretic behavior is always present. As already assumed from Fig. 3 A) of the main text, the *I–V* curves are non-linear with various features for both voltage polarities. The most striking observation is the behavior of the conductance gap Δ, defined by the current onset on both voltage branches. The current detection limit is 1 fA, but under low bias and fast scanning speeds rather 100 fA, as indicated by the noise floor in Fig. 9 A) and B). In contrast to the findings at 300 K and for compound **4′** at any temperature, the current onset for **2** at 50 K is different for positive and negative bias, defining two polarization-dependent conductance gaps Δ_1 and Δ_2 as depicted in Fig. 9 A) and B). As the current onset occurs when the first MO is close to resonance, this behavior indicates that the MO alignment changes depending on how the voltage has been swept. Fig. 9 C) shows a statistical analysis of all current onsets and the switching voltages found in the data. Clearly, there is a consistent difference in the two onset energies (V_2 - V_1) of approx. 0.08 eV. The switching voltage V_{Switch}, however, is found most often at approx. ± 1.2 V, close to the stability limit of our junction and only hardly visible in the *I–V* characteristics (blue arrow in Fig. 9 A). Within experimental resolution, the switching energy does not seem to depend on the voltage polarity.

The hysteretic switching behavior in Au–**2**–Au taking place at low temperatures in contrast to the exclusively monotonous curves for the Au–**4′**–Au system is in contrast to similar studies using Ru metal centers[11,12] in which no switching was observed at room temperature and at 5 K. The absence of this effect might be due to ensemble measurements when probing more than 100 molecules in parallel with a non-homogenous field gradient across the molecules in contact, which may smear out distinct features in the transport characteristics. Another explanation for the absence of redox functionality of that system is the different reversibility in the intramolecular redox process as

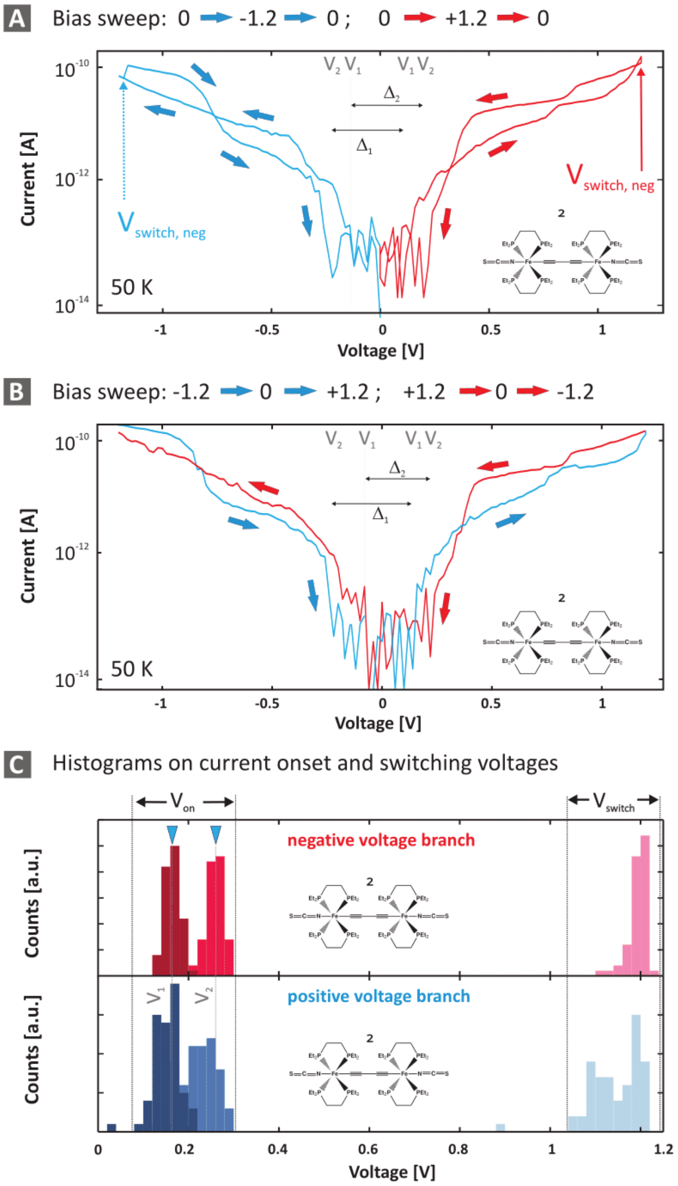

Figure 9: Individual I–V curves of Au-**2**-Au taken at 50 K for different bias sweep directions. A) Sweep starting at 0 V, and B) at -1.2 V. C) Statistical analysis of current onset voltages, V_1 and V_2, defining the conductance gap, Δ_i, and the switching voltage, V_{Switch}, extracted for positive and negative bias irrespective of the sweep direction.

measured in solution, which is highest for the unsaturated, rigid-rod and electronically versatile C_4 ligands,[13–15] and decreases dramatically if other types of sp/sp_2 systems were used as in the case of the Ru compounds.[11] In our experiment, however, the switching was pronounced and reproducible. Other effects than intramolecular redox processes responsible for conductance switching, such as stochastic switching in the molecule–metal contacts, can be excluded as the switching feature is robust against mechanical manipulation and highly reversible also at low temperatures. At zero bias, the hysteretic effect is preserved as indicated by a change and a bias asymmetry of the conductance gap that depend on the preceding bias sweep direction (and hence the sign of the electric field applied); therefore causing a memory effect to take place.

12 Transition Voltage Spectroscopy Representation

In contrast to low temperature data where the MOs contribute resonantly to transport and their energy levels are indicated by peaks in the differential conductance - voltage, *G*–*V* plot (as seen in Fig. 3 of the main text), the room temperature data shows less distinct features except from the current level and the functional current increase. One way to plot the data and to extract injection barriers without the need to apply high bias, is transition voltage spectroscopy (TVS),[16] where the natural log of I/V^2 is plotted against 1/V. Fig. 9 shows individual *I-V* traces that were selected with respect to their statistical appearance in the histograms of Fig. 2 of the main text. The TVS representation shows a local minimum, attributed to the injection barrier height related to the energetic position of the MO close to resonance. Within the spread of the experimental data, the minima are located at lower bias: (1.85 ± 0.3) V for **5′** and (1.75 ± 0.3) V for **4′**, in contrast to (4.2 ± 1.5) V for **3**, and (5.5 ± 1.5) V for **2**. Given the large number of assumptions,[17] we leave this discussion with a more qualitative statement, that the barriers are substantially lower for C–Au coupling compared to the NCS and NCSe coupling.

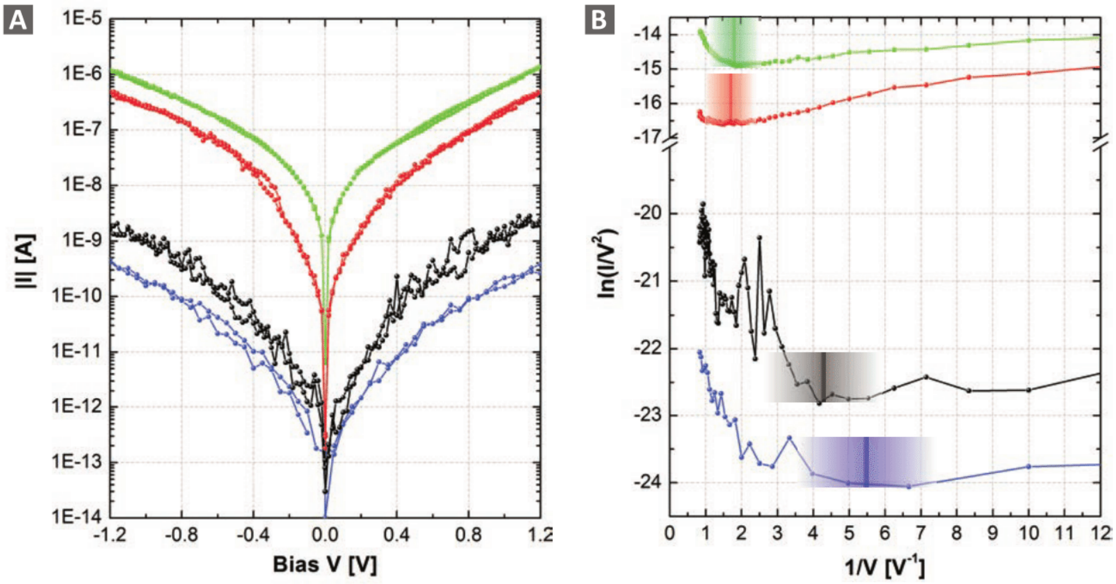

Figure 10: A) Individual *I*–*V* curves (blue: compound **2**, black: compound **3**, green: compound **4′** and red: compound **5′**) selected according to the statistical accumulations in the histogram (as displayed in Fig. 2 of the main text). B) Transition voltage spectroscopy (TVS) representation of selected *I*–*V* curves (blue: compound **2**, black: compound **3**, green: compound **4′** and red: compound **5′**) revealing possible injection barrier heights.

13 Comparison to State-of-the-Art Molecular Wires

A comparison of different conductances (measured or extracted at 100, 200 or 250 mV) for molecular wires[11,12,18,19] as a function of wire length is given in Fig. 11 and compared with our experimental and theoretical values for compound **4′**. A preliminary length-dependence for the dinuclear Fe complexes is made by taking into account the plausible dimer formation of **4′** forming Au–**4′**–**4′**–Au junctions with the repeating unit being the dinuclear [Fe–C_4–Fe] core.

The decay constants of β = 4.4 nm^{-1} (determined by experimental values at 200 mV or 1.0 V) and β = 3.5 nm^{-1} (DFT at zero bias, no k-point sampling for the dimer system Au–**4′**–**4′**–Au, mononuclear compound not taken into account for the fit) are both lower than for organometallic Ruthenium(II) Bis(σ-arylacetylide) complexes[11,12] (β = 1.02 - 1.64 nm^{-1}) or purely organic oligothiophenes (β = 1.0 nm^{-1}) and rather comparable to phenyls coupled via C–Au or amines (β = 4.0 - 6.0 nm^{-1}).

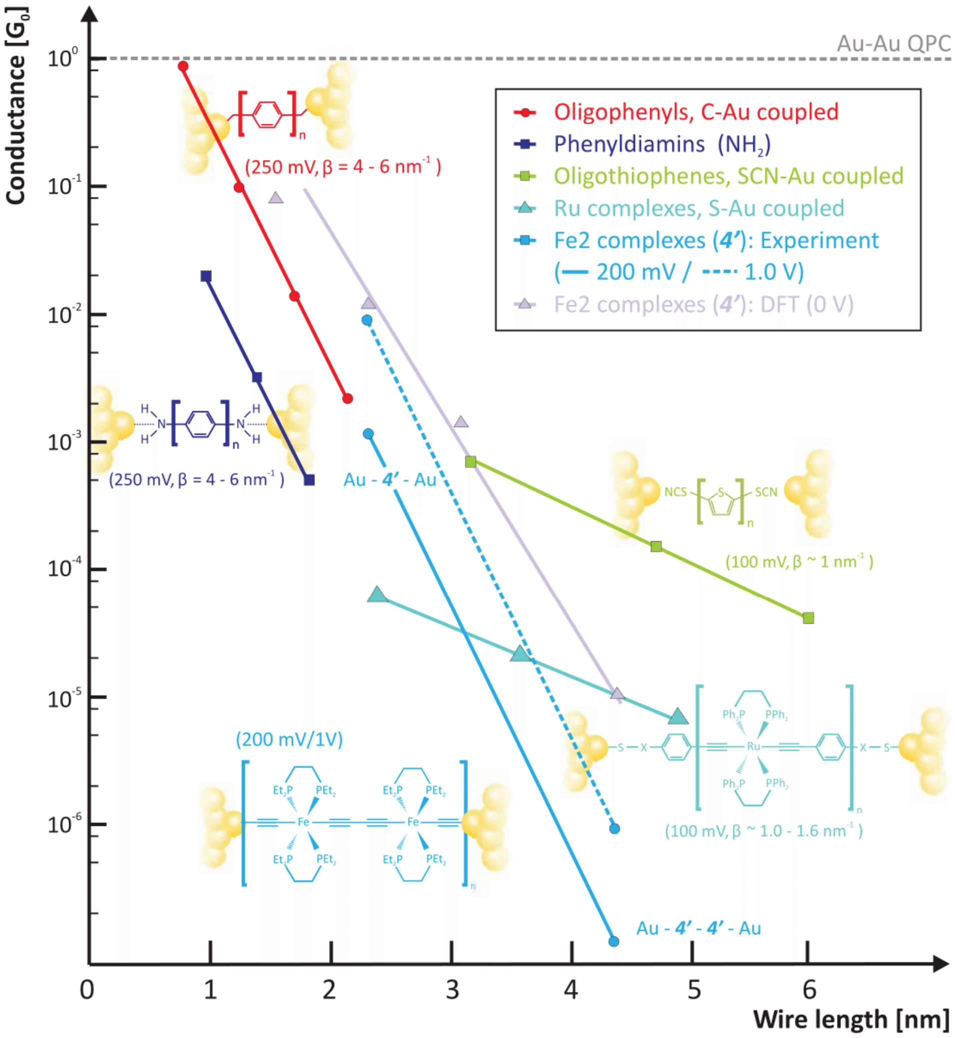

Figure 11: Conductances as a function of molecular wire length for purely organic oligophenyls and oligothiophenes compared with organometallic Ru(II) and Fe2 complexes. All data is taken at low bias of 100 mV, 200 mV or 250 mV for comparison.

References

(1) Lissel, F.; Schwarz, F.; Blaque, O.; Riel, H.; Lörtscher, E.; Venkatesan, K.; Berke, H. *Submitted* **2014**,

(2) Paulsson, M.; Zahidy, F.; Datta, S. In *Nanoscience, Engineering and Technology Handbook*; Goddard, W., Brenner, D., Lyshevski, S., Iafrate, G., Eds.; CRC Press, New York, 2003.

(3) Lörtscher, E.; Weber, H. B.; Riel, H. *Phys. Rev. Lett.* **2007**, *98*, 176807.

(4) Brandbyge, M.; Mozos, J.-L.; Taylor, J.; Stokbro, K. *Phys. Rev. B* **2002**, *65*, 165401.

(5) Xue, Y.; Datta, S.; Ratner, M. A. *Chem. Phys.* **2002**, *281*, 151.

(6) Rocha, A. R.; Garcia-Suarez, V. M.; Bailey, S. W.; Lambert, C. J.; Ferrer, J.; Sanvito, S. *Nature Mater.* **2005**, *4*, 335.

(7) Mortensen, J. J.; Hansen, L. B.; Jacobsen, K. W. *Phys. Rev. B* **2005**, *71*, 035109.

(8) Enkovaara, J.; Rostgaard, C.; Mortensen, J. J.; Chen, J.; Dulak, M.; Ferrighi, L.; Gavnholt, J.; Glinsvad, C.; Haikola, V.; Hansen, H. A.; Kistoffersen, H.; Kuisma, M.; Larsen, A. H.; Lehtovaara, L. *J. Phys.: Conf. Ser.* **2010**, *22*, 253202.

(9) Kastlunger, G.; Stadler, R. *Phys. Rev. B* **2013**, *88*, 035418.

(10) Quek, S. Y.; Neaton, J. B.; Hybertsen, M. S.; Venkataraman, L.; Choi, C. H.; Louie, S. G. *Nano Lett.* **2007**, *7*, 3477–3482.

(11) Luo, L.; Benameur, A.; Brignou, P.; Choi, S. H.; Rigaut, S.; Frisbie, C. D. *J. Phys. Chem. C* **2011**, *115*, 19955–19961.

(12) Kim, B.; Beebe, J. M.; Olivier, C.; Rigaut, S.; Touchard, D.; Kushmerick, J. G.; Zhu, X.-Y.; Frisbie, C. D. *J. Phys. Chem. C* **2007**, *111*, 7521–7526.

(13) Dembinski, R.; Bartik, T.; Bartik, B.; Jaeger, M.; Gladysz, J. A. *Journal of the American Chemical Society* **2000**, *122*, 810–822.

(14) Ward, M. D. *Chem. Soc. Rev.* **1995**, *24*, 121–134.

(15) de Montigny, F.; Argouarch, G.; Costuas, K.; Halet, J.-F.; Roisnel, T.; Toupet, L.; Lapinte, C. *Organometallics* **2005**, *24*, 4558–4572.

(16) Beebe, J. M.; Kim, B.; Gadzuk, J. W.; Frisbie, C. D.; Kushmerick, J. G. *Phys. Rev. Lett.* **2006**, *97*, 026801.

(17) Huisman, E. H.; Guédon, C. M.; van Wees, B. J.; van der Molen, S. J. *Nano Lett.* **2009**, *9*, 3909–3913.

(18) Chen, W.; Widawsky, J. R.; Vazquez, H.; Schneebeli, S. T.; Hybertsen, M. S.; Breslow, R.; Venkataraman, L. *J. Am. Chem. Soc.* **2011**, *133*, 17160–17163.

(19) Yamada, R.; Kumazawa, H.; Noutoshi, T.; Tanaka, S.; Tada, H. *Nano Lett.* **2008**, *8*, 1237–1240.

5. STRUCTURAL AND ELECTRONIC VARIATIONS OF CARBYL/METHYNE-BASED BRIDGES IN DI- AND TRINUCLEAR REDOX-ACTIVE IRON COMPLEXES BEARING FE(DIPHOSPHINE)$_2$X (X = I, NCS) MOIETIES

2.1 MANUSCRIPT

The manuscript and associated supplementary information were submitted as a full paper to Organometallics on June 6th 2014 as:

F. Lissel, O. Blacque, K. Venkatesan, H. Berke: *Structural and Electronic Variations of Carbyl/Methyne-Based Bridges in Di- and Trinuclear Redox-Active Iron Complexes Bearing Fe(diphosphine)$_2$X (X = I, NCS) Moieties*

and is currently under revision (accepted after major revisions on July 11th 2014). We kindly ask to treat the contents confidential.

Structural and Electronic Variations of Carbyl/Methyne-Based Bridges in Di- and Trinuclear Redox-Active Iron Complexes Bearing Fe(diphosphine)$_2$X (X = I, NCS) Moieties

Franziska Lissel, Olivier Blacque, Koushik Venkatesan and Heinz Berke*

† Department of Chemistry, University of Zurich, Winterthurerstrasse 190, CH-8057 Zurich, Switzerland

ABSTRACT: Starting from the mononuclear precursor *trans*-Fe(depe)$_2$I$_2$ (depe = 1,2-bis(diethylphosphino)ethane), 4 dinuclear complexes IFe(depe)$_2$–C$_n$–Fe(depe)$_2$I with C$_n$ = 1,4-(–C≡C–C$_6$H$_4$–C≡C–) **1**, 1,3-(–C≡C–C$_6$H$_4$–C≡C–) **2**, 4,4'-(–C≡C–C$_6$H$_4$–C$_6$H$_4$–C≡C–) **3**, 2,5-(–C≡C–thiophene–C≡C–) **4** as well as a trinuclear complex {I–Fe(depe)$_2$(C≡C–)}$_3$(1,3,5-C$_6$H$_3$)} **5** were prepared in a facile way by transmetalation from stannylated precursors. Substitution of the terminal iodides applying an excess of NaSCN yielded the corresponding isothiocyanate complexes **6** - **10** in very good yields. All complexes **1** - **10** are intrinsically functional due to the redox-active metal centres embedded in a structurally rigid and covalent sp/sp^2 framework. **1** - **10** were characterized by NMR, IR and Raman spectroscopy, as well as elemental analyses. X-ray diffraction studies carried out for **1**, **2**, **4**, **5**, **6**, **8** and **9** showed that the C$_2$ units of the bridging ligand are best described as acetylenic and that the endgroup-arene-endgroup angle is determined by the geometry of the arene bridging ligand. Cyclic voltammetry was employed to explore the redox behavior of **1** - **10**. The 1,4-(–C≡C–C$_6$H$_4$–C≡C–) and the 2,5-(–C≡C–thiophene–C≡C–) bridged compounds **1**, **4**, **6** and **9** exhibit two fully reversible oxidation waves, while the 1,3-(–C≡C–C$_6$H$_4$–C≡C–) and 4,4'-(–C≡C–C$_6$H$_4$–C$_6$H$_4$–C≡C–) bridged dinuclear complexes and the trinuclear complexes only show one reversible oxidation wave corresponding to 2 e$^-$ and 3 e$^-$ processes, respectively. Calculations were carried out for truncated model complexes to determine the HOMO/LUMO energies. The DFT results confirmed that by changing the sp/sp^2 bridging ligand, tuning the energies of the molecular orbitals, and modify the HOMO-LUMO gap $\Delta E_{(H\text{-}L)}$ and the chemical hardness is possible.

Introduction

The field of molecular electronics seeks to design and fabricate electronic circuits and ultimately devices on the molecular level.[1],[2] At the present stage of development a search has been started for suitable molecules. The requested physical properties are naturally determined by the structures of such molecules and this is the point where chemistry plays a crucial role constructing the basic elements of the circuitry. Three structural and physically related properties of the molecules are essential:[2,3] (1) a so-called "molecular wire" combining a rigid-rod structural layout with favorable orbital overlap along an electronic charge pathway to allow transport of electric charge over distances in the range of a few nanometres, (2) an intrinsically functional moiety capable of enabling operations, such as high conductivity, rectification, conductance switching, charge storing or quantum interference and (3) suitable endgroups of the "molecular wires" to establish firm anchoring and electronic contact of the molecules to the electrodes.

Introducing redox-active metal centers into the rigid-rod molecular architectures, the so-called "relay approach", was shown to enhance the overall conductivity (point (1)) by providing defined donor–acceptor sites, thus promoting electron hopping.[4,5] In case the molecular architectures are dominated by carbon frameworks the introduction of metal centers into certain molecular topologies is a domain of organometallic chemistry. According to point (1) and (3) strong organometallic bonds are required to ensure stable and rigid molecular structures. Also the energetic position of the electron carrying molecular orbitals (absolute electronegativity according to Pearson[6]) is expected to cope energetically with the Fermi level of the macroscopic electronic leads, which are separated by several eV when purely organic molecules are employed, but can be adjusted and tuned in a facile way in organometallic compounds due to the strong electronic dependence exerted by the kind of the metal center.[7] [8] [9–11] [12] By the same token organometallic molecules can be tuned for a certain size in the HOMO/LUMO gap (absolute hardness according to Pearson[6]), which again provides adjustment of the orbital interactions of the molecules with the electronic leads helping to accomplish an electronic charge pathway and certain intrinsic functions of the molecules (points (1) and (2)).

These basic facts, together with the rich structural chemistry of ligands and the high tunability of transition metals in an ancillary ligand environment, makes organometallic molecules highly promising candidates for applications in molecular electronics. Nonetheless, investigations into organometallic entities are restrained by the lack of suitable consanguineous series of molecules including their endgroups, which allow to probe the interdependencies of structure and electronic properties at the molecular level.

The class of (PP)MC$_n$M(PP) (M = redox-active metal centre, P = monodentate phosphine ligand or PP = bidentate phosphine ligand, C$_n$ = bridging organic π ligand) type compounds are interesting model complexes to study intramolecular charge transport properties.[13,14,15] The covalently bonded and electronically delocalized bridging π ligand acts as a structurally well-defined rigid-rod intramolecular electron pathway, and by successively varying the metal centre(s),[16,17]
the bridging[18] and non-bridging ligands,[19] it is possible to probe the relationship between molecular structure and spectroscopic and electrochemical properties. It was shown that the electronic delocalization extends over the length of the organometallic unit in most cases.[20,21,22,23] The reversibility of the intramolecular redox processes was found to be highest for the unsaturated, rigid-rod type and electronically versatile C$_4$ ligand,[24,18,25] yet the utilization of other types of π systems was shown to allow the tuning of the intramolecular charge transport pathway to decouple the redox-active metal centres and thus gradually localize the electronic charge.[26,27,28]

While such structural modifications and the accompanying changes in the electronic layout are promising towards the goal of creating functional molecular moieties, the compounds of the (PP)MC$_n$M(PP) class are mostly limited to so-called "stopper-type" molecules (Cp*)(PP)MC$_n$M(PP)(Cp*) (Cp*= η^5-C$_5$Me$_5$) which cannot be functionalized at the termini to enable the binding to molecular electronic leads. Terminally open molecules of the type X(PP)MC$_n$M(PP)X (X = anchoring group) are rare as their realization poses a significant synthetic challenge. Up to date, single-molecule transport measurements were only carried out on a limited number of the X(PP)MC$_n$M(PP)X type of fragments, such a mononuclear ruthenium[29] and platinum[30] complex, as well as selected di- and trinuclear ruthenium entities.[31,32,33,34] In this paper strongly electron donating diphosphines were chosen as ancillary ligands (PP = depe = 1,2-bis(diethylphosphino)ethane) to the iron centers, because we expected complexes of high solubility in organic solvents, stable ligand environments and an absolute electronegativity in the range needed for appropriate interaction with the gold leads.

We recently reported that through a series of transmetalation and substitution reactions, terminally open multinuclear compounds with the structural core {Fe}C$_4${Fe} ({Fe} = Fe(depe)$_2$) can be accessed and allow to stepwise build a homometallic tetranuclear Me$_3$SiC$_4${Fe}C$_4${Fe}C$_4${Fe}C$_4${Fe}C$_4$SiMe$_3$ unit exhibiting extensive charge-delocalization and vibrational coupling over the entire unsaturated organometallic backbone.[20] End-capping a dinuclear functional {Fe}C$_4${Fe} core with terminal isothiocyanate ligands allowed to investigate the electronic properties using the mechanically controllable break junction (MCBJ) technique.[35,36] It was found that the utilization of terminal isothiocyanate ligands allows a weak but stable molecule-electrode contact and furthermore leads to the observation of stable and reversible switching events at low temperature. This finding is unprecedented in organometallic molecular electronics, and opens new possibilities to design and rationalize functional molecular circuits.

Au electrodes are comparably soft according to the HSAB concept developed by Pearson,[37] with a Fermi level $E_F \approx -(4.8\text{-}5.4)$ eV. To achieve a resonant transport, the molecular orbitals of the probed molecule have to be aligned in way to allow an easy overlap with the orbitals of the macroscopic Au strands. Consequently, molecules should be soft and polarizable to be adjusted to Au_F. The absolute chemical hardness can be correlated to the HOMO-LUMO gap $\Delta E_{(H\text{-}L)}$ and allows to predict the strength of donor - acceptor interactions.[6] Molecules with small HOMO/LUMO gaps are denoted as soft, those with large HOMO/LUMO gaps as hard, while (I+A)/2 (I = ionization potential, A = electron affinity) at high negative energy means high electronegativity and vice versa.

We envisaged that the variation of the bridging ligand C_n of a SCN{Fe}C_n{Fe}NCS entity can allow to tune the energies of the molecular orbitals and thus modify the chemical hardness and the resulting molecule-electrode contact. Consequently we targeted to bridge redox-active {Fe} cores with different sets of unsaturated organic linkers to probe the effect of a gradual decoupling of the metal centres on the molecular orbital energies and the resulting chemical hardness.

In this study, we present the synthetic routes to access dinuclear fragments of the type I{Fe}C_nFe{Fe}I (C_n = 1,4-($-C\equiv C-C_6H_4-C\equiv C-$), 1,3-($-C\equiv C-C_6H_4-C\equiv C-$), 4,4'-($-C\equiv C-C_6H_4-C_6H_4-C\equiv C-$), 2,5-($-C\equiv C-$thiophene$-C\equiv C-$)) as well as a trinuclear complex {I–{Fe}($C\equiv C-$)}$_3$(1,3,5-C_6H_3). The reactive terminal iodo ligands can then be substituted with NCS groups to yield the corresponding isothiocyanate complexes. All compounds were characterized by NMR, IR and Raman spectroscopy as well as elemental analyses. X-ray diffraction studies were carried out on seven complexes and confirmed rigid structures, while cyclic voltammetry was employed to explore the redox behavior. All complexes are intrinsically functional due to the redox-active metal centres embedded in a structurally rigid and covalent sp/sp^2 framework.

The molecular geometries of the model complexes **6**-*Me*, **7**-*Me*, **8**-*Me*, **9**-*Me* and the C_4 bridged complex **C**-*Me*, for which the ethyl groups of the depe ligands were replaced by methyl groups were optimized at the PBE1PBE/LANL2DZ level. The corresponding Fe-Fe' and S-S' distances were determined and the HOMO/LUMO energies calculated to gain insight into the influence of the bridging arene on the molecular orbitals. The obtained results confirm that choosing different bridging ligands allows to tune the energies of the molecular orbitals.

Experimental Section

Syntheses and Spectroscopic Characterizations. All experiments and measurements were carried out under a dinitrogen atmosphere using Schlenk techniques or in a glove box (M. Braun 150B-G-II). All compounds were worked up to an analytically pure state without the use of column chromatography. The experimental part containing the description of the syntheses, one- and two-dimensional NMR experiments (Figures S1 - S55), IR and Raman (Figures S56 - S65, Table S1), cyclic voltammetry experiments at different chart speeds (Figures S67 - S73) as well as the results of the elemental analyses can be found in the Supporting Information.

X-ray structure analyses. The molecular structures of complexes **1**, **2** and **4** are depicted in Figure 1, the molecular structures of compounds **6**, **8** and **9** are shown in Figure 2, and complex **5** is illustrated in Figure S66. Selected bond lengths, bond angles and intramolecular distances are summarized in Table S4. The crystallographic data for all compounds are presented in Tables S2 and S3. Single-crystal X-ray diffraction data were collected at low temperatures (at 120(2) K for compound **5**, at 153(2) K for compounds **1** and **4**, and at 183(1) K for compounds **2**, **6**, **8** and **9**) on a Xcalibur diffractometer (Ruby CCD detector) for compounds **1**, **2**, **4**, and **6** and on a SuperNova area-detector diffractometer for compounds **5**, **8** and **9**, using a single wavelength Enhance X-ray source with MoK_α radiation (λ = 0.71073 Å)[38] for all compounds, except for compound **5** for which the CuK_α radiation (λ = 1.54184 Å) was used. The selected suitable single crystals were mounted using polybutene oil on the top of a glass fiber fixed on a goniometer head and immediately transferred to the diffractometer. Pre-experiment, data collection, data reduction and absorption corrections[39] were performed with the program suite *CrysAlis^{Pro}*.[38] Using WinGX[40] or Olex (for compound **5**),[41] the crystal structures were solved with *SHELXS97*[42] using direct methods and the structure refinements were performed by full-matrix least-squares on F^2 with *SHELXL97*[42] (*SHELXL2013*[42] for compound **5**). *PLATON*[43] was used to check the results of the X-ray analyses.

For more details about the refinements, see the *refine_special_details* and *iucr_refine_instructions_details* sections in the Crystallographic Information files (Supporting Information). CCDC-1002481 (for **1**), CCDC-1002482 (for **2**), CCDC-1002483 (for **4**), CCDC-1002484 (for **5**), CCDC-1002485 (for **6**), CCDC-1002486 (for **8**) and CCDC-1002487 (for **9**), contain the supplementary crystallographic data for this paper. These data can be obtained free of charge from The Cambridge Crystallographic Data Centre via www.ccdc.cam.ac.uk/data_request/cif.

Computational details. DFT calculations were performed with the Gaussian03 program package[44] using the hybrid functional PBE1PBE [45] in conjunction with the LanL2DZ basis set[46,47,48] for the geometry optimizations and with the 6-311+G(d) basis set [49,50,51] on all atoms for the determination of the energy levels. Geometries were optimized with a C_i (inversion center) or a C_2

(two-fold axis) symmetry, and the ethyl groups of the *depe* ligands were replaced by methyl groups.

Experimental Results

Synthesis and spectroscopic properties of the different dinuclear complexes.

Dinuclear iron complexes of the type (Cp*)(PP)Fe–C_n–Fe(PP)(Cp*) (with PP = bidentate phosphine ligand, Cp* = cyclopentadienyl, C_n = sp or sp^2 bridging ligand) can be accessed by reacting the mononuclear fragment (Cp*)(PP)FeCl with silylated alkynes in the presence of MeOH and a fluoride source. Depending on the chosen co-reactants and the type of alkyne used, this pathway either yields directly the targeted dinuclear complex or the corresponding mononuclear vinylidene complex, which then can be subjected to oxidative homocoupling. Employing this route, dinuclear iron complexes bridged by C_4[52] and C_8[53] spacers, 9,10-bis(ethynyl)anthracene,[54] 2,5-bis(ethynyl)thiophene,[55] 1,4-[56] and 1,3-bis(ethynyl)benzene[57,58] as well as a trinuclear complex bridged by an 1,3,5-tris(ethynyl)benzene[57,58] ligand were obtained. This route turned out to be useful to access so-called "stopper-type" molecules, which cannot be further functionalized. Applying the related reaction conditions to obtain terminally open complexes of the type {X–Fe$(PP)_2$(C≡C–)$\}_m$(C_n)} (PP = bidentate phosphine ligand, X = halide) this synthetic method was found to be less reliable. A dinuclear complex of the type Cl$(depe)_2$Fe–1,4-(–C≡C–C_6H_4–C≡C)–Fe$(PP)_2$X[59] and a trinuclear terminally open complex {Cl–Fe$(dmpe)_2$(C≡C–)$\}_3$(1,3,5-C_6H_3)}[60] (dmpe = (1,2-bis(dimethylphosphino)ethane)) could be prepared earlier, yet the authors report low yields due to side product formation, as well as unsuccessful attempts to adopt this method for other sp^2-carbon bridged ligand systems. Likewise, the efforts to prepare Cl$(depe)_2$Fe–C_4–Fe$(depe)_2$Cl using *in-situ* deprotection of Me_3Si–C_4–SiMe_3 and subsequent coupling to two mononuclear *trans*-Fe$(depe)_2Cl_2$ units was also not successful, instead leading to the formation of an interesting non-rod type trinuclear compound of low symmetry.[61] These findings are in all likelihood owed to the structural versatility of the bidentate phosphine ligands, which are reported to reversibly dissociate in various cases, thus allowing structural reorganization of the iron coordination sphere.[62,63,64]

The tendency of the bidentate phosphine ligands to dissociate increases with their sterical demand causing the structural stability of the Fe$(PP)_2$ fragment to decrease in the order Fe$(dmpe)_2$ > Fe$(depe)_2$ > Fe$(dprpe)_2$ (dprpe = 1,2-bis(diisopropylphosphino)-ethane), while the solubility follows the reverse trend and is highest for the sterically bulky Fe$(dprpe)_2$ fragment.[65]

Based on earlier experiments, we aimed to use transmetalation reactions to obtain dinuclear complexes of the X$(PP)_2$Fe–C_n–Fe$(PP)_2$X type. [20] To maintain a reasonable solubility of the targeted complexes, the depe ligand was chosen as the 'equatorial' ligands of the tetragonally distorted iron octahedra. Axial iodo substituents were selected as the anioninc groups of the starting materials. As compared to terminal chloro ligands, the iodides are more reactive with respect to replacement, since they are known to readily dissociate in mononuclear *trans*-Fe$(PP)_2X_2$ complexes.[66] In earlier studies we could show that it is possible to access the dinuclear I$(depe)_2$Fe–C_4–Fe$(depe)_2$I complex in a facile way by transmetalation of Me_3Sn–C_4–SnMe_3 replacing the tin groups with two mononuclear *trans*-Fe$(depe)_2$I units applying stoichiometric amounts of the reagents in THF.[20] The terminal iodo ligands are reactive and allow subsequent substitution with a number of different functional groups, while maintaining the intrinsic redox functionality of the highly delocalised $(depe)_2$Fe–C_4–Fe$(depe)_2$ core.[20,36] Based on these results, we targeted to access dinuclear entities of the type I$(depe)_2$Fe–C_n–Fe$(depe)_2$I by transmetalation of *trans*-Fe$(depe)_2I_2$ with different stannylated sp/sp^2 bridging ligands. The organic reagents 1,4-bis((trimethylstannylethynyl)-benzene, 1,3-bis((trimethylstannyl)ethynyl)benzene, 4,4'-bis((trimethylstannyl)ethynyl)biphenyl, 2,5-bis((trimethyl-stannyl)ethynyl)thiophene and 1,3,5-tris((trimethylstannyl)-ethynyl)benzene were obtained by lithiating the corresponding deprotected alkyne at low temperatures and subsequent reaction with stoichiometric amounts of Me_3SnCl.

All stannylated reagents were purified by two subsequent crystallizations from cold pentane. Transmetalation of the bis-stannylated reagents with two equivalents of *trans*-Fe$(depe)_2I_2$ yielded the dinuclear di-iodo complexes **1** - **4** in good to very good yields (see Scheme 1)

To obtain the trinuclear compound [{FeI$(depe)_2$(C≡C–)$\}_3$(1,3,5-C_6H_3)] the corresponding reaction with 1,3,5-tris((trimethylstannyl)ethynyl)benzene and 3 eq. of *trans*-Fe$(depe)_2I_2$ was carried out. Except for the 2,5-diethynyl-thiophene bridged **4**, which is well soluble in most organic solvents, the compounds show poor solubility. Reacting these di- and triiodo compounds with an excess of NaSCN in refluxing acetonitrile gave the corresponding isothiocyanate complexes **6** - **10** in very good to excellent yields (see Scheme 1). All complexes **1** - **10** were worked up to an analytically pure state without the use of column chromatography (see

Supporting Information). Like in the case of the (depe)$_2$Fe–C$_4$–Fe(depe)$_2$ fragment, the di-isothiocyanate substituted complexes show a higher solubility in organic solvents in comparison to the corresponding diiodo forms.[36,20] For highly symmetric structures with pseudo-octahedral geometries around the chemically and magnetically equivalent Fe(II) centres, a singlet is expected in the ^{31}P{^{1}H}NMR, which was indeed found for all complexes **1** - **10**. In contrast, a previously described "stopper-type" trinuclear iron complex [{Fe(Cp*)(η^2-dppe)(C≡C}$_3$(1,3,5-C$_6$H$_3$)] (dppe = bis(diphenylphosphino)ethane) showed a broad and temperature dependent signal in the ^{31}P{^{1}H}NMR. This behaviour was ascribed to the bulky ligands of the Fe cores, which result in different orientations of the organoiron building blocks with respect to the plane of the bridging ligand, thus rendering the molecule magnetically nonequivalent.[57,60] The signal of the di-iodo complexes in the ^{31}P{^{1}H}NMR appears between 64.8 ppm for **3** and 67.9 ppm for **4**, which is slightly shifted upfield in comparison to the C$_4$ bridged analogue described previously (singlet at 68.3 ppm).[20] The di-isothiocyanate substituted compounds **6** - **10** give rise to a ^{31}P{^{1}H}NMR signal between 73.8 ppm for **6** and 74.6 ppm for **10**, which is in the same range as the corresponding SCN(depe)$_2$Fe–C$_4$–Fe(depe)$_2$NCS, showing a singlet at 74.1 ppm.[36] When monitoring the substitution reactions in acetonitrile to give the compounds **6** - **10** using *in-situ* ^{31}P{^{1}H} NMR measurements, the emergence of a signal was observed in the range of 70 - 72 ppm. Over the course of the reaction, this signal disappeared again, while the one of the targeted product grows in. This observation was interpreted in terms of a synthetic pathway to SCN(depe)$_2$Fe–C$_4$–Fe(depe)$_2$NCS via the intermediacy of a bis(acetonitrile) substituted dicationic complex [MeC≡C–(depe)$_2$Fe–C$_4$–Fe(depe)$_2$–N≡CMe]$^{2+}$ as reaction intermediate. This dicationic complex gives indeed rise to a ^{31}P{^{1}H} NMR signal at 70.9 ppm and could subsequently be isolated in form of the di-iodide salt.[36] In the ^{13}C{^{1}H} NMR a quintet was expected for the C$_\alpha$ nuclei of the bridging ligands due to coupling with the four equatorial P. This quintet is found in the ^{13}C{^{1}H} NMR spectra of all compounds except the trinuclear tri-iodo complex and the 4,4'-diethynyl-biphenyl bridged di-iodo complex **3**, probably due to the low solubility of said complexes in most organic solvents.[57,20]The signals of the C$_\alpha$ nuclei appear

Scheme 1. Reaction pathways to obtain dinuclear compounds of the type I-(depe)$_2$Fe-C$_n$-Fe(depe)$_2$-I (**a** - **d**) as well as a trinuclear {I–Fe(depe)$_2$(C≡C–)}$_3$(1,3,5-C$_6$H$_3$) **5** (**e**) and subsequent substitution of the terminal iodo functions with isothiocyanate (**f** - **j**).

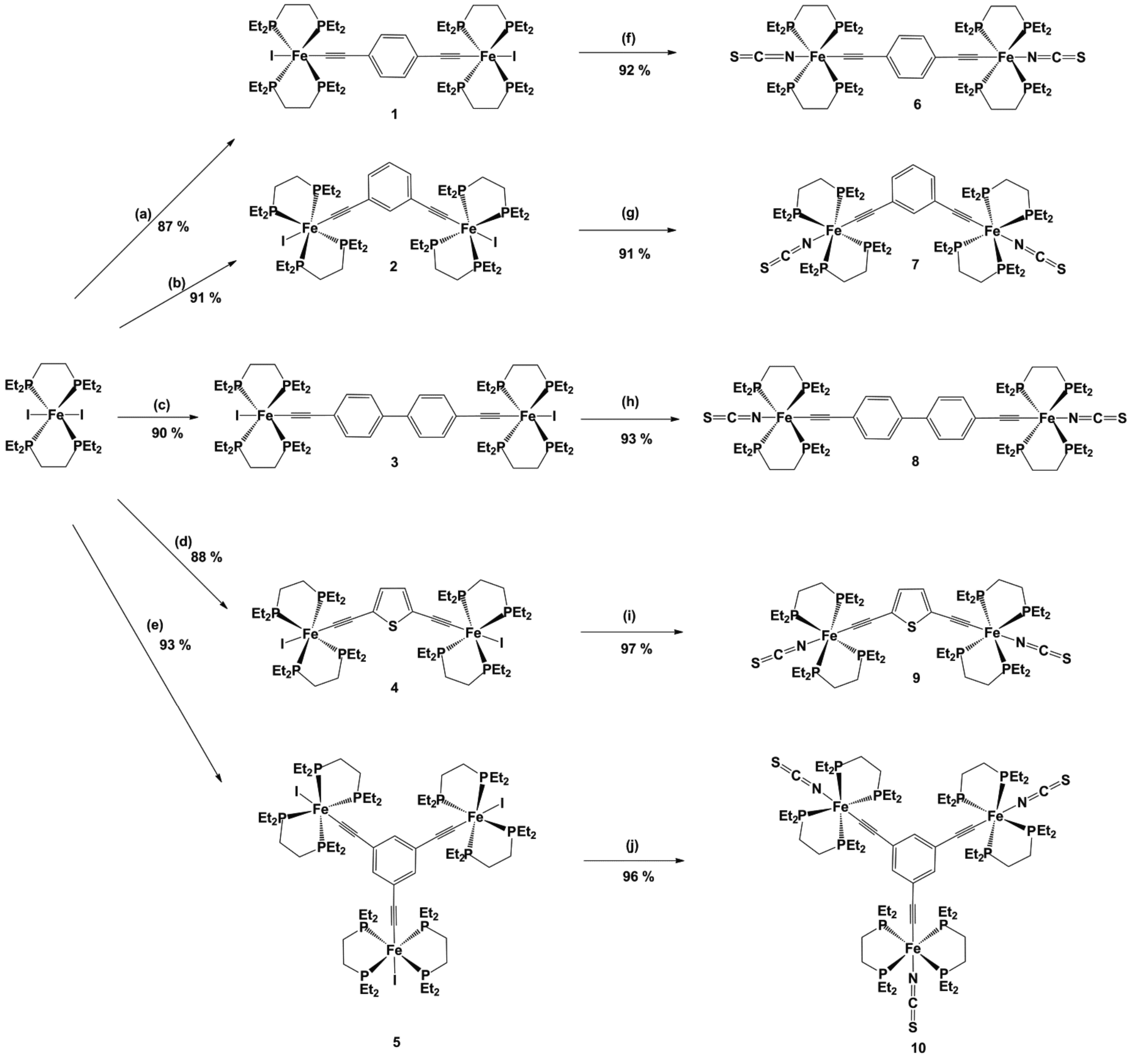

(**a**) 0.5 eq 1,4-bis((trimethylstannyl)ethynyl)benzene, THF, 12 h, reflux; (**b**) 0.5 eq 1,3-bis((trimethylstannyl)ethynyl)benzene, THF, 12 h, reflux; (**c**) 0.5 eq 4,4'-bis((trimethylstannyl)ethynyl)biphenyl, THF, 12 h, reflux; (**d**) 0.5 eq. 2,5-bis((trimethylstannyl)ethynyl)thiophene, toluene, 80 °C, 12 h; (**e**) 0.5 eq 1,3,5-tris((trimethylstannyl)ethynyl)benzene, THF, 12 h, reflux; (**f**) 20 eq. NaSCN, Me_3CN, reflux, 12 h; (**g**) 20 eq. NaSCN, Me_3CN, reflux, 5 h; (**h**) 20 eq. NaSCN, Me_3CN, reflux, 12 h; (**i**) 20 eq. NaSCN, Me_3CN, reflux, 12 h; (**j**) 20 eq. NaSCN, Me_3CN, reflux, 5 h.

Table 1. IR and Raman $\nu(C_4)$ bands of the bridging butadiyne unit of compounds **1** - **10**.

No.	**1**	**2**	**3**	**4**	**5**	**6**	**7**	**8**	**9**	**10**
ν_{as}(C≡C) [cm^{-1}]	2028 (vs)	2036 (vs)	2023 (vs)	2034 (s)	2046 (vs)	2044 (s)	2041 (vs)	2034 (vs)	2031 (s)	2043 (vs)
ν_s(C≡C) [cm^{-1}]	2030 (m)	2040 (s)	2040 (w)	2032 (m)	2049 (s)	2043 (m)	2040 (vs)	2045 (w)	2036 (m)	2053 (vs)
ν(C≡N) [cm^{-1}]	---	---	---	---	---	2092 (ν_{as}, s)	2092 (ν_{as}, s); 2097 (ν_s, m)	2094 (ν_{as}, s)	2094 (ν_{as}, s); 2097 (ν_s, w)	2096 (ν_{as}, vs); 2101 (ν_s, m)

between 122.7 ppm for **1** and 137.6 ppm for **4** marking an explicit downfield shift compared to the different previously described (depe)$_2$Fe–C$_4$–Fe(depe)$_2$ species, which C$_\alpha$ signals were found between 85 and 99 ppm.[20,36] This shift is related to different hybridizations of the bridging ligands and indicates a double bond character at the C$_\alpha$ atoms. All complexes **1** - **10** are highly symmetric. The 1,4-diethynyl-benzene bridged compound **1** and **6,** as well as the 4,4'-diethynyl-biphenyl bridged **3** and **8** are centrosymmetric with an inversion centre located at the centre of the bridging ligand. In an idealized arrangement, **2** and **7**, bridged by 1,3-diethynyl-benzene, as well as the 2,5-diethynyl-thiophene connected compounds **4** and **8**, which have a C$_{2v}$ structure and the trinuclear complexes**5** and **10** a structure of D$_{3h}$ symmetry.

For **1** - **10** the ν_{as}(C≡C) bands of the bridging ligands are a prominent feature in the IR spectra. The asymmetrical stretching band lies between a wavenumber of 2023 cm^{-1} for the 4,4'-diethynyl-biphenyl bridged **3** and of 2046 cm^{-1} for the trinuclear complex **5** (see Table 1).

Notably, the substitution of the terminal halides by the pseudohalide isothiocyanate does not have a pronounced effect of the position of the ν_{as}(C≡C) band. The isothiocyanate. ligand of complexes **6** - **10** gives rise to a sharp and intense band between 2092 cm^{-1} (for complexes **6** and **7**) and at 2096 cm^{-1} for the trinuclear complex **10**In addition, for the non-centrosymmetric compounds **7**, **9** and **10**, the ν_s(C≡N) are located in the Raman spectra at 2097 cm^{-1} for **7** and **9** and at 2101 cm^{-1} for the trinuclear complex **10**.

X-Ray Structure Analyses

Single crystals were grown of compounds **1**, **2**, **4**, **5**, **6**, **8** and **9** and allowed a structural characterization using X-ray diffraction studies. Figure 1 depicts the molecular structures of the diiodo substituted dinuclear complexes **1**, **2** and **4**, whereas the molecular structures of the diisothiocyanate complexes **6**, **8** and **9** are shown in Figure 2.

The low quality crystal structure of {IFe(depe)$_2$(C≡C–)}$_3$(1,3,5-C$_6$H$_3$) **5** is reported in the Supporting Information only (Figure S66) and the corresponding geometric parameters could not be used for further structural discussions. Selected bond lengths, distances and angles are summarized in Table S4.

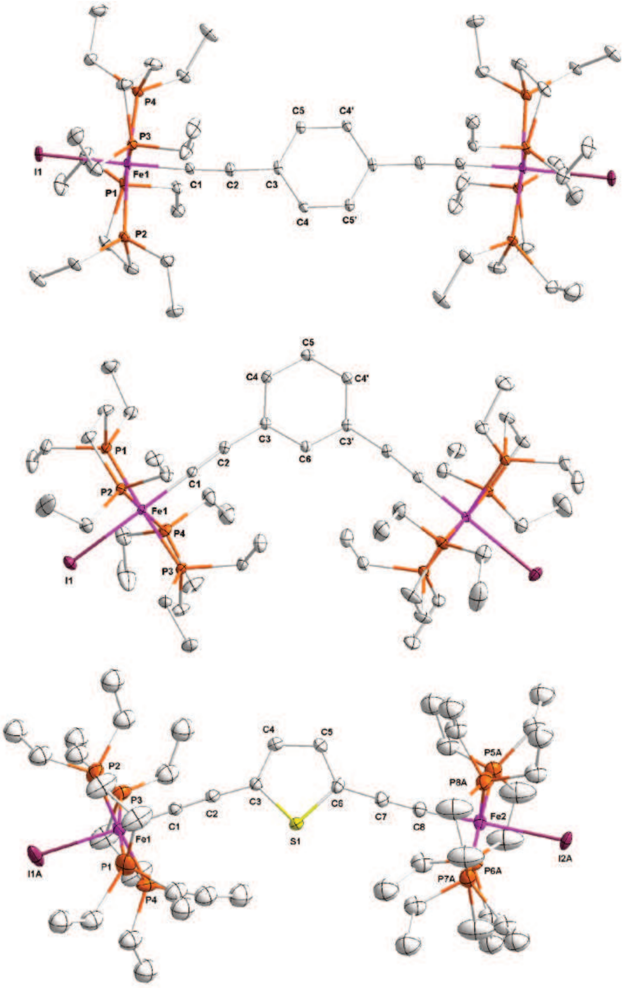

Figure 1. Molecular structures of **1** (*top*), **2** (*middle*) and **4** (*down*). Ellipsoids are set at 30% probability level. Solvent molecules and hydrogen atoms are omitted for clarity. See Table S4 for selected bond lengths, distances and angles.

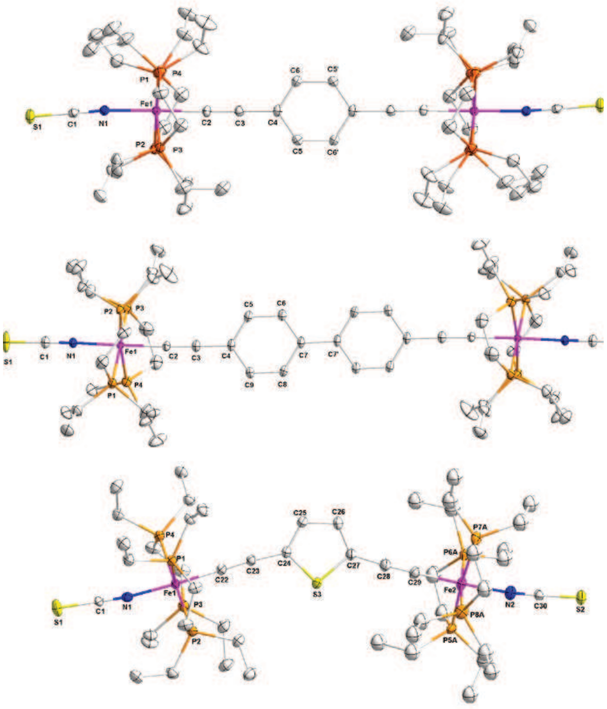

Figure 2. Molecular structures of **6** (*top*), **8** (*middle*) and **9** (*down*). Ellipsoids are set at 30% probability level. Solvent molecules and hydrogen atoms are omitted for clarity. See Table S4 for selected bond lengths, distances and angles.

For all molecules, the ligand geometry around the iron cores is pseudo-octahedral, with the four P atoms of the depe ligands occupying equatorial positions, whereas the respective terminal iodo or isothiocyanate groups are lying on an axial position *trans* to the bridging ligand. The introduction of the arene ligand causes a contraction of the coordinative Fe-P bonds from an average value of 2.309 Å in the mononuclear precursor[66] to values between 2.251 Å for **9** and 2.262 Å for **6**, consistent with a higher degree of σ-donation from the depe ligands to the metal centers. For all complexes discussed here, the bonds between the Fe and the C_α of the bridging ligand are lying between the values of 1.868(4)Å for **4** and 1.899(4) Å for **6**. The C_α-C_β bonds are between 1.210(6) Å for **4** and 1.222(9) Å for **9**, whereas the C_β-C_β' bonds have values between 1.408(6) Å for **4** and 1.441(5) Å for **6**.

These data are consistent with an acetylenic structure for the Fe–C≡C–R moieties (R = arene core). For the 1,4-diethynyl-benzene, the 4,4'-diethynyl-biphenyl and the 2,5-diethynyl-thiophene bridging ligands, cumulenic resonance structures can be drawn out. Yet, unlike in the case of the structurally related $(depe)_2Fe–C_4–Fe(depe)_2$ dinuclear compounds,[20,36] the structural data of the arene bridged molecules discussed here do not indicate a notable influence of this canonical structure. The Fe-I bond lengths lie between 2.6907(4) Å for **1** and 2.7146(9) Å for **4**, thus remaining practically unchanged compared to *trans*-$Fe(depe)_2I_2$ and the C_4 bridged dinuclear diiodo complex.[20,66]

Likewise, the bond lengths of the isothiocyanate endgroups of **6**, **8** and **9** (see Table S4) are consistent with Fe–N=C=S isothiocyanato structures and compare well with the data of the previously described C_4 bridged compound $SCN(depe)_2Fe–C_4–Fe(depe)_2NCS$.[36]

Due to the lone pairs on the N nuclei of the isothiocyanate groups, a Fe-N-C angle < 180° was expected. Yet, this angle is close to 180° for all complexes ((C1-N1-Fe1) 173.5(3)° for **6** and 176.56(15)° for **8**, see Table S4), and consequently the endgroup-arene-endgroup angle is determined purely by the geometry of the arene bridge.

The comparably short N-C bond (between 1.119(8) Å and 1.121(9) Å for **9**, see Table S4) suggests a considerable influence of the $M–N^+≡C–S^-$ canonical structure.[67] The molecular backbone of all described compounds is composed of carbyl or methyne units, which leads to the expectation of rigid structures, where the endgroup-arene-endgroup angle is determined purely by the substitution pattern of the arene bridging ligand. The bond angles of the X–Fe–C≡C–C fragments only deviate slightly from 180° (see Table S4), thereby confirming the expected structural rigidity. It can be reasoned that the observed minor deviations from linearity stem from secondary type intermolecular interactions and packaging effects within the crystal structures.[68,69,70]

Cyclic Voltammetry.

Cyclic voltammetry experiments were carried out to probe the electrochemical behaviour of the reported complexes in bulk in solution.

Based on studies carried out on stopper-type complexes $(Cp^*)(PP)Fe–C_n–Fe(PP)(Cp^*)$[54,52,53,55,56,57,58] it was hypothesized to find a significantly lower charge delocalization in compounds **1** - **10** compared to the previously reported molecules containing the $(depe)_2Fe–C_4–Fe(depe)_2$ fragment.[20, 36] These expectations were confirmed by the cyclic voltammetry experiments. The 1,4-diethynyl-benzene bridged compounds **1** and **6** (Figure 3), as well as the 2,5-diethynyl-thiophene bridged complexes **4** and **9** (Figure 5) exhibit two fully reversible oxidation waves.

The existence of two metal-based oxidations for symmetric molecules is a strong indicator for high charge delocalization over the length of the rigid-rod molecule,[71] and that the bridging ligand is actively supporting charge transport between the redox-active metal centres.[72] The comparably low

K_c values (see Table 2) indicate that thermodynamic stability of the mixed valence species is higher for the previously described C_4 bridged compounds.[20,36]

The electrochemical data of the related SCN(depe)$_2$Fe–C_4–Fe(depe)$_2$NCS complex **C**[36] are given in Table 2 for comparison. The 1,3-diethynyl-benzene and 4,4'-diethynyl-biphenyl bridged dinuclear complexes, as well as the trinuclear complexes, showed one reversible oxidation wave indicative of a localized charge.

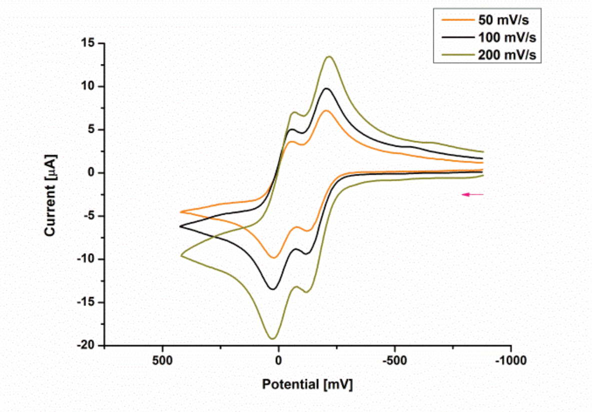

Figure 3. Cyclic voltammogram for **6** in THF/Bu_4NPF_6 (0.1M) at 300 K; Au working electrode, a Pt counter electrode, and an Ag reference electrode; chart speed: 50, 100, 200 mV/s; E vs. $Fc^{0/+}$ (external).

Consequently, the oxidation waves of the 1,3-diethynyl-benzene and 4,4'-diethynyl-biphenyl bridged systems correspond to 2e^- processes, and similary the one of the trinuclear complexes to 3e^- processes. The first oxidation wave of the 2,5-diethynyl-thiophene bridged complexes **4** and **9** appeared at a more negative potential compared to the C_4 bridged complex **C** (see Table 2). This finding suggested that the 2,5-diethynyl-thiophene bridge is less-electron withdrawing and consequently indicated that the HOMO should bear larger character of the bridging ligand.[54]

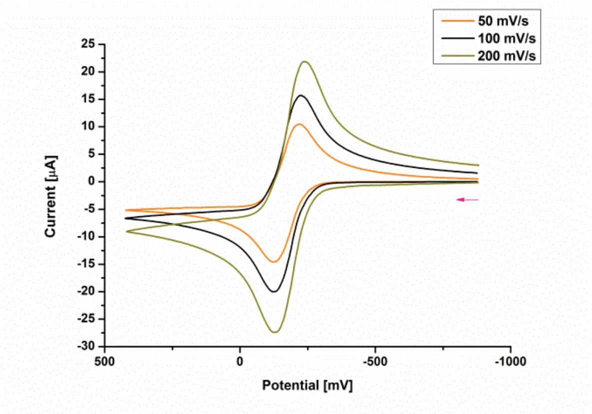

Figure 4. Cyclic voltammogram for **7** in THF/Bu_4NPF_6 (0.1M) at 300 K; Au working electrode, a Pt counter electrode, and an Ag reference electrode; chart speed: 50, 100, 200 mV/s; E vs. $Fc^{0/+}$ (external).

Table 2. Cyclic voltammetry data of the complexes **1** - **10**.

Compd	$E_{1/2}$ (0/+1) [mV]	$E_{1/2}$ (+1/+2) [mV]	ΔE [mV]	K_c
1	-385	-231	154	4.2 x 10^{2}
2	-312	--	--	--
3	-393	--	--	--
4	-472	-192	280	6.0 x 10^{4}
5	-221	--	--	--
6	-160	-18	142	2.7 x 10^{2}
7	-174	--	--	---
8	-252	--	--	--
9	-406	-131	275	5.0 x 10^{4}
10	-112	--	--	--
C[a]	-372	106	478	14.5 x 10^{7}

Measurements at 300 K in THF/Bu_4NPF_6 (0.1M) with an Au working electrode, a Pt counter electrode, and an Ag reference electrode. E vs $Fc^{0/+}$ (external). [a] see reference[36]

On a similar line, the occurrence of the single oxidation wave of the 1,3-diethynyl-benzene, 4,4'-diethynyl-biphenyl and the 1,3,5-triethynyl-benzene bridged compounds at more positive potentials (between -112 mV for **10** and -393 mV for **3**,) implies a less accentuated bridging ligand character in the respective HOMO. It has to be noted that for all five different types of bridges discussed, the oxidation waves shift to a less negative potential when the terminal iodo ligands are substituted with the isothiocyanate functional groups indicating the more electron withdrawing character of the pseudohalogenide.

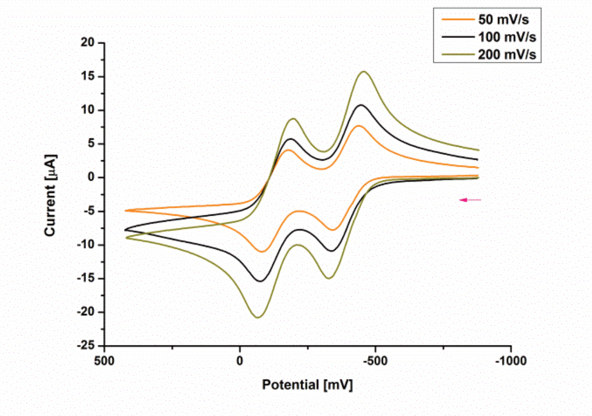

Figure 5. Cyclic voltammogram for **9** in THF/Bu_4NPF_6 (0.1M) at 300 K; Au working electrode, a Pt counter electrode, and an Ag reference electrode; chart speed: 50, 100, 200 mV/s; E vs. $Fc^{0/+}$ (external).

DFT Calculations

The molecular geometries of the model complexes **6**-*Me*, **7**-*Me*, **8**-*Me*, **9**-*Me* and the C_4 bridged **C**-*Me*, for which the ethyl groups of the depe ligands were replaced by methyl groups, were optimized at the PBE1PBE/LANL2DZ level.

The identified Fe⋯Fe' distances and S⋯S' distances of the isothiocyanato groups are reported in Table 3. The distances of the trinuclear compound **10**-*Me* are congeneric to the *meta* substituted dinuclear complex **7**-*Me.* In all cases, the computed non-bonding distances of the endgroups are slightly elongated compared to the structural data derived from the X-ray studies, which was attributed to intermolecular interactions and packaging effects within the crystal structures.[68,69,70] The deviation is highest for the C_4 bridged congeneric pair **C** and **C**-*Me*, where the computed S⋯S' distance of 17.34 Å is longer by about 2.5% compared to the distance of 16.940(3) Å found in the X-ray experiment[36] showing that the calculated and experimentally determined data compare very well.

The data show that the lengths of the molecular junctions of the 1,4-(–C≡–C_6H_4–C≡C–) bridged complex **6** and the 2,5-(–C≡C–thiophene–C≡C–) bridged **9** are in a comparable range. Also the 1,3-(–C≡C–C_6H_4–C≡C–) substituted **7**, the trinuclear complex **10** and the previously investigated C_4 bridged complex **C** are of a similar lengthAs the direct distance-dependent through space tunneling is an intrinsic part of molecular conductivity measurements of a given molecular junction, the different junction lengths would have to be taken into account when comparing the molecular conductance.[73]

For **6**-*Me*, **7**-*Me*, **8**-*Me*, **9**-*Me* and the C_4 bridged **C**-*Me*, the HOMO and LUMO energies are reported in Table 4 (see also Figure 6). The absolute energies of the HOMO lie between -5.03 eV for **7**-*Me* and -4.58 eV for **9**-*Me*. The absolute energies of the LUMO rise from -1.18 eV for **8**-*Me* to -0.57 eV for the C_4 bridged **C**-*Me*.

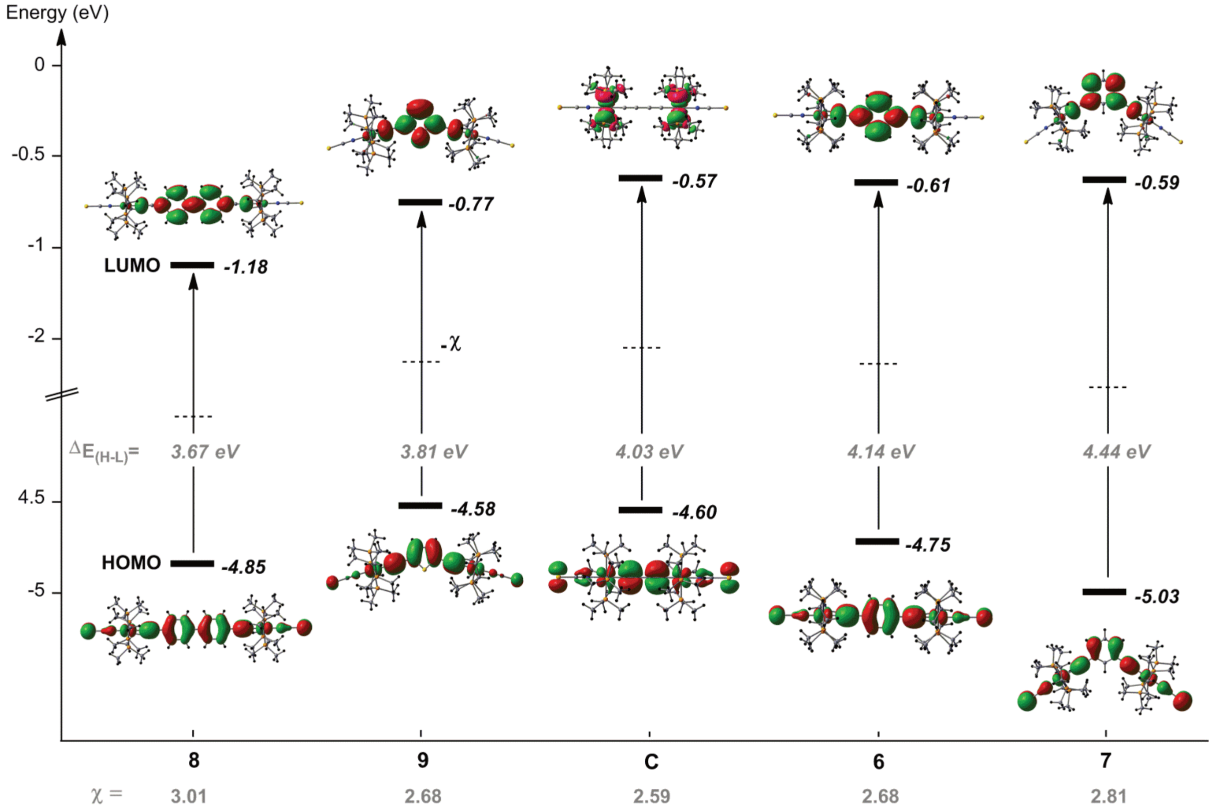

Figure 6. Energies of the frontier orbitals (HOMO and LUMO) of the model complexes **6**-*Me*, **7**-*Me*, **8**-*Me*, **9**-*Me* and of the C_4 bridged **C**-*Me* for comparison, computed at the PBE1PBE/LANL2DZ//PBE1PBE/6-311+g(d) level and arranged in increasing order of the HOMO/LUMO gap $\Delta E_{(H-L)}$. Spatial plots of the corresponding orbitals and their absolute electronegativity values χ (defined as (I+A)/2 with I = ionization potential, A = electron affinity)[6] are represented as a dashed lines halfway between the HOMO and LUMO.

Table 3. Selected distances (Å) computed at the PBE1PBE/LANL2DZ level and derived from X-ray studies

	Distances computed at the PBE1PBE/LANL2DZ level.			**Distances derived from X-ray diffraction studies**	
	Fe···Fe' (Å)	**S···S' (Å)**		**Fe···Fe' (Å)**	**S···S' (Å)**
6-*Me*	12.05	21.68	**6**	11.934(1)	21.426(2)
7-*Me*	10.23	18.16	**7**	--	--
8-*Me*	16.42	26.05	**8**	16.2610(4)	25.685(1)
9-*Me*	11.38	20.60	**9**	11.252(3)	20.609(3)
10-*Me*[b]	10.23	18.16	**10**	--	--
C-*Me*	7.71	17.34	**C**[a]	7.619(1)	16.940(3)

[a]see reference[36]; [b] data derived from the calculation of **7**-*Me*

To achieve a resonant transport in potential experiments of the measurement of molecular conductivity, which would be an important goal for this series of complexes, the molecular orbitals of the probed molecules should be aligned approximately to the Fermi level of the macroscopic electronic leads. The Fermi energy of Au electrodes is $E_F \approx -(4.8\text{-}5.4)$ eV and is consequently more in the energetic range of the HOMO's for all complexes discussed here. As expected for 18-electron metal complexes, the HOMO/LUMO gap $\Delta E_{(H-L)}$ is relatively large and lies between 3.67 eV for **8**-*Me* and 4.44 eV for **7**-*Me*.

Except for complex **8**-*Me*, for which an energetically very low-lying LUMO (E_L = -1.18 eV and $\Delta E_{(H-L)}$ = 3.67 eV)) was calculated, $\Delta E_{(H-L)}$ seems to be more dependent on theenergetic position of the HOMO, i.e. $\Delta E_{(H-L)}$ is smallest for **9**-*Me* (E_H = -4.58 eV and $\Delta E_{(H-L)}$ = 3.81 eV)) and highest for **7**-*Me* (E_H = 5.03 eV and $\Delta E_{(H-L)}$ = 4.44 eV).

Table 4. HOMO and LUMO energies (eV), HOMO/LUMO gap (eV) and absolute

electronegativity χ computed at the PBE1PBE/LANL2DZ//PBE1PBE/6-311+g(d) level.

	LUMO (eV)	HOMO (eV)	$\Delta E_{(H\text{-}L)}$ (eV)	χ (eV)
6-*Me*	-0.61	-4.75	4.14	2.68
7-*Me*	-0.59	-5.03	4.44	2.81
8-*Me*	-1.18	-4.85	3.67	3.01
9-*Me*	-0.77	-4.58	3.81	2.68
C-*Me*	-0.57	-4.60	4.03	2.59

χ is defined as (I+A)/2 where I is the ionization potential and A is the electron affinity, and here directly obtained from the HOMO and LUMO energies.

These results show that the energetic positions of the molecular orbitals and the extent of the HOMO/LUMO and the absolute chemical hardness gap to the position of E_F of Au can be tuned by varying the bridging ligand of a $X\{M\}C_n\{M\}X$, even if the metal centre, equatorial ligands and terminal ligands are kept constant.

For the discussed molecules, the chemical hardness[6] is consequently increasing in the order **8**-*Me* < **9**-*Me* < **C**-*Me* < **6**-*Me* < **7**-*Me*. Based on these findings, the coupling between the molecule and the gold electrode in measurements of the molecular conductivity can be expected to increase in the order **7**-*Me* < **6**-*Me* < **C**-*Me* < **9**-*Me* < **8**-*Me*.

Conclusion and Outlook

The transmetalation at stannylated carbyl/methyne bridging units with different structures with the mononuclear *trans*-Fe(depe)$_2$I fragment poses a new and facile synthetic pathway to access organometallic components suitable for molecular electronics. The dinuclear complexes I-(depe)$_2$Fe- C_n-Fe(depe)$_2$-I with C_n = 1,4-(–C≡C–C_6H_4–C≡C–) **1**, 1,3-(–C≡C–C_6H_4–C≡C–) **2**, 4,4'-(–C≡C–C_6H_4–C_6H_4–C≡C–) **3**, 2,5-(–C≡C–thiophene–C≡C–) **4**, as well as a trinuclear complex {I–Fe(depe)$_2$(C≡C–)}$_3$(1,3,5-C_6H_3) **5** were obtained in high yields. The terminal iodo ligands were substituted with the potentially electrode-binding isothiocyanate groups to give the corresponding di- and trinuclear complexes **6** - **10** in very good yields. X-ray diffraction studies of compounds **1**, **2**, **4**, **5**, **6**, **8** and **9** showed that the prepared compounds have the structural rigidity expected for carbyl/methyne composed systems and that the endgroup-arene-endgroup angles are determined by the geometry of the bridging arene.

The C_2 units of the bridging ligands are best described to exist in an acetylenic form. Cyclic voltammetry measurements confirmed that compared to the C_4 bridge used in our earlier studies, the charge delocalization is lower for the utilized cabyl/methyne constructed bridging units here. The 1,4-(–C≡C–C_6H_4–C≡C–) bridged compounds **1** and **6**, as well as the 2,5-(–C≡C–thiophene–C≡C–) bridged complexes **4** and **9** exhibit two oxidation waves under the given conditions. The derived K_c values (see Table 2) indicate that the thermodynamic stabilites of the mixed valence species is weak compared to the previously described C_4 bridged compounds. The 1,3-(–C≡C–C_6H_4–C≡C–) and 4,4'-(–C≡C–C_6H_4–C_6H_4–C≡C–) bridged dinuclear complexes, as well as the trinuclear complexes only show one reversible oxidation wave corresponding to $2e^-$ and $3e^-$ processes, respectively.

DFT calculations were carried out on model complexes **6**-*Me*, **7**-*Me*, **8**-*Me*, **9**-*Me*, as well as the C_4 bridged congener **C**-*Me* to investigate the energetic changes in the frontier orbitals with respect to the application of these complexes in molecular conductivity measurements. For all complexes the calculated energies of the HOMO's (between -5.03 eV for **7**-*Me* and -4.58 eV for **9**-*Me*) are in a close proximity of the Fermi energy of Au electrodes ($E_F \approx -(4.8\text{-}5.4)$ eV). The energetic positions of the molecular orbitals and the extent of the HOMO-LUMO gap can be tuned by varying the bridging ligand. Based on the findings, the coupling between the molecule and the soft gold electrode can be expected to increase in the order **7**-*Me* < **6**-*Me* < **C**-*Me* < **9**-*Me* < **8**-*Me*. To investigate the conductance profiles and the electronic behavior of complexes **6** - **10** on a single molecule level could further support the understanding of the electronic processes taking place at the molecular level. Ultimately this would contribute to the design and realization of molecular building blocks with tailored structural and electronic properties to fabricate functional devices on the molecular level.

ASSOCIATED CONTENT

Supporting Information. Experimental details describing the syntheses, the results of the elemental analyses, one- and two-dimensional NMR experiments (Figures S1 - S55), IR and Raman (Figures S56 - S65, Table S1), cyclic voltammetry experiments at different chart speeds (Figures S67 - S73) as well as) as well as summaries of the X-ray diffraction studies (Tables S2 – S4 and Figures S66) and a text file of all computed molecule Cartesian coordinates in a format for convenient visualization. This material is available free of charge via the Internet at http://pubs.acs.org.

AUTHOR INFORMATION

Corresponding Author

hberke@aci.uzh.ch

Notes

The authors declare no competing financial interests.

ACKNOWLEDGMENT

Funding from the National Research Program "Smart Materials" (NRP 62, grant 406240-126142) of the Swiss National Science Foundation (SNSF) and the University of Zürich is gratefully acknowledged.

REFERENCES

(1) Metzger, R. M. *J. Mater. Chem.* **2008,** *18* (37), 4364–4396.
(2) Carroll, R. L.; Gorman, C. B. *Angew. Chem. Int. Ed.* **2002** (41), 4378–4400.
(3) Cuniberti, G.; Fagas, G.; Richter, K. *Introducing molecular electronics;* Springer: Berlin, New York, **op. 2005**.
(4) Tuccitto, N.; Ferri, V.; Cavazzini, M.; Quici, S.; Zhavnerko, G.; Licciardello, A.; Rampi, M. A. *Nat Mater.* **2008,** *8* (1), 41–46.
(5) Wen, H.-M.; Yang, Y.; Zhou, X.-S.; Liu, J.-Y.; Zhang, D.-B.; Chen, Z.-B.; Wang, J.-Y.; Chen, Z.-N.; Tian, Z.-Q. *Chem. Sci.* **2013,** *4* (6), 2471.
(6) Pearson, R. G. *Chemical hardness;* Wiley-VCH: Weinheim, Germany, New York, **1997**.
(7) Zhao, X.; Huang, C.; Gulcur, M.; Batsanov, A. S.; Baghernejad, M.; Hong, W.; Bryce, M. R.; Wandlowski, T. *Chem. Mater.* **2013,** *25* (21), 4340–4347.
(8) Prins, F.; Monrabal-Capilla, M.; Osorio, E. A.; Coronado, E.; van der Zant, Herre S. J. *Adv. Mater.* **2011,** *23* (13), 1545–1549.
(9) Low, P. J. *Dalton Trans.* **2005** (17), 2821.
(10) Wuttke, E.; Pevny, F.; Hervault, Y.-M.; Norel, L.; Drescher, M.; Winter, R. F.; Rigaut, S. *Inorg. Chem.* **2012,** *51* (3), 1902–1915.
(11) Wuttke, E.; Hervault, Y.-M.; Polit, W.; Linseis, M.; Erler, P.; Rigaut, S.; Winter, R. F. *Organometallics.* **2014**.
(12) O'Hanlon, D. C.; Cohen, B. W.; Moravec, D. B.; Dallinger, R. F.; Hopkins, M. D. *J. Am. Chem. Soc.* **2014**.
(13) Aguirre-Etcheverry, P.; O'Hare, D. *Chem. Rev.* **2010,** *110* (8), 4839–4864.
(14) Costuas, K.; Rigaut, S. *Dalton Trans.* **2011,** *40* (21), 5643.
(15) Low, P. J. *Coord. Chem. Rev.* **2013,** *257* (9-10), 1507–1532.
(16) Szafert, S.; Paul, F.; Meyer, W. E.; Gladysz, J. A.; Lapinte, C. *C. R. Chimie.* **2008,** *11* (6-7), 693–701.
(17) Bruce, M. I.; Costuas, K.; Davin, T.; Ellis, B. G.; Halet, J.-F.; Lapinte, C.; Low, P. J.; Smith, M. E.; Skelton, B. W.; Toupet, L.; White, A. H. *Organometallics.* **2005,** *24* (16), 3864–3881.
(18) Montigny, F. de; Argouarch, G.; Costuas, K.; Halet, J.-F.; Roisnel, T.; Toupet, L.; Lapinte, C. *Organometallics.* **2005,** *24* (19), 4558–4572.
(19) Haines, D. E.; O'Hanlon, D. C.; Manna, J.; Jones, M. K.; Shaner, S. E.; Sun, J.; Hopkins, M. D. *Inorg. Chem.* **2013,** 52 (16), 9650–9658.
(20) Lissel, F.; Fox, T.; Blacque, O.; Polit, W.; Winter, R. F.; Venkatesan, K.; Berke, H. *J. Am. Chem. Soc.* **2013,** *135* (10), 4051–4060.
(21) Low, P. J.; Bock, S. *Electrochim. Acta.* **2013**.
(22) Pevny, F.; Di Piazza, E.; Norel, L.; Drescher, M.; Winter, R. F.; Rigaut, S. *Organometallics.* **2010,** *29* (22), 5912–5918.
(23) Wuttke, E.; Pevny, F.; Hervault, Y.-M.; Norel, L.; Drescher, M.; Winter, R. F.; Rigaut, S. *Inorg. Chem.* **2012,** *51* (3), 1902–1915.
(24) Ward, M. D. *Chem. Soc. Rev.* **1995,** *24* (2), 121.
(25) Frohnapfel, D. S.; Woodworth, B. E.; Thorp, H. H.; Templeton, J. L. *J. Phys. Chem. A.* **1998,** *102* (28), 5665–5669.
(26) Ghazala, S. I.; Paul, F.; Toupet, L.; Roisnel, T.; Hapiot, P.; Lapinte, C. *J. Am. Chem. Soc.* **2006,** *128* (7), 2463–2476.
(27) Lu, Y.; Quardokus, R.; Lent, C. S.; Justaud, F.; Lapinte, C.; Kandel, S. A. *J. Am. Chem. Soc.* **2010,** *132* (38), 13519–13524.
(28) Quardokus, R. C.; Lu, Y.; Wasio, N. A.; Lent, C. S.; Justaud, F.; Lapinte, C.; Kandel, S. A. *J. Am. Chem. Soc.* **2012,** *134* (3), 1710–1714.
(29) Marques-Gonzalez, S.; Yufit, D. S.; Howard, Judith A. K.; Martin, S.; Osorio, H. M.; Garcia-Suarez, V. M.; Nichols, R. J.; Higgins, S. J.; Cea, P.; Low, P. J. *Dalton Trans.* **2013,** *42* (2), 338–341.
(30) Major, M.; Hänisch, C. von; Weber, H. B.; Reichert, J.; Beckmann, D. *Angew. Chem. Int. Ed.* **2002,** *41* (7), 1183–1186.
(31) Wen, H.-M.; Yang, Y.; Zhou, X.-S.; Liu, J.-Y.; Zhang, D.-B.; Chen, Z.-B.; Wang, J.-Y.; Chen, Z.-N.; Tian, Z.-Q. *Chem. Sci.* **2013,** *4* (6), 2471.
(32) Benameur, A.; Brignou, P.; Di Piazza, E.; Hervault, Y.-M.; Norel, L.; Rigaut, S. *New J. Chem.* **2011,** *35* (10), 2105.
(33) Luo, L.; Benameur, A.; Brignou, P.; Choi, S. H.; Rigaut, S.; Frisbie, C. D. *J. Phys. Chem. C.* **2011,** *115* (40), 19955–19961.
(34) Kim, B.-S.; Beebe, J.; Olivier, C.; Rigaut, S.; Touchard, D.; Kushmerick, J.; Zhu, X.-Y.; Frisbie, C. *J. Phys. Chem. C.* **2007,** *111* (20), 7521–7526.
(35) Schwarz, F.; Kastlunger, G.; Lissel, F.; Riel, H.; Venkatesan, K.; Berke, H.; Stadler, R.; Lörtscher, E. *submitted.* **2014**.
(36) Lissel, F.; Schwarz, F.; Blacque, O.; Riel, H.; Lörtscher, E.; Venkatesan, K.; Berke, H. *to be submitted.* **2014**.
(37) Nath, S.; Ghosh, S.; Kundu, S.; Praharaj, S.; Panigrahi, S.; Pal, T. *J Nanopart Res.* **2006,** *8* (1), 111-116.
(38) Agilent Technologies (formerly Oxford Diffraction): Yarnton (England), **2011**.
(39) Clark, R. C.; Reid, J. S. *Acta Crystallogr A Found Crystallogr.* **1995,** *51* (6), 887–897.
(40) Farrugia, L. J. *J Appl Crystallogr.* **1999,** *32* (4), 837–838.
(41) Dolomanov, O. V.; Bourhis, L. J.; Gildea, R. J.; Howard, Judith A. K.; Puschmann, H. *J Appl Crystallogr.* **2009,** *42* (2), 339–341.
(42) Sheldrick, G. M. *Acta Crystallogr A Found Crystallogr.* **2008,** *64* (1), 112–122.
(43) Spek, A. L. *J Appl Crystallogr.* **2003,** *36* (1), 7–13.
(44) Frisch, M. J.; Trucks, G. W.; Schlegel, H. B.; Scuseria, G. E.; Rob, M. A.; Cheeseman, J. R.; Montgomery Jr, J. A.; Vreven, T.; Kudin, K. N.; Burant, J. C.; Millam, J. M.; Iyengar, S. S.; Tomasi, J.; Barone, V.; Mennucci, B.; Cossi, M.; Scalmani, G.; Rega, N.; Petersson, G. A.; Nakatsuji, H.; Hada, M.; Ehara, M.; Toyota, K.; Fukuda, R.; Hasegawa, J.; Ishida, M.; Nakajima, T.; Honda, Y.; Kitao, O.; Nakai, H.; Klene, M.; Li, X.; Knox, J. E.; Hratchian, H. P.; Cross, J. B.; Bakken, V.; Adamo, C.;

Jaramillo, J.; Gomperts, R.; Stratmann, R. E.; Yazyev, O.; Austin, A. J.; Cammi, R.; Pomelli, C.; Ochterski, J. W.; Ayala, P. Y.; Morokuma, K.; Voth, G. A.; Salvador, P.; Dannenberg, J. J.; Zakrzewski, V. G.; Dapprich, S.; Daniels, A. D.; Strain, M. C.; Farkas, O.; Malick, D. K.; Rabuck, A. D.; Raghavachari, K.; Foresman, J. B.; Ortiz, J. V.; Cui, Q.; Baboul, A. G.; Clifford, S.; Cioslowski, J.; Stefanov, B. B.; Liu, G.; Liashenko, A.; Piskorz, P.; Komaromi, I.; Martin, R. L.; Fox, D. J.; Keith, T.; Al-Laham, M. A.; Peng, C. Y.; Nanayakkara, A.; Challacombe, M.; Gill, P. M. W.; Johnson, B.; Chen, W.; Wong, M. W.; Gonzalez, C.; Pople, J. A. *Gaussian 03: revision D.01;* Gaussian Inc.: Wallingford, CT, **2003**.

(45) Adamo, C.; Barone, V. *Chemical Physics Letters*. **1999,** *314* (1-2), 152–157.

(46) Hay, P. J.; Wadt, W. R. *J. Chem. Phys.* **1985,** *82* (1), 270.

(47) Wadt, W. R.; Hay, P. J. *J. Chem. Phys.* **1985,** *82* (1), 284.

(48) Hay, P. J.; Wadt, W. R. *J. Chem. Phys.* **1985,** *82* (1), 299.

(49) Krishnan, R.; Binkley, J. S.; Seeger, R.; Pople, J. A. *J. Chem. Phys.* **1980** (72), 650.

(50) McLean, A. D.; Chandler, G. S. *J. Chem. Phys.* **1980** (72), 5639.

(51) Wachters, A. J. H. *J. Chem. Phys.* **1970** (52), 1033.

(52) Le Narvor, N.; Toupet, L.; Lapinte, C. *J. Am. Chem. Soc.* **1995,** *117* (27), 7129–7138.

(53) Coat, F.; Lapinte, C. *Organometallics*. **1996** (15), 477–479.

(54) Montigny, F. de; Argouarch, G.; Costuas, K.; Halet, J.-F.; Roisnel, T.; Toupet, L.; Lapinte, C. *Organometallics*. **2005,** *24* (19), 4558–4572.

(55) Le Stang, S.; Paul, F.; Lapinte, C. *Organometallics*. **2000,** *19* (6), 1035–1043.

(56) Le Narvor, N.; Lapinte, C. *Organometallics*. **1995** (14), 634–639.

(57) Weyland, T.; Lapinte, C.; Frapper, G.; Calhorda, M. J.; Halet, J.-F.; Toupet, L. *Organometallics*. **1997,** 2024–2031.

(58) Weyland, T.; Costuas, K.; Mari, A.; Halet, J.-F.; Lapinte, C. *Organometallics*. **1998,** *17* (25), 5569–5579.

(59) Colbert, Michael C. B.; Lewis, J.; Long, N. J.; Raithby, P. R.; Younus, M.; White, Andrew J. P.; Williams, D. J.; Payne, N. N.; Yellowlees, L.; Beljonne, D.; Chawdhury, N.; Friend, R. H. *Organometallics*. **1998,** *17* (14), 3034–3043.

(60) Hoffert, W. A.; Rappé, A. K.; Shores, M. P. *J. Am. Chem. Soc.* **2011,** *133* (51), 20823–20836.

(61) Hoffert, W. A.; Rappé, A. K.; Shores, M. P. *Chem. Commun.* **2010,** *46* (26), 4710.

(62) Allen, O. R.; Dalgarno, S. J.; Field, L. D.; Jensen, P.; Turnbull, A. J.; Willis, A. C. *Organometallics*. **2008,** *27* (9), 2092–2098.

(63) Field, L. D.; Li, H. L.; Dalgarno, S. J.; Turner, P. *Chem. Commun.* **2008** (14), 1680.

(64) Baker, M. V.; Field, L. D.; Hambley, T. W. *Inorg. Chem.* **1988,** *27* (16), 2872–2876.

(65) Baker, M. V.; Field, L. D.; Hambley, T. W. *Inorg. Chem.* **1988,** *27* (16), 2872–2876.

(66) Barclay, J. E.; Hills, A.; Hughes, D. L.; Leigh, G. J. *J. Chem. Soc., Dalton Trans.* **1988** (11), 2871.

(67) Forster, D.; Goodgame, D. M. L. *J. Chem. Soc.* **1965** (0), 268–274.

(68) Dembinski, R.; Lis, T.; Szafert, S.; Mayne, C. L.; Bartik, T.; Gladysz, J. *Journal of organometallic chemistry*. **1999,** *578* (1-2), 229–246.

(69) Zhuravlev, F.; Gladysz, J. A. *Chem. Eur. J.* **2004,** *10* (24), 6510–6522.

(70) Szafert, S.; Gladysz, J. A. *Chem. Rev.* **2003,** *103* (11), 4175–4206.

(71) Costuas, K.; Rigaut, S. *Dalton Trans.* **2011,** *40* (21), 5643.

(72) Aguirre-Etcheverry, P.; O'Hare, D. *Chem. Rev.* **2010,** *110* (8), 4839–4864.

(73) Gotsmann, B.; Riel, H.; Lörtscher, E. *Phys. Rev. B.* **2011,** *84* (20).

2.1 SUPPLEMENTARY INFORMATION

Manuscript in Revision (**Organometallics**, *accepted after major revisions*): F. Lissel, O. Blacque, K. Venkatesan, H. Berke: *Structural and Electronic Variations of Carbyl/Methyne-Based Bridges in Di- and Trinuclear Redox-Active Iron Complexes Bearing Fe(diphosphine)$_2$X (X = I, NCS) Moieties*

General Procedures

Reagent grade toluene, pentane, diethylether and tetrahydrofuran were dried and distilled from sodium prior to use. Reagent grade benzene and dichloromethane were dried and distilled from CaH_2, acetonitrile from P_2O_5. Deuterated solvents were dried and distilled likewise.

The stannylated linkers 1,4-bis((trimethylstannylethynyl)-benzene, 1,3-bis((trimethylstannyl)ethynyl)benzene, 4,4'-bis((trimethylstannyl)ethynyl)biphenyl, 2,5-bis((trimethyl-stannyl)ethynyl)thiophene and 1,3,5-tris((trimethylstannyl)-ethynyl)benzene were obtained by lithiating the corresponding deprotected alkyne at low temperatures and then reacting them with stochiometric amounts of Me_3SnCl. The stannylated reagents were purified by two subsequent crystallizations from cold pentane. Commercially available NaSCN was recrystallised from methanol prior to use.

NMR spectra were measured on a on a Bruker Biospin at 500 MHz for ^1H, 125.8 MHz for $^{13}C\{^1H\}$ and 202.5 MHz for $^{31}P\{^1H\}$. Chemical shifts for ^1H and ^{13}C are given in ppm relative to the solvent[3] and for ^{31}P relative to phosphoric acid. All NMR were recorded at room temperature. IR spectra were measured using an ATR bridge and recorded on a Perkin-Elmer Spectrum Two FT-IR spectrometer. Raman spectra were recorded on a Renishaw Ramanscope spectrometer (514 nm). CHN elemental analyses were performed with a LECO CHN-932 microanalyzer. Cyclic voltammograms were obtained with a BAS 100W Voltammetric Analyzer (low volume cell). The cell was equipped with an Au working electrode and a Pt counter electrode, and an Ag reference electrode. All sample solutions were 0.1M in Bu_4NPF_6 and recorded with a scan rate of 100 mV/s. Ferrocene was used as an external standard. A BAS 100W program was employed for the data analysis.

Syntheses

[I– (depe$_2$)Fe–1,4– (C≡C–C$_6$H$_4$–C≡C) –Fe(depe$_2$) –I] 1

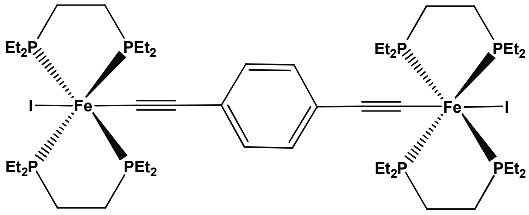

Fe(depe)$_2$I$_2$ (289 mg, 0.4 mmol) and 1,4-bis((trimethylstannyl)ethynyl)benzene (95 mg, 0.21 mmol) were suspended in THF (10 mL) and heated to reflux for 12 h. The THF was removed *in vacuo* and the obtained solid washed with pentane/diethylether (1:1, 3 x 10 mL). The product was extracted with toluene (40 mL) and the solution filtered over diatomite. Drying *in vacuo* gave the title compound as a red solid. Yield: 228 mg = 0.173 mmol = 86.7 %. Crystals suitable for X-ray were grown by slow diffusion of pentane into a THF solution at rt.

Anal. Calcd.: C: 45.68, H: 7.67. **Found**: C: 45.91, H: 7.51. **IR** (ATR, cm^{-1}): 2028 (vs, $\nu_{C\equiv C}$);1489 (m, $\nu_{C=C}$). **Raman** (cm^{-1}): 2030 (m, $\nu_{C\equiv C}$);1586 (s, $\nu_{C=C}$). **^{1}H – NMR** (500 MHz, THF-d$_8$): δ = 6.50 (s, 4H, Ar-**H**), 2.62 - 2.53 (m, 8H, C**H**$_2$-CH$_3$), 2.47 - 2.38 (m, 8H, C**H**$_2$-CH$_3$), 2.06 - 1.89 (m, 24H, C**H**$_2$-CH$_3$ and C**H**$_2$-CH$_2$), 1.83 - 1.75 (m, 8H, C**H**$_2$-CH$_3$, overlapping with THF), 1.26 - 1.14 (m, 48H, CH$_2$-C**H**$_3$). **^{13}C – NMR** (125.8 MHz, THF-d$_8$): 129.9 (s, o-**C**), 125.6 (s, *i*-**C**), 124.15 (s, Fe-C≡**C**), 122.7 (p, $^{2}J_{C\text{-}P}$ = 23.9 Hz, Fe-**C**≡C), 25.1 - 24.9 (m, **C**H$_2$-CH$_3$), 22.6 - 22.1 (m, **C**H$_2$-**C**H$_2$), 21.3 - 21.1 (m, **C**H$_2$-CH$_3$), 10.5 (d, $^{2}J_{C\text{-}P}$ = 75.5 Hz, CH$_2$-**C**H$_3$). **^{31}P – NMR** (202.5 MHz, THF-d$_8$): 66.0 (s).

[I– (depe$_2$)Fe–1,3– (C≡C–C$_6$H$_4$–C≡C) –Fe(depe$_2$) –I] 2

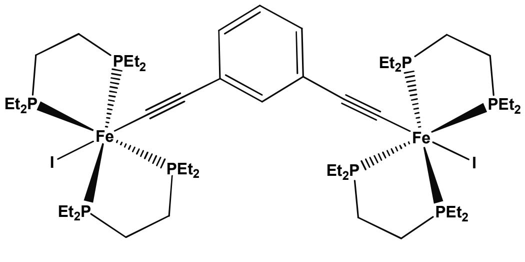

Fe(depe)$_2$I$_2$ (289 mg, 0.4 mmol) and 1,3-bis((trimethylstannyl)ethynyl)benzene (95 mg, 0.21 mmol) were suspended in THF (10 mL) and heated to reflux for 12 h. The solvent was removed in vacuo and the obtained pink solid washed with pentane (3 x 10 mL). The product was extracted with benzene (25 mL) and the solution filtered over a patch of celite. Drying *in vacuo* gave the title compound as a pink solid. Yield: 238 mg = 0.181 mmol = 90.5 %. Crystals suitable for X-ray were grown by slow diffusion of pentane into a THF solution at rt.

Anal. Calcd.: C: 45.68; H: 7.67. **Found**: C: 45,49; H: 7.53. **IR** (ATR, cm^{-1}): 2036 (vs, $\nu_{C\equiv C}$);1571 (s, $\nu_{C=C}$); 1551 (m, $\nu_{C=C}$). **Raman** (cm^{-1}): 2040 (s, $\nu_{C\equiv C}$);1574 (m, $\nu_{C=C}$);**^{1}H – NMR** (500 MHz, THF-d$_8$): δ = 6.62 (t, 1H, $^3J_{H\text{-}H}$ = 7.5 Hz, 5-Ar-**H**), 6.39 (s, 1H, 2-Ar-**H**), 6.31 (d, 1H, $^3J_{H\text{-}H}$ = 7.5 Hz, 4-Ar-**H**), 2.64 - 2.54 (m, 8H, C**H**$_2$-CH$_3$), 2.50 - 2.38 (m, 8H, C**H**$_2$-CH$_3$), 2.06 - 1.88 (m, 24H, C**H**$_2$-CH$_3$ and C**H**$_2$-CH$_2$), 1.83 - 1.75 (m, 8H, C**H**$_2$-CH$_3$), 1.26 - 1.14 (m, 48H, CH$_2$-C**H**$_3$). **^{13}C{^{1}H} NMR** (125.8 MHz, THF-d$_8$): δ = 132.1 (s, 2-Ar-**C**), 130.9 (p, $^2J_{C\text{-}P}$ = 37.7 Hz, Fe-**C**≡C), 130.6 (s, 1-Ar-**C**), 127.9 (s, 5-Ar-**C**), 124.9 (s, 4-Ar-**C**), 123.8 (Fe-C≡**C**), 25.1 - 24.8 (m Hz, **C**H$_2$-CH$_3$) 22.5 - 22.0 (m, **C**H$_2$-**C**H$_2$), 21.3 - 20.9 (m Hz, **C**H$_2$-CH$_3$), 10.6 (d, $^2J_{C\text{-}P}$ = 62.9 Hz, CH$_2$-**C**H$_3$). **^{31}P{^{1}H} NMR** (202.5 MHz, THF-d$_8$): δ = 66.1 (s).

[I– (depe$_2$)Fe–4,4–(C≡C–C$_6$H$_4$ –C$_6$H$_4$–C≡C)–Fe(depe$_2$) –I] 3

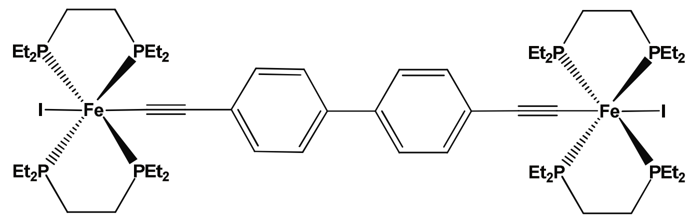

Fe(depe)$_2$I$_2$ (289 mg, 0.4 mmol) and 4,4'-bis((trimethylstannyl)ethynyl)biphenyl (110 mg, 0.208 mmol) were suspended in THF (10 mL) and heated to reflux for 12 h. After cooling down to rt, a yellow-orange precipitate formed. Pentane (30 mL) was added and the supernatant solution removed. The precipitate was washed with pentane (3 x 10 mL). After extraction with hot toluene (90°C, 40 mL), the solution was filtered hot over a patch of celite. The toluene was removed *in vacuo* to give the title compound as an orange solid. Yield: 251 mg = 0.181 mmol = 90.4 %.

Anal. Calcd.: C: 48.36; H: 7.54. **Found**: C: 48.56; H: 7.55. **IR** (ATR, cm^{-1}): 2023 (vs, $\nu_{C\equiv C}$);1595 (m, $\nu_{C=C}$); 1480 (s, $\nu_{C=C}$). **Raman** (cm^{-1}): 2040 (w, $\nu_{C\equiv C}$);1591 (vs, $\nu_{C=C}$). (500 MHz, CD$_2$Cl$_2$): δ = 7.23 (d, 4H, $^3J_{H\text{-}H}$ = 10.0 Hz, Ar-**H),** 6.88 (d, 4H, $^3J_{H\text{-}H}$ = 10.0 Hz, Ar-**H),** 2.63 - 2.51 (m, 8H, C**H**$_2$-CH$_3$), 2.10 - 1.90 (m, 24 H, C**H**$_2$-CH$_3$ and C**H**$_2$-CH$_2$), 1.88 - 179 (m, 8H, C**H**$_2$-CH$_3$), 1.32 - 1.17 (m, 48H, CH$_2$-C**H**$_3$) **^{13}C – NMR** (125.8 MHz, CD$_2$Cl$_2$): δ = 135.0 (s, Ar-**C**), 130.3 (s, Ar-**C**-H), 128.6 (s, Ar-**C**), 126.1 (s, Ar-**C**-H), 123.3 (s, Fe-C≡**C**), 24.4 - 24.0 (m Hz, **C**H$_2$-CH$_3$) 21.8 - 21.3 (m, **C**H$_2$-**C**H$_2$), 20.5 - 20.2 (m Hz, **C**H$_2$-CH$_3$), 10.3 (d, $^2J_{C\text{-}P}$ = 75.5 Hz, CH$_2$-**C**H$_3$). **^{31}P – NMR** (202.5 MHz, CD$_2$Cl$_2$): δ = 64.8 (s).

[I– (depe$_2$)Fe–4,4– (C≡C– SC$_4$H$_2$ –C≡C) –Fe(depe$_2$) –I] 4

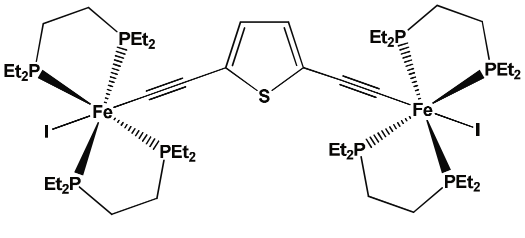

Fe(depe)$_2$I$_2$ (289 mg, 0.4 mmol) and 2,5-bis((trimethylstannyl)ethynyl)thiophene (96 mg, 0.21 mmol) were suspended in toluene (10 mL) and heated to 80°C for 12 h. After cooling down, the brown solution was concentrated to 5 mL before pentane was added (20 mL) causing a precipitate to form. the supernatant solution was removed and the precipitate washed with pentane (3 x 10 mL). The product was extracted with benzene (20 mL)) and the solution filtered over a patch of celite. Drying *in vacuo* gave the title compound as a brown solid. Yield: 234 mg = 0.177mmol = 88.4 %. Crystals suitable for X-ray were grown in benzene/pentane at rt.

Anal. Calcd.: C: 43.65; H: 7.48. **Found**: C: 43.81; H: 7.51. **IR** (ATR, cm^{-1}): 2034 (s, $\nu_{C\equiv C}$);1502 (w, $\nu_{C=C}$). **Raman** (cm^{-1}): 2032 (m, $\nu_{C\equiv C}$);1439 (vs, $\nu_{C=C}$). **^{1}H – NMR** (500 MHz, C$_6$D$_6$): δ = 6.38 (s, 2H, 3-Thiophene-**H**), 2.72 - 2.62 (m, 8H, C**H**$_2$-CH$_3$), 2.44 - 2.33 (m, 8H, C**H**$_2$-CH$_3$), 1.92 - 1.79 (m, 16H, C**H**$_2$-CH$_3$ and C**H**$_2$-CH$_2$), 1.77 - 1.61 (m, 16H, C**H**$_2$-CH$_3$ and C**H**$_2$-CH$_2$), 1.11 - 1.02 (m, 48H, CH$_2$-C**H**$_3$). **^{13}C{^{1}H} NMR** (125.8 MHz, C$_6$D$_6$): δ = 137.6 (p, $^2J_{C\text{-}P}$ = 28.9 Hz, Fe-**C**≡C), 125.4 (s, Fe-C≡**C**), 123.1(s, 3-Thiophene-**C**), 115.4 (s, 2-Thiophene-**C**), 24.5 - 24.3(m, **C**H$_2$-CH$_3$), 22.0 - 21.5 (m, **C**H$_2$-**C**H$_2$), 20.9 - 20.6(m, **C**H$_2$-CH$_3$), 10.3(d, $^2J_{C\text{-}P}$ = 62.9 Hz, CH$_2$-**C**H$_3$). **^{31}P{^{1}H} NMR** (202.5 MHz, C$_6$D$_6$): δ = 67.9 (s).

[{I– (depe$_2$)Fe– C≡C–}$_3$–(1,3,5– C$_6$H$_3$)] 5

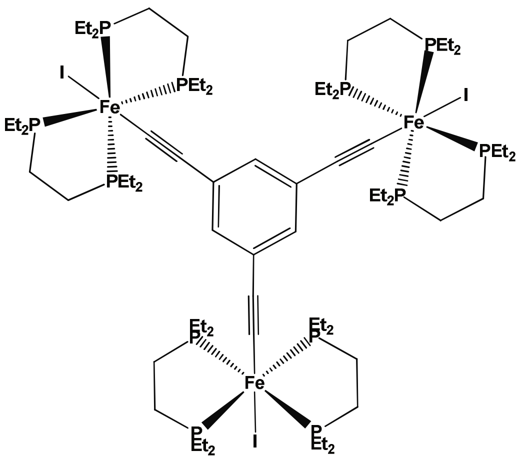

Fe(depe)$_2$I$_2$ (217 mg, 0.3 mmol) and 1,3,5-tris((trimethylstannyl)ethynyl)benzene (67 mg, 0.105 mmol) were suspended in THF (50 mL) and heated to reflux for 12 h. The red solution was then filtered hot over a patch of celite and concentrated to a volume of 20 mL, causing a pink precipitate to form. The supernatant solution was removed and the precipitate washed with diethylether (3 x 10 mL). Drying *in vacuo* gave the title compound as a pink solid. Yield: 180 mg = 0.0931 mmol =93.1 %.

Anal. Calcd.: C: 44.74; H: 7.67. **Found:** C: 44.95; H: 7.46. **IR** (ATR, cm^{-1}): 2046 (vs, $\nu_{C\equiv C}$); 1551 (vs, $\nu_{C=C}$). **Raman** (cm^{-1}): 2049 (s, $\nu_{C\equiv C}$);1561 (m, $\nu_{C=C}$). **^{1}H – NMR** (500 MHz, CD$_2$Cl$_2$): δ = 5.94 (s, 3H, Ar-**H),** 2.55 - 2.44 (m, 12H, C**H**$_2$-CH$_3$), 2.40 - 2.27 (m, 12H, C**H**$_2$-CH$_3$), 2.00 - 1.84 (m, 32H, C**H**$_2$-CH$_3$ and C**H**$_2$-CH$_2$), 1.76 - 1.67 (m, 12H, C**H**$_2$-CH$_3$), 1.20 - 1.12 (m, 72H, CH$_2$-C**H**$_3$) **^{13}C – NMR** (125.8 MHz, CD$_2$Cl$_2$): δ = 126.3 (s, Ar-**C**-H), 24.8 - 24.2 (m Hz, **C**H$_2$-CH$_3$), 22.1 - 21. 5 (m, **C**H$_2$-**C**H$_2$), 20.7 - 20.1 (m Hz, **C**H$_2$-CH$_3$), 10.4 (d, $^2J_{C\text{-}P}$ = 75.5 Hz, CH$_2$-**C**H$_3$). **^{31}P – NMR** (202.5 MHz, CD$_2$Cl$_2$): δ = 66-5 (s).

[SCN– (depe$_2$)Fe–1,4– (C≡C–C_6H_4–C≡C) –Fe(depe$_2$) –NCS] 6

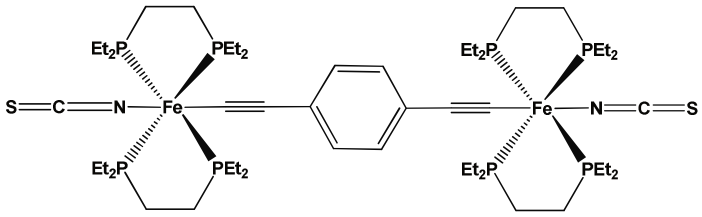

Compound **1** (66 mg, 0.05 mmol) and NaSCN (81 mg, 1 mmol) were dispersed in acetonitrile (15 mL) and heated to reflux for 12 h. Complex **1** gradually dissolved to give a yellow solution. The solution was concentrated to 5 mL, causing a yellow precipitate to form. The precipitate was filtered off using a patch of celite and washed with acetonitrile (3 x 5 mL). The product, a yellow solid, was extracted with benzene (40 mL) and dried *in vacuo*. Crystals suitable for X-ray were grown by slow diffusion of pentane into a THF solution at rt.

Anal. Calcd.. **Found**: C: 53.06; H: 8.56; N: 2.38. **Found**: C: 52.80; H: 8.61; N: 2.42. **IR** (ATR, cm^{-1}): 2092 (s, $\nu_{C=N}$); 2044 (s, $\nu_{C\equiv C}$); 1489 (m, $\nu_{C=C}$). **Raman** (cm^{-1}): 2043 (m, $\nu_{C\equiv C}$); 1590 (s, $\nu_{C=C}$). **^{1}H – NMR** (500 MHz, CD_2Cl_2): δ = 6.50 (s, 4H, Ar-**H**), 2.29 - 2.20 (m, 8H, C**H**$_2$-CH$_3$), 1.95 - 1.72 (m, 40H, C**H**$_2$-CH$_3$ and C**H**$_2$-CH$_2$), 1.24 - 1.14 (m, 48H, CH$_2$-C**H**$_3$). **^{13}C – NMR** (125.8 MHz, CD_2Cl_2): 139.5 (s, Fe-N=**C**=S), 129.6 (s, *o*-**C**), 127.7 (p, $^2J_{C\text{-}P}$ = 25.2 Hz, Fe-**C**≡C), 124.9 (s, *i*-**C**), 120.6 (s, Fe-C≡**C**), 21.3 - 20.7 (m, **C**H$_2$-CH$_3$), 20.0 - 19.6 (m, CH$_2$-**C**H$_2$ and **C**H$_2$-CH$_3$), 9.5 (d, $^2J_{C\text{-}P}$ = 37.7 Hz, CH$_2$-**C**H$_3$). **^{31}P – NMR** (202.5 MHz, CD_2Cl_2): 73.8 (s)

[SCN– (depe$_2$)Fe–1,3– (C≡C–C_6H_4–C≡C) –Fe(depe$_2$) –NCS] 7

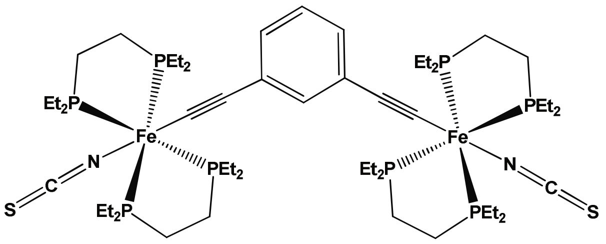

Compound **2** (66 mg, 0.05 mmol) and NaSCN (81 mg, 1 mmol) were dispersed in acetonitrile (15 mL) and heated to reflux for 5 h, yielding a yellow solution. The acetonitrile was removed *in vacuo* and the resulting solid washed with diethylether (3 x 5 mL). The product extracted with benzene/pentane (2:1, 40 mL). The solution was filtered over a patch of celite . Drying *in vacuo* gave the title compound as yellow solid. Yield: 53.6 mg = 0.046 mmol = 91.1 %.

Anal. Calcd.. **Found**: C: 53.06; H: 8.56; N: 2.38. **Found**: C: 53.31; H: 8.47; N: 2.15. **IR** (ATR, cm^{-1}): 2092 (s, $\nu_{C=N}$); 2041 (vs, $\nu_{C\equiv C}$); 1574 (s, $\nu_{C=C}$); 1552 (m, $\nu_{C=C}$). **Raman** (cm^{-1}): 2097 (m, $\nu_{C=N}$); 2040 (vs, $\nu_{C\equiv C}$); 1578 (m, $\nu_{C=C}$); 1552 (w, $\nu_{C=C}$). **^{1}H – NMR** (500 MHz, THF-d_8): δ = 6.59 (t, 1H, $^3J_{H\text{-}H}$ = 7.5 Hz, 5-Ar-**H**), 6.35 (s, 1H, 2-Ar-**H**), 6.31 (d, 1H,

$^3J_{H-H}$ = 10.0 Hz, 4-Ar-**H**), 2.38 - 2.26 (m, 8H, C**H**$_2$-CH$_3$), 2.00- 1.79 (m, 40H, C**H**$_2$-CH$_3$ and C**H**$_2$-CH$_2$), 1.27 - 1.18 (m, 48H, CH$_2$-C**H**$_3$). **^{13}C{^{1}H} NMR** (125.8 MHz, THF-d$_8$): δ = 142.8 (s, Fe-N=C=S), 132.3 (s, 2-Ar-**C**), 130.3 (s, 1-Ar-**C**), 127.9 (s, 5-Ar-**C**), 126.8 (p, $^2J_{C-P}$ = 25.2 Hz, Fe-**C**≡C), 125.2 (s, 4-Ar-**C**), 121.1 (Fe-C≡**C**), 21.8 - 21.3 (m Hz, **C**H$_2$-CH$_3$) 20.8 - 20.5 (m, **C**H$_2$-**C**H$_2$), 20.4 - 20.2 (m Hz, **C**H$_2$-CH$_3$), 9.7 (d, $^2J_{C-P}$ = 50.3 Hz, CH$_2$-**C**H$_3$). **^{31}P{^{1}H} NMR** (202.5 MHz, THF-d$_8$): δ = 74.4 (s).

[SCN- (depe$_2$)Fe-4,4-(C≡C-C$_6$H$_4$-C$_6$H$_4$-C≡C)-Fe(depe$_2$) -NCS] 8

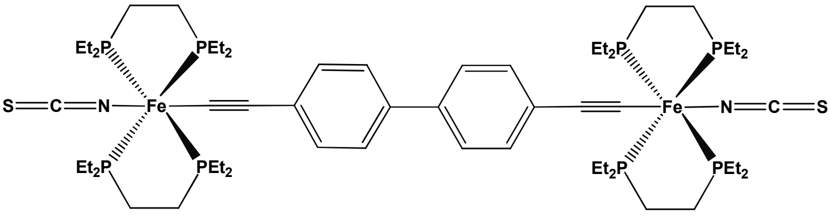

Compound 3 (70 mg, 0.05 mmol) and NaSCN (81 mg, 1 mmol) were dispersed in acetonitrile (15 mL) and heated to reflux for 12 h. The components never fully dissolved, over the course of the reaction, a yellow precipitate was always present. The solution was concentrated to 5 mL to further precipitation. The solid was filtered off using a patch of celite and washed with acetonitrile (3 x 5 mL). The product, a yellow-orange solid, was extracted with benzene (40 mL) and dried *in vacuo*. Yield: 58 mg = 0.047 mmol = 93.2 %. Crystals suitable for X-ray were grown by slow evaporation of a THF/acetonitrile solution at rt.

Anal. Calcd.: C: 55.59; H: 8.37; N: 2.24. **Found**: C: 55.78; H: 8.31; N: 2.16. **IR** (ATR, cm^{-1}): 2094 (s, $\nu_{C=N}$); 2034 (vs, $\nu_{C≡C}$); 1596 (s, $\nu_{C=C}$); 1481 (s, $\nu_{C=C}$). **Raman** (cm^{-1}): 2045 (w, $\nu_{C≡C}$); 1591 (vs, $\nu_{C=C}$); 1522 (vw, $\nu_{C=C}$). **^{1}H – NMR** (500 MHz, CD$_2$Cl$_2$): δ = 7.19 (d, 4H, $^3J_{H-H}$ = 8.0 Hz, Ar-**H**), 6.84 (d, 4H, $^3J_{H-H}$ = 8.0 Hz, Ar-**H**), 2.37 - 2.25 (m, 8H, C**H**$_2$-CH$_3$), 2.06 - 1.75 (m, 40H, C**H**$_2$-CH$_3$ and C**H**$_2$-CH$_2$), 1.30 - 1.13 (m, 48H, CH$_2$-C**H**$_3$) **^{13}C – NMR** (125.8 MHz, CD$_2$Cl$_2$): δ = 139.9 (s, Fe-N=**C**=S), 135.5 (s, Ar-**C**), 132.2 (p, $^2J_{C-P}$ = 28.3 Hz, Fe-**C**≡C), 130.4 (s, Ar-**C**-H), 128.7 (s, Ar-**C**), 126.2 (s, Ar-**C**-H), 120.3 (s, Fe-C≡**C**), 21.4 - 21.0 (m Hz, **C**H$_2$-CH$_3$) 20.2 - 19.9 (m, **C**H$_2$-**C**H$_2$), 19.9 - 19.7 (m Hz, **C**H$_2$-CH$_3$), 9.6 (d, $^2J_{C-P}$ = 62.9 Hz, CH$_2$-**C**H$_3$). **^{31}P – NMR** (202.5 MHz, CD$_2$Cl$_2$): δ = 73.9 (s).

[SCN-(depe$_2$)Fe-4,4-(C≡C-SC$_4$H$_2$-C≡C)-Fe(depe$_2$)-NCS] 9

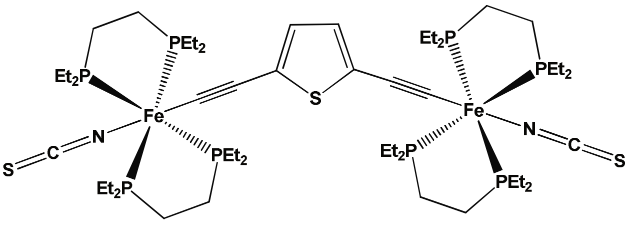

Compound 4 (66 mg, 0.05 mmol) and NaSCN (81 mg, 1 mmol) were dispersed in acetonitrile (15 mL) and heated to reflux for 12 h, yielding a brown solution. The acetonitrile was removed *in vacuo* and the resulting solid washed with cold diethylether (-20°C, 3 x 5 mL). Then the product was extracted with benzene/pentane (2:1; 40 mL). The solution was filtered over a patch of celite . Drying *in vacuo* gave the title compound as yellow-brown solid. Yield: 57 mg = 0.049 mmol = 97.0 % Crystals suitable for X-ray were grown by slow diffusion of pentane into a benzene solution at rt.

Anal. Calcd.: C: 50.76; H: 8.35; N: 2.37. **Found**: C: 50.71; H: 8.31; N: 2.30. **IR** (ATR, cm^{-1}): 2094 (s, $\nu_{C=N}$); 2031 (s, $\nu_{C\equiv C}$); 1503 (w, $\nu_{C=C}$). **Raman** (cm^{-1}): 2097 (w, $\nu_{C=N}$); 2036 (m, $\nu_{C\equiv C}$); 1434 (vs, $\nu_{C=C}$**^{1}H – NMR** (500 MHz, C_6D_6): δ = 6.24 (s, 2H, 4-Thiophene-**H**), 2.14 - 2.07 (m, 8H, C**H**$_2$-CH$_3$), 1.90 - 1.83 (m, 8H, C**H**$_2$-CH$_3$), 1.61 - 1.45 (m, 32H, C**H**$_2$-CH$_3$ and C**H**$_2$-CH$_2$), 1.03 - 0.94 (m, 48H, CH$_2$-C**H**$_3$). **^{13}C{^{1}H} NMR** (125.8 MHz, C_6D_6): δ = 142.5 (2, Fe-N=**C**=S), 133.6 (p, $^2J_{C-P}$ = 25.2 Hz, Fe-C≡**C**), 125.2 (s, 3-Thiophene-**C**), 123.4 (s, Fe-C≡**C**), 112.5 (s, 2-Thiophene-**C**), 21.1 - 20.0 (m, **C**H$_2$-CH$_3$), 20.0 - 19.7 (m, **C**H$_2$-**C**H$_2$), 19.7 - 19.5 (m, **C**H$_2$-CH$_3$), 9.3 (d, $^2J_{C-P}$ = 37.7 Hz, CH$_2$-**C**H$_3$). **^{31}P{^{1}H} NMR** (202.5 MHz, C_6D_6): δ = 74.0 (s)

[{SCN– (depe$_2$)Fe– C≡C–}$_3$–(1,3,5– C$_6$H$_3$)] 10

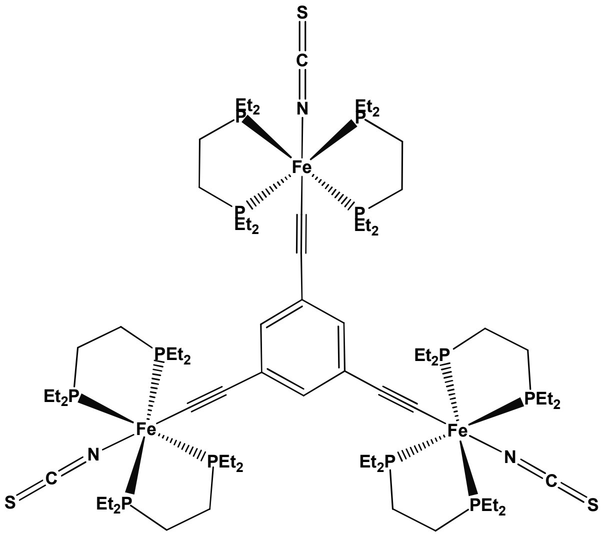

Compound **5** (97 mg, 0.05 mmol) and NaSCN (122 mg, 1.5 mmol) were dispersed in acetonitrile (15 mL) and heated to reflux for 5 h. The pink complex **5** gradually dissolved to give a yellow solution. The solution was concentrated to 5 mL, causing a yellow precipitate to form. The precipitate was filtered off using a patch of celite and washed with acetonitrile (3 x 5 mL). The product, a yellow solid, was extracted with benzene (40 mL) and dried *in vacuo*. Yield: 83 mg = 0.048 mmol = 96.2%.

Anal. Calcd.: C: 52.18; H: 8.58; N: 2.43. **Found:** C: 52.38; H: 8.45; N: 2.31. **IR** (ATR, cm^{-1}): 2096 (vs, $\nu_{C=N}$); 2043 (vs, $\nu_{C\equiv C}$); 1552 (s, $\nu_{C=C}$). **Raman** (cm^{-1}): 2101 (m, $\nu_{C=N}$); 2053 (vs, $\nu_{C\equiv C}$); 1556 (m, br, sh at 1575, $\nu_{C=C}$). **^{1}H – NMR** (500 MHz, THF-d_8): δ = 5.93 (s, 3H, Ar-**H**), 2.35 - 2.24 (m, 12H, C**H**$_2$-CH$_3$), 1.96 - 1.88 (m, 24H, C**H**$_2$-CH$_3$), 1.86 - 1.77 (m, 36H, C**H**$_2$-CH$_3$ and C**H**$_2$-CH$_2$), 1.24 - 1.17 (m, 72H, CH$_2$-C**H**$_3$). **^{13}C – NMR** (125.8 MHz, THF-d_8): 142.7 (s, Fe-N=**C**=S), 129.6 (s, Ar-**C**-C≡C), 127.5 (s, Ar-**C**-H), 123.8 (p, $^2J_{C-P}$ = 28.3 Hz, Fe-**C**≡C), 121.5 (s, Fe-C≡**C**), 21.5 - 21.3 (m, **C**H$_2$-**C**H$_2$), 20.7 - 20.4 (m, **C**H$_2$-CH$_3$), 9.6 (d, $^2J_{C-P}$ = 62.9 Hz, CH$_2$-**C**H$_3$). **^{31}P – NMR** (202.5 MHz, THF-d_8): 74.6 (s).

NMR - Studies

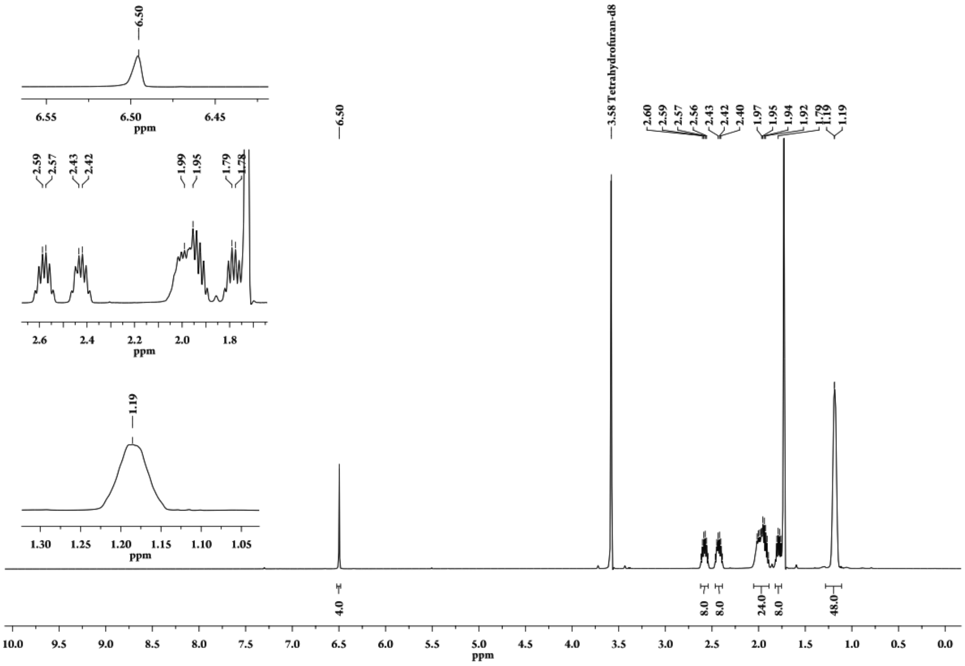

Figure S1. ^{1}H NMR of **1** in THF-d_8

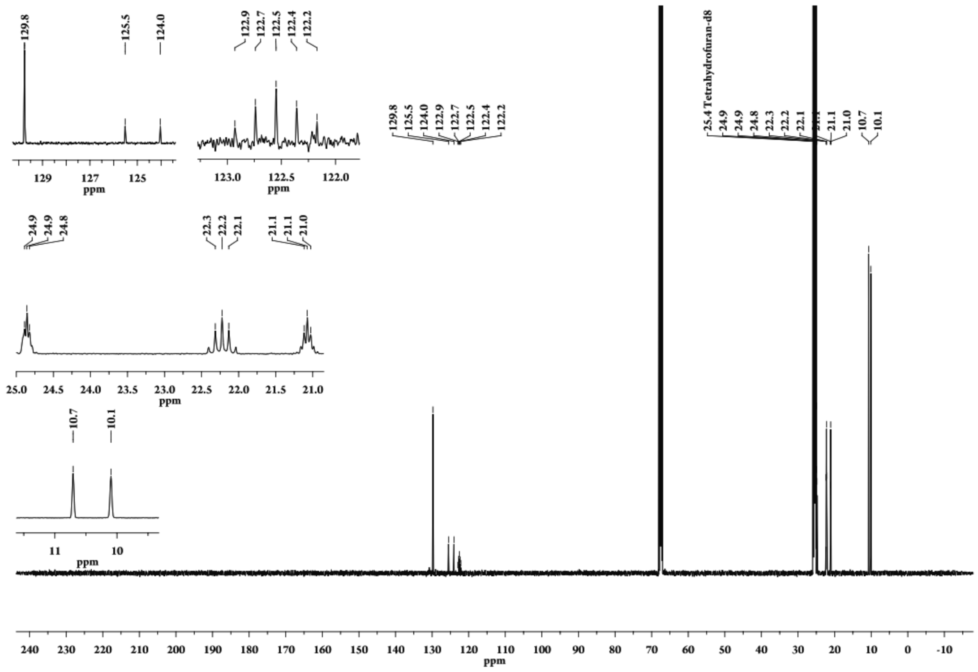

Figure S2. $^{13}C\{^{1}H\}$ NMR of **1** in THF-d_8

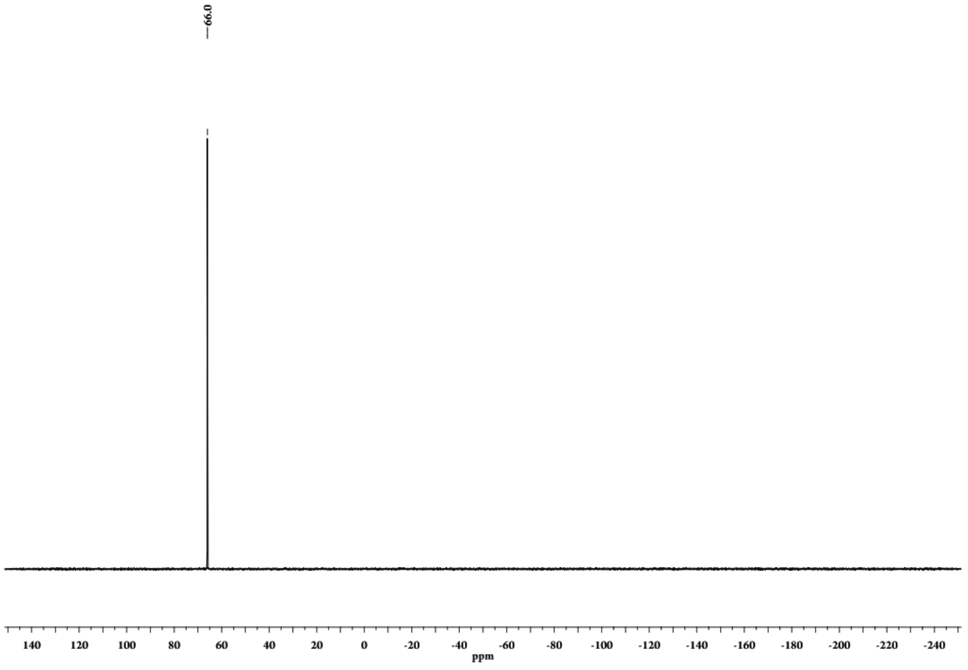

Figure S3. $^{31}P\{^{1}H\}$ NMR of **1** in THF-d_8

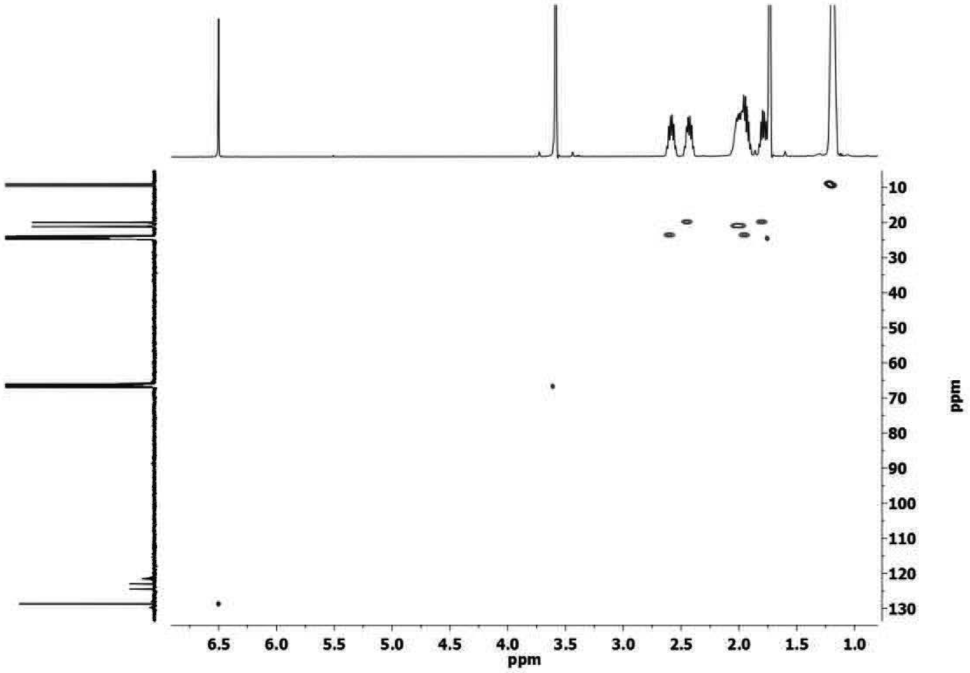

Figure S4. C,H Correlation NMR of **1** in THF-d_8

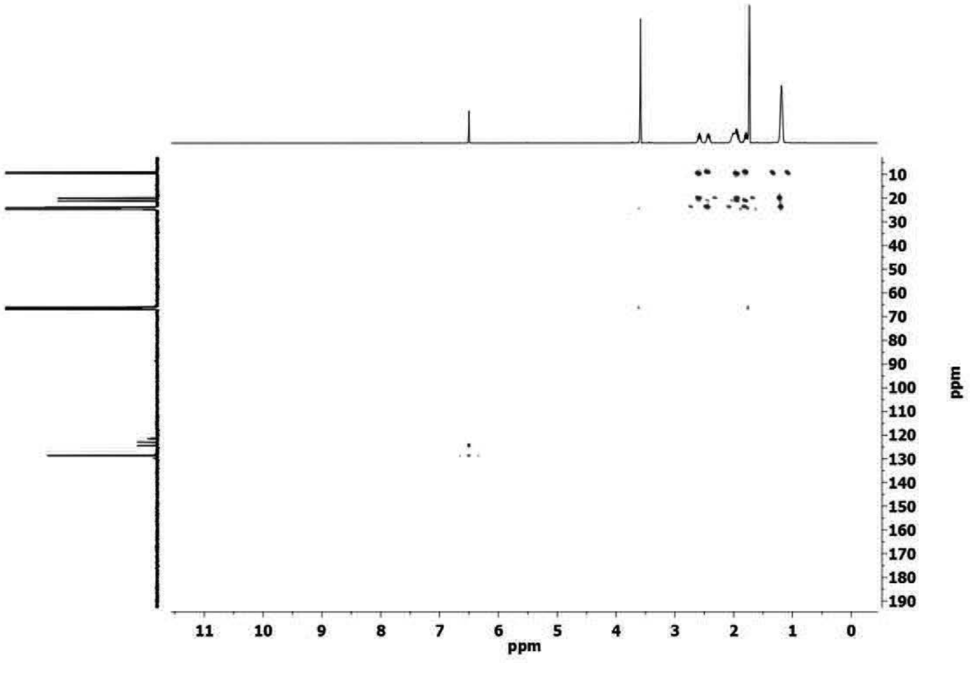

Figure S5. C,H Correlation (longrange) NMR of **1** in THF-d_8

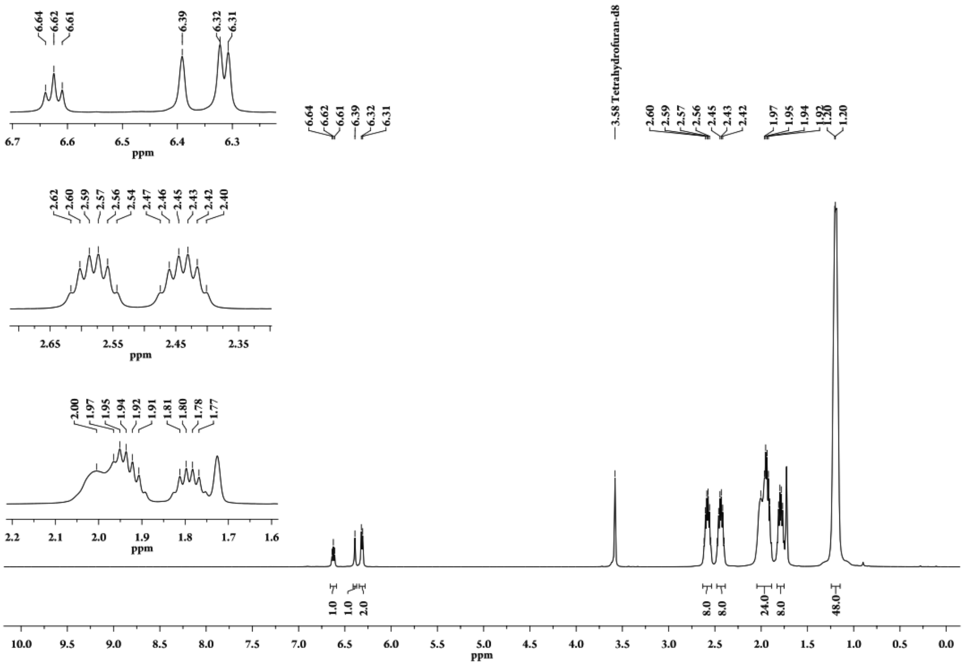

Figure S6. ^{1}H NMR of **2** in THF-d_8

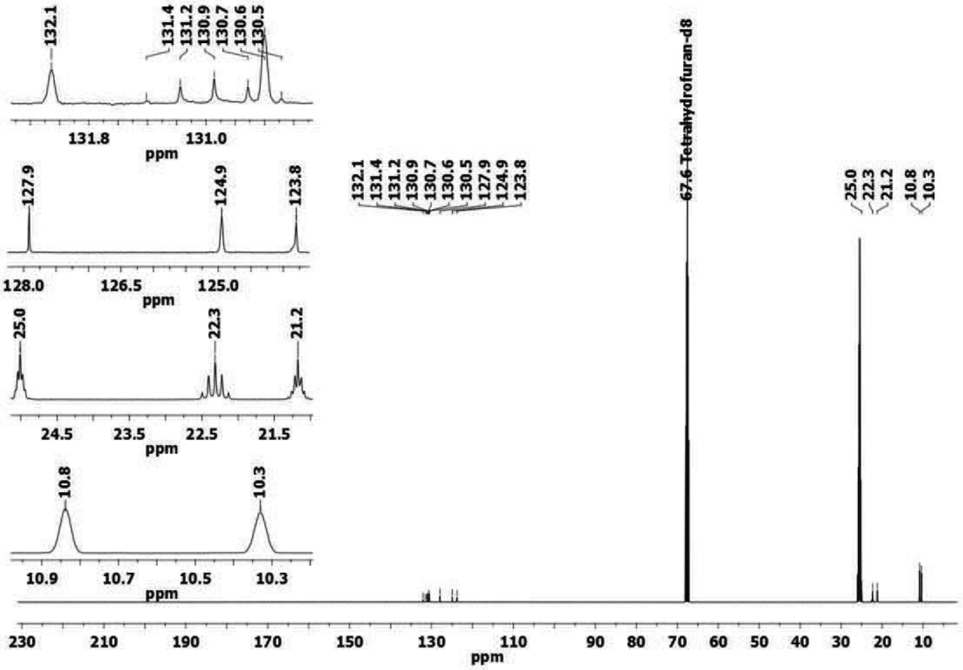

Figure S7. ^{13}C{^{1}H} NMR of **2** in THF-d_8

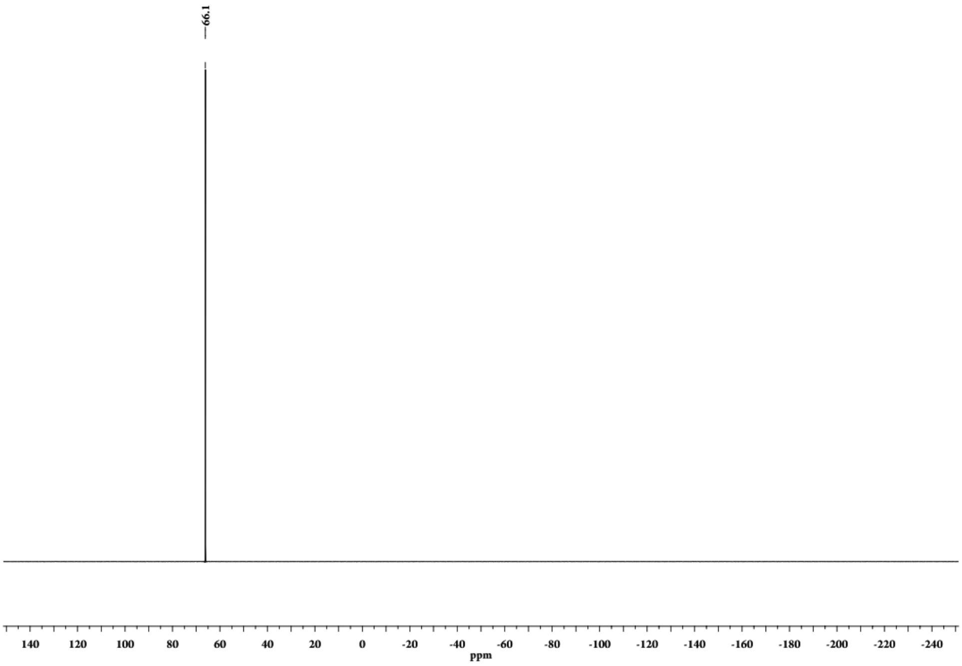

Figure S8. $^{31}P\{^1H\}$ NMR of **2** in THF-d$_8$

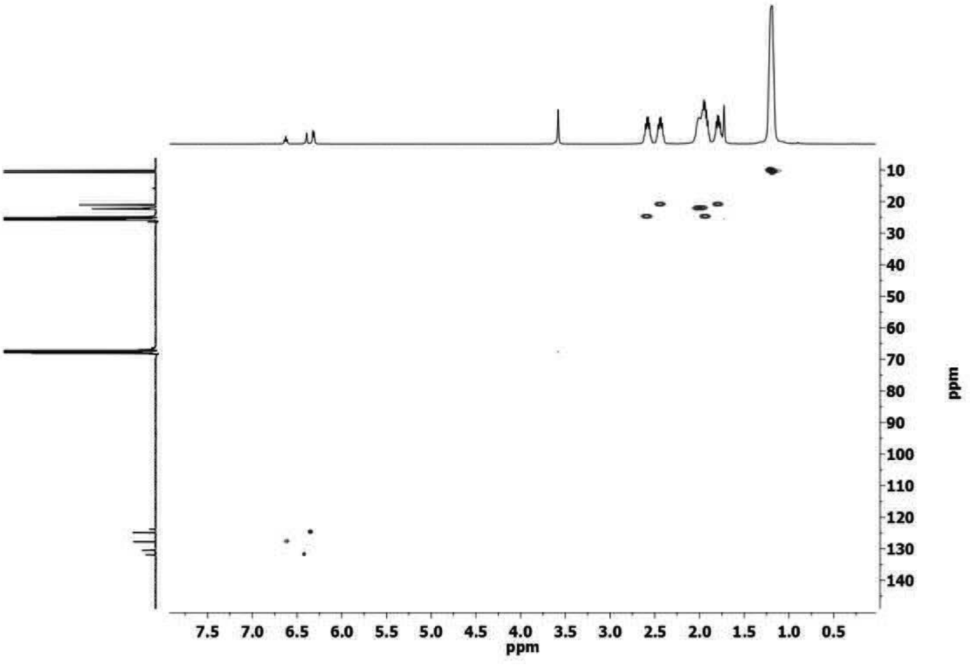

Figure S9. C,H Correlation NMR of **2** in THF-d$_8$

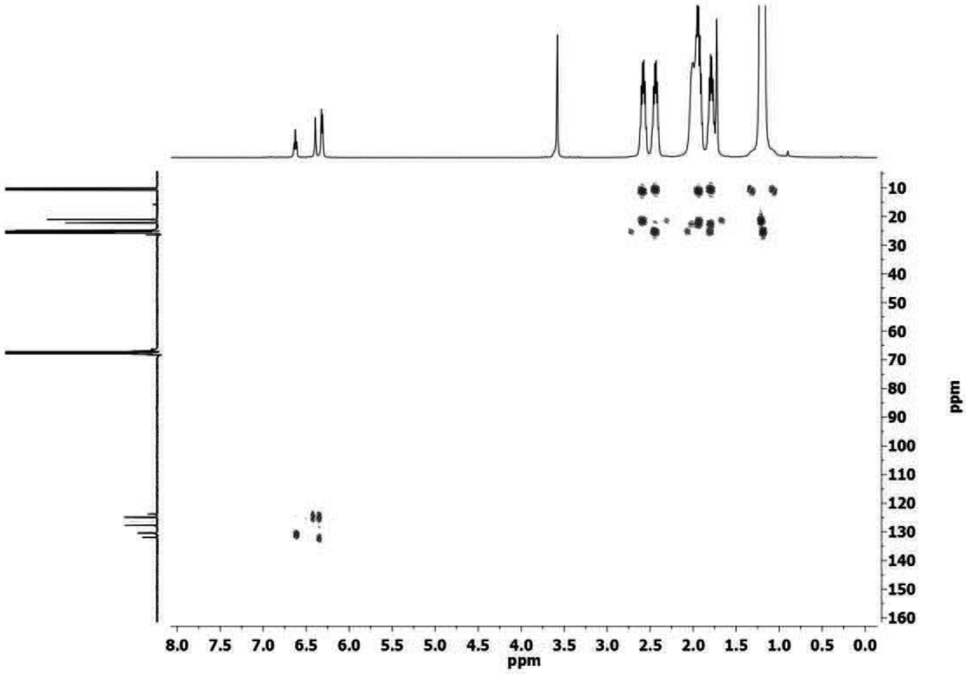

Figure S10. C,H Correlation (longrange) NMR of **2** in THF-d_8

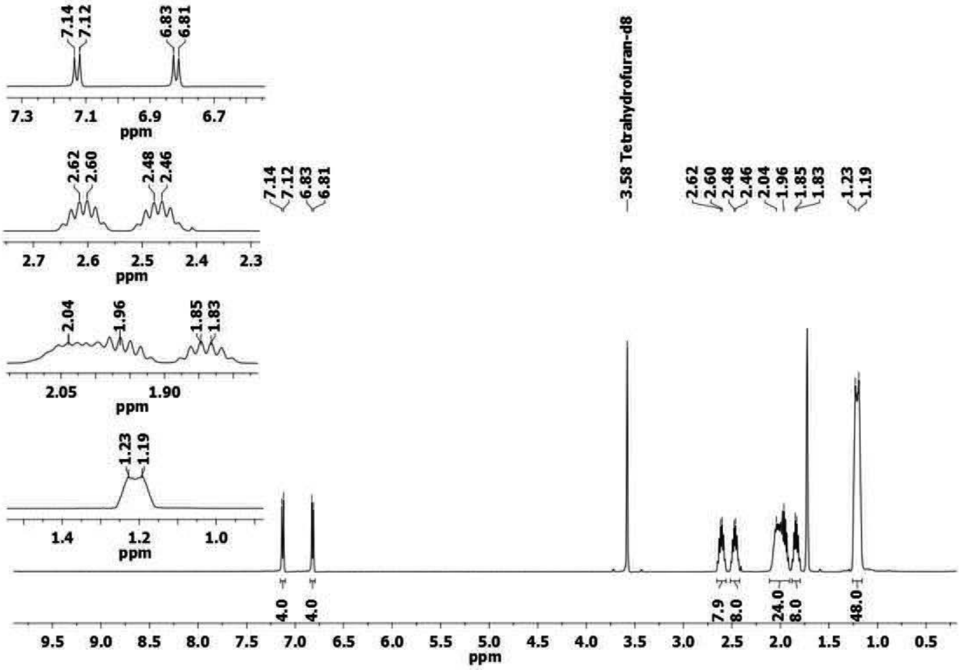

Figure S11. ^{1}H NMR of **3** in CD_2Cl_2

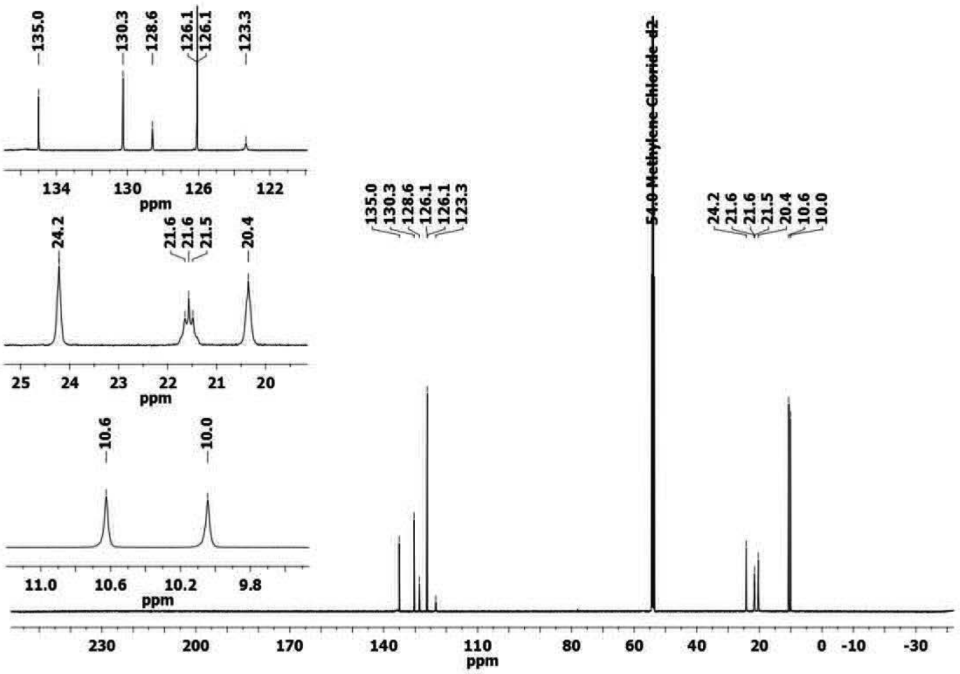

Figure S12. $^{13}C\{^1H\}$ NMR of **3** in CD_2Cl_2

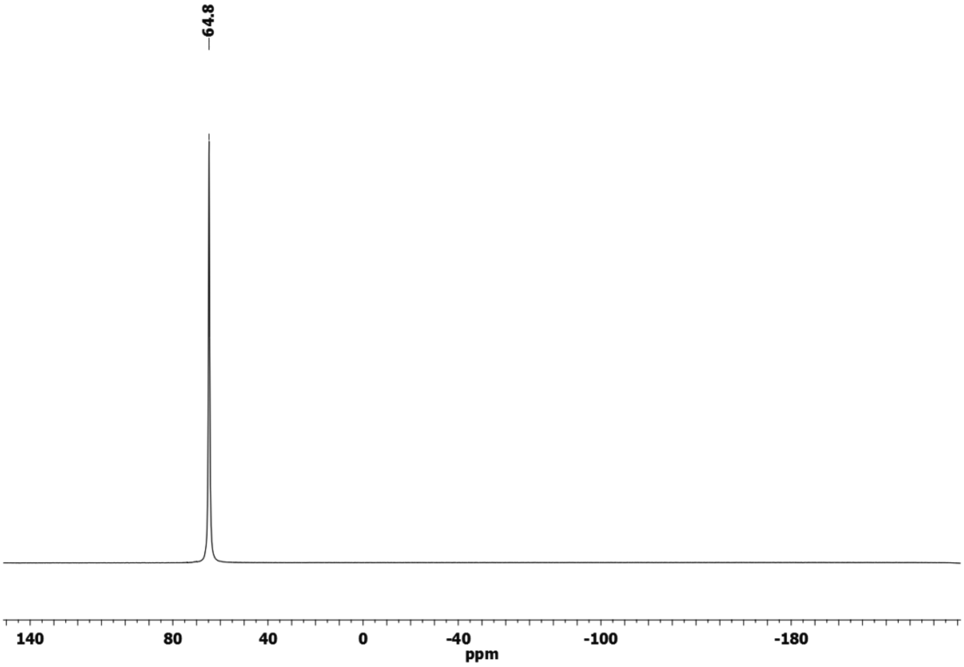

Figure S13. $^{31}P\{^1H\}$ NMR of **3** in CD_2Cl_2

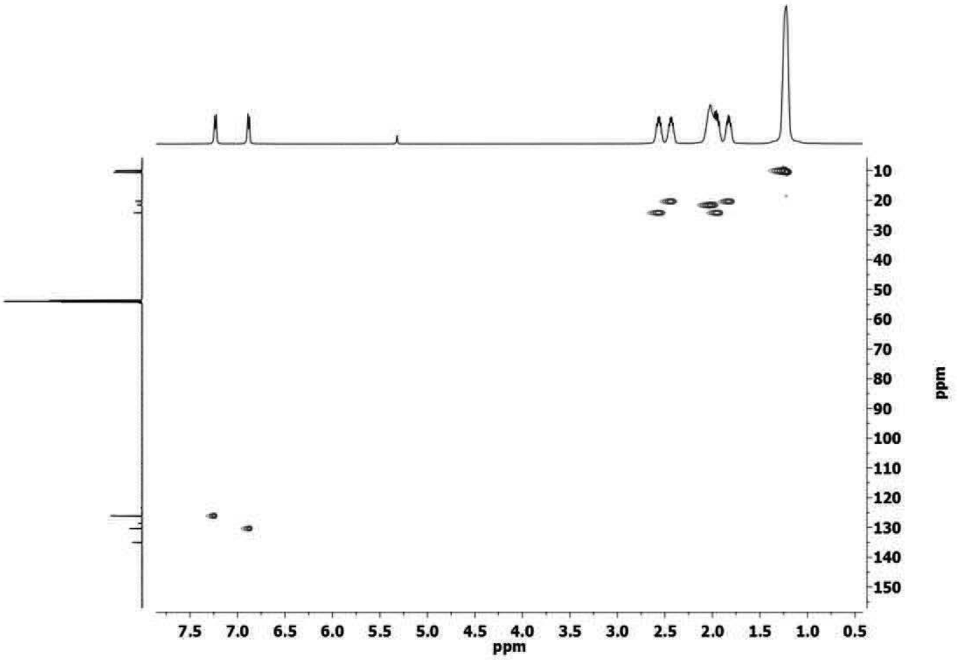

Figure S14. C,H Correlation of **3** in CD_2Cl_2

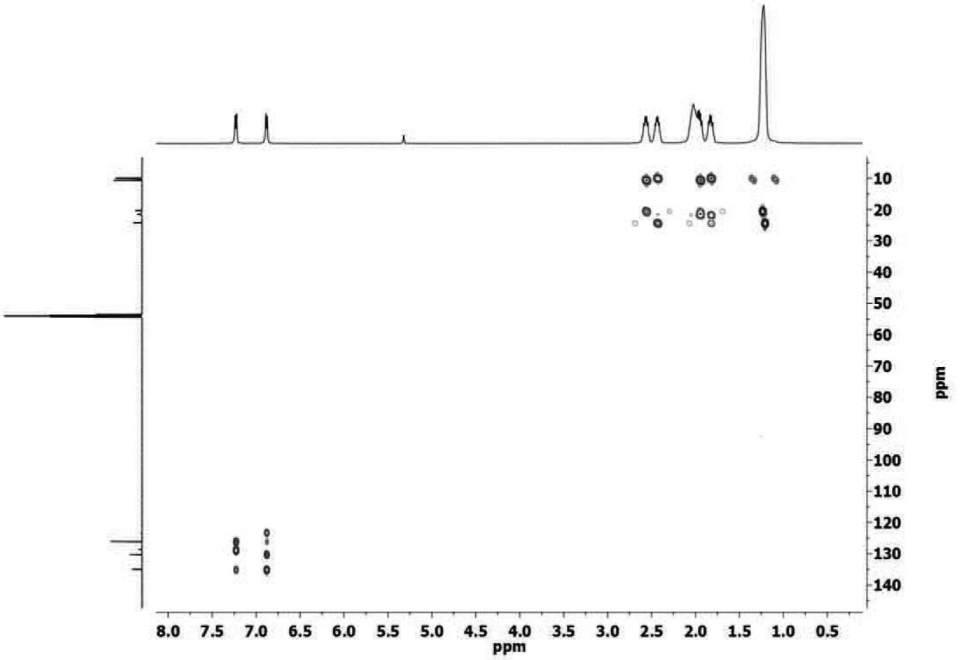

Figure S15. C,H Correlation (longrange) of **3** in CD_2Cl_2

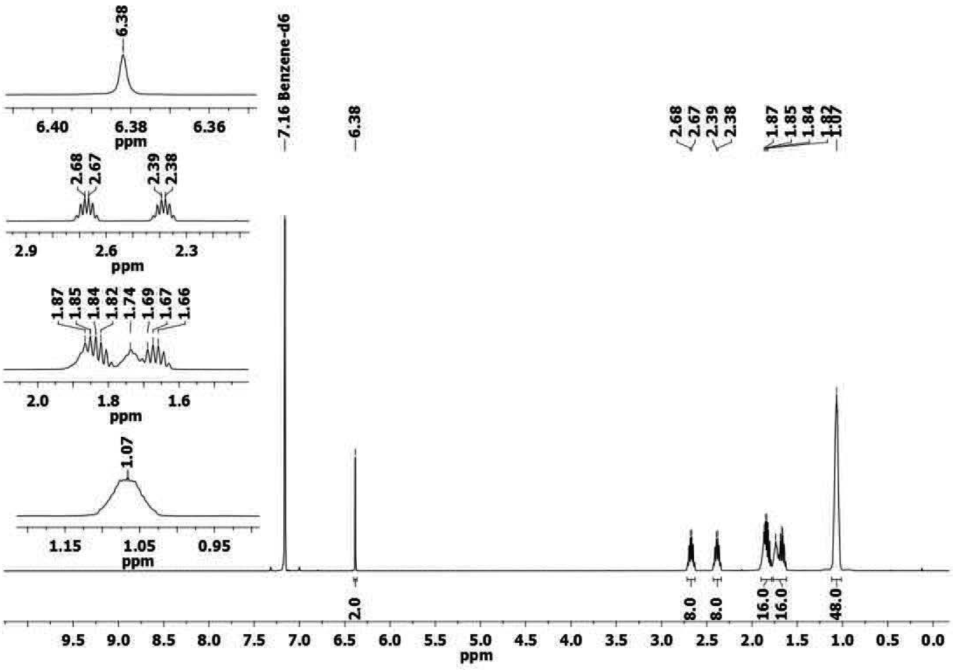

Figure S16. ^{1}H NMR of **4** in C_6D_6

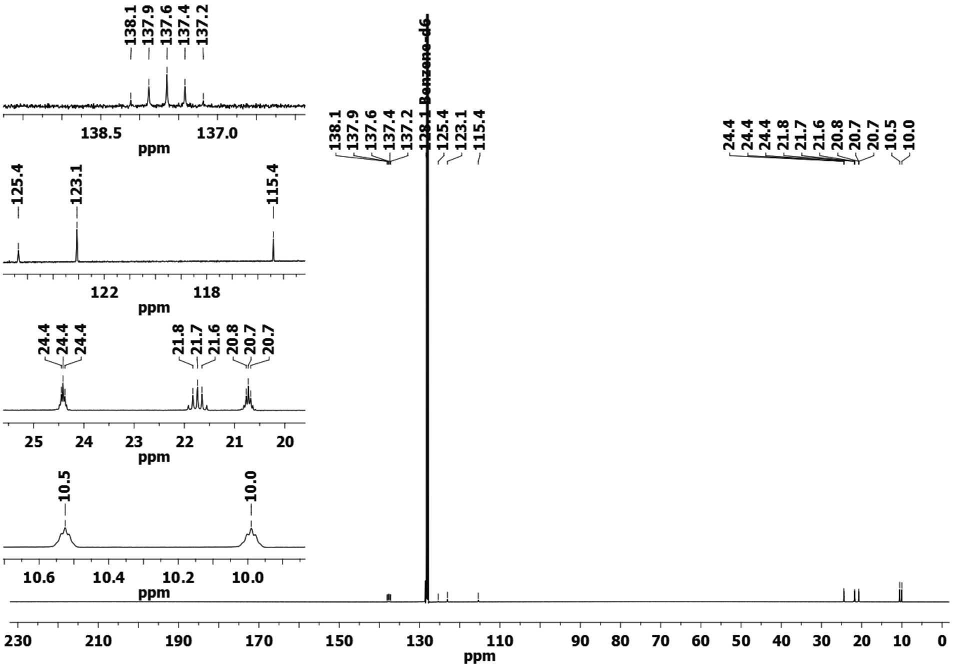

Figure S17. $^{13}C\{^1H\}$ NMR of **4** in C_6D_6

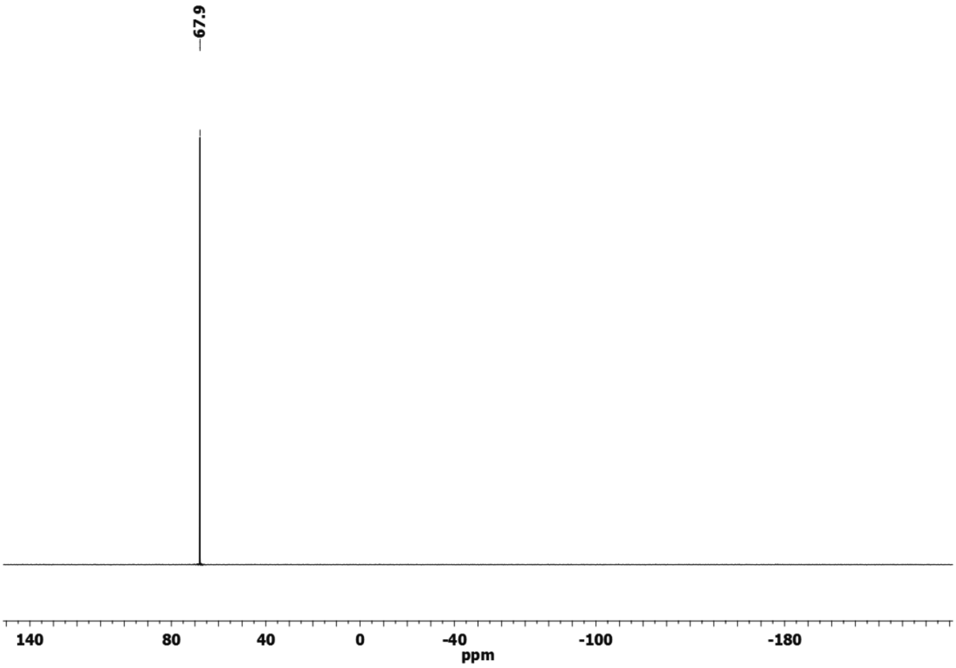

Figure S18. $^{31}P\{^1H\}$ NMR of **4** in C_6D_6

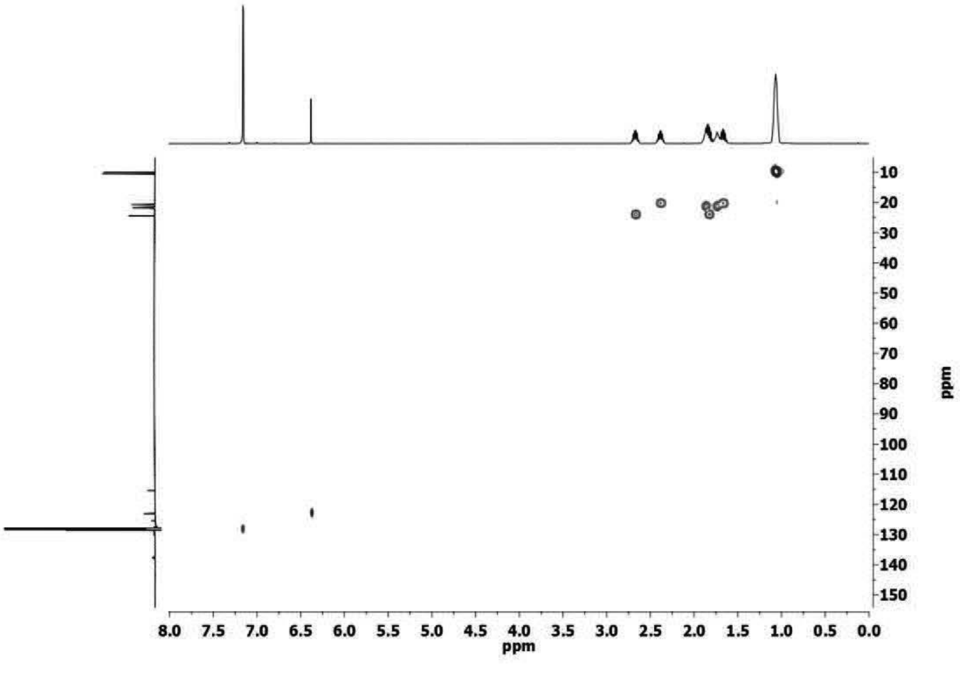

Figure S19. C,H-Correlation of **4** in C_6D_6

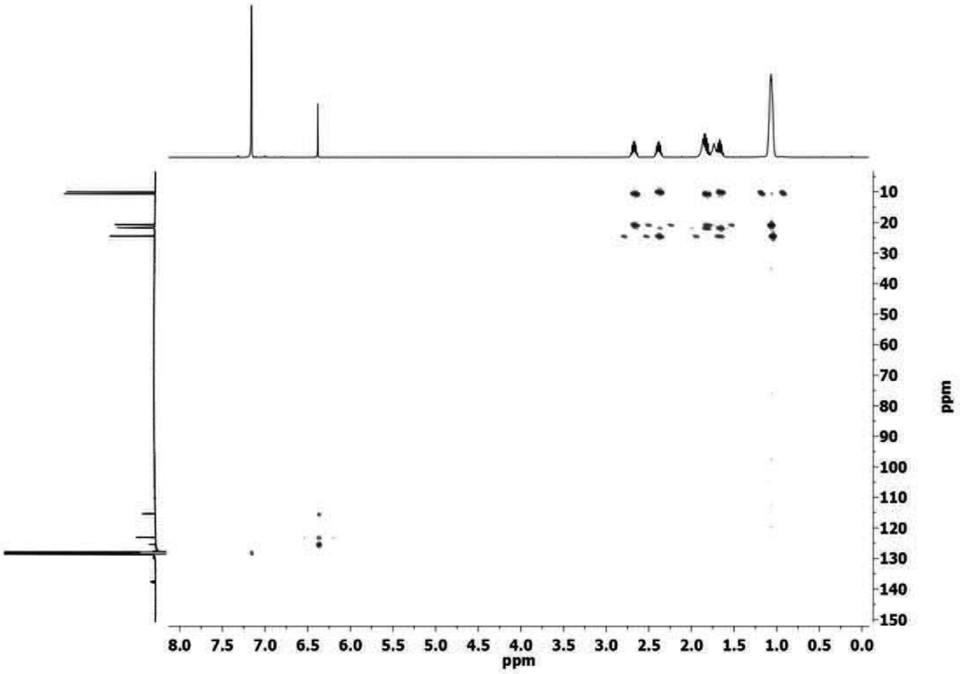

Figure S20. C,H-Correlation (longrange) of **4** in C_6D_6

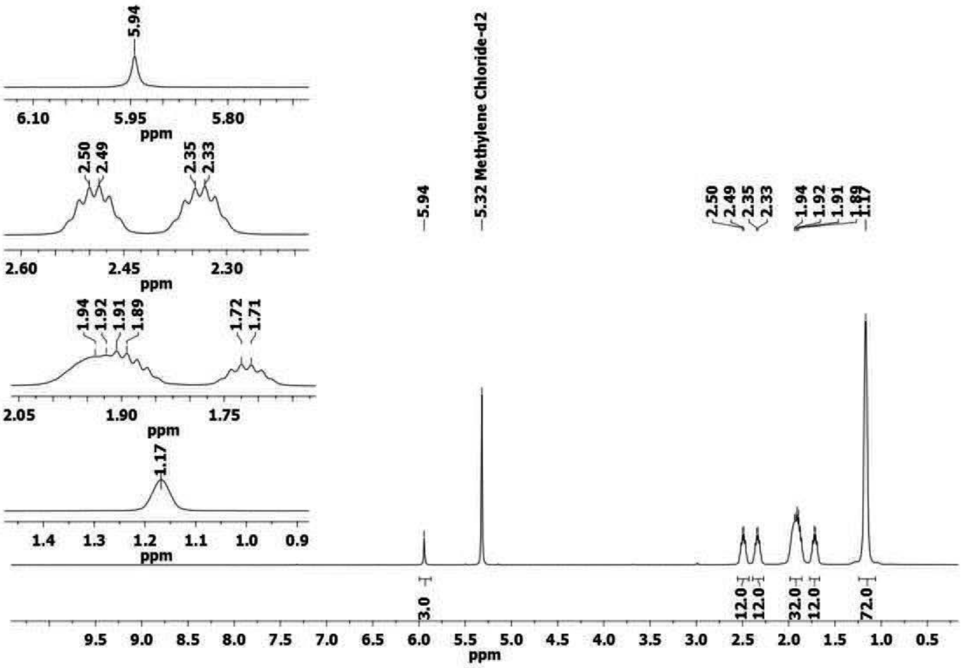

Figure S21. ^{1}H NMR of **5** in CD_2Cl_2

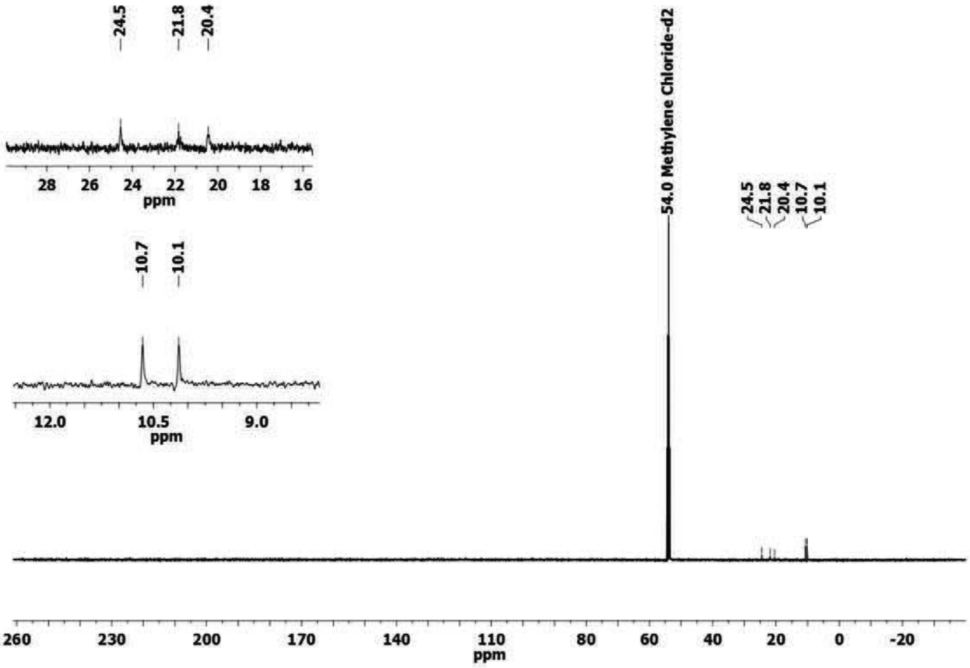

Figure S22. $^{13}C\{^{1}H\}$ NMR of **5** in CD_2Cl_2

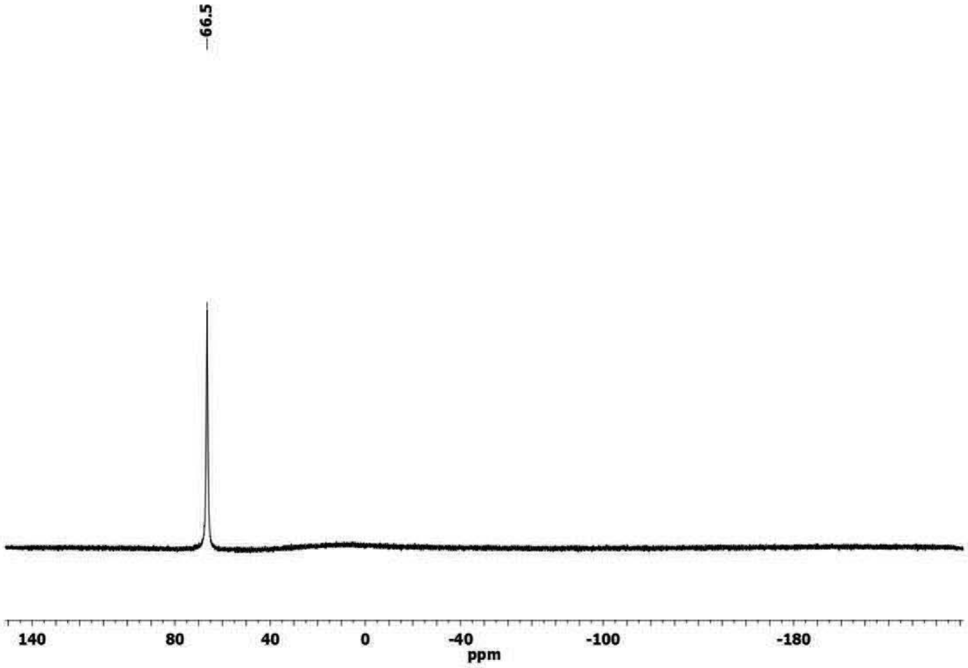

Figure S23. $^{31}P\{^{1}H\}$ NMR of **5** in CD_2Cl_2

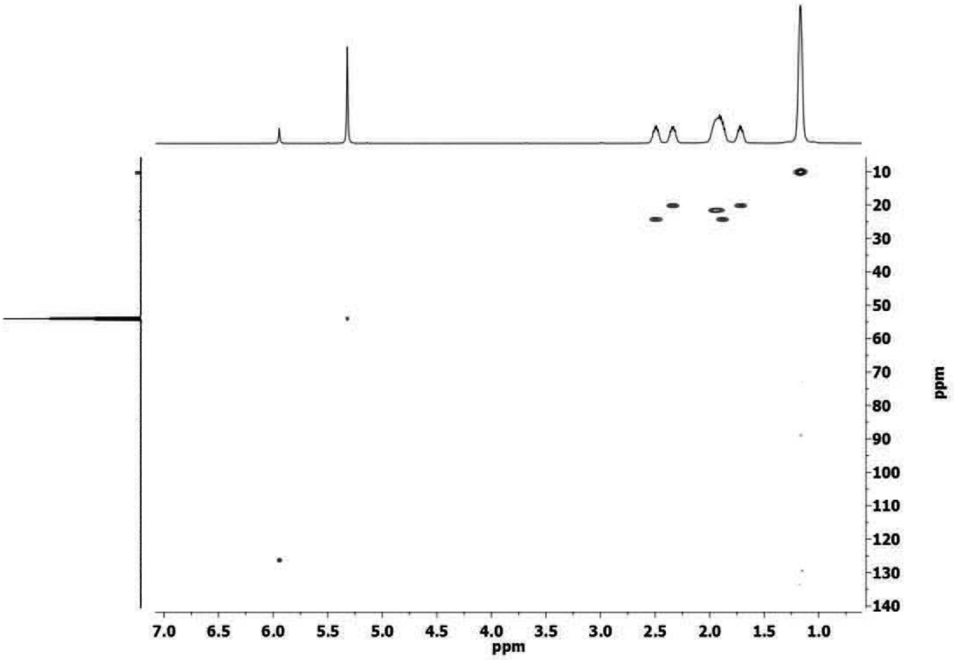

Figure S24. C,H Correlation of **5** in CD_2Cl_2

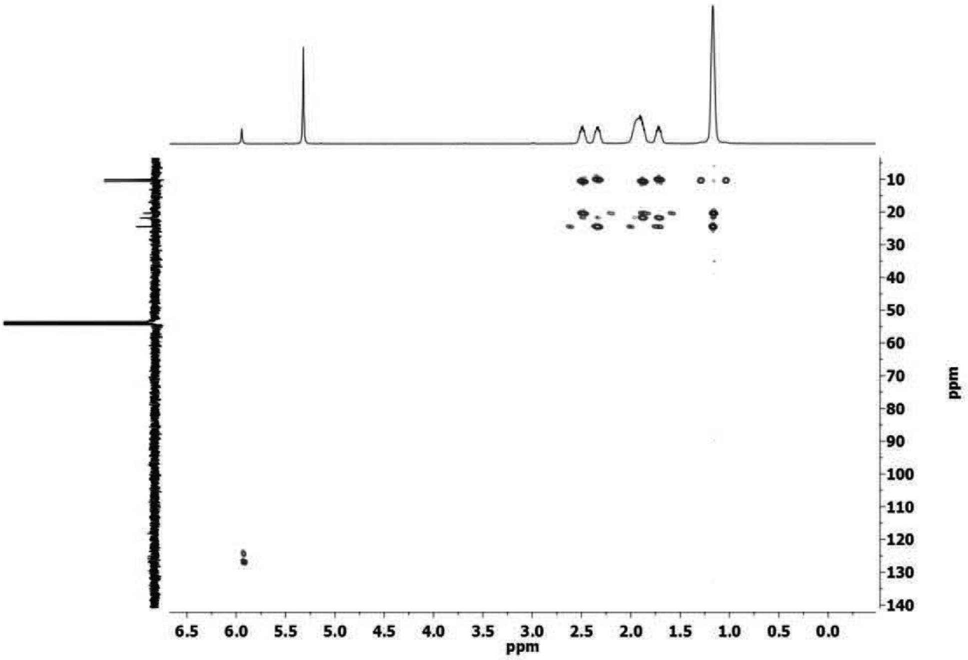

Figure S25. C,H Correlation (longrange) of **5** in CD_2Cl_2

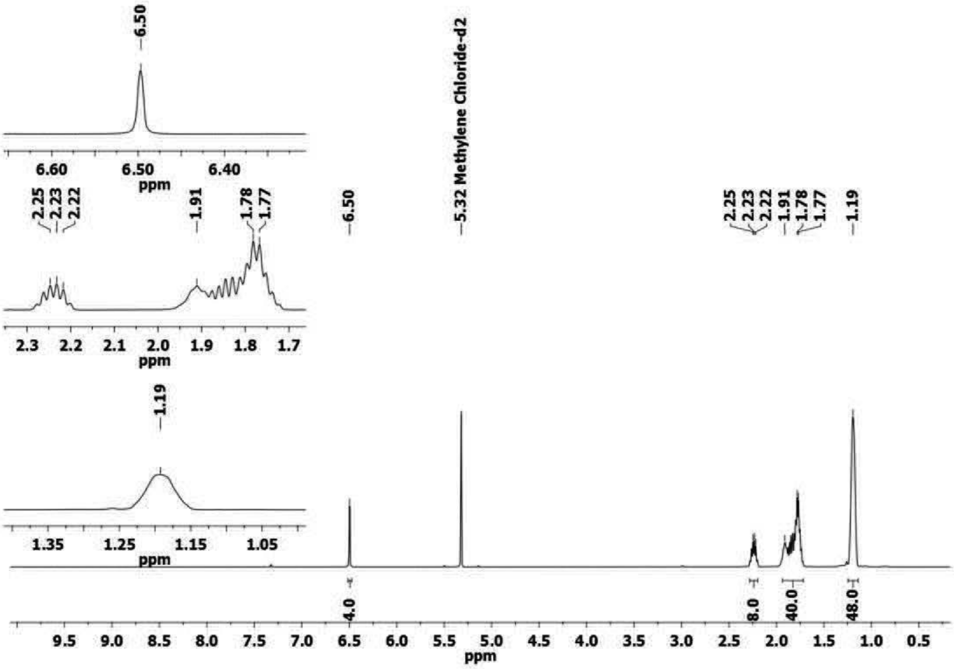

Figure S26. ^{1}H NMR of **6** in CD_2Cl_2

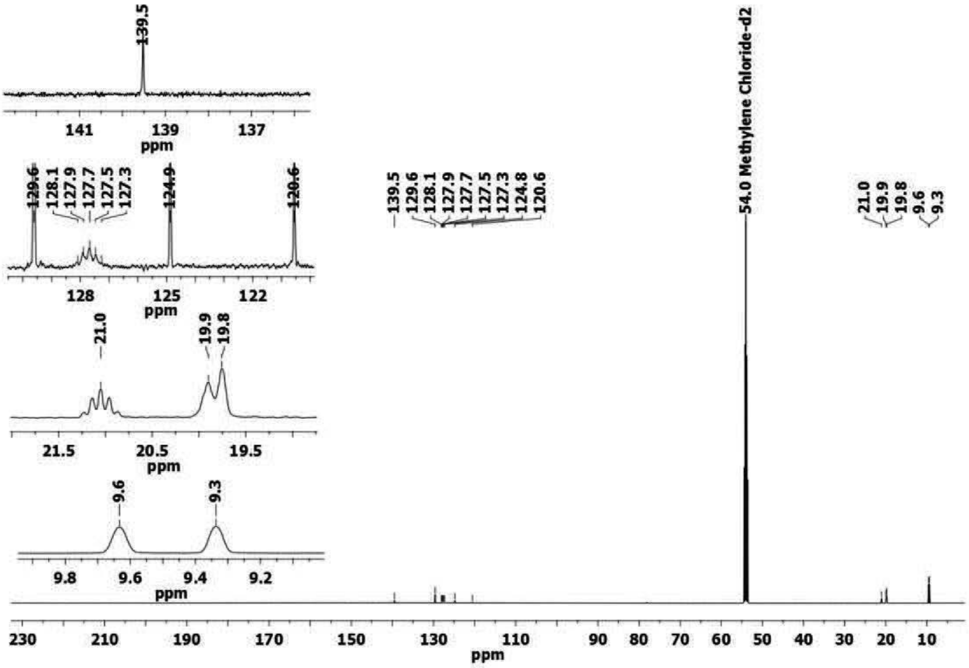

Figure S27. $^{13}C\{^1H\}$ NMR of **6** in CD_2Cl_2

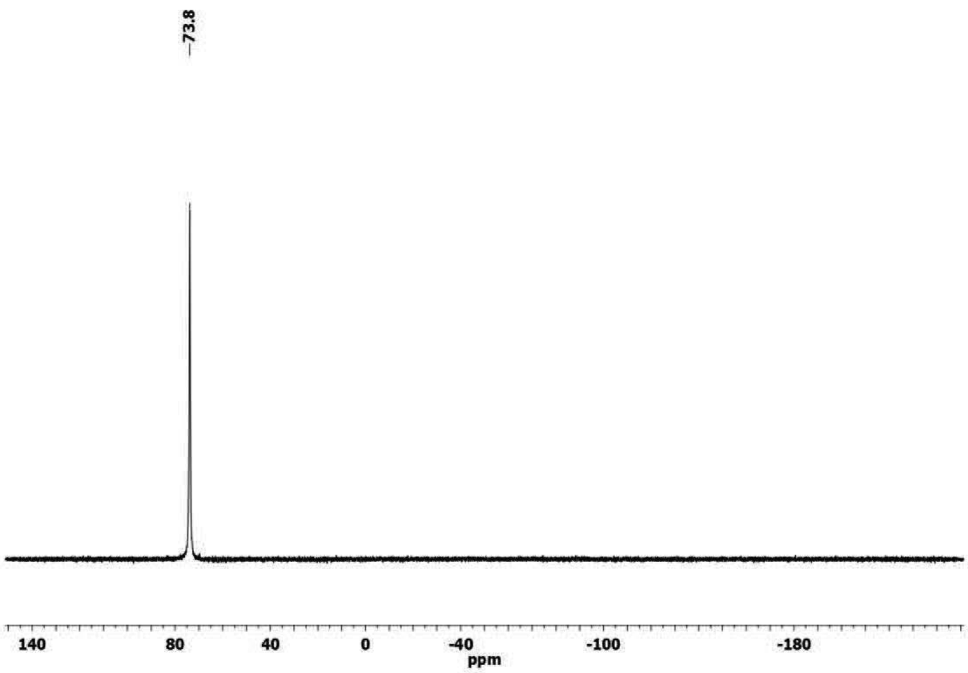

Figure S28. $^{31}P\{^1H\}$ NMR of **6** in CD_2Cl_2

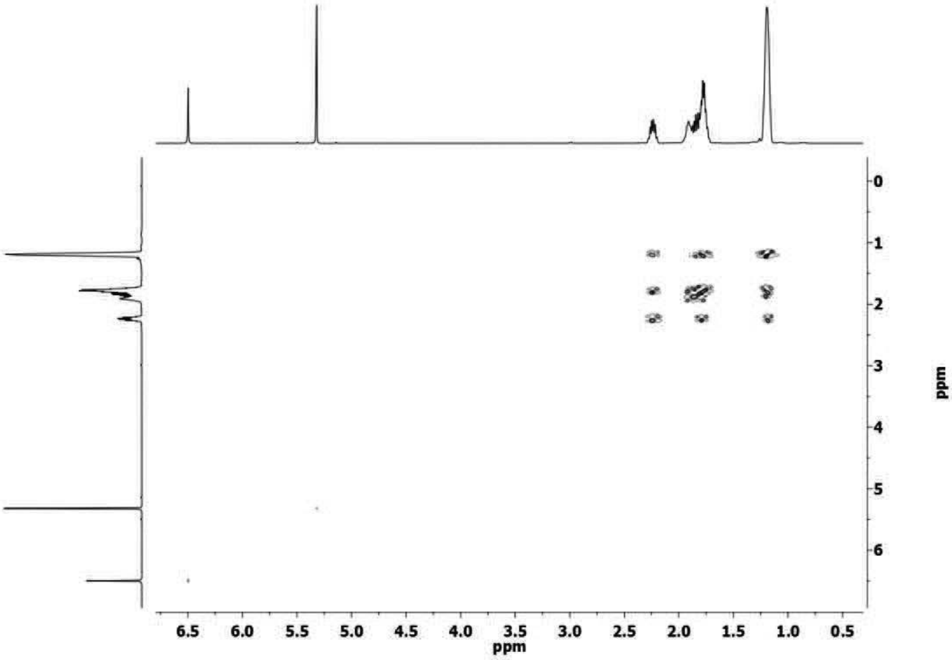

Figure S29. H,H Correlation (COSY) of **6** in CD_2Cl_2

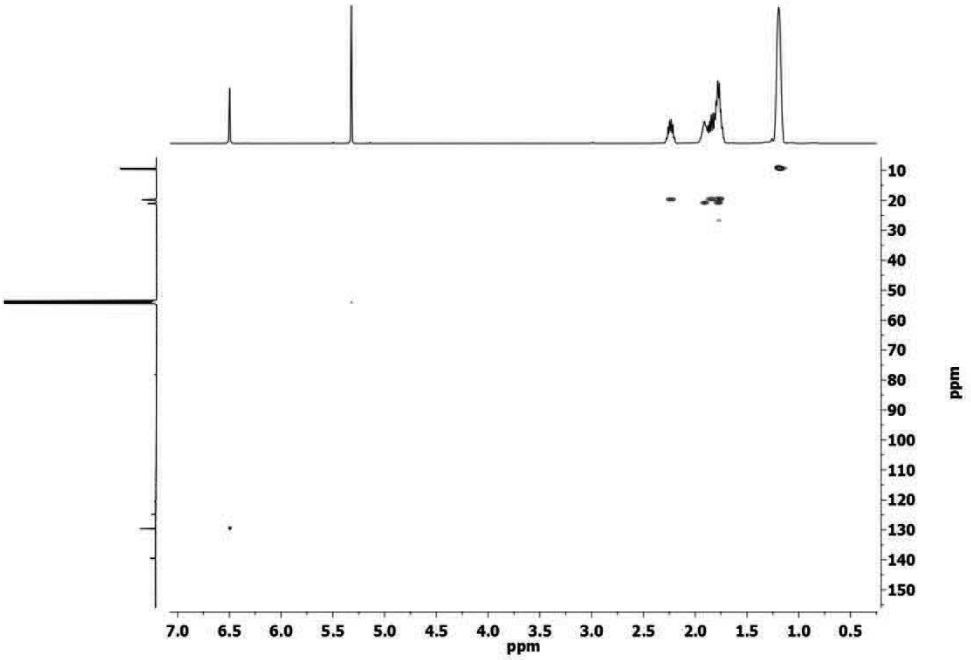

Figure S30. C,H Correlation of **6** in CD_2Cl_2

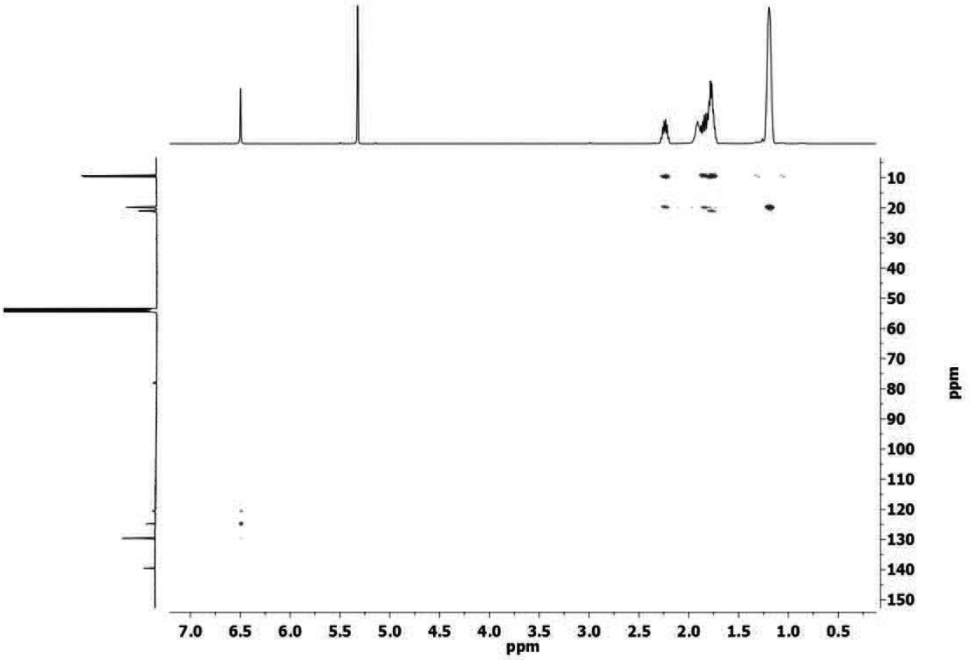

Figure S31. C,H Correlation (longrange) of **6** in CD_2Cl_2

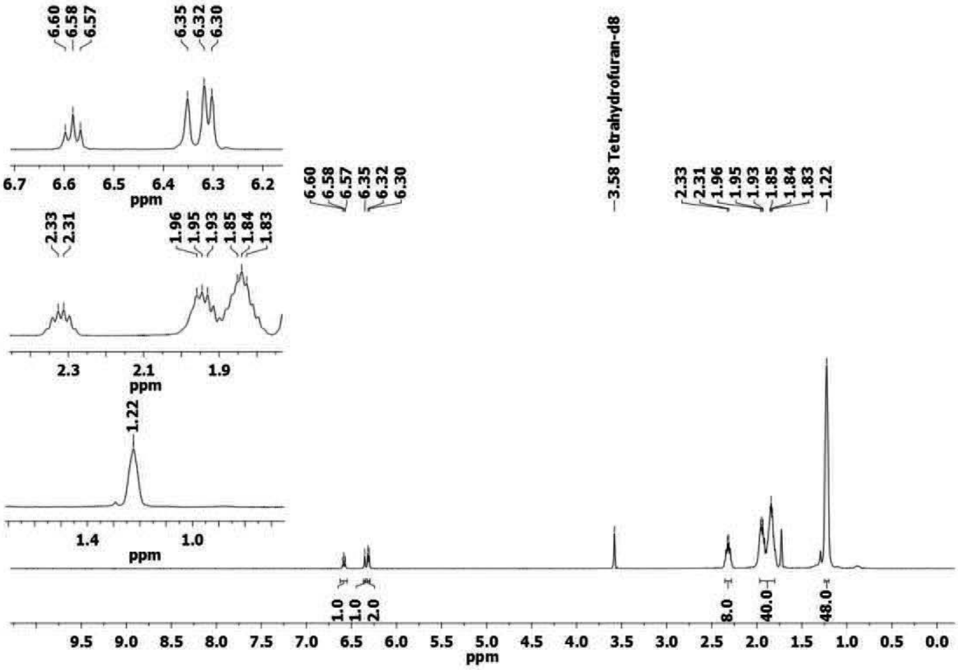

Figure S32. ^{1}H NMR of **7** in THF-d$_8$

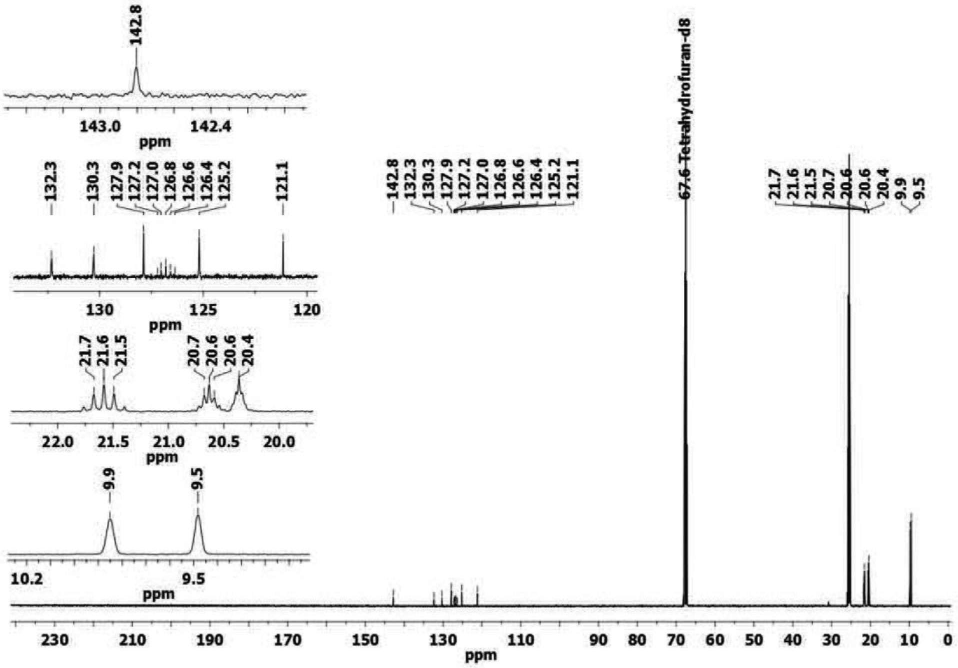

Figure S33. ^{13}C{^{1}H} NMR of **7** in THF-d$_8$

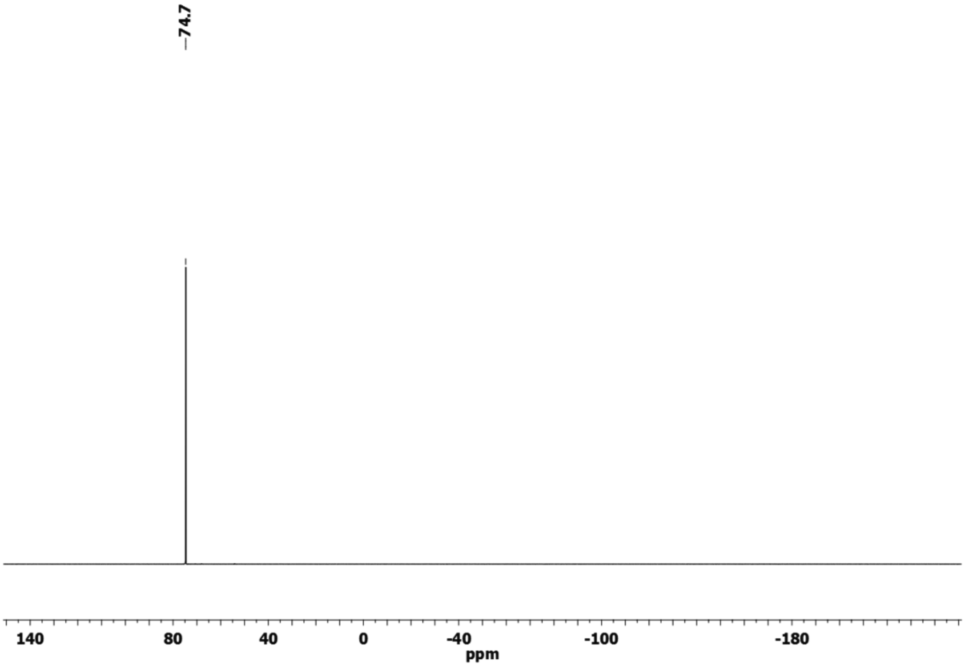

Figure S34. $^{31}P\{^{1}H\}$ NMR of **7** in THF-d_8

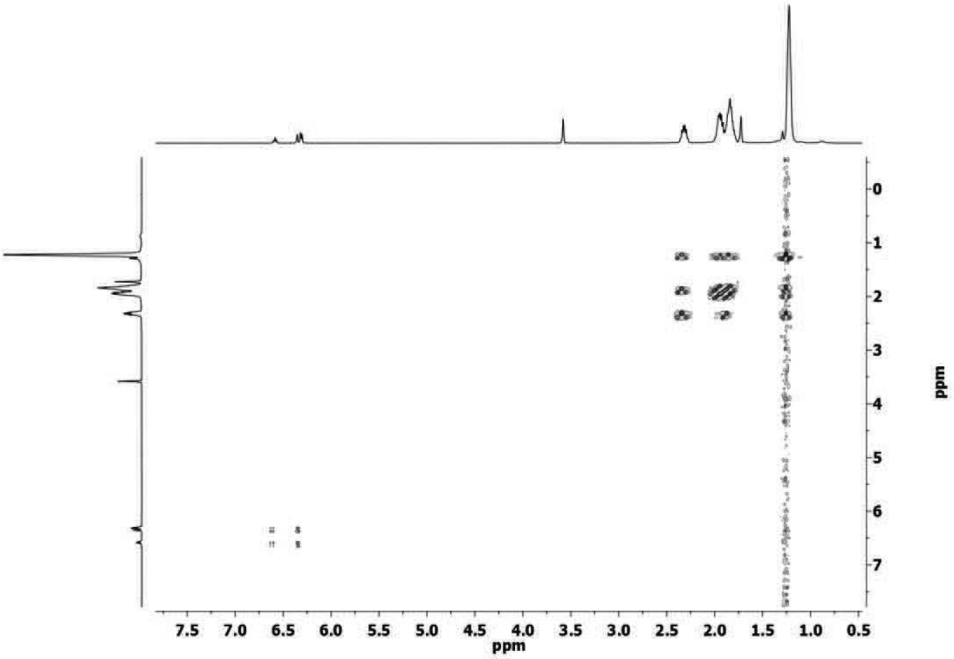

Figure S35. H,H Correlation (COSY) of **7** in THF-d_8

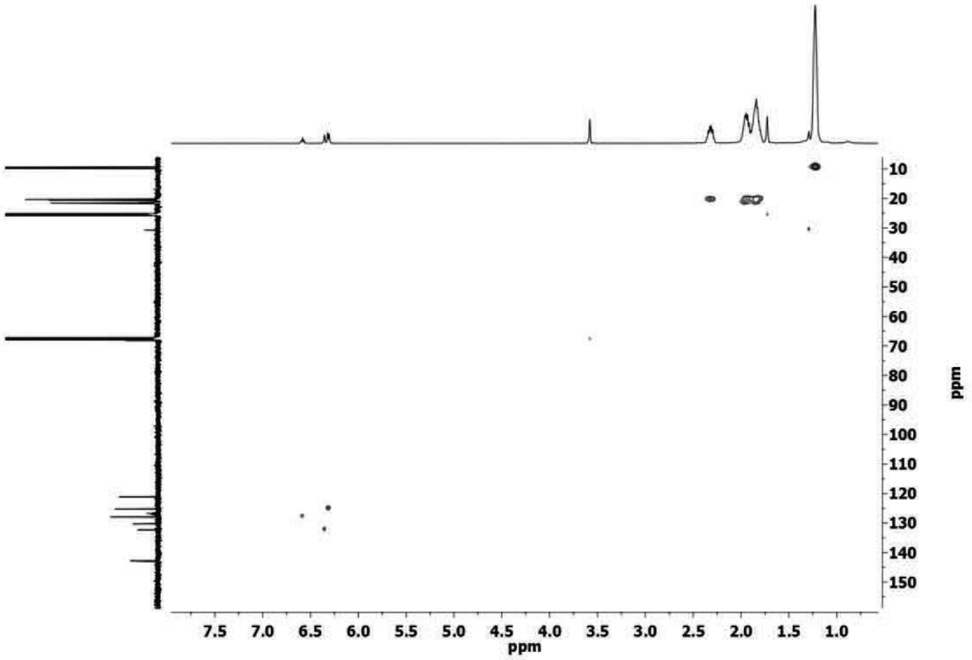

Figure S36. C, H Correlation of **7** in THF-d$_8$

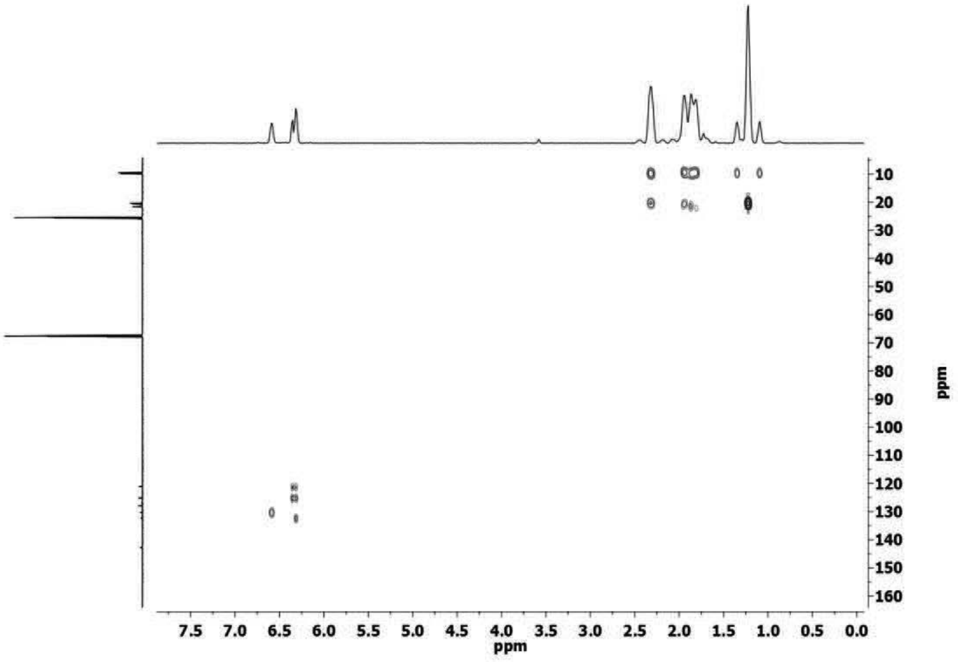

Figure S37. C, H Correlation (longrange) of **7** in THF-d$_8$

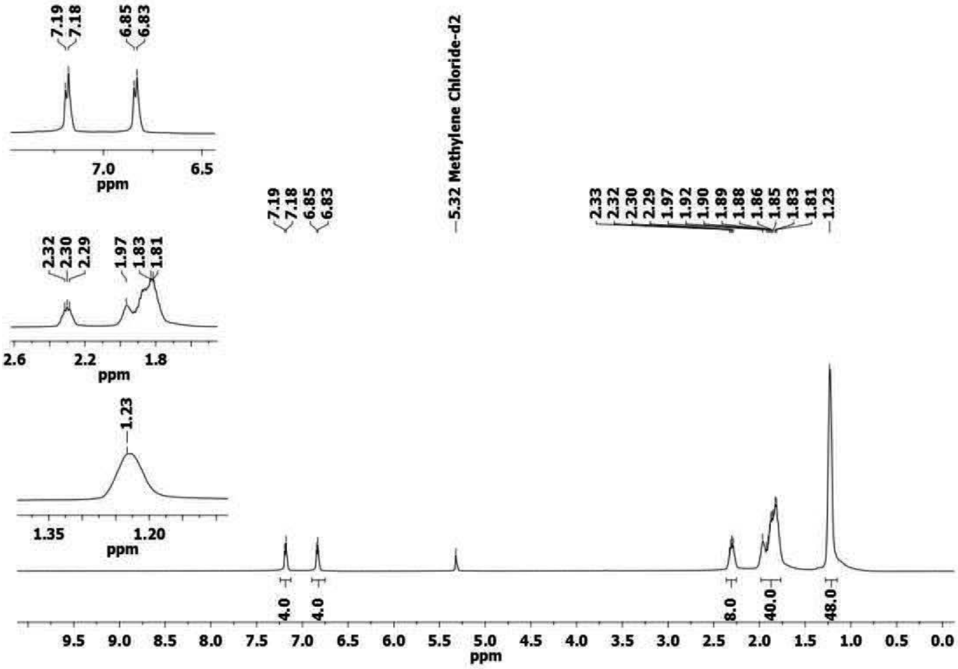

Figure S38. ^{1}H NMR of **8** in CD_2Cl_2

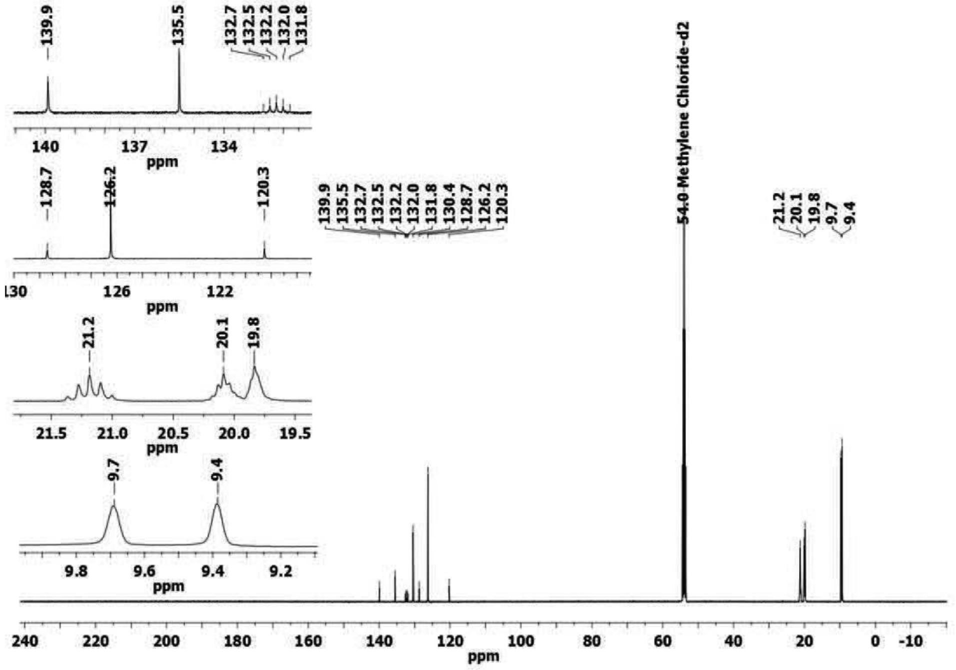

Figure S39. $^{13}C\{^1H\}$ NMR of **8** in CD_2Cl_2

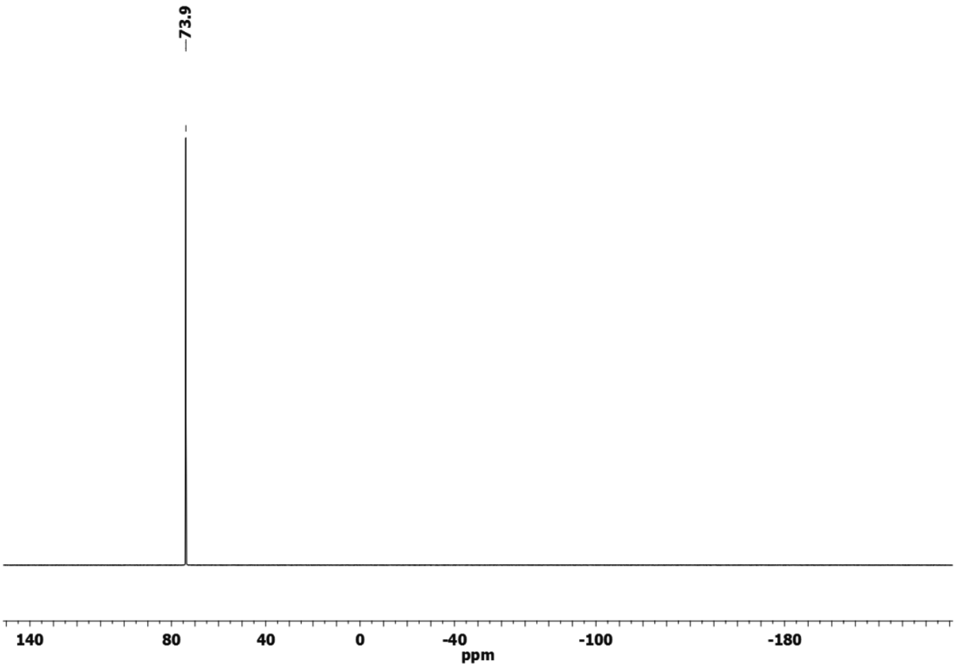

Figure S40. $^{31}P\{^{1}H\}$ NMR of **8** in CD_2Cl_2

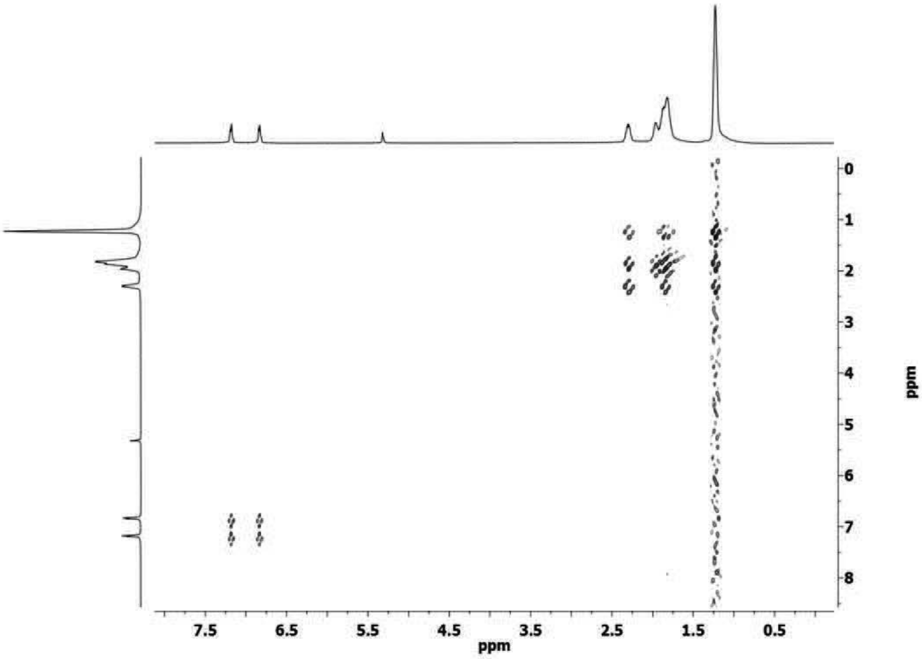

Figure S41. H,H Correlation (COSY) of **8** in CD_2Cl_2

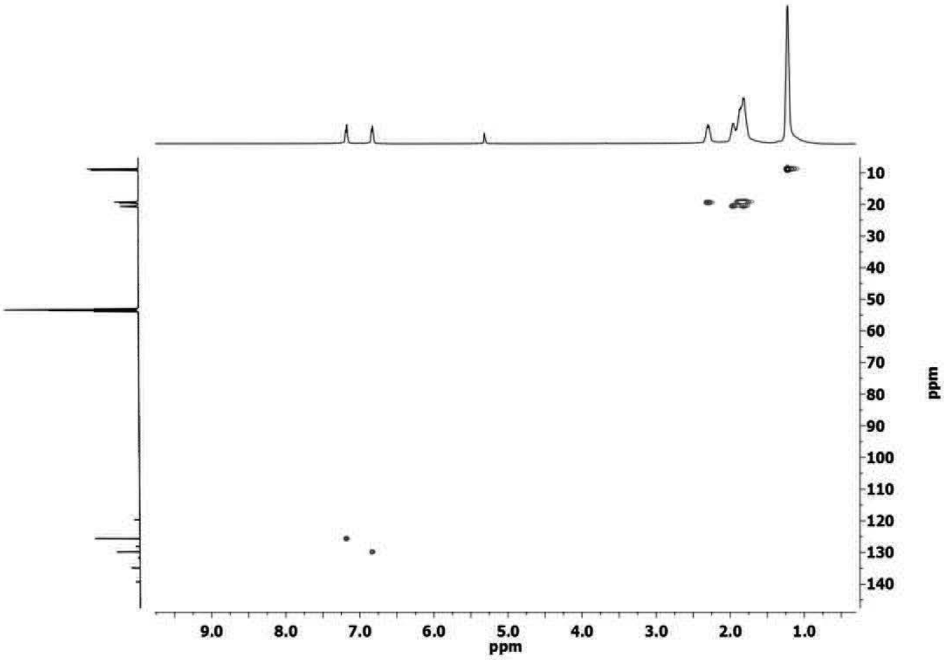

Figure S42. C,H Correlation of **8** in CD_2Cl_2

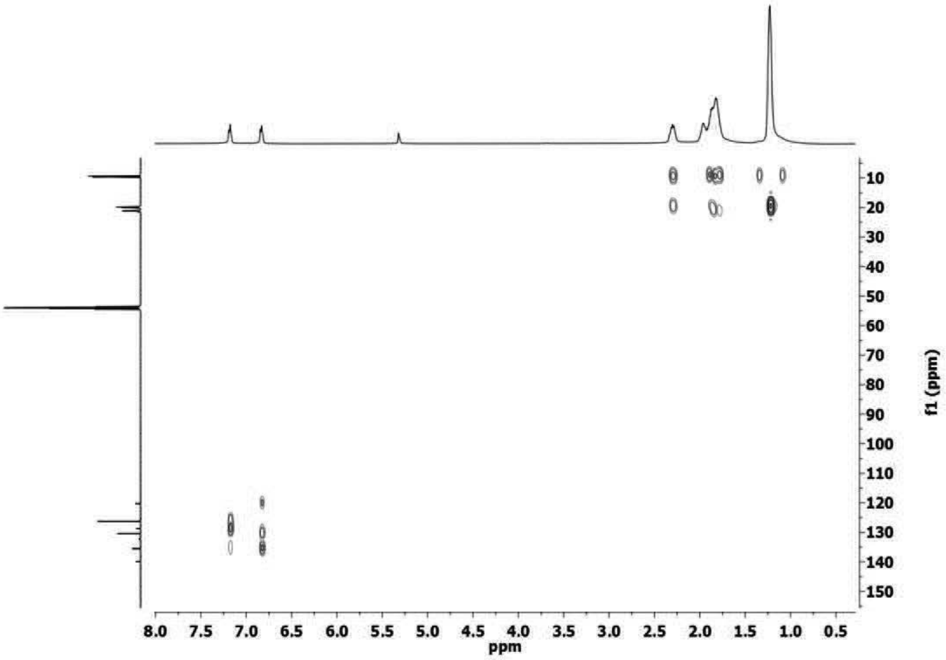

Figure S43. C,H Correlation (longrange) of **8** in CD_2Cl_2

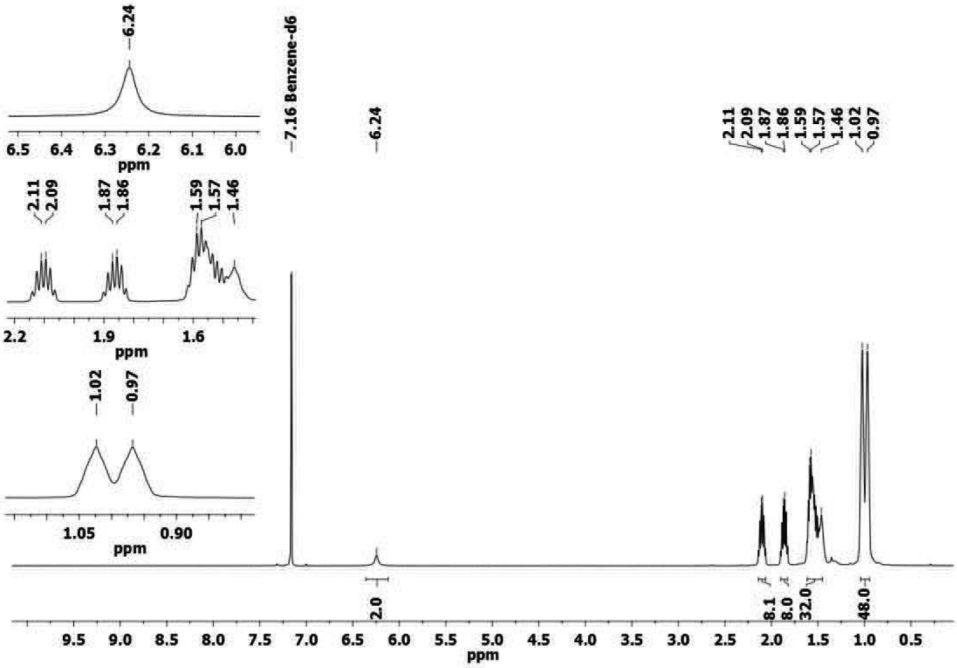

Figure S44. ^{1}H NMR of **9** in C_6D_6

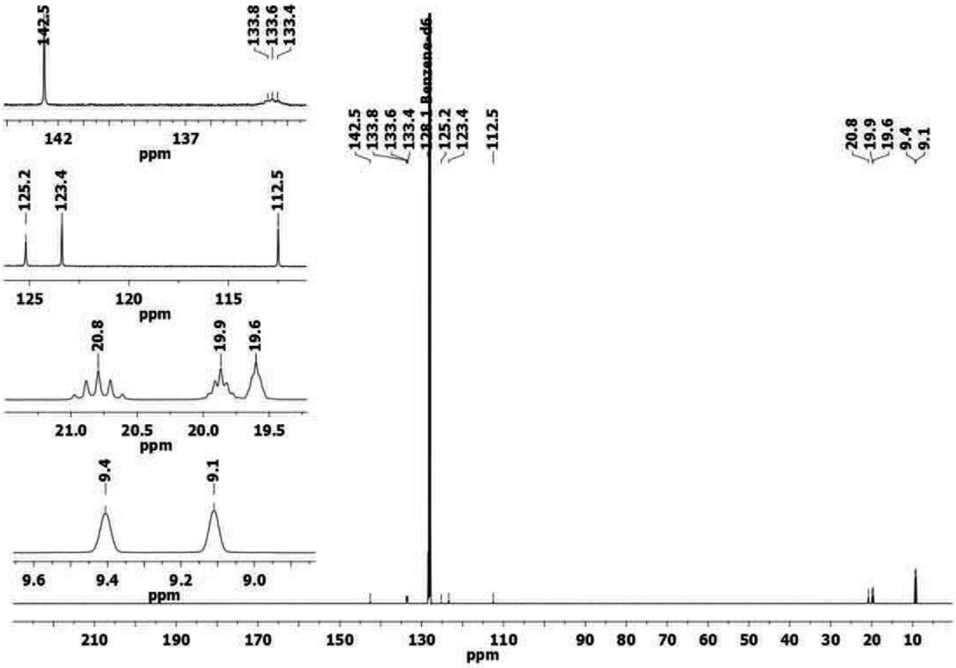

Figure S45. $^{13}C\{^1H\}$ NMR of **9** in C_6D_6

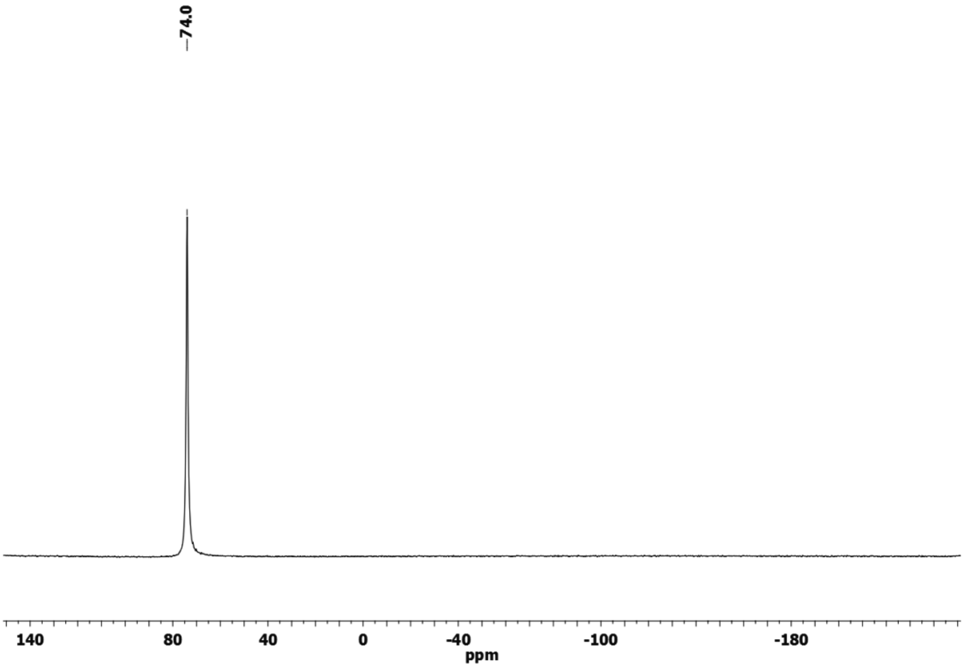

Figure S46. $^{31}P\{^{1}H\}$ NMR of **9** in C_6D_6

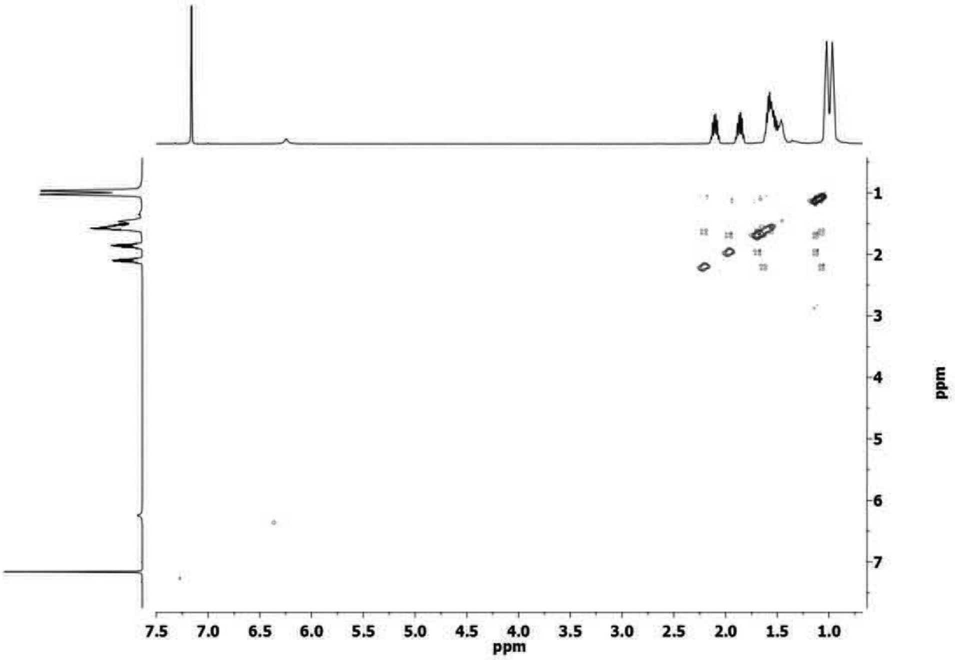

Figure S47. H,H Correlation (COSY) of **9** in C_6D_6

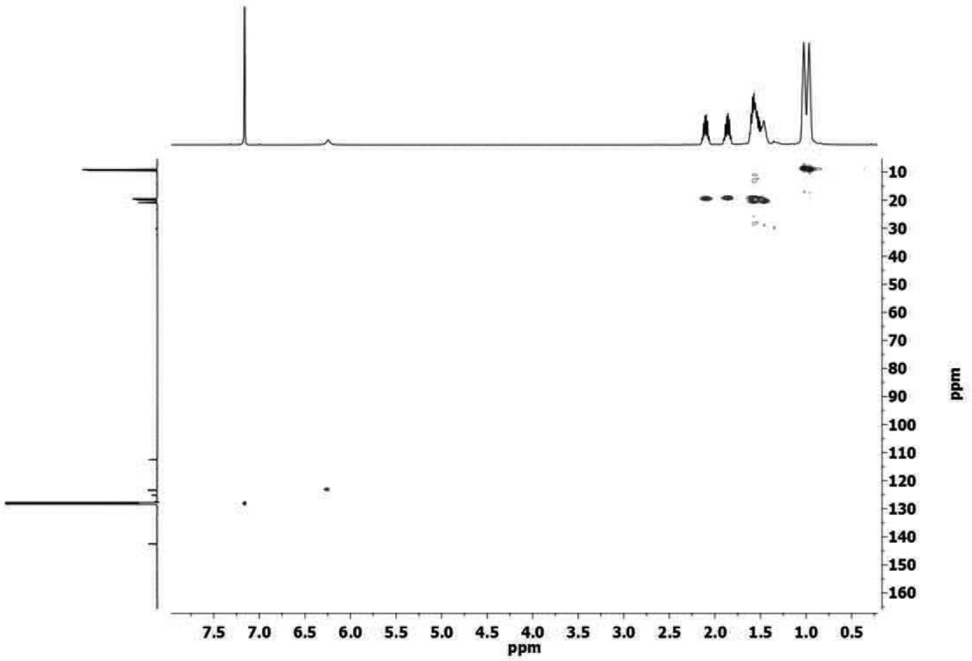

Figure S48. C,H Correlation of **9** in C_6D_6

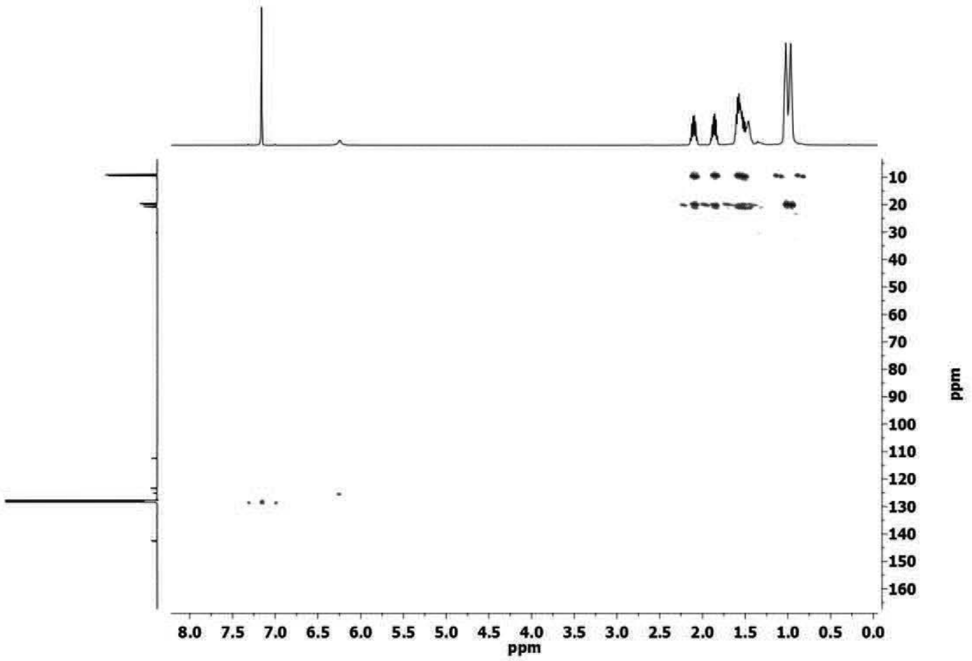

Figure S49. C,H Correlation (longrange) of **9** in C_6D_6

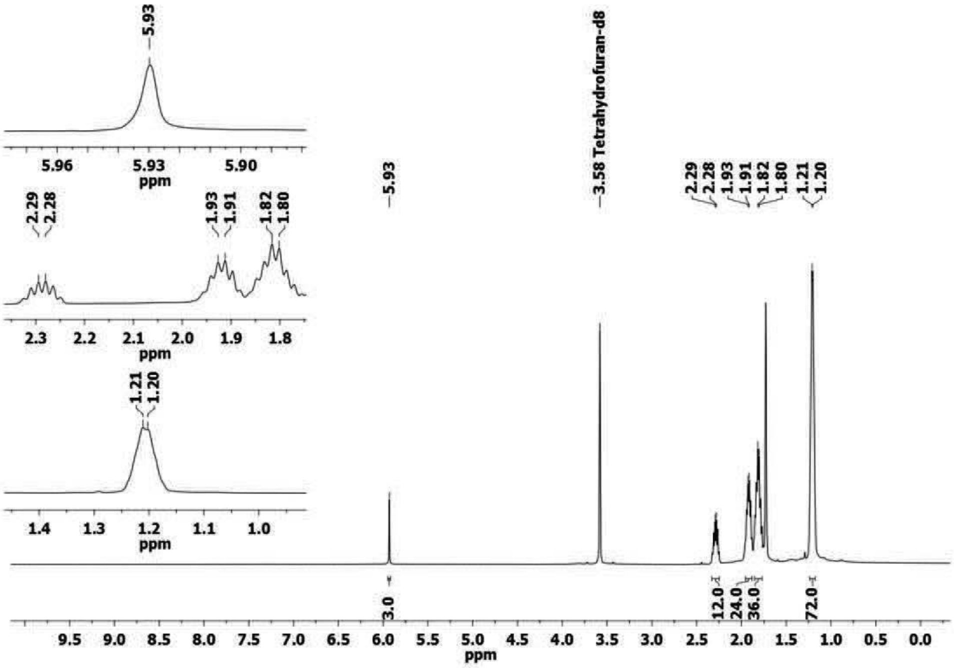

Figure S50. ^{1}H NMR of **10** in THF-d_8

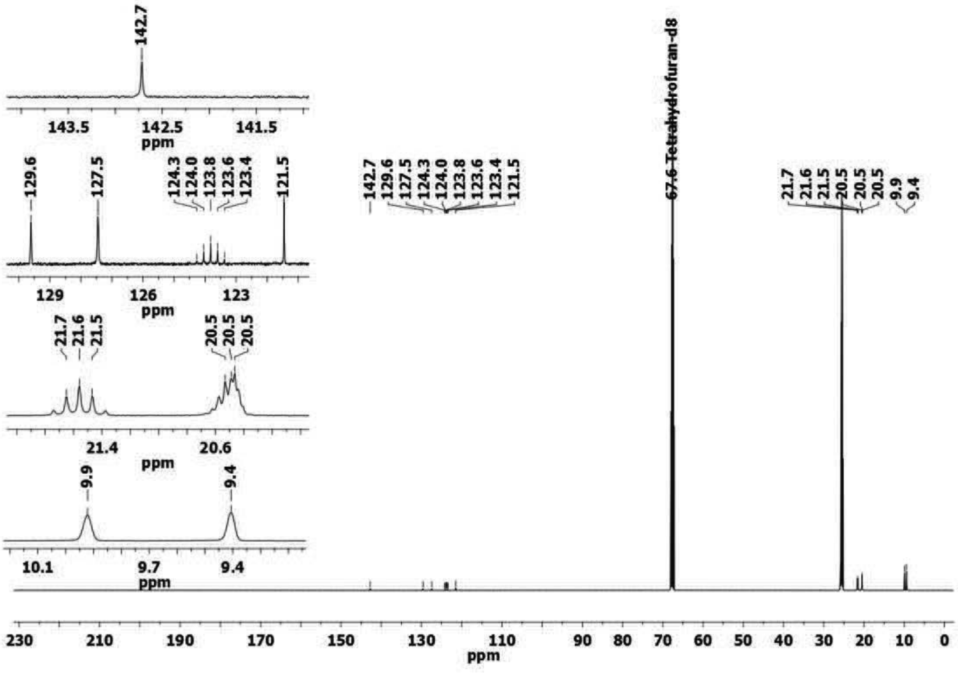

Figure S51. $^{13}C\{^1H\}$ NMR of **10** in THF-d_8

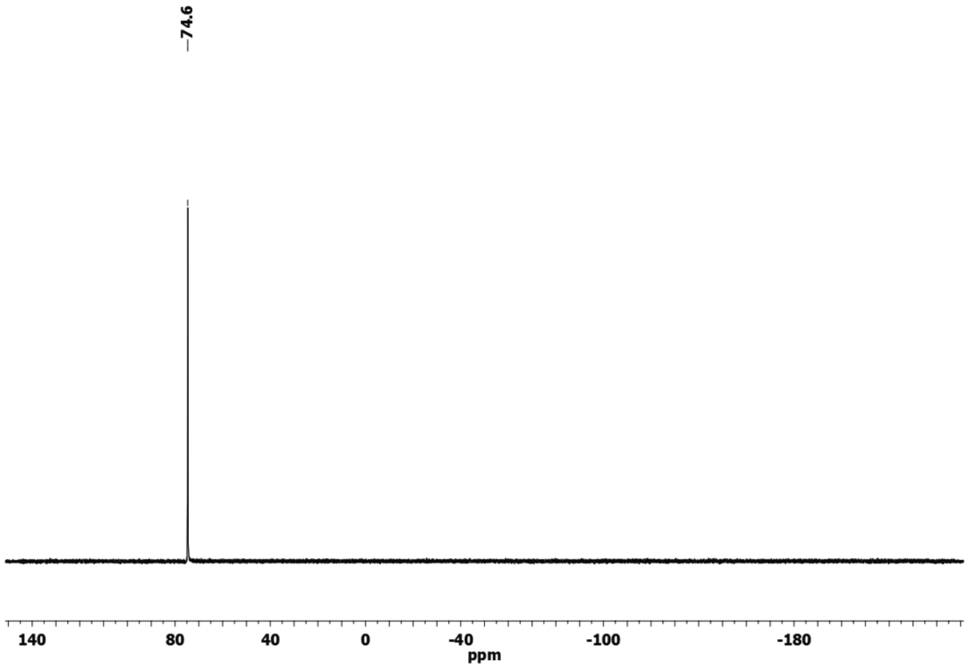

Figure S52. $^{31}P\{^{1}H\}$ NMR of **10** in THF-d$_8$

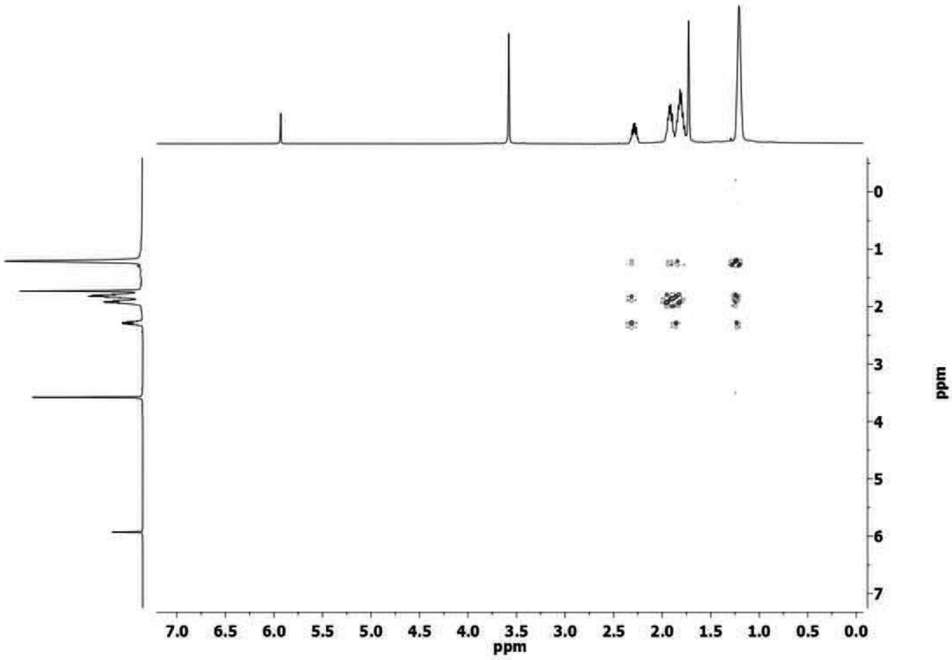

Figure S53. H,H Correlation (COSY) of **10** in THF-d$_8$

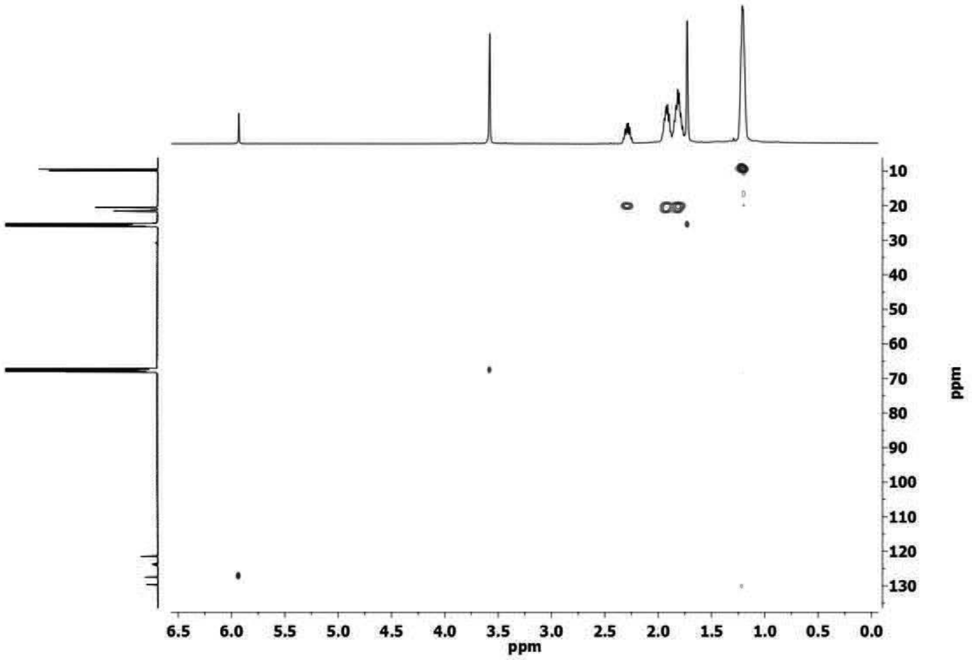

Figure S54. C,H Correlation of **10** in THF-d_8

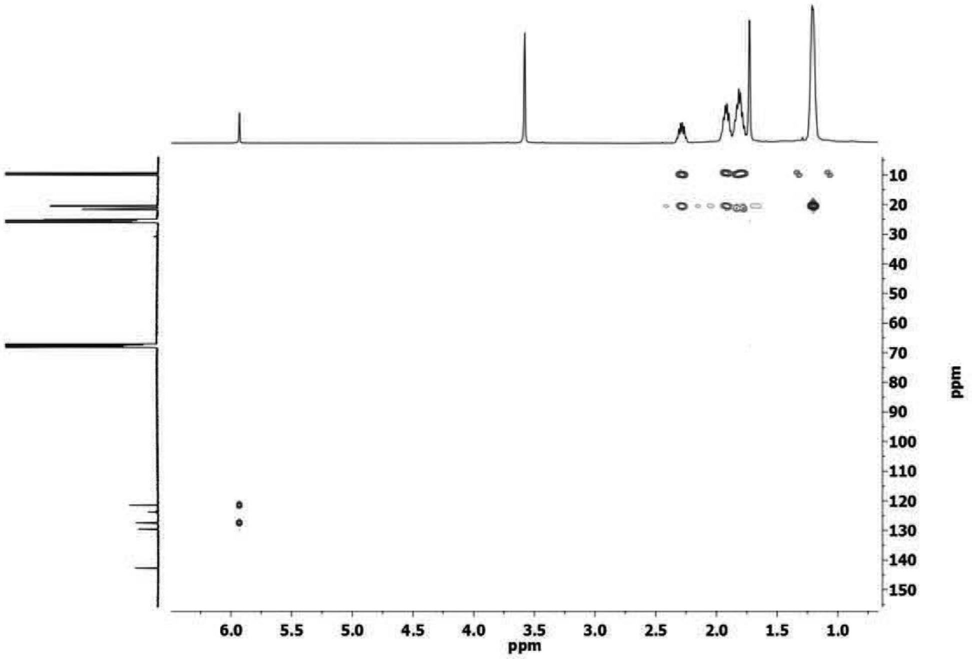

Figure S55. C,H Correlation (longrange) of **10** in THF-d_8

Infrared Spectra

Table S1. IR and Raman ν(C_4) bands of the bridging butadiyne unit of compounds **1 - 10**.

No.	**IR [cm^{-1}] ν_{as}(C≡C)**	**IR [cm^{-1}] ν_{as}(C=C)**	**Raman [cm^{-1}] ν_{s}(C≡C)**	**Raman [cm^{-1}] ν_{s}(C=C)**	**ν(C≡N) [cm^{-1}]**
1	2028 (vs)	1489 (m)	2030 (m)	1586 (s)	---
2	2036 (vs)	1571 (s), 1551 (m)	2040 (s)	1574 (m)	---
3	2023 (vs)	1595 (m), 1480 (s)	2040 (w)	1591 (vs)	---
4	2034(s)	1502 (w)	2032 (m)	1439 (vs)	---
5	2046 (vs)	1551 (vs)	2049 (s)	1561 (m)	---
6	2044(s)	1489 (m)	2043 (m)	1590 (s)	2092 (ν_{as}, s)
7	2041 (vs)	1574 (s), 1552 (m)	2040 (vs)	1578 (m), 1552 (w)	2092 (ν_{as}, s); 2097 (ν_{s}, m)
8	2034 (vs)	1596 (s), 1481 (s)	2045 (w)	1591 (vs), 1522 (vw)	2094 (ν_{as}, s)
9	2031(s)	1503 (w)	2036 (m)	1434 (vs)	2094 (ν_{as}, s); 2097 (ν_{s}, w)
10	2043 (vs)	1552 (s)	2053 (vs)	1556 (m, br, sh at 1575)	2096 (ν_{as}, vs); 2101 (ν_{s}, m)

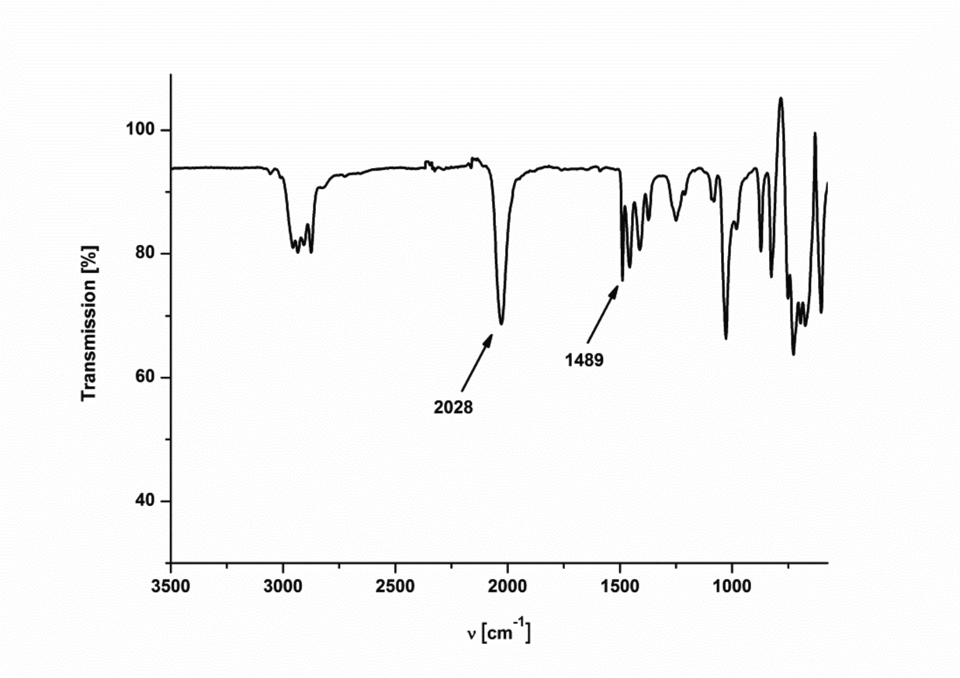

***Figure S56**.* IR spectrum (ATR) of **1**

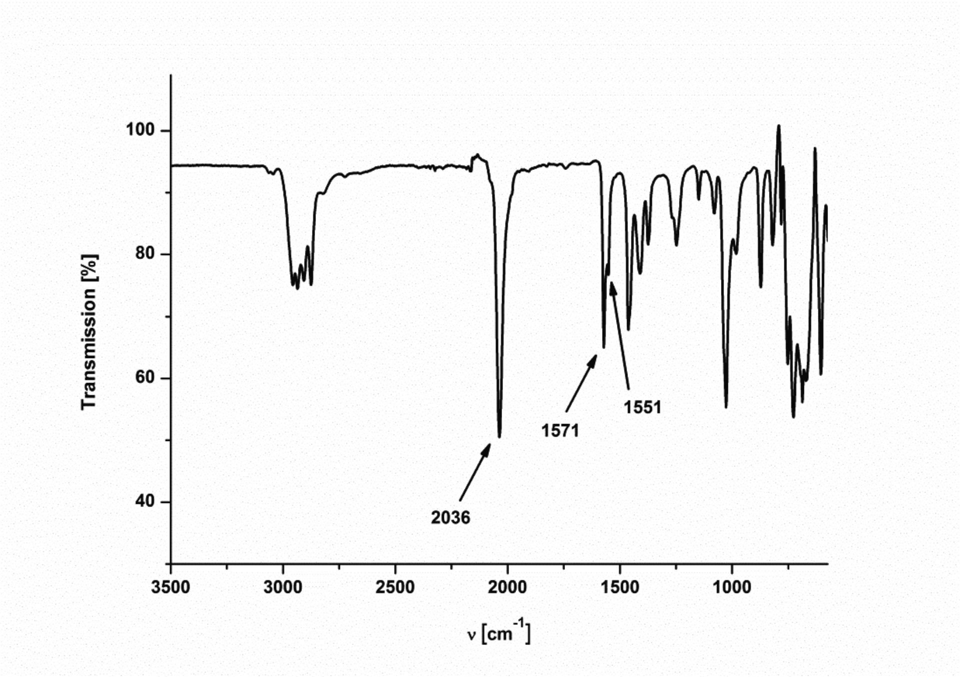

***Figure S57**.* IR spectrum (ATR) of **2**

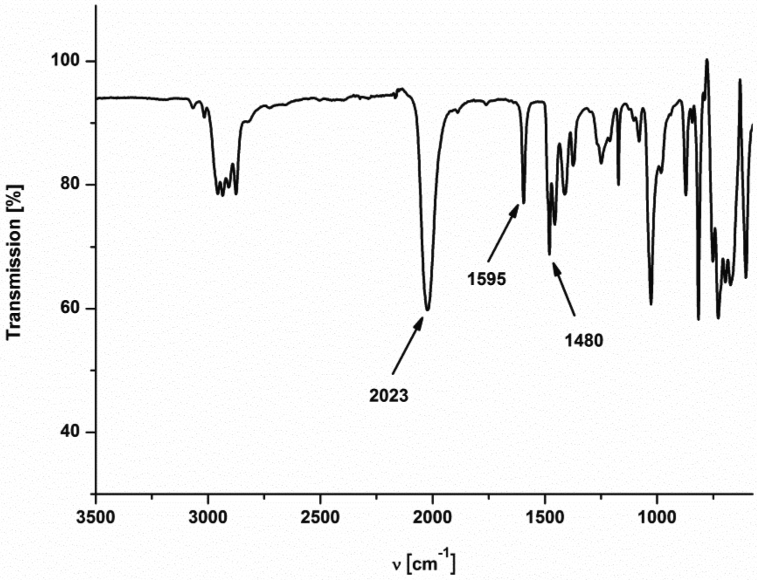

Figure S58. IR spectrum (ATR) of **3**

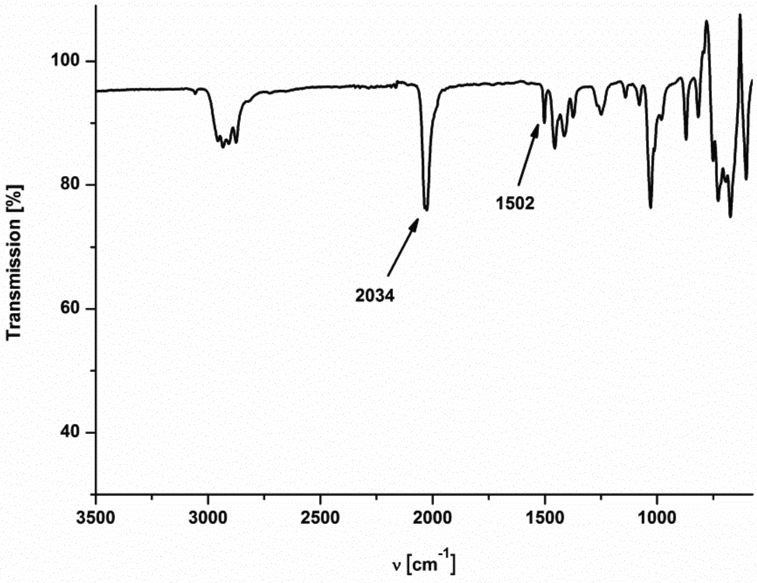

Figure S59. IR spectrum (ATR) of **4**

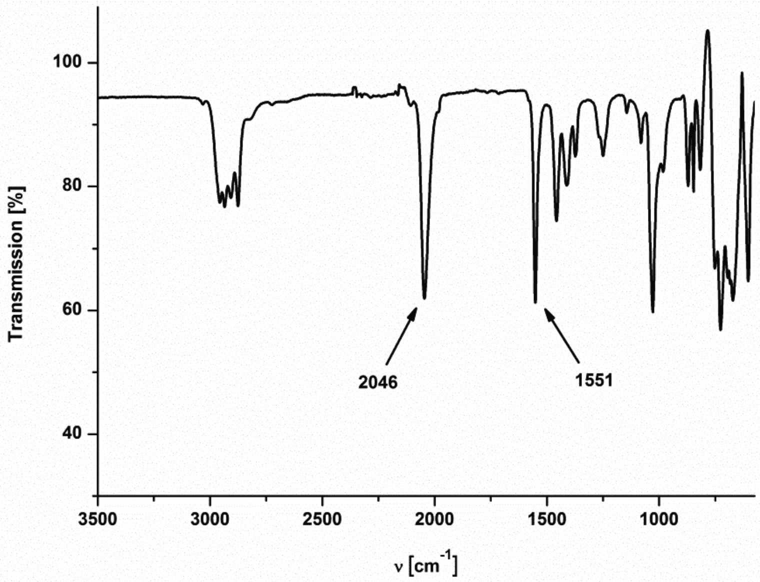

Figure S60. IR spectrum (ATR) of **5**

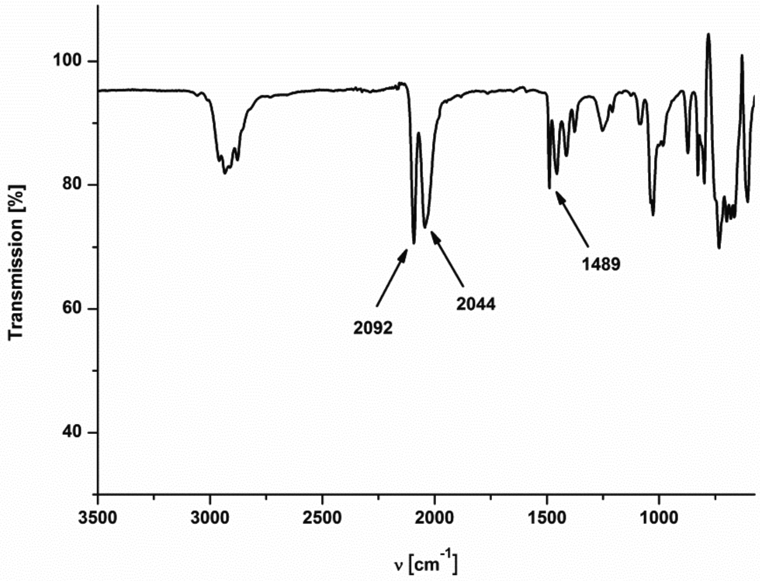

Figure S61. IR spectrum (ATR) of **6**

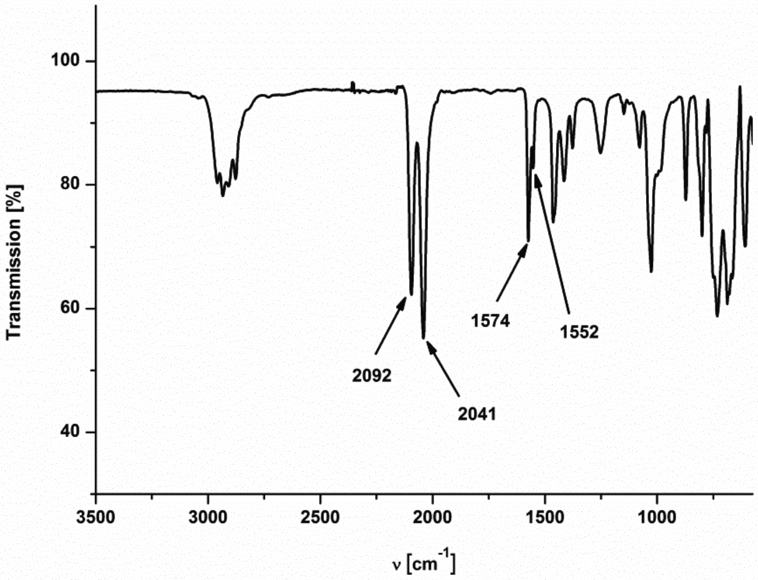

Figure S62. IR spectrum (ATR) of **7**

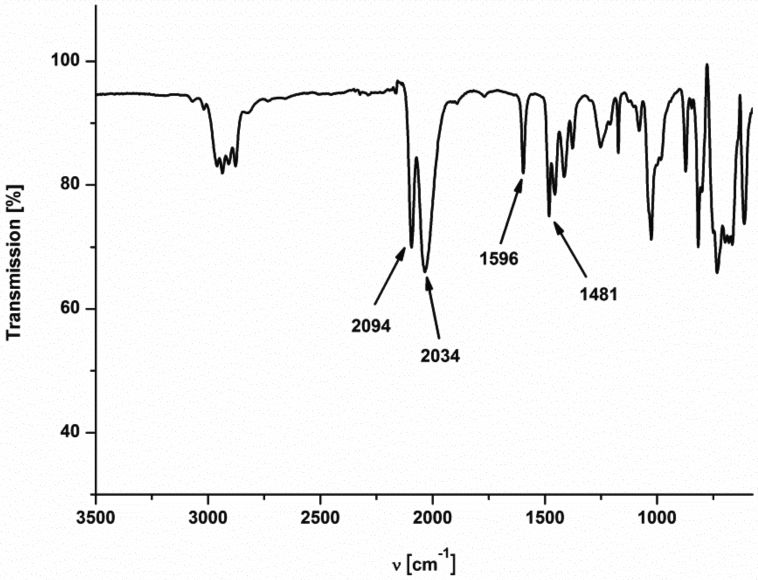

Figure S63. IR spectrum (ATR) of **8**

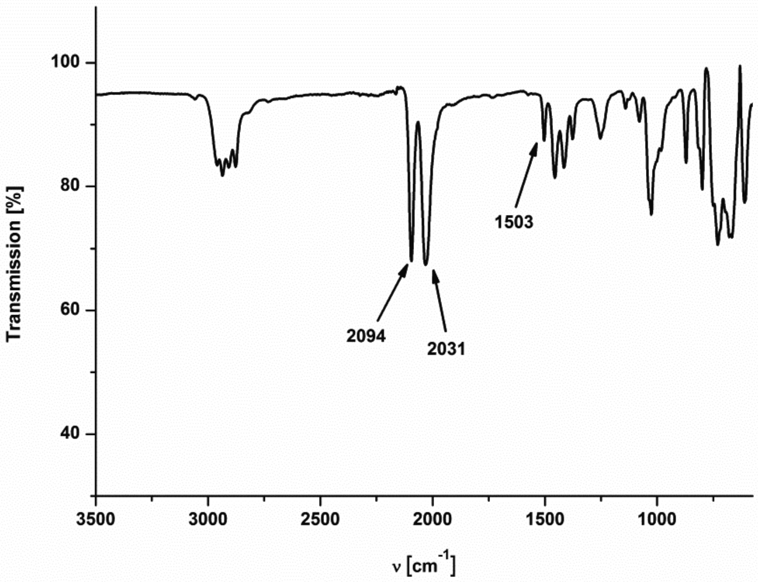

Figure S64. IR spectrum (ATR) of **9**

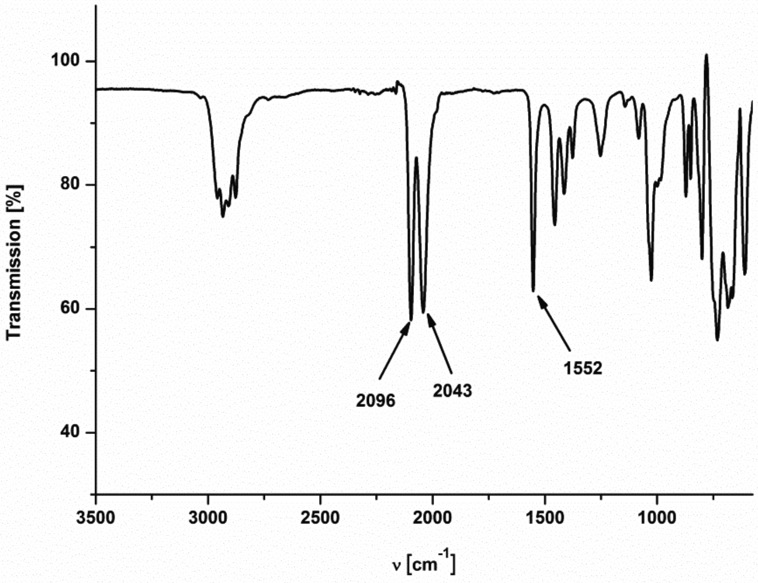

Figure S65. IR spectrum (ATR) of **10**

X-ray diffraction

Table S2. Crystallographic data for compounds **1**, **2** and **4**.

	1	**2**	**4**
empirical formula	$C_{50}H_{100}Fe_2I_2P_8$	$C_{50}H_{100}Fe_2I_2P_8$	$C_{48}H_{98}Fe_2I_2P_8S$
formula weight (g·mol^{-1})	1314.56	1314.56	1320.58
temperature (K)	153(2)	183(1)	153(2)
wavelength (Å)	0.71073	0.71073	0.71073
crystal system, space group	monoclinic, $P\,2_1/c$	monoclinic, $I\,2/a$	monoclinic, $P\,2_1/c$
a (Å)	16.5189(4)	16.1604(1)	12.1821(4)
b (Å)	9.9102(2)	13.9634(1)	29.8188(10)
c (Å)	18.2717(3)	27.1193(2)	19.5967(8)
α (deg)	90	90	90
β (deg)	97.748(2)	100.184(1)	124.521(3)
γ (deg)	90	90	90
volume (Å^3)	2963.87(11)	6023.17(7)	5865.2(4)
Z, density (calcd) (Mg·m^{-3})	2, 1.473	4, 1.450	4, 1.496
abs coefficient (mm^{-1})	1.779	1.750	1.832
F(000)	1356	2712	2720
crystal size (mm^3)	0.40 x 0.22 x 0.07	0.44 x 0.29 x 0.19	0.24 x 0.14 x 0.13
θ range (deg)	3.05 to 30.03	2.32 to 30.03	2.73 to 25.03
reflections collected	47537	62490	31417
reflections unique	8570 / R_{int} = 0.0459	8805 / R_{int} = 0.0325	10206 / R_{int} = 0.0371
completeness to θ (%)	98.9	100.0	98.3
absorption correction	analytical	semi-empirical from equivalents	analytical
max/min transmission	0.890 and 0.633	1.000 and 0.619	0.858 and 0.766
data / restraints / parameters	7514 / 2 / 308	8162 / 0 / 289	8009 / 74 / 518
goodness-of-fit on F^2	1.041	1.076	1.032
final R_1 and wR_2 indices [$I > 2\sigma(I)$]	0.0375, 0.0902	0.0235, 0.0602	0.0712, 0.1803
R_1 and wR_2 indices (all data)	0.0454, 0.0985	0.0263, 0.0625	0.0899, 0.1965
largest diff. peak and hole (e·Å^{-3})	2.722 and -1.061	0.745 and -0.588	1.790 and -1.777

The unweighted R-factor is $R_1 = \sum(Fo - Fc)/\sum Fo$; $I>2\sigma(I)$ *and the weighted R-factor is* $wR_2 = \{\sum w(Fo^2 - Fc^2)^2/\sum w(Fo^2)^2\}^{1/2}$

Table S3. Crystallographic data for compounds **5**, **6**, **8** and **9**.

	5	6	8	9
empirical formula	$C_{72}H_{147}Fe_3I_3P_{12}$, $0.5(C_6H_6)$	$C_{52}H_{100}Fe_2N_2P_8S_2$, $2(C_6H_5Cl)$	$C_{58}H_{104}Fe_2N_2P_8S_2$	$C_{50}H_{98}Fe_2N_2P_8S_3$
formula weight (g·mol^{-1})	1971.83	1402.02	1253.01	1182.98
temperature (K)	120(2)	183(1)	183(1)	183(1)
wavelength (Å)	1.54184	0.71073	0.71073	0.71073
crystal system, space group	monoclinic, $P\ 2_1/c$	monoclinic, $P\ 2_1/c$	orthorhombic, P b c a	monoclinic, $P\ 2_1/c$
a (Å)	16.5273(5)	9.4939(6)	12.3808(2)	17.8328(4)
b (Å)	28.5966(10)	12.9379(5)	17.8464(2	20.0399(4)
c (Å)	20.0805(7)	29.598(2)	29.4377(4)	18.9596(4)
α (deg)	90	90	90	90
β (deg)	101.221(4)	90.369(6)	90	117.489(3)
γ (deg)	90	90	90	90
volume (Å^3)	9309.1(6)	3635.5(4)	6504.34(16)	6010.6(2)
Z, density (calcd) (Mg·m^{-3})	4, 1.407	2, 1.281	4, 1.280	4, 1.307
abs coefficient (mm^{-1})	13.729	0.744	0.744	0.834
F(000)	4068	1492	2680	2528
crystal size (mm^3)	0.20 x 0.10 x 0.03	0.30 x 0.11 x 0.04	0.45 x 0.34 x 0.04	0.35 x 0.07 x 0.01
θ range (deg)	2.72 to 68.25	2.56 to 25.35	2.12 to 30.40	2.37 to 28.78
reflections collected	50707	20403	43906	69260
reflections unique	17043 / R_{int} = 0.1258	6596 / R_{int} = 0.0696	8994 / R_{int} = 0.0286	13917 / R_{int} = 0.0582
completeness to θ (%)	99.9	98.9	100.0	96.5
absorption correction	semi-empirical from equivalents	analytical	analytical	analytical
max/min transmission	1.000 and 0.368	0.967 and 0.850	0.980 and 0.853	0.991 and 0.851
data / restraints / parameters	7144 / 128 / 248	4869 / 110 / 366	7387 / 36 / 371	10153 / 84 / 584
goodness-of-fit on F^2	1.114	1.021	1.023	1.136
final R_1 and wR_2 indices [$I > 2\sigma(I)$]	0.1298, 0.3467	0.0598, 0.1362	0.0392, 0.0920	0.1054, 0.2174
R_1 and wR_2 indices (all data)	0.2208, 0.4288	0.0865, 0.1536	0.0513, 0.0992	0.1392, 0.2325
largest diff. peak and hole (e·Å^{-3})	3.537 and -1.500	0.654 and -0.628	0.947 and -0.464	1.240 and -1.482

The unweighted R-factor is $R_1 = \sum(Fo - Fc)/\sum Fo$; $I>2\sigma(I)$ *and the weighted R-factor is* $wR_2 = \{\sum w(Fo^2 - Fc^2)^2/\sum w(Fo^2)^2\}$

Table S4. Selected bond lengths [Å], non-bonding distances [Å] and angles [°] of compounds **1**, **2**, **4**, **6**, **8** and **9**.

	1	2	4	6	8	9
Space group	P 21/c	I 2/a	P 21/c	P 21/c	P b c a	P 21/c
Bond lengths [Å]	**Fe1-C1** 1.883(2)	**Fe1-C1** 1.8862(14)	**Fe1-C1** 1.868(4) **Fe2-C8** 1.889(4)	**Fe1-C2** 1.899(4)	**Fe1-C2** 1.8991(16)	**Fe1–C22** 1.890(6) **Fe2-C29** 1.891(7)
	C1-C2 1.218(4)	**C1-C2** 1.220(2)	**C1-C2** 1.226(6) **C8-C7** 1.210(6)	**C2-C3** 1.221(5)	**C2-C3** 1.217(2)	**C22–C23** 1.222(9) **C29–C28** 1.213(10)
	C2-C3 1.433(3)	**C2-C3** 1.4329(19)	**C2-C3** 1.408(6) **C7-C6** 1.415(6)	**C3-C4** 1.441(5)	**C3-C4** 1.435(2)	**C23–C24** 1.418(9) **C28–C27** 1.424(9)
	Fe1-I1 2.6907(4)	**Fe1-I1** 2.7026(2)	**Fe1-I1A** 2.7146(9) **Fe2-I2A** 2.7065(9)	**Fe1-N1** 1.953(3)	**Fe1-N1** 1.9534(14)	**Fe1-N1** 1.964(6) **Fe2-N2** 1.964(6)
	---	---	---	**N1-C1** 1.160(5)	**N1-C1** 1.150(2)	**N1-C1** 1.119(8) **N2-C30** 1.121(9)
	---	---	---	**C1-S1** 1.645(4)	**C1-S1** 1.6405(18)	**C1-S1** 1.673(7) **C30-S2** 1.661(7)
	Fe1-P 2.254[a]	**Fe1-P** 2.252[a]	**Fe1-P** 2.255[a] **Fe2-P** 2.235[a]	**Fe1-P** 2.262[a]	**Fe1-P** 2.253[a]	**Fe1-P** 2.256[a] **Fe2-P** 2.251[a]
Non-bonding distances [Å]	**Fe1···Fe1'** 11.8981(2)	**Fe1···Fe1'** 9.7504(3)	**Fe1···Fe2** 11.1638(9)	**Fe1···Fe1'** 11.9343(10)	**Fe1···Fe1'** 16.2610(4)	**Fe1···Fe2** 11.2517(29)
	---	---	---	**S1···S1'** 21.4257(21)	**S1···S1'** 25.6847(11)	**S1···S2** 20.6091(29)
Bond angles [°]	---	---	---	**S1-C1-N1** 179.7(4)	**S1-C1-N1** 178.85(18)	**S1-C1-N1** 178.0(6) **S2-C30-N2** 178.0(7)
	---	---	---	**C1-N1-Fe1** 173.5(3)	**C1-N1-Fe1** 176.56(15)	**C1-N1-Fe1** 173.2(6) **C30-N2-Fe2** 174.1(7)
	I1-Fe1-C1 176.98(8)	**I1-Fe1-C1** 178.90(4)	**I1A-Fe1-C1** 175.88(14) **I2A-Fe2-C8** 177.37(16)	**N1-Fe1-C2** 179.08(14)	**N1-Fe1-C2** 178.58(7)	**N1-Fe1-C22** 177.9(3) **N2-Fe2-C29** 177.0(3)
	Fe1-C1-C2 176.6(2)	**Fe1-C1-C2** 177.21(13)	**Fe1-C1-C2** 179.2(4) **Fe2-C8-C7** 176.2(4)	**Fe1-C2-C3** 177.4(3)	**Fe1-C2-C3** 177.61(16)	**Fe1-C22-C23** 179.1(6) **Fe2-C29-C28**
	C1-C2-C3 176.5(3)	**C1-C2-C3** 172.67(15)	**C1-C2-C3** 176.0(4) **C8-C7-C6** 175.2(5)	**C2-C3-C4** 175.9(4)	**C2-C3-C4** 176.4(2)	**C22-C23-C24** 175.8(7) **C29-C28-C27** 178.0(8)

[a] average bond length.

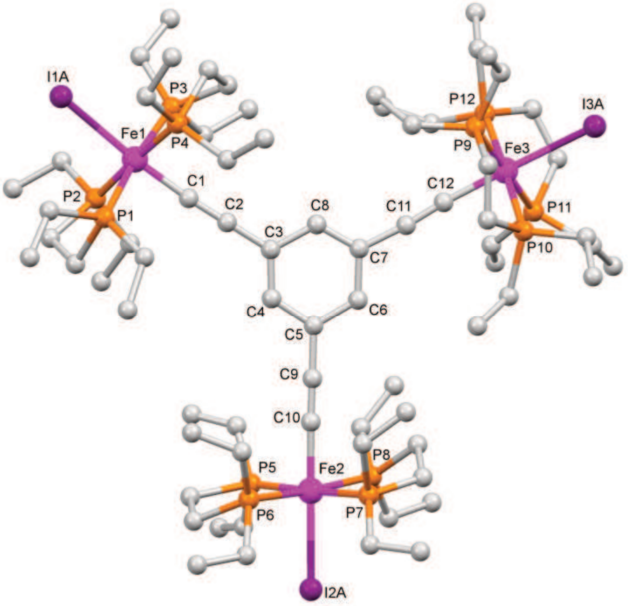

Figure S66. Molecular structures of: **5**. Solvent molecules and selected hydrogen atoms are omitted for clarity.

Refinement details. In the crystal structure of **1**, one ethyl group is disordered over two sets of positions with site-occupancy factors of 0.253(9) and 0.747(9). Some *SHELXL* bond distance restraints (*SADI*) were used to correct the geometry of the disordered components. All non-hydrogen atoms were refined anisotropically. All hydrogen positions were calculated after each cycle of refinement using a riding model, with C—H = 0.93 Å and $U_{\mathrm{iso}}(\mathrm{H}) = 1.2U_{\mathrm{eq}}(\mathrm{C})$ for aromatic H atoms, with C—H = 0.97 Å and $U_{\mathrm{iso}}(\mathrm{H}) = 1.2U_{\mathrm{eq}}(\mathrm{C})$ for methylene H atoms, and with C—H = 0.96 Å and $U_{\mathrm{iso}}(\mathrm{H}) = 1.5U_{\mathrm{eq}}(\mathrm{C})$ for methyl H atoms. In the crywstal structure of **2**, the molecule lies on a two-fold rotation axis that passes through the substituted benzene ring (symmetry code: *i* = -*x*-1/2, *y*, -z). All non-hydrogen atoms were refined anisotropically. All hydrogen positions were calculated after each cycle of refinement using a riding model, with C—H = 0.93 Å and $U_{\mathrm{iso}}(\mathrm{H}) = 1.2U_{\mathrm{eq}}(\mathrm{C})$ for the aromatic H atoms, with C—H = 0.97 Å and $U_{\mathrm{iso}}(\mathrm{H}) = 1.2U_{\mathrm{eq}}(\mathrm{C})$ for the methylene H atoms, and with C—H = 0.96 Å and $U_{\mathrm{iso}}(\mathrm{H}) = 1.5U_{\mathrm{eq}}(\mathrm{C})$ for the methyl H atoms. In the crystal structure of **4**, the main residue is disordered at 69%. The central part of the molecule $\mathrm{Fe-C_2-C_4H_2S-C_2-Fe}$ is not disordered which makes the determination unambiguous. The selected crystal was clearly a monocrystal: 99.7% of the diffraction peaks fit with the cell parameters. No merohedral twinning is observed. A total number of 74 restraints had to be used to correct the geometry of the disordered components of the molecule and the thermal parameters of the corresponding atoms. All non-hydrogen atoms were refined anisotropically. All hydrogen positions were calculated after each cycle of refinement using a riding model, with C—H = 0.93 Å and $U_{\mathrm{iso}}(\mathrm{H}) = 1.2U_{\mathrm{eq}}(\mathrm{C})$ for aromatic H atoms, with C—H = 0.97 Å and $U_{\mathrm{iso}}(\mathrm{H}) = 1.2U_{\mathrm{eq}}(\mathrm{C})$ for methylene H atoms, and with C—H = 0.96 Å and $U_{\mathrm{iso}}(\mathrm{H}) = 1.5U_{\mathrm{eq}}(\mathrm{C})$ for methyl H atoms. In the crystal structure of **5**, only the main core of the molecule, $\mathrm{C_{12}Fe_3}$, did not show any disorder. The whole molecule appeared clearly with most of the structure solution programs. Unfortunately, attemps to refine the model with a site-occupancy of 1 for all atoms resulted to very large isotropic parameters. The *depe* ligand is well know to exhibit disorders, sometimes even all atoms of the ligand are disordered, it seems to be the case here for all three *depe* ligands. The fact that the crystal and the data collection were of a good quality, and that the non-disordered core confirms the expected molecule, we did refine the crystal structure of the compound to present the result in the Supporting Information (Appendix). First, the main core including the P and I atoms were freely refined, and then all C positions were located in Fourier difference maps, their xyz coordinates and isotropic parameters were fixed

(U_{iso} = 0.08 for the ethane bridge C atoms, U_{iso} = 0.10 for the methylene C atoms of the ethyl groups, and U_{iso} = 0.015 for the methyl C atoms of the ethyl groups). Restraints had to be used to correct the geometry of some parts of the molecules, but we tried to check systematically bond distances and angles to unfix as many coordinates as possible. The Fe, I, P atoms as well as the central 12 C atoms were anisotropically refined. All hydrogen positions were calculated after each cycle of refinement using a riding model, with C—H = 0.93 Å and U_{iso}(H) = 1.2U_{eq}(C) for aromatic H atoms, with C—H = 0.97 Å and U_{iso}(H) = 1.2U_{eq}(C) for methylene H atoms, and with C—H = 0.96 Å and U_{iso}(H) = 1.5U_{eq}(C) for methyl H atoms. In the crystal structure of **6**, the dinuclear species lies on an inversion center located in the middle of the central benzene ring (symmetry code: *i* = -*x*+1, -*y*, -*z*+1). It cocrystallized with solvent molecules of dichloromethane in a ratio 1:2. The terminal CH_3 group of one ethyl ligand is disordered over two sets of positions with site-occupancy factors of 0.367(9) and 0.633(9). Some restraints had to be used to correct the geometry of the disordered parts and the thermal parameters of the corresponding atoms. All non-hydrogen atoms were refined anisotropically. All hydrogen positions were calculated after each cycle of refinement using a riding model, with C—H = 0.93 Å and U_{iso}(H) = 1.2U_{eq}(C) for aromatic H atoms, with C—H = 0.97 Å and U_{iso}(H) = 1.2U_{eq}(C) for methylene H atoms, and with C—H = 0.96 Å and U_{iso}(H) = 1.5U_{eq}(C) for methyl H atoms. In the crystal structure of **8**, the dinuclear species lie on a center of inversion located in the middle of the central C—C bond. The second part of the molecule is obtained by a symmetry operation (-1-*x*, -*y*, -*z*). Two ethyl ligands are disordered over two sets of positions with site occupancy ratios of 0.495 (8):0.505 (8) and 0.220 (4):0.780 (4). All hydrogen positions were calculated after each cycle of refinement using a riding model, with C—H = 0.93 Å and U_{iso}(H) = 1.2U_{eq}(C) for aromatic H atoms, with C—H = 0.97 Å and U_{iso}(H) = 1.2U_{eq}(C) for methylene H atoms, and with C—H = 0.96 Å and U_{iso}(H) = 1.5U_{eq}(C) for methyl H atoms. In the crystal structure of **9**, the diphosphine ligands bound to Fe2 are fully disordered over two sets of positions with a site-occupancy ratio of 0.5:0.5. Many *SHELXL* restraints and/or constraints (84 *vs.* 584 parameters) had to be used to correct the geometry of the disordered components (*DFIX*, *DANG*, *SAME*) and the thermal parameters of the corresponding atoms (*EADP*). All hydrogen positions were calculated after each cycle of refinement using a riding model, with C—H = 0.93Å and U_{iso}(H) = 1.2U_{eq}(C) for aromatic H atoms, with C—H = 0.97Å and U_{iso}(H) = 1.2U_{eq}(C) for methylene H atoms, and with C—H = 0.96Å and U_{iso}(H) = 1.5U_{eq}(C) for methyl H atoms.

Cyclic Voltammetry Studies

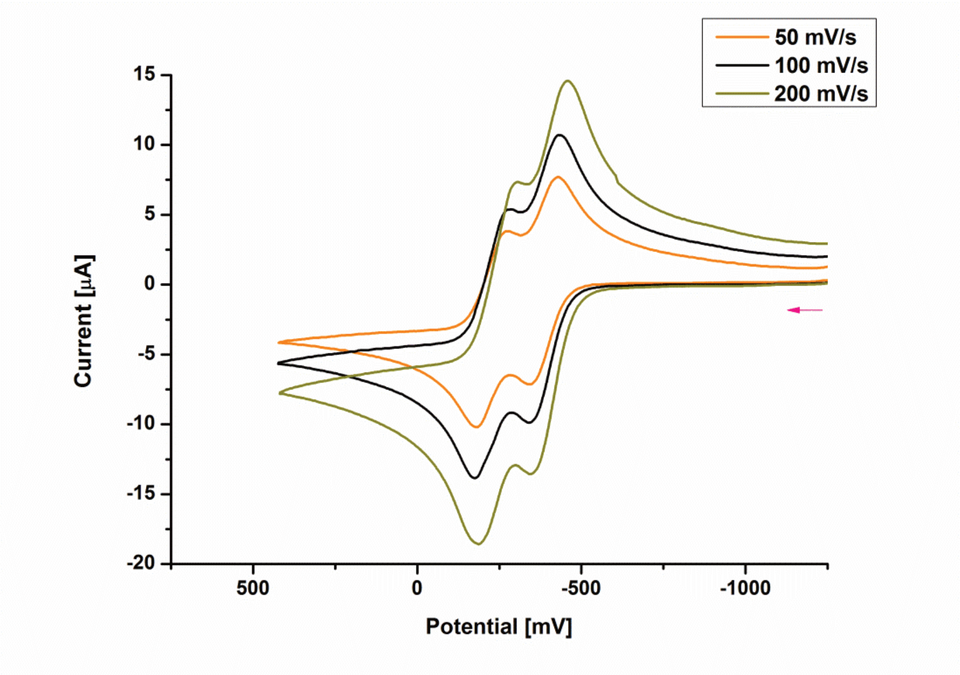

Figure S67. Cyclic voltammograms for **1** in NBu_4PF_6 (0.1M) at three different chart rates; rt, Au electrode; E vs. $Fc^{o/+}$ (external)

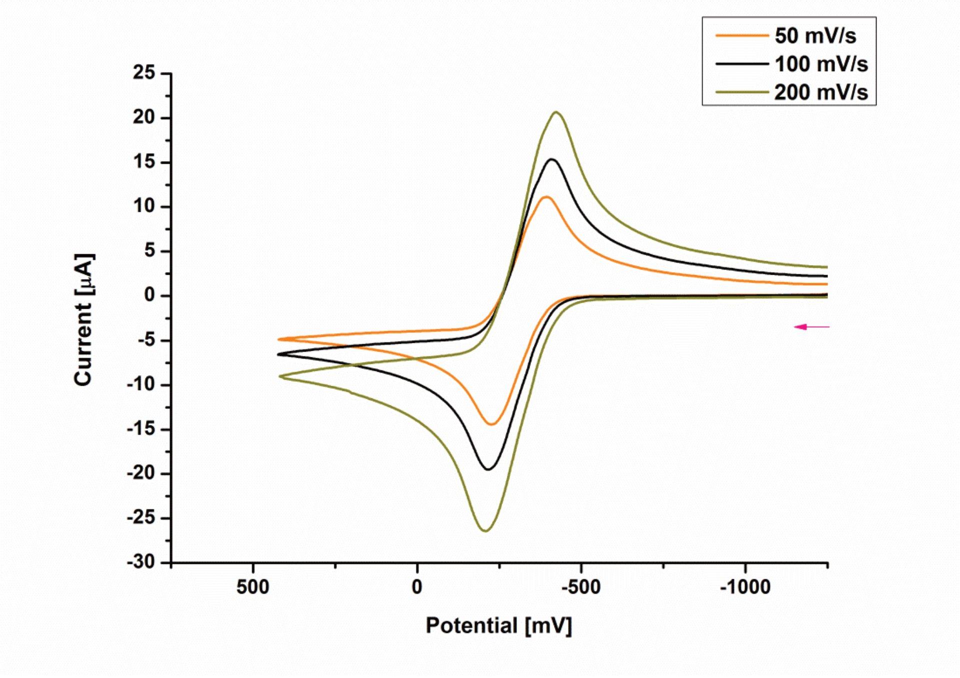

Figure S68. Cyclic voltammograms for **2** in NBu_4PF_6 (0.1M) at three different chart rates; rt, Au electrode; E vs. $Fc^{0/+}$ (external)

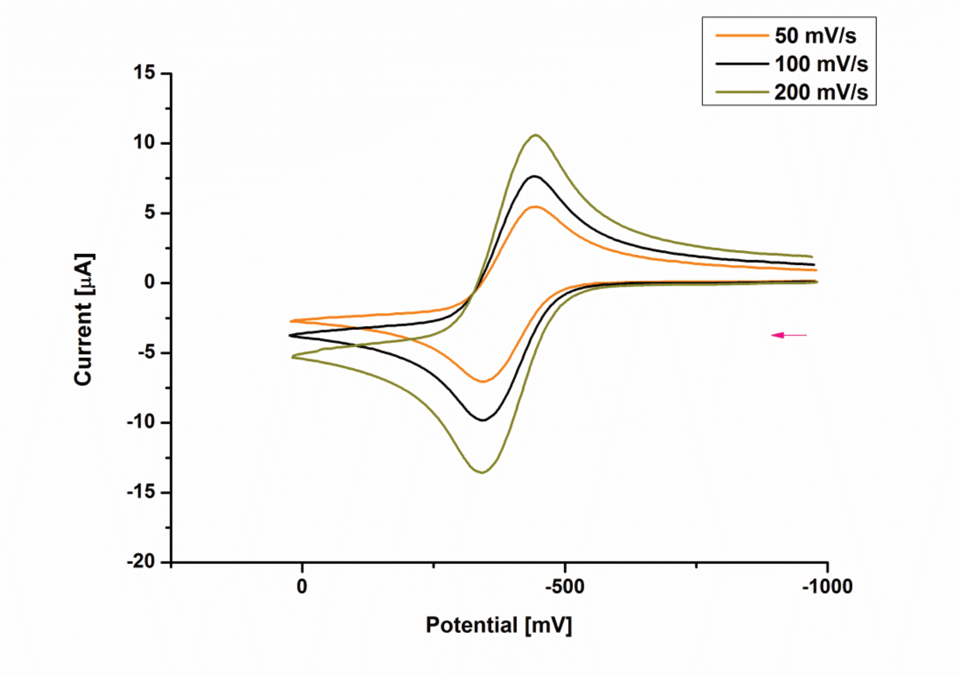

Figure S69. Cyclic voltammograms for **3** in NBu_4PF_6 (0.1M) at three different chart rates; rt, Au electrode; E vs. $Fc^{0/+}$ (external)

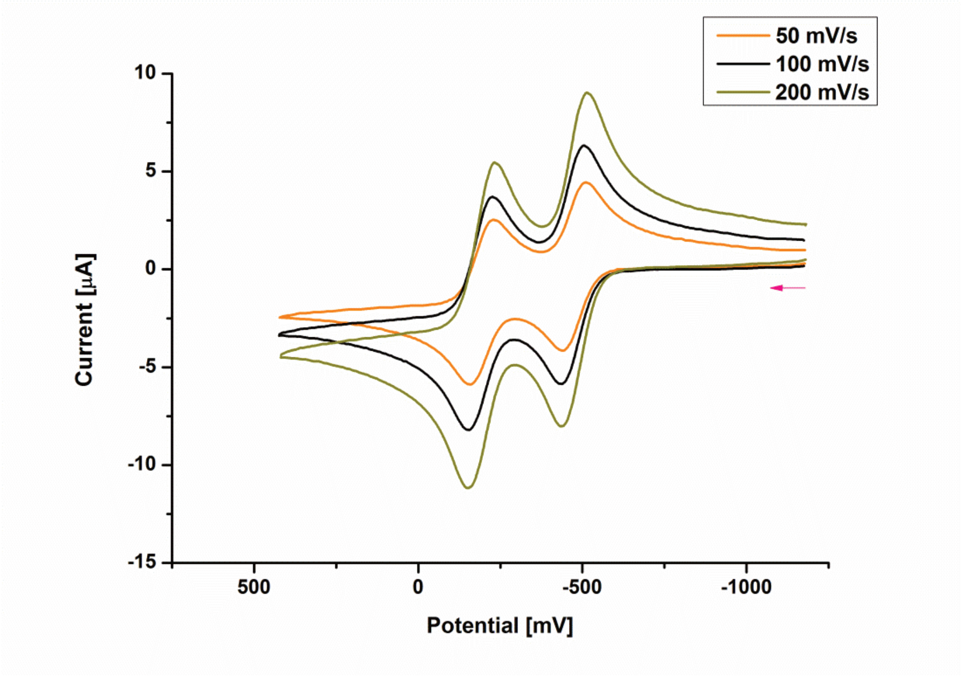

Figure S70. Cyclic voltammograms for **4** in NBu_4PF_6 (0.1M) at three different chart rates; rt, Au electrode; E vs. $Fc^{0/+}$ (external)

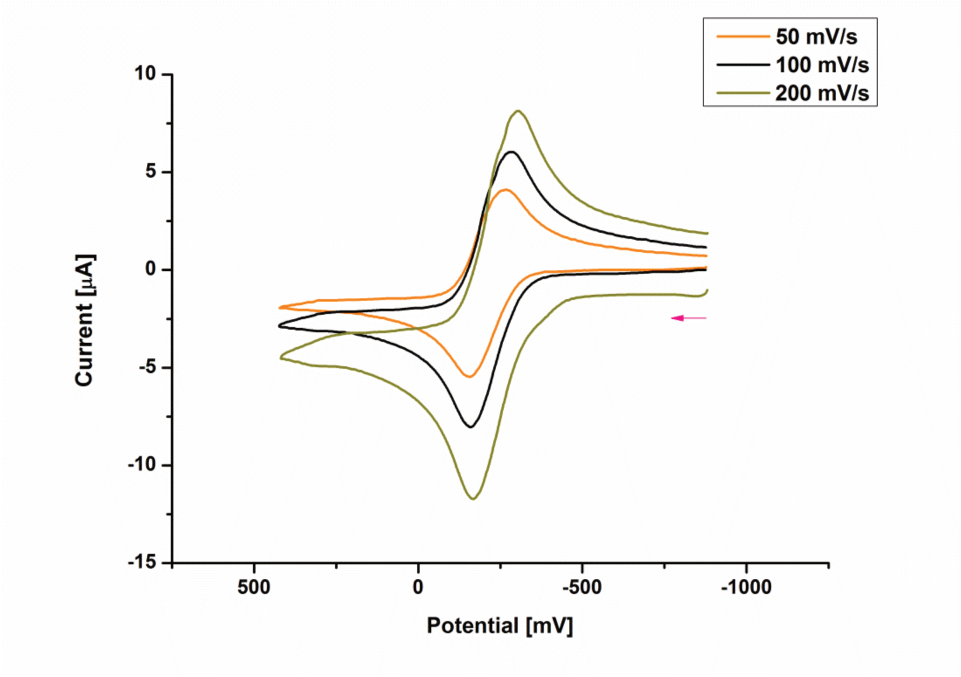

Figure S71. Cyclic voltammograms for **5** in NBu_4PF_6 (0.1M) at three different chart rates; rt, Au electrode; E vs. $Fc^{0/+}$ (external)

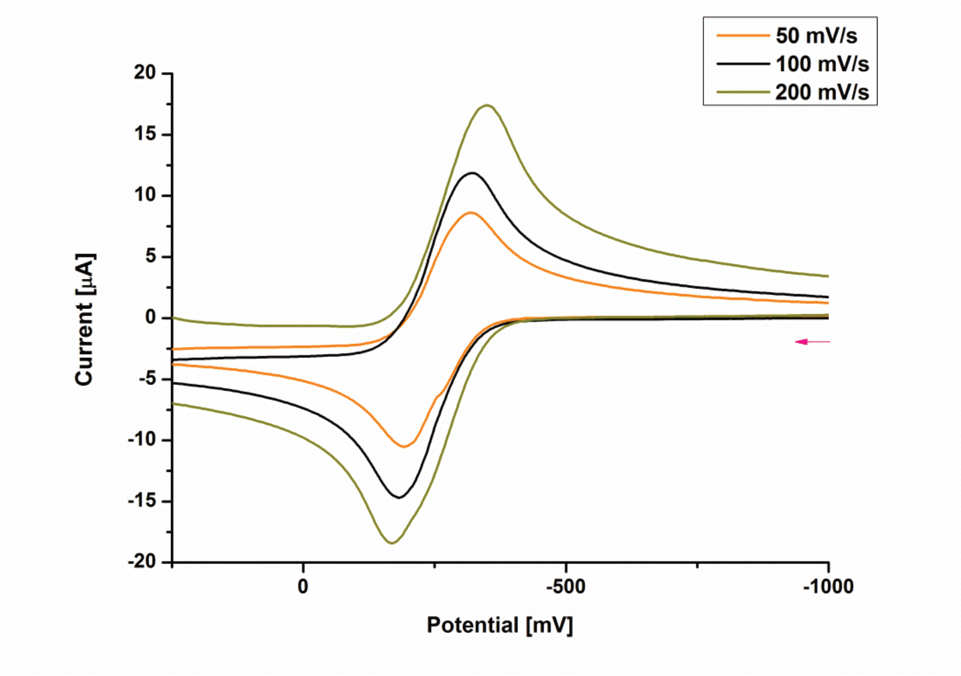

Figure S72. Cyclic voltammograms for **8** in NBu_4PF_6 (0.1M) at three different chart rates; rt, Au electrode; E vs. $Fc^{o/+}$ (external)

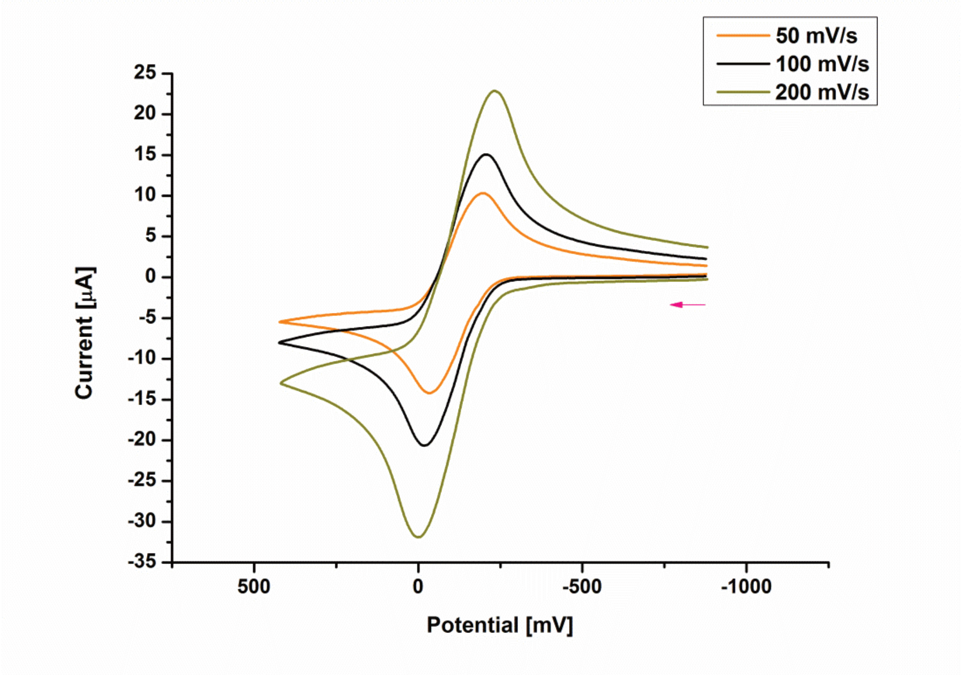

Figure S73. Cyclic voltammograms for **10** in NBu_4PF_6 (0.1M) at three different chart rates; rt, Au electrode; E vs. $Fc^{o/+}$ (external)

6. SCOPE OF THE THESIS

Single molecules constitute the smallest discrete units to build electronic devices at the molecular level. Key requirements for suitable molecular units are structural rigidity, resonant conductivity along chosen pathways and the option to manipulate and thus modulate the charge transport. One route towards such molecular units is to embed redox active metal centers in conjugated organic moieties, thereby deploying the metal centers as relays for the transported charge. Such organometallic architecture is also attractive due to the possibility to vary structural motifs, electron density and work functions, thus obtaining fundamental knowledge on the relationship between molecular structure and electronic properties.

This thesis aimed at constructing such organometallic fully conjugated systems by incorporating Fe centers into alkyne based scaffolds and investigating their physico-chemical and electronic properties.

Within the Subproject 1 a series of rigid-rod, one dimensional single molecules in the low nanometer range was synthesized, which were investigated using *in-situ* spectroelectrochemistry and found to exhibit strong electronic coupling over the length of the conjugated chain. The applied iterative synthetic technique prolongs the chain by forming new iron-carbon bonds.

The employment of different building blocks allows the modification of structural motifs (Figure 1). To probe the relationship between molecular structure and electrical as well as electronic properties, Subprojects 2 and 3 aimed at varying these motifs and investigating the induced property changes using electrochemical and single molecule conductance measurements.

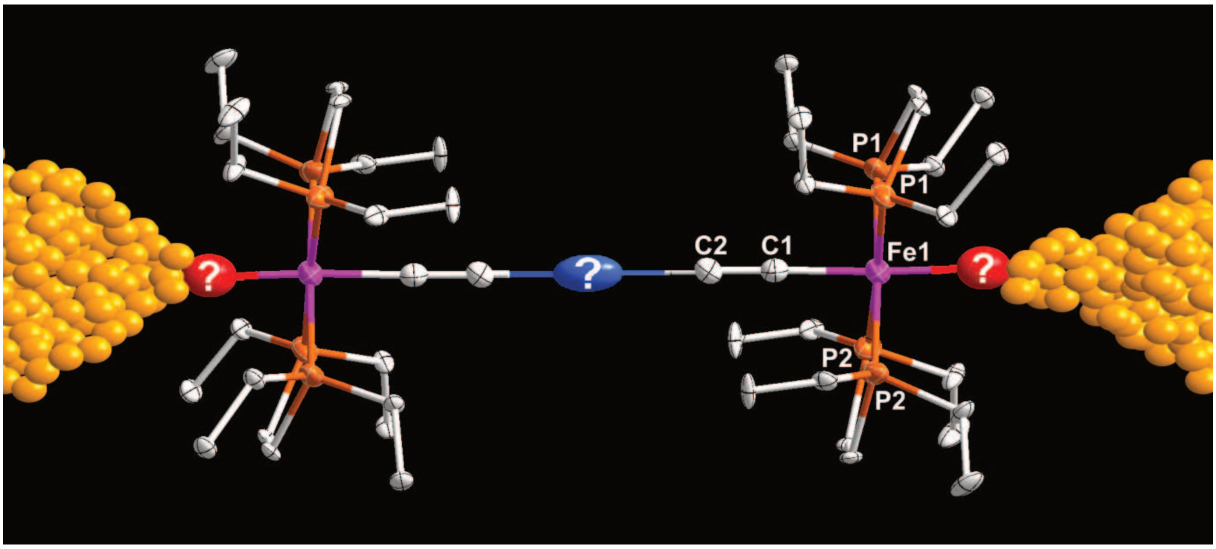

Figure 1. Structural drawing of a sp/sp^2 based framework containing two Fe centers and bound to molecular sized Au electrodes. Question marks indicate structurally variable sites: (red) electrode binding anchor group, (blue) bridging ligand.

Within Subproject 2 the electrode binding anchor groups of a highly delocalized {Fe}–C≡C−C≡C–{Fe} fragment were gradually varied from anchorgroups known in organic-based molecular electronics towards deploying selected delocalized substituents known in general organometallic chemistry in the new context of molecular electronics.

Subproject 3 entails the modification of the electron transfer pathway by varying the bridging ligand connecting the two iron cores whereas the anchoring group is kept unchanged.

6.1 STEPWISE CONSTRUCTION AND SPECTROELECTRIC PROBING OF A TETRA-IRON MOLECULE

Manuscript: F. Lissel, T. Fox, O. Blacque, W. Polit, R. F. Winter, K. Venkatesan, H. Berke "*Stepwise Construction of an Iron-Substituted Rigid-Rod Molecular Wire: Targeting a Tetraferra-Tetracosa-Decayne", J. Am. Chem. Soc.* **2013**, 135 (10), 4051-4060

Synthesis and Characterization

To probe the electric properties of iron-alkyne based scaffolds and their suitability for molecular electronic applications, it was necessary to develop the synthetic pathways to build-up highly symmetric frameworks with open termini in order to access higher analogues.

Starting from a simple and well-known mononuclear precursor *trans*-$Fe(depe)_2I_2$, two tetra-iron molecules $X\{Fe\}C_4\{Fe\}C_4\{Fe\}C_4\{Fe\}X$ ($\{Fe\} = Fe(depe)_2$; depe = 1,2-bis(diethylphosphino)ethane; X = I **6**, C_4SiMe_3 **7**) were assembled (Scheme 1). The stepwise build-up proceeds over a series of dinuclear intermediates $X\{Fe\}C_4\{Fe\}X$ ($\{Fe\} = Fe(depe)_2$; X = I **2**, C_4SiMe_3 **3**, C_4H **4**, C_4SnMe_3 **5**) which were all isolated.

All compounds were characterized by 1D and 2D NMR studies, IR, and Raman spectroscopies and by elemental analyses. X-ray diffraction of the dinuclear complexes (Figure 2) revealed highly symmetrical structures with rigid-rod $R{-}\{Fe\}{-}C_4{-}\{Fe\}{-}R$ backbones.

Scheme 1. Stepwise synthesis of the tetraferra-tetracosa-decayne complex **7**.

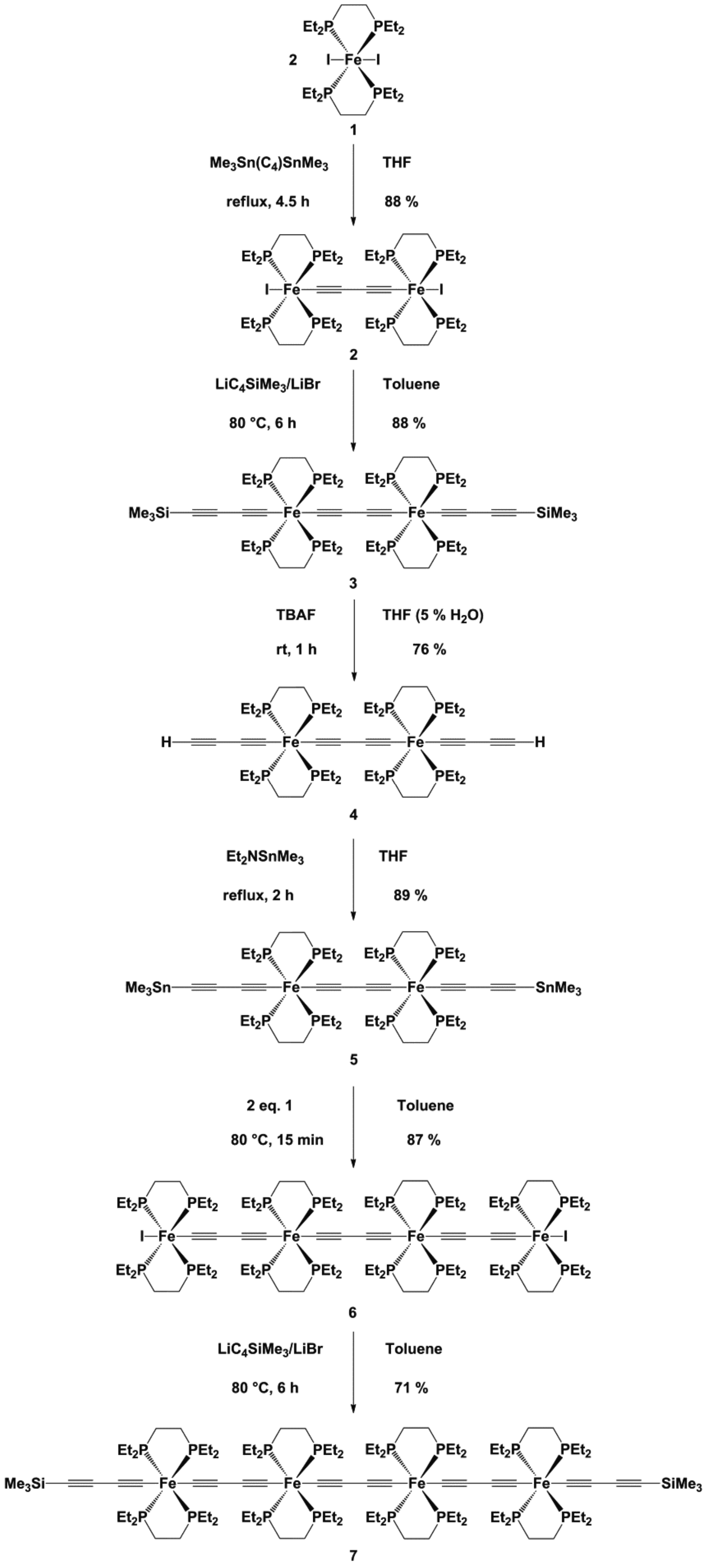

X-Ray Diffraction

X-Ray diffraction analyses of the three C_4R disubstituted compounds **3 - 5** showed structures with rigid-rod RC_4–{Fe}–C_4–{Fe}–C_4R backbones. Compared to the diiodo complex **2**, the Fe-Fe distance is clearly elongated. This can be attributed to the even more pronounced butadiyndiyl character of the bridge, marked by a slight contraction of the triple bonds, which is being overcompensated by elongations of the Fe–C and C–C single bonds.

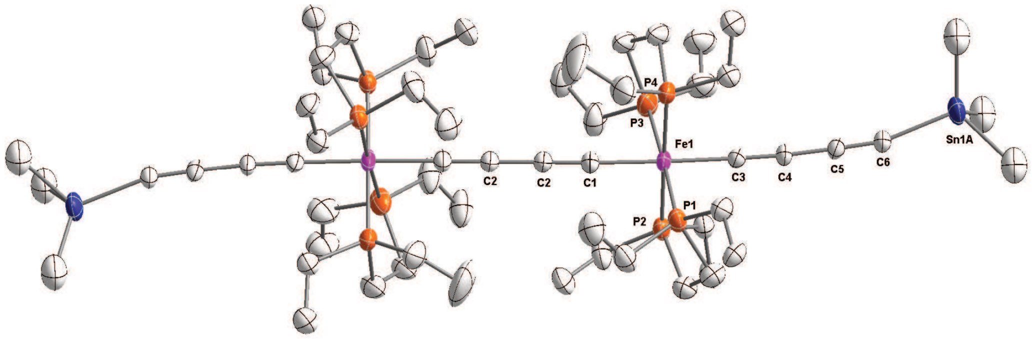

Figure 2. Molecular structure of 5. Ellipsoids are set at 30% probability level. Solvent molecules and selected hydrogen atoms are omitted for clarity.

Cyclic Voltammetry

Cyclic voltammetric studies showed that compounds **2 - 7** undergo reversible and well-defined oxidations with high K_c values indicating thermodynamically stable mixed valence species (Table 1). The dinuclear complexes **3 - 5** exhibit three reversible oxidation waves, two related to the gradual oxidation of the two metal centres and a third wave at a more positive potentials related to the oxidation of the bridging ligand. The cyclic voltammetric studies of the tetranuclear complexes **6** and **7** exhibited four individually resolved, reversible oxidation waves (Table 1) marking the successive oxidation of all four metal centers, at very negative potentials.

Table 1. Electrochemical data of the di- and tetranuclear complexes.

Compd.	**$E_{1/2}$ (0/+1) [mV]**	**$E_{1/2}$ (+1/+2) [mV]**	**$\Delta E_{(1,2)}$ [mV]**	**K_c**	**$E_{1/2}$ (+2/+3) [mV]**	**$E_{1/2}$ (+3/+4) [mV]**	**$\Delta E_{(3,4)}$ [mV]**
2 [a]	-905	-362	543	1.9×10^9	--	--	--
3 [a]	-863	-423	440	3.3×10^7	306	--	--
4 [a]	-880	-421	459	6.9×10^7	316	--	--
5 [a]	-893	-446	447	4.3×10^7	268	--	--
6 [b]	-1434	-1099	335	5.3×10^5	-650	-435	215
7 [a]	-1204	-873	331	4.5×10^5	-553	-421	135

Measurements performed with an Au working electrode and a Pt counter electrode, and a nonaqueous reference electrode (Ag/AgCl) with a scan rate of 100mV/s. Calibrated against $Fc^{0/+}$ as an external calibrant. [a] in THF/Bu_4NPF_6 (0.1M) at rt; [b] in CH_2Cl_2/Bu_4NPF_6 (0.1M) at rt.

Neither complex **6** nor complex **7** exhibited further reversible oxidation waves within the potential window of the given electrolyte that could be attributed to redox processes of the organic units. It has to be noted that the successive oxidations of the metal centers occur at very negative potentials, while the oxidation of the carbon-rich bridging ligand of **3**, **4** and **5** was observed at a much more positive potential. The separations of individual half-wave potentials for both tetranuclear compounds are not as large as for the dinuclear complexes, but still substantial and well sufficient to allow a spectroelectrochemical probing of individual oxidation states.

Spectroelectrochemical Studies

The electronic properties of complexes **2**, **3** and **7** were investigated by spectroelectrochemical measurements. In all cases, the first oxidation led to the growth of an intense and broad near infrared (NIR) band of electronic origin (Figure 3 for the dinuclear **3** and tetranuclear **7**) which is assigned as the Fe(II)/Fe(III) intervalence charge transfer (IVCT) absorption. For both dinuclear complexes **2** and **3**, the Γ value as introduced by Brunschwig, Creutz and Sutin as a measure of ground-state delocalization clearly exceeds the value of 0.50 delimiting the Class II-III transition and hence point to extensive charge-delocalization in this mixed-valence species. For the tetranuclear complex 7 the calculated Γ value of 0.51 places $\mathbf{7}^{+}$ still in the regime of strongly delocalized systems, yet at the Class II/III borderline. Spectral deconvolution of the NIR part of the electronic spectrum reveals the presence of a second NIR band whose calculated Γ value of 0.25 is typical of an IVCT transition within a mixed-valent system of Class II parentage.

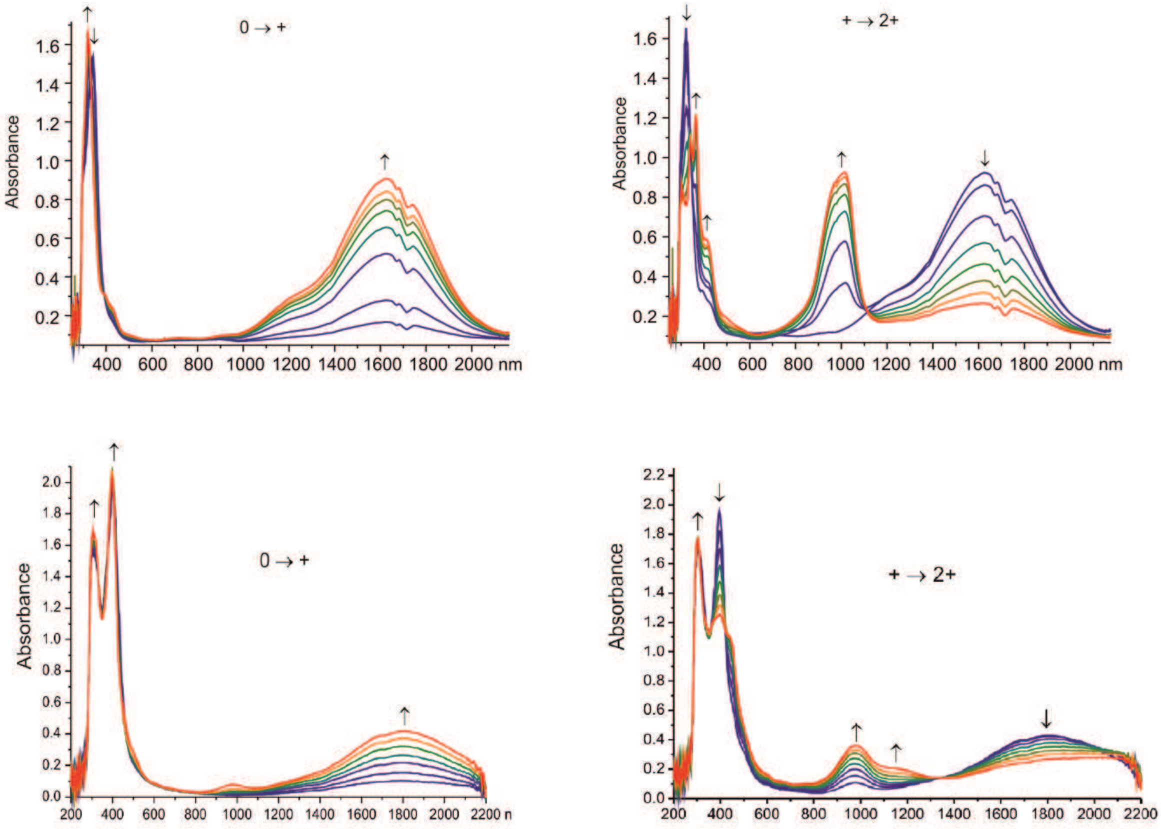

Figure 3. UV/Vis/NIR spectroscopic changes in an OTTLE cell ($1,2\text{-}C_2H_4Cl_2/NBu_4BAr^F{}_4$ 0.2 M at rt) during the first (*top left*) and the second oxidation (*top right*) of complex **3** and the first (*bottom left*) and the second (*bottom right*) oxidation of complex **7**

At variance with $\mathbf{3}^{2+}$, doubly oxidized $\mathbf{7}^{2+}$ still retains a rather strong NIR band with a corresponding Γ value of 0.21 (Figure 3). This finding provides a clue that both the first and the second oxidation within the bis(butadiynediyl) bridged tetra-iron molecule take place at the inner iron cores, thus leading to an electronic system of $\mathbf{7}^{2+}$ where only one type of IVCT transitions, that is from each of the outer to the neighbouring innersite, is observed. All three investigated molecules show extensive vibrational coupling along the unsaturated iron-alkyne backbone.

6.2 VARYING THE ANCHORING GROUPS OF AN ORGANOMETALLIC MOLECULAR JUNCTION

F. Lissel, F. Schwarz, O. Blacque, H. Riel, E. Lörtscher, K. Venkatesan, H. Berke *J. Am. Chem. Soc.,* **2014**, DOI: 10.1021/ja507672g

F. Schwarz, G. Kastelunger, F. Lissel, H. Riel, K. Venkatesan, H. Berke, R. Stadler, E. Lörtscher *NanoLetters* **2014**, DOI: 10.1021/nl5029045

Synthesis and Characterization

A homologous series of X{Fe}C≡C−C≡CFe{Fe}X complexes ({Fe} = Fe(depe)$_2$, depe = 1,2-bis(diethylphosphino)ethane; X = I **2**, NCMe **8**, N_2 **9,** C_4SnMe_3 **5**, C_2H **10**, C_2SnMe_3 **11**, NCSe **12**, NCS **13**, CN **14**, SH **15** and NO_2 **16**) was designed to systematically study the influence of the anchorgroup on organometallic single-molecule junctions to achieve high-conductive molecular wires (Scheme 2). All compounds were characterized by 1D and 2D NMR studies, IR, and Raman spectroscopies, elemental analyses and X-ray diffraction.

Scheme 2. Structures of a series of {Fe}–C≡C−C≡C–{Fe} based complexes.

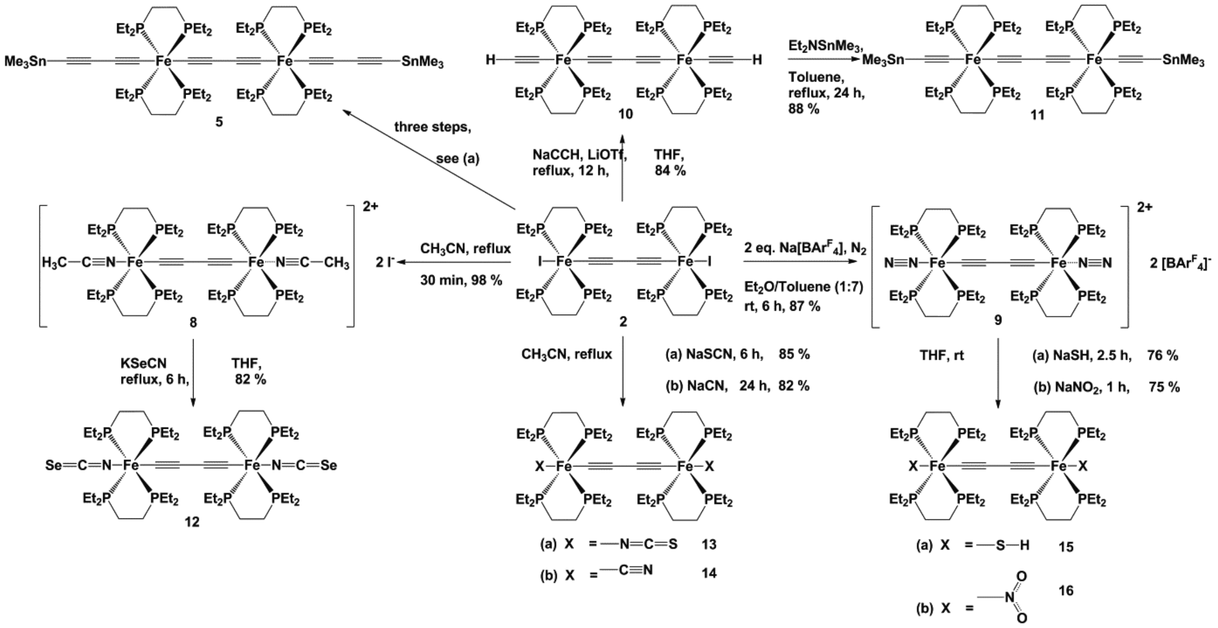

Cyclic Voltammetry

In cyclovoltammetric studies, complex **15** does not exhibit reversible oxidation processes probably due to the formation of dithiol compounds. All other compounds show reversible and well-defined oxidations with high K_c values, albeit at varying potentials (Table 2).

Table 2. Cyclic voltammetry data of the dinuclear complexes **10** - **16**

Compd.	**$E_{1/2}$ (0/+1) [mV]**	**$E_{1/2}$ (+1/+2) [mV]**	**ΔE [mV]**	**K_c**	**$E_{1/2}$ (+2/+3) [mV]**
5	-503	-48	456	6.0×10^7	671
10	-453	10	-462	7.7×10^7	799
11	-458	5	-463	7.9×10^7	---
12	-428	24	-452	5.1×10^7	---
13	-372	106	-478	14.5×10^7	848
14	-421	10	-431	2.2×10^7	729
15	---	---	---	---	---
16	-497	-14	-483	17.7×10^7	735

Measurements at rt in THF/NBu_4PF_6 (0.1M) with an Au working electrode, a Pt counter electrode, and an Ag reference electrode. Calibrated against $Fc^{0/+}$ as an external calibrant.

DFT I: MO Calulations

The molecular geometries of the model complexes **5**$_H$-*Me*, **10**-*Me*, **12**-*Me*, **13**-*Me*, **14**-*Me*, **15**-*Me* and **16**-*Me* were optimized with a C_i (inversion center) or a C_2 (two-fold axis) symmetry, and dmpe as equatorial ligands (dmpe = 1,2-bis(dimethylphosphino)ethane). As the $SnMe_3$ groups of **5** and **11** are expected to cleave off to form a covalent C-Au bond, calculations were carried out for the H terminated models **5**$_H$ -*Me* ($HC_4(dmpe)_2Fe-C_4-Fe(dmpe)_2C_4H$) and **10**-*Me* ($HC{\equiv}C(dmpe)_2Fe-C_4-Fe(dmpe)_2C{\equiv}CH$).

Single-point calculations were carried out for the determination of the molecular orbital energies. The HOMO and LUMO energies are given in Table 3.

To achieve a resonant transport, which would be an important goal for this series of complexes, the molecular orbitals of the probed molecule should be aligned to E_F of the macroscopic electronic leads. The work of Pearson established that $\Delta E_{(H-L)}$ derived from DFT calculations can be correlated to hardness associated with a weakening of polarizability and therefore an increase in chemical hardness.

The MO levels of the isolated molecules are aligned to E_F in the order **13**-*Me* **<** **14**-*Me* = **12**-*Me* **<** **16**-*Me* < **5**$_H$-*Me* < **15**-*Me* < **10**-*Me*. It has to be noted however, that the calculations were carried out for isolated molecules in the gas phase, whereas for the MCBJ experiments, a solid state behaviour of the complexes has to be assumed. The interactions with the Au electrodes are not considered by the chosen level of DFT. Still, the calculations show that the energetic positions of the molecular orbitals and the extent of the HOMO/LUMO gap can be tuned by varying the terminal ligand of a $X\{M\}C_4\{M\}X$, even if metal center, bridging and equatorial ligands are kept unaltered.

Table 3. Selected distances (Å) computed at the PBE1PBE/LANL2DZ level and derived from X-ray studies, HOMO and LUMO energies (eV), HOMO/LUMO gap (eV) and absolute electronegativity χ computed at the PBE1PBE/LANL2DZ//PBE1PBE/6-311+g(d) level.

X	**X···X (X-ray)**	**X···X (DFT)**	**LUMO**	**HOMO**	**$\Delta E_{(H-L)}$**	**X**
	[Å]	**[Å]**	**[eV]**	**[eV]**	**[eV]**	**[eV]**
SH	S···S = 12.3435(17)	12.54	-0.33	-4.16	3.83	2.25
NO$_2$	O···O = 12.830(3)	13.15	-0.57	-4.58	4.01	2.58
CN	N···N = 13.738(4)	13.93	-0.39	-4.41	4.02	2.40
C$_2$H	C···C = 13.896(6)	14.08	-0.28	-4.07	3.79	2.18
NCS	S···S = 16.940(3)	17.34	-0.57	-4.60	4.03	2.59
NCSe	Se···Se = 17.3280(15)	17.59	-0.60	-4.62	4.02	2.61
C$_4$H	C···C = 19.015(12)	19.26	-0.40	-4.33	3.93	2.37

Single-Molecule Transport Measurements

Based on the results of the spectroscopic and electrochemical studies as well as of the computational findings, complexes **5**, **11 - 14** were chosen for transport measurements at the single-molecule level using a MCBJ setup.

Figure 4 shows that compounds **12 -14** bind coordinatively to Au, whereas the $SnMe_3$ end capped compounds **5** and **11** allow for covalent bonding. The loss of the $SnMe_3$ leads to a reduction in length and a shorter electrode–electrode distance for resulting Au–molecule–Au system. The junction's lengthdetermines also the direct electron-tunneling contribution between the electrodes, a non-negligible electron path the parallel to the molecular-mediated one. The **Au–12–Au**, **Au–13–Au**, **Au–5'–Au** junctions are in a comparable length range, and also the lengths of the **Au–11′–Au Au–14–Au** systems are similar (Table 3).

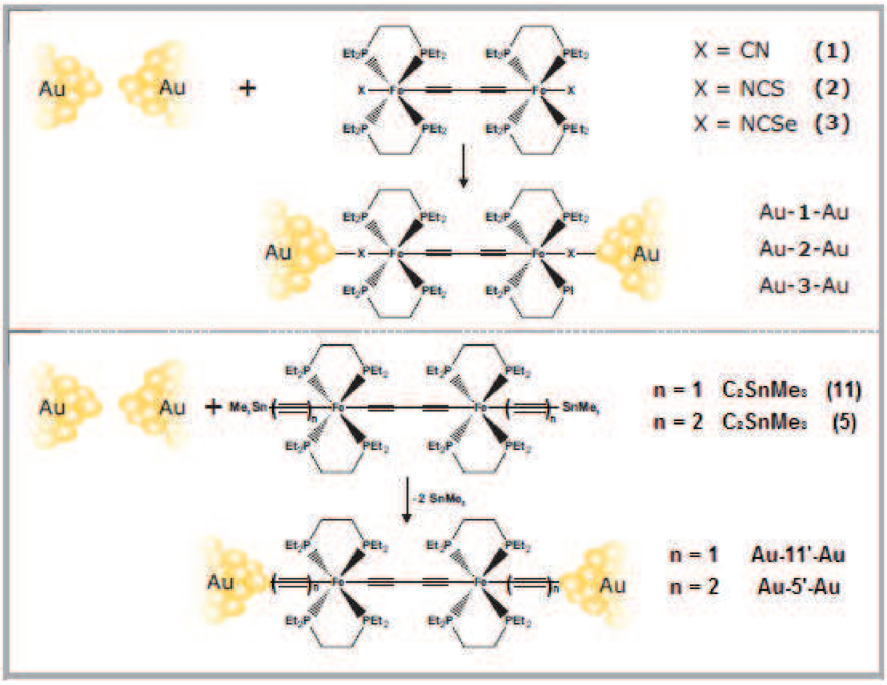

Figure 4. *top:* Compounds **12 - 14** with corresponding reaction schemes upon coupling to Au electrodes. *bottom*: The $SnMe_3$ endgroups of **5** and **11** cleave off and direct C–Au bonds are formed yielding the **Au–5'–Au** and Au–11'–Au junctions.

Conductance at Room Temperature

All complexes **5**, **11** - **14** were studied at room temperature under ultra-high vacuum (UHV) conditions. For **14**, only histograms could be acquired revealing a less pronounced accumulation at 8.1 x 10^{-7} G_0. Most likely the phosphine ligands sterically hinder the short CN anchor to bind to the Au surface, rendering the endgroup rather inefficient for electron injection. The statistical transport measurements of **11'**, **5'**, **12** and **13** provided reproducible and consistent results that are displayed in Figure 5. The data presented shows representative and individual I-V characteristics for Au-**11'** (green), **5'** (red), **12** (black) and **13** (blue). The current is increasing with increasing bias for all compounds, indicating that the frontier MOs get energetically better aligned with the chemical potentials of left or right leads. At 300 K the MOs are broadened thermally and generally a non-linear (almost exponential) functional I-V behavior with only a few distinguishable features is found. The transport curves differ strongly in A) the current amplitude at both low and high bias, B) the current onset (at zero bias) and C) the signal to noise ratio.

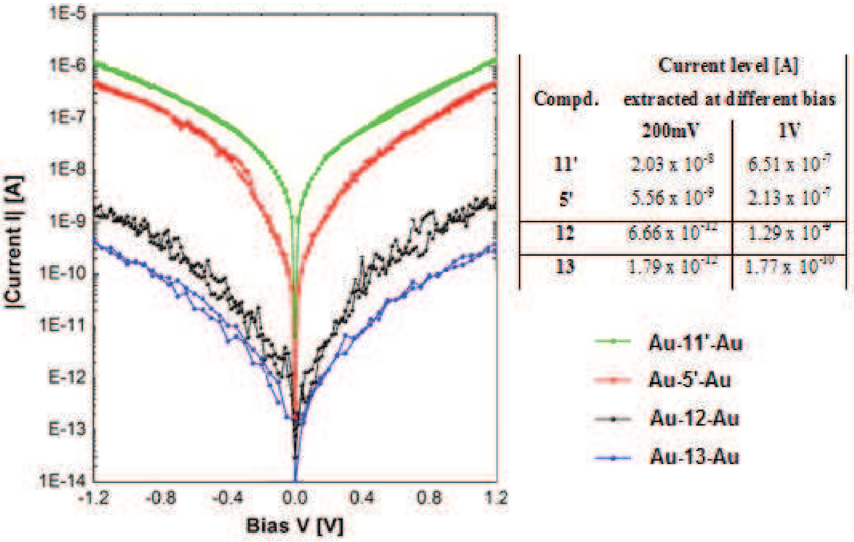

Compd.	Current level [A] extracted at different bias	
	200mV	1V
11'	2.03 x 10^{-8}	6.51 x 10^{-7}
5'	5.56 x 10^{-9}	2.13 x 10^{-7}
12	6.66 x 10^{-12}	1.29 x 10^{-9}
13	1.79 x 10^{-12}	1.77 x 10^{-10}

Figure 5. Current - Voltage (I-V) characteristics taken at 300 K for the junctions **Au-11'-Au** (green), **Au-5'-Au** (red), **Au-12-Au** (black) and **Au-13-Au** (blue).

A) The current levels of compound **13** (blue) and **12** (black) differ by almost one order of magnitude, rendering NCS coupling the weakest among all coupling motifs studied here. Compounds **11'** and **5'** with direct C-Au coupling revealed an approximately hundred and a thousand fold increase in current compared to NCSe and NCS termination. As the Fe-C_4-Fe molecular backbone is kept equal in all four compounds, charging effects that may shift the MO's energy levels in the Au-molecule-Au systems are expected to be similar for all compounds. Hence the current levels represent in a first-order approximation the electronic coupling strength of the corresponding endgroup, showing the NCSe termination couples better compared to NCS as the current is increased by a factor of ten. The current level of the direct C-Au bond is at least two orders of magnitude higher compared to NCSe and three orders of magnitude compared to the NCS termination.

B) The functional current increase when starting the bias sweep at zero is similar for NCS and NCSe. For the direct C-Au coupling, a very abrupt increase in current is found, indicating that resonant MOs or MOs close-to-resonance are available at E_F and that the contribution of the MOs next to the frontier ones to transport is minor in the bias window available

C) The noise in the current can be used as a measure for the junction stability under electrical load. The current fluctuations are one order of magnitude smaller for C-Au coupling compared with NCS coupling, in particular for voltages larger than ±0.4 V, indicating that the C-Au bond has very limited bond fluctuations.

Conductance at Low Temperature

In contrast to room temperature measurements, the MOs usually become apparent in *G–V* characteristics at low temperatures, because of the reduced thermal broadening. For **13,** a conductance gap and several discrete MO resonances are found at temperatures under 100 K (Figure 6). In addition, many *I–V* characteristics have the appearance of hysteretic conductance switching. For compound **5'**, only monotonous curves without a conductance gap were recorded at low temperatures. Figure 6 shows 100 *I–V* (C), and *GDiff -V* (D) characteristics of **5'**, taken at 50 K. Besides the absence of discrete MO peaks, the transport properties are more linear and the current levels are 3 to 4 orders of magnitude higher.

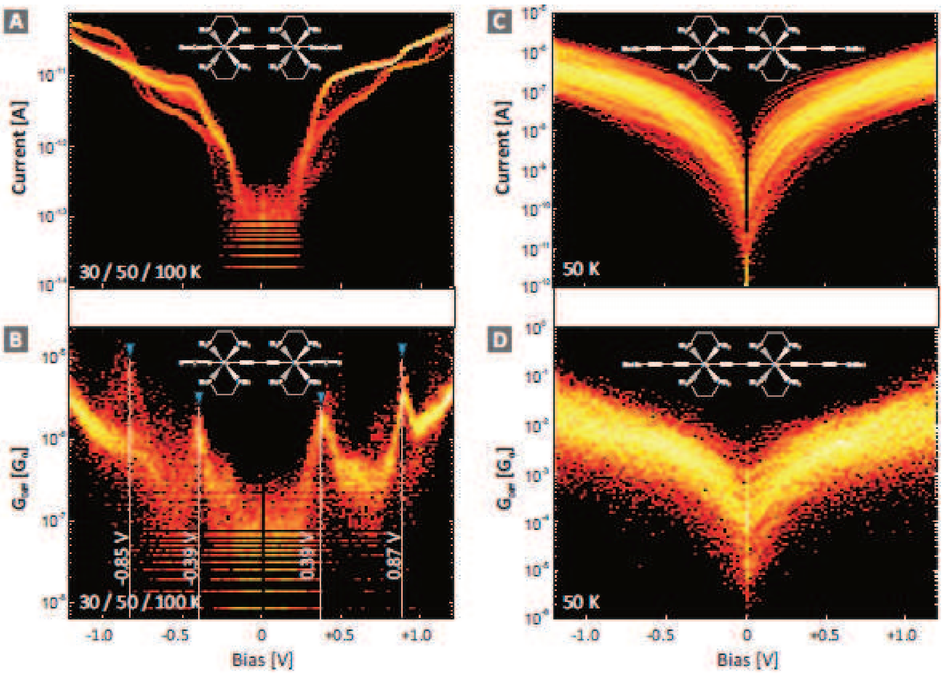

Figure 6. *I–V* and G_{Dif} - *V* characteristics taken at low temperatures for **Au−13−Au** (A, B) and for **Au−5'−Au** (C, D).

DFT II: Conductance

The results of further DFT calculations for the transmission functions and eigenenergies of the respective orbitals HOMO and HOMO^{-1} relative to E_F are presented in Figure 7 for the compounds **5'**, **11'**, **12** - **14**. Both the eigenvalues and the shape of the relevant MOs are similar for all systems, consisting of p-orbitals delocalized over the entire molecular backbone and containing equal amounts of both Fe d-states. For each system, the HOMO and HOMO^{-1} differ only in the sense that they are rotated by 90◦ to each other, which explains their energetical proximity and therefore the double-peak structure in the transmission function.

The conductance at zero bias is mainly influenced by the tails of the HOMO and HOMO^{-1} peaks, leading to quite different values among the compounds investigated.

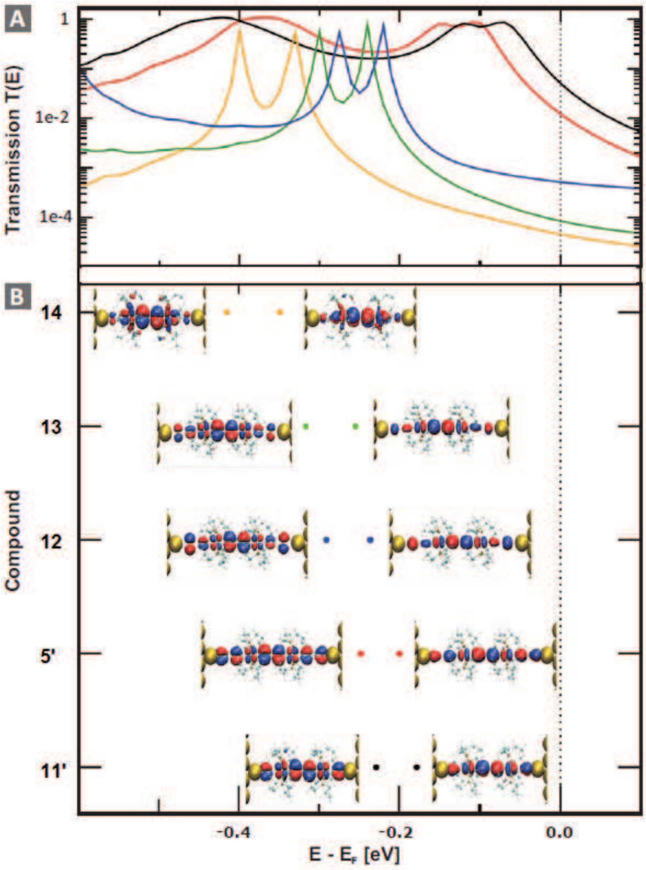

Figure 7. (A)Transmission functions for **14** (yellow),. **13** (green), **12** (blue), **5'** (red) and **11'** (black). (B). Spatial distributions of the HOMO and HOMO^{-1} and the energetic positions of the MOs with respect to E_F

Although the metal–molecule coupling is quite high for all anchorgroups, the two C–Au endgroups surpass the others with rather strong covalent bonding. As a consequence of the hybridization of the MOs and the leads, even the rather long C_4 anchors of **5'** lead to a higher conductance than the coordinatively bonding endgroups CN, NCS and NCSe. The strong hybridization might also be the reason why the hysteretic switching behavior found in **13** at low temperatures was not revealed in the C–Au coupled **5'** as the MOs are more pinned and intrinsic functionality is prohibited.

The hybridization of metal and molecular states in the case of **Au−5'−Au** extends the delocalized electronic system between the two Fe centers over the molecule–electrode interfaces, in contrast to the weakly bonded **Au−13−Au** system (Figure 8).

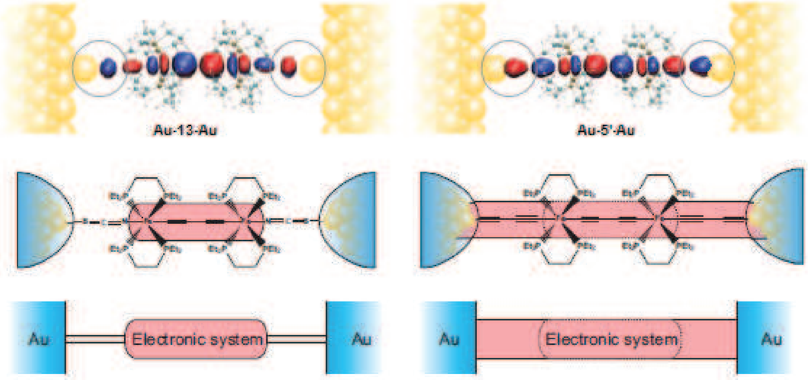

Figure 8. Schematic representation of the **Au−13−Au** (C) and the **Au−5'−Au** junction (D).

6.3 CARBYL/METHYNE-BASED BRIDGES IN DI- AND TRINUCLEAR REDOX-ACTIVE IRON COMPLEXES

Manuscript in Revision (**Organometallics**, *accepted after major revisions*): F. Lissel, O. Blacque, K. Venkatesan, H. Berke: *Structural and Electronic Variations of Carbyl/Methyne-Based Bridges in Di- and Trinuclear Redox-Active Iron Complexes Bearing Fe(diphosphine)$_2$X (X = I, NCS) Moieties*

Syntheses and Characterization

Assuming a resonant charge transport, the conductance pathway will follow the bonds of the organometallic backbone. Therefore a change of hybridisation and geometry of the bridging ligand can be expected to have a significant influence on molecular conductance and possibly allow a modification of the electric and electronic properties of a molecular junction. A series of di- and trinuclear molecules with varying bridging and terminal ligands was synthesized (Scheme 3).

Complexes **17** - **26** were characterised by 1D and 2D NMR studies, IR, and Raman spectroscopies and elemental analyses. Structural studies using X-ray diffraction were carried out for all compounds except **19** and **22**.

Scheme 3. Structures of dinuclear frameworks with varying bridging and terminal ligands

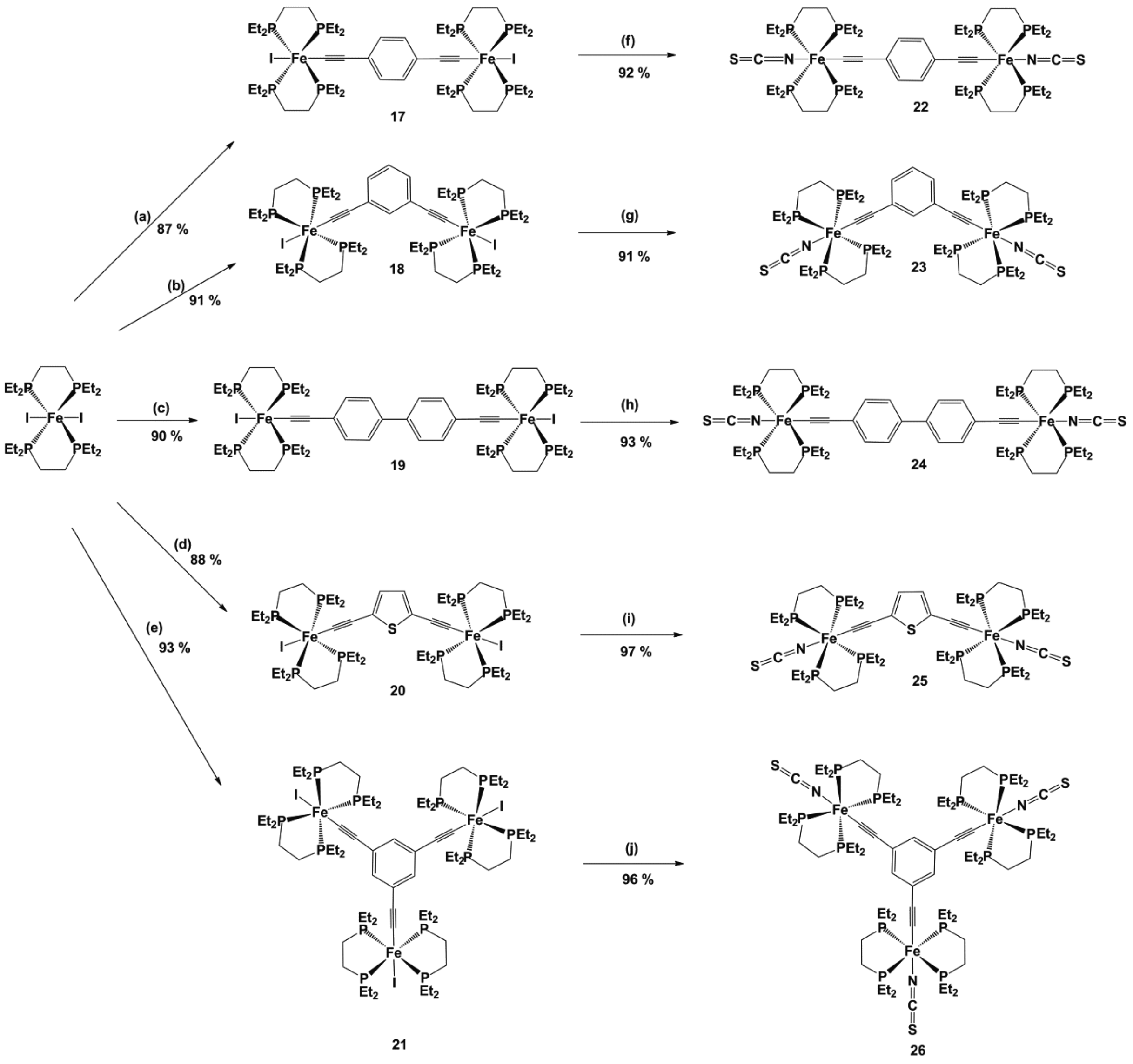

(a) 0.5 eq 1,4-bis((trimethylstannyl)ethynyl)benzene, THF, 12 h, reflux; **(b)** 0.5 eq 1,3-bis((trimethylstannyl)ethynyl)benzene, THF, 12 h, reflux; **(c)** 0.5 eq 4,4'-bis((trimethylstannyl)ethynyl)biphenyl, THF, 12 h, reflux; **(d)** 0.5 eq. 2,5-bis((trimethylstannyl)ethynyl)thiophene, toluene, 80 °C, 12 h; **(e)** 0.5 eq 1,3,5-tris((trimethylstannyl)ethynyl)benzene, THF, 12 h, reflux; **(f)** 20 eq. NaSCN, Me$_3$CN, reflux, 12 h; **(g)** 20 eq. NaSCN, Me$_3$CN, reflux, 5 h; **(h)** 20 eq. NaSCN, Me$_3$CN, reflux, 12 h; **(i)** 20 eq. NaSCN, Me$_3$CN, reflux, 12 h; **(j)** 20 eq. NaSCN, Me$_3$CN, reflux, 5 h.

Cyclic Voltammetry

As can be expected, the insertion of an sp^2 hybridized area into the conductance pathway causes a drastic decrease of thermodynamic the stabilisation of the mixed valence species in comparison to the butadiyne based frameworks. The 1,3-diethynyl-benzene and 4,4'-diethynyl-biphenyl bridged dinuclear complexes, as well as the trinuclear complexes, showed one reversible oxidation wave indicative of a localized charge. Consequently, the oxidation waves of the 1,3-diethynyl-benzene and 4,4'-diethynyl-biphenyl bridged systems correspond to $2e^-$ processes and similary the one of the trinuclear complexes to $3e^-$ processes.

The first oxidation wave of the 2,5-diethynyl-thiophene bridged complexes **20** and **25** appeared at a more negative potential compared to the C_4 bridged complex **13** (Table 4) suggesting that the 2,5-diethynyl-thiophene bridge is less-electron withdrawing and consequently indicative that the HOMO should bear larger character of the bridging ligand.

Table 4. Cyclic voltammetry data of the complexes **17 - 18**.

Compd.	**$E_{1/2}$ (0/+1) [mV]**	**$E_{1/2}$ (+1/+2) [mV]**	**ΔE [mV]**	**K_c**
17	-385	-231	154	4.2×10^2
18	-312	--	--	--
19	-393	--	--	--
20	-472	-192	280	6.0×10^4
21	-221	--	--	--
22	-160	-18	142	2.7×10^2
23	-174	--	--	---
24	-252	--	--	--
25	-406	-131	275	5.0×10^4
26	-112	--	--	--
13	-372	106	478	14.5×10^7

Measurements at 300 K in THF/Bu_4NPF_6 (0.1M) with an Au working electrode, a Pt counter electrode, and an Ag reference electrode. E vs $Fc^{0/+}$ (external).

On a similar line, the occurrence of the single oxidation wave of the 1,3-diethynyl-benzene, 4,4'-diethynyl-biphenyl and the 1,3,5-triethynyl-benzene bridged compounds at more positive potentials (between -112 mV for **26** and -393 mV for **19**,) implies a less accentuated bridging ligand character in the respective HOMO.

It has to be noted that for all five different types of bridges discussed, the oxidation waves shift to a less negative potential when the terminal iodo ligands are substituted with the isothiocyanate functional groups indicating the more electron withdrawing character of the pseudohalogenide.

DFT Calculations

The molecular geometries of the model complexes **22**-*Me*, **23**-*Me*, **24**-*Me*, **25**-*Me* and the C_4 bridged **13**-*Me*, for which the ethyl groups of the *depe* ligands were replaced by methyl groups, were optimized at the PBE1PBE/LANL2DZ level. The distances of the trinuclear compound **26-***Me* are congeneric to the *meta* substituted dinuclear complex **23-***Me*. In all cases the calculated and experimentally determined data compare very well and show that the lengths of the molecular junctions of the 1,4-($-C\equiv-C_6H_4-C\equiv C-$) bridged complex **22** and the 2,5-($-C\equiv C-$thiophene$-C\equiv C-$) bridged **25** are in a comparable range. Also the 1,3-($-C\equiv C-C_6H_4-C\equiv C-$) substituted **23**, the trinuclear complex **26** and the C_4 bridged complex **13** are of a similar length. As the direct distance-dependent through space tunneling is an intrinsic part of molecular conductivity measurements of a given molecular junction, the different junction lengths would have to be taken into account when comparing the molecular conductance.

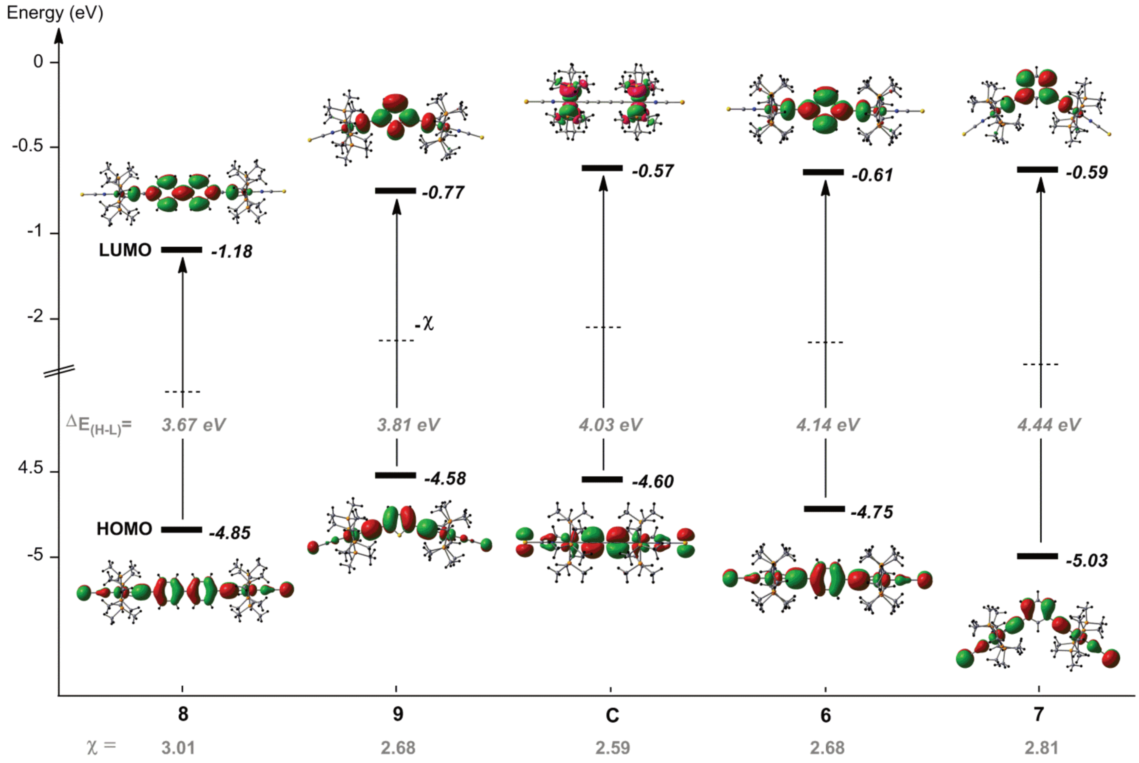

Figure 9. Energies of the frontier orbitals (HOMO and LUMO) of the model complexes computed at the PBE1PBE/LANL2DZ//PBE1PBE/6-311+g(d) level and arranged in increasing order of the HOMO/LUMO gap $\Delta E_{(H\text{-}L)}$. Spatial plots of the corresponding orbitals and their absolute electronegativity values χ (defined as (I+A)/2 with I = ionization potential, A = electron affinity) are represented as a dashed lines halfway between the HOMO and LUMO.

For **22**-*Me*, **23**-*Me*, **24**-*Me*, **25**-*Me* and the C_4 bridged **13**-*Me*, the HOMO and LUMO energies are reported in Table 5 and Figure 9. To achieve a resonant transport in potential experiments of the measurement of molecular conductivity, which would be an important goal for this series of complexes, the molecular orbitals of the probed molecules should be aligned approximately to the Fermi level of the macroscopic electronic leads, which is more in the energetic range of the HOMO's for all complexes discussed here.

Table 5. HOMO and LUMO energies (eV), HOMO/LUMO gap (eV) and absolute electronegativity χ computed at the PBE1PBE/LANL2DZ//PBE1PBE/6-311+g(d) level.

Compd.	**LUMO (eV)**	**HOMO (eV)**	**$\Delta E_{(H-L)}$ (eV)**	**χ (eV)**
22-*Me*	-0.61	-4.75	4.14	2.68
23-*Me*	-0.59	-5.03	4.44	2.81
24-*Me*	-1.18	-4.85	3.67	3.01
25-*Me*	-0.77	-4.58	3.81	2.68
13-*Me*	-0.57	-4.60	4.03	2.59

χ is defined as (I+A)/2 where I is the ionization potential and A is the electron affinity, and here directly obtained from the HOMO and LUMO energies.

As expected for 18-electron metal complexes, the HOMO/LUMO gap $\Delta E_{(H-L)}$ is relatively large and lies between 3.67 eV for **24**-*Me* and 4.44 eV for **23**-*Me*. Except for complex **24**-*Me*, for which an energetically very low-lying LUMO was calculated, $\Delta E_{(H-L)}$ seems to be more dependent on the energetic position of the HOMO (Table 5).

These results show that the energetic positions of the molecular orbitals and the extent of the HOMO/LUMO and the absolute chemical hardness gap to the position of E_F of Au can be tuned by varying the bridging ligand of a X{M}C_n{M}X, even if the metal centre, equatorial ligands and terminal ligands are kept constant.

For the discussed molecules, the chemical hardness is consequently increasing in the order **24**-*Me* < **25**-*Me* < **13**-*Me* < **22**-*Me* < **23**-*Me*. Based on these findings, the coupling between the molecule and the gold electrode in measurements of the molecular conductivity can be expected to increase in the order **23**-*Me* < **22**-*Me* < **13**-*Me* < **25**-*Me* < **24**-*Me*.

7. CONCLUSION AND OUTLOOK

The transmetalation of structurally different stannylated bridging units with the mononuclear *trans*-Fe(depe)$_2$I fragment poses a new and facile synthetic pathway to access organometallic components suitable for molecular electronics. The dinuclear complexes I{Fe}R$_n${Fe}I with {Fe} = Fe(depe)$_2$, depe = 1,2-bis(diethylphospino)ethane) and R$_n$ = −C≡C−C≡C− **2**, 1,4-(−C≡C−C$_6$H$_4$−C≡C−) **17**, 1,3-(−C≡C−C$_6$H$_4$−C≡C−) **18**, 4,4'-(−C≡C−C$_6$H$_4$−C$_6$H$_4$−C≡C−) **19**, 2,5-(−C≡C−thiophene−C≡C−) **20,** as well as a trinuclear complex {I−Fe(depe)$_2$(C≡C−)}$_3$(1,3,5-C$_6$H$_3$) **21** were obtained in high yields.

The terminal iodides react in facile ways with suitable nucleophiles, allowing the introduction of a range of ligands. It was demonstrated that the class of {Fe}C$_4${Fe} organometallic complexes can be modified to incorporate terminal substituents capable of binding to Au electrodes to form stable single-molecular junctions by establishing either covalent (e.g. C$_2$SnMe$_3$ **11**, C$_4$SnMe$_3$ **5**) or coordinative (e.g. NCS **13**, NCSe **12**, CN **14**) bonds to Au electrodes.

In a similar fashion the di- and trinuclear systems with different bridging ligands R$_n$ were substituted with terminal NCS ligands (complexes **22** - **26**)

Also, the {Fe}C$_4${Fe} system can extended to a homometallic tetranuclear Me$_3$SiC$_4${Fe}C$_4${Fe}C$_4${Fe}C$_4${Fe}C$_4$SiMe$_3$ ({Fe} = Fe(depe)$_2$, depe = 1,2-

bis(diethylphospino)ethane) complex **7**, which showed extensive charge delocalization and vibrational coupling over the entire unsaturated organometallic backbone.

For selected dinculear C_4 bridged molecules, investigations of the conductance profiles were carried out at the single-molecule level using a mechanically controlled break junction.

For the C_2 terminated **11'** a current level of 6.5×10^{-7} A at 1.0 V was achieved, reaching 1% of the maximal current available for Au-Au Quantum-Point-Contacts (77.6×10^{-6} A at 1.0 V assuming one conductance channel), outperforming the currently best conductive molecular wire systems (at comparable length), the poly-*p*-phenylene possessing a C-Au coupling.

The established systematic synthetic approach allows the structural motifs, such as metal centers, bridging ligand and equatorial ligand sphere, to be modified in order to modulate the charge transport properties.

Upon binding to molecular electrodes, the electron delocalization of the {Fe}–C≡C−C≡C–{Fe} core is electronically extended towards the leads by hybridization of MO and metal states.. The utilization of the sp-hybridized and electronically highly versatile butadiyne bridging ligand was demonstrated to drastically increase charge transport rates by lowering the injection barrier across the molecule-metal interface. The results show that the {Fe}C_4{Fe} class are promising to achieve long and highly conductive wires due to an extension of the electronic system over the molecule–metal interfaces due to strong hybridization.

Therefore the utilization of covalently bonded organometallic frameworks with metal centers embedded into the molecular backbone is an attractive concept to achieve low-ohmic molecular wires that are strongly required for future nanoelectronics. Beyond that, organometallic compounds are an attractive framework for the integration of intrinsic functionality for future applications such as redox activity for conductance switching and memory application.

SYNOPSIS

Single molecules constitute the smallest units to build electronic devices. In a fundamental research approach iron-alkyne based complexes of the type X(depe)$_2$FeYFe(depe)$_2$X (X endgroup, Y bridge) were probed for their spectroscopic and electrochemical properties as well as their molecular conductivities, which showed marked dependencies on the X and Y groups.

LIST OF COMPOUNDS

Chapter 2

$[I-Fe(depe)_2-C\equiv C-C\equiv C-Fe(depe)_2-I]$	1
$[Me_3Si-C\equiv C-C\equiv C-Fe(depe)_2-C\equiv C-C\equiv C-Fe(depe)_2-C\equiv C-C\equiv C-SiMe_3]$	2
$[H-C\equiv C-C\equiv C-Fe(depe)_2-C\equiv C-C\equiv C-Fe(depe)_2-C\equiv C-C\equiv C-H]$	3
$[Me_3Sn-C\equiv C-C\equiv C-Fe(depe)_2-C\equiv C-C\equiv C-Fe(depe)_2-C\equiv C-C\equiv C-SnMe_3]$	4
$[I-Fe(depe)_2-C_4-Fe(depe)_2-C_4-Fe(depe)_2-C_4-Fe(depe)_2-I]$	5
$[Me_3Si-C_4-Fe(depe)_2-C_4-Fe(depe)_2-C_4-Fe(depe)_2-C_4-Fe(depe)_2-C_4-SiMe_3]]$	6

Chapter 3 and 4

$[Me-C\equiv N-Fe(depe)_2-C\equiv C-C\equiv C-Fe(depe)_2-N\equiv C-Me]^{2+}[I^-]_2$	7
$[N\equiv N-Fe(depe)_2-C\equiv C-C\equiv C-Fe(depe)_2-N\equiv N]^{2+}[B_{Ar}{}^{F-}]_2$	8
$[H-C\equiv C-Fe(depe)_2-C\equiv C-C\equiv C-Fe(depe)_2-C\equiv C-H]$	9
$[Me_3Sn-C\equiv C-Fe(depe)_2-C\equiv C-C\equiv C-Fe(depe)_2-C\equiv C-SnMe_3]$	10
$[Se=C=N-Fe(depe)_2-C\equiv C-C\equiv C-Fe(depe)_2-N=C=Se]$	11
$[S=C=N-Fe(depe)_2-C\equiv C-C\equiv C-Fe(depe)_2-N=C=S]$	12
$[N\equiv C-Fe(depe)_2-C\equiv C-C\equiv C-Fe(depe)_2-C\equiv N]$	13
$[H-S-Fe(depe)_2-C\equiv C-C\equiv C-Fe(depe)_2-S-H]$	14
$[O_2N-Fe(depe)_2-C\equiv C-C\equiv C-Fe(depe)_2-NO_2]$	15

Chapter 5

I–Fe(depe$_2$)–1,4–(C≡C–C$_6$H$_4$–C≡C)–Fe(depe$_2$)–I]	16
I–Fe(depe$_2$)–1,3–(C≡C–C$_6$H$_4$–C≡C) –Fe(depe$_2$)–I]	17
[I–Fe(depe$_2$)–4,4–(C≡C–C$_6$H$_4$ –C$_6$H$_4$–C≡C)–Fe(depe$_2$)–I]	18
[I–Fe(depe$_2$)–4,4–(C≡C–Thiophene–C≡C)–Fe(depe$_2$)–I]	19
[{I–Fe(depe$_2$)–C≡C–}$_3$–(1,3,5–C$_6$H$_3$)]	20
[S=C=N–Fe(depe)$_2$–1,4–(C≡C–C$_6$H$_4$–C≡C)–Fe(depe)$_2$–N=C=S]	21
[S=C=N–Fe(depe)$_2$–1,3–(C≡C–C$_6$H$_4$–C≡C)–Fe(depe)$_2$–N=C=S]	22
[S=C=N–Fe(depe)$_2$–4,4–(C≡C–C$_6$H$_4$ –C$_6$H$_4$–C≡C)–Fe(depe)$_2$–N=C=S]	23
[S=C=N–Fe(depe)$_2$–4,4–(C≡C–Thiophene –C≡C)–Fe(depe)$_2$–N=C=S]	24
[{S=C=N–Fe(depe$_2$)–C≡C–}$_3$–(1,3,5–C$_6$H$_3$)]	25

ACKNOWLEDGEMENTS

I would like to express my deepest respect and thanks to everybody helping and supporting me in the last years. In particular, I would like to thank:

my Ph.D. supervisor **Prof. Dr. Heinz Berke** for giving me the great opportunity to work in his group and trusting me with a very interesting and challenging subject - and also for teaching me how to become a better scientist and researcher;

Dr. Koushik Venkatesan, for all the discussions, support and friendship - I learned a lot from you;

Prof. Dr. Roger Alberto, for his help and support and for being in my comitee, **Prof. Dr. Jürg Hutter** for reviewing my thesis and being in my comitee, and **Dr. Emmanuel Lörtscher** for discussions, support and being in my comitee

Dr. Olivier Blacque, for many beautiful crystal structures and DFT calculations, and also for your friendship and support;

Dr. Thomas Fox, for helping with NMR and answering all my questions patiently;

Our partners in the NRP 62 program '*Functional organic and organometallic materials for molecular electronic applications*' from **IBM Research Zurich**:
Florian Schwarz, for being as enthuiastic about our project as I am, for all MCBJ measurements and for the "physic" perspective;
Dr. Heike Riel, for all the support, discussions and good advice;

Michael Koch, for discussions, support and sharing a dream;

From the **University of Konstanz**:
Prof. Rainer Winter for his support and for sharing his knowledge about electrochemistry, and **Walther Polit** for all spectroelectrochemical measurements;

From the **University of Vienna**:
Dr. Robert Stadler and **Georg Kastelunger**, for sophisticated calculations, interesting discussions and insights;

The technical service of the former ACI for measurements and support: **Dr. Ferdinand Wild** for NIR measurements, **Barbara and Heinz Spring** for all the elemental analyses, **Hanspeter Stadler** for technical support;

All the other former and current Ph.D. students from the Berke group, especially, **Dr. Carolina Egler-Lucas** and **Dr. Sergey N. Semenov** for teaching me a lot about inert techniques and gloveboxes;

All former and current members of 32 H 90, especially the core: **Alexander Szentkuti**, **Michael Bachmann**, **Tobias von Arx**, for all your help and a good time;

My parents and sisters, **Sylvia Lissel** and **Dr. Manfred Lissel**, **Ariane** and **Natascha**, for their support and for believing in me. My friends, **Clara**, **Sebastian**, **Lemonia** and **Daphne** for grounding me when necessary and helping me to keep my head high.

Furthermore, I would like to thank the following institutions:
UZH, a well-equipped and beautifully situated university to conduct research, the **SNF** for financial support (NRP62; Grant No. 406240-126142) and the the Ph.D. programs within the NRP 62 Smart Materials, the **CMSZH** for the communication, management and leadership courses as well as for a travel grant, the **SCS** for a travel grant and **LERU** for the LERU summer school 2014.

CURRICULUM VITAE

Personal Information

Name:	Franziska Lissel
Date of Birth:	22.03.1982
Place of Birth:	Bielefeld, Germany
Nationality:	German

Work Experience

06/2010 – 06/2014:	University of Zurich (cooperation with IBM Research, Zurich, Switzerland) PhD candidate and research assistant 'Functional organic and organometallic materials for molecular electronic applications' Swiss National Science Foundation (SNF), National Research Program (NRP 62) Responsible for laboratory safety Responsible for glovebox maintenance
03/2010 – 05/2010:	ETH Zurich, Zurich, Switzerland Research internship, catalyst design for selective cross-coupling
03/2009 – 11/2009:	New Jersey Institute of Technology NJIT, Newark, New Jersey, USA Visiting researcher, syntheses of perfluorinated phthalocyanines
05/2007 – present:	University of Bremen, Germany; NJIT, USA; University of Zurich, Switzerland Supervising students at the undergraduate and graduate level

04/2006 – 10/2006: Alfred-Wegener-Institute (AWI, Helmholtz Gemeinschaft), Bremerhaven, Germany
Research internship, analysis of the atmospherical nitric oxides cycles

04/2004 – 10/2004: Bio-Circle Surface Technology GmbH, Gütersloh, Germany
Industrial internship, industrial waste management

01/2002 – 01/2003: Centre of Marine Tropical Ecology (ZMT, Leibnitz Gemeinschaft), Bremen, Germany
Scientific assistant, analytical laboratory

Education

10/2003 – 11/2009: University of Bremen, Bremen, Germany
Study of Chemistry, Degree: **Diplom – Chemikerin**
(overall grade: 1.5 in the German grade system)

10/2001 – 06/2003: University of Bremen, Bremen, Germany
Study of Biology

09/1992 – 06/2001: Kreisgymnasium Halle/Westf, Germany
Abitur (overall grade: 1.8 in the German grade system)

Extracurricular Activities

09/2011 – present: Language courses French

06/2012: Strategy workshop (Boston Consulting Group BCG)

11/2006 – 03/2007: Backpacking in Southeast Asia (Thailand, Cambodia, Vietnam, Southern China)

Certificates

07/2013 – 12/2013: Communication skills for leaders (transferable skills workshop)

02/2013 – 07/2013: Management skills for leaders (transferable skills workshop)

09/2013 – 02/2014: Leadership skills for leaders (transferable skills workshop)

05/2011: Patent Law (block course offered by the Swiss National Science Foundation)

Language Skills

German: Mother tongue

English: Excellent

French: Language courses since 2011. Current level: B2

Awards and Stipends

11/2013: Early Postdoc.Mobility Stipend for a 18 month postdoctoral stay at Stanford (USA), Swiss National Science Foundation (SNF)

05/2013: Travel award, Swiss Chemical Society (SCS)

03/2013: Travel award, Graduate School of Chemical and Molecular Science Zurich (CMSZH)

Presentations - Oral

10/2011: Smart Materials Meeting, Fribourg, Switzerland
'Organometallic Iron Scaffolds for Molecular Electronics'

03/2008: 19th Mountain/Sea Liposome Workshop, Oberjoch, Germany
'Cytotoxicity of Boron-Containing Artificial Lipids'

Presentations - Poster

09/2013: 12th European Conference on Electronic Materials (ECME), London, UK

09/2011: 11th European Conference on Electronic Materials (ECME), Barcelona, Spain

06/2011: Molecular Electronics Workshop, EMPA, Dübendorf, Switzerland

LIST OF PUBLICATIONS

Research Article - First author:

F. Lissel, T. Fox, O. Blacque, W. Polit, R. F. Winter, K. Venkatesan, H. Berke *J. Am. Chem. Soc.* **2013**, 135 (10), pp 4051 - 4060

F. Lissel, F. Schwarz, O. Blacque, H. Riel, E. Lörtscher, K. Venkatesan, H. Berke *J. Am. Chem. Soc.,* **2014***,* DOI: 10.1021/ja507672g

Research Article - Coauthor:

F. Schwarz, G. Kastelunger, F. Lissel, H. Riel, K. Venkatesan, H. Berke, R. Stadler, E. Lörtscher *NanoLetters* **2014**, DOI: 10.1021/nl5029045

T. Schaffran, F. Lissel, B. Samatanga, G. Karlsson, A. Burghardt, K. Edwards, M. Winterhalter, R. Peschka-Süss, R. Schubert, D. Gabel *J. Organomet. Chem.* **2009**, 694 (11), pp 1708 - 1712

Manuscript Submitted - First Author

Manuscript in Revision (**Organometallics**, *accepted after major revisions*): F. Lissel, O. Blacque, K. Venkatesan, H. Berke: *Structural and Electronic Variations of Carbyl/Methyne-Based Bridges in Di- and Trinuclear Redox-Active Iron Complexes Bearing Fe(diphosphine)$_2$X (X = I, NCS) Moieties*